DEBRIS FLOW AND RESERVOIR SEDIMENTATION

SHORT-TERM RAINFALL FORECASTING FOR LAHAR EARLY WARNING SYSTEM IN MERAPI, INDONESIA

MAGFIRA SYARIFUDDIN[(1)], SATORU OISHI[(2)], RATIH INDRI HAPSARI[(3)], YUKA ITO[(4)], DJOKO LEGONO[(5)]

[(1,4)]Graduate School of Engineering, Kobe University, Kobe, Japan
magfira@stu.kobe-u.ac.jp; 155t101t@stu.kobe-u.ac.jp
[(2)]Research Centre for Urban Safety and Security, Kobe University, Kobe, Japan
tetsu@phoenix.kobe-u.ac.jp
[(3)]Department of Civil Engineering, State Polytechnic of Malang, Malang, Indonesia
ratih@polinema.ac.id
[(5)]Department of Civil Engineering, Faculty of Engineering, Gadjah Mada University, Yogyakarta, Indonesia
legono@tsipil.ugm.ac.id

ABSTRACT

Severe rainfall intensity is the main triggering agent of hydrometeorology disaster. In the Merapi volcano of Indonesia, the major hydrometeorology disaster is lahar, which is a type of mudflow or debris flow composed of slurry pyroclastic material, rocky debris, and water. This paper discusses the development of an Early Warning System (EWS) framework according to the landform and rainfall characteristic. The landform analysis included the susceptibility classification of the sub-basins, while the rainfall analysis included numerical model of lahar and short-term rainfall forecasting. The proposed EWS framework could simulate real lahar event that happened on 17 Feb 2016 in Gendol and Woro river. The short-term rainfall forecasting required more improvement as the spatial distribution of rainfall gave weak correlation at 0.19 and decreased by the increment of time. However, the temporal fluctuation gave satisfactory results compared to the observed rainfall temporal fluctuation. Considering the lahar behavior that usually happens unexpectedly, the application of the rainfall prediction will give benefit on lahar disaster management to prevent more lost and human casualties.

Keywords: Early warning system; lahar, rainfall; short-term rainfall prediction; merapi.

1 INTRODUCTION

Lahar is a Javanese term used to describe a rapidly flowing, high concentration, poorly sorted sediment-laden mixture of rock debris and water from a volcano that goes along river stream. It is a continuum flow type which covers debris flows, hyper-concentrated, streamflow, and mudflows (Lavigne et al., 2007; Neal, 1976). Severe rainfall intensity is known to be the main agent on triggering lahar in Mount Merapi. An empirical study in Merapi found that lahar occurs at elevation over 1200 m after a minimum of 70 mm/h rainfall intensity (*r)* in 35 minutes (Legowo, 1981). While at 450-600 m above mean sea level, lahar is still hazardous after 40 mm rainfall within 2h (Lavigne et al., 2000a).

Studies on lahar and rainfall relationship are classified into two major groups: (1) direct measurement and field monitoring, and (2) physically based theoretical studies. In the first group, monitoring of lahar are done using several equipment's such as seismograph, wire sensor, automatic water level recording (AWLR), video camera and direct sampling of volcanic material to understand the characteristic of lahar in Mt. Merapi (de Belizal et al., 2013; Lavigne et al., 2000b; Legowo, 1981). Second group studies include both static and hydrodynamic approach. In the second group, rainfall information becomes the fundamental element (Jones et al., 2017; Castruccio and Claverro, 2015).

The second group studies are mostly based on ground measurement from rain gauges which are usually installed in the downstream. This led to the underestimation of rainfall induced lahar threshold values, because most lahars usually initiate in the upstream. Meanwhile, the study of lahar prediction based on the rainfall information is also limited. Some studies has applied rainfall or weather forecasting for debris flow prediction, such as Wei et al. (2004), where he applied the Numerical Weather Prediction for debris flow forecasting in China. Nevertheless, lahar occurs as small-scale phenomena which are frequently triggered by rainfall extremes at scales that will not be resolved by numerical weather prediction (NWP) or low-resolution rain gauge network.

An X-Band Multi Parameter (X-MP) radar measures 150 m mesh of rainfall intensity within 2 minutes time interval. In term of the disaster resilience, the X-MP radar can also be utilized to predict the variation of rainfall by applying the short-term rainfall forecasting (Hapsari, 2011; Kim et al., 2006). Short-term rainfall forecasting deals with short-term prediction for few hours of rainfall which in contrast to the medium-term (few hours out to 14 days) and long term (2 weeks out to 3 months or more). This method often is referred as now-casting, which is essentially required for real time flash-flood forecasting in an operational Hydrology (Hapsari, 2011). However, its application on lahar monitoring is relatively unexplored.

This paper discusses the possibility of applying the short-term rainfall prediction to an early warning system (EWS) in the Merapi Volcanic Area (MVA). In the first part, the EWS which is based on a numerical model of lahar and geomorphological condition in sub-basin scale will be discussed, followed by short-term rainfall prediction and its application in the EWS based on rainfall measurement by X-MP radar.

2 STUDY AREA

The study area is in the MVA (7°32.5'S and 110°26.5'E), at the border of two provinces, of Central Java and Yogyakarta. The volcano is known to be the most active and dangerous volcano in the world. Yearly average rainfall ranges from 2500 to 3000 mm. The study was focused in the area starting from 120 m amsl to 2700 m amsl that covered 696 km^2 and included 13 main rives that drains the volcano (Figure 1). The river stream was defined at 500 m threshold, which resulted in 316 sub-basin and all were identified at area of 0.06-7.65 km^2 radius.

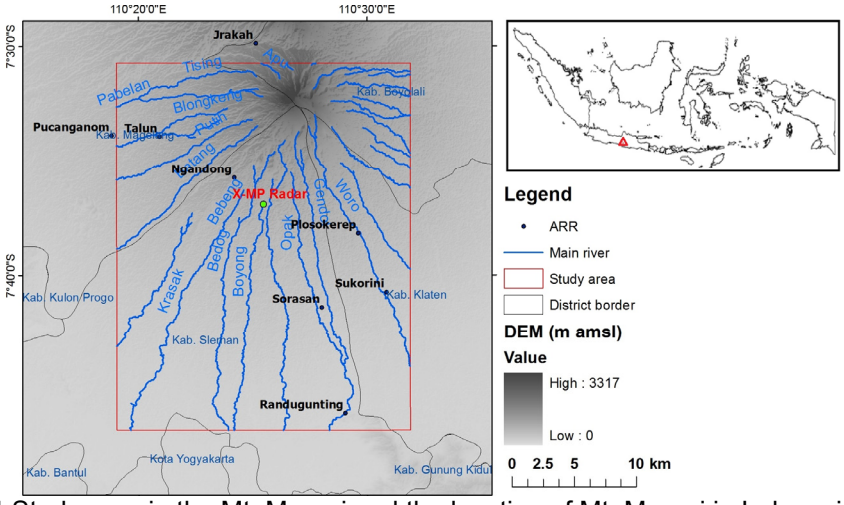

Figure. 1 Study area in the Mt. Merapi and the location of Mt. Merapi in Indonesia (index)

3 MATERIAL AND METHOD

3.1 Material

The digital surface model (DSM) of advanced land observation satellite (ALOS) with 5 m resolution from The Japan Exploration Agency (JAXA) provides the terrain information of MVA. The land use and land cover (LULC) in 2011 and soil information were provided by secondary sources of The Ministry of Forestry of The Republic of Indonesia, and Food and Agriculture Organization (FAO) respectively.

The rainfall information was estimated from the X-MP radar. This radar uses 3.3 cm wavelength (9.45 GHz) and gives rainfall intensity information of 150 m mesh for every 2 minutes within 30 km radius. The radar data preparation included the attenuation and ground clutter elimination, together with rainfall estimation from radar reflectivity products, which had been explained previously by Hapsari (2011).

The 1 hour mean rainfall depth from radar quantitative precipitation estimate (QPE) was compared with accumulated 1 hour rainfall depth from 8 stations in MVA (Figure. 1) for the period of May 2016. This was done to verify the reliability of radar (Figure 2). Rainfall from X-MP radar tended to have smaller values compared to the ARR resulted in low value of coefficient of determination, R^2.

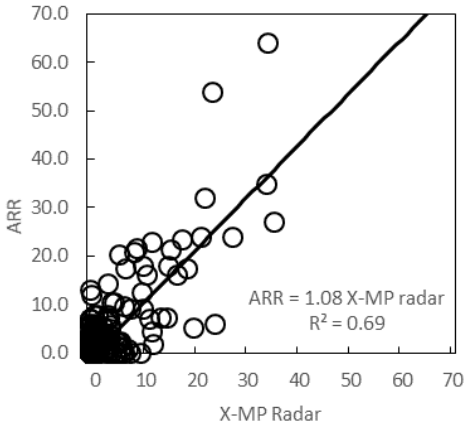

Figure 2. The average hourly rainfall depth [mm] from X-MP radar rainfall versus rain-gauge (ARR) data

The value of R2 could be influenced by radar attenuation and representativeness error. Attenuation was described as the problem of short wavelength of radar's characteristic that becomes weaker during severe rainfall. While the representativeness error is related to the use of radar data with its 22,500 m^2 pixel area in comparison to the point observation by ARR at an area of approximately 0.0033 m2 (Over et al., 2007). To handle these problems, some methods were used to correct the attenuation and the representativeness error (Hapsari, 2011; Aghakouchak et al., 2010). However, those studies are beyond the scope of current studies.

The X-MP radar data was used without any adjustment, as the data had 0 order magnitude with the ARR data. It also gave better spatial rainfall distribution that was required by the developed EWS. Lahar simulation by ARR data could not be done as some stations in the upstream area were unable to record any rainfall information during the lahar event.

The simulation period was on 17 Feb 2016, when a real lahar event happened and swept 2 vehicles in the upstream of Gendol catchment. The X-MP radar recorded the maximum rainfall intensity which was higher than 90 mm/h. Thus, considering the radar-rainfall intensity has smaller values tendencies; we used the maximum radar-rainfall intensity in each sub-basin to generate the discharge in the boundary condition. Average 1 hour and 2 hour rainfall intensity are given in Figure 3. The rainfalls were concentrated in the summit of Mt. Merapi rather than in the lower elevation, and the average rainfall intensity for 1 hour was 36.58 mm/h. The accumulated rainfall depth in upstream Gendol catchment for 2 hour was 42 mm.

The Meteorology, climatology and geophysics agency of Indonesia has classified the rainfall intensity as weak rainfall (1-5 mm/h), moderate rainfall (5-10 mm/h), heavy rainfall (10-20 mm/h) and extreme rainfall (> 20 mm). Based on this classification the rainfall on 17 Feb 2016 in Merapi was classified as heavy or extreme rainfall.

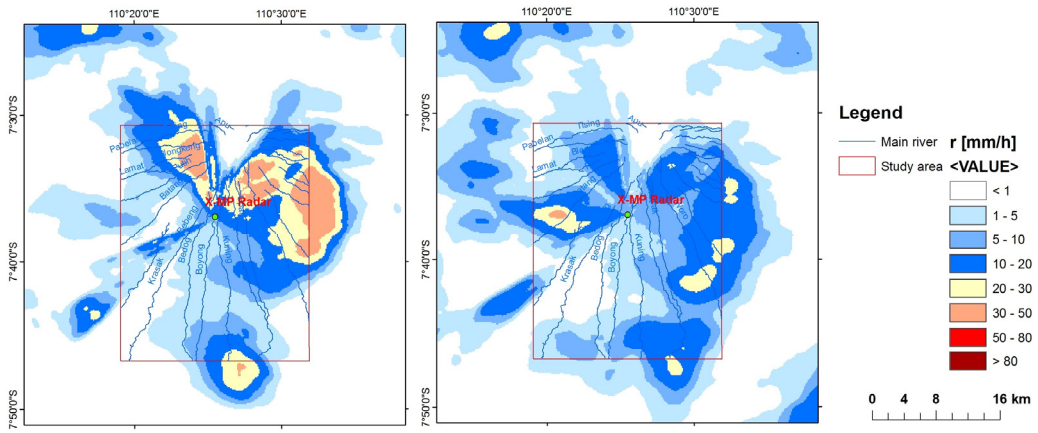

(a) 1 hour mean rainfall intensity (b) 2 hours mean rainfall intensity

Figure 3. Average rainfall intensity, *r* [mm/h] for 1 hour (a) and 2 hours (b) monitored by X-MP radar

3.2 Method and Model Description

3.2.1 Early warning system framework

The early warning system (EWS) was combined with landform information and rainfall condition as the static and dynamic variable respectively. The landform information was analyzed according to four extracted parameters from each sub-basin (Table 1). Those parameters were selected based on the study by Berenguer et al. (2015). Other information required is the historical lahar information in each sub-basin to know their reactivity of lahar hazard. This information was gathered from lahar prone area map of Mt. Merapi published by Center for Research and Technology Development of Geology Disaster. The reactivity of each sub-basin is given in Figure 4. The classification of sub-basins susceptibility was done by k-means cluster analysis (Equation [1]), where the sub-basins were classified into three classes: highly susceptible, moderate susceptible and low susceptible.

Table 1. Parameters used for analyzing sub-basin susceptibility by k-means cluster

Parameters	Description	Derived from	Unit
Maximum Elevation	The highest elevation in a sub-basin	GIS extraction	m amsl
Melton ratio	Ratios between the difference of sub-basin elevation (H_{max}-H_{min}) and square of area (A)	MR = (H_{max}-H_{min})/A^2	
Average slope	Average ratios between elevation and distance in each sub-basin	GIS extraction	o
Basin orientation	The aspect or orientation of sub-basin	GIS extraction	o

$$J = \sum_{a=1}^{b}\sum_{c=1}^{d}\left\|xk_c^{(a)} - ck_a\right\|^2 \quad [1]$$

where $||xk_a^{(a)}-ck_j||^2$ is the Euclidian distance measured between a data point $xk_a^{(a)}$ and cluster ck_j of the d data points for getting a as the objective function on how a data set behaves differently from their respective cluster centers.

Lahar simulation in each sub-basin was calculated by HyperKANAKO model. This model was developed by Nakatani et al. (2012) and considers debris flow to initiate a 1 Dimensional (1D) model which was transformed into a 2D model to form an alluvial pan. The model was based on Takahashi model for debris flow [Takahashi et al., 1992; Takahashi, 2014], where the continuity and momentum equation for transport and bed surface are calculated based on Equation [2] to [5].

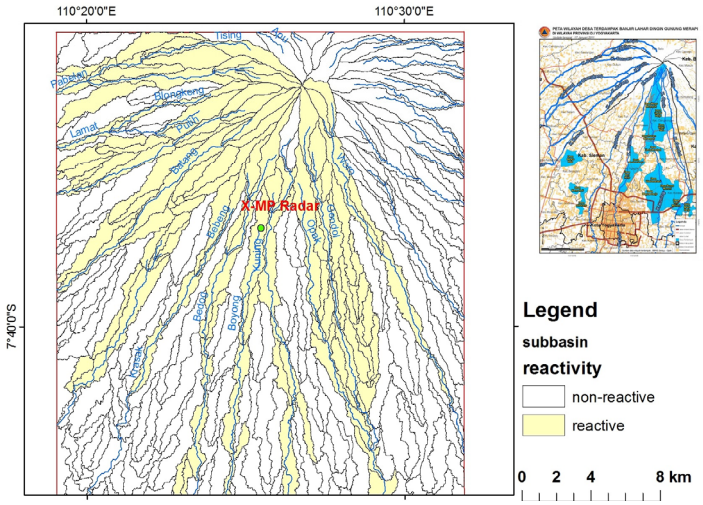

Figure 4. Sub-basin susceptibility and the affected lahar area map (index)

1) Transport and bed surface elevations equations

$$\frac{\partial C_k h}{\partial t} + \frac{\partial C_k uh}{\partial x} + \frac{\partial C_k vh}{\partial y} = i_k C_k \quad [2]$$

$$\frac{\partial u}{\partial t} + u\frac{\partial u}{\partial x} + v\frac{\partial u}{\partial y} = g\,\sin\theta_{wx} - \frac{\tau_x}{\rho_T h} \quad [3]$$

$$\frac{\partial v}{\partial t} + u\frac{\partial v}{\partial x} + v\frac{\partial v}{\partial y} = g\,\sin\theta_{wy} - \frac{\tau_y}{\rho_T h} \quad [4]$$

$$\frac{\partial Z}{\partial t} = -i \quad [5]$$

where h is flow depth, u is x-axis direction flow velocity, v is y-axis direction flow velocity, i is erosion/deposition velocity, ik is the k-th sediment erosion/deposition velocity, g is gravity acceleration, ρ_T is mixture density, θ_{wx} and θ_{wy} are the flow surface gradients in the x-axis and y-axis directions, and τ_x and τ_y are the riverbed shearing stresses in the x-axis and y-axis directions respectively and finally Z is erosion or deposition thickness of the bed measured from the original bed elevation.

2) Erosion and deposition velocity, i equation

Erosion velocity, if $C < C_\infty$

$$i = \delta\frac{C_\infty - C}{C_* - C_\infty}\frac{M}{d_m} \quad [6]$$

deposition velocity, if $C \geq C_\infty$

$$i = \delta'\frac{C_\infty - C}{C_*}\frac{M}{d_m} \quad [7]$$

where, δ is erosion coefficient, δ' is deposition coefficient, d_m is mean diameter of sediment (equals to 0.014 m, based on Ikhsan et al., 2009), C_* is maximum sediment concentration in the flow and C_∞ is the equilibrium sediment concentration described according to Nakagawa et al. (2003).

3) Bottom shear stress equations

in case of stony or dynamic debris flow, $C \geq 0.4C_*$

$$\tau = \frac{\rho_T}{8}\left(\frac{d_m}{h}\right)^2 \frac{u|u|}{\left\{C + \frac{(1-C)\rho}{\sigma}\right\}\left\{\left(\frac{C_*}{C}\right)^{1/3} - 1\right\}^2} \quad [8]$$

In case of immature debris flow, $0.01 \leq C \leq 0.4C_*$

$$\tau = \frac{\rho_T}{0.49}\left(\frac{d_m}{h}\right)^2 u|u| \quad [9]$$

In case of bed load, $C \leq 0.01$

$$\tau = \frac{\rho g n^2 u|u|}{h^{1/3}} \quad [10]$$

where n is the manning roughness coefficient (equals to 0.035)

The maximum concentration, C_* contained in the flow during simulation was used to classify whether the rainfall had potency to generate lahar in a sub basin. This classification was based on Takahashi (2014). If $0.2 \leq C_* \leq 0.5$, then the flow was a debris flow, hence the rainfall is severe. Hyper-concentrated flow happened when $0.02 \leq C_* < 0.2$ and the rainfall was classified as moderate rainfall. When there is no flow or $C_* < 0.02$, any rainfall that led to this concentration were considered as weak rainfall class.

The terrain data was resampled to have 10 m mesh resolution, while the discharge information in the boundary condition was calculated by using the Hydrologic Engineering Center of Hydrologic Modeling System (HEC-HMS) based on rainfall information provided by X-MP radar. The boundary condition for sub-basins in lower elevation was given by the discharge simulated from the upper sub-basins. If the simulated flow could not be transformed into 2D flow, the discharge was considered to be too weak for lahar genesis. Hence, the lahar simulation was stopped and no further analysis was done. The simulation were run for 3 hours

3.2.2 The short-term rainfall prediction

The short-term rainfall forecast was based on translation model proposed by Shiiba et al., (1984). The dynamic of the horizontal rainfall intensity distribution r(*x,y,t*) with the spatial coordinate (*x,y*) at time *t* is describe in Eq. [11] and [12].

$$\frac{\partial r}{\partial t} + m\frac{\partial r}{\partial x} + n\frac{\partial r}{\partial y} = w \quad [11]$$

where,

$$m = \frac{dx}{dt}, n = \frac{dy}{dt}, w = \frac{dz}{dt} \quad [12]$$

where, *m* and *n* are advection vector (AV) by which the horizontal rainfall distribution was assumed to be translated, and *w* is the growth/decay rate of rainfall intensity along its movement. The method assumed that *m*, *n* and *w* formations are specified on each grid linearly in the manner of:

$$m(x,y) = c_1x + c_2y + c_3 \quad [13]$$
$$n(x,y) = c_4x + c_5y + c_6 \quad [14]$$
$$w(x,y) = c_7x + c_8y + c_9 \quad [15]$$

The c_1 to c_9 parameters are optimized by linear least square using past observed X-MP radar data approximated by central difference scheme according to a method explained by Hapsari (2011).

Extrapolated pattern of rainfall for a time step σ into the future (t_0+t), is given by equation [16] and [17]

$$r(x,y,t_0+t) = r(x(t_0),y(t_0),t_0) - X(\sigma;c_1,\ldots,c_9)\begin{bmatrix}x\\y\\1\end{bmatrix} \quad [16]$$

$$\begin{bmatrix} x(t_0) \\ y(t_0) \end{bmatrix} = Y(-\sigma;\ c_1, \ldots, c_6) \begin{bmatrix} x \\ y \\ 1 \end{bmatrix} \quad [17]$$

where X and Y are 3x3 and 2x3 matrices respectively.

This translation vector was able to identify the horizontal movement of rainfall intensity distribution. Table 2 gives the examples of sets of parameters that can be used to define different model phenomena. While the main concern of this study was to obtain a flexible EWS that has easy interpretation and also was based on predicted rainfall, evaluating the performance of model is necessary. Lahar occurrence verification was done qualitatively as no discharge data were available in the upstream area. The rainfall prediction will be verified quantitatively by using Pearson correlation method. We used 3 past rainfall observation sheets, and the initial prediction time is 15:50 local time (UTC+7). The calculation domain is within radar observation and the mesh size is re-sampled to be 1 km. We applied an ensemble lagged forecast from 2 minutes to 6 minutes and assumed the phenomena were parallel, translation and rotation. The singular vector (SV) method to create the initial condition perturbations was also used, as it has been recommended to be one of the ensemble prediction techniques (Hapsari, 2011; Palmer and Zanna, 2013).

Table 2. Combination of advection vectors parameter for different rainfall phenomena

Phenomena	C_1	C_2	C_3	C_4	C_5	C_6	C_7	C_8	C_9
Parallel translation only			√			√			
Translation and rotation only	√	√	√	√	√	√			
Parallel translation, growth decay			√			√	√	√	√
Translation, rotation, growth-decay	√	√	√	√	√	√	√	√	√

4 RESULTS AND DISCUSSIONS

4.1 Early Warning System framework

4.1.1 Sub-basin susceptibility

The statistical analysis for each parameter (Table 1) is presented in Figure. 5. More reactive sub-basins were located in the higher elevation (> 1000 m amsl) compared to the non-reactive sub-basins. This finding confirmed the previous study that said lahar usually occurred at elevation higher than 1200 m amsl. Furthermore, the non-reactive sub-basins had lower Melton ratio and mean slope compared to the reactive sub-basins, and they were oriented to north until north-eastern part of Mt. Merapi. This was similar to Legono and Pamudji (2015) which stated that the rivers in west, southwest, south and southeast of Mt. Merapi experienced more lahar occurrence.

The result of the k-means cluster analysis is illustrated in Figure 6. In total, from 316 sub-basins, 31 were classified as highly susceptible while 87 and 194 are classified as moderate and low susceptible respectively. About 8% of the non-reactive sub-basins were classified to be high susceptible together with 14 sub-basins near the summit of Mt. Merapi. Almost all of the reactive sub-basin was classified as moderate susceptible. Nevertheless, some sub-basins which belong to three rivers i.e: Blongkeng, Bedog and Lamat that were previously classified as reactive are in low susceptible class

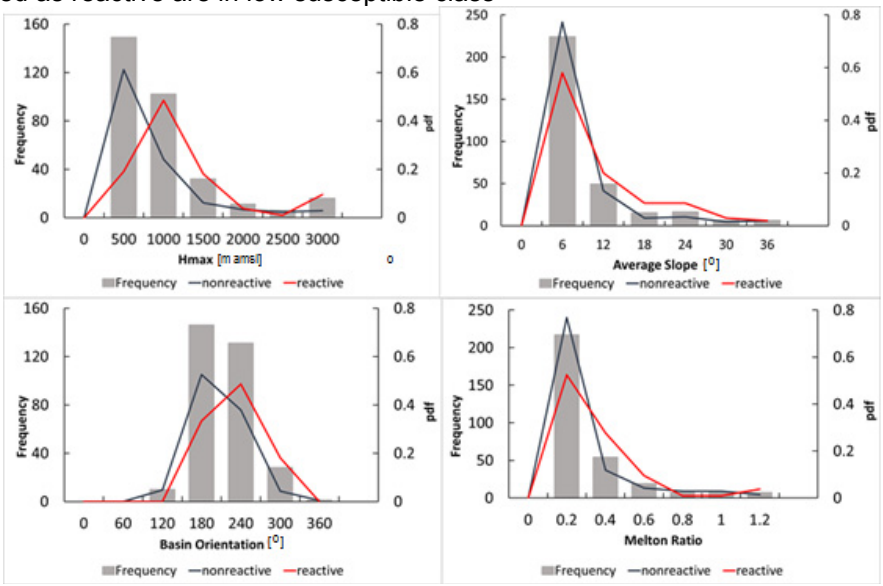

Figure 5. Statistical analysis of parameters extracted from each sub-basin

These results are in agreement with de Belizal et al. (2013) who noted that: Putih, Boyong, Ladon and Gendol Rivers had high to very high frequencies of lahar event. After the centennial eruption of Merapi in 2010, the frequency of lahar occurrence in those rivers was more than 25 to 50 events in the following rainy season. On the other side, they also noted that Lamat and Blongkeng rivers had less than 5 lahar events in the same period. This method classified upstream Woro River as highly susceptible class, different with previous study where it was said to have less frequent lahar occurrence as Lamat and Blongkeng River. However, the result is reasonable as Berenguer et al. (2015) who used fuzzy cluster analysis for Debris Flow (DF) susceptibility classification in eastern Pyrenees, Spain also found that the majority of reactive sub-basins belong to moderate susceptible class, and 10 % of non-reactive sub-basins were classified as high susceptible class.

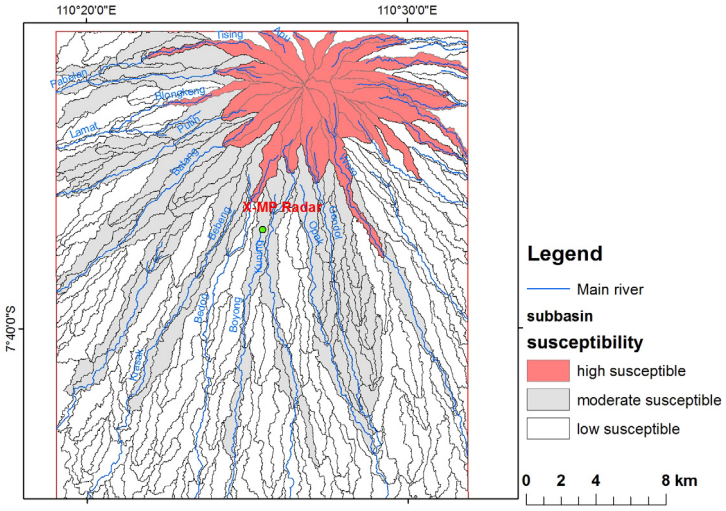

Figure 6. Susceptibility of sub-basin based on k-means cluster analysis

4.1.3 Rainfall analysis and numerical model results

Table 3 shows the summary results of maximum concentration within the flow for all sub-basins. As lahar compasses of debris flow, hyper-concentrated flow, stream flow and mudflow, thus our assumption to classify the flow concentration based on Takahashi (2014) is acceptable. The upstream Blongkeng sub-basin had the highest concentration of 0.39, caused by extreme rainfall intensity received on the day. More than 90% of Sub-basins had bed load flow concentration which were lower than 0.02. This indicated that the flows resulted from the simulation were diluted and contained less coarser particles, so that they were similar to the field measurement by Levigne et al. (2000).

Table 3. Summary of maximum sediment concentration resulted from lahar simulation.

Maximum concentration (% volume)	Numbers of sub-basin
<0.01	151
0.01-0.02	144
0.02-0.2	20
0.2-0.5	1

4.1.2 Combining the susceptibility of sub-basin and rainfall information

The classification of sub-basins (S) and rainfall condition (R) were combined by fuzzy logic (Equation [18]) to determine an occurrence of lahar in a sub-basin. Table 4 gives the summary of this combination rule, where C1, C2 and C3 are low hazard class, moderate hazard class and high hazard class respectively.

$$\text{If } \left\{\begin{array}{l}[(R \in R_1) \cap (S \in S_1)] \\ \cup\,[(R \in R_1) \cap (S \in S_2)] \\ \cup\,[(R \in R_1) \cap (S \in S_3)] \\ \cup\,[(R \in R_2) \cap (S \in S_1)]\end{array}\right\} \Rightarrow \text{C1;}$$

$$\text{If } \left\{\begin{array}{l}[(R \in R_2) \cap (S \in S_2)] \\ \cup\,[(R \in R_3) \cap (S \in S_1)]\end{array}\right\} \Rightarrow \text{C2} \qquad [18]$$

$$\text{If } \left\{\begin{array}{l}[(R \in R_3) \cap (S \in S_2)] \\ \cup\,[(R \in R_3) \cap (S \in S_2)] \\ \cup\,[(R \in R_3) \cap (S \in S_3)]\end{array}\right\} \Rightarrow \text{C3}$$

The logic in Table 4 is explained as follow: if the sub-basin is classified as C1 then the chance of lahar to occur is small and no measures need to be taken. The C2 class means that lahar is likely to occur and preventive measures should be considered, otherwise C3 means that lahar is about to occur and people must be evacuated from hazard prone area.

Table 4. The rule of combining the lahar hazard class based on sub-basin susceptibility and rainfall condition

Parameters		**Sub-basin susceptibility**		
		Low	**Moderate**	**High**
Rainfall condition	Weak	Low (C1)	Low (C1)	Low (C1)
	Moderate	Low (C1)	Moderate (C2)	High (C3)
	Severe	Moderate (C2)	High (C3)	High (C3)

Figure 7(a) shows the result of the classification. Three rivers were classified to have high lahar warning level (C3), i.e: Gendol, Woro and Putih River. This result was reasonable as the upstream sub-basin of those rivers received higher rainfall intensities compared to the other sub-basins (Figure 3(a)). Although the highest concentration happened in Blongkeng River according to the simulation, it however has moderate hazard level because the sub-basin was classified as low susceptible. Comparing the result with real condition, only Putih River was not reported to have lahar event on 17 Feb 2016. Lahar event was reported in upstream Gendol River, while hyper-concentrated-like flow was also caught by a CCTV in the upstream of Woro River (Figure 7(b)).

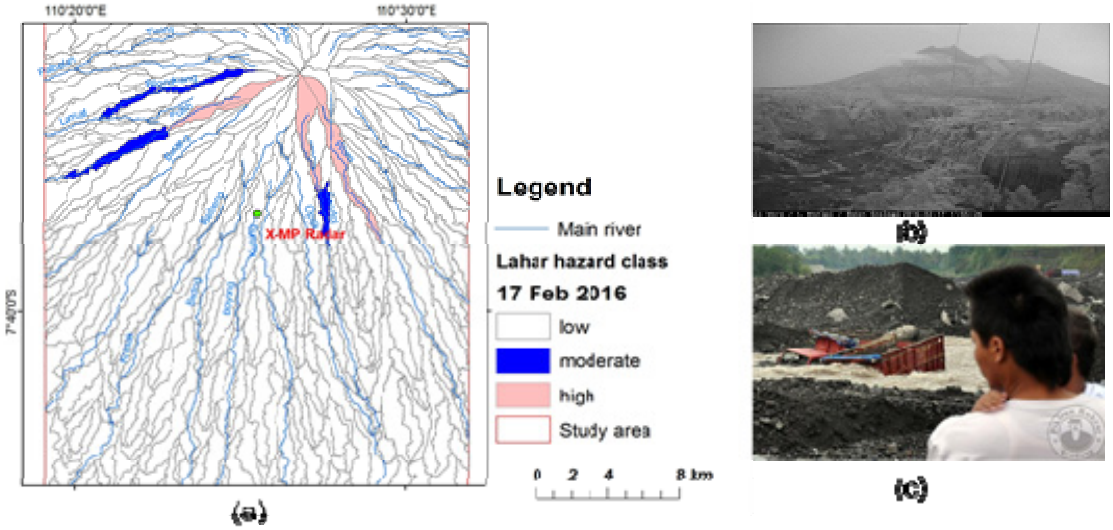

Figure 7. Lahar hazard class for 17 Feb 2016 based on the combination of sub-basin susceptibility and rainfall condition (a), CCTV image from Woro river on 17 Feb 2016 (b), Local people were watching two trucks trapped by Lahar flow in Gendol river on 17 Feb 2016, Kepuharjo (c); courtesy of pikiran-rakyat.com.

The similar classification had been done by Berenguer et al. (2015) which also combined the susceptibility sub-basins and rainfall condition to analyze the debris flow occurrence in Spain. The previous research involved large amount of data hence the change in the instability of soil could be monitored for period of months. Although the lahar was usually triggered instantaneously by extreme rainfall, it is also possible to extend the lahar simulation by using more rainfall data. This future work is needed because it will give better understanding on the hydorological condition in Merapi before the lahar occurs.

4.2 Short-term rainfall prediction

Best predicted areal rainfall intensity, *r* [mm/h] in Gendol catchment is given in Figure 8, and the spatial correlation between predicted and observed rainfall are given in Table 5. In general the short-term rainfall predictions were still unable to predict the spatial movement of rainfall, although the timely variation within the study area showed similar pattern.

Using the timelag (-4) at 15:46 with second perturbation or SV(+2) gave the closest rainfall pattern with the observed rainfall (Figure 8 and 9). All of the first singular vectors (SV(+1)), it gave the tendencies of rainfall to have negative growth, which showed that the second singular vector were more likely to project the leading eigenvalue in its transient time (Palmer and Zanna, 2013). Future error correction is required for getting a proper scale of this singular vector. The observed rainfall values also showed great decay rate, which could not be predicted by the model. This made the correlation between predicted was observed to be linearly weaker as simulation period went longer. These two factors, which were the growth decay rate. Thus, applying the second perturbation of singular vector should be the main consideration on further model improvement.

Table 5. Spatial correlation between predicted values and observed rainfall

Time	Pearson Correlation	
	15:46 (SV+2)	mean
16:20	0.10	0.36
16:50	0.19	0.18
17:20	0.01	0.04
17:50	0.05	-0.02

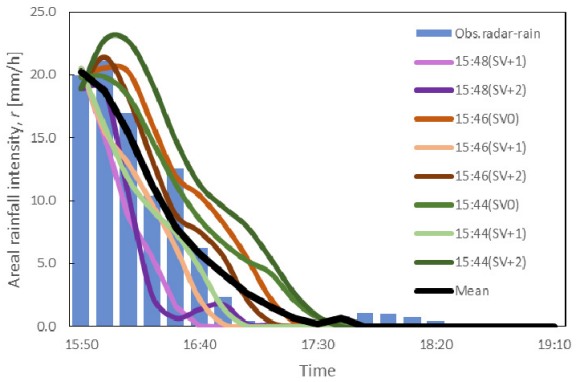

Figure 8. Areal rainfall intensity, *r* [mm/h] prediction in Gendol catchment by various methods of singular vector and its mean values, compared to the observed rainfall

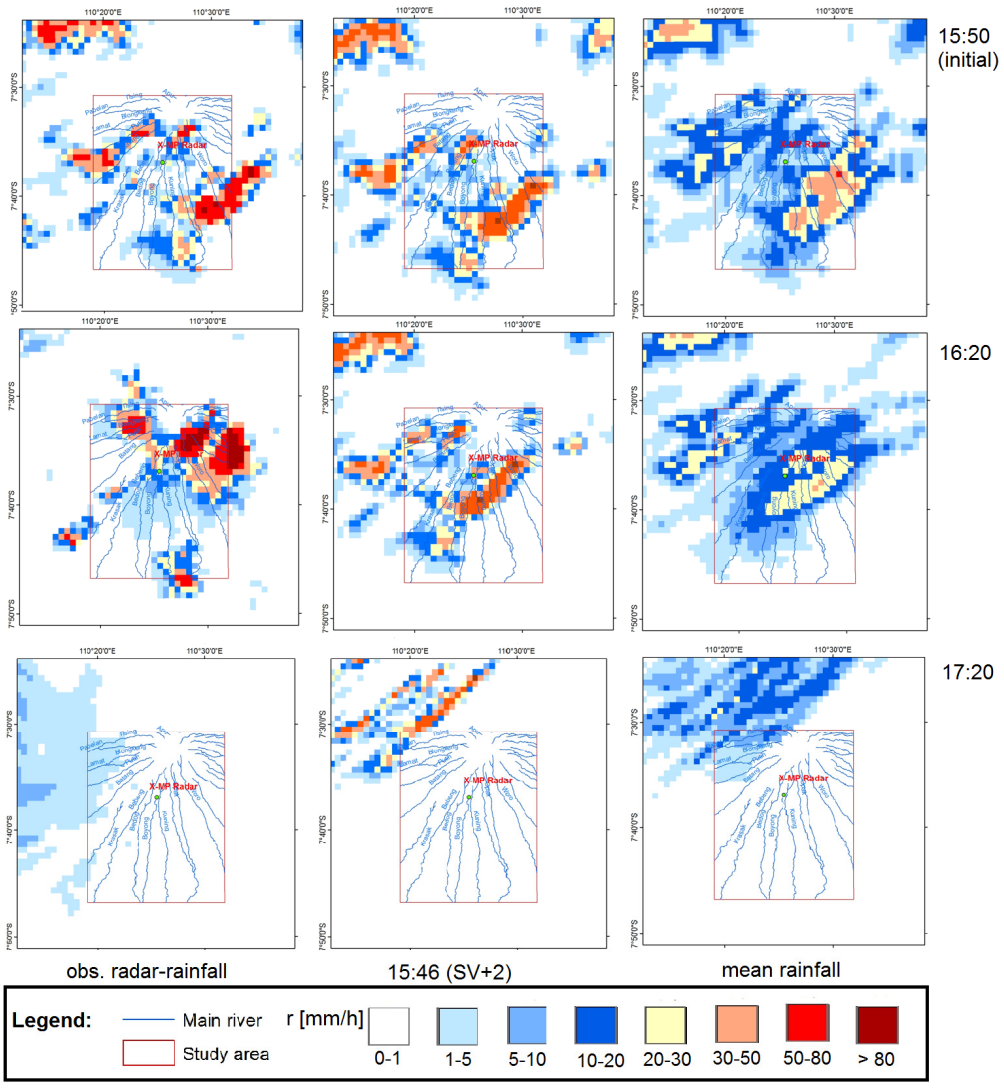

Figure 9. Spatial rainfall intensity, *r* [mm/h\] distribution of predicted rainfall compared with the real observed rainfall

5 CONCLUSIONS

A method to develop a short-term rainfall prediction and early warning system (EWS) has been done in MVA. Although the spatial variation of rainfall were still poor, but the temporal fluctuation of rainfall in catchment scale shows similar trend. The EWS framework that is based on geomorphological condition and rainfall information could identify the hazard level area for the selected study case on 17 Feb 2016. Improvement are still required especially for short-term rainfall prediction by applying the second singular vector (SV+2) and better growth and decay factor.

ACKNOWLEDGEMENTS

This study is supported by Integrated Study on Mitigation of Multi-modal Disaster Caused by Ejection of Volcanic Products, Science and Technology Research Partnership Sustainable Development Program (SATREPS).

REFERENCES

Aghakouchak, A., Habib, E. & Bardossy, A. (2010). Modelling Radar Rainfall Estimation Uncertainties: Random Error Model, *J.Hydrol. Engineering*, 15(4), 265-274.

Berenguer, M.,Sempere-Torres, D. & Hurlimann, M. (2015). Debris-flow Forecasting at Regional Scale by Combining Susceptibility Mapping and Radar Rainfall, *J. Nat. Hazard Earth Sys*, 15, 587-602.

Castruccio, A. & Clavero, J. (2015), Lahar Simulation at Active Volcanoes of the Southern Andes; Implications for Hazard Assessment, *J. Nat Hazards*., 693-716.

de Belizal, E., Lavigne, F., Hadmoko, D.S., Degai, J.P.,Dipayana, G.A., Bachtiar, W.M., Marfai, M.A., Coquet, M., Le Mauff, B., Robi, A.K., Vidal, C., Cholik, N. & Aisyah, N. (2013). Rain-triggered Lahar Following the 2010 eruption of Merapi Volcano Indonesia, *J. Volcanol. Geoth. Res*, 261, 330-347.

Hapsari, R.I, (2011). Development of Probabilities Hydro-Meteorological Prediction for Urban Flood Disaster Prevention. *Doctoral Thesis*. Yamanashi University.

Ikhsan, J., Fujita, M., Takabayashi, H. & M. Sulaiman. (2009). Concept on Sustainable Sand Mining Management in Merapi Area, *Annual Journal of Hydraulic Engineering, JSCE*. 2009, Vol. 53

Jones, R., Thomas, R. E., Peakall, J. & Manville, V. (2017), Rainfall-Runoff Properties of Tephra: Simulated Effects of Grain-Size and Antecedent Rainfall, *Geomorphology*, 39-51.

Kim, S., Tachikawa, Y. & Takara, K. (2006). Flood Forecasting System Using Weather Radar and Distributed Hydrological Model, *Annuals of Disas. Prev. Res. Inst*., Kyoto Univ., No. 49 B, 2006. 55-65

Legono, D. & Pamudji, R.A. (2015). *Lahar Flow Disaster, Human Activities and Risk Mitigation on Volcanic Rivers – Case Study of Rivers on Mt. Merapi Slope, Indonesia*, Disaster Prevention Research Institute Kyoto University.

Legowo, D. (1981). Volcanic Debris Control Applied in Indonesia. *J. Hydrol.*, 20, 122-1341.

Lavigne, F., Thouret, J.C., Voight, B., Suwa, H. & Sumaryono, A. (2000a). Lahar at Merapi Volcano, Central Java: An Overview, *J Volcanol. Geoth. Res.* 100, 423-456.

Lavigne, F., Thouret, J.C., Voight, B., Young, K., La Husen, R., Marso, J., Suwa, H., Sumaryono, A., Sayudi D.S., Dejean, M. (2000b). Instrumental Lahar Monitoring at Merapi Volcano, Central Java, Indonesia. *J. Volcanol. Geotherm. Res*. 100, 457-478.

Nakatani, K., E. Iwanami, H., Shigeo, Y. Satofuka, Y. & T. Mizuyama. (2012), Development of "Hyper Kanako", A Debris Flow Simulation System Based on Laser Profiler Data, *12th Congress INTERPRAEVENT,* Grenobel, France, Conference Proceedings.

Nakagawa, H., Takahashi, T., Satofuka, Y. & Kawaike, K. (2003). Numerical Simulation of Sediment Disasters Caused by Heavy Rainfall in Camuri Grande basin, Venezuela, *Proceedings of the 3rd Conference on Debris-Flow Hazards Mitigation.: Mechanics, Prediction, and Assessment*, 671-682.

Neall, V.E. (1976). Lahar as Major Geological Hazards. *Bull. Int. Assoc. Eng. Geol,* No. 14, 233– 240.

Over, T.M., Murphy, N, E.A., Ortel, T. W. & Ishii A.L. (2007). Comparisons between NEXRAD Radar and Tipping-Bucket Gage Rainfall Data: A Case Study for DuPage County, Illinois, *Conference Paper on: World Environmental and Water Resources Congress*.

Palmer, T.N, & L. Zanna, 2013: Singular Vectors, Predictability and Ensemble Forecasting for Weather and Climate, *J. Phys.*, 46, 254018.

Shiiba, M., Takasao, T. & Nakakita, E. (1984). Investigation of Short-Term Rainfall Prediction Method by a Translation Model, *Jpn. Conf. on Hydraul., 28th*, 423-428.

Takahashi T., Nakagawa H., Harada, T. & Yamashiki, Y. (1992). Routing Debris Flows with Particle Segregation, J. *Hydraul. Eng- ASCE,* Vol. 118, No.11, 1490-1507.

Takahashi, T. (2014), D*ebris flow: Mechanics, Prediction and Countermeasures*. 2nd edition. Taylor & Francis.

Wei, K., Gao, P., Cu K.i., Hu, K., Xu, J., Zhang, G. & Bi, B. (2006). Method of Debris Flow Prediction Based on A Numerical Weather Forecast and Its Application, *WIT Trans. Ecol. Envir.,* 90, 37-46.

FIELD CALIBRATION OF BEDLOAD MONITORING SYSTEM IN A SEDIMENT BYPASS TUNNEL: SWISS PLATE GEOPHONE

MICHELLE MUELLER-HAGMANN[(1)], ISMAIL ALBAYRAK[(2)] & ROBERT MICHAEL BOES[(3)]

[(1,2,3)]Laboratory of Hydraulics, Hydrology and Glaciology, ETH Zurich, Switzerland
mueller-hagmann@vaw.baug.ethz.ch; albayrak@vaw.baug.ethz.ch; boes@vaw.baug.ethz.ch

ABSTRACT

Under the impact of climate change, sediment transport in melting water draining from glacier basins and reservoir sedimentation tend to increase worldwide. As a consequence, three main problems arise: (1) the loss of reservoir storage volume for energy production, flood retention, water supply and irrigation; (2) increased hydro-abrasion at turbines and hydraulic structures; and (3) negative environmental impacts due to downstream sediment deficit. An effective countermeasure against reservoir sedimentation in small to medium-sized mountainous reservoirs is to route sediment around the dam by using a sediment bypass tunnel (SBT). A major problem affecting nearly all SBTs is severe hydro-abrasion on the tunnel invert due to high bed load transport rates in combination with high flow velocities. Depending on site-specific operating conditions and sediment properties, i.e. size, hardness and shape, invert abrasion can cause considerable refurbishment costs. For optimized operation of SBTs with respect to sustainable sediment management and cost efficiency, continuous real-time monitoring of bed load transport is necessary. Bed load transport can be monitored indirectly by using passive sensors like geophones or hydrophones. However, these techniques require a site-specific calibration depending on hydraulic conditions, particle-size and shape. This study deals with the field calibration of a so-called Swiss plate geophone system implemented at the outlet of Solis SBT located in Grisons in the Swiss Alps. The geophones with a sampling rate of 10 kHz are placed across the whole tunnel width and have an inclination of 10° against the invert slope. Three different particle size classes were tested 16-32 mm, 32-63 mm and 0-400 mm. The results indicate that calibration is independent from flow velocity due to the counter inclination of the geophones. However, a certain degree of signal saturation due to high bed load transport rate occurred and hence a further investigation is needed.

Keywords: Swiss plate geophone; bedload measurements; geophone calibration; sediment bypass tunnel; reservoir sedimentation.

1 INTRODUCTION

The role of sediment management considering sustainable and cost-effective operation and maintenance of hydraulic structures has been disregarded for a long time. However, sediment transport in watercourses increases due to the impact of climate change and promotes related problems such as a loss of storage volume for energy production, flood retention, water supply and irrigation, an increase of hydro-abrasive wear at turbines and hydraulic structures and negative environmental impact in the downstream due to the interrupted sediment transport by the dam (Sumi et al., 2004, Boes et al., 2014; Kondolf et al., 2014). Therefore, a holistic sediment management approach at hydraulic structures, in particular at reservoirs is globally required.

One of the effective and holistic countermeasures against reservoir sedimentation is to route sediment around a dam by using a sediment bypass tunnel (SBT). It restores the natural sediment transport and hence not only reduces reservoir sedimentation but also sediment deficit related problems in the downstream such as river bed incision, ground water lowering, degradation of eco-morphology, reduction of habitat quality and even nutrient and sediment deficit in coastal regions (Syvitski et al., 2005; Kantoush and Sumi, 2010; Fukuda et al., 2012; Fukuroi, 2012; Kondolf et al., 2014; Facchini et al., 2015; Martin et al., 2015). A major problem affecting nearly all SBTs is severe hydro-abrasion on the tunnel invert due to the high bed load transport rates in combination with high flow velocities (Figure 1). Depending on site-specific operating conditions and sediment properties, i.e. size, hardness and shape, invert abrasion can cause considerable refurbishment costs.

For optimized operation of SBTs with respect to sustainable sediment management and cost efficiency, continuous real-time monitoring of hydraulic operating conditions and sediment transport is required. The latter includes suspended sediment load and bed load and can be monitored by turbidity sensors and the Swiss Plate Geophone System (SPGS) described below, respectively. The number of impulses computed from the registered SPGS signals correlates with the transported bed load mass.

Using this relation, i.e. a calibration, bed load transport rates are estimated. Since flow velocity, particle-size and shape affect the calibration and because laboratory calibration cannot adequately reproduce prototype conditions, site-specific calibration in the field is highly recommended.

In the scope of a research project on the invert hydro-abrasion in SBTs, a field calibration of a SPGS was conducted. This system has been implemented at the outlet of Solis SBT located in Grisons in the Swiss Alps. The present study reports the results of the calibration and compares them with the results from two laboratory calibrations of the same system.

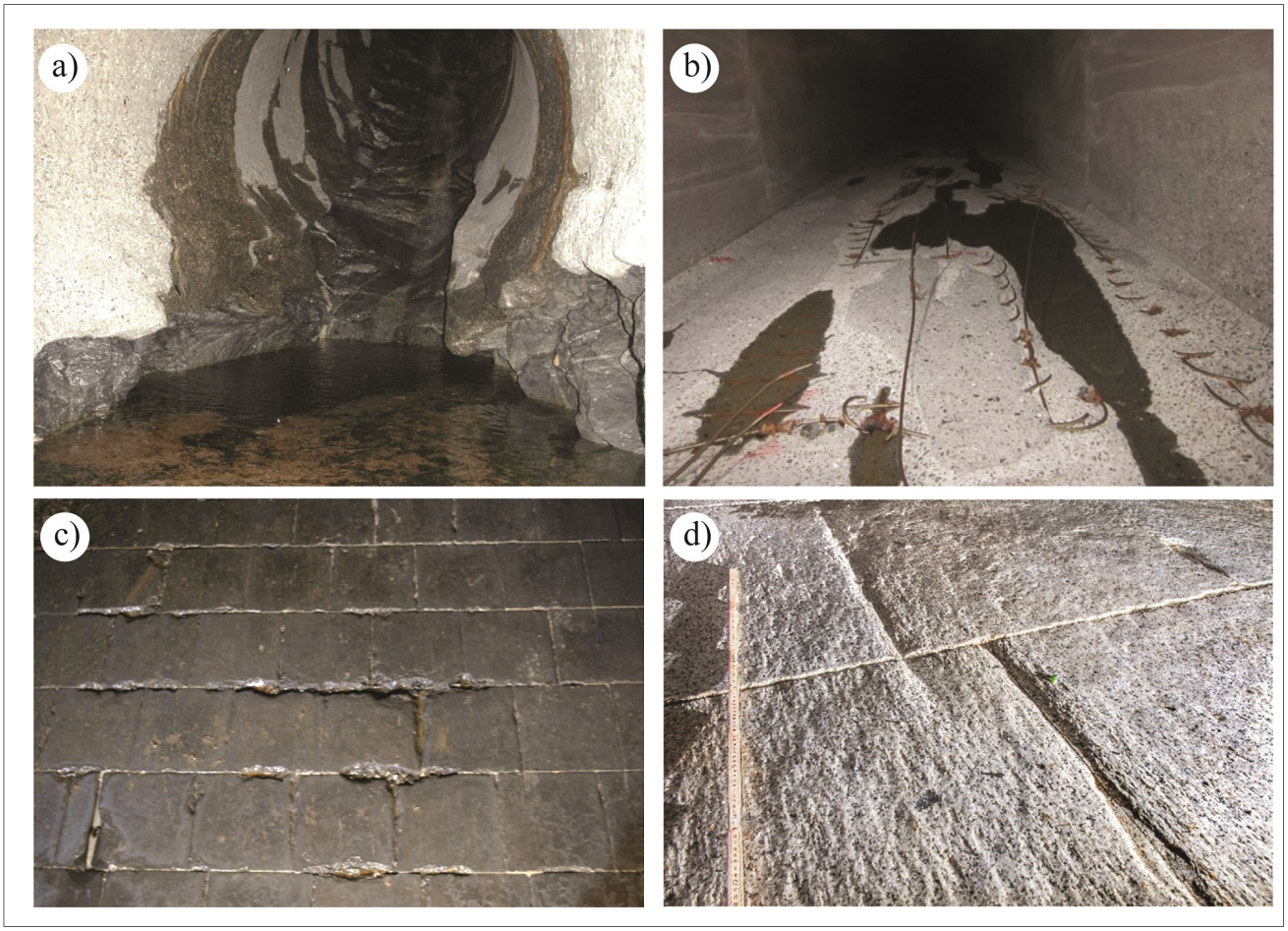

Figure 1. Hydroabrasion examples, a) abrasion at Val d'Ambra SBT (CH) into the concrete lining and rock underground (M. Müller-Hagmann), b) incision channels of the reinforced concrete lining of Asahi SBT (JP) (KEPCO, 2012), hydroabrasive damages at c) cast basalt tiles in Runchez SBT (CH) (M. Müller-Hagmann) and d) at the granite lining of Pfaffensprung SBT (CH) (VAW).

2 TEST SET-UP AND PROCEDURE

2.1 Solis SBT

The Solis reservoir located in the Swiss Alps was commissioned in 1986 and stores approximately 4.07 10^6 m^3 of which 1.46 10^6 m^3 are useful storage capacity for power generation by the electric power company of Zurich (ewz). Compared to the mean annual runoff of 853 10^6 m^3, the reservoir volume and the capacity inflow ratio of 0.0048 are small. The reservoir is fed by the Albula River and the reservoir head is located one kilometer downstream of the confluence with the Julia River.

Estimated annual transported and deposited sediment volumes in the Solis reservoir are on average 103'000 m^3 and 80'000 m^3, respectively. After twelve years of operation, 20% of the reservoir storage capacity was lost due to sedimentation, which significantly affects hydropower operation. Assuming a constant aggradation rate, the aggradation body was expected to reach the dam by 2012 and would consequently have endangered the operation safety of the dam (Auel et al., 2011; Oertli & Auel, 2015). To reduce the sedimentation and restore the interrupted sediment transport in the river reach, a one-kilometer long SBT was constructed (Figure 2) and commissioned in 2012. The function of the SBT is to bypass incoming sediments during flood events. Bed load particles enter the reservoir and propagate towards a guiding structure in the reservoir, which diverts bed load to the SBT intake structure to be routed around the dam (Figure 2). With this design, the lower part of the reservoir between the guiding structure and the dam is protected from

sedimentation by both bed load and suspended load up to the SBT design discharge of 170 m^3/s, representing a five-year flood when the SBT is in operation. For reservoir inflows exceeding the design discharge, all the bed load is diverted to the SBT intake, whereas a part of the suspended load is conveyed towards the dam with the surplus flow passing the guiding structure. If not conveyed via the power waterway, the bottom outlet or the spillway to the tailwater, a considerable amount of fines may thus settle in the lower part of the reservoir, which is periodically flushed through the bottom outlet.

Since the SBT intake is located below the drawdown level, the inflow is pressurized and no acceleration section is required. After the intake, the SBT flow is decelerated but remains supercritical with Froude number F ≈ 1.7 and an average flow velocity of U ≈ 11 m/s. Hence, a sufficient sediment transport capacity is ensured along the whole tunnel. The bottom slope of the SBT is 1.9%, and the arched cross sectional area amounts to 18.5 m^2.

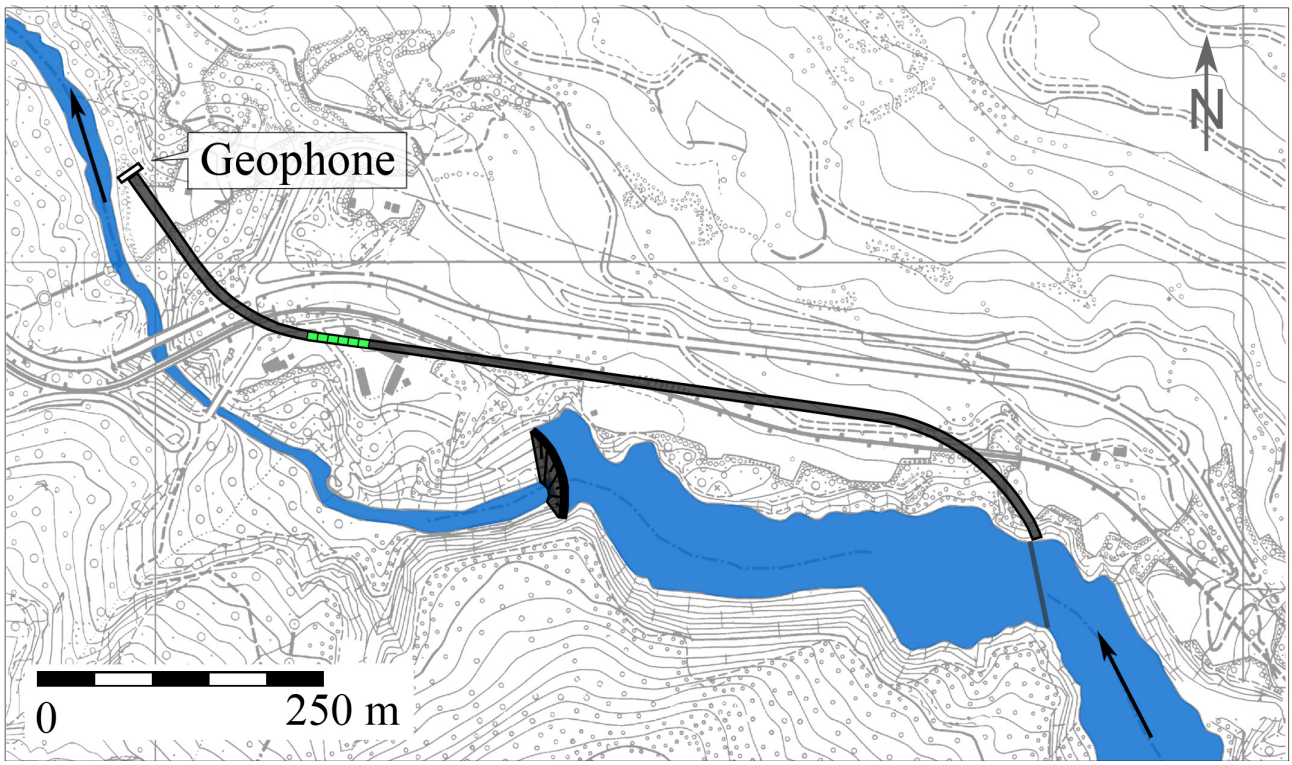

Figure 2. Overview of the Solis SBT with the dam (center), the guiding structure and intake (right) and the geophone system at the outlet (left).

2.2 Swiss plate geophone system

The SPGS developed by the Swiss Federal Institute for Forest, Snow and Landscape Research (WSL) is a robust device allowing for continuous bed load transport monitoring (Rickenmann & Fritschi, 2010; Koshiba et al., 2017). There is a long-time experience with SPGS at a number of torrents and mountain streams with flow velocities up to 5 m/s and flow depth of a few decimeters, mainly in the Swiss and Austrian Alps. The submersible device consists of an elastically bedded steel plate mounted flush to the channel bed. The plate is equipped with a geophone sensor (shown in Figure 3a: GS-20DX, manufactured by "Geospace Technologies", Houston, Texas), encased by a waterproof aluminum housing (Figure 3b). The length of the plate in flow direction is 36 cm, the width is 50 cm and the thickness is 1.5 cm. The bearing between the steel plate and the mounting steel box is made of rubber (elastomer type CR/SRB-standard 65±5, manufactured by "Angst + Pfister", Zurich, Switzerland). Besides signal damping issues, this bearing serves for isolation of vibrational energy generated in the surroundings.

The sensor does not directly measure bed load transport, but registers the vibration signals of the geophone plate, i.e. the vertical plate oscillations induced by impingement of passing particles. The signal output is a voltage with a sampling frequency of 10 kHz (Figure 4). To filter out background noise and vibrations generated by clear water discharge, a threshold signal value of 0.1 V is defined in accordance with other applications (Rickenmann et al., 2013; Wyss, 2016; Chiari et al., 2016). However, this threshold value can be changed depending on background noise and other electronic interferences (Morach, 2011).

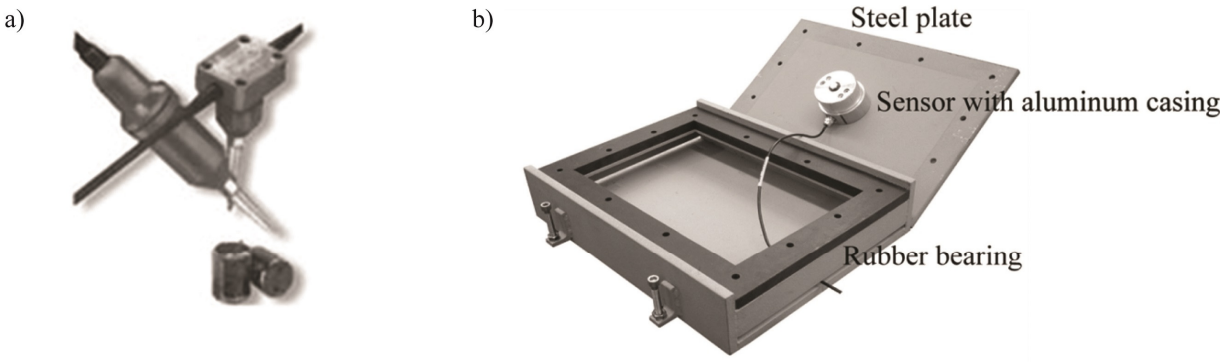

Figure 3. SPGS: a) geophone sensor (courtesy of Geospace Technologies) and b) open measuring unit showing steel plate and waterproof aluminum housing of the sensor.

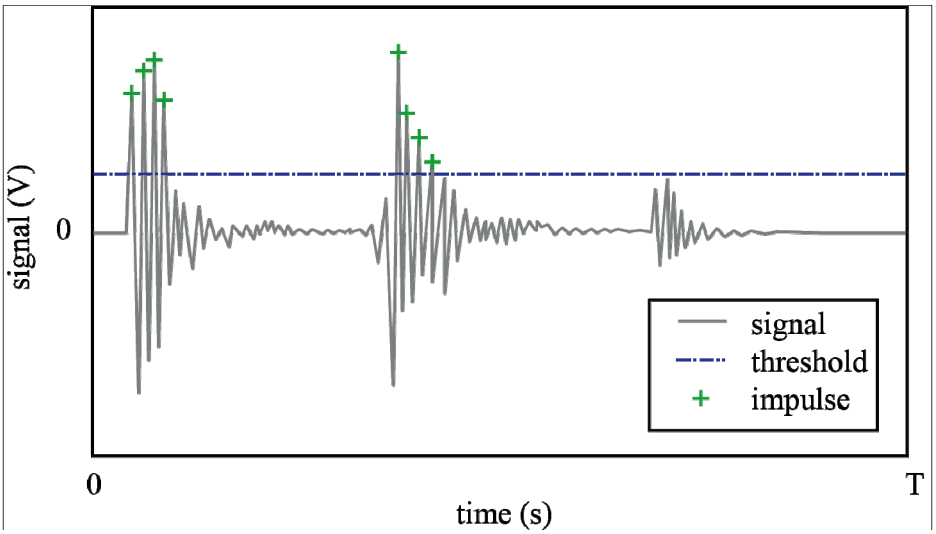

Figure 4. Schematic geophone signal.

2.3 Calibration coefficient K_b

The number of impulses Imp above the threshold value (Figure 4) correlates linearly with bed load mass m (Rickenmann 1997, Rickenmann et al. 2012). The linear correlation coefficient between impulses and bedload mass K_b is used to estimate sediment transport rate. It constitutes a calibration coefficient and is defined as:

$$K_b = \frac{\mathrm{Imp}}{m} \quad (1/\mathrm{kg}) \qquad [1]$$

Recent investigations reveal that not only sediment transport rate but also grain size information can be extracted from the amplitude of the geophone signals (Wyss et al., 2014; Wyss, 2016; Wyss et al., 2016a). Since the calibration coefficient is affected by flow conditions, grain size and shape, a site-specific calibration is required (Rickenmann and McArdell, 2007; Rickenmann et al., 2012; Rickenmann et al., 2013; Wyss et al., 2014; Wyss et al., 2015; Wyss et al., 2016a and 2016b). The calibration is generally based on monitored sediment deposition volumes in retention basins or on basket sampling of transported sediment (Rickenmann and McArdell, 2008; Rickenmann et al., 2012; Rickenmann et al., 2014; Wyss, 2016). However, as none of these methods is possible at Solis SBT, a field test described in Section 2.2. was performed to calibrate the geophone system at the Solis SBT.

The SPGS was implemented near the SBT outlet, 100 m downstream of a right hand bend (radius = 145 m, angle = 46.5°, Figure 2). In order to capture not only temporal but also spatial variations of bed load transport, the SPGS at Solis SBT consists of 8 units covering the entire tunnel width (Figure 5a). In contrast to the general geophone applications, the flow regime in the Solis SBT is supercritical. To address this issues, a laboratory investigation was conducted before the implementation of the SPGS in the Solis SBT (Morach, 2011). The tests revealed that particle detection rates increased when inclining the geophone plate against the flow direction compared to the horizontal mounting. Thus, the geophone system in Solis was accordingly implemented with an inclination angle of 10° (Figure 5b). After the implementation, further laboratory tests

similar to Morach (2011) were conducted, the results of which are compared with the present results in Section 3.

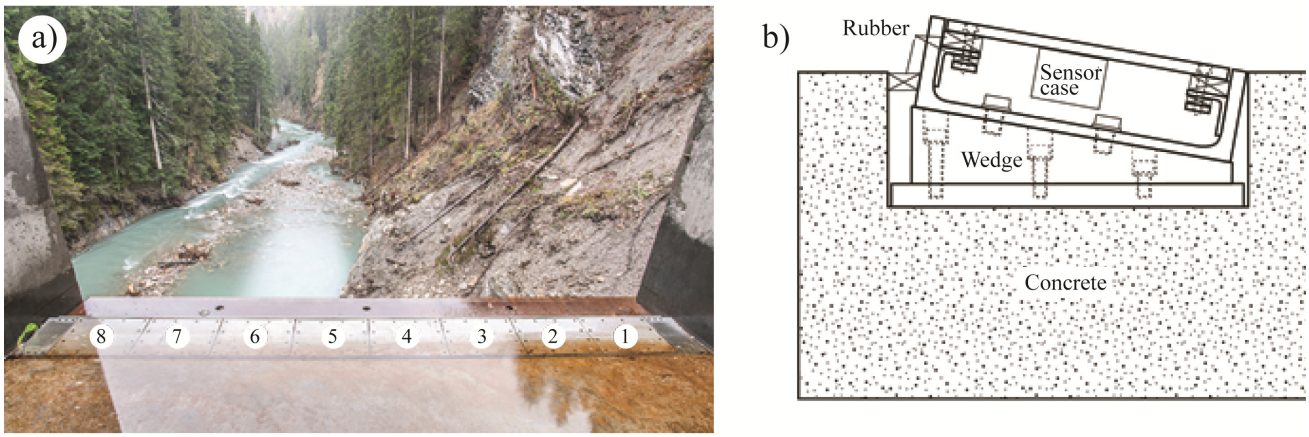

Figure 5. a) Counter-inclined SPGS installed at the Solis SBT outlet; view in flow direction; b) Cross section of the geophone construction (flow from right to left).

2.4 Procedure and characteristics of sediments used

The Solis SPGS (Figure 5a) was calibrated using three sediment grain size classes. Three test runs, one for each sediment size class, were conducted. The calibration procedure consisted of: (I) placing of a 10 m^3 sediment deposit volume downstream of the intake gate, (II) SBT operation and signal recording, and (III) analysis of the raw geophone signals. The sediment deposit was located at the inlet in order to achieve characteristic bedload transport of typical SBT operation. To limit water loss from the reservoir, a discharge of 50 m^3/s was selected. To avoid additional sediment transport from the reservoir, the reservoir level was kept high (i.e. 0.83-0.85 m below the full supply level), so that bed shear stresses were too low to entrain settled sediments. The sediments used for the geophone calibration were taken from a gravel plant, located on the Albula at the reservoir head so that the sediment properties were identical to the sediment transported through the SBT in typical operations. The grain size distributions (GSD) were provided by the supplier and checked by line-sampling (Table 1 and Figure 6a). Based on the latter, the corresponding gravimetric GSD was calculated according to Fehr (1987). Therefore, the fraction of the particles smaller than 16 mm was assumed to 15%.For each test run, the sediments were weighed at the gravel plant and transported to the test site by truck. Due to limited space, a side- and back-dumper was used. At a distance of 20 m from the intake, the sediments were damped and distributed by a small excavator. The sediment deposition covered the whole tunnel width with a layer thickness of 20 cm and a wedged forehead (Figure 6b).

Table 1. Sediment of the calibration test runs and the natural Solis sediment.

	Name	D (mm)	d_m (mm)	Volume (m^3)	Mass (to)
Fine material	Test 1	16-32 mm	25±2	10.01	15.3
Coarse material	Test 2	32-63 mm	45±4	9.94	15.4
Mixture	Test 3	0-400 mm	210±20	11.53	18.4
Solis natural (assumed)	Solis GSD	0-300 mm	60	-	-

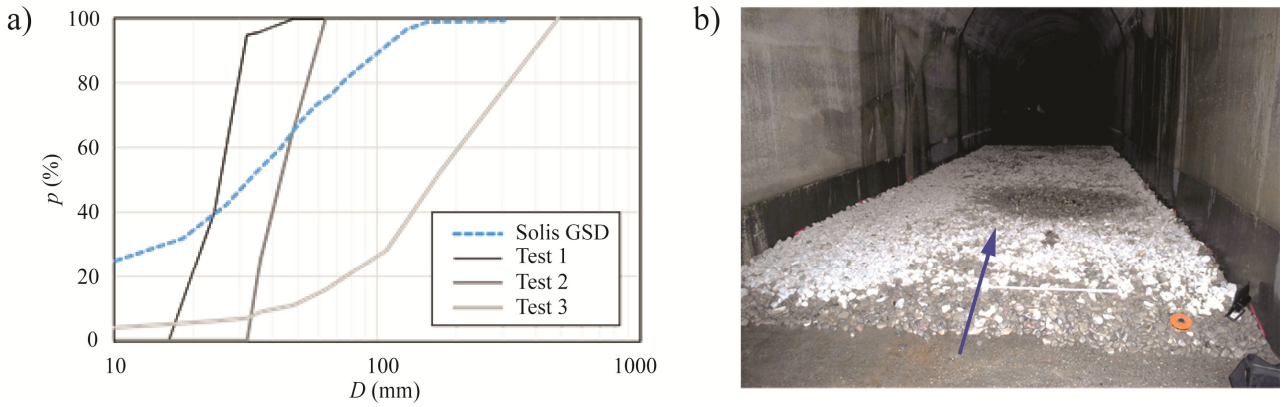

Figure 6. a) GSD of the natural sediments flushed through the SBT and of the sediments used for geophone field calibration; b) photo of damped sediments of size class 32-63 mm, view in flow direction.

3 RESULTS ON THE CALIBRATION COEFFICIENT K_b

Figure 7a shows the sediment-laden flow at the SBT outlet structure, depicting that: (1) bed load distribution across the tunnel width was uneven during all three test runs, (2) sediment transport was concentrated at the right tunnel side, see darker flow area, and (3) almost no particles were transported on the left side. These qualitative observations were confirmed by the quantitative geophone measurements indicating a strong effect of the upstream bend on the lateral sediment transport distribution (Figure 7b). The relative number of registered impulses, i.e. the number of impulses per plate divided by the total number of impulses across the SBT width, collapses well independent from test run and thus GSD (Figure 7b). During normal SBT operation, similar lateral bed load transport distributions were measured, which confirms that the geophone calibration tests reproduced the real sediment transport conditions in the Solis SBT.

The bedload calibration coefficient K_b was determined for each test run (Table 2). Figure 8 shows K_b versus grain size D for the Solis field and laboratory calibration tests as well as Morach's (2011) tests. The geophone can detect the particles with a size above D = 16 mm and thus around this threshold particle size, K_b is approx. zero (Figure 8). As expected, K_b varies with particle size (Morach, 2011; Wyss, 2016). Despite different hydraulic and bed load transport conditions, all K_b values are in a comparable range, in particular for particles larger than 50 mm. For $D \approx 25$ mm the K_b value of the field calibration is higher than for the laboratory calibration, while it is the contrary for $D \approx 45$ mm. This is attributed to the higher flow velocity prevailing in the Solis SBT. The difference between Morach's (2011) and the presented results may originate from electric interferences affecting Morach's experiments. Her measurements exhibit a significantly higher background noise, which can amplify the signal and hence bias the results, in particularly for small sediment with low amplitudes in the range of the detection threshold.

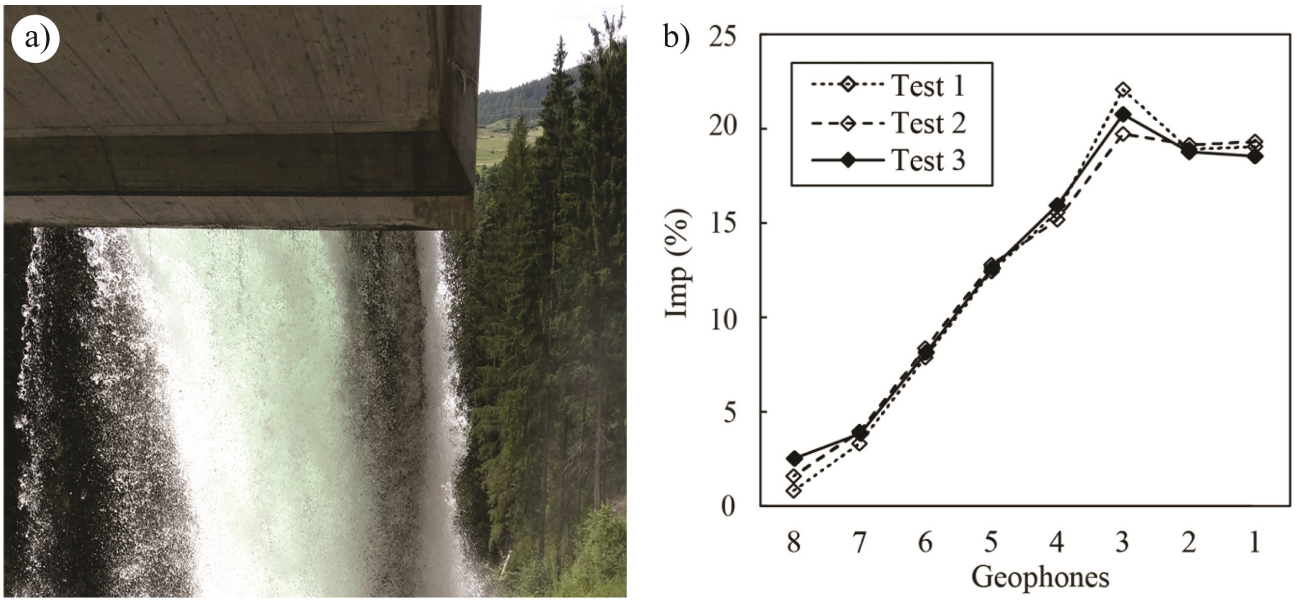

Figure 7. a) SBT outlet with clear water and black sediment jet on the right side during the test run 3 with D=0-400 mm ,view in flow direction from underneath the SBT outlet; b) relative number of impulses registered by each geophone plate.

Table 2. Grain size and K_b based on the field calibration.

	Test 1	Test 2	Test 3
D (mm)	16-32	32-63	0-400
d_m (mm)	25±2	45±4	210±20
K_b (1/kg)	6.80	13.6	5.05

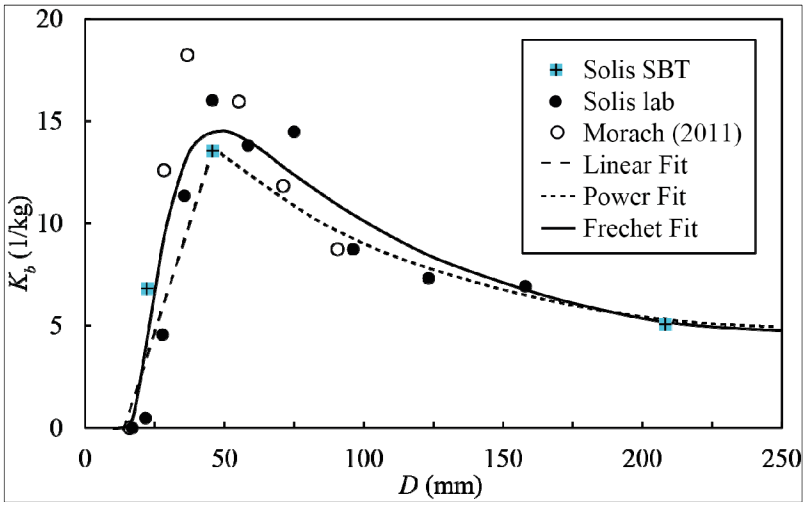

Figure 8. K_b versus D for the laboratory and field calibration as well as Morach's (2011) results with a bimodal correlation as well as a Frechet fit for the field data.

The data sets from the field and laboratory calibrations were fitted with (I) a bimodal function containing a linear raising (Equation [2a]) and a power law falling limb (Equation [2b]) and (II) a Frechet distribution (Equation [3]), which was already successfully applied by Wyss (Wys,s 2016; Wyss et al., 2016a, b), where c_1 to c_8 are the coefficients determined for each data set (Table 3).

$$K_b = c_1 \cdot D + c_2 \quad [2a]$$

$$K_b = c_3 \cdot D^{c4} \quad [2b]$$

$$K_b = c_5 \cdot c_6 \cdot c_7 \cdot c_8{}^{c_7} \left[1 - \mathrm{e}^{-\left(\frac{c_8}{D}\right)^{c7}} \right]^{c_6 - 1} \cdot D^{(c_7+1)} \cdot \mathrm{e}^{-\left(\frac{c_8}{D}\right)^{c7}} \quad [3]$$

The K_b values to be used for the typical Solis SBT operating conditions, i.e. outside the calibration tests presented herein, were determined by applying a weighted averaging method based on the GSD of the Solis natural sediment (Table 1) using Eqs. [2a], [2b] and [3] with the corresponding coefficients c_1 to c_8. Considering only the expected GSD at Solis, K_b values determined from the field calibration vary from 9.6 to 10.8 1/kg, which are comparable to those obtained from the laboratory calibration tests (Table 3). The K_b values determined from Morach's (2011) test data are 10 to 20% higher than those from the other two calibrations (Table 3). This difference is attributed to different impulse threshold values among the calibration tests, i.e. 0.2 V for Morach (2011) and 0.1 V for the other two calibrations. Therefore, these results are only used for a plausibility check confirming the field results. Finally, K_b = (9.6+10.8)/2 = 10.2 1/kg, i.e. the averaged K_b from the field calibration, is used for the Solis SBT SPGS.

The bimodal (Eqs. [2a] and [2b]) and the Frechet fits (Eq. [3]) were also applied to the GSD of Test 3 (Figure 6a) to verify the applicability of the weighted averaging method. The calculated K_b values for Test 3 are 5.1 1/kg and 5.8 1/kg and deviate by only 1 and 15%, respectively, from K_b = 5.05 1/kg directly obtained from the field calibration (Table 2). This result confirms that for a given GSD the method using either bimodal or Frechet fits results in a good prediction of K_b.

Table 3. Bimodal and Frechet fits for the field and laboratory calibration as well as for Morach's (2011) data describing the correlation between K_b and D with the corresponding coefficients of determination and resulting weighted averaged K_b for the expected GSD in Solis (Table 1)

	Bimodal fit							Frechet fit					
	Linear fit			Power fit									
	c_1	c_2	R^2	c_3	c_4	R^2	K_b (1/kg)	c_5	c_6	c_7	c_8	R^2	K_b (1/kg)
Field	0.50	-6.7	0.92	175	-0.66	1.0	9.6	15'000	0.044	1.85	48	0.93	10.8
Lab	0.61	-11.4	0.98	344	-0.79	0.90	10.1	7'800	0.054	2.77	43	0.98	10.7
Morach	0.90	-13.8	0.99	367	-0.81	0.91	12.2	2'200	0.279	2.4	40	0.99	11.6

The effect of geophone inclination on the calibration coefficient K_b is analyzed by comparing the present laboratory and field data as well as Morach's (2011) data (10° inclination) with the data from Rickenmann et al. (2013) (approximately 0° inclination). In Figure 9 the K_b values of the particles with D > 16 mm are plotted as a function of average flow velocities. Rickenmann et al. (2013) data feature a decreasing trend with increasing flow velocity, whereas the rest of the data does not show a velocity dependency. This difference can be attributed to the geophone inclination. However, to support this hypothesis, further tests with different relative grain submergence, grain size, sediment transport rates and impulse counting thresholds values are required.

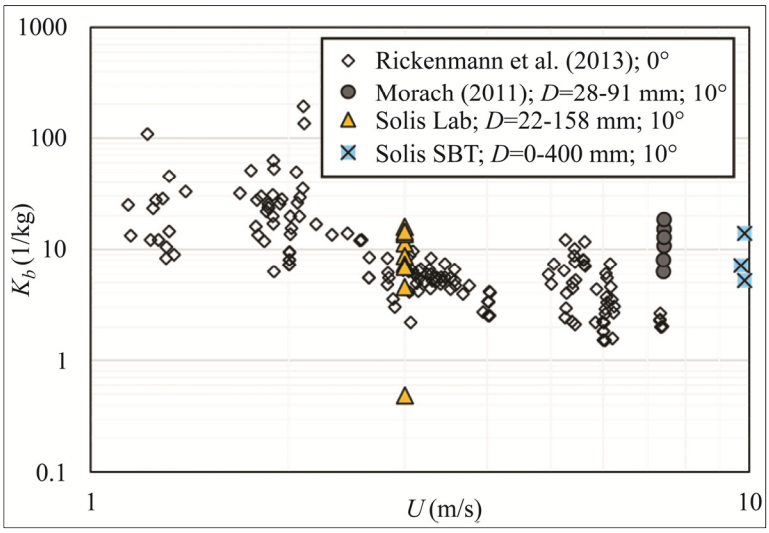

Figure 9. K_b as a function of mean flow velocity and geophone inclination; data from Rickenmann et al. (2013), Morach (2011) and from laboratory as well as field calibration experiments for the Solis SBT

4 CONCLUSIONS

A Swiss plate geophone system (SPGS) at Solis SBT was calibrated with three sediment size classes under field conditions. This system differs from the typical SPGS applications by an inclination of 10° against the bottom slope. The results are compared with those from two laboratory calibration tests with the same inclination and literature data for approximately 0° inclination slightly varying depending on the river bed slope. The calibration coefficient K_b obtained from the laboratory and field tests did not show any dependency on averaged flow velocity, while the literature values indicate a decreasing trend with increasing flow velocity. This leads to a general conclusion that the geophone inclination affects K_b. A comparison between the laboratory and field tests reveals that K_b varies with particle size, relative particle submergence and hydraulic conditions. Therefore, a field calibration of the SPGS is recommended to limit the uncertainties in bed load transport prediction. Furthermore, the weighted averaging method based on GSD is recommended to determine K_b.

The presented results are site-dependent and are only valid for the Solis SBT conditions and SPGS configuration. Based on the results of the laboratory and field calibrations, K_b = 10.2 1/kg was found for the geophone system at the Solis SBT. To improve the accuracy of the calibration, further tests with more uniform and mixed sediment samples and a range of sediment transport rates similar to typical SBT operation are needed.

ACKNOWLEDGEMENTS

The authors thank *swisselectric research*, *cemsuisse*, the Swiss Federal Office of Energy SFOE and Fondazione Lombardi Ingegneria for the financial support. Further thanks go to the staff of the electric power company of Zurich *ewz* and of the Swiss Federal Railways *SBB* for their purposeful and straightforward support during the planning and execution of this research project. This project is embedded into the framework of the Swiss Competence Center of Energy Research – Supply of Electricity (SCCER-SoE).

REFERENCES

Auel, C., Boes, R., Ziegler, T. & Oertli, C. (2011). Design and Construction of the Sediment Bypass Tunnel at Solis. *Hydropower and Dams* 3, 62-66.

Boes, R.M., Auel C., Hagmann, M. & Albayrak I. (2014). Sediment Bypass Tunnels to Mitigate Reservoir Sedimentation and Restore Sediment Continuity. *Proceedings of International River flow Conference* (A. J. Schleiss et al., eds.), Lausanne, Switzerland, 221-228.

Chiari, M., Berktold, M., Jäger, G. & Hübel, J. (2016). Geschiebemessstelle im Suggadinbach (Vorarlberg) ('Bedload monitoring staion at Suggadinbach (Vorarlberg)'). *Feststofftransport und Sedimentmanagement* (Sediment trasnport and sediment management'). Verien der Diplomingenieure der Wildbach und Lawinenverbauung Österreichs, 50-58.

Facchini, A., Siviglia, A. & Boes, R.M. (2015). Downstream Morphological Impact of a Sediment Bypass Tunnel - Preliminary Results and Forthcoming Actions. *Proceedings of First International Workshop on Sediment Bypass Tunnels*, VAW-Mitteilungen 232 (R. Boes, ed.), VAW, ETH Zurich, Switzerland: 137-146.

Fehr, R. (1987). *Geschiebeanalysen in Gebirgsflüssen ('Bed load analysis of Mountain Rivers')*. VAW-Mitteilungen 92 (D. Vischer, ed.), VAW ETH Zurich, Switzerland.

Fukuda, T., Yamashita, K., Osada, K. & Fukuoka, S. (2012). Study on Flushing Mechanism of Dam Reservoir Sedimentation and Recovery of Riffle-Pool in Downstream Reach By a Flushing Bypass Tunnel. *Proceedings of International Symposium on Dams for a changing World*, Kyoto, Japan.

Fukuroi, H. (2012). Damage from Thyphoon Talas to Civil Engineering Structures for Hydropower and the Effect of the Sediment Bypass System at Asahi dam. *Proc. International Symposium on Dams for a changing world*, Kyoto.

Hagmann, M., Albayrak, I. & Boes, R.M. (2015). Field Research: Invert material resistance and sediment transport measurements. *Proc. First International Workshop on Sediment Bypass Tunnels*, VAW-Mitteilungen 232 (R. M. Boes, ed.), ETH Zurich, Switzerland: 123-136.

Jacobs, F. & Hagmann, M. (2015). Sediment Bypass Tunnel Runcahez: Invert Abrasion 1995-2014. *Proceedings of First International Workshop on Sediment Bypass Tunnels*, VAW-Mitteilungen 232 (R. M. Boes, ed.), Zurich, Switzerland: 211-222.

Kantoush, S.A. & Sumi, T. (2010). *River Morphology and Sediment Management Strategies for Sustainable Reservoir in Japan and European Alps*. Annuals of Disaster Prevention Research Institute.

KEPCO (2012). *Sediment Bypass System at Asahi Dam*, Powerpoint Presentation 12.06.2012, Japan. The Kansai Electric Power Co. (KEPCO).

Kondolf, G.M., Gao, Y., Annandale, G.W., Morris, G.L., Jiang, E., Zhang, J., Cao, Y., Carling, P., Fu, K., Guo, Q., Hotchkiss, R., Peteuli, C., Sumi, T., Wang, H.W., Wang, Z., Wie, Z., Wu, B., Wu, C. & Yang, C.T. (2014). Sustainable Sediment Management in Reservoirs and Regulated Rivers: Experiences from Five Continents. *Earth's Future* 2(5), 256-280.

Koshiba, T., Auel, C., Tsutsumi, D., Kantoush, S. & Sumi, T. (2017). Application of an Impact Plate - Bedload Transport Measuring System for High-Speed Flows. *International Journal of Science and Research - Special Issue from the Interntational Symposium on River Sedimentation*, Submitted.

Martin, E.J., Doering, M. & Robinson, C.T. (2015). Ecological Effects of Sediment Bypass Tunnels. *Proceedings of First International Workshop on Sediment Bypass Tunnels*, VAW-Mitteilungen 232 (R. Boes, ed.), VAW, ETH Zurich, Switzerland, 147-156.

Morach, S. (2011). Geschiebemessung mittels Geophonen bei hohen Fliessgeschwindigkeiten - Hydraulische Modellversuche ('Bedload transport measurement at high flow velocities - hydraulic model tests'). *Master Thesis*, VAW, ETH Zurich, Switzerland.

Müller, B. & Walker, M. (2015). The Pfaffensprung Sediment Bypass Tunnel: 95 Years of Experience. *Proc. First International Workshop on Sediment Bypass Tunnels*, VAW-Mitteilungen 232 (R. Boes, ed.), VAW, ETH Zurich, Switzerland, 247-258.

Oertli, C. & Auel, C. (2015). Solis Sediment Bypass Tunnel: First Operation Experiences. *Proceedings of First International Workshop on Sediment Bypass Tunnels*, VAW-Mitteilungen 232 (R. Boes, ed.), VAW, ETH Zurich, Switzerland: 223-234.

Rickenmann, D. (1997). Sediment Transport in Swiss Torrents. *Earth Surface Processes and Landforms,* 22(10), 937-951.

Rickenmann, D. & McArdell, B.W. (2007). Continuous Measurement of Sediment Transport in the Erlenbach Stream Using Piezoelectric Bedload Impact Sensors. *Earth Surface Processes and Landforms,* 32(9), 1362-1378.

Rickenmann, D. & McArdell, B.W. (2008). Calibration of Piezoelectric Bedload Impact Sensors in the Pitzbach mountain stream. *Geodinamica Acta*, 21(1-2), 35-51.

Rickenmann, D. & Fritschi, B. (2010). Bedload Transport Measurements Using Piezoelectric Impact Sensors and Geophones. *Proceedings International Bedload-Surrogate Monitoring Workshop*, U.S. Geological Survey Scientific Investigations Report, 2010-5091.

Rickenmann, D., Turowski, J. M., Fritschi, B., Klaiber, A. & Ludwig, A. (2012). Bedload Transport Measurements at the Erlenbach Stream with Geophones and Automated Basket Samplers. *Earth Surface Processes and Landforms,* 37(9), 1000-1011.

Rickenmann, D., Turowski, J.M., Fritschi, B., Wyss, C., Laronne, J., Barzilai, R., Reid, I., Kreisler, A., Aigner, J., Seitz, H. & Habersack, H. (2013). Bedload Transport Measurements with Impact Plate Geophones: Comparison of Sensor Calibration in Different Gravel-Bed Streams. *Earth Surface Processes and Landforms,* 39(7), 928-942.

Rickenmann, D., Wyss, C.R., Turowski, J.M., Weitbrecht, V. & Boes, R.M. (2014). Geschiebemessungen mit Geophonsensoren: Ableitung der Kalibrierungsfunktion durch Messungen im Feld und Labor. ('Bedload transport measurement by geophon sensors: derivation of the calibration function by field and laboratory measurements'). *Proceedings Wasserbausymposium "Wasserbau und Flussbau im Alpenraum"*, VAW-Mitteilung 227, ETH Zurich, Switzerland, 355-366.

Sumi, T., Okano, M. & Takata, Y. (2004). Reservoir Sedimentation Management with Bypass Tunnels in Japan. *Proceedings of 9th International Symposium on River Sedimentation*, Yichang, 1036-1043.

Syvitski, J. P.M., Vörösmarty, C.J., Kettner, A.J. & Green, P. (2005). Impact of Humans on the Flux of Terrestrial Sediment to the Global Coastal Ocean. *Science,* 308(5720), 376-380.

VAW (2010). *Geschiebumleitstollen Solis - Hydraulische Modellversuche ('Bedload bypass tunnel Solis - Hydraulic modell investigation')*. VAW Bericht 4269, ETH Zürich, Switzerland.

Wyss, C.R., Rickenmann, D., Fritschi, B., Weitbrecht, V. & Boes, R.M. (2014). Bedload Grain Size Estimation from the Indirect Monitoring of Bedload Transport with Swiss Plate Geophones at the Erlenbach Stream. *Proceedings of River Flow 2014*, Lausanne, 1907-1912.

Wyss, C.R., Rickenmann, D., Fritschi, B., Turowski, J.M., Weitbrecht, V. & Boes R.M. (2015). Measuring Bedload Transport Rates by Grain-Size Fraction Using the Swiss Plate Geophone Signal at the Erlenbach. *Journal of Hydraulic Engineering,* 142(5), 1-11.

Wyss, C.R. (2016). Sediment Transport Measurements with Geophone Sensors. VAW-Mitteilungen 234 (R. M. Boes, ed.), Also Published as a *Doctoral Thesis*. Nr. 23353, ETH Zurich. ETH Zurich, Switzerland.

Wyss, C.R., Rickenmann, D., Fritschi, B., Turowski, J.M., Weitbrecht, V. & Boes R.M. (2016a). Laboratory Flume Experiments With the Swiss Plate Geophone Bed Load Monitoring System: 1. Impulse Counts and Particle Size Identification. *Water Resources Research,* 52(10), 7744-7759.

Wyss, C.R., Rickenmann, D., Fritschi, B., Turowski, J.M., Weitbrecht, V., Travaglini, E., Bardou, E. & Boes, R.M. (2016b). Laboratory Flume Experiments with The Swiss Plate Geophone Bed Load Monitoring System: 2. Application to field sites with direct bed load samples. *Water Resources Research,* 52(10), 7760-7778.

ESTIMATION OF SEDIMENT INFLOW INTO A RESERVOIR USING COMBINED APPROACH OF RAINFALL – RUNOFF MODELLING AND SEDIMENT TRANSPORT ASSESSMENT

AZWIN ABDUL RAZAD[(1)], LARIYAH MOHD SIDEK[(2)], JANSEN LUIS ALEXANDER[(3)] & THAMER AHMED MOHAMED[(4)]

[(1)] TNB Research Sdn Bhd, No. 1, Lorong Air Hitam, Kawasan Institusi Penyelidikan Bangi, 43000 Kajang, Selangor
azwin.razad@tnb.com.my
[(2)]Sustainable Technology & Environment Group, Institute for Energy Infrastructure, University Tenaga Nasional, Selangor, Malaysia
[(3)] Major Project Dept, Energy Ventures Division, Tenaga Nasional Berhad
[(4)] Civil Engineering Dept, Engineering Faculty, Universiti Putra Malaysia

ABSTRACT

Reservoir sedimentation can affect both operation and safety of dam if it is not properly managed. It adversely affects the multiple functions of dam and has become one of the major concerns for its owner and operator. This study describes the attempt to predict total inflow of sediment into the Ringlet Reservoir in Cameron Highlands using integrated approach of catchment rainfall runoff modeling and sediment rating curves derived from field sampling. MIKE NAM are used to simulate the runoff generated from the Cameron Highlands' catchment. This model is developed, calibrated and validated using the flow data of Sg Bertam. Field sampling is conducted to measure the Total Suspended Solids (TSS), Bed Load and grab samples at major rivers of the catchment. Sediment rating curves are developed to describe the relationship between the total sediment load and discharge. The available sampling data, hydrology records and catchment ratio are used in determining the total sediment inflow into Ringlet Reservoir, which is between 150,000 m^3/year to 200,000 m^3/year. This information is useful for the reservoir manager to plan for the most suitable sediment management.

Keywords: Reservoir sedimentation; rainfall runoff model; sediment rating curve; dam; field sampling.

1 INTRODUCTION

Reservoir sedimentation can affect both operation and safety of dam if it is not properly managed. It adversely affects the multiple functions of dam and has become one of the major concerns for its owner and operator. Storage loss reduces the reservoir capacity hence affecting the available storage for power generation and flooding. Excessive sedimentation could also affect dam structural stability as well as disturbing the ecosystem that it supports; through the reduction of light penetration and sediment being the pollutant carrier. Abrasive sediment particles could also affect the mechanical equipment, increasing its rate of wear and tear (Abdul Razad et al., 2011). Although the storage loss is undeniably anticipated by the reservoir operators, reservoirs worldwide are experiencing accelerated sedimentation and losing the storage capacity rapidly, possibly as fast as 1% per year (Mahmood, 1987). Sedimentation in reservoir is characterized by the geometry of the reservoir, operation rules, inflow, and sediment material which govern the reservoir trapping efficiencies (Borland, 1960; Strand, 1982; Lara, 1962; Brune, 1953; Churchill, 1948). Large initial storage volumes and erosion control have traditionally been recommended to reduce sediment inflow to reservoir, however, these alone could not achieve the required reservoir stabilization (Morris, 1998). Furthermore, many erosion control programs are poorly implemented due to many reasons, and fail to achieve the desired reductions in sediment yield.

To design an effective sediment management, it is important to accurately estimate sediment load originating from the catchment and transported by the river system, by means of comprehensive monitoring, survey and combination of modelling works.

2 PREDICTION OF SEDIMENT INFLOW

Prediction of sediment inflow is predominantly based on reservoir survey information, obtained from the relevant bathymetry survey using echo sounding technique. Storage is calculated using either Triangular Irregular Network (TIN), simplified using GIS software or conventional cross section method. Difference in storage indicates sedimentation rate, provided that information on sediment removal via dredging, flushing or others is known. However, this method does not provide spatial and temporal variation of sediment inflow, but rather useful for long term sediment management and planning. The use of soil loss equation such as Universal Soil Loss Equation (USLE) is feasible to estimate potential erosion generated within the catchment, but the rate needs to be multiplied by the estimated Sediment Delivery Ratio (SDR) to determine the sediment yield. In Malaysian context, Design Guides for Erosion and Sediment Control in Malaysia (DID, 2010) is

available for estimation of potential erosion and sediment yield but it requires site verification to reflect the actual site condition. Another common method to predict sediment inflow is by using the trap efficiency concept, which is defined as the ratio between sediment deposition inside the reservoir and sediment inflow into the reservoir. This is further described by Brune (1953) and Churchill (1948).

In view of the temporal variation of the sediment load, sediment monitoring is preferred to estimate the sediment inflow. Sediment load is much higher during storm event, and can multiply by many folds in comparison to that of normal flow. Sediment monitoring consists of measuring the concentration of sediment and discharge to develop the sediment rating curves and if it is done on a continuous basis, information obtained can be used to generate the total sediment inflow on a yearly basis. In the event that continuous sediment data is not available, extrapolation or interpolation can be applied to compute the sediment load then applied to a much longer discharge record to estimate long-term sediment yield. However, monitoring sediment flow data over a long period and periodic reservoir survey are exhaustive and expensive (Silva et al., 2007). Therefore, the concept of modelling becomes useful to overcome the previous shortcomings. Models can be divided into empirical, conceptual and physical-based. Erosion, sediment and nutrient transport models generally consist of both hydrological and nutrient and sediment transport components. (Merritt et al., 2006). Bedri et al. (2014) developed the water quality prediction system which comprises an integrated catchment-coastal model and water quality database. Choudhury and Sundar Sil (2010) developed new models which combine Muskingum model and the sediment rating model leading to integrated water discharge–sediment concentration model (WSCM). In this view, the use of hydrological modelling is feasible to predict sediment inflow, provided that information on concentration – discharge is sufficient.

3 STUDY AREA

Cameron Highlands is located in the state of Pahang, near the mountain range of Peninsular Malaysia, as illustrated in Figure I. The area is famous for its active highland agriculture and tourism activities, owing to its nice and cool weather throughout the year. There are three (3) major catchments namely Bertam, Telom and Lemoi. Cameron Highlands is also a home to seven hydro power stations owned and run by the national utility company Tenaga Nasional Berhad (TNB). With the total installed capacity of 262 MW, the scheme is an important asset to TNB due to it being one of the sources of green energy (Abdul Razad et al., 2011).

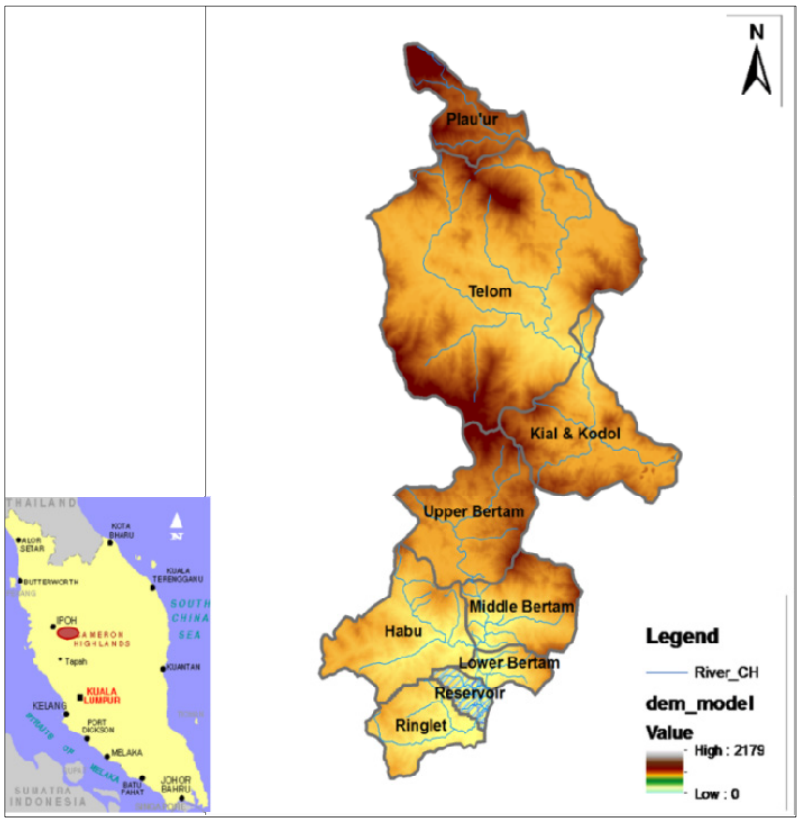

Figure 1. Catchment of Cameron Highlands.

Ringlet Reservoir is 0.5km^2 multipurpose reservoir located in Cameron Highlands, which is used to regulate flow from the upper catchment for hydropower generation at Jor Power Station. The reservoir has the original design storage of 6.7 million m^3, of which 2 million m^3 is dead storage and 4.7 million m^3 is live storage. The reservoir and its Sultan Abu Bakar Dam also serves as a flood control in the downstream area of

Bertam Valley, a home to almost 3000 residents. The total catchment area that drains into Ringlet is 183km^2, divided into two (2) major catchment of Bertam and Telom. Owing to its topography, 26% of the terrain of Cameron Highlands is steeper than 25º and 60% of the land is steeper than 20° (Abdul Razad et al., 2016). Prior to the completion of the hydropower scheme, most of the areas in Cameron Highlands were covered in forest and the sediment concentrations in the rivers were not very high. It was estimated that the Ringlet Reservoir would have a useful life of approximately 80 years, with no special provisions to cope with sedimentation (Tenaga Nasional Berhad, 2000). It has been reported that Ringlet Reservoir has suffered storage reduction up to 53% of its storage due to sedimentation since its operation in 1963 (TNB Hidro, 2006). Study by various researchers specific to Cameron Highlands indicated critical soil loss and sedimentation rate, ranging from 150,000 m^3/year up to 530,000 m^3/year (Adroit, 2004; Toriman et al., 2010; TNB Hidro, 2006). Significant changes in land use within the catchment over the years associated with the high intensity farming and urban development on the steep valley slopes could have been the major contributor to the increasing rate of erosion and sedimentation from the catchment, which is eventually deposited into Ringlet Reservoir (Abdul Razad et al., 2016). Figure 1 illustrates the location of the study area and its contributing catchment.

During the course of a year, the Cameron Highlands' catchment experiences two rainy seasons associated with southwest (April to May) and northeast (September to November) monsoons. Cameron Highlands receives an average annual rainfall of more than 2,800 mm. January and February are the driest month with rainfall amounts of 100 mm per month while October and November are the wettest with rainfall amounts of 350 mm per month (Cranbrook and Edwards, 1994). Changes in land use in Cameron Highlands have been significant from 1947 to 2010 with forest area reducing by 33%, while market gardening rose by 18%. Agriculture is the second major land use, represented by 23% of the total land area. Catchment urbanisation has increased by 4% since 1947. Tea and scrub forest remain fairly constant at about 7% of the total catchment area (Abdul Razad et al., 2011). Land use evolution between 1947 and 2010 in Cameron Highlands is shown in Figure 2.

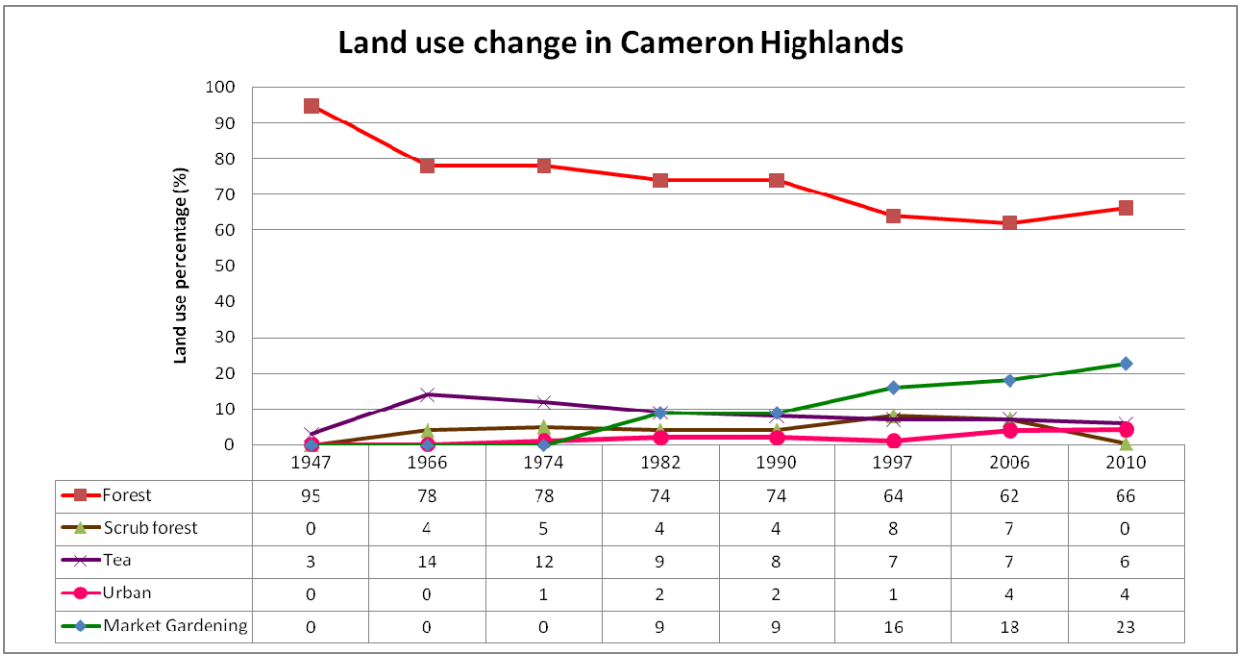

	1947	1966	1974	1982	1990	1997	2006	2010
Forest	95	78	78	74	74	64	62	66
Scrub forest	0	4	5	4	4	8	7	0
Tea	3	14	12	9	8	7	7	6
Urban	0	0	1	2	2	1	4	4
Market Gardening	0	0	0	9	9	16	18	23

Figure 2. Land use changes in Cameron Highlands' catchment.

4 METHODOLOGY

4.1 Rainfall runoff modelling

The objective of the hydrological assessment is to determine the hydrological characteristics of the rivers located within the study area. MIKE NAM rainfall-runoff analysis was used to derive the runoff hydrographs generated by the contributing sub-catchments of Cameron Highlands. Only the Bertam catchment was considered in the rainfall-runoff modelling. However, water channeled through the Telom tunnel (originating from the Telom catchment) was added as a constant source discharge in the hydraulic model. MIKE NAM is a parametric, lumped hydrologic model that simulates the land phase of the hydrologic cycle, of which the meteorological inputs to the model such as daily rainfall and daily evapotranspiration were used. Thiessen polygon was used to generate the areal rainfall for each sub-catchments. The general structure of the model with its four different and mutually interrelated storages and their corresponding flows is shown in Figure 3.

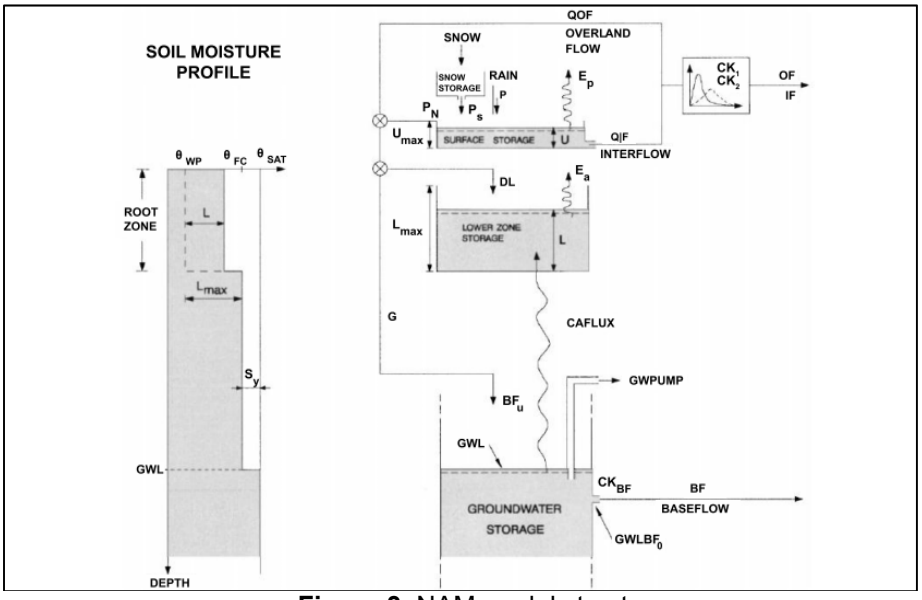

Figure 3. NAM model structure.

MIKE NAM model was prepared by digitizing the catchment of Cameron Highlands into several sub-catchments using GIS. Input data required to set up MIKE NAM include land use, rainfall, evaporation, topography, and streamflow data for calibration. In this model, at least five (5) rainfall stations and one (1) weather station located within Bertam Catchment were used, using complete ten (10) years of data available from 1999 to 2009, as shown in Figure 4. Double mass curve analysis showed straight line describing the data consistency for the model. To estimate the final NAM parameters, the model must be calibrated against the observed runoff, described by a streamflow station 6003 within Upper Bertam sub-catchment. The auto-calibration was used first followed by manual adjustment of the relevant parameters to achieve; (a) minimum error in the water balance error (%WBL) such that the average simulated agrees to the observed runoff; and (b) minimum error in the overall Root Mean Square Error (RMSE) for the entire flow spectrum to achieve overall agreement of the shape of the hydrograph, as explained by Madsen (2000; 2003). The key parameters involved in calibration are explained in Table 1.

The reliability of MIKE NAM can be evaluated based on Root Mean Square Error (RMSE) and Efficiency Index (EI) or known as Nash-Sutcliffe Efficiency (NSE) (Nash and Sutcliffe, 1970). It is important to note that to achieve good calibration, a good rainfall dataset representative of the sub-catchment is needed. Depending on the aim of the model, calibration on event-basis as well as long term period would enhance the reliability of the model. Once the model was calibrated, MIKE NAM was used to simulate the inflows from various sub-catchments, using the calibrated parameters. Land use differences were used to determine the suitable NAM parameters.

Table 1. Associated NAM parameters.

Parameters	Description	Lower Bound	Upper Bound	Final Value	Effect if increases
U_{max} (mm)	Maximum water content in surface storage	10	20	15.1	Volume decreased Peak runoff decreased
L_{max} (mm)	Maximum water content in the root zone storage	100	300	171	Volume decreased Peak runoff decreased
CQOF	Overland flow runoff coefficient	0.1	1	0.132	Volume increased Peak runoff increased
CKIF (hr)	Time constant for interflow	200	1000	200	Not tested
$CK_{1,2}$ (hr)	Time constant for routing interflow and overland flow	1	50	4.11	Hydrograph expands
TOF	Root zone threshold value for overland flow	0	0.99	0.0128	Peak runoff decreased Volume decreased
TIF	Root zone threshold value for interflow	0	0.99	0.409	
CKBF (hr)	Baseflow time constant	1000	4000	2301	Baseflow decreased

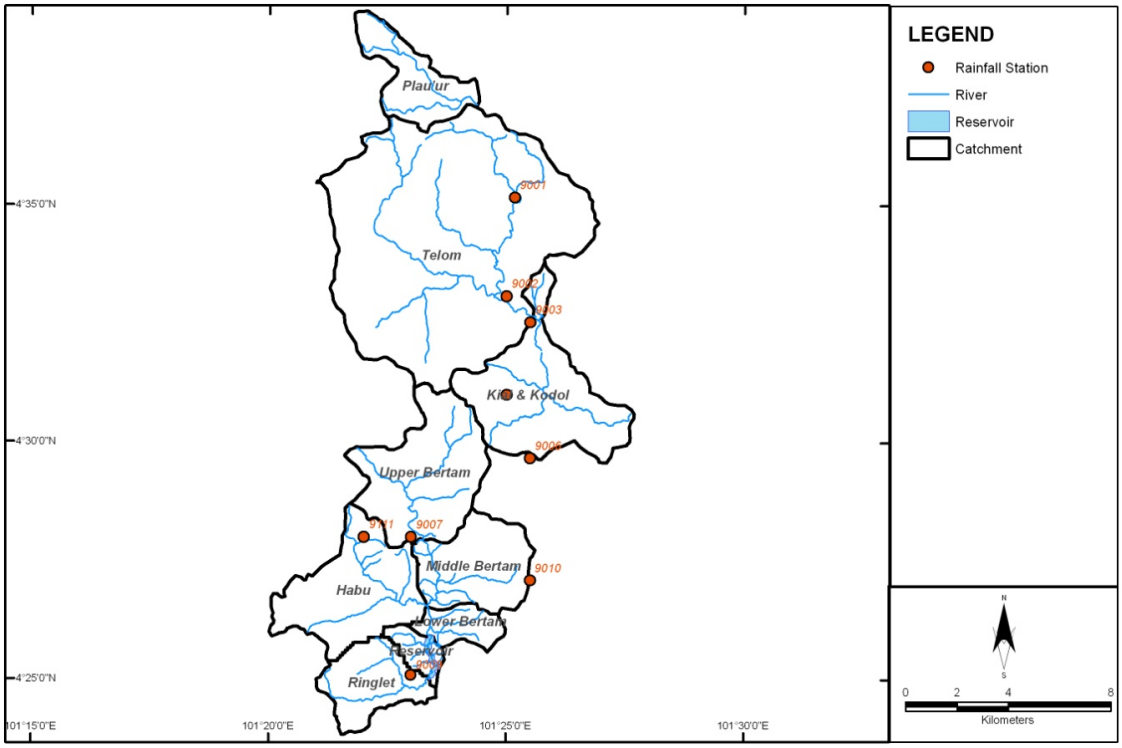

Figure 4. Rainfall stations used in the model.

4.2 Sediment rating curves

Comprehensive sediment monitoring was conducted on major rivers such as Sg Bertam, Sg Habu and Sg Ringlet, by measuring total suspended solids (TSS), bed load and discharge, since 1999 until 2009. Bed material was collected using Van Veen gab sampler and analysed using particle size distribution. Bed load was sampled using Helley Smith sampler and analysed in the laboratory using drying and weighing technique. US DH-48 or US DH-59 Depth Integrating Suspended Sediment Sampler was used to obtain the TSS samples, and analysed in the laboratory according to APHA – 2540D. Attempts were made to capture samples during heavy flow event, as most sediment is transported in magnitude far greater than during the normal flow. In general, the observed TSS in rivers of Cameron Highlands was generally above that of the suggested limit for Class II (50 mg/l) and easily exceeded 1000 mg/L during heavy flow. Sediment rating curves were derived to obtain the relationship between the discharge (Q) in m^3/s and sediment load (Qs) in kg/s, which can be described as a power function, power function with constant (Asselman, 2000) and linear function (Tananaev, 2014). Among all sediment rating curves, the power function (refer Equation 1) is the most common function to describe the average relation between streamflow (Q) and suspended sediment concentration (SSC) or sediment load for a certain location (Wang et al., 2013). The rating curves were derived from multiple data sets based on sampling period and compared for consistency by combining the rating curves with the discharge timeseries and annual sediment load contributed by the selected rivers. Summary of the data collected is tabulated in Table 2 below.

$$Q_s = aQ^b \quad [1]$$

Table 2. Summary of field data.

Rivers	Discharge, Q (m^3/s)	Width B, (m)	Average Slope, S0	D_{50} (mm)	Bed Load Transport, Tb (kg/s)	Suspended Load Transport, Ts (kg/s)	Total Load Transport, Tt (kg/s)
Sg. Ringlet	0.12-3.57	3-7.3	0.0037	1.2	0.003-6.217	0.001-9.326	0.014-15.543
Sg. Habu	0.69-5.84	3-7.3	0.0025	0.9	0.027-4.633	0.004-30.23	0.074-30.23
Sg. Bertam	3.23-9.16	14-16.5	0.0007	0.7	0.012-2.451	0.106-2.661	0.225-3.06

4.3 Estimation of sediment inflow

Using the rating curves derived at the sampling location and hydrographs simulated using MIKE NAM, sediment inflow from rivers namely Sg Habu, Sg Bertam and Sg Ringlet which flow into Ringlet Reservoir was calculated by multiplying the relevant discharge with the rating curves equations.

5 RESULTS AND DISCUSSION

5.1 Flow simulation from MIKE NAM

Model for Upper Bertam was calibrated with the observed discharge at Station 6003 Sg Bertam. Figure 5 and Figure 6 illustrate the simulated and observed discharge hydrographs during calibration period of 1999 to 2006. In this calibration, NSE value of 0.629, WBL percentage error of 2.4% and RMSE 0.386 were observed, which indicate good agreement between the observed and simulated runoff in terms of timing, rate and volume. The calibration parameters were then used in MIKE NAM to simulate flow from other sub-catchments, as illustrated in Figure 7.

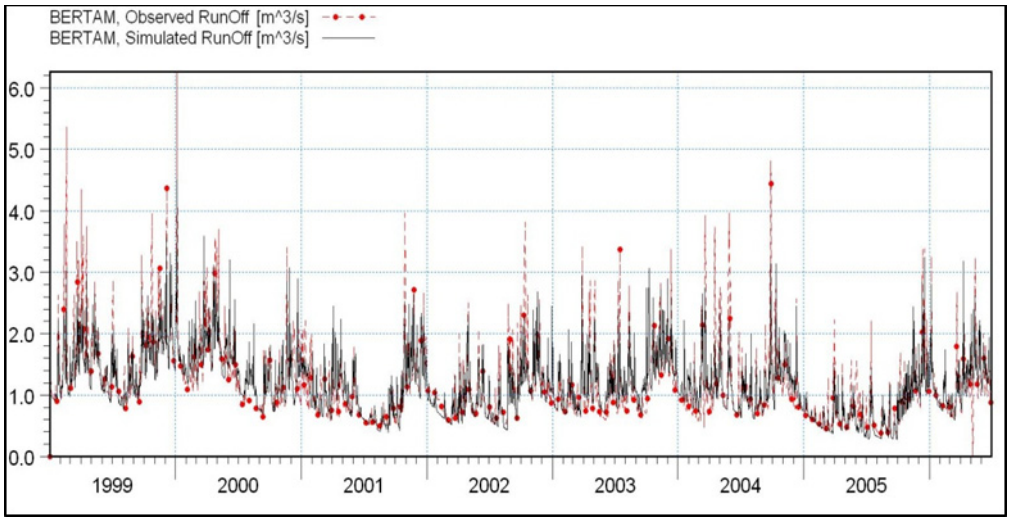

Figure 5. Observed and simulated runoff hydrograph during model calibration for upper Bertam.

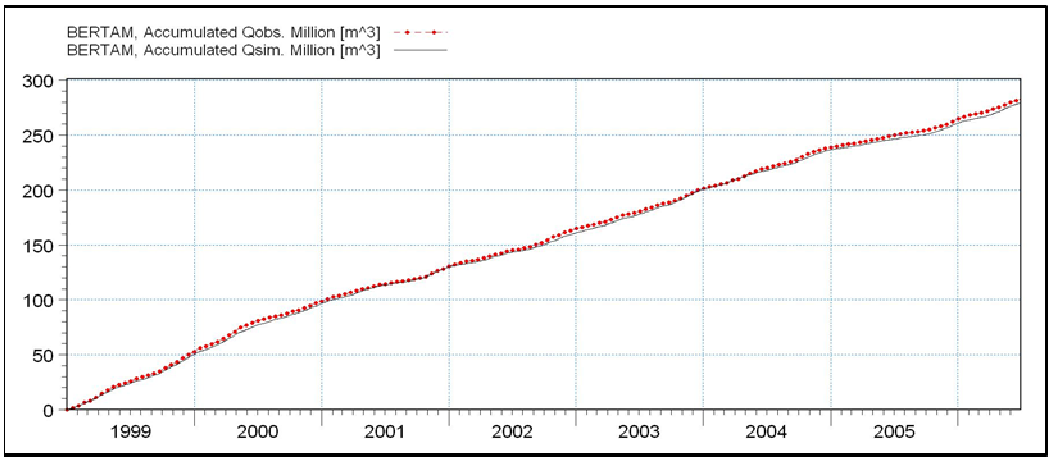

Figure 6. Observed and simulated accumulated runoff hydrograph for upper Bertam.

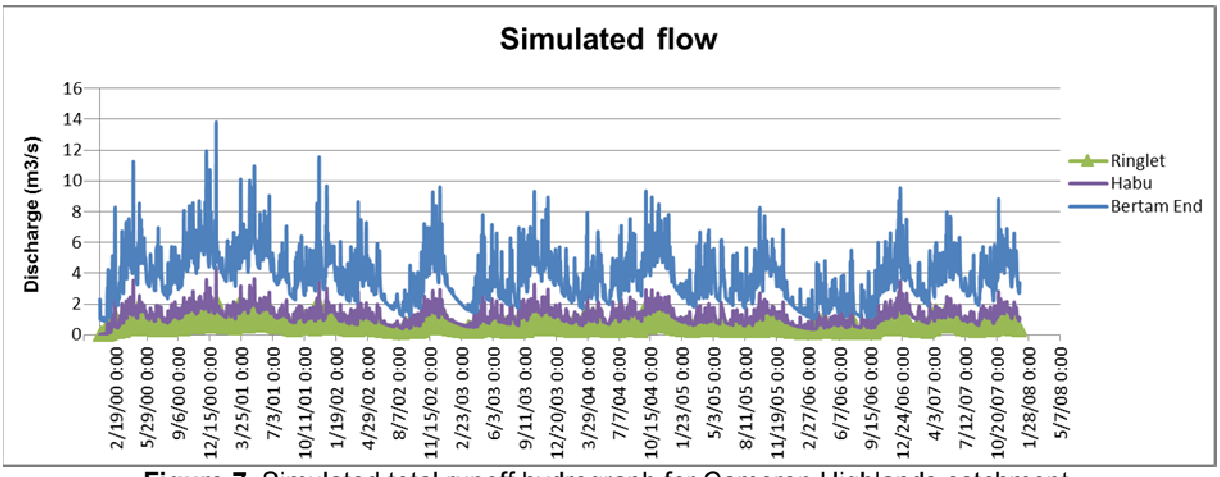

Figure 7. Simulated total runoff hydrograph for Cameron Highlands catchment.

5.2 Estimation of sediment inflow

Strong correlations exist between river discharge, TSS concentration and bed load for all rivers ($p<0.05$). The trend of sediment transport is almost identical for all rivers during low flow event but varies as the river discharge exceeded its baseflow. Rating curves developed based on sampling results using dataset from 1999 to 2009 indicated good correlation, of which $R^2 > 0.8$. Dataset 1 refers to data from 1998 to 2004, while dataset 2 refers to sampling data from 2005 to 2009. To derive a good rating curve, each data should be considered carefully prior to removing any outlier. Medium to high flow data should exhibit similar pattern of sediment transport. Figure 8, Figure 9 and Figure 10 below illustrates sediment load rating curve for Sg Ringlet, Sg Habu and Sg Bertam, respectively.

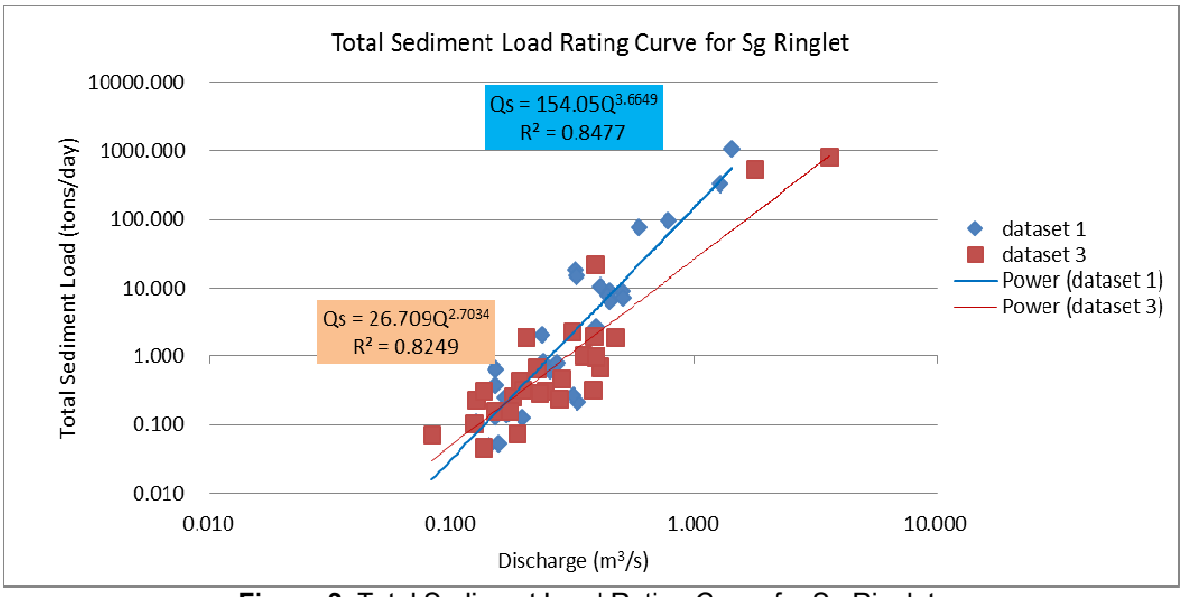

Figure 8. Total Sediment Load Rating Curve for Sg Ringlet.

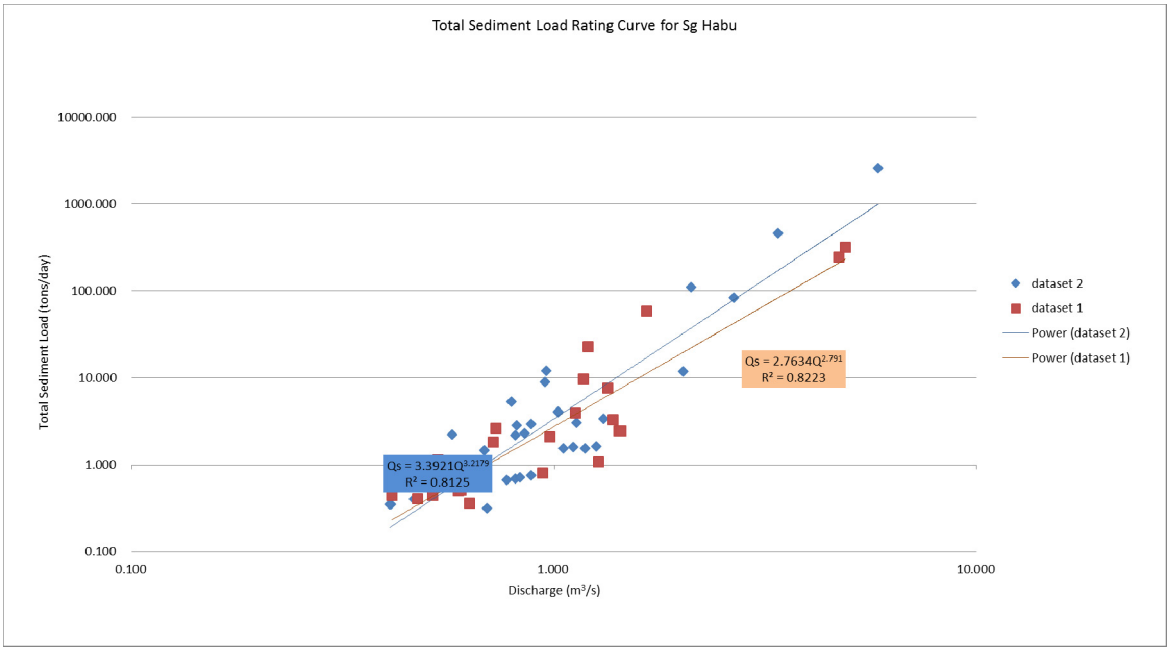

Figure 9. Total Sediment Load Rating Curve for Sg Habu.

Sediment rating curves equations were multiplied with the simulated flow of the rivers feeding into Ringlet Reservoir to obtain the total sediment load. Using the specific density of 1.62 ton/m^3, the total sediment load flowing into Ringlet Reservoir is estimated at 150,000 to 200,000 m^3/year based on the dataset range from 1999 to 2009. This should serve as an early indication on how the sediment inflow can be predicted although it is acknowledged that certain sediment transport modelling along the rivers should be undertaken.

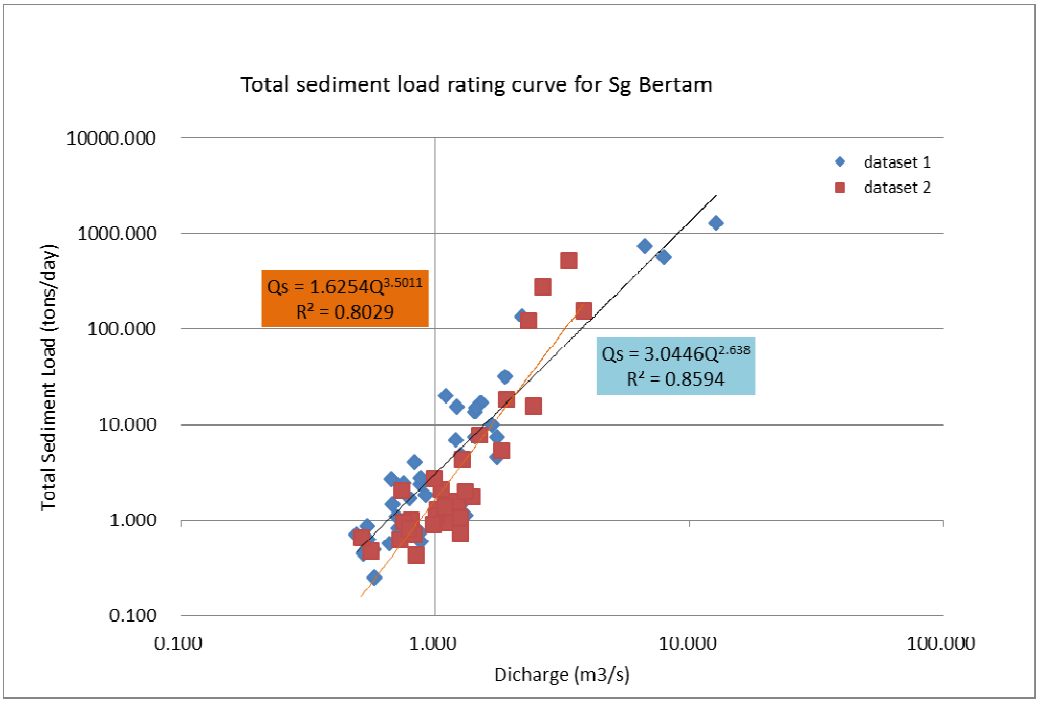

Figure 10. Total Sediment Load Rating Curve for Sg Bertam.

6 CONCLUSIONS

There are many methods capable of predicting sediment inflow into a reservoir. However, some are labour intensive and require high costs to be implemented. The use of calibrated rainfall runoff modelling such as MIKE NAM to simulate flow at relevant rivers in Cameron Highlands provides opportunity to understand the flow variations that goes into Ringlet Reservoir. The establishment of sediment rating curves at selected rivers and coupled with simulated flow is proven useful to allow estimation of sediment inflow into a reservoir. The concept is acceptable but it requires further dataset from sediment sampling and certain degree of assessment using sediment transport modelling. In summary, the total annual sediment inflow into Ringlet Reservoir is estimated to be between 150,000 m^3/year to 2000,000 m^3/year. This information is useful for the reservoir manager to plan for the most suitable sediment management.

DISCLAIMER

The information contained in this paper is purely based on research work and specifically for research purpose; it does not represent opinion of Tenaga Nasional Berhad and its subsidiaries.

ACKNOWLEDGEMENT

Author would like to express gratitude to Tenaga Nasional Berhad and TNB Research Sdn Bhd for the research fund to conduct this project.

REFERENCES

Abdul Razad, A., Abbas, A.R., Alexander, J.L. & Mohd Radzi, M.R. (2011). Design of Effective Sediment Entrapment Basin, *3rd International Conference on Managing Rivers* in the 21st Century, Penang, Malaysia.

Abdul Razad, A.Z., Alexander, J.L., Sidek, L.M. & Basri, H. (2016). Sediment Inflow Prediction towards Effective Reservoir Sedimentation Management. *International Conference on Hydropower and Dams (HYDRO 2016),* Montreaux, Switzerland.

Adroit Consulting Engineers. (2004). *A Study on Pollution Prevention and Water Quality Improvement Program of Rivers in Cameron Highlands*, Consultation Project. Adroit Consulting Engineers.

Asselman, N.E.M. (2000). Fitting and Interpretation of Sediment Rating Curves. *Journal of Hydrology*. 234, 228–248.

Bedri, Z. Corkery, A. & O'Sullivan, J.J. (2014). Integrated Catchment-Coastal Modelling System for Real-Time Water Quality Forecasts. *Environmental Modelling & Software,* 61, 458-476.

Borland, W.M. (1960). Sediment Problems of the Lower Colorado River. *Journal of Hydraulics Division*, 86(245), 61-87.

Brune, G. (1953). Trap Efficiency of Reservoirs. *American Geophysical Union*, 34(3), 407-418.

Churchill, M.A. (1948). Discussion of Analysis and use of Reservoir Sedimentation. *Federal Interagency Sedimentation Conference*, Denver, Colorado: Gottschalk, L.C., 139-140.

Choudhury, P & Sil, B.S. (2010). Integrated Water and Sediment Flow Simulation and Forecasting Models for River Reaches, *Journal of Hydrology*, 385, 313–322.

Cranbrook, E. & Edwards, D.S. (1994). *A Tropical Rainforest: The Nature of Biodiversity in Borneo and Belalong, Brunei*. First Edition, VVB Laufersweiler.

Lara, J. (1962). *Revision of Procedures to Compute Sediment Distribution in Large Reservoirs*. Denver, Colorado: Unites States Bureau of Reclamation.

Madsen, H. (2000). Automatic Calibration of a Conceptual Rainfall–Runoff Model using Multiple Objectives. *Journal of Hydrology* 235, 276-288.

Mahmood, K. (1987). *Reservoir Sedimentation: Impact, Extent and Mitigation*, Technical Paper No 71. Washington DC: The World Bank.

Merritt, W.S., Letcher, R. A. & Jakeman, A. J. (2006). A Review of Erosion and Sediment Transport Models. *Environmental Modelling & Software* 18(2003), 761–799.

Morris, G. a. (1998). *Reservoir Sedimentation Handbook: Design and Management of Dam, Reservoirs and Watersheds for Sustainable use*. New York: Mc Graw-Hill Book Co.

Silva, R.M., Santos, C.A.G. & Silva, L.P. (2007). Evaluation of Soil Loss in Guaraira Basin by GIS and Remote Sensing Based Model. *Journal of Urban Environmental Engineering,* 1(2), 44–52.

Strand, R. (1982). *Reservoir Sedimentation,* Technical Guidelines for Bureau of Reclamation. Colorado: United States Bureau of Reclamation.

Tananaev, N. I. (2014). Fitting Sediment Rating Curves using Regression Analysis: A Case Study of Russian Arctic Rivers. *Proceedings of the International Association of Hydrological Sciences*, 367, 11–14.

TNB Hidro Sdn Bhd. (2006). *IEA Hydropower Implementing Agreement Annex VIII - Hydropower Good Practices: Environmental Mitigation Measures and Benefits Case study 04-03:* Reservoir Sedimentation - Cameron Highlands Hydroelectric Scheme, Malaysia, TNB Hidro Sdn Bhd.

Wang, J., Ishidaira, H., Sun, W. & Ning, S. (2013). Development and Interpretation of New Sediment Rating Curve Considering the Effect of Vegetation Cover for Asian basins. *The Scientific World Journal*, 2013, 1-9.

Proceedings of the 37th IAHR World Congress
August 13 – 18, 2017, Kuala Lumpur, Malaysia

INVESTIGATION OF TURBIDITY CURRENT VENTING FOR TWO DIFFERENT RESERVOIR BED SLOPES

SABINE CHAMOUN[1], GIOVANNI DE CESARE[2] & ANTON J. SCHLEISS[3]

[1,2,3] Laboratory of Hydraulic Constructions (LCH), Ecole Polytechnique Fédérale de Lausanne (EPFL), Lausanne, Switzerland, sabine.chamoun@epfl.ch

ABSTRACT

Reservoirs represent an important source of energy that should be preserved and sustained. However, the lifetime of reservoirs is being reduced due to natural processes such as sedimentation. To face this problem, different sediment mitigation techniques are employed in numerous reservoirs. These techniques sometimes require the complete emptying of reservoirs. In the particular case where sedimentation is due to the presence of turbidity currents, the most adequate technique for the evacuation of sediments is by venting these currents through bottom or low-level outlets. Venting is investigated in the present work using an experimental model where turbidity currents are generated and vented under different conditions through a bottom outlet. Several measuring instruments are used to monitor the turbidity currents and two bed slopes are tested. The effect of the slope variation on the release efficiency of venting is studied. Additionally, venting is shown to induce no retrogressive erosion. Results from this research can provide useful input for reservoir operators where sedimentation occurs.

Keywords: Reservoir sediment management; turbidity currents; venting; bottom outlets; slopes.

1 INTRODUCTION

In the last decades, thousands of reservoirs were built around the world due to their multifunctional use. Some reservoirs have a long lifetime and serve efficiently for decades or centuries. However, the efficiency of other reservoirs is endangered by processes hindering their sustainability such as sedimentation. The latter is by definition the transport and deposition of sediments from watersheds into reservoirs during flood events. In the long term, sedimentation reduces the storage capacity of the reservoir, blocks and erodes hydraulic machinery and causes the impoverishment of the downstream river in essential sediments for fish habitats (Kantoush and Sumi, 2010). To reduce the impact of sedimentation, many techniques are being tested and applied worldwide. Some methods consists on managing sediments in the watershed such as reforestation, bypassing etc. Other techniques are applied in the reservoir by drawing down the water level causing retrogressive erosion (i.e., pressurized or free-flow flushing) or by mechanically dredging sediments from the reservoir into the downstream river (Brandt, 2000).

However, in some cases, the transported sediments form sediment-laden currents called turbidity currents. The latter are a type of density current, advancing because of density differences with the clear water of the reservoir (Fan and Morris, 1992). Due to their high sediment concentration, turbidity currents plunge below the clear water surface of the reservoir and can advance along the thalweg until reaching the dam structure. In order to evacuate the sediments introduced by turbidity currents into reservoirs, low-level outlets or intakes should be used to vent the currents once they reach the dam. If no outlet structures are present/operated, the turbidity current hits the dam and forms a muddy lake before settling and filling up the reservoir in the vicinity of the dam. The sediments reaching the dam are generally very fine (i.e., silt and clay). They can solidify and block outlets if they are left to deposit. Therefore, the turbidity current should be ideally transited downstream while it is reaching the dam and not after the deposition of the sediments.

Venting of turbidity currents, if performed under controlled and optimal conditions, can be very beneficial both economically and ecologically. It allows the restoration of the downstream river conditions by providing the required fine sediments while using relatively small release discharges, leading to low water losses. However, venting of turbidity currents requires good knowledge of both operational conditions and turbidity currents' dynamics. Despite the fact that venting is applied in reservoirs around the world (Chamoun et al., 2016a), dam operators are still lacking considerable information that allows them to optimize the release efficiency during venting operations. Several researchers discussed venting turbidity currents but very few investigated this technique quantitatively (Fan, 1986; Lu, 1992; Lee et al., 2014; Chamoun et al., 2017;). The most influential parameters are nevertheless known due to field investigation (Morris and Fan, 1997). In this paper, venting of turbidity currents is investigated using an experimental model. Two bed slopes are tested. The generated turbidity currents are firstly described and characterized. Then, the effect of the slope variation on the efficiency of venting is evaluated.

The experimental model is first described, followed by the test procedure and measuring instruments. Then, the results are discussed: velocity profiles, deposition and venting efficiencies are analyzed. Finally, conclusions and recommendations are provided.

2 EXPERIMENTAL MODEL

The experimental tests are performed in a long and narrow flume of 8.55 m length, 0.27 m width and 0.9 m height. It can be tilted from 0% to a 5% slope. In the present paper, the 2.4% and 5% slopes are discussed. As shown in Figure 1, there are three main compartments in the flume: the head tank, the main flume, and a downstream compartment. The head tank receives the sediment-water mixture from the mixing tank placed below the flume. The main flume represents the reservoir where the turbidity current advances. Finally, the downstream compartment receives the residual water that overflows the wall in order to keep the clear water level constant during the tests. A sliding gate separates the head tank from the main flume. The inlet is placed at the bottom of the sliding gate, and links the head tank to the main flume once the gate is opened. At 6.7 m from the inlet, a wall of 80 cm (for the 2.4% slope) and 92 cm (for the 5% slope) is placed and simulates the dam. It has an opening at the bottom simulating the outlet. The latter is centered on the width of the flume and has a rectangular shape (12 cm x 9 cm).

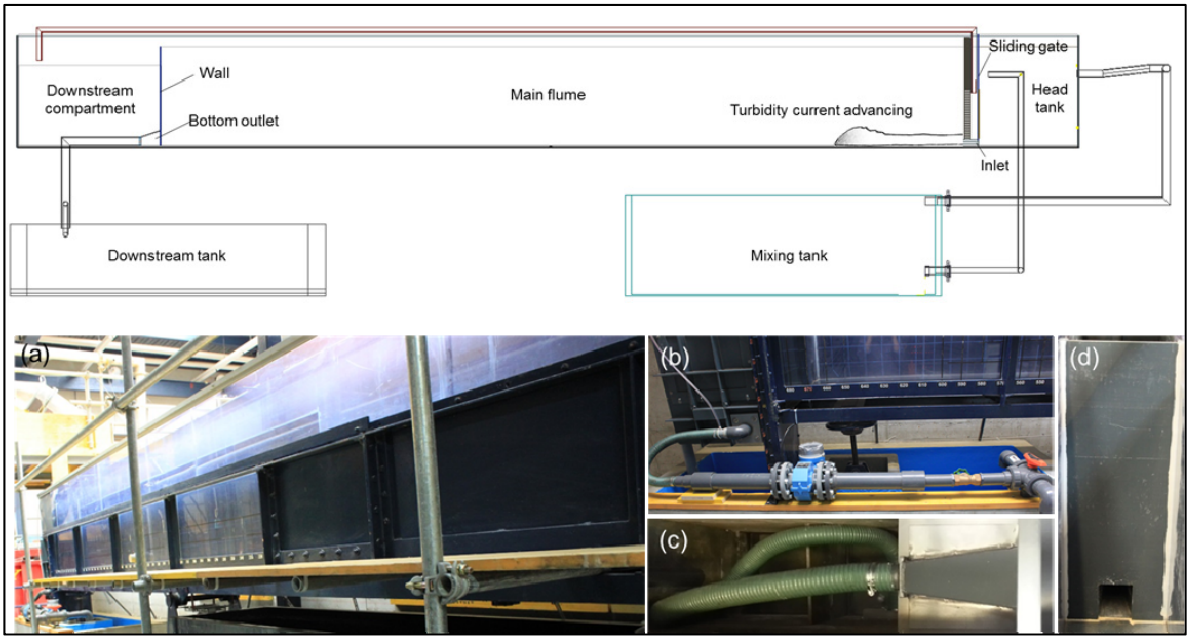

Figure 1. Annotated scheme of the experimental set-up and photos of (a) the main flume, (b) the downstream installation, (c) top view and (d) front view of the bottom outlet.

2.1 Test procedure and measurements

First of all, a water-sediment mixture is prepared in the mixing tank by adding a specific mass of sediments resulting in the required initial concentration of the current. This mixture is continuously mixed using a recirculating pump placed inside the tank. It ensures the suspension of the sediments in the water and thus keeps the concentration constant.

When the mixture is ready, it is pumped into the head tank and is recirculated between both tanks until it reaches the tested concentration in the head tank. Once this condition is fulfilled, the recirculation between the mixing tank and the head tank is stopped and the sliding gate is opened. The mixture is then directly pumped into the main flume. Due to the density difference, a turbidity current is formed and advances on the bed of the flume. The turbidity currents are continuously-fed throughout the duration of the test. Once the current reaches the bottom outlet, venting starts and the current is evacuated with a specified outflow discharge. The released mixture then reaches the downstream basin.

The sediments contained in the turbidity currents are represented by a powdery material (thermoplastic polyurethane). The particle density of the material is ρ_s = 1160 kg/m^3, the characterizing diameters are d_{10} = 66.5 µm, d_{50} = 140 µm, and d_{90} = 214 µm; d_x being the diameter for which x% of the sediments have smaller diameters. Based on the d_{50}, the settling velocity v_s was estimated by 1.5 mm (Stokes' Law and Cheng, 1997).

Care was taken to generate turbidity currents having steady and similar initial conditions (i.e., inflow discharge and concentration). Throughout the tests, different measurements were undertaken to characterize the turbidity currents generated and control the operation of venting:

i. The initial and outflow concentrations C_{TC} and C_{VENT} were measured in the head tank and in the downstream basin respectively using calibrated turbidity probes.
ii. The initial and outflow discharges Q_{TC} and Q_{VENT} were measured in the pumping pipe between the head tank and the mixing tank and at the pipe used for venting (Figure 1.b) respectively.
iii. Deposition was measured in space and time using an electrical resistance-based depositometer (De Rooij et al., 1999). It is formed by two electrodes. A reference electrode is suspended 50 cm above the bed of the flume and 62 bottom electrodes are implemented inside the bed of the flume. Bottom electrodes are separated by 10 cm; the first one is placed 10 cm downstream of the inlet and the last one 620 cm from the inlet (50 cm from the outlet). Through a calibration procedure (Chamoun et al., 2016b), the electrical resistance measured between the reference and bottom electrodes was then converted to a mass (or thickness) of sediments. Therefore, deposition was measured during the whole test at 62 different points.
iv. Velocity profiles are measured using UVP (UVP, Metflow, Switzerland, 2014) transducers placed at 6 different locations of the main flume (i.e., 2.8 m, 4.1 m, 5.5 m, 5.8 m, 6.0 m, and 6.2 m from inlet).
v. Water levels in the head tank and in the main flume were measured using ultrasonic level probes.
vi. Temperatures in the head and in the main flume were measured before and after the test, to make sure that density differences are majorly due to the suspended sediments and not due to a temperature difference between the mixture and the clear water.
vii. Videos and photos were recorded throughout the tests using a camera placed in front of the flume.

3 RESULTS

3.1 Tests

The considered tests are shown in Table 1. Two bed slopes were tested: 2.4% and 5.0%. The initial concentration of turbidity currents generated are of 26 g/l on average. Apart from reference tests where no venting was applied, two different venting degrees were tested. The latter represent the ratio between the outflow discharge Q_{VENT} and the turbidity current inflow discharge Q_{TC}. The latter is constant for all the tests and Q_{TC} = 1 l/s. Figure 2 below shows an example of a typical turbidity current while approaching the wall (at 620 cm from the inlet) before venting is applied.

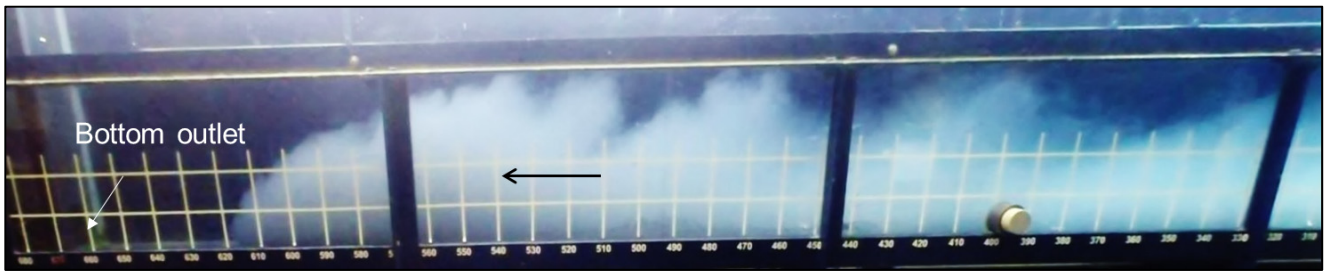

Figure 2. The turbidity current approaching the bottom outlet on the 2.4% slope.

Table 1. Characteristics of the tests.

Slope s (%)	Initial concentration C_{TC} (g/l)	Initial density ρ_{t0} (kg/m^3)	Venting degree Φ (%)
2.4	26.1	1003.3	0
2.4	28.4	1003.6	50
2.4	22.1	1002.7	100
5.0	22.8	1002.8	0
5.0	28.7	1003.6	50
5.0	26.2	1003.3	100

3.2 Velocity

Velocity profiles of turbidity currents provide useful information for their characterization. The profiles taken by the UVP at 4.1 m from the inlet are used to characterize the currents (Figure 3) in terms of velocity U and height h. Turner's equations are used for this goal (Ellison and Turner, 1959):

$$Uh = \int_0^{\infty} udz = \int_0^{h_t} udz \qquad [1]$$

$$U^2 h = \int_0^{\infty} u^2 dz = \int_0^{h_t} u^2 \, dz \qquad [2]$$

where u and z are the local velocity and height, respectively, measured by the UVP profiles and h_t is the height at which u tends to 0.

Based on the velocity and height determination (results are shown in Figure 3), the regime of the currents can be determined through the estimation of Richardson number $Ri = (g'H\cos\alpha)/U^2$ where g' is the estimated reduced gravity at 4.1 m from the inlet (average of the initial reduced gravity g'_0 and the reduced gravity during the approach of the current to the bottom outlet). Additionally, the turbulence rate of the current can be quantified by Reynolds number Re = UH/v where v is the kinematic viscosity of water.

The velocity obtained on the 2.4% slope $U_{2.4} < U_{5.0}$ obtained on the 5.0% slope. Since equal inflow discharges are applied at the inlet for all the tests, the height $h_{2.4} > h_{5.0}$. Reynolds numbers calculated for both slopes are $Re_{2.4} = 6600$ and $Re_{5.0} = 7070$ showing that the currents are fully turbulent (condition applied when Re > 2000 as suggested by Kneller and Buckee (2000)).

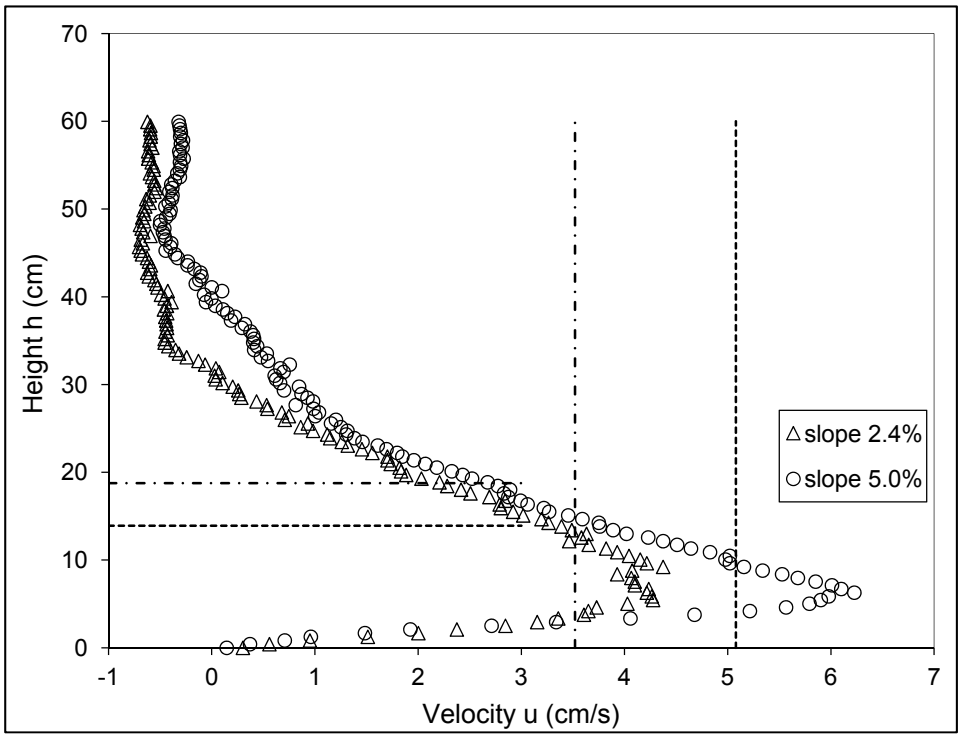

Figure 3. Averaged velocity profiles obtained on the 2.4% and the 5.0% slopes.

3.3 Deposition

The variation of deposition in time and space is shown in Figure 4. Each of the curves corresponds to the deposition in space accumulated during a time step of Δt = 30s. The gray curve corresponds to the deposition obtained when the current reaches the wall and venting starts.

Spatially, the highest deposition occurs close to the inlet due to the phase of development of the current where the coarse sediments settle. While it advances, the deposition mass decreases because the sediments contained in the current become finer. Temporally, a first phase of high depositional rate can be observed which is also explained by the phase of development of the current. This is followed by a decrease approaching a steady rate of deposition. This is probably linked to the arrival of the current to the wall and the formation of the muddy lake. At this stage, the deposition decreases and more sediments are suspended. A better assessment of the temporal variation of the deposition is done by plotting the integral of the sediment mass in time.

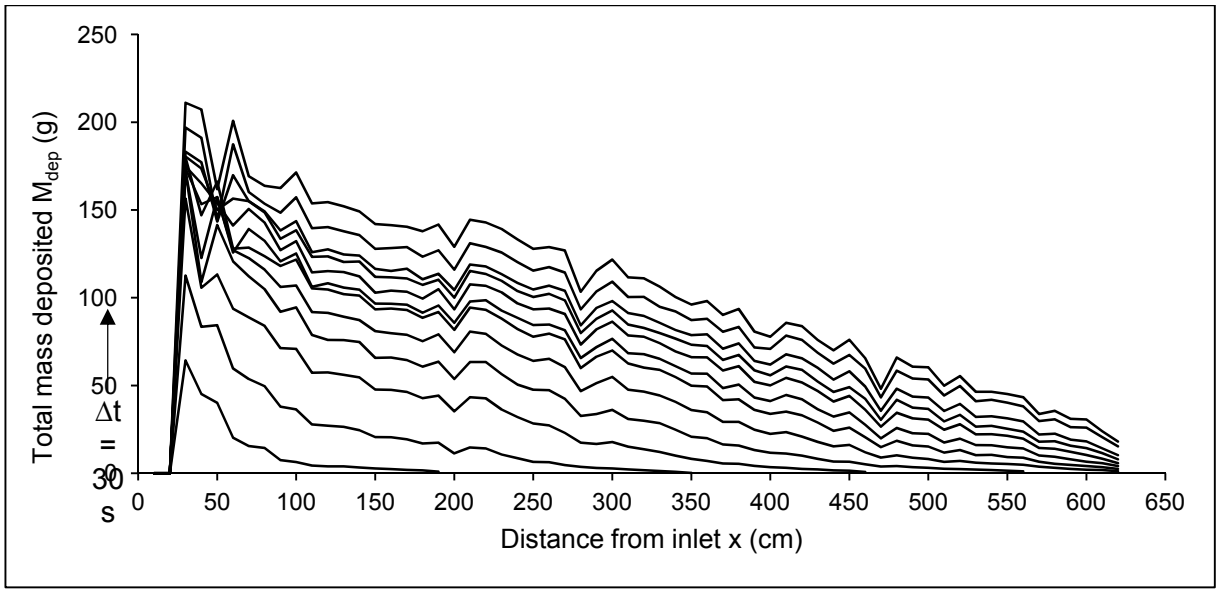

Figure 4. Variation of deposition in time and space obtained on the 2.4% bed slope using a venting degree Φ = 50%.

Figure 5 and Figure 6 below show the variation of the total deposited mass M_{deptot}, normalized by the total inflow mass M_{TCtot} relatively to time t (t = 0 corresponds to the beginning of the test) for each of the slopes used and for the three cases of outlet discharge (Φ = 0%; 50% and 100%). Reference lines were added for the cases where venting was performed and correspond to the time at which the outlet was opened (arrival of the current to the wall).

First of all, the currents are shown to be highly depositive. Deposition increases the most during the phase before the current reaches the wall, which corresponds to more or less the first 150s for all cases. Then, around the time where the current reaches the wall, a slow decrease in deposition is observed, for all the cases. The variation of the relative deposition is very similar when comparing the reference test (Φ = 0%) with the tests where venting was applied with Φ = 50% and Φ = 100%. This means that the venting operation itself does not induce an effect on the deposition and unlike flushing for instance, does not cause a retrogressive erosion. However, one shall note that deposition is measured until 620 cm from the inlet while the wall is located at 670 cm. The effect on deposition might be present in the closer vicinity of the wall where deposition is not measured.

The major effect on the variation of deposition seems to be due to the arrival of the turbidity current to the wall, rather than to the operation of venting. When it reaches the wall, the turbidity current rebounds and is reflected upstream. Therefore, more sediments are suspended and deposition is slowed down due to the formation of the muddy lake.

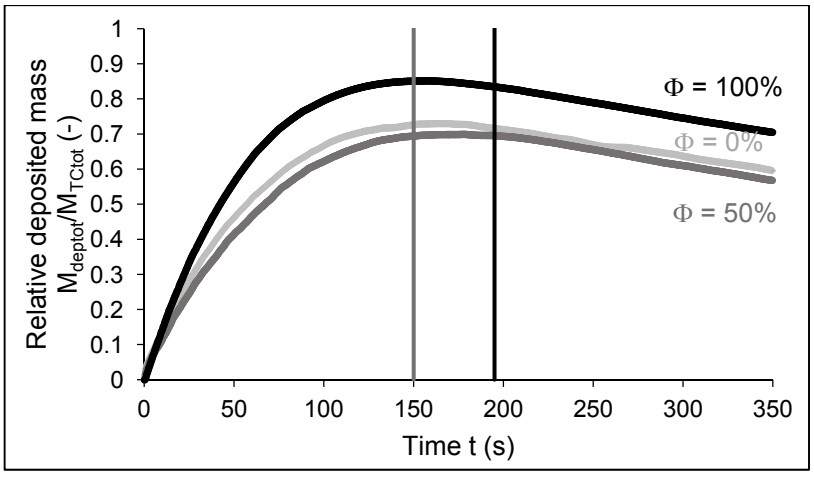

Figure 5. Variation of the relative deposited mass in time for the 2.4% slope.

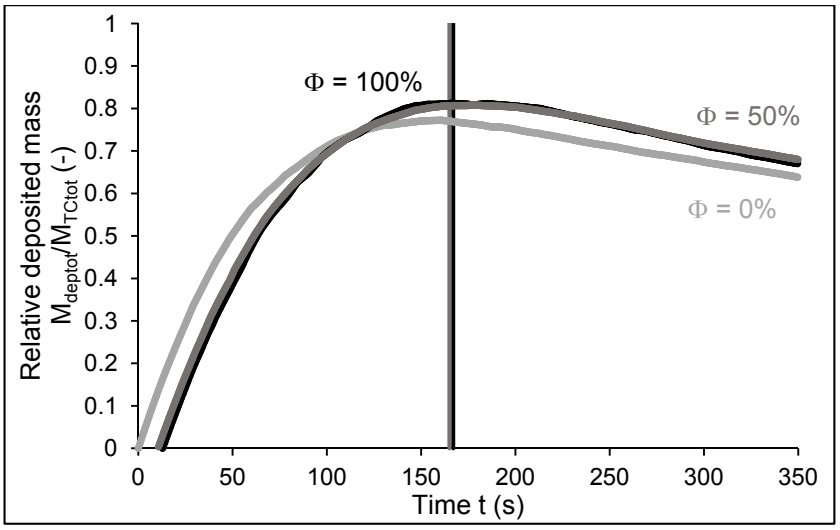

Figure 6. Variation of the relative deposited mass in time for the 5.0% slope.

3.4 Efficiency of venting

The efficiency of venting is evaluated using the criteria of the local venting efficiency LVE (Chamoun et al., 2017) which is defined by the ratio between the total vented mass of sediments $M_{VENTtot}$ to the total inflow (turbidity current) mass of sediments M_{TCtot} while subtracting the total deposited mass from the total inflowing mass M_{deptot}. This subtraction is done due to the fact that there is not retrogressive erosion caused during venting. By accounting for the deposited sediments within the inflowing sediments, the efficiency of venting will be artificially decreased. In Figure 7 and Figure 8 below, LVE = $M_{VENTtot}/(M_{TCtot}-M_{deptot})$ is applied at each time step and the results are compared for the two cases of bed slopes and for two different venting discharges Φ = 50% and Φ = 100%. The time $t-T_v$ where T_v is the time at which venting begins.

The results show that by increasing the bed slopes, higher venting efficiencies are obtained. Venting efficiencies generally increase at the beginning of the operation for both slopes before stabilizing or slowing decreasing for the rest of the venting duration. The increase is due to the arrival of the turbidity current and the formation of the concentrated muddy lake. The slow decrease can be explained by the upstream reflection of the continuously-fed turbidity current.

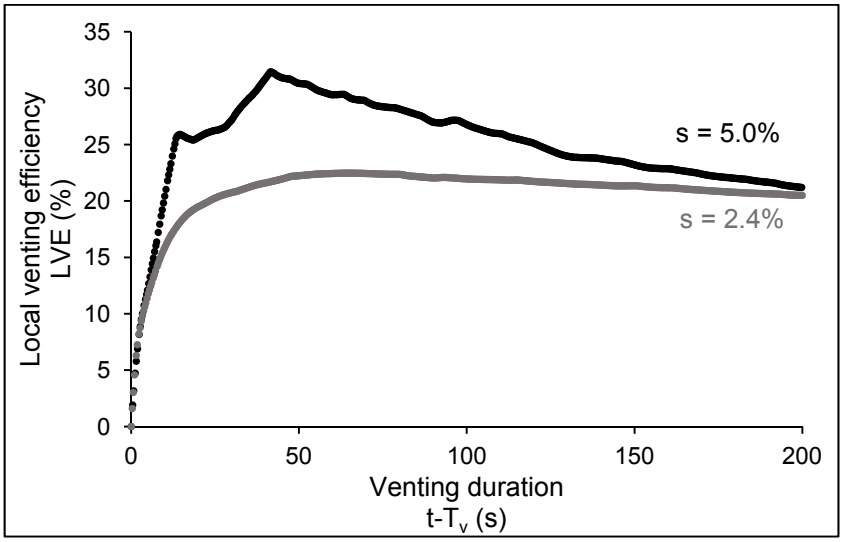

Figure 7. Local venting efficiency LVE in time for the two different slopes using a venting degree Φ = 100%.

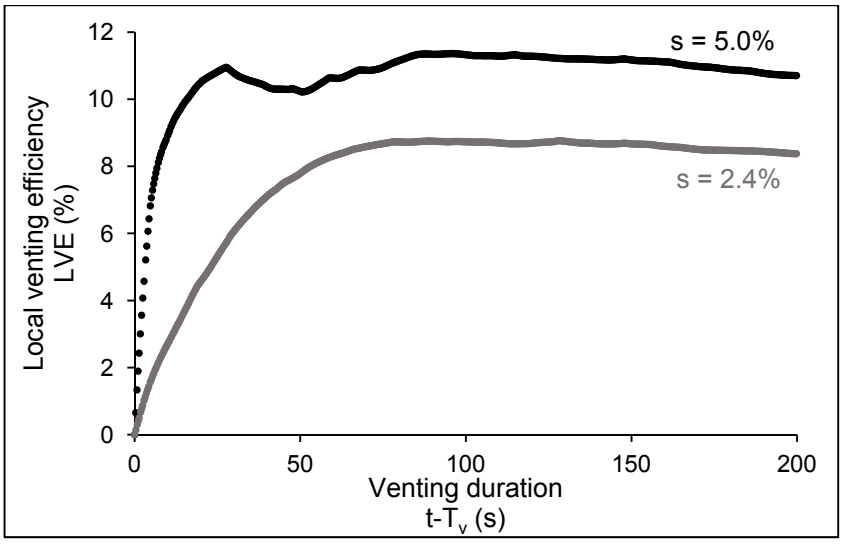

Figure 8. Local venting efficiency LVE in time for the two different slopes using a venting degree Φ = 50%.

4 CONCLUSIONS

Reservoir sedimentation is a global issue causing the loss of storage capacity of reservoirs as well as the blockage and abrasion of outlet structures and hydraulic machineries. Downstream impoverishment also results due to the lack of sediments transited. In the case where sedimentation is due to the presence of turbidity currents, venting through outlets or intakes should be considered.

In the present work, venting of turbidity currents through a bottom outlet is investigated experimentally using two different bed slopes (i.e., 2.4% and 5.0%). Two venting degrees (relative outlet discharge) are discussed (i.e., 50% and 100%) as well as reference tests where venting was not applied.

The measuring instruments used throughout the tests allowed a good understanding of the type of turbidity currents vented, by determining the regime, the Reynolds number and characterizing height and velocity. This information is useful when upscaling to prototype conditions. On another hand, deposition showed that the venting operation did not induce any retrogressive erosion as far as 50 cm from the outlet. Additionally, venting efficiencies were assessed in time and showed an increase with an increasing slope and for the same venting degree. Therefore, the steeper the thalweg in the vicinity of the dam, the higher the venting efficiencies.

Finally, venting of turbidity currents is one of the most favorable technique of sediment mitigation in reservoirs in both economic and environmental terms. Many parameters can affect the efficiency of this operation. These can be related to the morphology, hydrology, shape of the reservoir, outlet characteristics and the operation itself. However, for a healthy downstream environment, both coarse and fine sediments are required. Therefore, venting should also be combined with other techniques that is able to transport the coarse sediments located mostly at the upstream region of reservoirs.

ACKNOWLEDGMENTS

The study titled ‘‘Efficiency of turbidity currents venting under varied outflow discharge’’ was funded by Swisselectric Research and the Swiss Committee on Dams.

REFERENCES

Brandt, S.A. (2000). A Review of Reservoir Desiltation. *International Journal of Sediment Research*, 15(3), 321–342.

Chamoun, S., De Cesare, G. & Schleiss, A.J. (2016a). Managing Reservoir Sedimentation by Venting Turbidity Currents: A Review. *International Journal of Sediment Research*, 31(3), 195–204.

Chamoun, S., Zordan, J., De Cesare, G. & Franca, M.J. (2016b). Measurement of the Deposition of Fine Sediments in a Channel Bed. *Flow Measurement and Instrumentation*, 50, 49–56.

Chamoun, S., De Cesare, G. & Schleiss, A.J. (2017). Venting of Turbidity Currents Approaching a Rectangular Opening on a Horizontal Bed. *Journal of Hydraulic Research*, 1-15.

Cheng, N. (1997). Simplified Settling Velocity Formula for Sediment Particle. *Journal of Hydraulic Engineering*, 123(2), 149–152.

De Rooij, F., Dalziel, S.B. & Linden, P.F. (1999). Electrical Measurement of Sediment Layer Thickness under Suspension Flows. *Experiments in Fluids*, 26(5), 470–474.

Ellison, T.H. & Turner, J.S. (1959). Turbulent Entrainment in Stratified Flows. *Journal of Fluid Mechanics*, 6(3), 423–448.

Fan, J. (1986). Turbid Density Currents in Reservoirs. *Water International*, 11(3), 107–116.
Fan, J. & Morris, G.L. (1992). Reservoir Sedimentation II: Reservoir Desiltation and Long-Term Storage Capacity. *Journal of Hydraulic Engineering*, 118(3), 370–384.
Kantoush, S. A. & Sumi, T. (2010). River Morphology and Sediment Management Strategies for Sustainable Reservoir in Japan and European Alps. In *Annuals of Disaster Preventive Research Institute, 53,* 821–839. Kyoto, Japan.
Kneller, B. & Buckee, C. (2000). The Structure and Fluid Mechanics of Turbidity Currents : A Review of Some Recent Studies and their Geological Implications. *Sedimentology*, 47(s1), 62–94.
Lee, F.Z., Lai, J.S., Tan, Y.C. & Sung, C.C. (2014). Turbid Density Current Venting through Reservoir Outlets. *KSCE Journal of Civil Engineering*, 18(2), 694–705.
Lu, X. (1992). An Approximate Method for Calculating The Efficiency of Venting Density Current Through Outlet. In *5th International Symposium on River Sedimentation,* 829–835. Karlsruhe.
Metflow, S. (2014). *UVP Monitor - User's guide*, Lausanne, Switzerland.
Morris, G. & Fan, J. (1997). *Reservoir Sedimentation Handbook: Design and Management of Dams, Reservoirs, and Watersheds for Sustainable Use*. McGraw-Hill, New York.

Proceedings of the 37th IAHR World Congress
August 13 – 18, 2017, Kuala Lumpur, Malaysia

DISCUSSION ON DESILTING MEASURES FOR RESERVOIR SEDIMENTATION

HONG BIN LIU[(1)], CAI PING WU[(2)] & WEN JIAO ZHANG[(3)]

[(1,2,3)]Yellow River Institute of Hydraulic Research, Zhengzhou, China,
wjzhang2006@163.com

ABSTRACT

Reservoir sedimentation is a serious problem to make a reservoir gradually lose its normal function. As a result, the issues of reservoir deposition have been clearly studied and some technological improvements in China have been achieved. The traditional desilting measures for reservoir deposition contain hydraulic desilting, mechanical dredging and some other comprehensive measures. According to the specific condition of reservoir deposition, different desilting equipment and measure are applied. In this paper, the common desilting measures, such as mechanical dredging, empty-reservoir desilting, density current desilting, flood detention desilting and self-suction sediment transport piping system, are summarized. Those desilting measures' principle, effect and application condition are demonstrated, especially from a high-efficient, low-carbon and environmental point of view. The studies show that self-suction sediment transport piping system has an advantage of improving efficiency, lowering energy, saving water and reducing cost. Moreover, the desilted sediment is easy to be collected and recycled. The desilting that measures about self-suction sediment transport piping system has broad prospects in engineering application.

Keywords: Reservoir sedimentation, desilting measures; high-efficient desilting; environmental protection; self-suction sediment transport piping system.

1 INTRODUCTION

Sediment deposition is a common problem in various reservoirs with different objectives and functions as a result of the change of natural river course and sediment movement law. Especially for the sediment-laden river, this problem is more serious. Sediment deposition greatly decreases the usable capacity of a reservoir, which leads to the benefit reduction of flood control, irrigation, water supply, power generation and so on. In recent years, the abnormal weather always exists in China. Considering the influence from the large areas of continuous drought, rainstorm and floods, reservoir sedimentation has been more evident and adverse in impact of normal reservoir function. Sediment deposition not only influences the safety and normal use of the reservoir, but also becomes the key factor restricting comprehensive utilization of water resources and intensifying water environment deterioration (Cao et al., 2011). Reservoir sedimentation has become a problem that needs to be urgently solved.

The researcher studies about reservoir desilting measures in China which begun in the 1960s, when a lot of research results and engineering experience have been accumulated. In general, the reservoir desilting measures mainly contain hydraulic desilting and mechanical dredging. The hydraulic desilting measures contain empty-reservoir desilting, density current desilting, flood detention desilting, self-suction sediment transport piping system and etc. The mechanical dredging measures contain mud bucket dredger, suction dredger, jetting suction dredger, dredge pump, ground excavating equipment and etc. Because each reservoir has different natural condition, engineering scale, structure, surrounding climate and geological factors, which causes different sediment generation reason and mode, will contribute to the different desilting measures adopted that have different effects on water resource utilization and water environment protection. Therefore, the desilting mechanism, applicable conditions, advantages and disadvantages, and cost of those sediment desilting measures need to be studied. According to the reservoir's condition and foundation, the scientific and reasonable desilting method can be chosen to ensure the normal reservoir function.

In this paper, the desilting principle, effects and suitable conditions of several typical reservoir desilting measures are discussed based on the new research progress of reservoir desilting measures in recent years. The view of improving the sediment dredging efficiency, lowering cost, promoting environmental protection and reducing pollution is always taken into consideration. Through the recognition of those desilting measures from the aspects of high efficiency, low carbon and low environmental impact will lead to various desilting measures that can be achieved where the best effect will out bring the greatest efficiency.

2 RESERVOIR DESILTING MEASURES

2.1 Mechanical dredging technology

Mechanical dredging, which contains mud bucket dredger, cutter suction dredger and jetting suction dredger was divided according to the working principle, means of utilizing additional power like dredge pump, pneumatic pump, dredger and some transportation equipment to dig and discharge the reservoir sedimentation, as shown in Figure 1. Mud bucket dredger digs and transports the sediment depending on the mechanical force of the dredger. This dredger can only unload the sediment into the hopper of the dredger or nearby barge, so it cannot do long distance transport and has low efficiency. Cutter suction dredger cuts and stirs the reservoir bottom sediment through the rotating cutter device in front of the suction pipe, and it transports the sediment by the powerful force from dredge pump or pneumatic pump. It can be used for long distance transportation and sediment resource utilization by adding a connecting pump station. Jetting suction dredger generally uses high-pressure water jet to break the sediment, and inhales the mud through submersible pump and gas lift device. Then, the mud was transported to the centrifugal slurry pump through the pipe, and after pressurization, it is sent to the appropriate site for resource utilization along the floating pipeline.

Figure 1. Schematic diagram of mechanical dredger.

Mechanical dredging is a direct and effective method to clear reservoir sediment. While the mechanical dredging equipment's working scope was almost 80 m^3/h - 500 m^3/h [b]. The desilting scale and depth were small. If the dredging depth was greater than 10 m, the field operation is rather difficult. The mechanical desilting cost is relatively high, and it was limited to do small-scale desilting work for small reservoirs. In recent years, with the research and development of key equipment and automatic monitoring technology of mechanical dredging, the design and manufacture of modern dredger gradually tend to be at large-scale, highly efficient and intelligent. The mechanical dredging depth had reached more than 100 m, and the dredging scale had increased to 3000 m^3/h - 4000 m^3/h. For instance, Jiangyin Water Conservancy Mechanization Engineering Co., Ltd. and Beijing Xinhui Water Conservancy Construction Co., Ltd. developed a new pneumatic deep-water dredging system with the maximum operating depth of 120 m specific for the suspended load, bed load and other sediment. The new dredging system had been successfully applied in both Fuxian Lake in Yunnan Province and Wanzhou section of the Three Gorges Reservoir. The cutter suction dredger had also developed faster recently. In order to reduce the secondary pollution from common reamer, the environmental reamer was quipped with mud flap, seal cover and level regulator which was developed. In general, the environmental machineries such as environmental reamer heads, antifouling screen and etc. have become more and more important. Most of the advanced positioning and monitoring of instruments, such as GPS and pollution monitors, were usually installed on the dredger to improve the dredging accuracy and control the dredging quantity. At the same time, the sediment transport system has been improved to reduce the mud leakage to avoid the secondary pollution to the environment, and lower the desilting cost through the reasonable utilization of sediment resources. Hence, mechanical dredging will play an important role in reservoir sedimentation management in the future.

2.2 Hydraulic desilting technology based on reservoir operation

The traditional hydraulic desilting measures contain density current desilting, empty-reservoir desilting and flood detention desilting, which were all implemented through the reservoir operation, as shown in Figure 2. Those measures have significant desilting effect under certain conditions, but the effect was directly related to reservoir hydrologic condition, upstream and downstream river bed structure, and water head. In addition, the reservoir sediment was usually discharged into the downstream river channel through water release

[b] /h represents unit hour.

structures, which was unable to realize the rational utilization and development of the value of sediment resources.

Figure 2. Schematic diagram of density current desilting.

Density current desilting is an effective desilting measure for the reservoirs in a sediment-laden river, especially for the full reservoirs during the flood season. This measure had been applied in many reservoirs in China. For example, since Xiaolangdi Reservoir began to store water, it mainly made use of the reservoirs natural density flow and artificial density flow to reduce the reservoir sedimentation. However, the desilting effect of density flow was closely related to the flood flow, incoming sediment amount and grading, discharged flow, gate opening time, reservoir terrain, the height of discharge outlet and etc. The desilting condition of density current was not easy to be formed, so the density current desilting was only suitable for the reservoirs with certain boundary, hydraulic condition and sediment condition. In addition, density current desilting technology can only be carried out during the water-sediment regulation period before the flood season or during the upstream flood period in the flood season. With this method, only the sediment in front of the dam coming from density flow's transport or previous sedimentation can be desilted and discharged. The desilting capacity was greatly limited due to the continuous power of density current.

Empty-reservoir desilting means discharging the deposition out of the reservoir area through the water level lowering scour where headwater erosion or artificial hydraulic flushing in the process of emptying reservoir is used and this is one of the effective ways of restoring reservoir capacity. The sediment erosion quantity was related to erosion time, erosion flow and lowering range of reservoir water level. The larger the erosion time, erosion flow and lowering range of reservoir water level are, the higher the desilting efficiency will be. The advantage of empty-reservoir desilting was that high sediment concentration will be discharged, which has an immediate desilting effect. While its disadvantage is that it need abundant of water when working plus that the reservoir sediment will deposit again soon after the desilting work. Moreover, emptying reservoir influences the slope stability of river channel which leads to the danger of collapse and landslide, and it also affects the economic benefits from reservoir power generation, irrigation, and shipping and the growing of aquatic animals and plants. Empty-reservoir desilting was applicable to the region with abundant of water resources, the reservoir with large natural river slope or the seasonal reservoir.

Flood detention desilting is a way of storing the clear and releasing the mud of a reservoir. In the flood detention period, the reservoir water keeps certain moving velocity. The coarse-particle sediment deposits in the reservoir, and fine-particle sediment was discharged by the flow out of the reservoir, avoiding the potential and serious silting induced during the reservoir storage period. The effect of flood detention desilting was significant with regard to the impounding reservoir. By this method, the desilting efficiency is affected by desilting time, the lasting time of flood detention, gate opening time, flood discharge capacity, and the flood overbank situation. The amount of reservoir water discharged along with flood detention desilting is large. This needs abundant upstream inflow which may carry a mass of sediment.

2.3 Self-suction sediment transport piping system

In recent years, a new method for reservoir desilting, self-suction sediment transport piping system has been popular. This technique takes advantage of the natural water head difference on the upstream and downstream of a reservoir as the desilting energy to transport the sedimentation out of the reservoir through the suction-head and moved pipeline. Figure 3 displays the schematic diagram of self-suction sediment transport piping system.

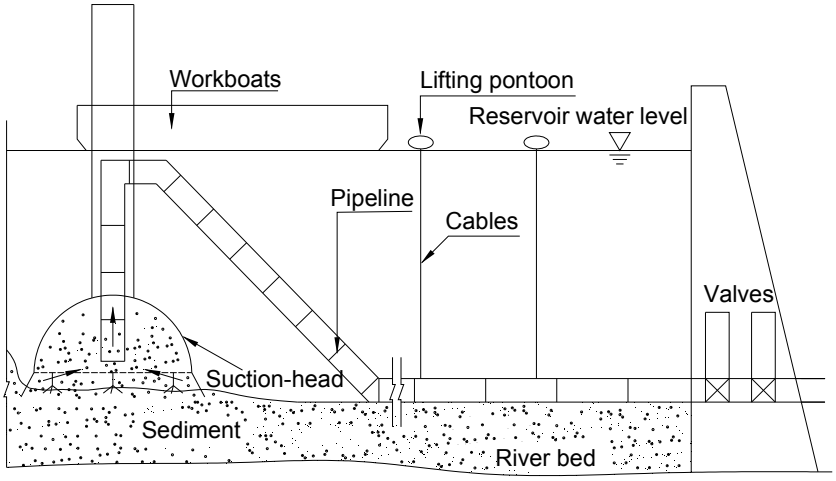

Figure 3. Schematic diagram of self-suction sediment transport piping system.

The technology of self-suction sediment transport piping system has been widely studied by the scholars from many countries and has achieved some achievements (Gu, 1993). In the 1970s, this method was applied and developed in some African reservoirs which deposited seriously and couldn't be cleared by hydraulic desilting. For instance, the dam of Wufoda Reservoir is 90 m high, and the sediment thickness in front of the dam reached 50 m. The amount of sediment discharge capacity of this desilting system can be 3 million m3 every year which was more than the inlet sediment amount when the diameter of suction pipe is 0.4 m and the length of it is 1 km-2 km with 4000 hours' working time a year. In China, several small and medium-sized reservoirs, such as Xiaohuashan, Tianjiawan, Xintian, Beichaji and etc., adopted the self-suction sediment transport piping system to do some desilting experiments in the 1970s (Gansu, 1987). By means of those experiments where a set of hydraulic suction device with relatively perfect performance was gradually formed, and the desilting work achieved preliminary good results. For example, the hydraulic suction device of Beichaji haa an average sediment transport rate of 550000 kg/h, on 500 hours' working time a year combined with irrigation. It can desilt the sediment up to 172000 m3 and discharge volume of water about 450000 m3 in a year. For 15 years, the desilting amount can reach 2.58 million m3. This not only controls the reservoir sedimentation, but also restores previous desilted capacity of 780000 m3. The desilting cost was counted as 0.069 yuan/m3 in China which equals to 0.0185 dollars per cubic meter with the exchange rate in 1987. This is one tenth of the mechanical dredging cost during the same period. Moreover, Jiang et al. (2009) studied the dredging key technology of self-suction sediment transport piping system for deep reservoir based on special public industry of the Xiaolangdi Reservoir. The studies included the self-suction head size and form (Chen et al., 2012), piping layout scheme passing the dam, construction connection technology of pipe and tunnel, new technology of pipe connection, laying and disassembly, pipeline flow pattern and flow state, the relationship of hydraulic parameters like sediment transport concentration and etc. They put forward a specific dredging scheme for Xiaolangdi Reservoir. According to the desilting time for 6 months each year, the annual desilting amount was approximately 300 billion kg and the discharged water volume was approximately 900 million m3. For a long time, it could permanently remain that the reservoir area located in front of the dam of 20 km and over the elevation of 145 m had no sedimentation. However, because of the great difficulty in piping layout passing of the dam of Xiaolangdi, the dredging scheme was restricted. Yang and Luo (2009) of Tianjin University carried out the tests of several styles of suction-head for Qingtongxia Reservoir. According to the test results, the structure and control mode of the suction-head got optimized. Meng and Yin (2013) studied the efficiency of the suction-head with different types based on the hydraulic model test, and they put forward effective suction-head type. Zhao L.J. and Zhang W.J. et al. from Yellow River Institute of Hydraulic Research developed a kind of suction-head for self-suction sediment transport piping system in the deep reservoir by adjusting the structure style, combination, hydrodynamic condition, layout scheme of suction-head and high speed jet, considering the factors of environmental protection, low energy consumption, high efficiency and high stability. At present, this system is applied in a reservoir as the dredging demonstration project in Xinjiang Province, China. Combining the advanced positioning and monitoring instruments, the self-suction sediment transport piping system will gradually form a complete set of practical equipment to face the market.

3 CONCLUSIONS

Desilting reservoir sediment in an effective way can make the reservoir work for a long time, which is of great social and economic benefits. For different reservoirs, the most appropriate desilting measure and equipment are selected in light of reservoir's function, water and sediment characteristic, erosion and deposition regularity, morphological characteristics of reservoir area, and so on. Table 1 shows the comparison results of different desilting measures. As the research and development of the key environmental

and mechanical equipment and the automatic monitoring technology, mechanical dredging will play an important role in reservoir sedimentation management in the future.

Table 1. Comparison results of different desilting measures.

Desilting measures	Advantages	Limitations	Cost
Mechanical dredging	High maneuverability and flexibility	Small dredging scale and difficult field operation	High
Hydraulic desilting	Sufficient utilization of reservoir operation	Big water consumption, desilting condition formed with difficulty and low sediment resource utilization ratio	Low
Self-suction sediment transport piping system	Utilization of reservoir natural water head, saving of external power and small water consumption	existence of enough water head	Low

Compared with the traditional reservoir desilting method, the self-suction sediment transport piping system has many advantages on realizing the effective desilting work. It has strong applicability, high desilting efficiency and long-time operational capability, which is less influenced by hydrogeological conditions and does not affect the reservoir scheduling. Moreover, this system is energy-efficient and environmental friendly without external energy input when compared with the mechanical dredging. It can combine the desilting work with irrigation, making full use of water resources. By this method of self-suction sediment transport piping system. It is also conducive to reduce the reservoir capacity loss rate effectively, prolong the service life of the reservoir, improve the comprehensive benefit of the reservoir flood control and power generation, transport the reservoir sediment to the appointed places for effective utilization, and finally promote efficient ecological economic virtuous circle and sustainable development of the reservoir area.

ACKNOWLEDGMENTS

This work is supported by the National Natural Science Foundation of China under Grant No. 51539004, the Special Fund from Ministry of Water Resources for Scientific Research in Public Welfare Industry of China under Grant No. 201501003, and the Special Research Fund of Yellow River Institute of Hydraulic Research under Grant No. HKY-JBYW-2016-35.

REFERENCES

Chen, J.J., Li Y.F., Guo H.M. & Ren Y.F. (2012). Experimental Study on Body Shape of Suction-Head of Self-Suction Sediment Transport Piping System. *Yellow River*, 34(3), 22-23. (In Chinese)

Cao, H.Q. & Zhou J.J. (2011). Development and Prospect of Dredging at Water Conservancy Works in China. *Journal of Sediment Research*, 5, 67-72. (In Chinese)

Gu, S.P. (1993). Study on a Technique for Sediment Disposal from Reserviors. *Norwegian Institute of Technology*, 6-9.

Gansu Hydraulic Research Institute. (1987). *Report of research results of reservoir desilting tests in Gansu Province*. Gansu Hydraulic Research Institute (In Chinese)

Jiang, E.H., Gao H. & Li Y.F. (2009). *Report of Comparative Study of Sediment Incipient Motion and Transport Scheme.* Yellow River Institute of Hydraulic Research, Zhengzhou, China. (In Chinese)

Luo, D.X. (2009). Experimental Study on the Sediment Flushing Characteristics with Pipeline. Tianjin University. (In Chinese)

Meng, K. & Yin, S.H. (2013). Experimental Study on Suction-Head of Reservoir Siphon Desilting Pipeline. *Jinlin Water Conservancy*, 12, 39-41. (In Chinese)

VENTING OF TURBIDITY CURRENTS: WHEN TO ACT?

SABINE CHAMOUN[(1)]

[(1)] Laboratory of Hydraulic Constructions (LCH), Ecole Polytechnique Fédérale de Lausanne (EPFL), Lausanne, Switzerland, sabine.chamoun@epfl.ch

ABSTRACT

During floods, sediments are transported from watersheds into reservoirs, slowly decreasing water volumes and this leading to economic losses. Thus, in the long term, sedimentation endangers reservoirs' sustainability. Sediments can also block low-level hydraulic structures such as bottom outlets and powerhouse intakes and cause abrasion of gates and turbines. Additionally, the trapped sediments induce downstream starvation and thus the impoverishment of the river's morphology and ecosystem. Many measures are taken to deal with the sedimentation of reservoirs. Among the most common methods is venting turbidity currents approaching the dam. In fact, these sediment-laden currents carry the major part of sediments found near the dam and thus their evacuation before they settle can be a very effective method to reduce sedimentation. However, dam operators lack information and guidelines to perform efficient venting operations. The present research experimentally and numerically investigates the venting of turbidity currents applied with different timings of outlet opening: (1) before the current reaches the outlet, (2) after the current has reached the outlet and climbed up to the top of the dam, and (3) after the upstream reflection of the muddy lake has begun. The high data acquisition frequency offers the possibility to examine temporal variations of inflow and outflow concentrations and discharges and thus variations of the efficiency of venting in time during the tests. In addition, the experimental results are extended numerically for a better understanding of the effect of opening timing on venting. Results show that opening the outlet before the current reaches the wall can be more efficient than opening after the current has reached the wall. Outputs of this study lead to crucial information for dam operators dealing with reservoirs facing high sedimentation rates due to the formation of turbidity currents.

Keywords: Reservoir sedimentation; turbidity currents; venting; bottom outlets; timing.

1 INTRODUCTION

The management of reservoirs to ensure their sustainability is a task that requires technical intervention on many levels. It includes works of maintenance, management of operations under different hydrological conditions, adaptation to possible changes in demands, and most importantly making sure the capacity of reservoirs is not significantly reduced. Sedimentation is a serious problem affecting reservoirs worldwide (Schleiss et al., 2016).

In order to reduce the impact of sedimentation, different methods exist to remove the deposited sediments. One of the most common techniques is to open the outlets and drawdown of the water level, causing retrogressive erosion and moving sediments towards the downstream river. This method is called free-flow flushing (Brandt, 2000). Another method is to mechanically dredge (wet or dry) the sediments, transporting them from upstream to downstream of the dam or other dump areas. However, these methods can be harmful for the downstream environment since large amounts of sediments are introduced in the river in a short time compared to the natural transport process (Espa et al., 2016). Other methods take place in the watershed to bypass or block sediments (Kantoush and Sumi, 2010).

In some cases, however, sediment-laden flows form and plunge below the clear water surface of the reservoir due to their higher density. They are called turbidity currents. Depending on the reservoir's geometry, the sediment concentration and also temperature differences (between the current and the clear water), a turbidity current can travel long distances until reaching the dam. The current then rebounds, its kinetic energy is transformed into potential energy and it climbs up the dam before reflecting upstream. A muddy lake is formed during this process and if no low-level outlets or intakes are opened, the sediments of the muddy lake settle and consolidate. Sediments depositing close to the dam not only reduce the reservoir's capacity but can also obstruct/abrade hydraulic structures (e.g., low-level outlets, turbines, intakes). In order to avoid such consequences, a direct transit or venting of turbidity currents reaching the dam through outlets is the most adequate technique if well performed. Besides reducing the amount of sediments in the vicinity of the dam, venting can be beneficial for the downstream environment and relatively economic since it is performed using relatively low outlet discharges.

However, this technique requires information on the turbidity currents and thus their monitoring, which can be costly. Moreover, guidelines on the operational conditions that can lead to high release efficiencies are also needed. In this context, several knowledge gaps exist and optimal conditions to perform efficient venting

have not been sufficiently investigated. Researchers have highlighted the importance of this technique in the past (Bell, 1942; Chen and Zhao, 1992; Fan and Morris, 1992; Morris and Fan, 1997; Müller and De Cesare, 2009; Nizery et al., 1952; Schneider et al., 2007) but very few have performed quantitative research on the subject (Yu et al., 2004; Lee et al., 2014; Chamoun et al., 2017). Based on literature and particularly on field data, some influential parameters can be determined. Among these parameters is the timing of the outlet opening.

In the present work, venting of turbidity currents is investigated using an experimental set-up, as well as a numerical analysis. The effect of the opening timing of a bottom outlet on the amount of sediments that are evacuated is studied. The experimental model and procedure are firstly described, followed by the tests' boundary conditions and experimental results. The numerical model is then briefly described and more insight on the operation of venting under different timings is given.

2 EXPERIMENTAL SET-UP AND MATERIAL

The experimental set-up is formed by a long (L = 8.55 m) and narrow flume (b = 0.27 m) with a 1 m height. A mixing tank serves the purpose for the preparation of the water-sediment mixture (Figure 1.e). The flume is divided into three parts: (i) the head tank located in the upstream part of the flume and connected to the mixing tank using two pipes, a ''pumping pipe'' (Figure 2) that serves to pump the mixture from the mixing tank into the head tank and a ''restitution pipe'' used to siphon the mixture back into the mixing tank; (ii) the main flume which has a length of 6.7 m represents the reservoir in which the turbidity current is triggered; and (iii) a downstream compartment that receives residual clear water from the main flume while the turbidity current advances. The inlet consists of a tranquilizer of 4.5 cm height (Figure 1.c). It links the head tank to the main flume when the sliding gate is opened. A wall (0.8 m height for the 2.4% slope and 0.92 m for the 5% slope) is placed at 6.7 m from the inlet. It represents the dam with a rectangular outlet placed at its bottom (Figure 1.b). The outlet is centered on the width of the flume. It has a height of 12 cm and a width of 9 cm. A downstream tank is located at the exit of the outlet and receives the vented turbidity current.

Note that for the cases where the outflow is larger than the inflow and in order to avoid the decrease of the water level in the main flume, a part of the spilled clear water in the downstream compartment of the flume is pumped back into the main flume through a ''recirculation pipe''. A diffusor placed above the inlet (Figure 1.c) receives this ''residual'' water and homogeneously divides it over its height.

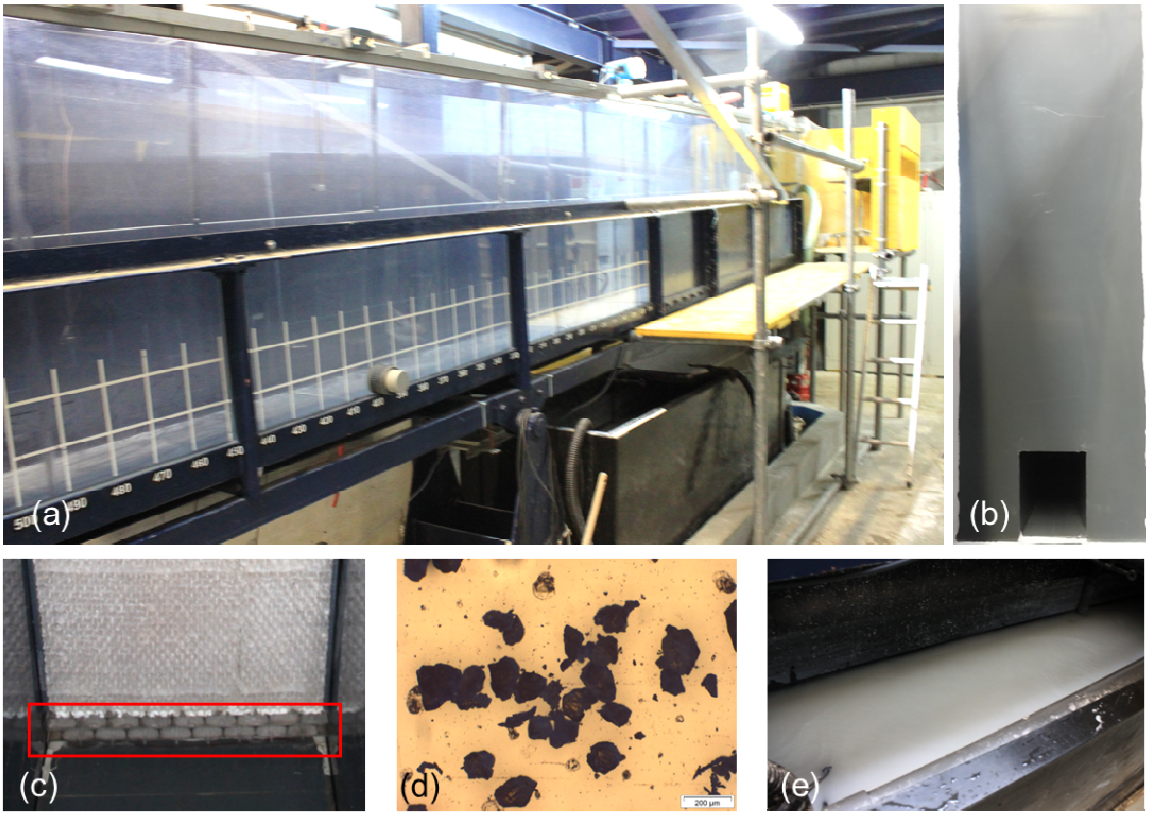

Figure 1. Experimental set-up showing (a) the main flume (b) the bottom outlet and the wall (c) the inlet highlighted in red below part of the diffusor (d) a microscopic photo of the sediment material and (e) the sediment-water mixture in the mixing tank before the beginning of a test.

2.1 Sediment material

A thermoplastic polyurethane (polymer) powder is used to simulate the sediments contained in the turbidity currents. It has a particle density of ρ_s = 1160 kg/m^3 and diameters of d_{10} = 66.5 µm, d_{50} = 140 µm, and d_{90} = 214 µm, where d_x represents the diameter for which x% of the sediments have smaller diameters. As shown in the microscopic photo, the sediments are angular (Figure 1.d). The settling velocity is thus not only estimated using Stokes' Law (appropriate for spherical particles) but also using an empirical formula proposed by Cheng (1997) for natural sediments. An average settling velocity v_s = 1.5 mm/s is considered.

3 PROCEDURE

At the beginning of each test, the main flume was filled with clear water up to the height of the downstream wall and the water-sediment mixture was simultaneously prepared in the mixing tank. The latter was equipped with a submerged pump that keeps the sediments suspended before and during the test. After adding the adequate mass of sediments, the mixture was pumped into the head tank and recirculated between the two compartments for a few minutes. This procedure ensures the homogeneity of the mixture and lasts until reaching the fixed concentration of the test in the head tank. The recirculation was then stopped and the sliding gate was opened triggering a turbidity current inside the main flume. Due to its higher density, the latter advanced on the bed of the flume below the clear water. Depending on the timing of opening tested, the bottom outlet was operated and the evacuated flow reached the downstream tank where discharge and concentration were measured.

3.1 Measurements

Several measuring instruments are employed throughout the tests. The different parameters monitored and the locations of the instruments are summarized in Table 1 and Figure 2. Inflow conditions in terms of discharge and concentrations were kept as steady as possible during one test and between the different tests. Temperature measurements serve to check that density differences between the mixture and the clear water is majorly due to the suspended sediments and not affected by temperature differences. More details about the measuring techniques and accuracy can be found in Chamoun et al., (2017).

Table 1. List of the measuring instruments and parameters measured.

Instrument	Parameter	Location
Turbidity probe	Concentration C_{TC} and C_{VENT}	Head tank; Downstream tank
Flowmeter	Discharge Q_{TC}, Q_{VENT} and Q_{res}	Pumping, venting, and recirculation pipes
Depositometer	Deposition	62 different points at the bed of the flume
Level probe	Water level	Head tank; main flume
UVP transducer	Velocity profile	2.8 m, 4.1 m, 5.5 m, 5.8 m, 6.0 m, and 6.2 m from the inlet
Thermometer	Temperature	Head tank; Downstream tank
Camera	Photos/videos	Facing the channel

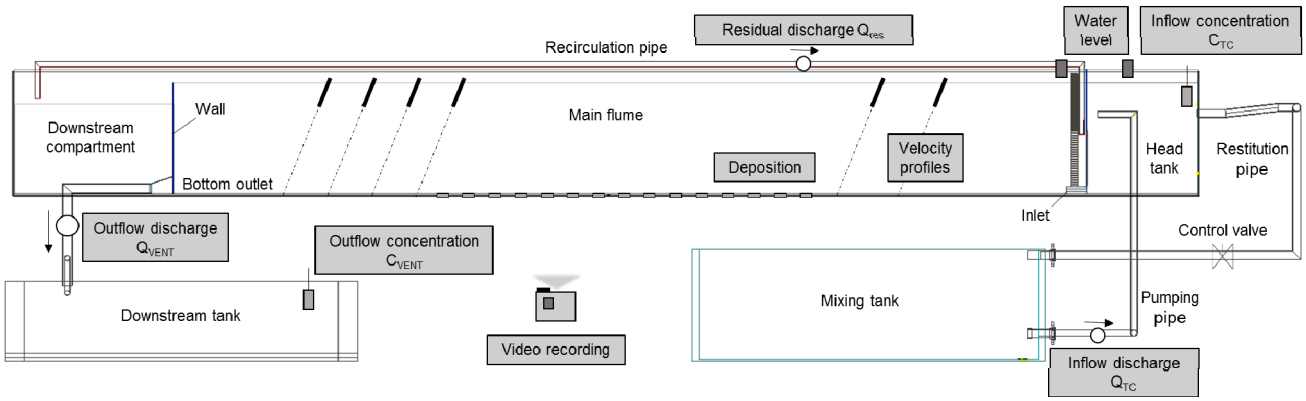

Figure 2. Scheme of the experimental set-up summarizing the different measurements (in gray highlight).

4 EXPERIMENTAL RESULTS

4.1 Tests

The characteristics of the tests considered for the present paper are listed in Table 2. Two different bed slopes are used: 2.4% and 5%. The initial concentration C_{TC} and density ρ_{t0} of the turbidity currents are shown. The tested ratio Φ between outflow discharge and turbidity current inflow discharge is 115% for all the

cases. Three different timings of outlet opening are tested: (i) before the arrival of the turbidity current to the bottom outlet, at a distance d/h = 5, where d is the distance from the outlet and h is the height of the outlet (12 cm); (ii) after the arrival of the turbidity current to the bottom outlet and when it has climbed up the wall and reached its top (~ 30s after arrival); and (iii) after the formation of the muddy lake and the beginning of the reflection of the turbidity current upstream (~ 60s after arrival).

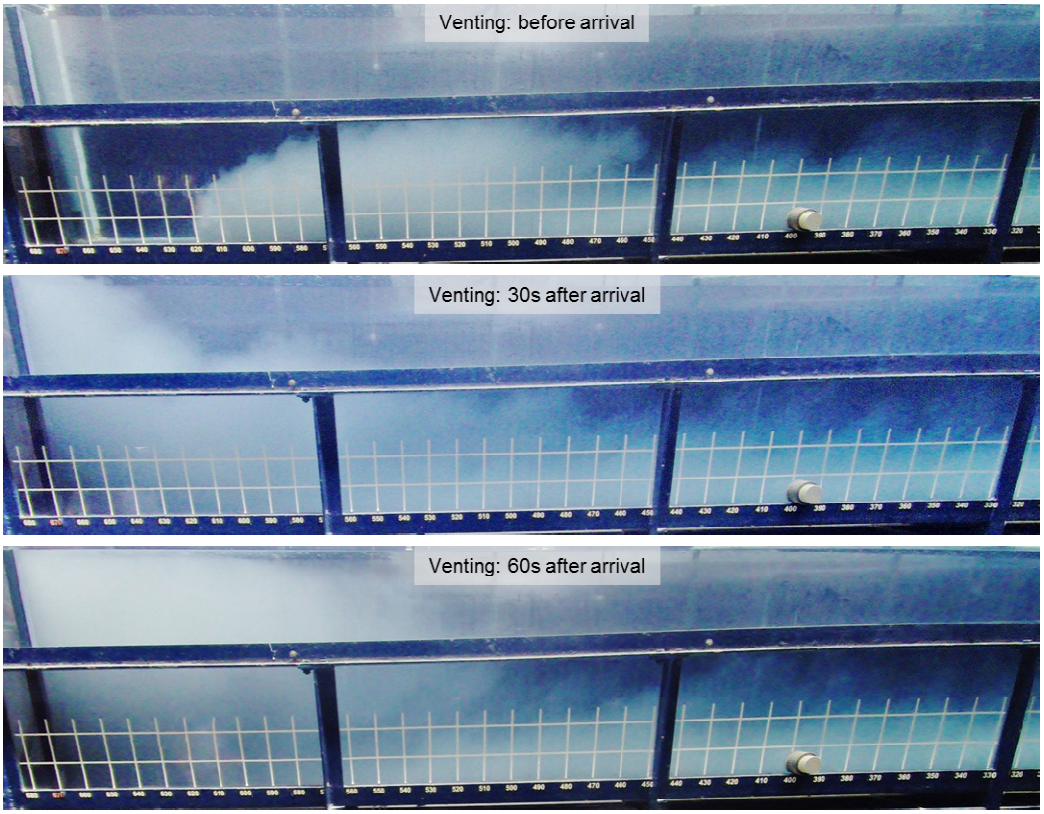

Figure 3. The different outlet opening timings tested (2.4% slope).

Table 2. Characteristics of the tests.

Test number	Slope s (%)	Initial concentration C_{TC} (g/l)	Initial density ρ_{t0} (kg/m^3)	Venting degree Φ (%)	Timing of outlet opening
T1.b	2.4	20.0	1002.4	115	Before d/h = 5
T1.a30	2.4	27.4	1003.4	115	After 30 s
T1.a60	2.4	28.0	1003.5	115	After 60 s
T2.b	5.0	27.8	1003.5	115	Before d/h = 5
T2.a30	5.0	26.0	1003.2	115	After 30 s
T2.a60	5.0	26.2	1003.3	115	After 60 s

4.2 Outflow concentration

The outflow concentration was measured at the downstream tank where the vented current is restituted. The frequency of the measurement is high enough (2.75 Hz) to detect the detailed temporal variation of the outflow concentration. As shown in Figure 4, the concentration increases once the vented current reaches the downstream tank before slightly decreasing and becoming quasi-steady. This behavior is observed for all the tests with more or less the same trend, and only with different slope of the phase preceding the quasi-steady state.

Outflow concentrations were used to deduce two important parameters, which are the reduced gravity acceleration of the turbidity current while approaching the wall and the height of aspiration of the outlet . Both require the value of the density of the turbidity current in the approaching phase right before venting starts (in the vicinity of the wall). However, this value was not measured. Therefore, the highlighted part of the outflow concentration (Figure 4) is averaged and considered as representative of the concentration of the body of the current reaching the wall. The concentration at the approaching phase is called C_{app}. The height of aspiration h_L represents the height that the outlet can reach above its central axis to vent the dense fluid approaching it. It is expressed as such (Craya, 1949; Gariel, 1949; Fan, 1960):

$$\left[\frac{\Delta\rho}{\rho_w}\frac{g(-h_L)^5}{Q_{VENT}^2}\right]^{1/5} = -1.2 \qquad [1]$$

where $\Delta\rho = \rho_{tapp} - \rho_w$ represents the density difference between the approaching turbidity current ρ_{tapp} and the clear water ρ_w and g is the gravitational acceleration. According to Graf and Altinakar (1995), the density of the turbidity current approaching the outlet is $\rho_{tapp} = C_{app}\rho_s + (1-C_{app})\rho_w$ and thus the reduced gravity acceleration of the current is $g'_{app} = g[(\rho_s-\rho_w)/\rho_w]C_{app}$.

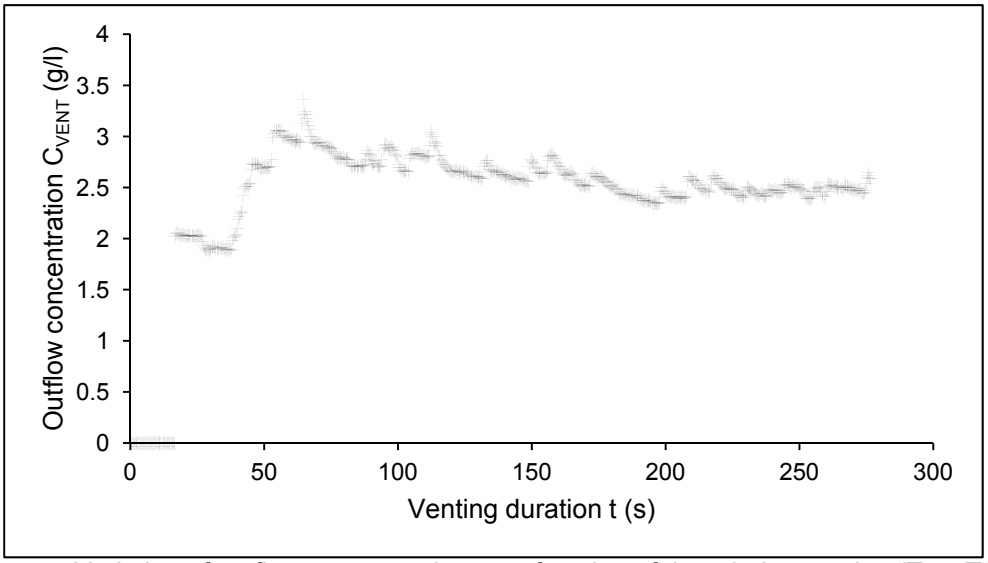

Figure 4. Variation of outflow concentration as a function of time during venting (Test T2.b).

4.2.1 Height of aspiration

As shown in Eq. [1], the height of aspiration depends on the density of the turbidity current reaching the outlet (C_{app}) and the discharge of the outlet. Based on the results shown in Table 3, the zone of influence of the outlet during venting is limited to a height of 21.2 cm on average with very similar values for the different tests. This height corresponds to 25% of the total water depth in the flume. This shows that the effect of venting is very local and that the timing of opening does not affect the height that the bottom outlet can reach out to evacuate from the turbidity current/muddy lake.

Table 3. Height of aspiration of the outlet for the different tests.

Test number	Height of aspiration h_L (cm)
T1.b	22.1
T1.a30	21.2
T1.a60	19.4
T2.b	21.4
T2.a30	21.4
T2.a60	21.8

4.3 Venting release efficiency

The release efficiency of venting is evaluated based on the ratio between the total mass of sediments vented M_{VENT} and the total mass of sediments introduced into the reservoir (main flume) by the turbidity current M_{TC}. In Figure 5, this efficiency is plotted in time for the 2.4% and 5% slopes. For both slopes, during the beginning of venting, the efficiency obtained when operating the outlet before the arrival of the current is lower than the cases where the outlet is opened after the arrival of the current. However, the curves of T1.b and T2.b increase faster and the efficiency obtained in a longer term tends to surpass that obtained when the outlet is opened after the arrival of the current.

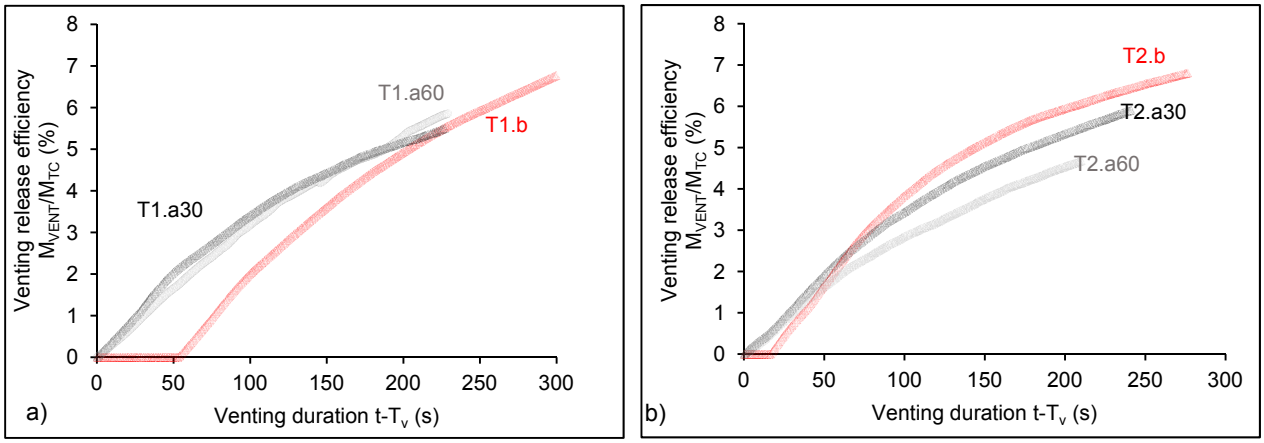

Figure 5. Venting release efficiency as a function of venting duration for the 2.4% slope (left) and the 5% slope (right) (tests numbering according to Table 2).

This is observed in particular for the 5% slope where venting before the arrival of the current gives higher efficiencies starting t-T_v = 60s, where T_v is the time corresponding to the beginning of venting. In order to take into account the major parameters that can affect the efficiency, such as the height of aspiration h_L and the reduced gravity of the approaching current g'_{app}, a normalized time defined by Chamoun et al. (2017) and expressed by $\bar{t} = (t-T_v)^2 g'_{app}/h_L$ is used in Figure 6.

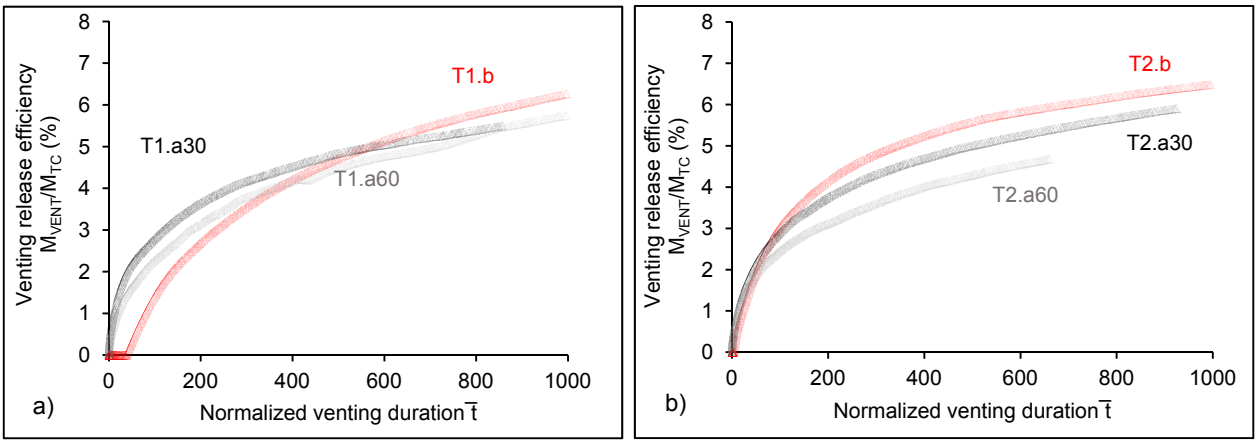

Figure 6. Venting release efficiency as a function of the normalized time for the 2.4% slope (left) and the 5% slope (right) (tests numbering according to Table 2).

The results now show a clearer trend. Log-shaped curves obtained for the different cases suggest that there are two phases in venting. The first phase where venting starts, the increase in efficiency is fast. The second phase, where the current has already climbed up the wall and started reflecting upstream, yields more and more steady efficiencies in time (especially that inflow and outflow have steady conditions in the present work). The graphs in Figure 6 show more clearly that venting before the current reaches the outlet, particularly for long-term operations, can be more efficient than venting after the current has reached the outlet.

5 NUMERICAL MODEL

5.1 Description

In order to extend the analysis based on some visual and unmeasured features, a 3D numerical model was built using ANSYS CFX Inc. The geometry of the numerical model represents the experimental set-up. The mesh is tetrahedral (516'997 elements) except for a hexahedral inflation applied at the bed.

One of the advantages of ANSYS CFX Inc. is that it offers the possibility for users to insert equations to better represent the specific phenomenon simulated. In the present case, equations for the drag coefficient (Cheng, 1997), the settling velocity of the sediments (Richardson and Zaki, 1997; Zhiyao, et al., 2008) and the mixture's dynamic viscosity (Van Rijn, 1987) were added. An inhomogeneous multiphase model was used with the SST turbulence model. The sediment diameter of 140 µm (corresponding to the d_{50} of the material used experimentally) was used with a particle density, ρ_s = 1160 kg/m^3 and a uniform grain size distribution.

The geometry and boundary conditions applied are shown in Figure 7. The calibration of the numerical model was done based on the experimental results.

The numerical model was used to simulate the tests performed with the 5% slope. The release efficiency of venting was computed and the behavior of the vented flow in the vicinity of the dam was evaluated. The three cases of opening timing are called ''before'', ''after 30s'' and ''after 60s'' hereafter.

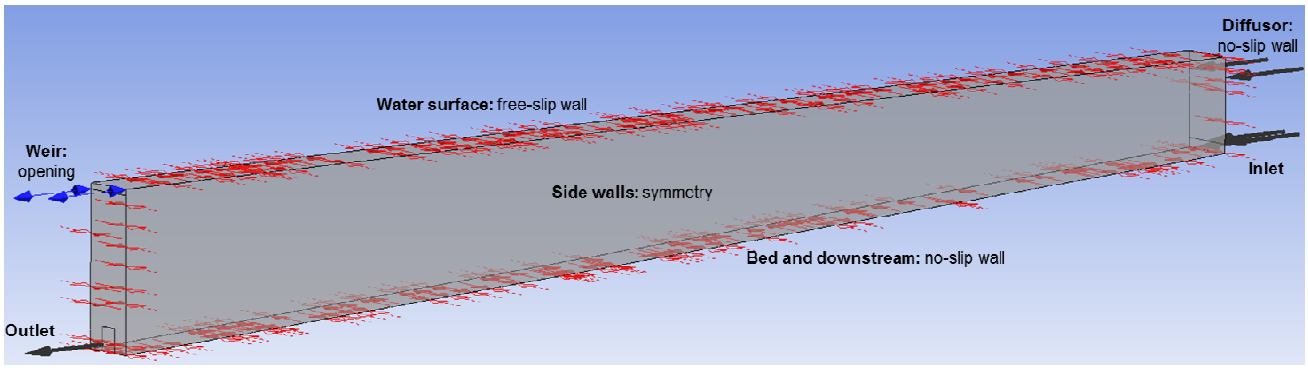

Figure 7. Geometry and boundary conditions used in the numerical model for the 5% slope.

6 NUMERICAL RESULTS

6.1 Venting release efficiency

The results of the release efficiency of venting obtained numerically show quite similar trends in comparison with the experimental results. The efficiency ''before'' is the lowest at the beginning of venting, then it increases faster than the two other cases until reaching efficiencies similar to the ''after 30s'' case and higher than the ''after 60s'' case. Opening the outlet 60s after the arrival of the current to the wall yields the lowest efficiencies.

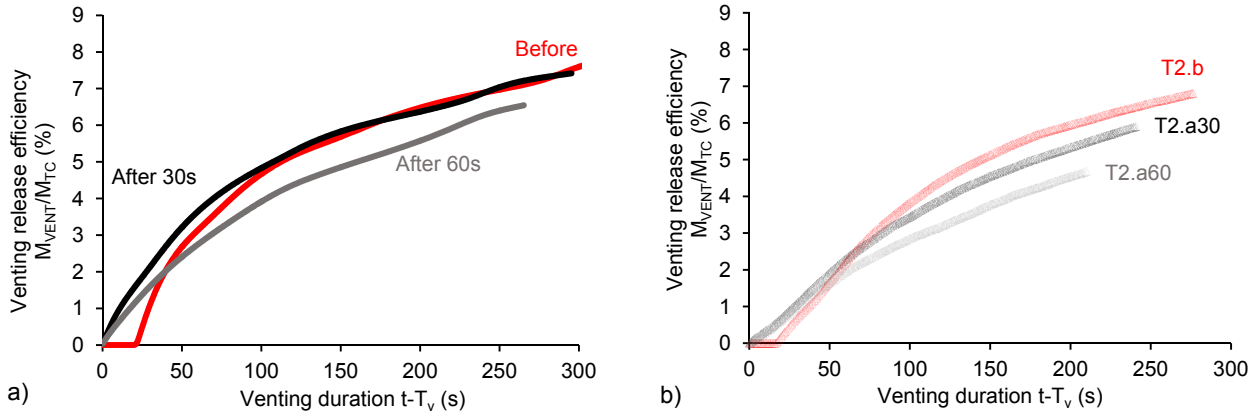

Figure 8. Venting release efficiency as a function of time for the three different timing cases obtained (a) numerically and (b) experimentally for the 5% slope.

A comparison was made between the ''before'' and ''after 60s'' cases based on the volume rendered sediment concentrations. Figure 9 shows that at t = 430s (venting started at t = 125s for the ''before'' case and at t = 205s for the ''after 60s'' case), the ''after 60s'' case shows higher concentrations close to the outlet, while the ''before'' case shows very low concentrations. The latter simply looks like the continuation of the linear decrease of concentrations close to the bed when moving from upstream to downstream. In order to better assess the difference between the two cases, sediment concentrations of ''before'' case were subtracted from the sediment concentrations ''after 60s''. Positive values (Figure 10) were obtained in the vicinity of the wall explaining the lower efficiencies obtained with the ''after 60s'' case. In fact, in the latter case, the muddy lake is well developed before venting has started, rendering the suction of the current continuously reaching the outlet more complicated. Moreover, a kind of interflow seems to form in the ''after 60s'' case due to the high reflection upstream.

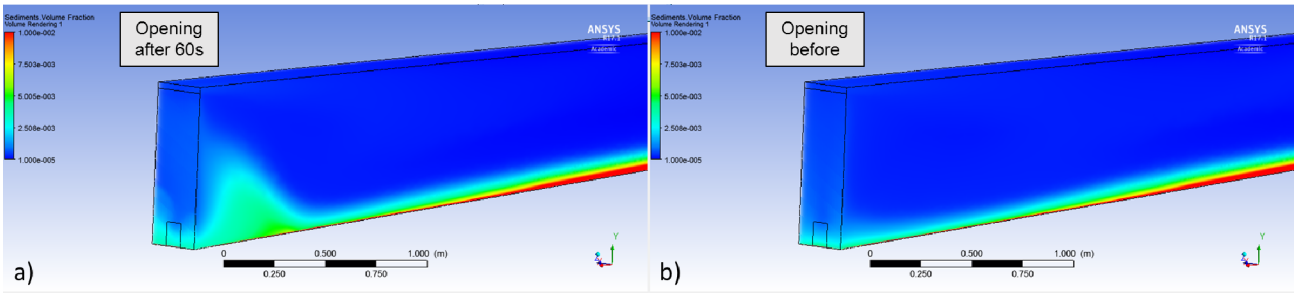

Figure 9. Rendered volumes showing the sediment concentration at t = 430s for the (a) ''before'' and (b) ''after 60s'' cases (slope 5%).

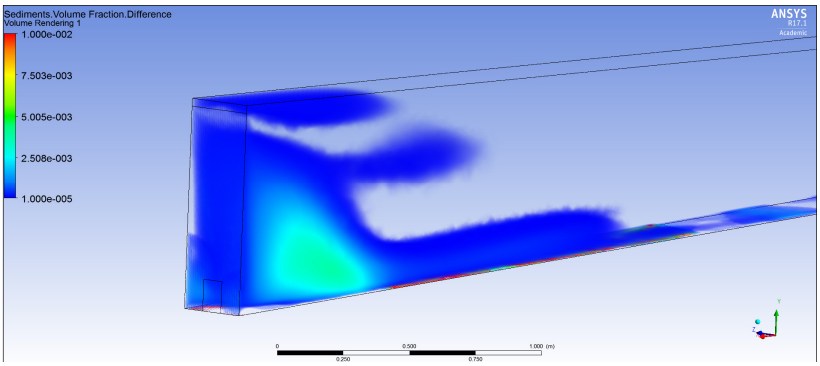

Figure 10. Difference between concentration values of the ''after 60s'' and ''before'' cases obtained numerically at t = 430s in the vicinity of the wall (slope 5%).

Furthermore, the sediment velocity streamlines during venting were computed to improve the understanding of the phenomenon (Figure 11). In fact, the streamlines obtained with the ''after 60s'' case are not well developed between the current and the outlet compared with the ''before'' case. Opening before the current reaches the outlet ensures a better suction of the current once it reaches the dam. Contrarily, when venting is timed after the formation of the muddy lake, parts of the sediments are stuck close to the outlet due to a recirculation (stagnant zone). This zone seems to force the continuously flowing turbidity current to bound over it and reach the outlet at higher levels rendering its transit more complicated and less efficient.

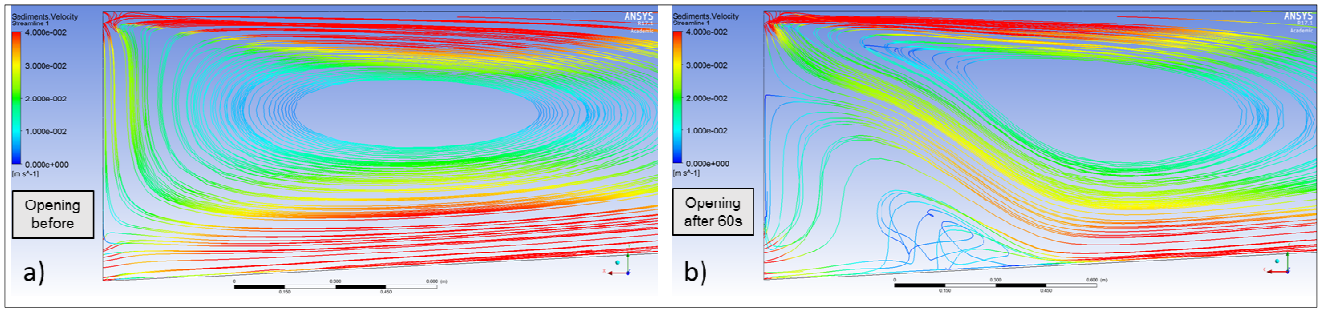

Figure 11. Streamlines in the vicinity of the dam for the case of venting ''before'' and ''after 60s''.

7 CONCLUSIONS

Reservoir sedimentation is an increasing problem that numerous reservoirs are facing worldwide. Preventing or reducing large amounts of sediments that can settle in reservoirs during floods is a must to ensure the sustainability of these structures.

Venting of turbidity currents is among the most economic and efficient mitigation techniques, if performed under optimal conditions. One of the most important operational parameters of venting is the timing of the opening of the outlets. This parameter is discussed in the present paper based on experimental and numerical data. Three different timings are discussed: opening the outlet before the arrival of the current to the dam, after the current has reached the top of the dam (before it starts reflecting upstream), and after the muddy lake has formed and began reflecting upstream.

Based on the calculation of the height of aspiration for the different tests, venting is shown to have a very local influence in terms of height where the aspiration level reached 25% of the total clear water depth. The venting release efficiencies are experimentally shown to be slightly more favorable when opening after the current reaches the dam, during a certain time at the beginning of venting. After this duration, efficiencies

obtained in the case of opening the outlet before the arrival of the current to the wall become higher. It seems that the earlier the opening takes place, the longer the time it takes to produce higher efficiencies than the case of operating the outlet after the current has reached the dam. This suggests that opening the outlet when the current is the closest to the dam can be the best timing.

These trends were more or less identical numerically, particularly when comparing the efficiencies obtained when the outlet is opened before the current has reached the wall and the ones obtained after the muddy lake has started reflecting upstream. Sediment concentration contours and streamlines were computed numerically and show the formation of a recirculation zone upstream of the outlet that forces the continuously inflowing current to bounce and renders its suction more complicated. On the opposite, in the case where the outlet is opened before the arrival of the current to the wall, it is smoothly evacuated and streamlines are well developed.

Finally, the output of the present research can provide missing input for dam operators needing crucial information on the optimal conditions to perform venting and reduce sedimentation rates.

ACKNOWLEDGEMENTS

The study titled ''Efficiency of turbidity currents venting under varied outflow discharges'' is funded by Swisselectric Research and the Swiss Committee on Dams. This work is supervised by Prof. Anton J. Schleiss and co-supervised by Dr. Giovanni De Cesare from the Ecole Polytechnique Fédérale de Lausanne.

REFERENCES

Bell, H.S. (1942). Density Currents as Agents for Transporting Sediments. *The Journal of Geology*, 50(5), 512–547.

Brandt, S.A. (2000). A Review of Reservoir Desiltation. *International Journal of Sediment Research*, 15(3), 321–342.

Chamoun, S., De Cesare, G. & Schleiss, A.J. (2017). Venting of Turbidity Currents Approaching a Rectangular Opening on a Horizontal Bed. *Journal of Hydraulic Research* (Accepted For Publication).

Chen, J. & Zhao, K. (1992). Sediment Management In Nanqin Reservoir. *International Journal of Sediment Research*, 7(3), 71–84.

Cheng, N. (1997). Simplified Settling Velocity Formula for Sediment Particle. *Journal of Hydraulic Engineering*, 123(2), 149–152.

Craya, A. (1949). Recherches Théoriques Sur L'écoulement De Couches Superposées De Fluides De Densités Différentes [Theoretical Research On Multiple-Layer Stratified Flows]. *La Houille Blanche*, 35(1), 44–55 (In French).

Espa, P., Brignoli, M.L., Crosa, G., Gentili, G. & Quadroni, S. (2016). Controlled Sediment Flushing at the Cancano Reservoir (Italian Alps): Management of the Operation and Downstream Environmental Impact. *Journal of Environmental Management*, 182, 1–12.

Fan, J.-H. (1960). Experimental Studies on Density Currents. *Scientia Sinica*, 4(2).

Fan, J. & Morris, G.L. (1992). Reservoir Sedimentation II: Reservoir Desiltation and Long-Term Storage Capacity. *Journal Of Hydraulic Engineering*, 118(3), 370–384.

Gariel, P. (1949). Recherches Expérimentales Sur L'écoulement De Couches Superposées De Fluides De Densités Différentes [Experimental Research On Mutiple-Layer Stratified Flows]. *La Houille Blanche*, 35(1), 56–64 (In French).

Graf, W.H. & Altinakar, M.S. (1995). Courants De Turbidité [Turbidity Currents]. *La Houille Blanche*, 81(7), 28–37.

Kantoush, S.A. & Sumi, T. (2010). *River Morphology and Sediment Management Strategies for Sustainable Reservoir In Japan and European Alps*. In Annuals of Disaster Preventive Research Institute (Pp. 821–839). Kyoto, Japan.

Lee, F.Z., Lai, J.S., Tan, Y.C. & Sung, C.C. (2014). Turbid Density Current Venting Through Reservoir Outlets. *KSCE Journal of Civil Engineering*, 18(2), 694–705.

Morris, G. & Fan, J. (1997). *Reservoir Sedimentation Handbook: Design and Management of Dams, Reservoirs, and Watersheds for Sustainable Use*. Mcgraw-Hill, New York.

Müller, P.J. & De Cesare, G. (2009). Sedimentation Problems in the Reservoirs of the Kraftwerke Sarganserland - Venting of Turbidity Currents as the Essential Part of the Solution. General Report Q.89-R.21. In *Proceedings of The 23rd Congress of the International Commission On Large Dams CIGB-ICOLD*. Brasilia: Vol. 2, Brasilia, Brazil, Q.89-R.21.

Nizery, A., Braudeau, G. & Bonnin, J. (1952). La Station Du Sautet Pour L'étude De L'alluvionnement Des Réservoirs [The Sautet Station For Studying The Sedimentation Of Reservoirs]. In *Proceedings Transport Hydraulique Et Décantation Des Matériaux Solides [Hydraulic Transport And Settling Of Solid Material]* (P. 180–218) (In French). France.

Richardson, J.F. & Zaki, W.N. (1997). Sedimentation and Fluidisation: Part I. *Chemical Engineering Research and Design*, 75, 82–100.

Schleiss, A.J., Franca, M.J., Juez, C. & De Cesare, G. (2016). Reservoir Sedimentation. *Journal of Hydraulic*

Research, 54(6), 595–614.
Schneider, J., Badura, H., Troy, W. & Knoblauch, H. (2007). Determination of Parameters for Venting Turbidity Currents. In *IAHR Congress* (P. 425). Venice, Italy.
Van Rijn, L.C. (1987). Mathematical Modelling of Morphological Processes in the Case of Suspended Sediment Transport. *Delft Hydraulic Communication No. 382*.
Yu, W.-S., Hsu, S.M. & Fan, K.-L. (2004). Experiments on Selective Withdrawal of a Codirectional Two-Layer Flow Through a Line Sink. *Journal of Hydraulic Engineering*, 130(12), 1156–1166.
Zhiyao, S., Tingting, W., Fumin, X. & Ruijie, L. (2008). A Simple Formula for Predicting Settling Velocity of Sediment Particles. *Water Science And Engineering*, 1(1), 37–43.

FEASIBILITY STUDY OF SEDIMENT FLUSHING FROM A MEXICAN RESERVOIR LOCATED IN THE VALLEY OF MEXICO BASIN; BY USING NUMERICAL MODELS IN 2D AND 3D

MIGUEL ANGEL BRIBIESCA RODRIGUEZ [(1)], JORGE IVAN JUAREZ DEHESA [(2)] & FERNANDO J. GONZALEZ VILLARREAL [(3)]

[(1,2,3)] Institute of Engineering, National Autonomous University of Mexico, Mexico City, Mexico.
mbribiescar@iingen.unam.mx; jjuarezd@iingen.unam.mx; fgonzalezv@iingen.unam.mx

ABSTRACT

One of the main problems that affect reservoirs is the loss of long-term capacity due to sedimentation problems. When a reservoir gets designed, there is always an available volume for the sediments to be stored, however, in many occasions this volume gets exceeded, and leads to loss of useful volume in the reservoir. This paper discusses the feasibility of flushing sediments from a Mexican reservoir in the State of Mexico where this dam will become an important source of drinkable water to the population of both the Valley of Mexico basin and Mexico City. However, recent studies have shown that this dam will get severe sedimentation problems in no longer than five years period, that leads to the main reason of this paper which is to demonstrate the feasibility of flushing sediments from the reservoir in order to get an efficient operation policy and increase the reservoir useful lifespan.

Keywords: Flushing sediments; reservoirs useful life; atkinson method; low level outlets; valley of mexico basin.

1 INTRODUCTION

As a river gets an obstruction with structures like dams, it gets a stagnation that leads the sediments to get transported and it will behave according to the next mechanism (Figure 1): as the stream goes in to the reservoir, the thicker material will dispose according to the narrowing of the water speed due to the effect of the stream´s enlargement and the water´s depth growing, created at the reservoir´s "tail", leading to a accumulation of the thicker material called "delta". The finer sediment will continue up to inside of the reservoir as a density stream for further stagnation and accumulation at the bottom of the reservoir. There are many reservoirs in which density stream don´t get to generate itself, and a generalized turbidity is produced at the reservoir, or at least at most of it, that will evolve per the particular settle dynamics.

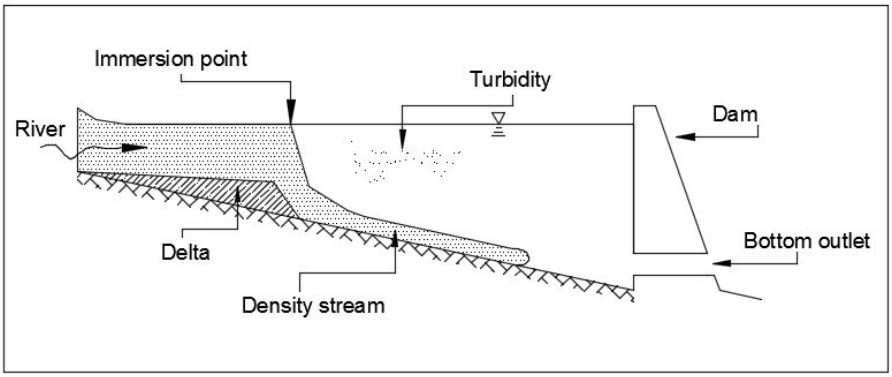

Figure 1. Scheme of the sediment behavior within a reservoir (Gracia, 1997)

The sedimentation mechanism described above is more complex in reality, because it depends of many other factors as it is: temperatures stratification, shape, dimensions and reservoir´s special features, operation policies, sediment´s physiochemical features and the incoming water flood, among others.

When it comes to large reservoirs, the generation of the delta has a major importance due to its river´s upstream effect and because of the occupant volume within the reservoir. The backwater occasionally floods areas that before of the delta generation, were not used to be flooded. And when the dam is not that large and has frequent spills, it is possible for the delta to occupy a major part of the reservoir and, in such case, the thicker sediment is the main reason of the loss of useful capacity, due to most of the fine sediment probably will not be deposed, it will move on, downstream.

Settled material at the bottom of the reservoir, will be restricted to compaction as time goes by. This effect will get accentuated as the levels of the reservoir sensibly change, making it to produce an alternated dry-off and moistening of the settled material. This leads to two important problems: one, the volume change deposited throughout the time that affects the quantity of stored water. Two, the removal difficulties of highly compacted sediment.

1.1 Reservoir clogging.

The final destination of the reservoirs is to get filled with the sediment or get silted. If the sediment input is bigger comparing with the reservoir´s capacity, its useful life could be very short. For example, in a small storage reservoir in the state of Lara, Venezuela, it got filled with sediments within the first year after their opening, even before of the aqueduct´s inauguration. The planning of a reservoir must include the most likely silting rate, in order to, determinate if the reservoir´s useful life will be enough to guarantee their construction.

A small reservoir over a large stream, passes most of its sediment contribution so quickly that the finer sediments will not be deposited, but they will be discharged downstream. On the other hand, a large reservoir can storage water for years and allows the almost complete removal of the hanging sediment. The trapping efficiency in a reservoir gets diminished as the reservoir´s useful life goes by. Thus, the reservoirs capacity gets diminish by the sediment accumulation. Thereby, a complete reservoir clogging can happen in a short time, but in reality, the reservoir´s useful life ends when the volume of sediment is enough to avoid the reservoir to accomplish its purpose which was originally bound to.

1.2 Sediment flushing

Dams are getting silted at an approximately rate of 1% worldwide. This implies that by half of the 21st century, the world´s water storage will be half of the current one. This will lead to important economics and environmental consequences.

Flushing is scouring out of deposited sediment from reservoirs with the use of low level outlets in a dam to lower water levels, and so increase the flow velocities in the reservoir. The technique is not widely practice because:

- It is usually only effective in narrow reservoirs
- It involves large volumes of water being passed through the dam.
- It requires the reservoir to be emptied.

However, flushing has proved to be highly effective at some sites. For example, the Tarbela Dam in Pakistan, Gebidem Dam in Switzerland, the Unazuki Dam in Japan and the Baira Dam in India, just to name a few. The most influential factors for the flushing to be successful are:

- Shape of the reservoir (it has better results and greater efficiency when it comes about large and narrow reservoirs).
- Volume of the reservoir (the shorter the reservoir is -comparing with the annual volume of water- the better the result is)
- Hydraulics conditions (it has been better results through the induction of river conditions in the reservoir).
- Predictability and annual flood magnitude.
- Mobility of the sediments within the reservoir.

Mexican reservoirs are not exempted of the sedimentation problem, and that is the main topic of this paper. It is to demonstrate the flushing feasibility of a Mexican reservoir through 2D and 3D numerical models. In the first place, the 2D model were simulated by a Spanish software named IBER, and in the second place the 3D model were simulated by the FLOW 3D software.

2 METHODOLOGY

The studied dam had an imminent problem of reservoir sedimentation. This is the reason, why both simulations were done by using 2D and 3D models. But in order to prove the flushing feasibility, the Atkinson method was carried out by using the dam´s actual conditions and once the flushing feasibility was proved, the Atkinson method helped to calibrate both models.

2.1 The Atkinson method

This numerical method is the most used and recommended by the International Commission of Large Dams (ICOLD). By applying this criteria, reservoirs at which flushing might be viable can be identified, and a preliminary estimate of the sustainable storage capacity can be made.

In order to get a successful flushing of sediment, this criterion was based on a fully satisfaction of the sediment balance ratio (SBR), the long term capacity ratio (LTCR), the draw down ratio (DDR), the flushing width ratio (FWR) and top width ratio (TWR).

An equation expressing the sediment balance ratio, SBR (Equation1), is defined:

$$SBR = \frac{M_f}{M_{dep}} = \frac{86400(T_f)(Q_s)}{M_{in} \cdot TE} \quad [1]$$

where,

$$Q_s = \psi \frac{Q_f^{1.6} \cdot S^{1.2}}{W^{0.6}} \quad [2]$$

According to the Equation 1, the term *Qs* is referred to the flushing discharge (m^3/s) and *W* is the flushing width by taking the minimum value between a representative reservoir width in the reach upstream from the dam at the flushing water surface elevation, and, the width of the flow at the bed of flushing channel. The ψ term is defined as a constant for sediment type according to the University of Tshinghua criterion (Table XX). And the T.E term refers to the trapping efficiency of the reservoir according to the Brone´s curve (Figure 2).

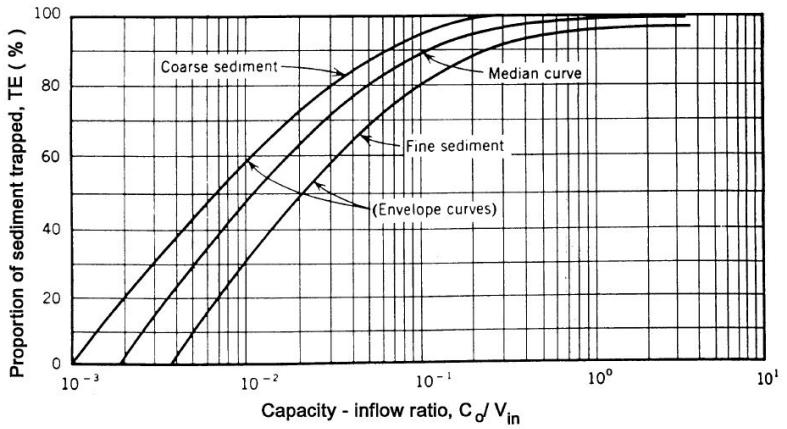

Figure 2. Brone´s curve for estimating reservoir trapping efficiency

If SBR > 1.0 then is expected that a sediment balance can be achieved and so this criterion is satisfied.

The criterion based on the long term capacity was based on a simplified geometry of the reservoir. A trapezoidal shaped scoured channel with its bottom at the original river elevation and the total reservoir volume which can be calculated from that assumed final cross sections has been termed the “sustainable capacity”. A long term capacity ratio, LTCR, can be defines as follow:

$$LTCR = \frac{A_f}{A_r} \quad [3]$$

Where the *Af* term is the sustainable capacity of the reservoir and the *Ar* term would be the original capacity. Values of LTCR greater than about 0.5 would indicate that the capacity criterion is partially satisfied with values approaching unity indicate that the criterion is fully satisfied. An acceptable value for LTCR will depend on the costs associated with flushing, which, in this will not be determined.

It had been observed that a tending full drawdown flushing is more effective when it comes about sediments transportation. The Atkinson method suggested that a minimum drawdown of 70% during flushing will be enough to get the DDR criterion fully satisfied. This ratio, termed DDR, is defined as follows:

$$DDR = 1 - \frac{El_f - El_{min}}{El_{max} - El_{min}} \quad [4]$$

The scoured valley formed by flushing will have a bottom width approximately equal to the flushing width previously calculated from the SBR, unless this calculated width exceeds the width of the reservoir at that elevation. Flushing channel width should also be assessed independently of the extent of drawdown, so a flushing width ratio, FWR, can be defined:

$$FWR = \frac{W_f}{W_{bot}} \quad [5]$$

If FWR is significantly less than unity the flushing width can be considered an important constraint. An exception will arise, however, for reservoirs where the side slope of the exposed deposits is shallow according to Atkinson (1996).

Finally it is the TWR criterion, which is related with the simplified geometry of the reservoir, according to Atkinson, TWR values approaching unity are sufficient. TWR can be defined:

$$TWR = \frac{W_{td}}{W_t} \quad [6]$$

2.2 Iber software (bidimensional modeling)

The software IBER is a free surface turbulent flow simulation numerical model in a non-permanent regime and with environmental and fluvial hydraulics processes. Iber´s application rank embraces fluvial hydrodynamics, dam rupture simulation and assessment of flood zones, sediments transportation calculation, and tidal flow in estuaries.

The Iber model features about three main calculation modules: one hydrodynamic module, one turbulence module and one sediments transportation module. Each of these modules work with a finite volume of non-structured mesh, featured by triangular or squared elements.

In the sediments transportation module, the bedload transport and suspended load transport equations get solved. Having both ways of sediment transportation, the evolution of the bottom height gets calculated due to silting and erosion processes through Exner´s equation. In the updated version (used in this paper) there were only considered for uniform granulometries. The sediments transportation module used the velocities, depths and turbulence fields provided by the hydrodynamic and turbulence modules.

The bottom solid flow was calculated through an empirical formulation where it could be chosen among the Meyer-Peter Muller formulation and the Van Rijn´s one. The suspended load transport was modeled through an average turbulent transport equation.

The current simulation done for this paper was proposed with the Meyer-Peter Muller´s equation, which was deducted for gravel bottoms of up to 30 mm diameters and it calculates the solid flow in m^2/s as follows:

$$q_{sb} = 8 \cdot (\tau^*_{bs} - \tau^*_c)^{3/2} \quad [7]$$

The q^*_{sb} term is the non-dimensional solid flow and it is gotten the sediment own characteristics in the studied zone (density and particle diameter), and it is calculated as follows:

$$q^*_{sb} = \frac{q_{sb}}{\sqrt{\left(\frac{\rho_s}{\rho} - 1\right) g D_s^3}} \quad [8]$$

It is important to mention that some considerations were made when the transportation bottom is not flat. In other word, if there is a flat bottom in equation 7, the critical tension value will be τ_c*=0.047. On the other hand if the bottom is not flat at all (as in this case), a correction by bottom slope has to be made and the equation above should be corrected in order to consider the gravity´s effect both in the way to increase the bottom transportation with positive slope, and to diminish it with adverse slope. [1]

2.3 Flow 3D (three-dimensional modeling)

The three-dimensional sediment scour model allows multiple non-cohesive species of soil and considers entrainment, deposition, bedload transport and suspended load transport. The sediment scour model assumes multiple sediment species with different properties including grain size, mass density, critical shear stress, angle of repose and parameters for entrainment and transport. The FLOW 3D model also calculates all the sediment transport processes including bedload transport, suspended load transport, entrainment and deposition for each species of soil.

According to the FLOW 3D manual, “entrainment” is the process by which turbulent eddies remove the grains from the top of the packed bed and carry them into suspension.

For this particular case, it was only considered that the bedload transport due to the suspended load transport has very or non-influence in the flushing process. The dimensionless form of the bedload transport rate for species “n” is defined as:

$$\Phi_n = \frac{q_{b,n}}{\sqrt{\left(\frac{\rho_s}{\rho} - 1\right) g d_n^3}} \quad [9]$$

[1] For further information, please check the Iber´s reference manual

Where $q_{b,n}$ is the volumetric bedload transport rate per unit bed width (in units of volume per width time). Φ_n Is calculated by using the Meyer-Peter and Muller equation where we notice the similarities between the bidimensional Meyer-Peter and Muller equation and this one.

It is important to mention that all the simulations were made by using the Meyer-Peter and Muller equation

The sediment flushing was simulated, on one hand, by using Iber and on the other hand, FLOW 3D helped to simulate the sediment passing through the bottom outlets. The sedimentation model was used with a sediment diameter of D_{50}= 1.75 mm and one specific weight of 2.65 ton/m^3

In order to get the three-dimensional simulation, a solid dam was built where CAD tools was used to feed the model (Figure 2)

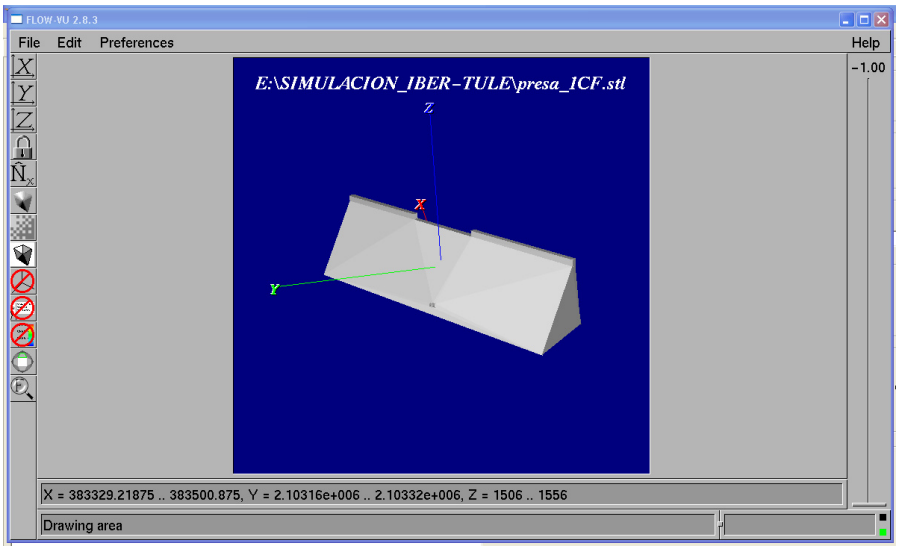

Figure 3. Solid dam uploaded in the FLOW 3D

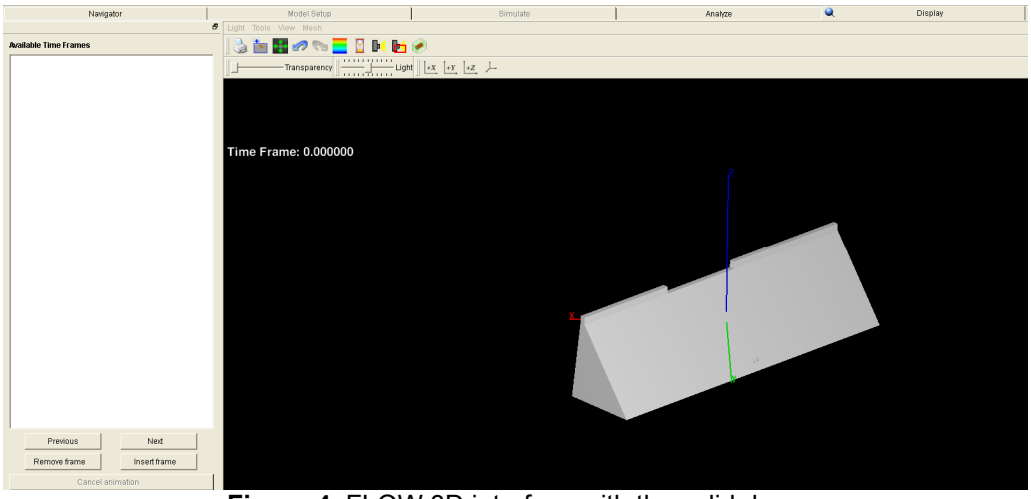

Figure 4. FLOW 3D interface with the solid dam.

The solid dam above was built for both numerical models, however, due to timing reasons, the complete flushing process was simulated on the bidimensional model and the scoured out sediment was simulated with the three-dimensional model by meshing only the bottom oultets, to get a further comparative among these two models.

3 PROBLEM AVAILABLE DATA

3.1 Characteristics of the dam

According to the previously collected data this dam will be considered as a large dam (ICOLD rank), and in a no longer than 5 years period. This dam will get severe sedimentation issues, leading it to a complete loss of useful capacity in approximately 9 years.

For the Atkinson criterion, it was necessary to use a constant for sediment type provided by the Thsinghua University in China, and in this particular case (D_{50}= 1.75 mm) the constant value was 300.

Table 1. Parameter in the Tshinghua University method for sediment load prediction.

Ψ=1600	For fine loess sediment
Ψ=650	For $D_{50} < 0.1\ mm$
Ψ=300	For $D_{50} \geq 0.1\ mm$
Ψ=180	If the flushing discharge is low (say less than 50 m³/s)

Finally, Tables 2 and 3 showed all the characteristics of the studied dam for two different water levels, which are the Ordinary Maximum Water Level and the Operational Minimum Water Level. The Atkinson criteria was carried out by using both water levels. And once the Atkinson criterion was obtained, the most efficient result will be used to calibrate both the 2D and 3D models.

Table 2. Atkinson criterion parameters for the Ordinary Maximum Water Level[2]

Atkinson Criterion		
Original storage capacity (C_o)	10,480,456	m³
Reservoir length (L)	3,400	m
Dam height	50	m
Bottom outlets hydraulic dimensions x2	400x400	cm
Elevation of top water (El_{max})	1551.75	masl
Minimum bed elevation immediately upstream from the dam (El_{min})	1504.4	masl
Constant for sediment type (ψ)	300	
Proposed duration of flushing (T_f)	0.1	days
Outlet sill elevation and outlet design (El_f)	1508	masl
Representative discharge passing through reservoir during flushing (Q_f)	383	m³/s
Mean annual sediment inflow (M_{in})	2,659,750.9	ton
Mean annual water inflow volume (V_{in})	271,700,000	m³
Trapping Efficiency (TE)	0.8	
Representative side slope for the reservoir (SS_{res})	1.37	
Representative side slope for the deposits exposed by flushing (SS_s)	0.45	

4 OUTPUT RESULTS

4.1 Atkinson criterion

By applying the Atkinson criterion to the studied dam the following results are gotten.

Table 4. Atkinson criterion results for the Ordinary Maximum Water Level.

Atkinson criterion results		
Criterion	**Value**	**Required value**
SBR	3.24	> 1
LTCR	1.44	> 0.5
DDR	0.92	> 0.7
FWR	6.06	> 1
TWR	0.6	~1

At first sight the sediment flushing will be successful for this particular dam as four of the five criteria get completely satisfied for the water levels. However, as the flushing involves large volumes of water passing through the reservoir, this could mean tremendous loss of money as the water passes by, therefore, in order to get the cheapest project as possible, the water level used to get the simulation done was the Operational Minimum Water Level.

The previous statement is because both results for the Atkinson criterion were very similar, so in order to get the most efficient proposition, the Operational Minimum Water Level will secure the least loss of money possible.

[2] The term “masl” is for “meters above the sea level”

4.2 Iber and FLOW 3D software

To build the most accurate model for simulation, a digital elevation model (DEM) was used and in turn the bathymetric data was previously gotten (Figure 4). For the bottom outlets, they were considered as well-finished concrete (n= 0.018) with a rectangular geometry. For the Iber simulation the hydrodynamic module was activated with an initial elevation of 1551.75 masl (meters above the sea level) which is the minimum water level of operation.

Unlike the Atkinson criterion, for the Iber simulation, a 1-day flushing time was proposed (86,400 seconds). For the sediment initial conditions, only the bedload transport condition was activated, due to that in this case, the suspended load transport has no influence. Thus by having low water levels in the dam and by opening the bottom outlets a supercritical regime is obtained in order to get sediment out of the dam.

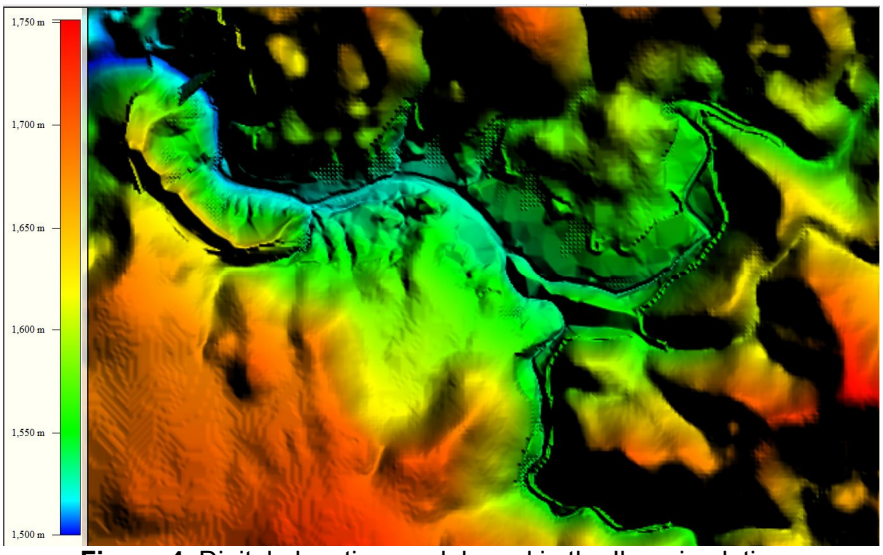

Figure 4. Digital elevation model used in the Iber simulations

It must be mentioned that the input hydrograph was not a hydrograph itself, but a constant flow of the river upstream the dam. This flow is the mean annual flow and it is about 8.4543 m^3/s.

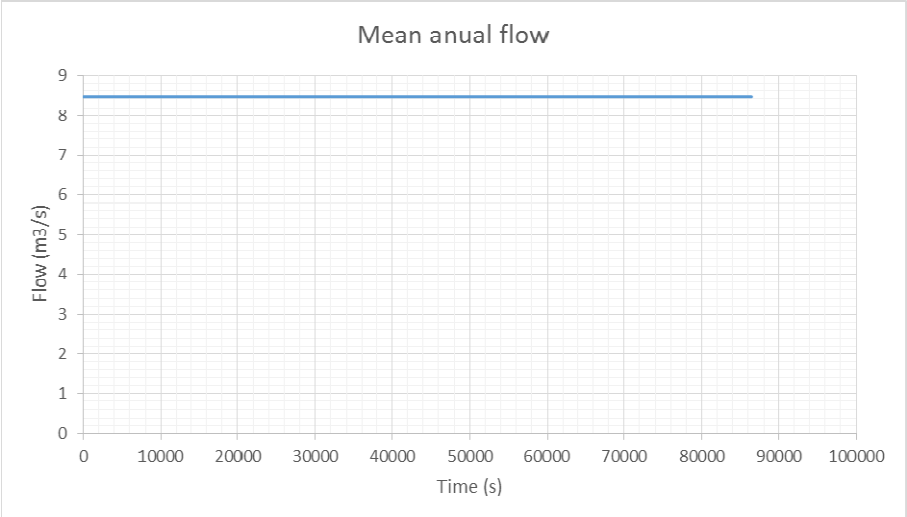

Figure 5. Mean annual flow graph for the bidimensional simulation.

4.3 Simulation results

According to the bidimensional simulation, different kinds of results were displayed by Iber. Among the displayed results are the “Bottom height” results which showed the main effects of erosion within the reservoir during the simulation.

Figures 7, 8 and 9 show the simulation results at the beginning and at the end of the 1-day flushing simulation. The displayed results were for water depth, water velocities at the bottom outlets and bedload transport.

Figure 6 shows the cross section immediately at upstream of the dam´s curtain at the beginning of the simulation and at the end of the same one.

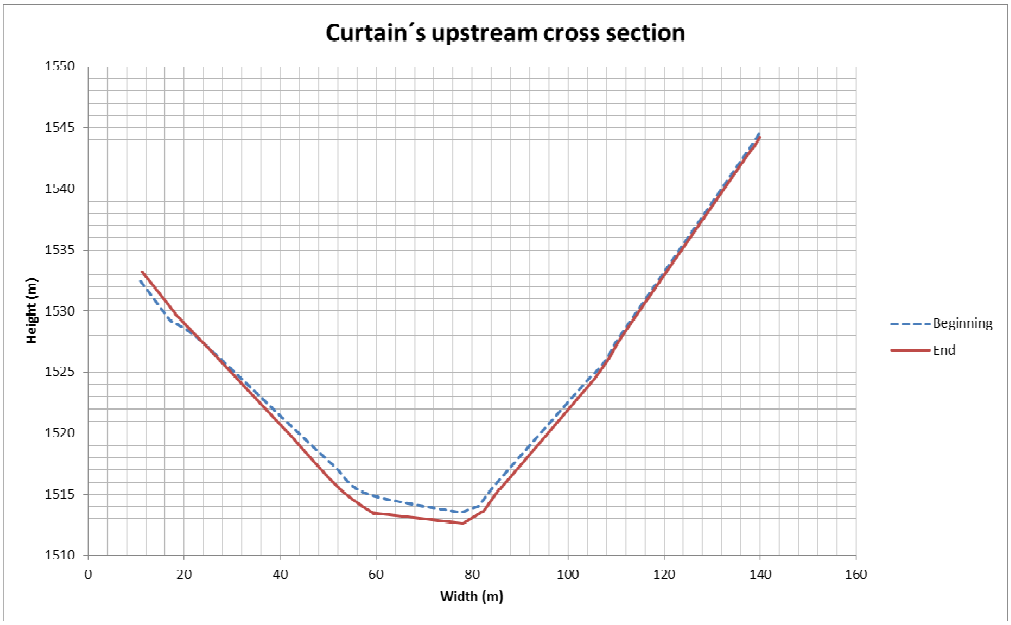

Figure 6. Sediment flushing results in the immediate cross section upstream the dam´s curtain

According to the above figure, the erosion results showed that the height difference between the beginning of the simulation and the end is 16 meters that implies a flushed sediment volume of 3.6 Hm3, which represents 34% of the reservoir's useful capacity.

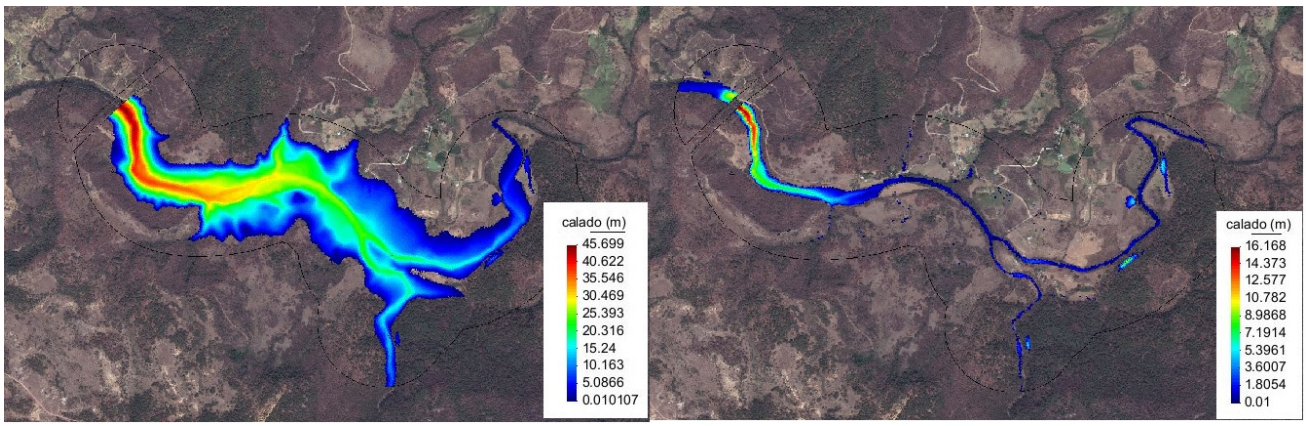

Figure 7. Water depth at the beginning and at the end of the 1-day simulation.

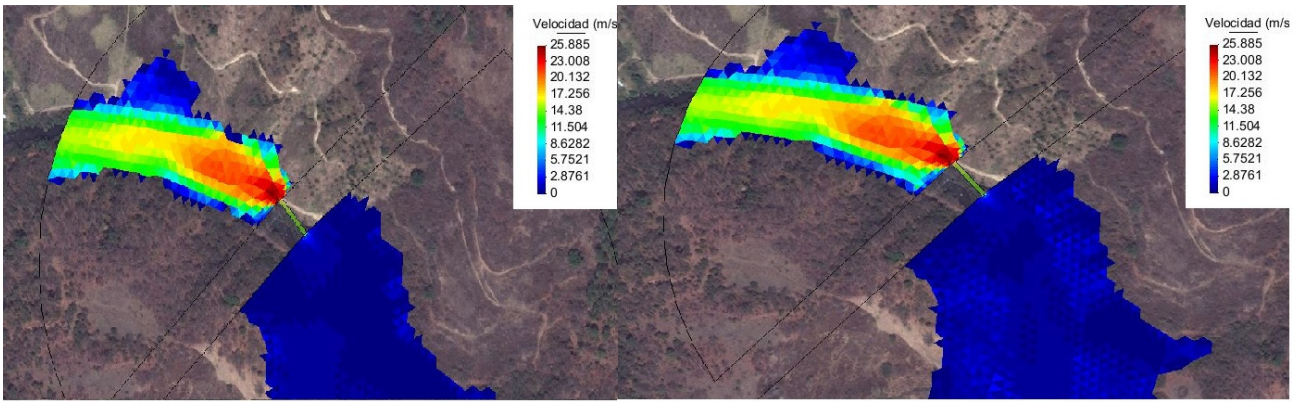

Figure 8. Water velocity within the bottom outlet at the beginning and at the end of the 1-day simulation.

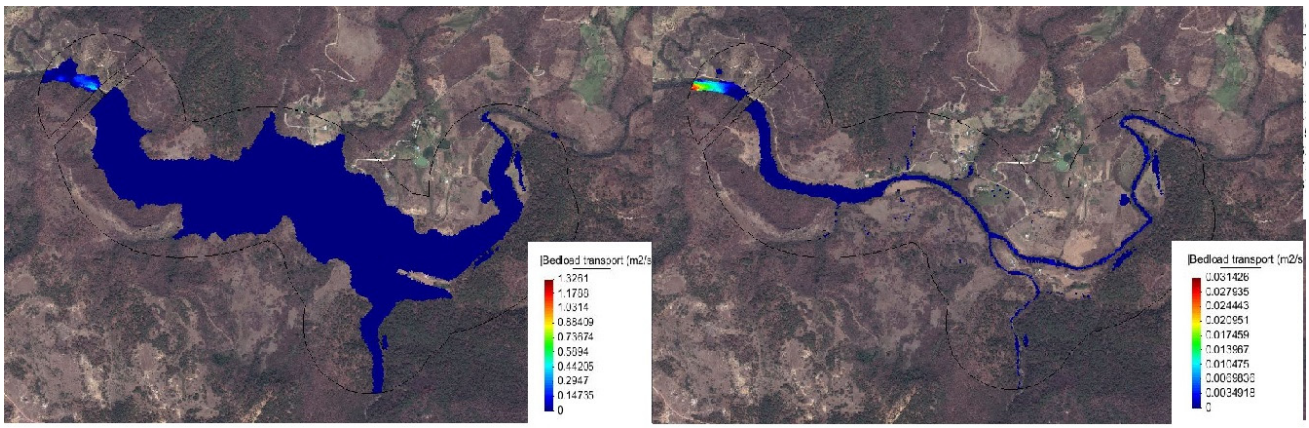

Figure 9. Bedload transport at the beginning and at the end of the 1-day simulation.

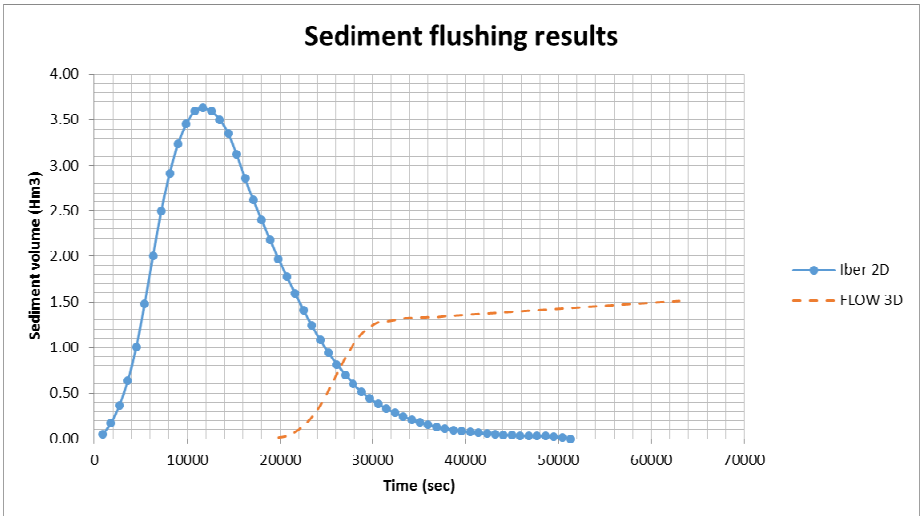

Figure 10. Sediment scouring results by using both numerical models.

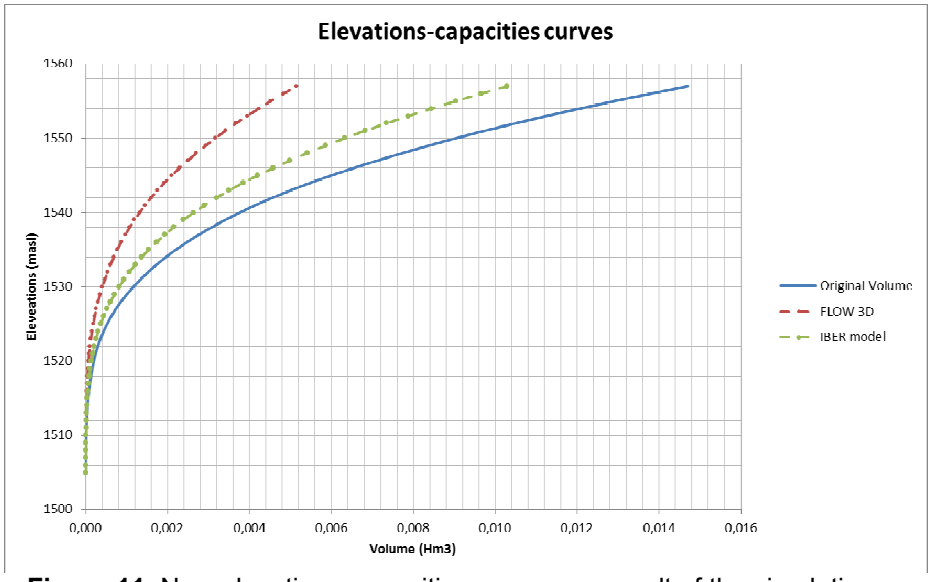

Figure 11. New elevations-capacities curve as a result of the simulations.

According to Figure 9, the elevations-capacities curves generated by the IBER and FLOW 3D software were very similar. However, for the 3D model the curve was shorter than the other ones because of the lack of time to simulate and the lack of RAM within the computer.

5 CONCLUSIONS

Out of the criteria proposed by Atkinson, four of those five get satisfied and the last one gets partially satisfied.

The SBR value is higher than recommended and with this the sediment mass flushed annually will be at least 3 times greater than the sediment mass depositing annually. The LTCR value estimates that the area of the flushing channel (the one free of sediments within the reservoir) is 1.44 times of the reservoir´s cross section.

As far as the DDR is concerned, it will have a 92% reservoir drawdown, which satisfies the criterion. Based on the results of the FWR criterion it is observed that the flushing channel bottom width is approximately 6.06 times greater than the reservoir´s bottom width, and with this the criterion gets fully satisfied.

Regarding to Figure 8 and 9, it is clear that the flushing will be successful and it will bring a lot of long term benefits to the dam. The elevations-capacities curve in Figure 9, shows the original one and the other two, resulted of the simulations. Figure 8 shows that by using the bidimensional model, at least 66% of the reservoir´s capacity would be recovered, and the 3D model showed that 35% of the sediment near of the curtain will be scoured out for that period of time specifically.

If the sediment flushing is carried out at least once every 5 years, it could lead to long term capacity recovery of the dam, as the simulations showed that if this technique is applied, at least the 70% of the reservoir will be recovered. The authors have to mentions that further actions have to be done downstream of the dam´s curtain in order to manage the scoured sediment. This is because as Figure 8 shows both the water and the scoured sediment velocities are so high that they could affect the nearest ecosystems.

The authors recommended to use sediment flushing once every 5 years with a 1 day duration in order to not to lose too much water volumes in the process.

ACKNOWLEDGEMENTS

First and foremost, we would like to thank to Dr. Jesus Gracia Sanchez., for his immense patience and above all his accurate advices to get this paper done. Second, we would like to thank Dr. Jose Luis Aragón for all his advices and for his big help at the use of the Iber software.

REFERENCES

Atkinson, E. (1996). The Feasibility of Flushing Sediment from Reservoirs. HR Wallingford, UK. Report No. OD 137.

Gracia Sánchez, Jesús (1997). *Sedimentación en embalses*. Capítulo 18 del Manual de Ingeniería de Ríos, Serie del Instituto de Ingeniería 601, April 1997.

IBER, Transporte de sedimentos. Retrieved from Website. URL: http://iberaula.es/modelo-iber/transporte-de-sedimentos on January 2017.

IBER, *Manual de Referencia Hidráulico*. Retrieved from Website. URL: http://iberaula.es/modelo-iber/descarga on January 2017.

Sotelo, A.G. (2002). Hidráulica de Canales. México, *UNAM*, Facultad de Ingeniería, 2002, 836.

EFFECTS OF CONSTITUTIVE RELATIONS ON TURBIDITY CURRENT EVOLUTIONS

JING WANG[(1)]

[(1)] State Key Laboratory of Water Resources and Hydropower Engineering Science, Wuhan University, Wuhan, China, wjn@whu.edu.cn

ABSTRACT

Turbidity currents are often hyperconcentrated flows of which the constitutive relations are typically non-Newtonian. Evolutions of these turbidity currents are quite distinct from those of Newtonian turbidity currents due to different viscous resistance laws. However, existing turbidity current models are mostly based on the Navier-Stokes equations, which implicitly assume the currents to be Newtonian. Here, new non-Newtonian turbidity current models are presented by first incorporating two essential non-Newtonian properties; yield stress and shear thinning, to the previous fully coupled model in the form of Herschel-Bulkley and bilinear constitutive relations, respectively. Both non-Newtonian models can be degenerated to traditional Newtonian model in dilute current cases. The models are numerically solved by Slope Limiter Centered (SLIC) scheme under the framework of finite volume method. A systematic series of lock-exchange experiments are revisited. In contrast with the limited prediction capability of traditional Newtonian model at low initial concentration of turbidity currents, the proposed models are demonstrated to perform equivalently well at low initial concentrations, in consistent with the measured data appreciably better in intermediate initial concentrations and partially reproduce the abrupt transitions at high initial concentrations. Nevertheless, the quantitative differences between numerical results and measured data necessitate further detailed investigations on the non-Newtonian properties of hyperconcentrated turbidity currents.

Keywords: Herschel-Bulkley constitutive relation; bilinear constitutive relation; turbidity currents; abrupt transition.

1 INTRODUCTION

Turbidity currents are subaqueous, sediment-laden underflows, which are driven by density excess between the intruding and ambient fluids. Hyperconcentrated turbidity currents, the constitutive relations of which are non-Newtonian, are common in natural and anthropogenic situations, such as those generated by submarine sediment slumping on continental slopes and reservoir operation in alluvial rivers with heavy sediment load (Parker et al., 1986; YRCC, 2007). Given the rheological and resulting viscous resistance law differences, non-Newtonian and Newtonian turbidity current propagation characteristics are notably different (Hallworth and Huppert, 1998; Chowdhury and Testik, 2011).

However, our knowledge on turbidity currents is mainly gained through investigations with dilute mixtures of which exhibiting Newtonian behavior. For example, various laboratory experiments have focused on turbidity currents with low initial sediment volume concentrations on the order of 10^{-2} (Bonnecaze et al., 1993; Dade and Huppert, 1994; Bonnecaze et al., 1995; Lee et al., 1997; Fedele and Garcia, 2009). In a complementary approach, turbidity currents were also numerically simulated using diverse mathematical models based on the classical Navier-Stokes equations, which implicitly presume the currents to be Newtonian fluids (Parker et al., 1986; Choi, 1998; Felix, 2002; Hu and Cao, 2009; Hu et al., 2012; Espath et al., 2013; Bhaganagar, 2014; Cao et al., 2015).

Unlike the abundant studies on dilute turbidity currents of which exhibiting Newtonian behavior, only a few attempts have been done with respect to relatively highly concentrated turbidity currents of which exhibiting non-Newtonian behavior. Hallworth and Huppert (1998) experimentally surveyed on this issue by conducting a series of lock-exchange experiments by gradually increasing the initial sediment concentrations. Abrupt transitions were observed beyond a critical initial concentration, indicating the qualitative differences between the evolution processes of high and low concentration turbidity currents. More recent studies by Huppert (2006) as well as Jacobson and Testik (2013) revealed that non-Newtonian constitutive relations of those highly concentrated currents were closely related to this phenomenon. On the other hand, Imran et al. (2001) numerically addressed this problem by developing a one-dimensional (1D) mathematical model that incorporated Herschel-Bulkley and bilinear rheologies, respectively. Yet, sediment exchange and bed deformation were completely neglected in this model, thus rendering in inconclusive results as most turbidity currents in nature with active sediment exchange and rapid bed deformation. Furthermore, another 1D single layer-averaged model for turbidity currents, which only incorporated the yield stress in Bingham constitutive relation was proposed by Hu (2012). Despite of comprehensive consideration of sediment exchange and feedbacks of bed deformation on turbidity currents, the model performed poorly as compared to the experimental data, owing to the rough treatment of non-Newtonian properties.

In principle, shear thinning and yield stress are both keys of non-Newtonian properties of hyperconcentrated flows. Hence, new non-Newtonian turbidity current models are presented in this study by first incorporating two essential non-Newtonian properties to fully coupled layer-averaged turbidity current model in the form of Herschel-Bulkley and bilinear constitutive relations, respectively. It is the goal of this study to use the proposed model to gain an insight into the underlying physical mechanisms of abrupt transitions and to preliminarily elucidate the effects of constitutive relations on turbidity current evolutions.

2 MATHEMATICAL FORMULATIONS

2.1 Governing equations

The general equations of motion for a vertical two-dimensional (2D) turbidity current can be expressed in the following form using the small slope assumption and shallow water approximations.

$$\frac{\partial \rho_m}{\partial t} + \frac{\partial \rho_m u_x}{\partial x} + \frac{\partial \rho_m u_z}{\partial z} = 0 \quad [1]$$

$$\frac{\partial \rho_m u_x}{\partial t} + \frac{\partial \rho_m u_x^2}{\partial x} + \frac{\partial \rho_m u_x u_z}{\partial z} = -\frac{\partial p_r}{\partial x} + \frac{\partial \tau}{\partial z} \quad [2]$$

where ρ_m = density of turbidity current, u_x, u_z = velocity components in the streamwise and upward normal direction, respectively, p_r = pressure at elevation z, and τ = shorthand for the component τ_{xz} of the deviator stress tensor. A consequence of the shallow water approximation is that the vertical component of the momentum equation reduces to the hydrostatic condition as Eq. [3].

$$p_r = \rho_w g h_w + \int_z^{z_{in}} \rho_m g dz \quad [3]$$

where ρ_w = density of clear water, h_w = thickness of ambient fluid, and z_{in} = elevation of interface between ambient fluid and turbidity current.

2.1.1 Newtonian constitutive relation

Newtonian constitutive relation is the simplest constitutive model in which viscous stress is linearly proportional to strain rate, which can be expressed as

$$\tau = \mu_N \gamma \quad [4]$$

where $\gamma = \partial u_x / \partial z$ = strain rate and μ_N = dynamic viscosity. The simplified form of celebrated Navier-Stokes equations can be obtained provided that we substitute Eq. (6) to Eq. (2). Then, integrating over the thickness of turbidity current, taking into account the suitable kinematic boundary conditions on the interface and bed and using shear velocity to approximate the resistance term, one obtains (Hu and Cao, 2009; Parker et al., 1986)

$$\frac{\partial \rho_m h}{\partial t} + \frac{\partial \rho_m h U}{\partial x} = \rho_w e_w U - \rho_0 \frac{\partial z_b}{\partial t} \quad [5]$$

$$\frac{\partial \rho_m h U}{\partial t} + \frac{\partial \rho_m h U^2}{\partial x} + \frac{\partial}{\partial x}\left(\frac{1}{2}(\rho_m - \rho_w) g h^2\right) = -(\rho_m - \rho_w) g h \frac{\partial z_b}{\partial x} - (1 + r_w) \rho_m u_*^2 \quad [6]$$

where h = thickness of turbidity current, U = depth-averaged velocity in streamwise direction, e_w = water entrainment coefficient, ρ_0 = density of saturated bed, z_b = bed elevation, r_w = ratio of interface resistance to bed resistance, and u_* = shear velocity.

2.1.2 Herschel-Bulkley constitutive relation

The non-Newtonian behaviors of “shear thinning” and “yield stress” are key effects in hyperconcentrated particle suspension mechanics. Probably, the most popular model that incorporates both non-Newtonian effects is the Herschel-Bulkley (H-B) model, expressed as (Balmforth and Provenzale 2010):

$$\begin{cases} \tau = \left(\tau_Y + K|\gamma|^n\right)\mathrm{sgn}(\gamma) & |\tau| > \tau_Y \\ \gamma = 0 & |\tau| \le \tau_Y \end{cases} \quad [7]$$

where τ_Y = yield stress and K = consistency of the fluid. If the index $n = 1$, Eq. [7] reverts to the Bingham constitutive model and the consistency is just the dynamic viscosity.

Proceeding with the same mathematical manipulations as Newtonian rheology, the 1D integral forms of mass and momentum conservation are obtained. As compared to those of Newtonian turbidity currents, the only difference lies in the extra viscousity term in the momentum conservation equation (Eq. [8]). When $n=1$, the extra viscous force of Bingham rheology becomes τ_Y, which is consistent with the hypothesis of Hu (2012). Moreover, the extra viscous force vanishes and Eq. [8] is degenerated into Eq. [6] of which Newtonian currents under the condition of $n=1$ and $\tau_Y=0$.

$$\frac{\partial \rho_m hU}{\partial t}+\frac{\partial \rho_m hU^2}{\partial x}+\frac{\partial}{\partial x}\left(\frac{1}{2}\left(\rho_m-\rho_w\right)gh^2\right)=-\left(\rho_m-\rho_w\right)gh\frac{\partial z_b}{\partial x}$$
$$-\left(1+r_w\right)\rho_m u_*^2-\left(1+r_w\right)\left[\left(\frac{\tau_Y}{\left|\partial u_x/\partial z\right|}+K\left|\frac{\partial u_x}{\partial z}\right|^{n-1}-\mu_N\right)\left|\frac{\partial u_x}{\partial z}\right|\right]_{z=z_b} \quad [8]$$

2.1.3 Bilinear constitutive relation

The concept of yield stress has received some criticisms, with evidence presented to suggest that most materials weakly yield or creep near zero strain rate (Barnes 1999). Moreover, in terms of mathematics, the discontinuous surface defined by the yield condition may introduce undesirable features into the non-Newtonian fluid model. Such criticisms have fueled the introduction of further models that go some way to avoid the problems, such as the present bilinear model as Eq. [9] (Balmforth and Provenzale 2010). The bilinear constitutive model characterizes the smooth transformation from a high viscosity (μ_l) Newtonian relation to a relatively low viscosity (μ_h) of Bingham relation with apparent yield stress, τ_Y when the strain rate increases.

$$\tau=\left(\mu_h+\frac{\tau_Y}{\left|\gamma\right|+\gamma_0}\right)\gamma\,,\qquad \gamma_0=\frac{\tau_Y}{\mu_l-\mu_h} \quad [9]$$

Analogy to the aforementioned two cases, the 1D layer-averaged equations for bilinear turbidity currents can be obtained in the following form. In the case of $r=\mu_l/\mu_h-1=0$, the extra viscous force is vanished and Eq. [10] of bilinear turbidity currents reverts to that Eq. [6] of Newtonian turbidity currents.

$$\frac{\partial \rho_m hU}{\partial t}+\frac{\partial \rho_m hU^2}{\partial x}+\frac{\partial}{\partial x}\left(\frac{1}{2}\left(\rho_m-\rho_w\right)gh^2\right)=-\left(\rho_m-\rho_w\right)gh\frac{\partial z_b}{\partial x}$$
$$-\left(1+r_w\right)\rho_m u_*^2-\left(1+r_w\right)\left[\left(\frac{\tau_Y}{\left|\partial u_x/\partial z\right|+\gamma_0}+\mu_h-\mu_N\right)\frac{\partial u_x}{\partial z}\right]_{z=z_b} \quad [10]$$

Combined with the mass conservation equations for sediment and bed material (Eqs. [11] and [12]), the governing equations for turbidity currents with Newtonian, Herschel-Bulkley, bilinear constitutive relations, respectively, were obtained. Note that the only difference lies in the momentum conservation equation, or more specifically, in the formulation of viscous force and both non-Newtonian models can be degenerated to Newtonian models under certain rheological parameter selections.

$$\frac{\partial hC}{\partial t}+\frac{\partial hUC}{\partial x}=E-D \quad [11]$$

$$\frac{\partial z_b}{\partial t}=-\frac{E-D}{1-p} \quad [12]$$

where $C=$ layer-averaged sediment volume concentration, E, $D=$ sediment entrainment and deposition fluxes, respectively, and $p=$ porosity of saturated bed.

To expedite numerical solution using conservative variables, it is advisable to recast the mass and momentum conservation equations of water-sediment mixture in the following form (Cao et al. 2004):

$$\frac{\partial h}{\partial t}+\frac{\partial hU}{\partial x}=e_w U+\frac{E-D}{1-p} \quad [13]$$

Newtonian constitutive relation:

$$\frac{\partial hU}{\partial t}+\frac{\partial}{\partial x}\left(hU^2+\frac{1}{2}R_\rho gh^2\right)=-R_\rho gh\frac{\partial z_b}{\partial x}-u_*^2\left(1+r_w\right)$$
$$+R_\rho e_w U^2+\frac{U\left(E-D\right)\left(\rho_m-\rho_0\right)}{\rho_m\left(1-p\right)}-R_\rho gh^2\frac{\rho_s-\rho_w}{2\rho_m}\frac{\partial C}{\partial x} \quad [14]$$

Herschel-Bulkley constitutive relation:

$$\frac{\partial hU}{\partial t}+\frac{\partial}{\partial x}\left(hU^2+\frac{1}{2}R_\rho gh^2\right)=-\frac{1+r_w}{\rho_m}\left[\left(\frac{\tau_Y}{\left|\partial u_x/\partial z\right|}+K\left|\frac{\partial u_x}{\partial z}\right|^{n-1}-\mu_N\right)\left|\frac{\partial u_x}{\partial z}\right|\right]_{z=z_b}$$
$$-R_\rho gh\frac{\partial z_b}{\partial x}-u_*^2\left(1+r_w\right)+R_\rho e_w U^2+\frac{U\left(E-D\right)\left(\rho_m-\rho_0\right)}{\rho_m\left(1-p\right)}-R_\rho gh^2\frac{\rho_s-\rho_w}{2\rho_m}\frac{\partial C}{\partial x} \quad [15]$$

Bilinear constitutive relation:

$$\frac{\partial hU}{\partial t}+\frac{\partial}{\partial x}\left(hU^2+\frac{1}{2}R_\rho gh^2\right)=-\frac{1+r_w}{\rho_m}\left[\left(\frac{\tau_Y}{\left|\partial u_x/\partial z\right|+\gamma_0}+\mu_h-\mu_N\right)\frac{\partial u_x}{\partial z}\right]_{z=z_b}$$
$$-R_\rho gh\frac{\partial z_b}{\partial x}-u_*^2\left(1+r_w\right)+R_\rho e_w U^2+\frac{U\left(E-D\right)\left(\rho_m-\rho_0\right)}{\rho_m\left(1-p\right)}-R_\rho gh^2\frac{\rho_s-\rho_w}{2\rho_m}\frac{\partial C}{\partial x} \quad [16]$$

2.2 Model closure

To close the governing equations above, a set of empirical relationships have to be introduced to determine the mass exchange fluxes, rheological parameters and the velocity gradient at the bottom boundary.

2.2.1 Mass exchange

The water entrainment coefficient, e_w is determined as (Parker et al., 1986):

$$e_w=\frac{0.00153}{0.0204+R_i} \quad [17]$$

where $R_i=\left(RgCh\right)/U^2=$ Richardson number and $R=\left(\rho_s-\rho_w\right)/\rho_m=$ submerged specific gravity of sediment. Sediment entrainment and deposition fluxes are estimated by (Parker et al., 1986):

$$E=\omega E_s,\ E_s=\begin{cases}0.3 & Z>Z_m\\ 3\times10^{-12}Z^{10}\left(1-Z_c/Z\right) & Z_c<Z\le Z_m\\ 0 & Z<Z_c\end{cases} \quad [18]$$

$$D=\omega c_b,\ c_b=c\left[1+31.5\left(u_*/\omega\right)^{-1.45}\right] \quad [19]$$

where $E_s=$ sediment entrainment coefficient; $Z=R_{ep}^{\ 0.5}\left(u_*/\omega\right)$, in which $R_{ep}=\left(d\sqrt{Rgd}\right)/\nu$, $d=$ particle diameter, $\nu=$ kinematic viscosity of clear water, $u_*=\sqrt{c_D}U=$ shear velocity, $c_D=$drag coefficient, $Z_c=5$, $Z_m=13.2$ are the critical and maximum values of Z, respectively, $c_b=$sediment volume concentration near the bed, and $\omega=$ sediment settling velocity calculated using formula of Zhang and Xie (1993).

2.2.2 Rheological parameters

The two crucial rheological parameters; yield stress and dynamic viscosity, are estimated as (Fei, 1991):

$$\tau_Y=\varphi 0.098e^{8.45\left(C-C_{v0}\right)/C_{vm}+1.5} \quad [20]$$

$$\mu=\mu_0\left(1-kC/C_{vm}\right)^{-2.5} \quad [21]$$

where,

$$C_{vm}^{cal}=0.92-0.2\lg\sum\left(P_i/d_i\right),\ C_{vm}=\left(C_{vm}^{\exp}+C_{vm}^{cal}\right)/2 \quad [22a]$$

$$C_{v0}=1.26C_{vm}^{3.2},\ k=1+2.0\left(C/C_{vm}\right)^{0.3}\left(1-C/C_{vm}\right)^4 \quad [22b]$$

where d_i, $P_i=$ average diameter of a certain grade of sediment and the corresponding percentage by weight, respectively. The correction coefficient, φ is introduced herein because the original form of Eq. [20] is derived from limited sediment samples. When $\varphi=1$, the original formula is retained. As shown by Eq. [22a], the calculated limiting particle concentration, C_{vm}^{cal} is calibrated using an empirical value of $C_{vm}^{exp}=0.45$ by Hallworth and Huppert (1998). The computed results of Eq. [21], by multiplying with a modification coefficient, α is used to estimate μ_N, K, and μ_l in corresponding constitutive relations due to the lack of measured rheological data. Apart from the two parameters, the index n in Herschel-Bulkley rheology and r in bilinear rheology are assumed to be constant and calibrated according to the experimental data.

2.2.3 Velocity gradient near bed

The velocity gradient at the bottom boundary is estimated by:

$$\left.\frac{\partial u_x}{\partial z}\right|_{z=z_b} = \frac{2U}{h} \quad [23]$$

2.3 Numerical algorithm

Governing equations for either Newtonian or the present non-Newtonian turbidity currents constitute a fourth order hyperbolic system, which can be solved numerically using schemes that can capture shocks and sharp fronts reasonably well (Toro 2001). With a simple form, the bed deformation equation is separated from the remaining three equations. Then, taking the governing equations of Herschel-Bulkley turbidity currents as an example, Eqs. (13), (15) and (11) can be rearranged in a compact form of:

$$\frac{\partial \mathbf{U}}{\partial t} + \frac{\partial \mathbf{F}}{\partial x} = \mathbf{S} \quad [24]$$

where,

$$\mathbf{U} = \begin{bmatrix} h \\ hU \\ hC \end{bmatrix} \quad \mathbf{F} = \begin{bmatrix} hU \\ hU^2 + \frac{1}{2}R_\rho g h^2 \\ hUC \end{bmatrix} \quad \mathbf{S} = \begin{bmatrix} e_w U + (E-D)/(1-p) \\ S_2 \\ E-D \end{bmatrix} \quad [25a]$$

$$S_2 = -R_\rho g h \frac{\partial z_b}{\partial x} - \frac{1+r_w}{\rho_m}\left[\left(\frac{\tau_Y}{\left|\frac{\partial u_x}{\partial z}\right|} + \left(K\left|\frac{\partial u_x}{\partial z}\right|^{n-1} - \mu_N\right)\right)\frac{\partial u_x}{\partial z}\right]_{z=z_b} \quad [25b]$$

$$- u_*^2(1+r_w) + R_\rho e_w U^2 + \frac{U(E-D)(\rho_m - \rho_0)}{\rho_m(1-p)} - R_\rho g h^2 \frac{\rho_s - \rho_w}{2\rho_m}\frac{\partial C}{\partial x}$$

An explicit discretization of Eq. [24] gives:

$$\mathbf{U}_i^{adv} = \mathbf{U}_i^m - \frac{\Delta t}{\Delta x}\left[\mathbf{F}_{i+1/2} - \mathbf{F}_{i-1/2}\right] \quad [26]$$

$$\mathbf{U}_i^{m+1} = \mathbf{U}_i^{adv} + \Delta t \mathbf{S}\left(\mathbf{U}_i^{adv}\right) \quad [27]$$

where $\Delta t =$ time step, $\Delta x =$ spatial step, $i =$ spatial node index, $m =$ time step index, and $\boldsymbol{F}_{i+1/2} =$ numerical flux at $x = x_{i+1/2}$. In present study, the SLIC solver and MINBEE slope limiter are employed to compute the numerical fluxes at interfaces (Toro, 2001). The scheme is monotone and has linear stability condition of:

$$Cr = \frac{\Delta t \max\left(\left|\lambda_{1,2,3}\right|\right)}{\Delta x} < 1 \quad [28]$$

where $\lambda_{1,2,3} =$ eigenvalues of the Jacobian matrix $\partial\mathbf{F}/\partial\mathbf{U}$.

Bed deformation is calculated from Eq. [12] using the state information due to Eq. (26).

$$z_{bi}^{m+1} = z_{bi}^{m} + \Delta t\left(D-E\right)_i^{adv}/(1-p) \quad [29]$$

3 ABRUPT TRANSITIONS IN HYPERCONCENTRATED TURBIDITY CURRETNS

The present non-Newtonian models as well as previous Newtonian model of turbidity currents are tested against the whole series of experiments using the 9 μm particles by Hallworth and Huppert (1998). In these experiments, the channel was horizontal and measured as 2 m long, 0.2 m wide and 0.25 m deep. The lock-gate was 0.03 m from the upstream boundary and initial thicknesses of both sides were 0.1 m. The density of particles is 3217 $\mathrm{kg/m^3}$. Other parameters used here are: spatial step, $\Delta x =$ 0.001 m; Courant number, $C_r =$ 0.9; bed porosity, $p =$ 0.4; coefficient, and $\alpha =$ 1.0, 1.0, 1.2, respectively, in Newtonian, H-B (including Bingham), and bilinear models. The drag coefficient, c_D is first calibrated to 0.02 using the measured data of low concentrations, in which the resistance of shear velocity dominants, and then directly applied to all the cases. Modification coefficients and some rheological parameters for each case are as follows:

Table 1. Modification coefficients and special rheological parameters for each modelling case.

Case		1	2	3	4	5	6	7	8	9
C_0		0.025	0.15	0.25	0.275	0.3	0.325	0.35	0.375	0.4
Bilinear	r	0.0	0.3	0.5	1.0	5.0	5.0	10.0	200.0	200.0
H-B	φ	0.0	0.02	0.08	0.1	0.3	0.3	0.4	0.4	0.4
	n	1.0	0.7	0.7	0.7	0.6	0.5	0.5	0.5	0.5
Bingham	φ	0.0	0.02	0.02	0.05	0.2	0.3	0.3	0.3	0.4

To quantify the differences between numerical solutions and measured data, the non-dimensional discrepancy is defined based on the L^1 norm:

$$L^{1f} = \frac{\sum \mathrm{abs}\left(x^f - \hat{x}^f\right)}{\sum \hat{x}^f}, \quad L^{1d} = \frac{\sum \mathrm{abs}\left(m^d - \hat{m}^d\right)}{\sum \hat{m}^d} \qquad [30]$$

where L^{1f} and L^{1d} are L^1 norms of front location and final deposit density, respectively. The deposit density is defined as the mass of dried deposit per unit area by $m^d = (z_b - z_{b0})(1-p)\rho_s$. x^f and m^d are front location and final deposit density from a numerical solution whilst $\hat{x}^f$ and $\hat{m}^d$ are measured data correspondingly.

Note that the following “low”, “intermediate”, “high” concentrations are classified by the performance of non-Newtonian models as compared to the measured data and Newtonian models, respectively, which can also be demonstrated quantitatively by the values and differences of aforementioned norms.

3.1 Low concentrated turbidity currents

As shown in Table 2, two cases, in which the initial sediment volume concentrations are no more than 0.15, are classified as low concentrated turbidity currents. Figure 1 shows the computed front evolution and final deposit density by the Newtonian, Bilinear, H-B and Bingham turbidity current models for these cases, as well as corresponding measured data. For Case 1, with sediment concentration less than the threshold concentration of non-Newtonian fluids, all non-Newtonian models can be degenerated to Newtonian model and consequently all numerical results coincide. Similarly, in Case 2, the sediment concentration is slightly higher than the threshold concentration of non-Newtonian fluids and small differences exists between Newtonian models and non-Newtonian models, except the relatively better deposit density of Herschel-Bulkley model. Succinctly, these results confirm the feasibility of present non-Newtonian models to dilute turbidity currents, which can be assumed as Newtonian fluids.

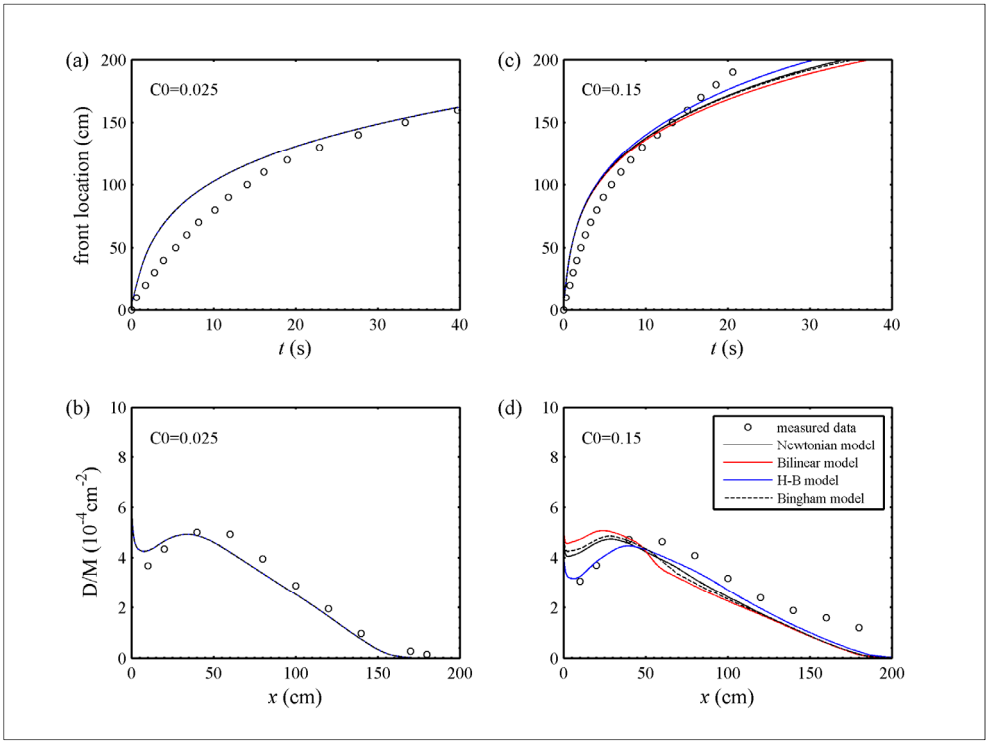

Figure 1. Front location and deposit density for low concentrated cases ($C_0 = 0.025$: (a), (b); $C_0 = 0.15$: (c), (d)).

Table 2. L^1 norms of Newtonian, bilinear, H-B, and Bingham models for low concentrated turbidity currents.

	Newtonian		Bilinear		H-B		Bingham	
	L^{1f}	L^{1d}	L^{1f}	L^{1d}	L^{1f}	L^{1d}	L^{1f}	L^{1d}
$C_0 = 0.025$	0.1518	0.1282	0.1518	0.1282	0.1518	0.1282	0.1518	0.1282
$C_0 = 0.15$	0.1472	0.2639	0.1493	0.3234	0.1476	0.1678	0.1477	0.2808

3.2 Intermediate-concentrated turbidity currents

Four experimental runs with initial sediment volume concentrations in the range of $0.25 \le C_0 < 0.35$ are classified as "intermediate concentrated" turbidity currents. Figures 2 and 3 illustrate the performances of both non-Newtonian and Newtonian models by comparing with the experimental data. From a qualitative perspective, in contrast with the smooth curves of Newtonian model, all non-Newtonian models reproduce the point of deviation in the front evolution process and the deposit phenomenon characterized by "thick layer around the inlet and very thin layer downstream" as the initial sediment concentration increases. Referring Figures 2 and 3, the values of L^{1f} and L^{1d} (Table 3) provide further testament for the improved performance of the present non-Newtonian models over the traditional Newtonian models in comparison with measured data. Specifically, Bingham and bilinear models, in almost all intermediate concentrated cases, feature respectively the minimum L^{1f} and L^{1d} values, whilst the Newtonian model features the maximum L^{1f} and L^{1d} values that can be nearly double than those of non-Newtonian models.

As stated above, both H-B and bilinear constitutive relations incorporate shear thinning and yield stress of non-Newtonian fluids in different mathematical forms. Therefore, the differences between two models can preliminarily indicate the profound effects of constitutive relations on turbidity current evolutions. Furthermore, the present Bingham results is indeed better than that of Hu (2012) both qualitatively and quantitatively. This is probably a consequence of different empirical formulations used for rheological parameters, which suggests the importance of rheological parameter selection in non-Newtonian turbidity current mathematical modelling.

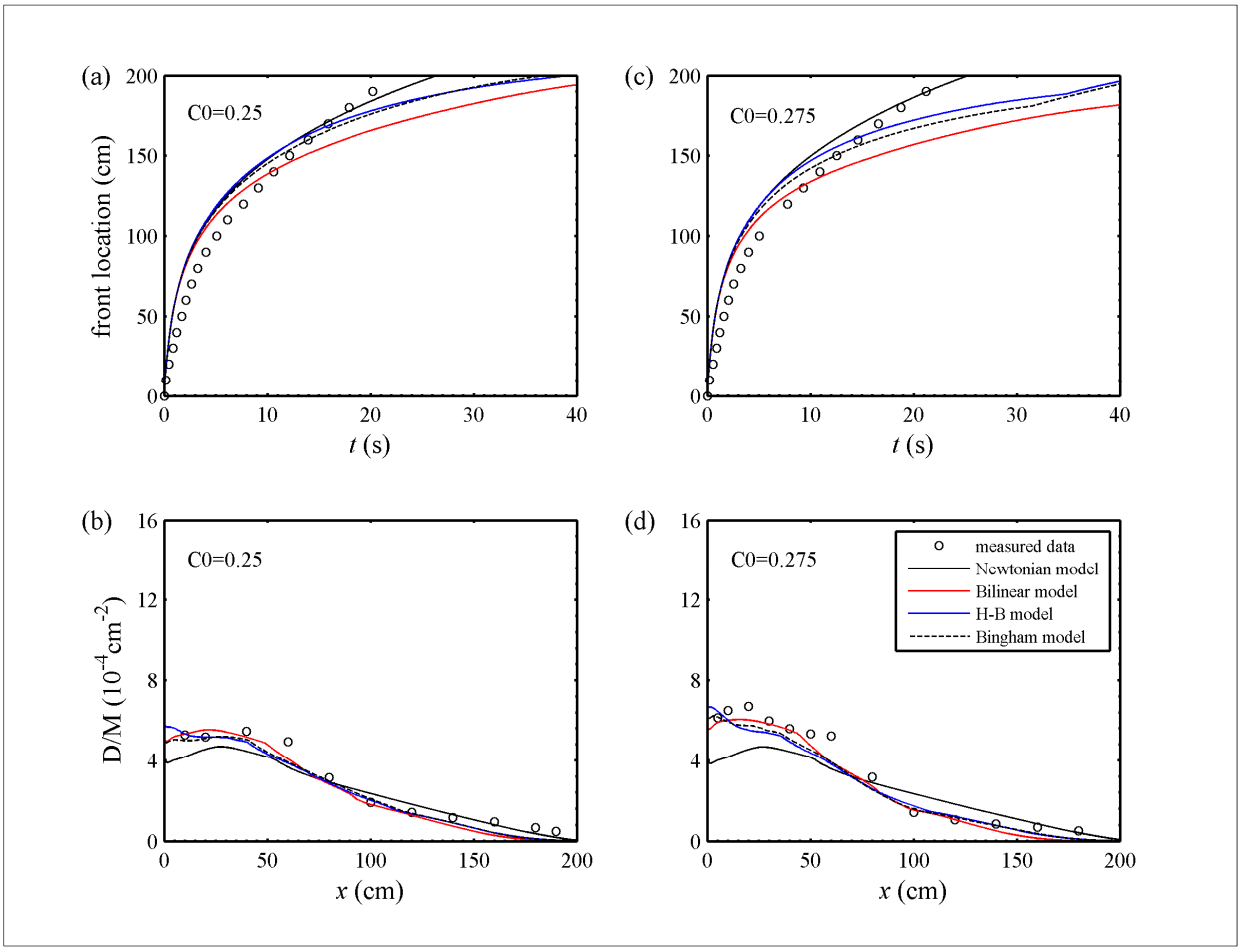

Figure 2. Front location and deposit density for intermediate concentrated cases ($C_0 = 0.25$: (a), (b); $C_0 = 0.275$: (c), (d)).

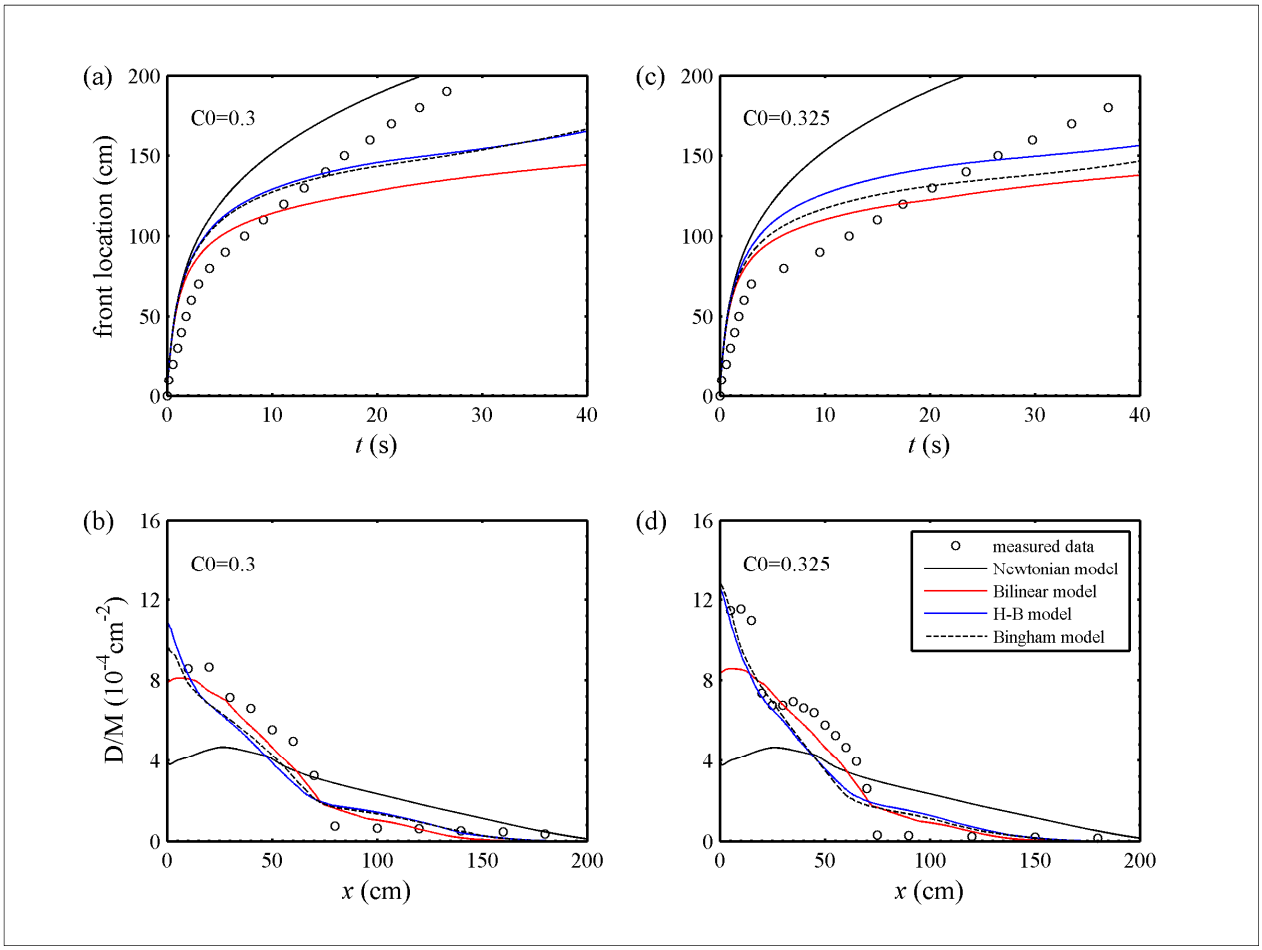

Figure 3. Front location and deposit density for intermediate concentrated cases ($C_0 = 0.3$: (a), (b); $C_0 = 0.325$: (c), (d)).

Table 3. L^1 norms of Newtonian, bilinear, H-B, and Bingham models for intermediate concentrated cases.

	Newtonian		**Bilinear**		**H-B**		**Bingham**	
	L^{1f}	L^{1d}	L^{1f}	L^{1d}	L^{1f}	L^{1d}	L^{1f}	L^{1d}
$C_0 = 0.25$	0.1409	0.1953	0.1436	0.1410	0.1515	0.1302	0.1410	0.1310
$C_0 = 0.275$	0.1590	0.2987	0.1632	0.1124	0.1609	0.1533	0.1549	0.1314
$C_0 = 0.3$	0.2784	0.4734	0.2155	0.1772	0.1981	0.2683	0.1988	0.2477
$C_0 = 0.32$	0.4578	0.4998	0.2137	0.2056	0.2198	0.2529	0.2111	0.2414

3.3 Highly concentrated turbidity currents

The front evolution and final deposit density by Newtonian model and the present non-Newtonian models along with the measured data are illustrated in Figure 4 for cases in which the initial sediment volume concentration is no less than 0.35. Note that results of Case 8, which is in line with the other cases, are omitted in this figure due to space constraints. Obviously, the Newtonian model performs poorly as compared to the measured data. Comparatively, three non-Newtonian models are all relatively better than the Newtonian model allowing for their capability of reflecting the abrupt transition properties qualitatively in the front evolution process and the final deposit morphology. However, significant differences exist between non-Newtonian numerical results and measured data (as shown in Table 4), which implies the rough estimation of rheological parameters by empirical formulas as well as the unknown non-Newtonian properties in extremely hyperconcentrated turbidity currents that have not been considered in bilinear, Herschel-Bulkley and Bingham constitutive relations.

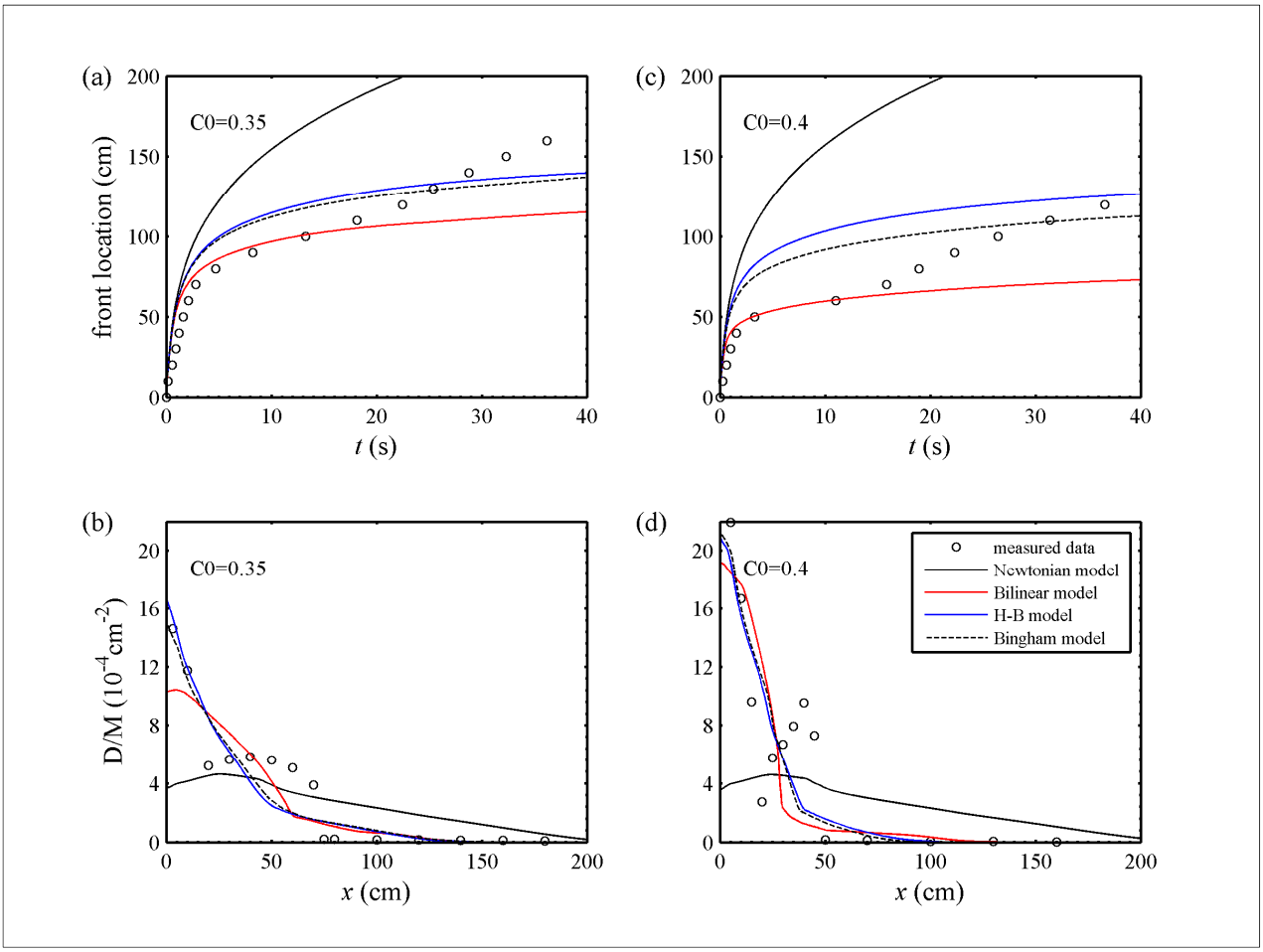

Figure 4. Front location and deposit density for highly concentrated cases ($C_0 = 0.35$: (a), (b); $C_0 = 0.4$: (c), (d)).

Table 4. L^1 norms of Newtonian, bilinear, H-B, and Bingham models for highly concentrated cases.

	Newtonian		**Bilinear**		**H-B**		**Bingham**	
	L^{1f}	L^{1d}	L^{1f}	L^{1d}	L^{1f}	L^{1d}	L^{1f}	L^{1d}
$C_0 = 0.35$	0.4991	0.6409	0.2334	0.3634	0.1987	0.3123	0.1956	0.3078
$C_0 = 0.375$	0.6570	0.5727	0.2949	0.4704	0.2331	0.3499	0.2182	0.3592
$C_0 = 0.4$	0.9872	0.7246	0.3201	0.5606	0.2775	0.4190	0.2507	0.4284

4 CONCLUSIONS

Physically enhanced non-Newtonian models (including bilinear and Herschel-Bulkley models) are developed for all low, intermediate, and highly concentrated turbidity currents. To the author's knowledge, it is the first to incorporate two key non-Newtonian properties; yield stress and shear-thinning, into the existing fully coupled turbidity currents model. As for dilute turbidity currents, these non-Newtonian properties become negligible and the present non-Newtonian models are degenerated to the traditional Newtonian model. The SLIC scheme is employed to numerically solve the governing equations under the framework of finite volume method. Both traditional Newtonian model and proposed non-Newtonian models are applied to the systematic series of lock-exchange turbidity current experiments. As expected, equivalent numerical results of non-Newtonian and Newtonian models are obtained for low concentrated cases. Enhanced performances of the non-Newtonian models, especially the prediction capability of final deposit morphology, are demonstrated over that of traditional Newtonian model as for intermediate concentrated cases. Whilst for hyperconcentrated turbidity currents, non-Newtonian models are able to qualitatively reproduce abrupt transitions, which is beyond the capability of Newtonian model. However, due to lack of rheological data and unknown physical mechanisms of hyper concentrated turbidity currents, quantitative discrepancies with experimental data still exist. Consequently, the complex constitutive relations and their profound influence in turbidity current evolutions, which partially revealed in this study, necessitate further detailed investigation.

ACKNOWLEDGEMENTS

The author acknowledges the warm support from Professor M. A. Hallworth for the original experimental data and helpful e-mail communication.

REFERENCES

Bonnecaze, R.T., Hallworth, M.A., Huppert, H.E. & Lister, J.R. (1995). Axisymmetric Particle-Driven Gravity Currents. *Journal of Fluid Mechanics*, 294, 93-121.

Bonnecaze, R.T., Huppert, H.E. & Lister, J.R. (1993). Particle-Driven Gravity Currents. *Journal of Fluid Mechanics*, 250, 339-369.

Balmforth, N.J. & Provenzale, A. (2010). *Geomorphological Fluid Mechanics*. Springer, Berlin.

Barnes, H.A. (1999). The Yield Stress - A Review Everything Flows? *Journal of Non-Newtonian Fluid Mechanics*, 81, 133-178.

Bhaganagar, K. (2014). Direct Numerical Simulation of Lock-Exchange Density Currents Over the Rough Wall in Slumping Phase. *Journal of Hydraulic Research*, 52(3), 386-398.

Cao, Z.X., Li, J., Pender, G. & Liu, Q.Q. (2015). Whole-Process Modeling of Reservoir Turbidity Currents by a Double Layer-Averaged Model. *Journal of Hydraulic Engineering*, 141(2), 04014069.

Cao, Z.X., Pender, G., Wallis, S. & Carling, P. (2004). Computational Dam-Break Hydraulics over Erodible Sediment Bed. *Journal of Hydraulic Engineering*, 130(7), 689-703.

Chowdhury, M.R. & Testik, F.Y. (2011). Laboratory Testing of Mathematical Models for High-Concentration Fluid Mud Turbidity Currents. *Ocean Engineering*, 38(1), 256-270.

Choi, S.U. (1998). Layer-Averaged Modeling of Two-Dimensional Turbidity Currents with a Dissipative-Galerkin Finite Element Method Part Ⅰ: Formulation and Application Example. *Journal of Hydraulic Research*, 36(3), 339-362.

Dade, W.B. & Huppert, H.E. (1994). Predicting the Geometry of Channelized Deep-Sea Turbidities. *Geology*, 22(1994), 645-648.

Espath, L.F.R., Pinto, L.C., Laizet, S. & Silvestrini, J.H. (2013). Two- and Three- Dimensional Direct Numerical Simulation of Particle-Laden Gravity Currents. *Computers & Geosciences*, CAGEO, 1, 9-16.

Fedele, J.J. & Garcia, M.H. (2009). Laboratory Experiments on the Formation of Subaqueous Depositional Gullies By Turbidity Currents. *Marine Geology*, 258(1), 48-59.

Fei, X.J. (1991). A Model for Calculating Viscosity of Sediment Carrying Flow in the Middle and Lower Yellow River. *Journal of Sediment Research*, 1991(2), 1-13.

Felix, M. (2002). Flow Structure of Turbidity Currents. *Sedimentology*, 49(3), 397-419.

Hu, P., Cao, Z.X., Pender, G. & Tan, G.M. (2012). Numerical Modelling of Turbidity Currents in the Xiaolangdi Reservoir, Yellow River, China. *Journal of Hydrology*, 464(41), 41-53.

Hu, P. & Cao, Z.X. (2009). Fully Coupled Mathematical Modeling of Turbidity Currents Over Erodible Bed. *Advances in Water Resources*, 32(1), 1-15.

Hu, P. (2012). Coupled Modelling of Turbidity Currents Over Erodible Beds. *PhD Thesis*, Heriot-Watt Univ., Edinburgh, U.K.

Hallworth, M.A. & Huppert, H.E. (1998). Abrupt Transitions in High-Concentration, Particle-Driven Gravity Currents. *Physics of Fluids*, 10(5), 1083-1087.

Huppert, H.E. (2006). Gravity Currents: A Personal Perspective. *Journal of Fluid Mechanics*, 554, 299-322.

Imran, J., Parker, G., Locat, J. & Lee, H. (2001). 1D Numerical Model of Muddy Subaqueous and Subaerial Debris Flows. *Journal of Hydraulic Engineering*, 127(11), 959-968.

Jacobson, M.R. & Testik, F.Y. (2013). On the Concentration Structure of High-Concentration Constant-Volume Fluid Mud Gravity Currents. *Physics of Fluids (1994-Present)*, 25(1), 016602-016602-24.

Lee, H.Y. & Yu, W.S. (1997). Experimental Study of Reservoir Turbidity Current. *Journal of Hydraulic Engineering*, 123(6), 520-528.

Parker, G., Fukushima, Y. & Pantin, H.M. (1986). Self-Accelerating Turbidity Currents. *Journal of Fluid Mechanics*, 171, 145-181.

Toro, E.F. (2001). *Shock-Capturing Methods for Free-Surface Shallow Flows*, Wiley, Chichester, England.

Yellow River Conservancy Commission (YRCC). (2007). *The Third Test of Water And Sediment Regulation Conduced On The Yellow River*. Yellow River Conservancy Press, Zhengzhou, China (In Chinese).

Zhang, R.J. & Xie, J.H. (1993). *Sedimentation Research in China: Systematic Selections*. China Water Power Press, Beijing. (In Chinese)

LABORATORY EXPERIMENTS ON DENSITY CURRENTS FLOWING OVER ARRAYS OF ROUGHNESS ELEMENTS

REZA NASROLLAHPOUR[1], MOHAMAD HIDAYAT JAMAL[2] & ZULHILMI ISMAIL[3]

[1,2,3] Department of Hydraulics and Hydrology, Faculty of Civil Engineering, Universiti Teknologi Malaysia, 81310 Johor Bahru, Malaysia
[2.3] Center for Coastal and Ocean Engineering (COEI), Universiti Teknologi Malaysia Kuala Lumpur, 54100 Kuala Lumpur, Malaysia
mhidayat@utm.my

ABSTRACT

In most practical cases, density currents flow over non-flat surfaces. This work uses laboratory experiments to collect velocity profiles of the currents flowing over different bed types. Herein, three different configurations of beam-roughened beds are examined and compared with that of the flat surface. The adjustments in the vertical velocity profiles at the presence of different roughened beds are investigated. Furthermore, this work analyses the impact of bed roughness on entrainment of ambient water into these currents. The primary results of the research show that increasing the spacing between the roughness elements causes further deceleration of the currents and it enhanced water entrainment rates into the dense underflows.

Keywords: Turbidity currents; bottom roughness; water entrainment; acoustic doppler velocimetry.

1 INTRODUCTION

Density currents (also known as gravity currents) are generated when fluid of one density is released into fluid of a different density. The density difference can be resulted from temperature gradients, dissolved contents, suspended particles or a combination of them (Fragoso et al., 2013). These currents are known as turbidity currents in case the main driving mechanism is obtained from suspended sediments.

Density currents occur in many natural and man-made environments. The most usual type of these currents is an underflow, produced as a flow is introduced into an ambient fluid of a less density. In oceanic and river systems, such currents occur because some of the water in an estuary, ocean or lake is colder, saltier or contains more suspended sediment and hence is denser than the surrounding water.

These flows are the main sediment transport mechanism in deep submarine environment, traveling long distances and transforming the topography of ocean floor. Sediment discharge of rivers flowing into reservoirs is typically very high during flood events. In dam reservoirs, these currents are believed to be responsible for sediment transport and subsequently effecting the dam's operation (Cesare et al., 2001).

These currents have been actively studied to improve understanding of their processes and dynamics. Most of the works regard the case of gravity currents flowing over smooth beds, for example, (Altinakar et al., 1996; Cortés et al., 2014; Cossu and Wells, 2012; Hosseini et al., 2006; Islam and Imran, 2010; Kneller et al., 1999; Nasrollahpour et al., 2015; Nasrollahpour et al., 2016). However, in practical cases, these currents usually flow over the beds which are not flat. This involves mobile beds, obstacles, grain roughness (e.g. sand or gravel) and form roughness (e.g. ripples or dunes).

Simulations of (Tokyay, 2010) showed considerable qualitative and quantitative differences in comparison with the simpler and much more investigated case of gravity currents advancing over smooth beds. There have been limited investigations in respect with the effect of form roughness on gravity currents (Batt, 2008; Bhaganagar, 2014; Chowdhury, 2013; Nasrollahpour et al., 2015; Negretti et al., 2008; Peters and Venart, 1999; Tokyay, 2010). However, these works have been focused on the frontal region of the currents, and understanding of bottom roughness effects on the body of these currents is still lacking. In general, decelerated, thicker, rounder and more diluted fronts have been noticed in their observations as a result of bottom roughness.

The main aim of this research is to provide a better understanding on the structure of density currents propagating over different rough beds. For this, vertical structures of the streamwise velocities are recorded in the body of density currents, and variations in the velocity profiles of the currents at the presence of different bed roughness configurations are analysed. Also, the effect of different bed configurations on entrainment of ambient fluid into these currents are quantified.

The interaction between arrays of roughness elements and gravity currents can be a representative of various natural scenarios where density currents flow over non-flat beds. Therefore, there is a need to

investigate adjustments in the structure of these currents encountering roughness arrays. This can contribute towards explaining the evolution of these currents over rough beds, which is of significant concern in many engineering areas due to its impact on the environment.

The rest of this paper is structured as follows: firstly, a brief overview of the experimentation is presented. This is followed by an analysis of the velocity of the currents flowing over different bed configurations. The influence of bottom roughness on water entrainment into the currents is also investigated, and the alterations in the entrainment rate are investigated. Finally, concluding remarks are drawn.

2 Methodology

The experimental set up consisted of an open channel 10 m long, 0.30 m wide and 0.7 m deep flume capable of having variable bed slopes. There was a water supply system providing tap water for the flume as the lighter ambient fluid with mixing tanks and a head tank, as seen in Figure 1.

This experimental research created density currents in lock-exchange configuration in which a gate separated two fluids with different densities and there was a rear wall at one end of the flume. In this setting, a denser lock fluid initially occupied the volume between the rear wall and the lock gate, and the lighter fluid (fresh water) occupied the area downstream of the gate.

The density current was initiated by the sudden removal of a vertical lock gate. Once the gate was opened, a gravity current containing heavier fluid propagated within the lighter ambient fluid as an underflow, which was referred to as the front of the current. After the front reached downstream end of the channel, it was directed for withdrawal via drainage valves placed inside the body of a weir at the downstream end of the channel. Thereafter, a shallower steady and quasi-uniform source of layer formed the body of the currents where there was the focus of this study.

The continuous flux currents were used at this work where there was an unceasing supply of intruding dense fluid, because the steady state of the body of the currents can only be marinated in this case. Salt was added to tap water inside the mixing tanks to create dense fluids with required salinities. A WP-84 conductivity meter (from TPS Pty Ltd, Australia) with a K=10 sensor and a DA-130N Portable Density Meter (from Kyoto Electronics Manufacturing, Japan) were employed to measure the salinities and densities, respectively.

Dense fluids were transferred to the area behind the gate via a head tank. The use of dissolved salt can be a surrogate for fine-grained sediments that does not settle out readily. Thus, all the currents can be considered to model turbidity currents (Abad *et al.*, 2011; Sequeiros *et al.*, 2010).

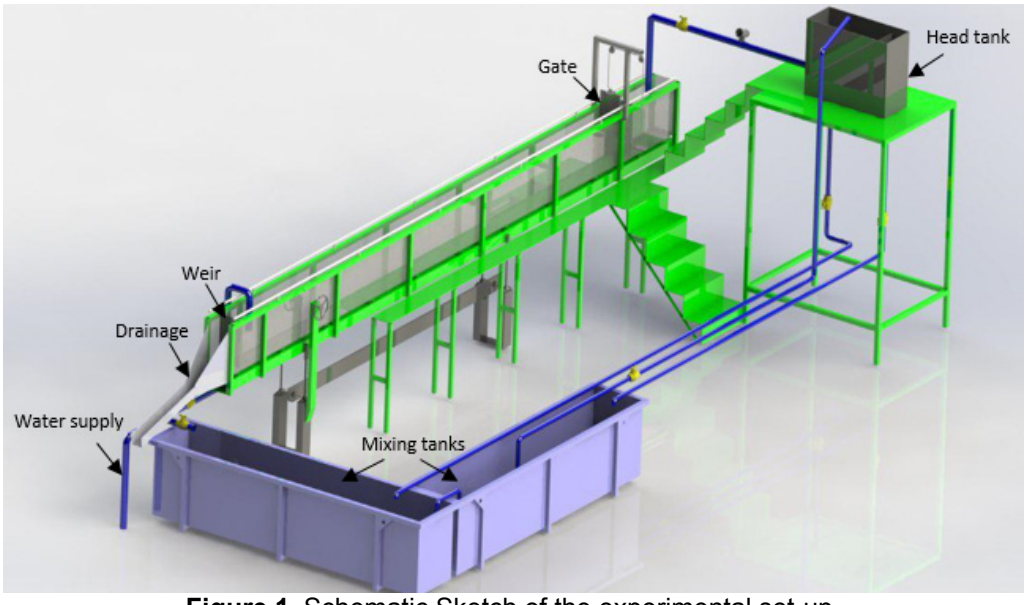

Figure 1. Schematic Sketch of the experimental set-up

In the present study, the case of roughness elements at the channel bed was also investigated. Particularly, the interaction of density currents with bottom roughness was considered. These rough beds consisted of arrays of square cross-section beams fabricated from wood with side dimensions of 1.2 cm, spanning the full channel width, extending along the laboratory channel. The rough beds included different configurations of the beam-roughened surfaces.

The desired roughness was obtained by gluing roughness elements on the bed with the required spacing. The elements spanned the full flume width perpendicular to the flow direction, in a repeated array extended over a 8 m region from the gate. One smooth bed (λ/K_r =0) and three roughness configurations (λ/K_r=1, 4 and 8) were tested herein adopting both dense and spare bottom roughness elements. The diagram of the roughness array is schematically shown in Figure 2 where λ is the downstream spacing between each

two subsequent beams, and K_r is roughness height. These beds are illustrated in Figure 3. A total of eight experiments were performed, as listed in Table 1 where S, C_{in} Q_{in} and h_{in} denote bed slope, concentration of dense fluid at the inlet, inlet discharge, and inlet opening height respectively.

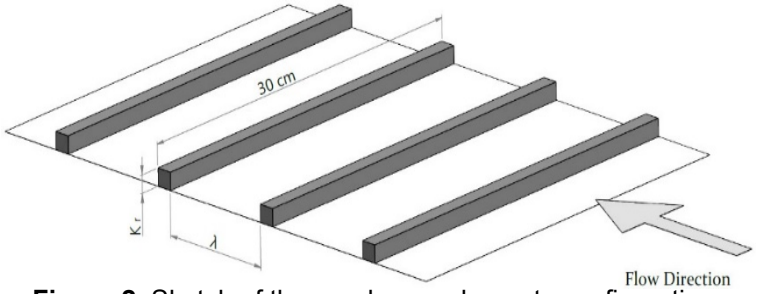

Figure 2. Sketch of the roughness elements configuration

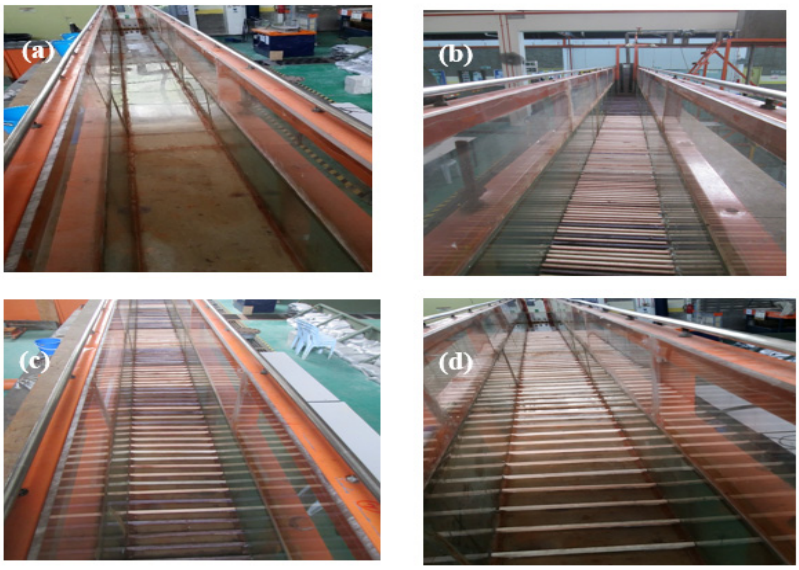

Figure 3. Photographs of different bed configurations corresponding to (a) $\lambda/K_r=0$ (b) $\lambda/K_r=1$ (c) $\lambda/K_r=4$ (d) $\lambda/K_r=8$

Table 1. Experimental conditions

Experiment Number	Bed configuration	S (%)	C_{in} (gr/lit)	ρ_{in} (kg/m^3)	Q_{in} (lit/s)	h_{in} (m)
1	Smooth	1.75	5	1002.6	1	0.07
2	Smooth	1.75	15	1009.6	1	0.07
3	$\lambda/K_r=1$	1.75	5	1002.6	1	0.07
4	$\lambda/K_r=1$	1.75	15	1009.6	1	0.07
5	$\lambda/K_r=4$	1.75	5	1002.6	1	0.07
6	$\lambda/K_r=4$	1.75	15	1009.6	1	0.07
7	$\lambda/K_r=8$	1.75	5	1002.6	1	0.07
8	$\lambda/K_r=8$	1.75	15	1009.6	1	0.07

This research also investigates velocity structure of gravity currents. To this end, vertical profiles of streamwise velocities flowing over various bed roughnesses were examined. A Vectrino Plus Velocimeter with a lab probe made by Nortek AS (Norway) was used to record the velocity profiles in the body (see Figure 4) of density currents at three locations (i.e. X= 3 m, 4 and 5 m from the gate) along the centerline of the channel. This is a high-resolution 10 MHZ Acoustic Doppler Velocimeter (ADV), having a down looking fixed-stem probe. A sampling frequency of 100 HZ was used herein.

In the experiments, the density current's color was roughly the same as that of fresh water. Thus, for visibility purposes, dye was added to the dense fluid in the mixing tanks. The velocity profile in any required section was determined by changing the vertical location of the sensor. The measurements began from the top part of the dense layer and continued into the lower parts by lowering the probe into the current till all the necessary points were covered. In this study, samples with signal-to-noise (SNR) values less than 15 dB and correlation less than 70% were filtered according to the manufacture recommendation.

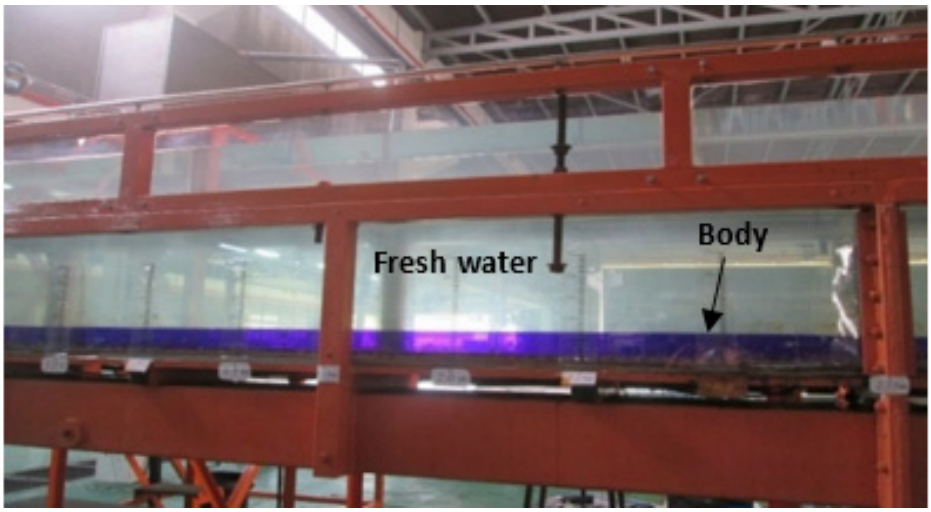

Figure 4. Body of a density current flowing under the fresh water

3 Results and Discussions

3.1 Influence of roughness on velocity profiles

Density currents flowing over roughness elements with various spacing (λ/K_r= 1, 4, 8) were tested in this work and their velocity profiles were recorded. Following (Perry et al., 1969), the roughened beds with λ/K_r=1 are categorized as d-type and the beds with λ/K_r =4, 8 are considered as k-type.

Herein, the influence of different configurations of roughness elements on the velocity profiles for selected number of experiments are illustrated in Figure 5. The dense layer height (z) and velocity (u) are normalized with the inlet opening height (h_{in}) and inlet velocity (u_{in}), respectively. Note that all these currents have the same initial conditions, and the adjustments in the profiles were solely induced by the roughness elements.

As seen in the Figures 5, the primary influence of roughness is decreasing the velocity of the currents. The current loses its kinetic energy as travelling over the elements due to adverse pressure gradient being induced by inclined upstream surface of the beams, leading to deceleration of the currents. Moreover, within the body, the velocity maximum was located higher in the current in comparison with the smooth case. The magnitude of these effects depends on the configuration of roughness elements, as discussed afterwards.

In this work, for the d-type bed roughness (i.e. λ/K_r=1), the velocity profiles depict close similarity with the smooth bed and noticeably differ from the k-type case. As seen in Figure 5, for the rough bed with λ/K_r =1, the maximum velocity was only slightly lower than that of the smooth bed. This indicates the minimal interaction of the currents with the elements for this roughness configuration. For λ/K_r =1, the position of peak velocity shifts further upward reaching to z/hin=0.65 as opposed to the corresponding current flowing over the λ/K_r=0 where z/h_{in}=0.4. This suggested that for λ/K_r =1 the current lifts above the roughness elements.

The initial density difference between the ambient water and the dense fluid was small; therefore, the currents flowing over the dense array of beams (e.g. d-type bed roughness) can lift above the beams and show a dynamics similar to their counterparts travelling over the smooth bed. Yet, they were still slightly slower which can be a result of energy loss due to trapped vortices between the elements.

The front of gravity currents flowing over d-type roughness was examined by (Peters and Venart, 1999) (Peters and Venart, 2000). A similar mechanism was found in which the head floats over the beams having only a slight interaction with them. In addition, they observed the rotating vortices trapped between the elements were weak, which was in agreement with the findings herewith.

For the k-type rough beds, the roughened beds with λ/K_r=4 and 8, the retardation of the density current increases with increasing the beams spacing. Moreover, increasing the spacing between elements increases the distance above the bed where maximum velocity attains.

Further deceleration of the current for k-type rough beds λ/K_r=4 and 8 was attributed to the larger spacing between the beams. As the current propagates over the elements, flow separation occurs above each beam, reattaching in the area between the beams. This creates a vortex below the separated flow at the downstream side of the beams ejecting to the overlying flow, as also shown in simulations (Leonardi et al., 2004) for single-phase flows. The larger gaps between the beams required more energy to maintain a vortex in motion in that area. Also, the volume of the released fluid from between the elements to the current was more significant in making more disruption leading to deceleration of the currents.

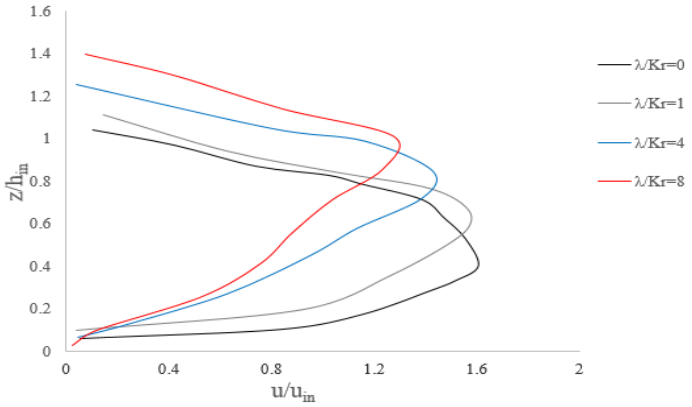

Figure 5. Comparison of velocity profiles for different bed types at X=4 m corresponding to X= 4 m, h_{in}=7 cm, C_{in}=5gr/lit, S=1.75%, Q_{in}= 1 lit/s

3.2 Bed-roughness induced entrainment

A distinct dividing boundary was maintained between the density current and ambient fluid throughout its entire lifetime. However, intense mixing occurs across this boundary due to shear stress at the interface between the density current and ambient fluid. Water entrainment was referred to the mass of ambient fluid crossing the interface and mixes with the dense underflow. Herein, an attempt was made to quantify mixing using entrainment rate.

Velocity at which fluid was entrained across an interface was proportional to some velocity scale of the flow. The constant of proportionality is known as water entrainment coefficient or rate (E_w). This coefficient is calculated using (Ellison and Turner, 1959):

$$E_w \bar{u} = \frac{d(\bar{u}\bar{h})}{dx} \quad [1]$$

To calculate the entrainment coefficient between two stations (*j* and *j+1*), the Eq. 1 can be rewritten as:

$$(E_w)_{j,j+1} = \left(\frac{2}{\bar{u}_{j+1} + u_j}\right)\left(\frac{(\bar{u}\bar{h})_{j+1} - (\bar{u}\bar{h})_j}{x_{j+1} - x_j}\right) \quad [2]$$

Where $\bar{u}$ is depth-averaged velocity, $\bar{h}$ is depth-averaged height, and x is the distance from the gate.

The depth-averaged velocity ($\bar{u}$) and height ($\bar{h}$) of the currents are estimated by equations introduced by (Ellison and Turner, 1959) as:

$$\bar{u} = \frac{\int_o^{h_d} u^2\, dz}{\int_0^{hd} u\, dz} \quad [3]$$

$$\bar{h} = \frac{\left(\int_0^{h_d} u\, dz\right)^2}{\int_0^{h_d} u^2\, dz} \quad [4]$$

Where u is the local velocity at the depth of z, and h_d is the depth where u=0.

In this work, the velocity profiles were recorded at three stations along a laboratory channel. For a given experiment, the entrainment rates were calculated between each two stations and the average of the calculated values was considered as the entrainment rate for that experiment.

Herein, the influence of different configurations of roughness elements on the entrainment rate was investigated. To this end, the entrainment rate for each bed type ($\overline{E}_w$) was yielded through averaging the calculated entrainment rates for the experiments conducted over that bed type. Then, the entrainment coefficient of each rough bed was divided to that of the smooth surface, as seen in Table 2.

Table 2. Comparison of the entrainment rate for different beds

Bed type	$\overline{E}_w$	$\frac{(\overline{E}_w)_{rough\ bed}}{(\overline{E}_w)_{smooth\ bed}}$
λ/K_r=0	0.002283	1
λ/K_r= 1	0.003401	1.49
λ/K_r= 4	0.005319	2.33
λ/K_r= 8	0.012009	5.26

For the d-type rough beds, the dense spacing of the beams helps the vortices to keep the fluid trapped between the elements while the current passes over the beams. This brings only little disruption to the overlying currents, influencing the entrainment rates only marginally compared to the case of the plane bed, as found in the entrainment rates presented in Table 2.

In case of k-type rough beds, the strong flow separation can engulf the fluid between the beams. Therefore, altered entrainment rates were expected for various roughness configurations, as shown in Table 2. For λ/K_r=4, 8, the entrainment rate grows with increasing the spacing between the elements, indicating further disruption to the currents as a result of ejected vortices from between the beams. This agrees with the result of field studies on natural density currents by (Fernandez and Imberger, 2006) where the water entrainment was found to be strongly dependent on the roughness of the bottom over which they travel.

The density difference between the current and ambient fluid was the driving force of the gravity currents. Thus, the currents were decelerated by the reduction in buoyancy forces due to further water entrainment into the current. Given the extreme water entrainment rate at λ/K_r= 8, the currents flowing over this rough bed were expected to demonstrate the smallest velocities, which was in confirmation with the velocity profiles seen in Figure 5. In natural flows, this can influence the vertical transport of particles to higher regions within the currents.

4 CONCLUSIONS

This work investigates velocity structure of density currents flowing over beam-type roughness. Overall, it is found that rough beds reduce the velocity of the currents compared to that of the smooth surface. However, the extend of this deceleration varies with the configuration of the bed roughness. The currents flowing over dense arrays of roughness elements (λ/K_r=1) depict a velocity similar to that of the flat bed, while the corresponding currents flowing over spare arrays of beams (λ/K_r=4, 8) resulted in deceleration of the currents.

Analysing the entrainment rates revealed entrainment of ambient water into dense layers improves with increasing of the cavities between the elements, suggesting an improved strength of ejection from between the beams. This produces significant disruption in the density currents flowing over the elements, resulting in enhanced water entrainment and deceleration of the currents.

This research contributes toward the explanation of the dynamics of density currents in many man-made and natural scenarios where these currents travel over non-plane beds. In particular, findings of this work can contribute toward dealing with the control of these currents in dam reservoirs using arrays of obstacles. This, in turn, leads to decreasing maintenance costs and increasing useful life time of the dams.

ACKNOWLEDGEMENTS

The funding for this work is provided by the Fundamental Research Grant Scheme (reference number: FRGS/1/2015/STWN01/UTM/02/2), under the Ministry of Education, Malaysia. The authors would also like to acknowledge the support of Universiti Teknologi Malaysia through the Research University Grant (reference number: PY/2014/02346).

REFERENCES

Abad, J.D., Sequeiros, O.E., Spinewine, B., Pirmez, C., Garcia, M.H. & Parker, G. (2011). Secondary Current of Saline Underflow in a Highly Meandering Channel: Experiments and Theory. J*ournal of Sedimentary Research*, 81(11), 787-813.

Altinakar, M., Graf, W. & Hopfinger, E. (1996). Flow Structure in Turbidity Currents. J*ournal of Hydraulic Research*, 34(5), 713-718.

Batt, R.L. (2008). The influence Of Bed Roughness on The Dynamics of Gravity Currents. *PhD Thesis*. University of Leeds.

Bhaganagar, K. (2014). Direct Numerical Simulation of Lock-Exchange Density Currents Over the Rough Wall in Slumping Phase. *Journal of Hydraulic Research*, 52(3), 386-398.

Cesare, G.D., Schleiss, A. & Hermann, F. (2001). Impact of Turbidity Currents on Reservoir Sedimentation. *Journal of Hydraulic Engineering*, 127(1), 6-16.

Chowdhury, R.A. (2013). Effect of Roughness on Density Currents, *Thesis*, The University Of Texas at San Antonio.

Cortés, A., Rueda, F. & Wells, M. (2014). Experimental Observations of The Splitting of a Gravity Current at a Density Step in a Stratified Water Body. *Journal of Geophysical Research: Oceans*, 119(2), 1038-1053.

Cossu, R. & Wells, M.G. (2012). A comparison of The Shear Stress Distribution in the Bottom Boundary Layer of Experimental Density and Turbidity Currents. *European Journal of Mechanics-B/Fluids*, 32, 70-79.

Ellison, T. & Turner, J. (1959). Turbulent Entrainment in Stratified Flows. *Journal of Fluid Mechanics*, 6(03), 423-448.

Fernandez, R.L. & Imberger, J. (2006). Bed Roughness Induced Entrainment in a High Richardson Number Underflow. J*ournal of Hydraulic Research*, 44(6), 725-738.

Fragoso, A., Patterson, M. & Wettlaufer, J. (2013). Mixing in Gravity Currents. J*ournal of Fluid Mechanics*, 734, R2.

Hosseini, S., Shamsai, A. & Ataie-Ashtiani, B. (2006). Synchronous Measurements of The Velocity and Concentration in Low Density Turbidity Currents Using an Acoustic Doppler Velocimeter. *Flow Measurement and Instrumentation*, 17(1), 59-68.

Islam, M.A. & Imran, J. (2010). Vertical structure of Continuous Release Saline and Turbidity Currents. *Journal of Geophysical Research: Oceans*, 115(C8).

Kneller, B.C., Bennett, S.J. & McCaffrey, W. D. (1999). Velocity Structure, Turbulence and Fluid Stresses in Experimental Gravity Currents. *Journal of Geophysical Research: Oceans*, 104(C3), 5381-5391.

Leonardi, S., Orlandi, P., Djenidi, L. & Antonia, R. (2004). Structure of Turbulent Channel Flow with Square Bars on One Wall. I*nternational Journal of Heat and Fluid Flow*, 25(3), 384-392.

Nasrollahpour, R., Jamal, M. H., Ismail, Z., Ghomeshi, M. & Roushenas, P. (2015). The Influence of Roughness on The Propagation of Density Currents. *Malaysian Journal of Civil Engineering*, 27(Special Issue 2), 266-272.

Nasrollahpour, R., Jamal, M.H., Ismail, Z. & Rusli, N.M. (2016). Experiments on the Dynamics of Density Currents. *Jurnal Teknologi*, 78(9-4), 71-76.

Negretti, M.E., Zhu, D.Z. & Jirka, G.H. (2008). The Effect of Bottom Roughness in Two-Layer Flows Down a Slope. *Dynamics of Atmospheres and Oceans*, 45(1), 46-68.

Perry, A.E., Schofield, W.H. & Joubert, P.N. (1969). Rough Wall Turbulent Boundary Layers. *Journal of Fluid Mechanics*, 37(02), 383-413.

Peters, W.D. & Venart, J. (1999). Rough-surface Gravity Current Flows. *PhD Thesis*. University of New Brunswick.

Peters, W.D. & Venart, J. (2000). Visualization of Rough-Surface Gravity Current Flows Using Laser-Induced Fluorescence. Paper presented at the Proceedings of *9th international symposium of flow visualization*, Edinburgh, Scotland.

Sequeiros, O.E., Spinewine, B., Beaubouef, R.T., Sun, T., García, M.H. & Parker, G. (2010). Characteristics of Velocity and Excess Density Profiles of Saline Underflows and Turbidity Currents Flowing Over a Mobile Bed. *Journal of Hydraulic Engineering*, 136(7), 412-433.

Tokyay, T.E. (2010). A LES study on Gravity Currents Propagating Over Roughness Elements, *PhD Thesis*. University of Iowa.

Proceedings of the 37th IAHR World Congress
August 13 – 18, 2017, Kuala Lumpur, Malaysia

2D NUMERICAL SIMULATION FOR EROSION BASED MORAINE DAM FAILURE AND MORPHOLOGICAL BED EVOLUTION

SAZEDA BEGAM[(1)], DHRUBAJYOTI SEN[(2)] & SUBHASISH DEY[(3)]

[(1)]School of Water Resources Engineering, Indian Institute of Technology Kharagpur, India
sbsazeda@swr.iitkgp.ernet.in
[(2,3)]Department of Civil Engineering, Indian Institute of Technology Kharagpur, India
djsen@civil.iitkgp.ernet.in, sdey@civil.ernet.iitkgp.in

ABSTRACT

The glacial lakes are increasing both in number and size and becoming more susceptible to causing Glacial Lake Outburst Flood (GLOF) due to global warming. The numerical simulation of moraine dam breach with better accuracy would help in understanding the extent of flash floods like GLOF more precisely. Moraine dam is a natural earthen dam formed by the material accumulated from a glacier which usually forms a glacial lake behind from the glacier melting water originating from its snout. This paper presents an approach for simulating the failure of a moraine dam by overtopping using a coupled numerical simulation model for flow and sediment movement (TELEMAC-2D and SISYPHE). The model simulates the breach formation of the dam and computes the resulting outflow hydrograph at the downstream of the dam. The embankment material is considered as non-cohesive and uniformly graded sand. The breaching process depends upon the shear stresses induced by the water flowing over the crest and downstream slope of the dam. After an initial breach is formed, the erosion of the dam proceeds spatially, which includes both vertical and lateral erosion. The study presents the simulation results from the 2D numerical model of the eroding embankment dam, which is compared with previously published experimental results. The numerical hydrodynamic model (TELEMAC-2D) is based on the shallow-water equations, which is coupled with the sediment erosion model (SISYPHE) in an interactive manner that takes into account the feedback between the water flow field hydraulics and the morphological changes of the dam surface profile. The governing law for sediment erosion code is that of Fredsoe and Rouse and is implemented by considering the material characteristics like critical erosion shear stress and erodibility factor. The results obtained from the numerical model are seen to match quite closely with the reported experimental results.

Keywords: Moraine dam failure; overtopping; Glacial lake outburst flood (GLOF); TELEMAC-2D; SISYPHE.

1 INTRODUCTION

In the twenty-first century, global warming has been identified as the main cause of climate change and perhaps the most significant threat to living organisms. The significant shrinking and recession of mountain glaciers worldwide and development of glacial lakes is one of the most convincing evidences of the changing global climate. The glacial lakes are expanding both in number and size and becoming increasingly susceptible to causing Glacial Lake Outburst Flood (GLOF) due to climate change. The GLOF events have devastating consequences resulting in loss of lives and destruction of roads, houses and other infrastructures. To minimize the disastrous effects of GLOF and to estimate the vulnerability of the regions downstream of the glacier lakes, it is necessary, to prepare a systematic inventory of such lakes, analyse their growth rates, estimate the failure chances of moraine dams (forming the lakes) and simulation of dam breach effects with better accuracy. The history of past glacier lake outburst flood events indicates that generally moraine-dammed lakes are the most potentially vulnerable to trigger a GLOF event and they are initially derived from supra-glacier lakes (Mool et al., 2001). A study carried out jointly by the International Centre for Integrated Mountain Development (ICIMOD), United Nations Environment Programme/Regional Resource Centre for Asia and the Pacific (UNEP/RRC-AP) and Asia-Pacific Network for Global Change research (APN) between 1999 and 2003 estimated that there are about 9000 large and medium glacial lakes in the Himalayas and more than 200 potentially dangerous glacial lakes in Bhutan, Nepal, Pakistan and selected basins of China and India (Bajracharya et al., 2008).

Moraine dam can be described as a natural earthen dam formed by the material accumulated from the downward movement of a glacier (the moraine) and one which accumulates water behind the dam due to the glacier melting from its snout. Though a moraine dam is usually unstable due to the unconsolidated ingredients with which it is made of, it requires a trigger event to initiate partial or complete failure of the dam by breaching and result in a GLOF (e.g. Costa and Schuster, 1988; Richardson and Reynolds, 2000). The failure of a moraine dam is, mainly caused by: (i) seepage and piping, and (ii) over-topping. Though the occurrence of piping is related to the materials state of un-consolidation, damage by overtopping and erosion

of a moraine dam may be caused due to a passing wave of water generated by extreme precipitation, landslide or avalanche generated impulse wave, excessive glacier melts, or an upstream GLOF reaching a lower glacier lake (Clague and Evans, 2000; Westoby et al., 2014).

Two broad approaches are followed for predicting the outburst flood hydrograph (or peak discharge) from moraine dam failures. In the first, empirical equations are derived to calculate the peak discharge depending on the data sets obtained from historical records of moraine dam failure (Costa and Schuster, 1988; Walder and O'Connor, 1997). However, these empirical equations are based upon a limited number of past events or confined to a particular study area and thus may not be applicable elsewhere. The other approach employs physically based models for numerically simulating a dam breach event under the assumed conditions. Most of these models emphasize a certain feature or characteristic of the material or phenomena being modeled. While some consider the dam material to be porous and non-cohesive (Yusof et al., 2010; Fred, 1991) or cohesive (Yusof et al., 2010), others consider an erosion law based on local shear stress (Takahashi and Nakagawa, 1993) or include wind effects (Awal et al., 2010). Some studies have also estimated the flood hydrograph resulting from dam breach (Bajracharya et al., 2007; Rivas et al., 2015). Most of these researches have made use of the BREACH model (Fread, 1991) and some have specifically used the model or some empirical formula to obtain GLOF generated flood peak. Another approach of generating flood hydrograph from rockfill dam breaching was made by Franca and Almeida in 2004. However, apparently there is not much study reported on a purely process based numerical simulation of a moraine dam failure and estimation of resulting hydrograph. The present work attempts to fill in this gap by modelling the breaching by overtopping of a moraine dam, represented by an embankment, using open source two-dimensional numerical flow simulation model TELEMAC-2D (TELEMAC-2D, 2014) coupled with the sediment movement simulation model SISYPHE (SISYPHE, 2010). The work further looks into verifying the results with published data obtained from physical model experiments reported by Schmocker and Hager (2012).

2 NUMERICAL SCHEME

The open source two-dimensional numerical flow model TELEMAC-2D is used for simulating the hydrodynamics of the flow, taking place during a GLOF event caused by an erosional breaching of a moraine dam. The general steps to run the model are setting initial bathymetry, mesh generation, application of appropriate boundary conditions, including the input parameters like discharge and setting of a time step. TELEMAC-2D solves the shallow water equations in two dimensions by the finite volume or finite element methods. The hydrodynamic variables (water velocity and depth) calculated are then passed on to SISYPHE, a sediment transport model, where the erosion of the dam and its eventual failure are simulated numerically. In SISYPHE, the bed load and the sediment continuity equation are solved by the finite element method to compute the new bathymetry (new set of bed elevation) at each time step, which becomes the initial bathymetry for the next time step. The governing equations used by the two simulation models described above are briefly discussed in the following section.

3 GOVERNING EQUATIONS USED IN NUMERICAL MODELLING

The two-dimensional flow model TELEMAC-2D employs the shallow water (Saint-Venant) equations of continuity and momentum which are derived from the vertically averaged Navier-Stokes equations and may be expressed as follows:

$$\frac{\partial h}{\partial t} + \frac{\partial (hu)}{\partial x} + \frac{\partial (hv)}{\partial y} = 0 \qquad [1]$$

$$\frac{\partial (hu)}{\partial t} + \frac{\partial (hu^2)}{\partial x} + \frac{\partial (huv)}{\partial y} = -hg\frac{\partial z}{\partial x} + \frac{\tau_{xx}}{\rho} + F_x \qquad [2]$$

$$\frac{\partial (hv)}{\partial t} + \frac{\partial (huv)}{\partial x} + \frac{\partial (hv^2)}{\partial y} = -hg\frac{\partial z}{\partial y} + \frac{\tau_{yy}}{\rho} + F_y \qquad [3]$$

Where, h = depth of water (L), u,v = depth averaged velocity components in x and y directions respectively (LT^{-1}), g = gravitational constant ($M^{-1}L^3T^{-2}$), ρ = density of water (ML^{-3}), z = free surface elevation (L), t = time (T), x,y = horizontal Cartesian coordinates (L), τ_{xx}, τ_{yy} = depth-averaged turbulent stresses ($ML^{-1}T^{-2}$), and F_x, F_y = Coriolis forces.

The model SISYPHE which simulates bed morphodynamics by calculating the bed elevation change when coupled with the flow simulation model TELEMAC-2D uses the Exner equation (Equation 4) for sediment continuity.

$$(1-p)\frac{\partial Z_b}{\partial t} + Div.(Q_b) + E - D = 0 \qquad [4]$$

Where, ρ = porosity (in fraction, unit less), Z_b = bottom or bed elevation (L), Q_b = volume of sediment transport (bed load) per unit width (L^2T^{-1}), E = net flux for erosion (as per Rouse formula, Rouse, 1961) and D = net flux for deposition (as per Fredsoe formula, Zyserman and Fredsoe, 1994).

In the present work, only bed load is presumed to be active and simulated by the morphodynamic model SISYPHE, which considers the Rouse concentration sediment profile and the Zyserman and Fredsoe equations (Zyserman and Fredsoe, 1994) respectively. Further, a hydrostatic assumption is considered by the model, in which the vertical accelerations generated from the pressure are assumed to be balanced by gravity only in case of small bed slopes. To make the model simpler for better understanding, the classical k-ε turbulence scheme is chosen in the hydrodynamic model (TELEMAC-2D) and the turbulence viscosity coefficient is set to a constant value 10^{-2} m^2s^{-1}. Similarly, the velocity diffusivity is considered as 10^{-2} m^2s^{-1} for taking into account the eddies and making the model more realistic. The bottom friction for the channel is estimated but the Strickler Law, which has an influence on both water velocity and bed shear stress for controlling the erosion and sediment transport.

To calculate the bed load for erosion modelling in SISYPHE, the following formula by Van Rijn (Van Rijn, 1984) is considered:

$$Q_b = 0.053(s-1)^{0.5} g^{0.5} D_{50}^{1.5} D_*^{-0.3} \tau^{1.5} \quad \text{for } \tau \le 3 \qquad [5]$$

$$Q_b = 0.1(s-1)^{0.5} g^{0.5} D_{50}^{1.5} D_*^{-0.3} \tau^{1.5} \quad \text{for } \tau > 3 \qquad [6]$$

Where,

$$D_* = D_{50}\left(\frac{(\rho_s - \rho)g}{\rho \upsilon^2}\right), \quad \tau = \frac{u_*^2 - u_{*cr}^2}{u_{*cr}^2} \qquad [7]$$

In the above equations, the notational representations are: Q_b = bed load transport rate, s = relative density, g = gravitational acceleration ($M^{-1}L^3T^{-2}$), D_{50} = mean sediment diameter (L), D_* = dimensionless particle size, u_* = bed shear velocity (LT^{-1}), u_{*cr} = critical bed shear velocity (LT^{-1}), τ = non-dimensional excess bed shear stress, ρ = density of water (ML^{-3}), ρ_s = density of sediments (ML^{-3}) and υ = kinematic viscosity (L^2T^{-1}).

4 DAM FAILURE MODELLING: NUMERICAL SIMULATION

This study attempts to replicate the breach by overtopping experiments reported by Schmocker and Hager (2012) carried out in the laboratory of ETH Zürich. The numerical simulation of the same phenomena is conducted by the coupled models TELEMAC-2D and SISYPHE, described in the previous section. Further, the modelling is done in two parts; at first, the breaching process is simulated by erosion, which is physically related to the fluid flow and material properties of the moraine dam, while the second obtains the flood discharge hydrograph resulting from the breaching. The modelling study is initiated by generating the channel section (or bathymetry) geometry. A schematic diagram of the model geometry taken from Schmocker and Hager (2012) is shown in Figure 1, while Figure 2 illustrates the corresponding triangular computational mesh generated for the numerical study for a certain length of channel section including the dam to serve as an input for the numerical model. The mesh containing 1606 nodes and 2900 elements, was generated with the help of the open source software tool Blue Kenue (NRC-CHE, 2010).

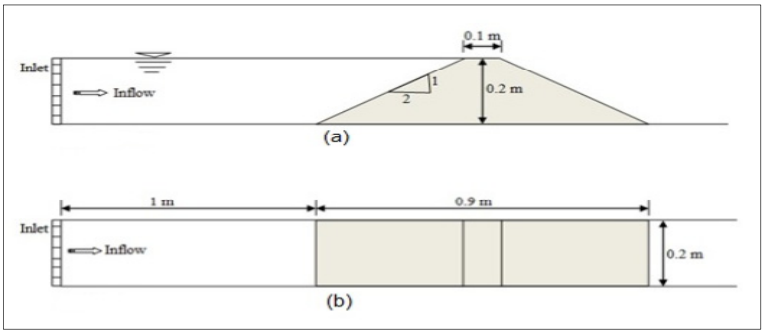

Figure 1. Schematic diagram of model geometry (not in scale): (a) Side View, (b) Plan View.

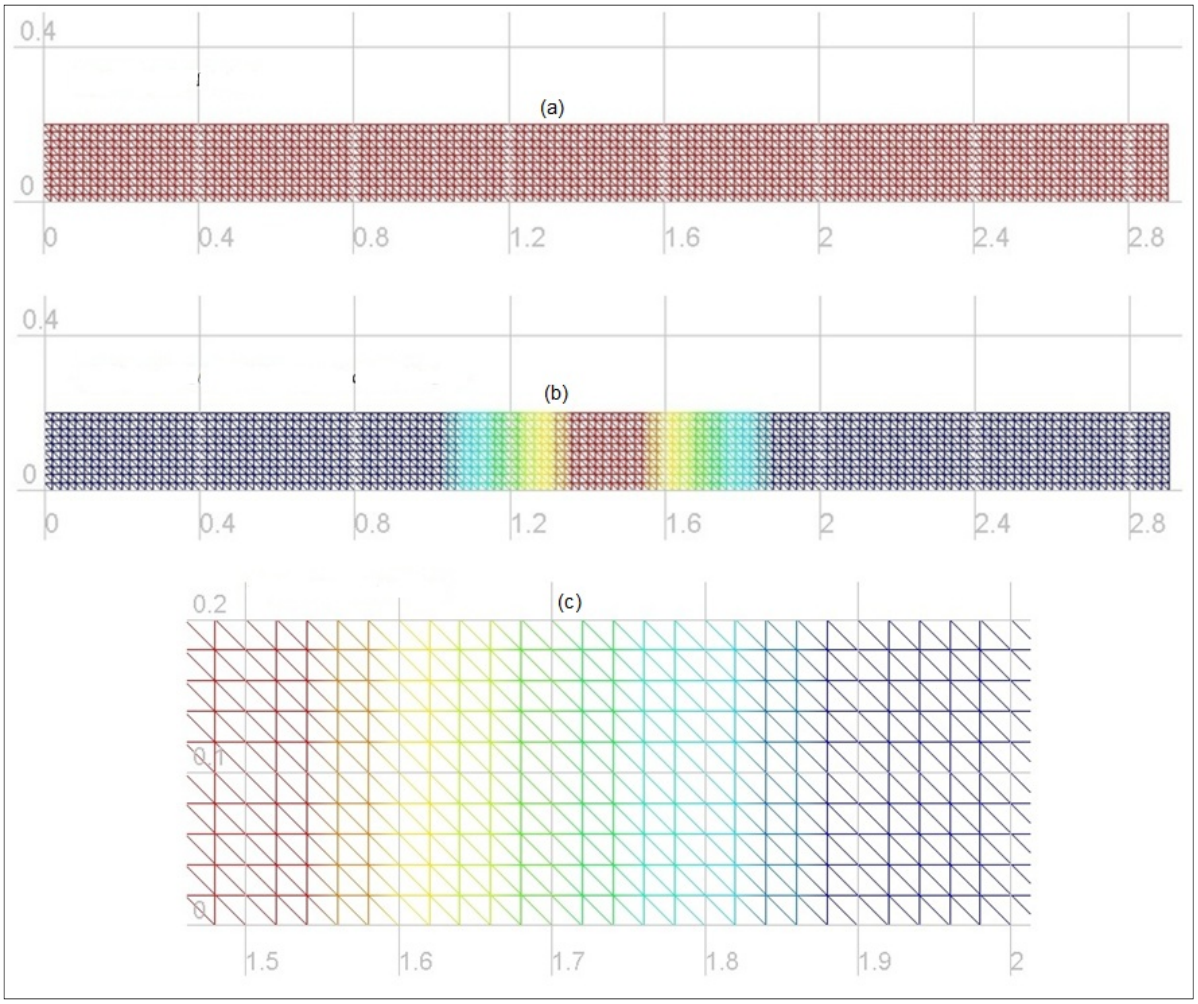

Figure 2. Computational mesh of channel section: (a) Triangular mesh grid, (b) Triangular mesh grid incorporated with elevation, (c) Close view of mesh grid.

The model embankment dam used by Shocker and Hager (2012) for their experimental studies of its breaching is reported to be made of non-cohesive, very coarse sand (D_{50} = 2 mm; density ρ_s = 2650 kg-m^{-3}; uniformity coefficient $\sigma_g = (D_{84}/D_{16})^{0.5} < 1.2$); has a flat crest width, W_d = 0.1 m; and the upstream and downstream dam slopes are set as 2H:1V with a dam height H_d = 0.2 m. The dam is located at a distance of 1m from the inlet of the channel which is 0.2m wide. The inflow discharge Q_{in} = 0.06 m^3/s. Figure 1 illustrates the model setup in section and plan, where the flow inlet is towards the left of the domain.

For the present numerical study, the physical model setup of Schmocker and Hager (2012), Figure 1 is replicated in the computational mesh shown in Figure 2. The hydrodynamic model TELEMAC-2D and the morphodynamic model SISYPHE both work on a two-dimensional mesh and for the present case, triangular mesh in two-dimensions (in plan) is used to model the physical model setup. The image at the top of Figure 2 shows this mesh while the middle image provides a colour gradation according to the elevation of the bed, where the location of the dam may be identified. The bottom image of Figure 2 shows a close up of the region modeled as the dam. There are 2900 triangular cells and 1606 nodes in the complete domain. The entire bed is assumed to be made up of erodible material conforming to the properties of the physical setup (Schmocker and Hager, 2012). Since the porosity of the physical model setup is not available, it is assumed as 40 percent for the numerical simulation. The inflow discharge is kept same as that reported for the physical model and is assumed to enter the flow domain from the left. The exit channel is imposed with a normal depth boundary condition for the sake of the present numerical simulation.

5 COMPARISON OF NUMERICAL AND PHYSICAL MODEL RESULTS

5.1 Dam morphology

Figure 3 presents a comparison between the numerical model outcomes of surface profiles for embankment dam breach reported by Schmocker and Hager (2012) for their experimental observations. The simulated breaching profiles computed at different times (Figure 3-a) seem to tally well with experimental observations (Figure 3-b) except for some discrepancies at the initial times. At time steps t = 2s and t = 4s, the

eroded profiles predicted by the model appear to be slightly high, that is, the sediment transport and erosion rates are marginally more than that reported by the laboratory experiment. This mismatch may perhaps be due to a difference in porosity values of the material used in the experiment and that considered in the model. As mentioned in the previous section, there is no reference to porosity for the model dam used in the experiment of Schmocker and Hager (2012), but a porosity of 40% has been adopted for the present numerical study.

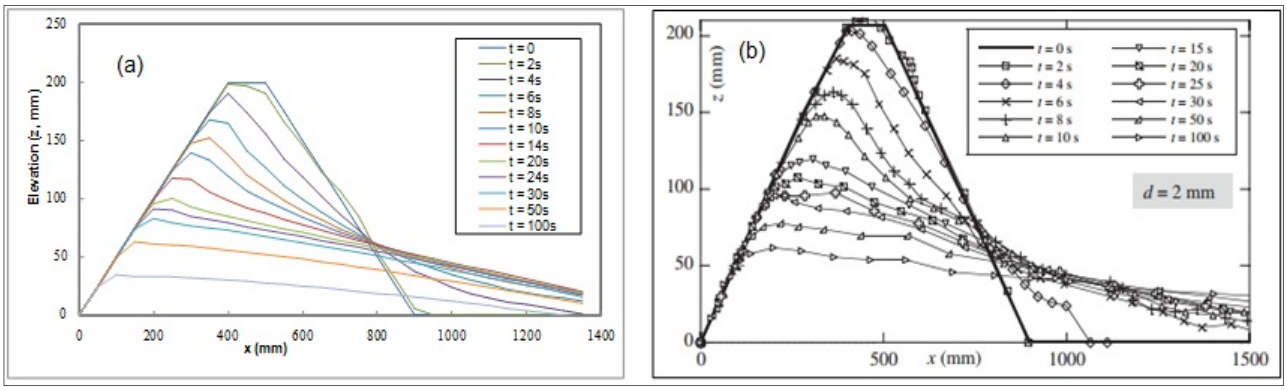

Figure 3. Comparison of breaching profiles between numerical model and experiment; (a) Numerical Model (b) Experimental result done by Schmocker and Hager, 2012.

5.2 Variations in flow conditions

The temporal evolution of the dam surface profiles over the entire channel length is illustrated in Figure 4 along with the free surface water levels at different times corresponding to t = 0s, 4s, 10s, 20s, 50s and 100s. The images are not exactly longitudinal sectional profiles, but visuals are captured from a slightly tilted three-dimensional angle as viewed from the top right corner of the domain. The continuous horizontal line represents the initial water level at the beginning of the numerical simulations and also serves as a reference line for comparison of the profiles in all the figures. The flow, which remains subcritical at upstream of the dam as the breach progresses, may be visually judged as becoming supercritical as it glides down over the downstream surface at t = 4s, from the occurrence of a hydraulic jump is noticeable at the extreme right end of the domain where the rapid flow meets the otherwise tranquil flow of the downstream and forms a hydraulic jump. With the downstream channel also getting eroded with time, the flow eventually appears to attain a uniform supercritical flow condition by bed adjustment.

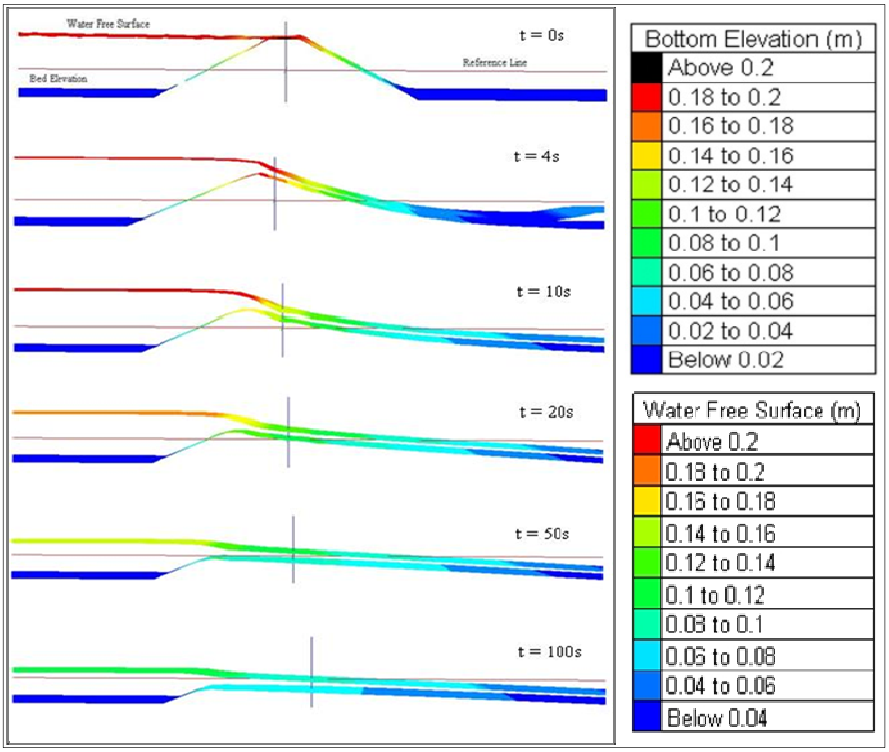

Figure 4. Elevated side view of dam domain from numerical model.

5.3 Dam-breach flood hydrograph

The flood hydrograph resulting from a breach of the dam is computed by TELEMAC-2D. This predicted hydrograph, similar to that resulting from a GLOF event at the downstream of moraine dam, is represented in Figure 5. It is noticed that the flood peak (0.08 m^3/s) is almost 33% higher than the continuous inflow rate (0.06 m^3/s). The estimation of this hydrograph is important for studying the propagation of the flood wave along the channel and in computing possible inundation and other damages in the event of a GLOF.

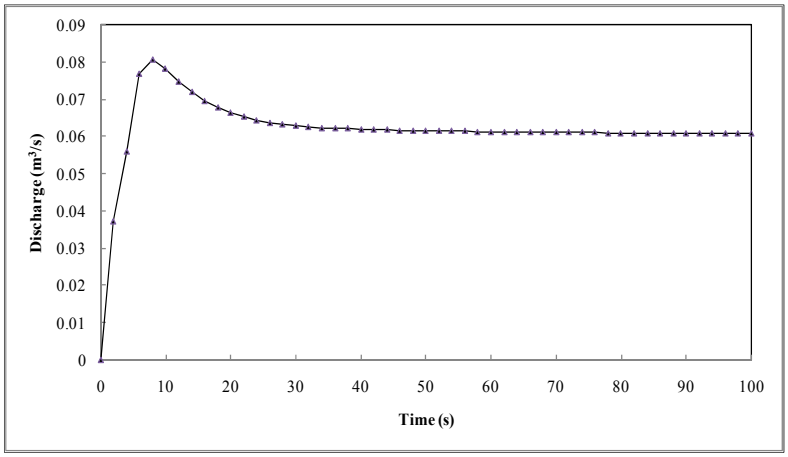

Figure 5. Breach Hydrograph from numerical simulation.

6 CONCLUSIONS

The current study reflects on a 2D numerical modelling approach in analyzing an erosion based moraine dam failure and predicting the outflow flood hydrograph due to breaching of the dam. Here, a moraine dam is considered as a trapezoidal embankment composed of non-cohesive sediments. The numerical model is assessed with given particle properties of sediment (mean diameter, density, porosity) as reported by a similar study on a physical model by Schmocker and Hager (2012). The numerical model was tested with the continuous steady inflow, as in the physical model, resulting in a falling water level behind the dam and generation of a flood on the downstream as the breaching of dam progressed after getting overtopped. The resulting dam erosion profiles are observed to be a good match with those reported from the laboratory experimental data. The major part of erosion occurs just after the initial overtopping and generates a flood peak, which is higher than the average steady inflow. The flood hydrograph generated is similar to that experienced with the breaching of a moraine dam. Though the present test demonstrates the failure of such a dam by overtopping, other failure models like the damage due to the passing of an impulse wave over the dam needs to be tested numerically, and matched with physical experiments. The numerical model too can be improved by considering cohesiveness of the sediments or investigating the piping failure of a moraine dam. However, the contribution of the current effort is the demonstration on the use of a numerical model in predicting the flood hydrograph that is similar to a GLOF generated with the breaching of a moraine dam. For simulating the failure of an actual moraine dam and predicting the resulting flood hydrograph, however, the surveyed bathymetry of the lake behind the dam and the actual profile of such a dam need to be taken into account.

ACKNOWLEDGEMENTS

The authors would like to specially thank Prof. W. Hager and Dr. L. Schmocker for their research and references on the dike breach at laboratory physical model extends.

REFERENCES

Awal, R., Nakagawa, H., Fujita, M., Kawaike, K., Baba, Y. & Zhang, H. (2010). *Experimental Study on Glacial Lake Outburst Floods Due to Waves Overtopping and Erosion of Moraine Dam*, Annals of Disaster Prevention Research Institute, Kyoto University. 53, 583-594.

Bajracharya, B., Shrestha, A.B. & Rajbhandari, L. (2007). Glacial Lake Outburst Floods in the Sagarmatha Region: Hazard Assessment Using GIS and Hydrodynamic Modelling. *Mountain Research and Development*, 27(4), 336-344.

Bajracharya, S.R., Mool, P.K. & Shrestha, B.R. (2008). *Global Climate Change and Melting of Himalayan Glaciers. Melting Glaciers and Rising Sea Levels: Impacts and Implications*. Icfai University Press, India. 28-46 pp.

Clague, J.J. & Evans, S.G. (2000). A review of Catastrophic Drainage of Moraine-Dammed Lakes in British Columbia. *Quaternary Science Reviews*, 19(17), 1763-1783.

Costa, J.E. & Schuster, R.L. (1988). The Formation and Failure of Natural Dams. *Geological Society of America Bulletin*, 100(7), 1054-1068.

Franca, M.J. & Almeida, A.B. (2004). A Computational Model of Rockfill Dam Breaching Caused by Overtopping (Rodab). *Journal of Hydraulic Research*, 42(2), 197-206.

Fread, D.L. (1991): *BREACH: An Erosion Model for Earthen Dam Failures*, U.S. National Weather Service, Office of Hydrology, Silver Spring, Maryland.

Mool, P.K., Wangda, D., Bajracharya, S.R., Kunzang, K., Gurung, D.R. & Joshi, S.P. (2001). *Inventory of Glaciers, Glacial Lakes and Glacial Lake Outburst Floods*, Bhutan Monitoring and Early Warning Systems, Hindu Kush-Himalayan Region: Bhutan.

NRC-CHE. (2010). *Reference Manual for Blue Kenue*, Canadian Hydraulic Centre National Research Council. 207 pp.

Richardson, S.D. & Reynolds, J.M. (2000). An Overview of Glacial Hazards in the Himalayas. *Quaternary International*, 65, 31-47.

Rivas, D.S., Somos-Valenzuela, M.A., Hodges, B.R. & McKinney, D.C. (2015). Predicting Outflow Induced by Moraine Failure in Glacial Lakes: The Lake Palcacocha Case from an Uncertainty Perspective. *Natural Hazards and Earth System Sciences*, 15(6), 1163-1179.

Rouse, H. (1961). *Fluid Mechanics/or Hydraulic Engineers.* Dover, New York, 422 pp.

Schmocker, L. & Hager, W.H. (2012). Plane Dike-Breach Due to Overtopping: Effects of Sediment, Dike Height and Discharge. *Journal of Hydraulic Research*, 50(6), 576-586.

SISYPHE. (2010). Sisyphe 6.0 User Manual. *EDF-R&D* <https//www.opentelemac.org>.

Takahashi, T. & Nakagawa, H. (1993). Flood and Debris Flow Hydrograph Due to Collapse of a Natural Dam by Overtopping. *Proceedings of Hydraulic Engineering*, 37, 699-704.

TELEMAC-2D. (2014). *TELEMAC-2D modelling system*: *TELEMAC-2D v7p0 User Manual, EDF-R&D* <https//www.opentelemac.org>.

Van Rijn, L.C. (1984). Sediment Transport, Part I: Bed Load Transport. *Journal of Hydraulic Engineering*, 110(10), 1431-1456.

Walder, J.S. & O'Connor, J.E. (1997). Methods for Predicting Peak Discharge of Floods Caused by Failure of Natural and Constructed Earthen Dams. *Water Resources Research*, 33(10), 2337-2348.

Westoby, M.J., Glasser, N.F., Brasington, J., Hambrey, M.J., Quincey, D.J. & Reynolds, J.M. (2014). Modelling outburst floods from moraine-dammed glacial lakes. *Earth-Science Reviews*, 134, 137-159.

Yusof, Z., Hargreaves, D. & Morvan, H. (2010). Development of A Porous Model to Characterise Erosion of a Breached Embankment. In *First European Congress of the IAHR,* Edinburgh, 4-6.

Zyserman, J.A. & Fredsøe, J. (1994). Data analysis of bed concentration of suspended sediment. *Journal of Hydraulic Engineering*, 120(9), 1021-1042.

LABORATORY EXPERIMENTS OF PULSED SUBAQEOUS SEDIMENT DENSITY FLOWS: INTERNAL STRATIFICATION AND LAYERING

MARIANGELA SFOUNI-GRIGORIADOU[(1)], CARMELO JUEZ[(2)], MARIO J. FRANCA[(3)] & BENOIT SPINEWINE[(4)]

[(1,4)] Fugro GeoConsulting, Brussels, Belgium,
m.sfouni@fugro.com
[(1,4)] Department of Civil Engineering, Université catholique de Louvain, Louvain-la-Neuve, Belgium,
[(2,3)] Laboratory of Hydraulic Constructions, École Polytechnique Fédérale de Lausanne, Lausanne, Switzerland

ABSTRACT

This paper reports on an experimental study which focuses on reproducing small scale sediment density flows in a laboratory flume. The observations are aimed at improving the parametrization of the relations that govern the transition between different phases of the flows. Dense mixtures of plastic sediment of variable grain size (thermoplastic polyurethane) and water were fed into the water-filled flume by gravity from a supply tank. Different grain-size and slope combinations were examined and the resulting velocity fields were obtained using UVP (Ultrasonic Velocity Profile) at various points along the channel. The flow was imaged through the transparent sidewall to track the velocity of the flow head for each test case. Image analysis also allowed a qualitative characterization of the vertical density stratification and water entrainment during runout. The runout distance and flow thickness are used to highlight the differences in the dynamic behavior of the flow for each test case. Data gathered from the experiments will be exploited in the further development of predictive numerical models for slide-induced debris flows transitioning to turbidity currents.

Keywords: Debris flow; density flow; mass movement; submarine landslide; turbidity current.

1 INTRODUCTION

Submarine debris flows and turbidity currents constitute a major geohazard as they are capable of transporting vast quantities of soil at significant velocities down channels and escarpments in deep-water environments. As subsea infrastructure continuously develops, a proper assessment of the risk of impact from these types of flows becomes increasingly important. The understanding of the internal processes governing the dynamics of these mass transport events, which are intrinsically transient and stratified, is critical.

The transition from a dense debris flow to a dilute turbidity current, as a result of downslope propagation and interaction with the sea floor and ambient sea water, can be divided into three main phases: (i) the initial failure and break-up of blocks and slumps, (ii) the transformation of the released material to a viscoplastic fluid and the development of a debris flow, and (iii) the generation of a turbidity current due to friction and mixing at the top interface of the debris flow producing a cloud of dilute suspended matter (Locat and Lee, 2005).

A predictive model of turbidity current generation from submarine debris flows was presented by Mohrig and Marr (2003). Their laboratory experiments confirmed that the influence of the dynamic stresses, developed at the very fronts of the parent debris flows, on the turbidity current development depends on their magnitude relative to an effective yield strength for the parent mixture of sediment and water (Mohrig and Marr, 2003).

Felix and Peakall (2006) worked on lock exchange experiments to study the generation of turbidity currents from debris flows. The transformation of debris flows occurs through multiple processes like erosion of the dense mass, breaking apart of the dense underflow, breaking of internal waves and turbulent mixing. Some of these processes take place simultaneously in a flow event, while others occur at different phases and positions. It was observed that a more efficient transformation to a turbidity current layer occurs for less-cohesive debris flows (Felix and Peakal, 2006).

Zakeri et al. (2010) studied the process in which a submarine debris flow and the overriding turbidity form the seabed deposits and how the deposits relate to the parent flow. In a series of flume experiments, slurries with different clay content were tested.

The experiments presented in the current work are focused on triggering dense subaqueous debris flows in a laboratory flume, and monitoring their propagation and associated degree of mixing and dilution. The effects of sediment size and bed slope on the propagation and the internal stratification of such flows are investigated. Two superposed layers are seen to coexist, a dense basal layer and a dilute top layer, which we interpret as a debris flow and a turbidity current, respectively. It is expected that the obtained dataset will provide a validation database for the development of a two layer depth-integrated mode of subaqueous landslides, currently in development.

The details of the experimental set-up are presented in section 2. Section 3 focuses on the instrumentation and processing of acquired images. Section 4 details the experimental procedure, and results are presented in section 5.

2 EXPERIMENTAL SET-UP

The experiments were conducted in a flume of 2.7 m long, 0.14 m wide and 0.21 m deep, with a variable bottom slope at the Hydraulic Constructions Laboratory of the École Polytechnique Fédérale de Lausanne (Figure 1). The glass-plastic flume can be tilted using adjustable supports at slopes ranging from 0% to 4.4%. The flume was initially filled with fresh water. Due to the water free surface, the maximum attainable water depth decreases in the upstream direction when the flume is tilted.

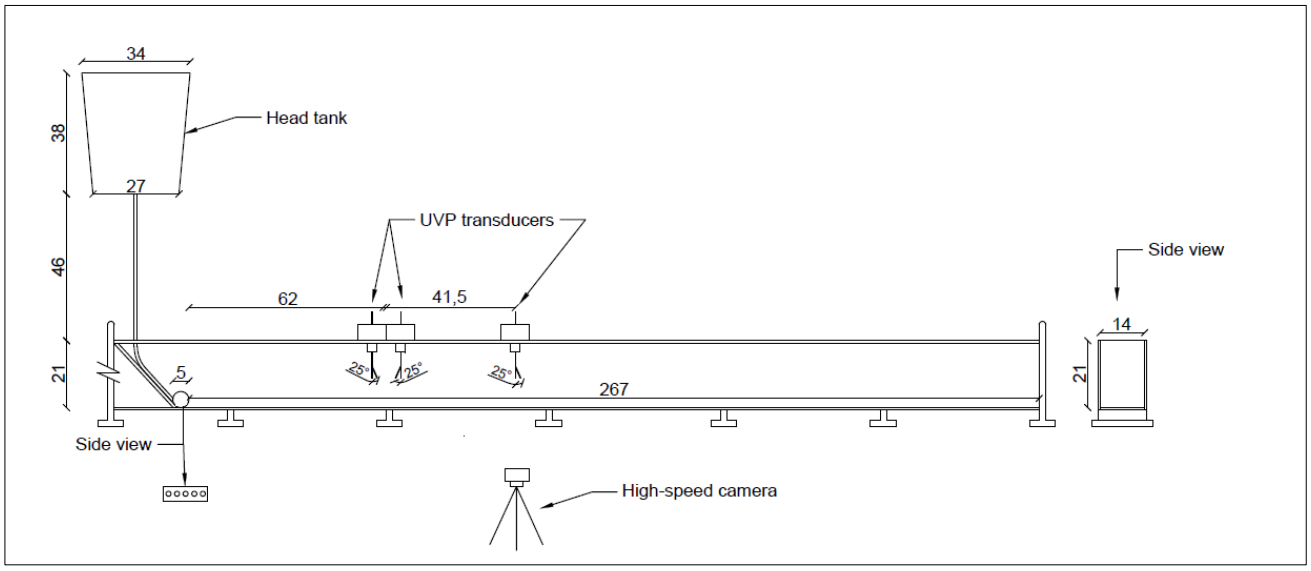

Figure 1. Sketch of the experimental set-up. All dimensions are in centimeters.

Mixtures of plastic sediments (thermoplastic polyurethane) and water were fed into the flume from an eight-litre head tank through a plastic tube ending in a perforated screen, to ensure uniform release of the material across the flume width. The sediment mass concentration in the head tank was set equal to 30% for most experiments. This percentage indicates a high density flow that could potentially reproduce the behavior of a debris flow. A few experiments were performed with a reduced initial sediment mass concentration equal to 8%.

Three different grades of sediment were used, with a median diameter (D_{50}) of 80 µm, 160 µm and 200 µm, respectively. For each sediment grain size, three different channel slopes were investigated. For each slope, an additional experiment was performed with a mixture of equal parts of sediments with D_{50} of 80 µm and 200 µm (Table 1).

In overall, the combinations of channel slope, sediment mixture, and initial sediment concentration resulted in a total of 15 individual experiments, as detailed in Table 2.

Table 1. Characteristics of the sediments.

Sediment name	D_{50} (µm)	Density (g/cm^3)
S	80	1.16
M	160	1.16
L	200	1.16

Table 2. List of experiments.

Experiment name	Sediment Type	Slope (%)	Mass Concentration (%)
S1	S	0	30
M1	M	0	30
L1	L	0	30
MIX1	50%S + 50%L	0	30
TC1	M	0	8
S2	S	2.2	30
M2	M	2.2	30
L2	L	2.2	30
MIX2	50%S + 50%L	2.2	30
TC2	M	2.2	8
S3	S	4.4	30
M3	M	4.4	30
L3	L	4.4	30
MIX3	50%S + 50%L	4.4	30
TC3	M	4.4	8

3 INSTRUMENTATION

3.1 Velocity measurement

Velocity profiles were measured using an Ultrasonic Doppler Velocity Profiler (Met-Flow, UVP). Three transducers have been immersed near to the water surface at an angle of 25° to the normal of the flume bottom. The position of the transducers is illustrated in Figure 1. The basic frequency of the transducers for the emitting ultrasonic pulse was 4 MHz. The velocity resolution of UVP DUO was set at 0.764 mm/s and its spatial resolution was set at 0.74 mm. A fixed number of 128 points were measured in each profile and the sampling period was equal to 0.161 s. The measurements gave the projected vertical profiles in the middle of the width of the flume. Each of the three UVPs was interrogated in sequence with a multiplexer throughout the duration of the experiment, and the time interval between successive measurements at a given transducer is in the order of 2.3 s.

3.2 Flow imaging and image processing

The flow was observed through the transparent side wall of the flume. A SMX-160 camera with acquisition frequency of 10 frames per second was used to obtain gray scale digital images with a resolution of 2208 by 400 pixels. The position of the camera is illustrated in Figure 1. On average 350 frames were taken for each experiment.

Four steps of image processing are applied to the raw images. First, the images are ortho-rectified using a number of reference points with known coordinates to correct for image distortion, and the resulting ortho-rectified image is resampled at a resolution of one pixel per mm, with the x-axis being defined as streamwise, tilted along-slope direction, and the y-axis orthogonal upwards. Second, a correction is applied to account for uneven illumination of the flow from the single light source used. A bell-shaped brightness correction factor is applied, which is calibrated on the basis of the observed illumination of a reference plate along the bottom of the flume sidewall. Third, the image background is removed by subtracting the initial image, prior to flow initiation, from the entire image sequence. Due to the bright color of the plastic sediment used, the current appears on the resulting image sequence as variable shades of grey on a perfectly black background, and the local brightness of the flow is, to a good approximation, a direct proxy for the local sediment concentration at that location. Lastly, for better visualization, the grey image is transformed into a color image with a jet color map featuring variations of blue-green-yellow-red shades that highlight regions of dense and dilute flow. The color map is altered so that the image regions indiscernible of the image background (with a pixel value of zero) are painted white for better visualization of the limits of the propagating current.

4 EXPERIMENTAL PROCEDURE

All the mixtures were prepared using a mixer device in order to ensure the uniformity of the mixture. The flume was filled with fresh water. The flume water and tank mixtures had approximately the same temperature, therefore temperature effects are considered negligible in the flow dynamics. When the mixing procedure was completed, the resulting mixture was immediately released in the head tank to avoid any settling of the sediments, and discharged into the flume under gravity. The gradual lowering of the mixture level in the head tank was tracked with another camera, and was roughly constant for all experiments with a total emptying duration of ~25 s, which corresponds to a feeding discharge of ~1/3 L/s. The release of the mixture was synchronized with the start of the UVP measurements. Simultaneously, the recording with the digital camera was triggered. After each experiment, the flume was drained out and refilled with fresh water prior to the next experiment.

5 RESULTS

5.1 General down-channel evolution

Preliminary results are presented in this paper for the configuration with a bed slope of 4.4%, and an initial mass concentration of sediment equal to 30% and composed solely of the larger sediment size of 200 μm. Analysis for the other configurations is ongoing and will be reported at a later stage.

Figure 2 shows snapshots of the current evolution at selected instants after release. As discussed in section 3.2, pixel values on the processed images are a good proxy for local sediment concentration in the current; however, in the absence of a robust calibration, the correlation cannot be precisely constrained and therefore the pixel brightness is presented in digital values rather than sediment concentration in percent. Nevertheless, what appears in shades of red color on the processed images is considered as a dense flow, while shades of yellow, green, cyan and blue correspond to gradually more dilute sediment suspensions.

The sequence of images on Figure 2 reveals the general down-channel propagation of the current, the preservation of a relatively dense and thick current head followed by a region where the dense basal layer is thinner, and the distinctive pattern of billows that govern the dilution of the top layer of the current and the formation of a turbidity cloud.

The current head is seen to preserve a density in the order of that in the most upstream section of the current. Mixing with the ambient fluid is initiated at the top of the head region, but the resulting turbidity is simultaneously slowed down and therefore trails behind the front, while additional dense current is fed into the frontal head from the basal layer, allowing it to remain dense. The sediment concentration in the front and dense basal layer is however not expected to be as high as 30% as in the head tank, but more probably in the range of 10 to 15%. This is due to immediate turbulent mixing at the exit of the perforated tube ending. A more robust calibration of the brightness-to-concentration correlation is planned for future experiments to confirm this.

Behind the front, the generation of lower density turbidity is quite apparent on the images, and is a result of large-scale mixing processes with the ambient water.

5.2 Frontal velocity

Visualization of the current head on the ortho-rectified images allows tracking the front position and velocity in time. These are presented in Figure 3, with readings of the front position on the left vertical axis and front velocity on the right vertical axis. The current is propagating with linearly increasing velocity for a duration of 30 s while for the last 5 s it has a constant velocity until the flow reaches the end of the flume. The maximum velocity is approximately 72 mm/s.

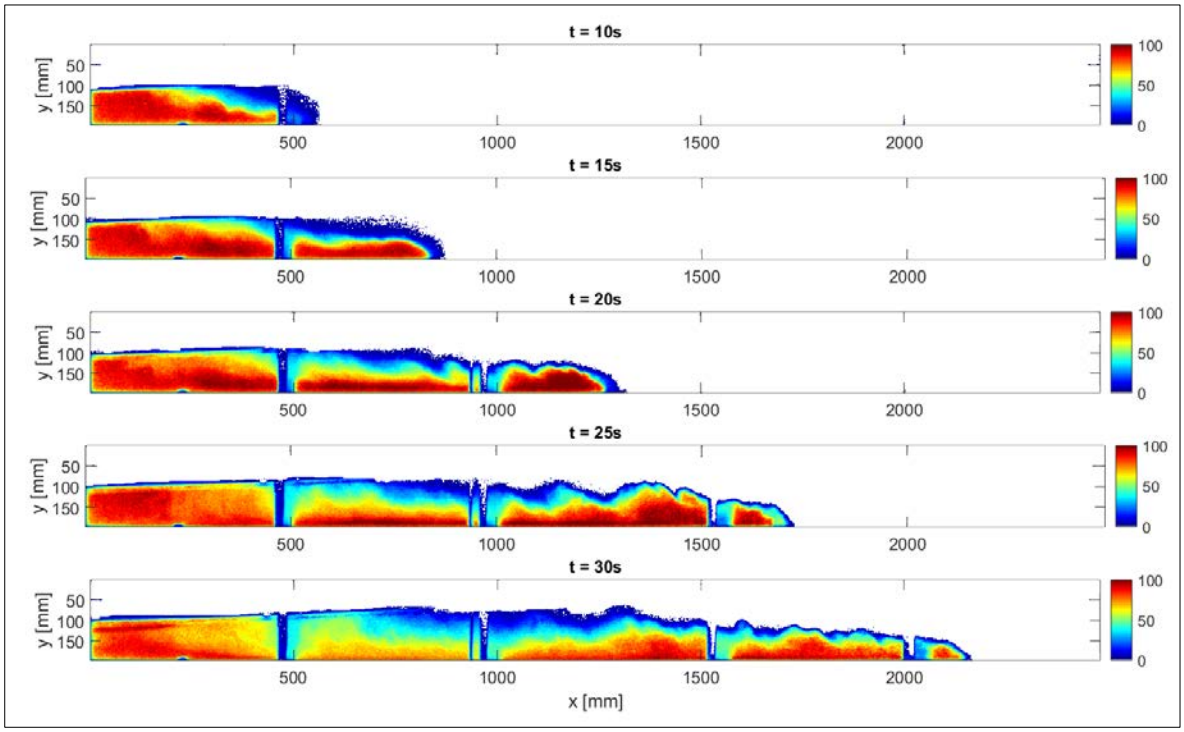

Figure 2. Snapshots of the flow for the test with a slope of 4.4% and 200μm grain size. Dashed lines define regions where the existence of shadows do not allow proper illumination of the flow.

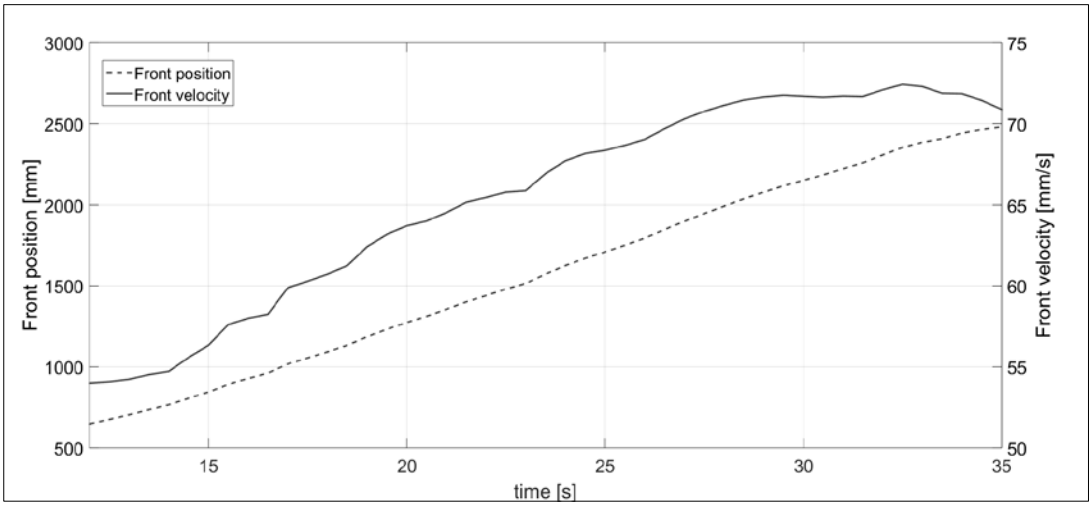

Figure 3. Time evolution of the front velocity (solid line, right axis) and position (dashed line, left axis).

5.3 Velocity and density stratification

The aim of this work was to investigate the internal stratification and layering of dense subaqueous sediment flows, by simultaneously measuring velocity and density profiles. This appears possible for the present experiments by combining the UVP velocity profiles and the qualitative density information encapsulated in the brightness of the digital images, interrogated at the same position than the UVP probes.

In Figure 4 to Figure 7, the downstream velocity and the brightness profiles are presented for selected time instants at the location of the third transducer (x = 910mm).

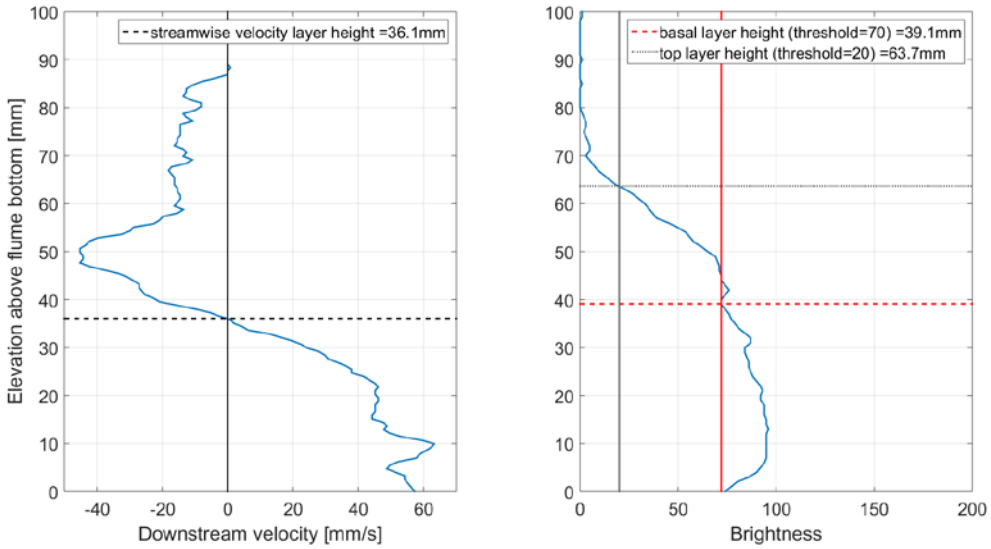

Figure 4. Downstream velocity and brightness profiles at position x = 910 mm and time t = 18.3 s.

On all velocity profiles (left panels), the height corresponding to a zero streamwise velocity is highlighted by a dashed line. While the bottom layer propagates down the channel, the top portion of the current propagates in the opposite direction. This is a direct result of the fact that the current is propagating in an enclosed basin, and any current in one direction must be balanced by an opposite current in the other direction, with only minor deviations possible that result from the generation of mild free surface waves at the flume free surface. Due to the limited depth available in the flume, the backward current incorporates some of the turbidity generated at the top of the density current.

The density/brightness profiles shown on the right panels of the figures reveal a pattern of upward stratification, with the brightness decreasing to zero at the top of the current. A qualitative partition of the current in a dense basal current and a dilute top current can be made by adopting a brightness threshold of 70, which corresponds to orange color on the flow images of Figure 2 and is slightly smaller than the maximum observed brightness. On Figure 4 to Figure 7, it is observed that this partition based on density corresponds quite well with the partition between down-channel and reverse currents based on the velocity profiles.

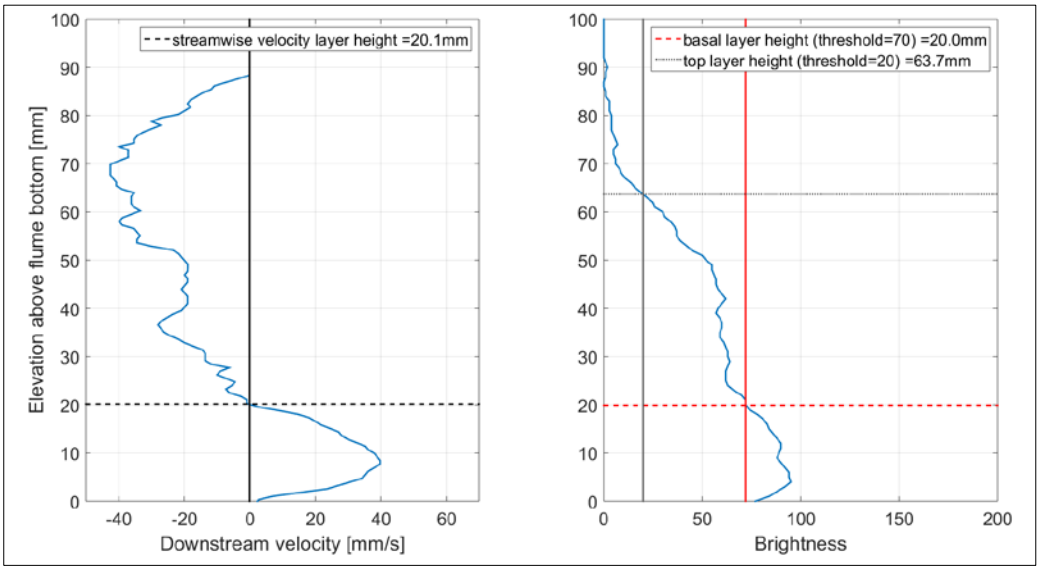

Figure 5. Downstream velocity and brightness profiles at position x = 910 mm and time t = 20.6 s.

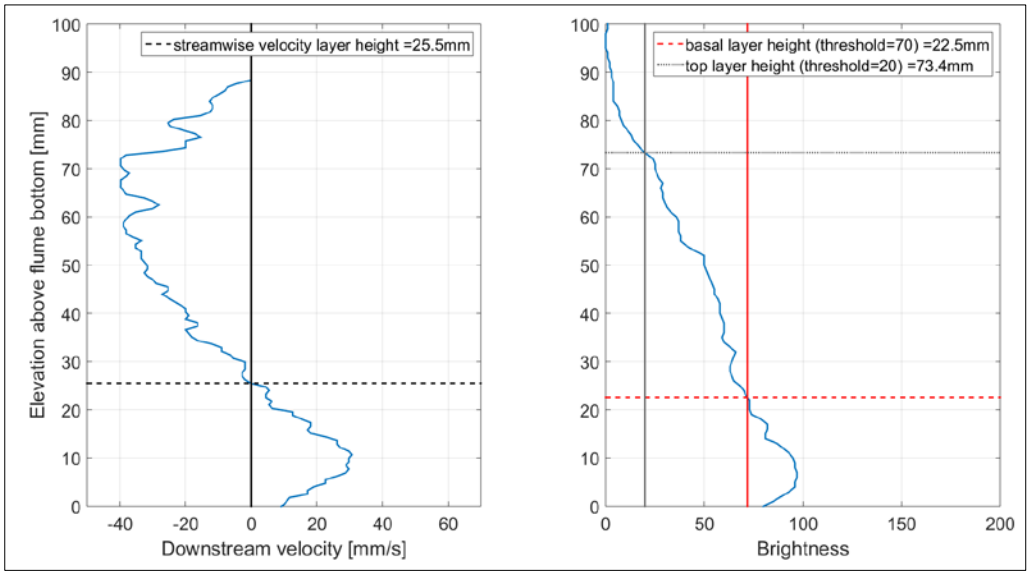

Figure 6. Downstream velocity and brightness profiles at position x = 910 mm and time t = 22.9 s.

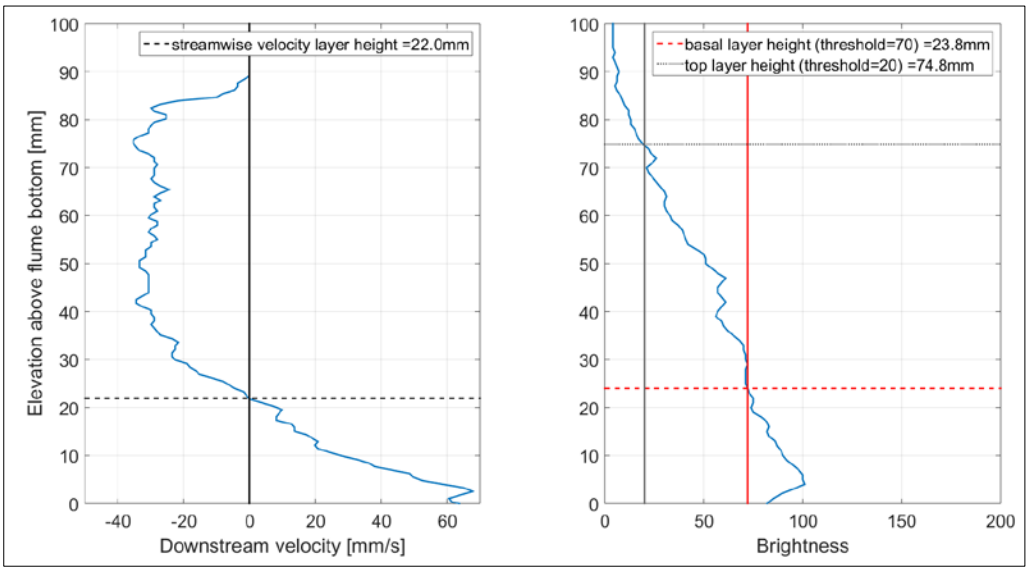

Figure 7. Downstream velocity and brightness profiles at position x = 910 mm and time t = 25.2 s.

This suggests indeed that the flow can be abstracted into two distinct layers: a basal layer that remains dense and rapid and dictates the down-channel propagation of the density current, and a top layer, which is much more dilute as a result of mixing, and propagates at a much slower velocity – which in the present case may result in backward velocity due to the lock-exchange configuration and the finite water depth in the flume.

Flow brightness profiles for different time instances at the same location x = 910 mm are given in Figure 8. At t = 15 s, the flow has not reached this location yet as it is evidenced by the near zero values of brightness. The very front of the flow passes from the location of the transducer at t = 16 s and is characterized by the low brightness values. Immediately after, the denser part of the flow head passes, with a thickness of circa 40 mm having a brightness above the adopted threshold of 70. From time t = 18.3 s to 25.2 s, the thickness of the dense layer of the flow is decreasing, while the total flow thickness is increasing due to the growth of the turbidity cloud. Passed t = 30 s, the dense layer has vanished but the total flow thickness surpasses 120 mm.

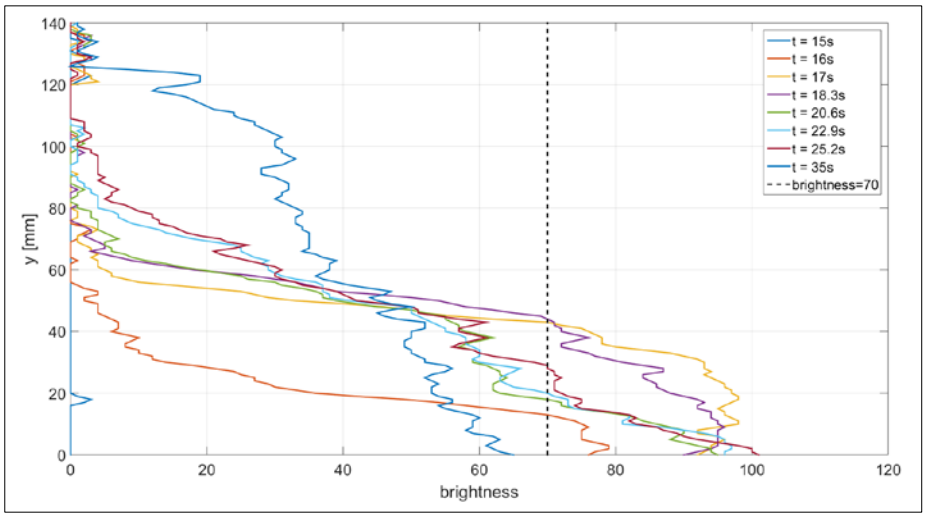

Figure 8. Brightness profiles for different time instances at position x = 910 mm.

A second threshold can be considered to investigate stratification, which distinguishes the dilute turbidity cloud from the background water. A brightness threshold of 20 is adopted for that purpose. The associated levels are also shown on the right panels of Figure 4 to Figure 7. By applying the same methodology to all images, on the top panel of Figure 9 the time evolution of the thickness of the dense and basal layers, with respective thresholds of 20 and 70, is presented, along with intermediate contours at multiples of 10. The lower panel of Figure 9 shows the fraction of the flow thickness that is occupied by the dense basal flow. The dense flow initially occupies roughly 90% of the flow thickness, while toward the end of the experiment it vanishes to zero as the dilute turbidity current thickens and the dense flow stops.

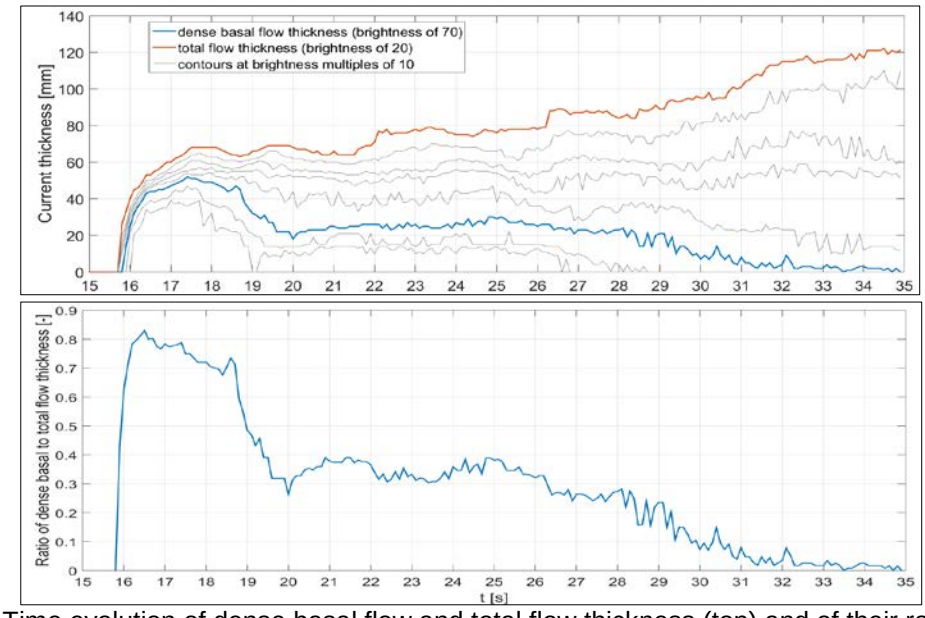

Figure 9. Time evolution of dense basal flow and total flow thickness (top) and of their ratio (bottom).

5.4 Space-time visualization of depth-integrated quantities

The density flows investigated in the present experiments may be considered as shallow flows, in the sense that their development in the streamwise direction is more than an order of magnitude larger than their thickness. It is therefore of interest to derive depth-integrated quantities. Figure 10 and Figure 11 show the space-time evolution of the flow thickness and depth-averaged flow brightness, respectively. The flow thickness is here defined as the portion of the current whose brightness is larger than the previously set threshold of 20 distinguishing the turbidity cloud from the surrounding clear water. In Figure 10, the highest density is observed near to the front of the flow. As the propagation continues, mixing starts to develop immediately behind the front and the thick mixing billows recirculate backwards, as can be seen from the curved trajectories of the regions of thick flow in Figure 10. The brightness is then averaged over the current thickness to yield the values reported in Figure 11. In that figure, the dense region of the current head and the "ejection" events associated with the formation of mixing billows are also clearly identified.

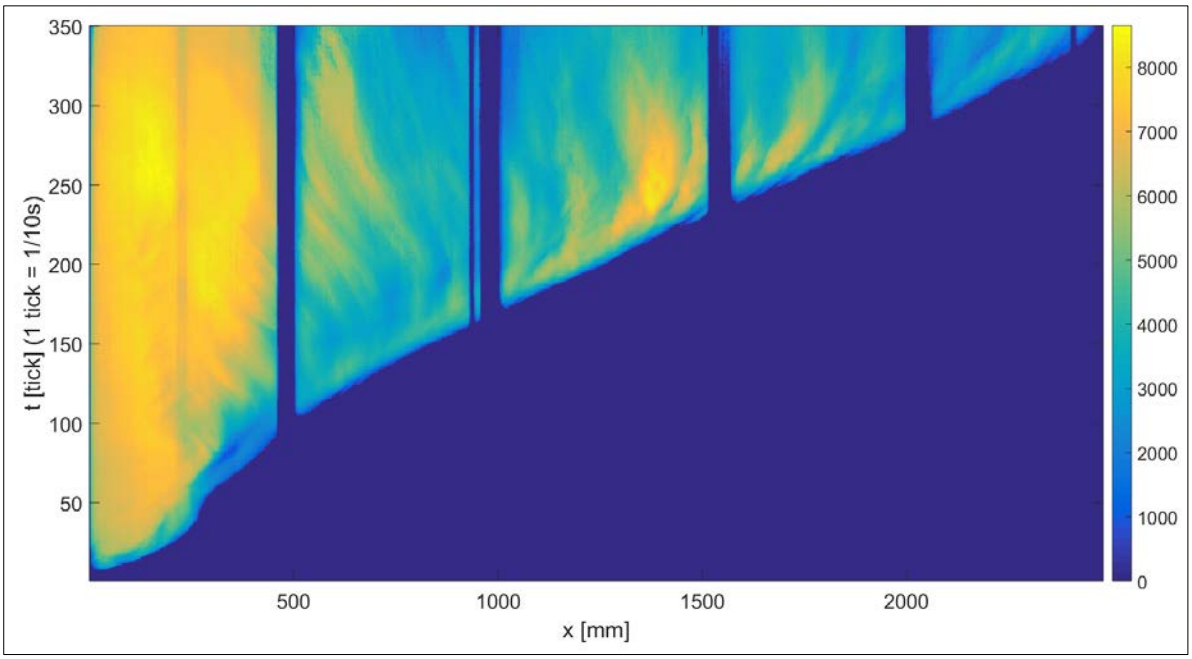

Figure 10. Flow thickness (defined as all pixels brighter than a set threshold of 20).

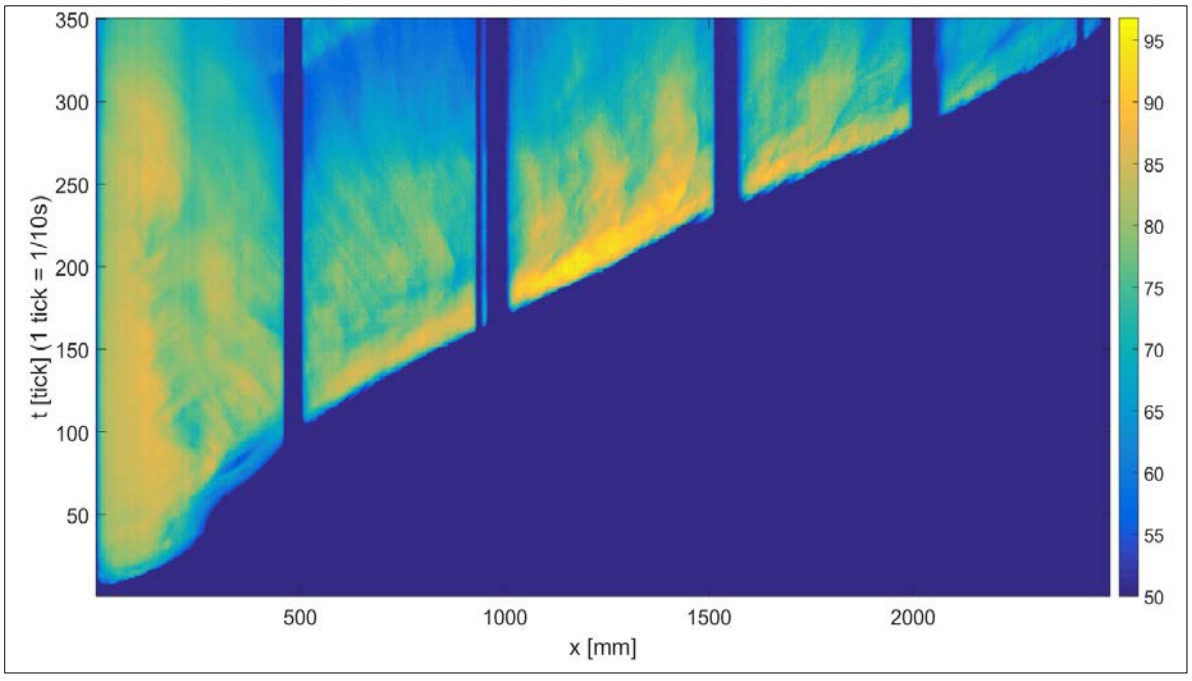

Figure 11. Depth-averaged flow brightness (averaged over flow thickness).

6 CONCLUSIONS

In this study, the behavior of subaqueous sediment density flows was investigated. Plastic sediment-water mixtures of different grain sizes were tested in a series of flume experiments with varying bed slopes. Velocity profiles were acquired at selected positions using UVP probes. A camera captured the flow with a frequency of 10 frames per second through the transparent sidewall. The images were processed to correct for image distortion and uneven illumination, to allow tracking of the current front velocity, thickness, and brightness which is a qualitative for sediment concentration. Preliminary results, restrained to the case with a bed slope of 4.4%, sediment's median grain size of 200 μm and initial sediment mass concentration of 30 %, are presented in this paper.

Analyses of the image sequence allows to highlight the partition of the flow into a basal layer, which remains dense throughout the current propagation, and a dilute turbidity cloud resulting from mixing with ambient water at the rear of the current head. The two layers were defined using the image brightness as an indication of concentration. The brightness thresholds used for the definition of each layer, were obtained after a correlation of the brightness profiles with the velocity profiles acquired with the UVPs. The height of the bottom layer as defined by the brightness threshold coincided well with the height of the flow region characterized by streamwise velocity, indicating rapid propagation of the dense basal layer and much slower, or even reverse, velocity for the dilute turbidity cloud.

The space-time evolution of depth-integrated quantities reveals that the front of the flow remains dense throughout the experiment, suggesting that near to the front, the sediment lost to turbidity trailing behind at the top of the current is balanced by additional dense current fed from the basal layer. The formation of mixing billows results in "ejection" events with a distinctive curved path on the space-time plots.

To our knowledge, these experiments are quite unique in the sense that they allow simultaneous measurements of velocity and density within the density currents, and allow investigating their internal stratification. Performing a quantitative analysis on the entire set of test cases is ongoing, and will hopefully lead to a characterization of the dynamic behavior that governs the transition between different phases of subaqueous sediment density flows. Parametrization of the vertical stratification and water entrainment relations will be important for predictive numerical models for slide-induced debris flows transitioning to turbidity currents.

ACKNOWLEDGEMENTS

This work was funded by the ITN-Programme (Marie Curie Actions) of the European Union's 36 Seventh Framework Programme FP7-PEOPLE-2013-ITN under REA grant agreement n° 607394-37 SEDITRANS.

REFERENCES

Felix, M. & Peakall, J. (2006). Transformation of Debris Flows into Turbidity Currents: Mechanisms Inferred From Laboratory Experiments*. Sedimentology*, 53,107-123.

Locat J. & Lee H.J. (2005). *Subaqueous Debris Flows Chapter 9. Debris-flows Hazards and Related Phenomena,* Springer*,* 203-245.

Mohrig D. & Marr J.G. (2003). Constraining the Efficiency of Turbidity Current Generation from Submarine Debris Flows and Slides Using Laboratory Experiments*. Marine and Petroleum Geology,* 20(6), 883-899.

Zakeri A., Si G., Marr J.G. & Høeg, K. (2010). Experimental Investigation of Subaqueous Clay-Rich Debris Flows, Turbidity Generation and Sediment Deposition*. Submarine Mass Movements and Their Consequences* of the series *Advances in Natural and Technological Hazards Research*. D.C. Mosher (Eds.), Springer Science, 28, 105-115.

Proceedings of the 37th IAHR World Congress
August 13 – 18, 2017, Kuala Lumpur, Malaysia

ASSESSMENT OF EFFICIENCY AND ENVIRONMENTAL IMPACT OF SEDIMENT FLUSHING FROM WLINGI AND LODOYO CASCADE RESERVOIRS, INDONESIA

FAHMI HIDAYAT[1], PITOJO TRI JUWONO[2], AGUS SUHARYANTO[3], ALWAFI PUJIRAHARJO[4], DJOKO LEGONO[5], DIAN SISINGGIH[6] & FIRMAN SARIFUDIN EFFENDI[7]

[1,7]Jasa Tirta I Public Corporation, Malang, Indonesia
hidayat.f@jasatirta1.net, firmanne@jasatirta1.net
[2,6,7]Water Resources Engineering Department, Brawijaya University, Malang, Indonesia
pitojo_tj@ub.ac.id, singgih@ub.ac.id
[1,3,4] Civil Engineering Department, Brawijaya University, Malang, Indonesia
agus.s@ub.ac.id, alwafi@ub.ac.id
[5]Civil and Environmental Engineering Department, Gadjah Mada University, Yogyakarta, Indonesia
djokolegono@ugm.ac.id

ABSTRACT

This paper addresses the sedimentation issues in Wlingi and Lodoyo reservoirs, in the Brantas River basin, Indonesia, and the efficient and environmentally sediment flushing operations in both reservoirs which are designed to achieve their long-term use. The sedimentation problem in Wlingi and Lodoyo reservoirs, is very severe due to sediment input from the recurrent eruptions of Mt. Kelud, one of the most active volcanoes in Indonesia. The latest eruption of Mt. Kelud occurred on 13 February 2014. After the eruption, the effective storage capacity of Wlingi and Lodoyo reservoirs decreased dramatically to 1.01 MCM and 1.33 MCM, respectively. To cope with the sedimentation problem, diverse sediment management strategies have been applied in these reservoirs and their catchments since the 1990 eruption of Mt. Kelud. One of the strategies is to recover the reservoirs' storage capacity by hydraulic flushing to remove accumulated sediment deposits from the reservoirs. Sediment flushing operation in Wlingi and Lodoyo reservoirs is a paradox. It is expected to remove accumulated sediment as much as possible from both reservoirs by consuming as little as possible of water in order to have a high flushing efficiency. On the other side, high efficiency flushing operation will cause adverse environmental impacts in the downstream water quality. Based on the observations done during sediment flushing operations, the impacts on water quality and aquatic organisms are considered to be significant for several days. The sediment flushing in Wlingi and Lodoyo reservoirs caused extremely high concentration of suspended solids in the downstream of both reservoirs.

Keywords: Reservoir sedimentation; sediment flushing; efficiency; environmentally friendly; Wlingi and Lodoyo reservoirs.

1 INTRODUCTION

Annually 0.5-1% of global storage volume is estimated to be lost due to sedimentation (Basson, 2009), figures that have been persisted since the World Bank report by Mahmood (1987). This means that without further measures, one quarter of all dams in the world will lose their storage to sedimentation in the next 25 to 50 years (WCD, 2000). Strategies for reservoir sedimentation management may be broadly classified as follows: (1) methods to reduce sediment inflow from upstream, (2) methods to pass sediment through or around the impoundment to minimize sediment trapping, and (3) methods to recover, increase, or reallocate storage or to modify intake or other structures, after sediment has been deposited (Morris, 2014). Among sediment management alternatives, sediment flushing has been successfully implemented in many dams globally (Lai & Shen, 1996; Sumi, 2005; Kondolf et al., 2014).

Flushing is a sediment removal technique where deposited sediment is scoured from the reservoir, by increasing the flow velocity, and then transported through low level outlets or spillway. Flushing can be operated in two ways: by lowering the water level or without lowering the water level, called pressure flushing and empty (free-flow) flushing, respectively. Pressure flushing is to release water through the bottom outlets by keeping the reservoir water level high. On the other hand, empty (free-flow) flushing is releasing water by emptying the reservoir and also to route inflowing water from upstream by providing riverine condition (Tigrek & Aras, 2012). Efficiency of sediment flushing through reservoir, calculated as the ratio between the volume of flushed sediment and the corresponding volume of water employed in the sediment flushing operation including water for dilution purpose, is very important to determine the feasibility of flushing operations.

However, the flushing of large amount of sediment from reservoirs can significantly impact downstream water quality and riverine ecosystems (Liu et al., 2004; Schleiss et al., 2016; Quadroni et al., 2016). In this paper, we present sedimentation problem in Wlingi and Lodoyo reservoirs due to sediment inflow from the eruptions of Mt. Kelud, the efficiency of flushing to remove sediment from both reservoirs and the impact of

flushing to the downstream water quality to study the paradox of sediment flushing since sediment flushing operation can be effective to remove sediment from reservoir, but will cause adverse environmental impacts.

2 MATERIALS AND METHODS

2.1 Study area

The study was carried out in Wlingi and Lodoyo cascade reservoirs. Wlingi Dam, with a catchment area of 2,890 km^2, is located on the southern skirts of Mt. Kelud in the upstream reach of the Brantas River basin, approximately 30 km downstream of Sutami Dam (Figure 1). Wlingi Dam was completed in 1979 for the purpose of peak demand hydropower generation (54 MW), irrigation water supply (12,687 ha irrigation area), and flood control. Lodoyo Barrage is located 7.9 km downstream of Wlingi Dam. Construction of Lodoyo Barrage, the second stage of the Wlingi Raya Project, started in 1978 and was completed in 1980. The function of Lodoyo Barrage is for hydropower generation (4.7 MW) and flood control. Wlingi and Lodoyo are very small reservoirs with capacity to inflow (C:I) ratios of about 0.007 and 0.001, respectively. The original gross storage volume of Wlingi reservoir was 24.00 MCM and the effective storage volume was 5.20 MCM between the high water level (HWL) of 163.50 m and the low water level (LWL) of 162.00 m. The original gross storage volume of Lodoyo reservoir was 5.20 MCM and the effective storage volume was 5.00 MCM between the HWL of 136.00 m and the LWL of 125.50 m.

Mt. Kelud is a composite stratovolcano built by the accumulation of numerous lava flows, pyroclastic flows, pyroclastic surges, and lahar deposits (Thouret et al., 1998). Mt. Kelud has erupted more than 30 times since 1000AD, and these eruptions include very large eruption of VEI 5 (Global Volcanism Program, 2014). In the recent past, eruptions occurred in 1901, 1919, 1951, 1966, 1990, 2007 and 2014 (Hidayat et al., 2017). These eruptions were generally similar, characterized by very short durations and a low volume of eruptive products (100-200 MCM). Explosive activity typically started with a phreatomagmatic outburst followed by a short plinian eruption with convective columns reaching an altitude of more than 10 km. These eruptions produced devastating lahars, pyroclastic surges and flows as well as ash fall deposits.

The most recent eruption occurred in February 2014. The eruption sent an ash plume to 17,000 m which triggered ash and volcanic debris fall as far as 350 km away (Global Volcanism Program, 2014). This eruption caused ash fall to the northeast, northwest and west of the volcano and produced about 150 MCM of volcanic material. A proportion of the large volumes of volcanic materials produced by the eruptions of Mt. Kelud is mobilised by flood waters and transported from the major tributaries to the Brantas River, i.e. the Putih, Jari and Lekso Rivers, which drain the southern slopes of Mt. Kelud. The sediments are ultimately trapped by Wlingi and Lodoyo Dams, and severe sedimentation take place in the reservoirs.

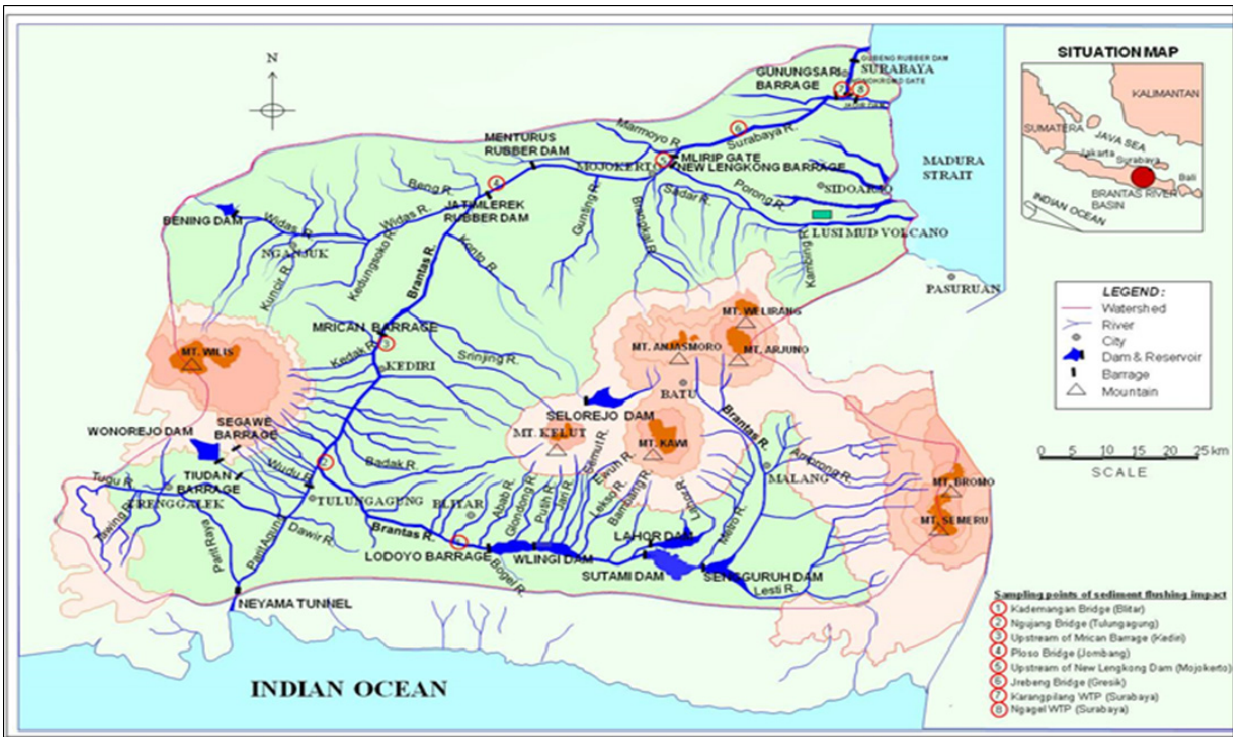

Figure 1. Location of sampling points of sediment flushing impact during sediment flushing operations in Wlingi and Lodoyo reservoirs.

2.2 Methods

2.2.1 Assessment of reservoir sedimentation

Assessments of sedimentation in Wlingi and Lodoyo reservoirs were conducted at three different periods of Mt. Kelud's eruptions: (1) before the 1990 eruption, (2) after the 1990 eruption, and (3) after the 2014 eruption. The sedimentation rates in both reservoirs were estimated from published and unpublished data by comparison of periodic reservoir capacity surveys performed by the range method. This method uses a series of permanent ranges or cross-section lines across the reservoirs which are resurveyed at intervals and used to compute the intersurvey volume change in each reach by geometric formulas. The data before 2015 were obtained from Jasa Tirta I Public Corporation (PJT-I), the river basin management organization of the Brantas, Bengawan Solo, Jratunseluna, Serayu Bogowonto and Toba Asahan River basins in Indonesia, which has responsibility for operation and maintenance of Wlingi dam and Lodoyo barrage. The May 2015 reservoir capacities and the reservoir capacities before after the sediment flushing operation in 2016 were obtained from bathymetric surveys by this study using automated surveying techniques which are applicable to range surveys in order to eliminate errors due to displacement of range lines during data collection. Reservoir volume was calculated using the Average End-area Method (Morris & Fan, 1997):

$$Volume = \frac{L(E_1 + E_2)}{2} \quad [1]$$

where L = length between ranges (m), and E_1 and E_2 are the cross-sectional end areas (m^2) of the ranges bounding the downstream and upstream limits of the reach.

2.2.2 Assessment of sediment flushing efficiency

The efficiency of the sediment flushing process can be expressed in different ways. Several studies on flushing efficiency have been made (Mahmood, 1987, Atkinson, 1996, Brandt, 2000, Lai & Shen, 1996, Morris & Fan, 1997). The sediment flushing efficiency in cascade reservoirs is defined as a ratio of total flushed sediment volume (V_s) from the reservoirs to total consumed water during flushing (V_w). The volume of water consumption during sediment flushing is calculated from the reservoir drawdown period until the end of flushing period.

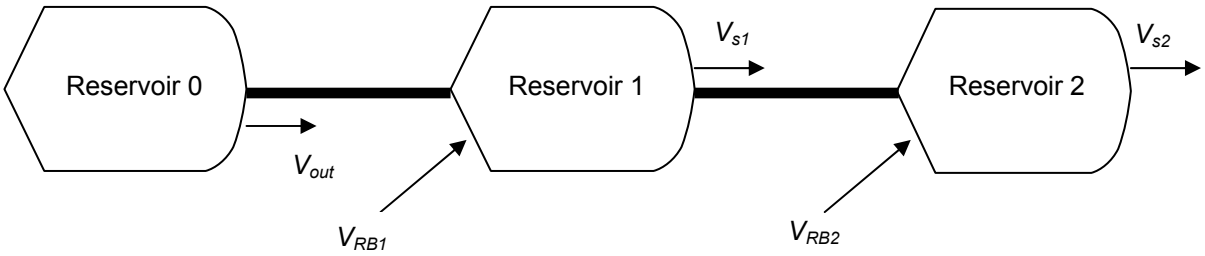

Figure 2. Ilustration of sediment flushing from cascade reservoirs.

In this study, the sediment flushing efficiency of Wlingi and Lodoyo cascade reservoirs was calculated using formula below (Hidayat et al., 2016).

$$Eff = \frac{Vs}{Vw} = \frac{Vs_1 + Vs_2}{V_{out} + V_{RB1} + V_{RB2}} \quad [2]$$

$$Eff = \frac{\left(V_{1after} - V_{1before}\right) + \left(V_{2after} - V_{2before}\right)}{V_{out} + V_{RB1} + V_{RB2}} \quad [3]$$

where E_{ff} is sediment flushing efficiency, V_s is flushed sediment volume (m^3), V_w is consumed water during flushing (m^3), V_{out} is outflow volume from upstream reservoir (m^3), V_{RB1} is inflow volume of reservoir 1 from its remaining basin (m^3), V_{RB2} is inflow volume of reservoir 2 from its remaining basin (m^3), $V_{1before}$ is volume of reservoir 1 before flushing (m^3), V_{1after} is volume of reservoir 1 after flushing (m^3), $V_{2before}$ is volume of reservoir 2 before flushing (m^3), and V_{2after} is volume of reservoir 2 after flushing (m^3). In this research study, Sutami reservoir, Wlingi reservoir and Lodoyo reservoir represent the reservoir 0, reservoir 1 and reservoir 2, respectively (Figure 2). The data of reservoirs' volume before and after flushing operations, and outflow discharge data were also obtained from PJT-I.

2.2.3 Assessment of sediment flushing impact to downstream environment

To understand the adverse environmental impacts of sediment flushing in Wlingi and Lodoyo reservoirs on the downstream reaches, two investigations were carried out by PJT-I during flushing operations in 2009 and 2016 to monitor water quality parameters i.e. dissolved oxygen (DO), biochemical oxygen demand (BOD), chemical oxygen demand (COD), Total Suspended Solids (TSS), Total Phosphate (T-P) and nitrate. The investigations were carried out at eight sampling sites i.e. Kademangan Bridge in Blitar, Ngujang Bridge in Tulungagung, Mrican Barrage in Kediri, Ploso Bridge in Jombang, Lengkong Barrage in Mojokerto, Jebreng Bridge in Gresik, Karang Pilang Water Treatment Plant (WTP), and Ngagel WTP in Surabaya. The location of sampling sites can be seen in Figure 1. The water sampling was carried out following the Indonesian National Standard: SNI 06-2412-1991, using appropriate sampling apparatus to meet the stipulated requirements. The water quality tests were conducted in the Water Quality Laboratories of PJT-I in Malang and Mojokerto.

3 RESULTS AND DISCUSSION

3.1 Sedimentation in Wlingi and Lodoyo reservoirs

The sedimentation in Wlingi and Lodoyo reservoirs is mainly caused by sediment inflow from the areas most affected by ejecta from eruptions of Mt. Kelud, one of the most active volcanoes in Indonesia. Sedimentation in Wlingi reservoir is caused by sediment-laden floods from the major tributaries to the Brantas River, i.e. the Putih, Jari, and Lekso Rivers, which drain the southern slopes of Mt. Kelud. Sedimentation in Lodoyo reservoir is caused by sediment outflow from Wlingi reservoir (66%), and the remainder is largely from tributary streams draining the slopes of Mt. Kelud and the southern catchment area.

The sedimentation rate in Wlingi reservoir has been very rapid, with annual average sediment deposition from its completion in 1979 to January 1990 (before the eruption on 10 February 1990) of about 1.49 MCM. The sedimentation rate increased over the 1977 to 1988 period, from 1.14 MCM/year in 1977-1982, 1.29 MCM/year in 1982-1985 to 1.65 MCM/year for the 1985-1988 period. This increase in yield rate is attributed to sediment outflow from lahar pockets and sabo check dams, which had mostly filled to capacity by the 1990 eruption of Mt. Kelud. In the period of 1977 to January 1990, shortly before the February 1990 eruption of Mt. Kelud, the gross capacity had decreased to 4.6 MCM (19.16 % of the initial volume) and the effective storage decreased to 2.20 MCM, 42.31% of the initial volume (Table 1).

The total sediment deposited in Wlingi reservoir from construction in 1977 to immediately prior to the 1990 eruption is estimated at 19.40 MCM (Table 1). Sediment inflow from the area between Sutami dam and Wlingi dam (catchment area: 430 km^2) which was not affected by Mt. Kelud during the survey period, is estimated at 0.43 MCM/year, 5.59 MCM over the 13 year period (Nippon Koei, 1990). Thus, net sediment inflow from the tributaries (Putih, Jari and Lekso) carrying ejecta from Mt. Kelud over that period is estimated at 13.81 MCM, which corresponds to an average sediment inflow rate of 1.06 MCM/year.

After the eruption of Mt. Kelud on 10 February 1990, Wlingi reservoir completely filled with sediment. According to the 1995 survey by PJT-I, the gross storage and effective storage of Wlingi reservoir were then 4.94 MCM and 1.59 MCM respectively. As a result of the continuous removal works, the effective storage capacity of Wlingi reservoir in 2013 recovered to 2.01 MCM, which corresponds to 38.65% of the designed effective storage capacity of 5.2 MCM. Changes in surveyed storage capacity since 1990 are significantly affected by the sediment removal works. Mt. Kelud erupted again on 13 February 2014. The reservoir capacity survey in May 2015 indicates that the gross storage and effective storage capacities of Wlingi reservoir were decreased to 2.20 MCM and 1.01 MCM, respectively (Table 1).

Table 1. Storage capacity transition of Wlingi reservoir.

Survey years	Gross storage		Effective storage		Dead storage	
	Volume (MCM)	Percentage (%)	Volume (MCM)	Percentage (%)	Volume (MCM)	Percentage (%)
1977	24.00	100.00	5.20	100.00	18.80	100.00
1982	18.32	76.33	NA	NA	NA	NA
1985	14.44	60.17	NA	NA	NA	NA
1988	9.50	39.58	NA	NA	NA	NA
January 1990	4.60	19.16	2.20	42.31	2.40	12.77
Eruption of Mt. Kelud in February 1990						
March1990	1.60	6.67	NA	NA	NA	NA
1995	4.94	20.58	1.59	30.58	3.35	17.82
2004	4.41	18.38	2.01	38.65	2.41	12.82
2009	4.38	18.25	2.01	38.65	2.37	12.61
2013	4.83	20.13	2.01	38.65	2.82	15.00
Eruption of Mt. Kelud in February 2014						
2015	2.20	9.17	1.01	19.42	1.19	6.33

Notes: NA = Not Available

The rate of storage capacity decline in Lodoyo reservoir is, like Wlingi reservoir, very high. After the eruption of Mt. Kelud in February 1990, when Wlingi reservoir completely filled with sediment and the trapping efficiency of Wlingi dam was very low, sediment outflow from Wlingi reservoir deposited in Lodoyo reservoir. According to the 1996 survey by PJT-I, the gross storage capacity of Lodoyo reservoir was 2.35 MCM, 45.19% of the initial volume. The capacity of Lodoyo reservoir continued to decrease until 2003. In 2013, the effective storage capacity of Lodoyo reservoir was reduced to 2.72 MCM, despite the implementation of flushing activities from 1999 and dredging from 2003. This represents 52.31% of the designed effective storage capacity of 5.20 MCM. Largely as a result of the 2014 eruption, storage capacity in Lodoyo reservoir decreased by about 50% between the surveys of 2013 and 2015. The reservoir capacity survey in May 2015 indicates that the effective storage capacity of Lodoyo reservoir was decreased to 1.33 MCM (Table 2).

Table 2. Storage capacity transition of Lodoyo reservoir.

Survey years	Gross storage		Effective storage		Dead storage	
	Volume (Mm ^{3})	Percentage (%)	Volume (Mm ^{3})	Percentage (%)	Volume (Mm ^{3})	Percentage (%)
1980	5.20	100.00	5.00	100.00	0.20	100.00
Eruption of Mt. Kelud in Februari 1990						
1990	3.69	70.96	3.69	73.80	0.00	0.00
1993	2.84	54.62	2.84	56.80	0.00	0.00
1996	2.35	45.19	2.35	47.00	0.00	0.00
2003	2.03	39.04	1.86	37.20	0.17	85.00
2006	2.73	52.50	2.73	54.60	0.00	0.00
2009	2.67	51.35	2.67	53.40	0.00	0.00
2011	2.65	50.96	2.65	53.00	0.00	0.00
2013	2.72	52.31	2.72	54.40	0.00	0.00
Eruption of Mt. Kelud in February 2014						
2015	1.33	25.78	1.33	26.60	0.00	0.00

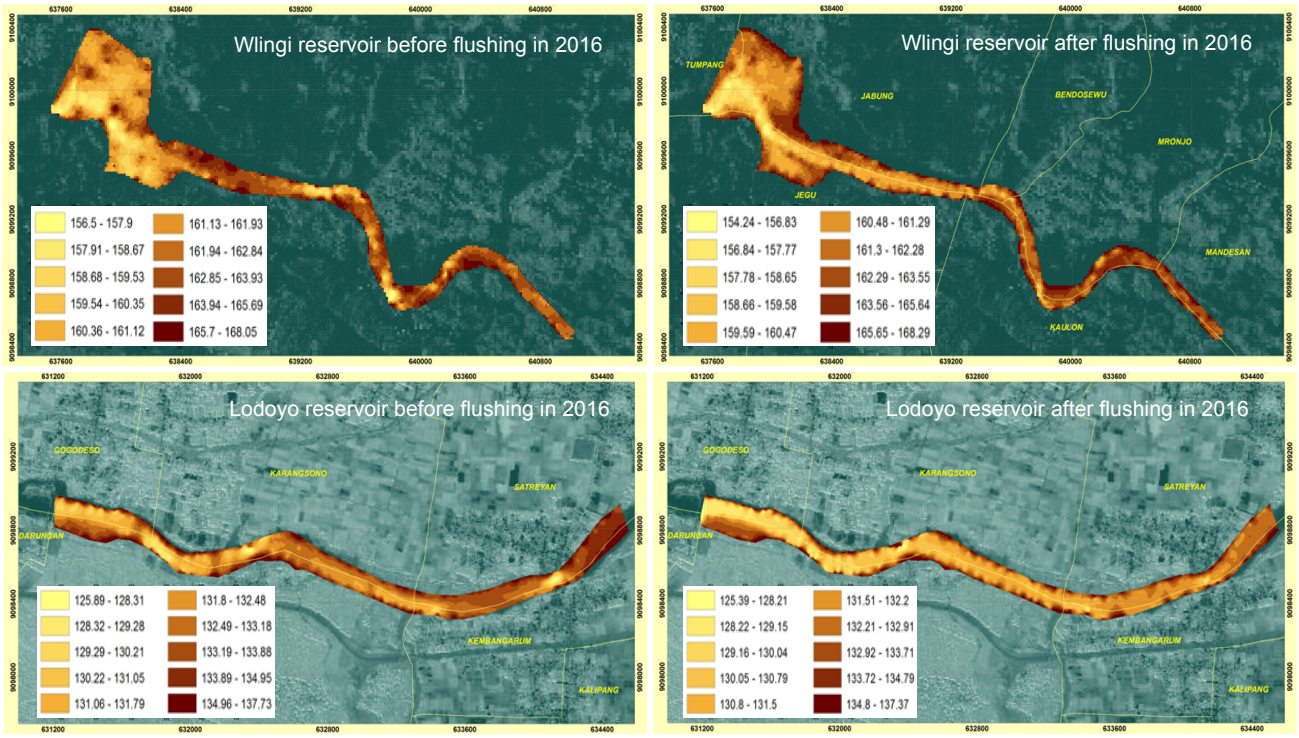

Figure 3. Bathimetry of Wlingi (top) and Lodoyo (bottom) reservoirs before and after sediment flushing operation in 2016.

3.2 Sediment flushing efficiency in Wlingi and Lodoyo reservoirs

It is very important to know how much efficiencies have been obtained by sediment flushing operations because water has economic value. Figure 4 shows the relationship of total water volume and flushed sediment volume of sediment flushing operations in Wlingi and Lodoyo reservoirs since 1990 until the most recent flushing operation in both reservoir in March 2016. From this relationship we calculated the sediment flushing efficiency in both reservoirs as a ratio of total flushed sediment volume from the reservoirs to total consumed water during flushing using Equation [3]. The sediment flushing operations on 17-19 March 2009 removed 145,513 m^3 and 64,367 m^3 of sediments from Wlingi and Lodoyo reservoirs respectively, and

consumed total water of 14.14 MCM. The sediment flushing operations on 24-26 March 2016 removed 1,026,500.48 m^3 and 604,535.51 m^3 of sediments from Wlingi and Lodoyo reservoirs respectively (Figure 3 shows bathimetry of Wlingi and Lodoyo reservoirs before and after sediment flushing operation in 2016), and consumed total water of 38.38 MCM. From the calculation we found that the sediment flushing efficiency of flushing operations in Wlingi and Lodoyo cascade reservoirs in 2009 and 2016 were 0.015 and 0.042 respectively. The efficiencies of sediment flushing in Wlingi and Lodoyo reservoirs after the eruption of Mt. Kelud were high since tremendous volume of sediment deposited in both reservoirs. The sediment flushing efficiency of the later flushing operations in both reservoirs then decrease since the flushed sediment volume decrease. Moreover, the sediments in Wlingi and Lodoyo reservoirs have become compacted by consolidation, and large amount of water remain consumed during flushing considering the downstream river environment, so that the flushing efficiency may be decreased.

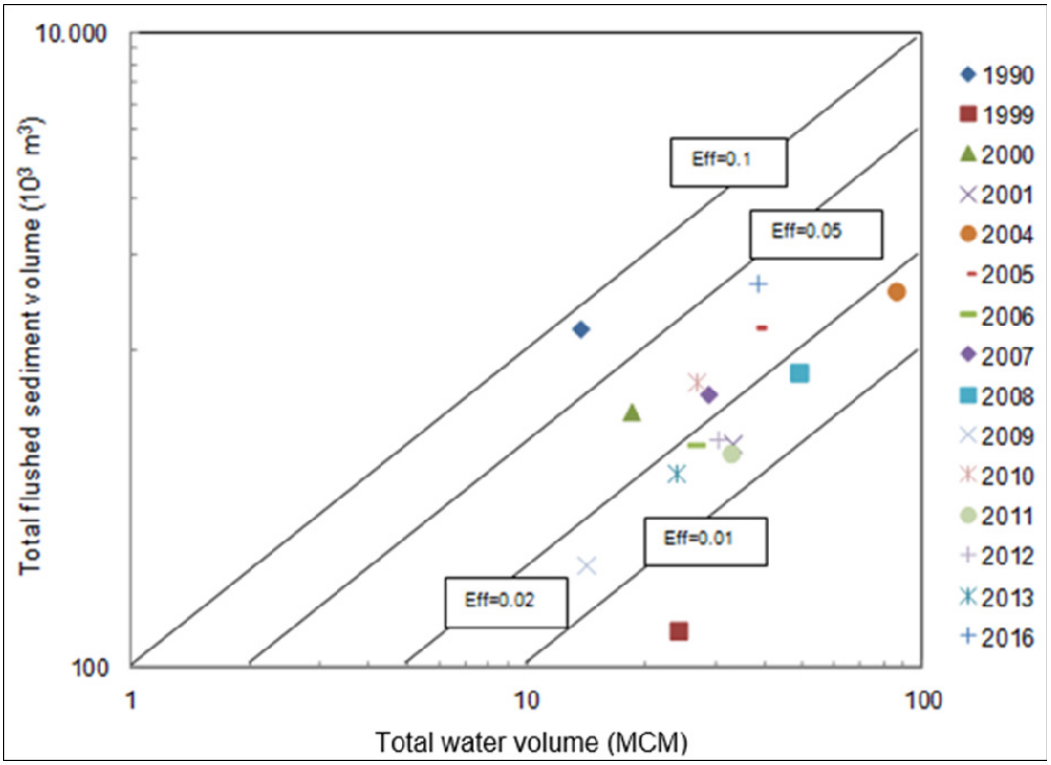

Figure 4. Total water volume and flushed sediment volume of sediment flushing operations in Wlingi and Lodoyo reservoirs (1990-2016).

3.3 Impact of sediment flushing on environment downstream of Wlingi and Lodoyo reservoirs

The results of investigations conducted during flushing operations in 2009 and 2016 reveal that the identified impacts were high turbidity and weakened or dead fish in the reservoirs and downstream river. Regarding the impacts on aquatic organisms, sediment fushing in Wlingi and Lodoyo Reservoir have severe impacts to fish in the reservoirs and its downstream reach (Soekistijono et al., 2005; Hidayat et al., 2014; Hidayat et al., 2015). Virtually almost all of fish in the reservoirs will be flushed downstream or killed during emptying, and fish nests will be desiccated. This phenomenon was remarkable until Ploso Bridge in Jombang (approx. 113 km from Lodoyo Barrage), but not observed at New Lengkong Barrage in Mojokerto (approx. 150 km from Lodoyo Barrage). Weakened or died fish was observed remarkable until Mrican Barrage in Kediri (approx. 75 km from Lodoyo Barrage). The results of water quality monitoring during sediment flushing in 2009 and 2016 can be seen in Figure 5 and are summarized as follows:

- Measured DO concentrations ranged from 0.2 to 9.8 mg/L in 2009 and from 0.5 to 6.9 mg/L in 2016. Sharp decline of DO concentrations was observed during both flushing operations in 2009 and 2016 at D/S of Lodoyo Barrage at Kademangan Bridge in Blitar. Low DO concentration in downstream area at Karangpilang WTP and Ngagel WTP were mostly affected by pollutant load from domestic and industry in Surabaya City.
- Measured BOD concentrations had a wide range from 2.3 to 28.4 mg/L and 4.6 to 81.7 mg/L in 2009 and 20016 respectively. It was recorded higher value at downstream of Lodoyo Barrage at Kademangan Bridge and between Lodoyo Barrage and Mrican Barrage at Ngujang Bridge in Tulungagung.
- Measured COD concentrations had the same tendency and timing as that of BOD concentrations. A wide range from 4.7 to 382.8 mg/L in 2009 and from 7.3 to 224.9 mg/L. It recorded higher value at

D/S of Lodoyo Barrage at Kademangan Bridge, between Lodoyo Barrage and Mrican Barrage at Ngujang Bridge, and D/S of Mrican Barrage in Kediri.

- Measured TSS concentrations had a wide range from 24.1 to 9,990.8 mg/L in 2009 and from 5.9 to 7,684.0 mg/L in 2016. We recognized a noticeable feature at U/S of New Lengkong Barrage, Jrebeng Bridge, Karangpilang WTP and Ngagel WTP, recorded less fluctuated values of TSS due to dilution effect. In the D/S of Lodoyo Barrage at Kademangan Bridge, extremely high values of SS were recorded during sediment flushing operation in 2009.
- Measured nitrate concentrations ranged from 0.2 to 2.7 mg/L in 2009 and from 0.9 to 2.9 mg/L in 2016. Sampling points on the lower reaches i.e. U/S of New Lengkong Barrage, Jrebeng Bridge, Karangpilang WTP and Ngagel WTP, recorded stable measurement results in 2016.
- Measured Total Phosphate (T-P) concentrations ranged from 0.07 to 1.38 mg/L in 2009 and from 0.07 to 0.10 mg/L in 2016. Sampling points on the downstream of Lodoyo barrage until lower reaches at U/S of Mrican Barrage, Ploso Bridge, U/S of New Lengkong Barrage, Jrebeng Bridge, Karangpilang WTP and Ngagel WTP recorded stable measurement results in 2016.

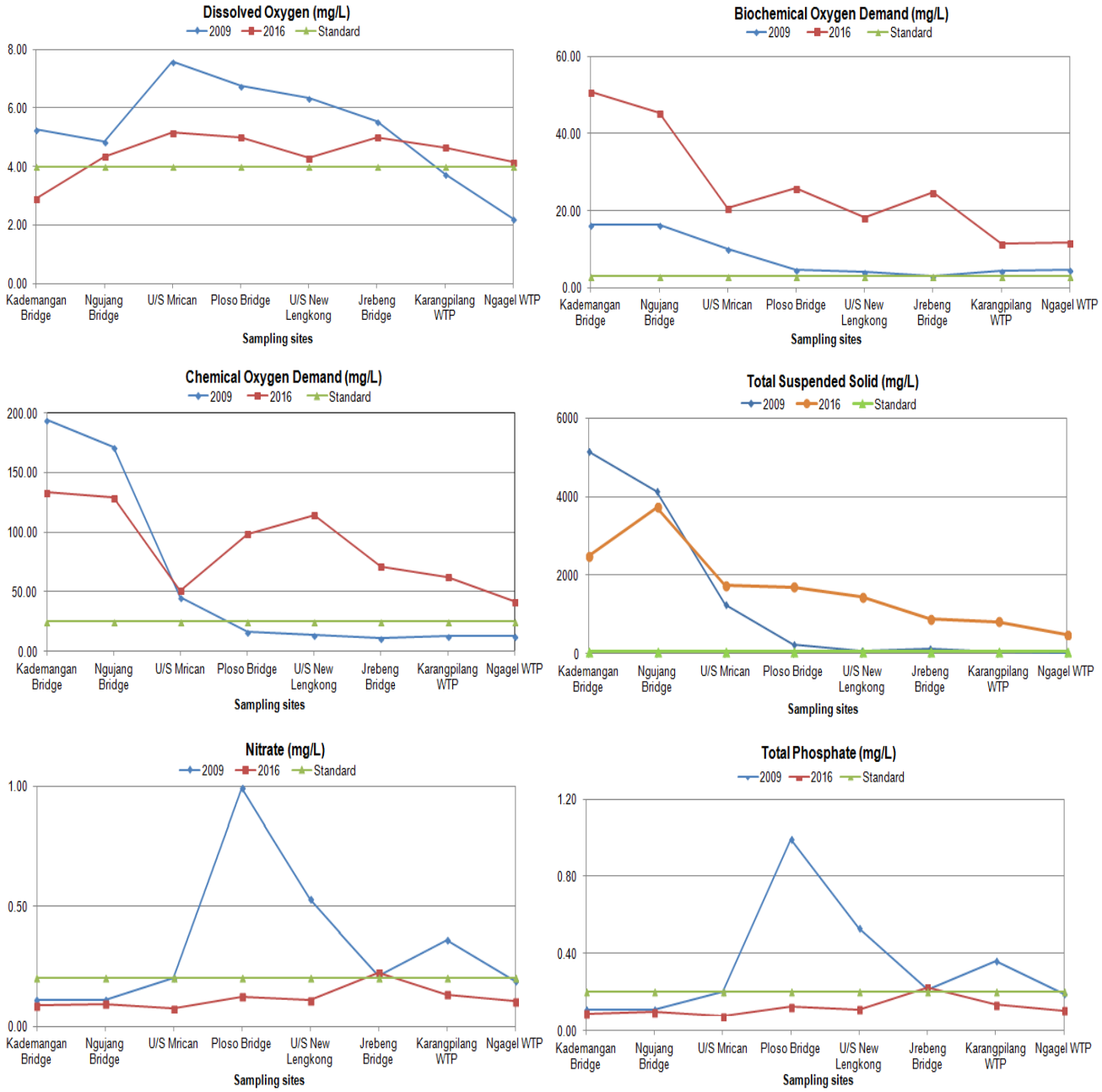

Figure 5. Water quality at downstream of Wlingi and Lodoyo reservoirs during sediment flushing operations in 2009 and 2016.

3.4 Discussion

Tremendous amount of sediments have accumulated in reservoirs in the world, thus reducing their performance and function for water supply, energy production, navigation, flood control, etc. The sedimentation problem most commonly occurs in small-and medium-sized reservoirs, where the contributing rivers have high sediment transport. In order to remove and reduce reservoir sedimentation, several approaches such as flushing, sluicing, dredging and upstream water and soil conservation have been developed; of these approaches, flushing is the only economic approach to restore the storage capacity of the reservoir with severe deposition (Liu et al., 2004). On the other hand, the high concentration of suspended solids of water released during sediment flushing operation will cause downstream environmental impacts. If the efficiency of sediment flushing is high, the downstream environmental impacts will be also high.

Wlingi and Lodoyo reservoirs, small-sized reservoirs in the Brantas River basin, Indonesia have problem on severe sedimentation due to sediment input from the recurrent eruptions of Mt. Kelud. The reservoir capacity survey in May 2015 indicated that the effective storage capacities of Wlingi and Lodoyo reservoir were decreased to 1.01 MCM (19.42% of the initial effective storage capacity) and 1.33 MCM (26.60% of the initial effective storage capacity), respectively. To cope with the sedimentation problem in Wlingi and Lodoyo cascade reservoirs, sediment flushing has been implemented since 1990. The sediment flushing in Wlingi and Lodoyo reservoirs is very effective to remove deposited sediment, same as sediment flushing operations in other cascade reservoirs in the world such as in Verbois and Chancy-Pougny reservoirs on the Rhone River in Europe as reported by Bollaert et al. (2014), and Dashidaira and Unazuki reservoirs on the Kurobe River in Japan as reported by Sumi (2005; 2008).

The efficiency of sediment flushing operation in Wlingi and Lodoyo cascade reservoirs in 2016 was 0.042, almost three times of the efficiency sedimen of sediment flushing operation in 2009. This was mainly caused by the volume of deposited sediment in both reservoirs which was very huge after the eruption of Mt. Kelud in February 2014. The efficiency of sediment flushing operation in Wlingi and Lodoyo reservoirs in 2016 was higher compared to other cascade reservoirs in the world. In Dashidaira and Unazuki reservoirs, the flushing efficiency calculated from the water consumption including the discharge during drawdown and the sediment volume flushed out is about 0.02 (Kantoush et al., 2010). In four hydropower reservoirs in the Italian central Alps i.e. Cancano, Valgrosina, Sernio and Madesimo, sediment flushing efficiency varied between 0.001 and 0.006. This parameter was also calculated as the ratio between the volume of evacuated sediment and the corresponding volume of water employed in the Controlled Sediment Flushing Operations (CSFO) including water for dilution purpose (Brignoli et al., 2017).

In term of capacity to inflow (C:I) ratio, Wlingi and Lodoyo as very small reservoirs with capacity to inflow (C:I) ratios of about 0.007 and 0.001, respectively, can be considered having high efficiency of hydraulic flushing. Several authors indicate that the efficiency of the hydraulic flushing depends on the relationship between the storage volume of the reservoir and the annual amount of incoming runoff. Annandale (1987) indicates that the flushing is effective if this ratio is less than 0.02, whereas Basson and Rooseboom (1996) raised this threshold to 0.05 (Castillo et al., 2015).

Flushing releases high sediment loads with limited water volumes, frequently producing downstream environmental impacts including low dissolved oxygen, high sediment concentration that interferes with the function of gills and smothers stream benthos, reduction in visibility and light penetration, and channel morphological impacts such as infilling of pools and clogging of river gravels with fine sediment, thereby eliminating spawning sites and habitat (Annandale et al., 2016). In Wlingi and Lodoyo reservoirs, sediment flushing caused impacts to environment and water quality in downstream of the reservoirs mainly due to very high concentration of suspended solids. Currently this impact is not considered very well, because it is only significant in several days during the flushing operation. However, flushing is not feasible at many sites because there have been severe impacts on the downstream aquatic environment, principally where heavy deposition or high concentration of suspended solids affects the habitat and survival of fish and other wildlife. In this respect, short periods of flushing are particularly problematic, therefore flushing time should be long enough to mitigate the adverse influences of flushing if water needed is available (Liu et al., 2004). By adding clear water during flushing operation, high peak suspended sediment concentrations may be damped diminishing negative ecological impacts (Sumi et al., 2009). Sediment flushing operation in Wlingi and Lodoyo reservoirs should be supported by additional water available from Sutami and Wonorejo reservoirs to provide dillution effect and should be timed to coincide with natural high-flow events.

In addition, Liu et al. (2004) mentioned that an attention to the environmental effects of sediment flushing has been noted in Europe after the flushing at Genissiat reservoir on the Rhone River in France produced severe damage on the downstream fishery due to enough water not being available from the upstream reservoirs in Switzerland in 1965 and 1978. Since then, reservoir operations for flushing have been subject to regulatory limits on downstream sediment loads or concentrations, which have to be taken into account in the detailed planning of every flushing. For example, Switzerland stipulates that the mean SS concentrations during flushing should not exceed 10 mg/L at the reservoirs in crystalline areas and 70 mg/L at the reservoirs in non-crystalline areas and the peak concentrations should range from 1 to 10 g/L except one river with 70 g/L (Staub, 2000); and France specifies maximum SS concentration should not be over 10 g/L during flushing.

In order to meet the environmental regulations, the flushing at Genissiat reservoir has been performed in concert with Verbois and Chancy- Pougny dams in Switzerland since 1978 (Habara et al., 2001). To control the environmental effects of sediment flushing operations in Wlingi and Lodoyo reservoirs, it is necessary to regulate the limit of SS concentration during flushing and take it into account in the detailed planning of flushing.

4 CONCLUSIONS

The sedimentation problem in Wlingi and Lodoyo reservoirs is very severe due to sediment input from the recurrent eruptions of Mt. Kelud, one of the most active volcanoes in Indonesia. After the eruption of Mt. Kelud in 2014, the effective storage capacity of Wlingi and Lodoyo reservoirs decreased dramatically to 1.01 MCM and 1.33 MCM, respectively. The sediment flushing operation in Wlingi and Lodoyo reservoirs is very effective to remove deposited sediment in order to preserve water storage in the reservoirs. The high efficiency of flushing was achieved during the sediment flushing operation in March 2016, caused high concentration of suspended solids just downstream the reservoirs. For the reservoirs in series on the same river system with high sediment deposition like Wlingi and Lodoyo reservoirs, a concerted action for controlled sediment flushing needs to be taken as mitigation measure to minimize the environmental impacts on the downstream areas and obtain an optimum sediment removal. The sediment flushing in Wlingi and Lodoyo reservoirs should be timed to coincide with natural high-flow events or additional water available from Sutami and Wonorejo reservoirs to provide dillution effect. More frequent sediment flushing from Wlingi and Lodoyo reservoirs can result in smaller sediment concentration during each event, which would normally be considered favorable and cause less impact to downstream environment. Moreover the Government of Indonesia needs to stipulate that the mean SS concentrations during flushing should not exceed the standards i.e, 50 mg/L and 400 mg/L for river water class I-II and river water class III according to the Regulation of the Government of the Republic of Indonesia No 82 of 2001 regarding Water Quality Management and Water Pollution Control.

ACKNOWLEDGEMENTS

The authors thank Jasa Tirta I Public Corporation (PJT-I), Indonesia for providing data used in this paper. The authors would like to acknowledge the financial support for this research from the Indonesia Endowment Fund for Education, the Ministry of Finance, the Government of the Republic of Indonesia.

REFERENCES

Annandale, G.W. (1987). Reservoir sedimentation. Elsevier Science, Amsterdam, Netherlands, 220.

Annandale, G.W., Gregory L., M. & Pravin Karki (2016). Extending the Life of Reservoirs: Sustainable Sediment Management for Dams and Run-of-River Hydropower, Directions in Development. Washington, DC: World Bank.

Atkinson, E. (1996). The Feasibility of Flushing Sediment from Reservoirs, Report OD 137 HR Wallingford, Wallingford, 21.

Basson, G.R. & Rooseboom, A. (1996). Sediment Pass through Operations in Reservoirs. Proceeding, of International Conference on Reservoir Sedimentation, Fort Collins, 1107–1130.

Basson, G.R. (2009). Management of Siltation in Existing and New Reservoirs. General Report Q. 89. Proceedings of the 23rd Congress of the International Commission on Large Dams CIGBICOLD, 2.

Bollaert, E.F.R., Diouf, S., Zanasco, J.L. & Barras J. (2014). Sequential Flushing of Verbois and Chancy-Pougny Reservoirs,Geneva, Switzerland. In Reservoir Sedimentation. CRC Press/Balkema, Leiden, the Netherlands.

Brandt, S.A. (2000). A Review of Reservoir Desiltation. International of Journal Sediment Research, 15(3), 321-342.

Brignoli, M.L., Quadroni, S., Crosa, G., Gentili, G. & Batalla, R., J. (2017). Experiences of Controlled Sediment Flushing from Four Alpine Reservoirs, River Sedimentation. CRC Press/Balkema, Leiden, the Netherlands.

Castillo, L.G., Carrillo, J.M. & Alvares, M.A. (2015). Complementary Methods for Determining the Sedimentation and Flushing in a Reservoir. Journal of Hydraulic Engineering, 141(11), 1-10.

Global Volcanism Program. (2014). Report on Kelud (Indonesia) In: Wunderman, Bulletin of the Global Volcanism Network, 39(2). Smithsonian Institution.

Habara, S., Suzuki, N., Tokito, Y. & Asaka, M. (2001). The Measures for the Sediment at the Dam Reservoirs in Europe, Water Resources Environment Technology Center, Tokyo.

Hidayat, F., Lesmana, S. & Suhartanto, E. (2014). Effect of Reservoir Sediment Flushing from Wlingi and Lodoyo Reservoirs on Downstream River Water Quality. 2nd International Conference on Sustainable Innovation, Yogyakarta, Indonesia.

Hidayat, F., Juwono, P.T., Suharyanto, A. & Pujiraharjo, A. (2015). Evaluation of Environmentally Friendly Flushing in Wlingi and Lodoyo Reservoirs. 1st Young Scientist International Conference of Water Resources Development and Environmental Protection. Malang, Indonesia.

Hidayat, F., Harianto, Juwono, P.T., Suharyanto, A., Pujiraharjo, A. & Marsudi, A.S. (2016). Efficient Sediment Flushing for Sustainable Sediment Management in Wlingi and Lodoyo Reservoirs. Proceeding of the 5th International Seminar of HATHI, 29-31 July 2016, Bali, Indonesia, 151-161.

Hidayat, F., Juwono, P.T., Suharyanto, A., Pujiraharjo, A., Sisinggih, D. & Legono, D. (2017). Sedimentation in Rivers and Reservoirs following the Eruptions of Kelut Volcano, Indonesia. River Sedimentation, CRC Press/Balkema, Leiden, the Netherlands.

Kantoush, S.A., Sumi, T., Suzuki, M. & Murasaki, M. (2010). Impacts of Sediment Flushing on Channel Evolution and Morphological Processes: Case Study of the Kurobe River, Japan. International Conference of Fluvial Hydraulics, River Flow, Bundesanstalt für Wasserbau.

Kondolf, G.M., Gao, Y., Annandale, G.W., Morris, G.L., Jiang, E., Zhang, J., Cao, Y., Carling, P., Fu, K., Guo, Q., Hotchkiss, R., Peteuil, C., Sumi, T., Wang, H.W., Wang, Z., Wei, Z., Wu, C. & Yang, C.T. (2014). Sustainable Sediment Management in Reservoirs and Regulated Rivers: Experiences from Five Continents. Earth's Future, 2, 256–280.

Lai, J.S. & Shen, H.W. (1996). Flushing Sediment through Reservoirs. Journal of Hydraulic Research, 34(2), 237-255.

Liu, J., Minami, S., Otsuki, H,. Liu, B. & Ashida, K. (2004). Environmental Impacts of Coordinated Sediment Flushing. Journal of Hydraulic Research, 42(5), 461-472.

Mahmood K. (1987). Reservoir Sedimentation: Impact, Extent and Mitigation (Tech. Rep. No. 5), International Bank for Reconstruction and Development, Washington, DC, USA.

Morris, G.L. & Fan, J. (1997) Reservoir Sedimentation Handbook: Design and Management of Dams, Reservoir and Watersheds for Sustainable Use. McGraw Hill, New York, USA.

Morris, G.L. (2014). Sediment Management and Sustainable Use of Reservoirs, in Modern Water Resources Engineering. Humana Press, 321–323.

Nippon Koei Co., Ltd. (1990). Recommendation Report on Countermeasures Against Sediment Inflow to Wlingi Reservoir. Nippon Koei Co., Ltd. Consulting Engineers, Tokyo, Japan.

Quadroni, S., Brignoli, M.L., Crosa, G., Gentili, G., Salmaso, F., Zaccara, S. and Espa, P. (2016). Effects of Sediment Flushing from a Small Alpine Reservoir on Downstream Aquatic Fauna. Ecohydrology, 9, 1276–1288.

Schleiss A.J., Franca, M.J., Juez, C. & Cesare, G.D. (2016): Reservoir Sedimentation. Journal of Hydraulic Research, 54(6), 595-614.

Soekistijono, Harnanto, A. & Hidayat, F. (2005). Coordinated Sediment Flushing in Wlingi-Lodoyo Reservoirs and the Study of its Economics Benefits and Effect to Water Quality and Ecosystem in the Downstream Reaches. Proceeding of International Symposium on Ecohydrology, Bali, Indonesia, 299-308.

Staub, E. (2000). Effects of Sediment Flashing on Fish and Invertebrates in Swiss Alpine Rivers. International Workshop and Symposium on Reservoir Sedimentation Management, October, Toyama, Japan, 109–118.

Sumi, T. (2005). Sediment Flushing Efficiency and Selection of Environmentally Compatible Reservoir Sediment Management Measures. International Symposium on Sediment Management and Dams, 2nd EADC Symposium. Yokohama, Japan.

Sumi, T. (2008). Evaluation of Efficiency of Reservoir Sediment Flushing in Kurobe River. In Fourth International Conference on Scour and Erosion, Tokyo, Japan, 5-7.

Sumi, T., Nakamura, S.Y. & Hayashi, K. (2009). The Effect of Sediment Flushing and Environmental Mitigation Measures in the Kurobe River. 23rd ICOLD Congress.

Thouret, J.C., Abdurachman K.E. & Bourdier, J.L. (1998). Origin, Characteristics and Behaviour of Lahars Following the 1990 Eruption of Mt. Kelud, Eastern Java (Indonesia), Bulletin of Volcanology 59, 460-480.

Tigrek, S. & Aras, T. (2012). Reservoir Sediment Management. CRC Press/Balkema, Leiden, the Netherlands.

WCD (World Commission on Dam) (2000). The Report of the World Commission on Dams, London: World Commission on Dams/Earthscan Publications.

Proceedings of the 37th IAHR World Congress
August 13 – 18, 2017, Kuala Lumpur, Malaysia

IMPLEMENTATION OF NON-NEWTONIAN RHEOLOGY FOR DEBRIS FLOW SIMULATION WITH REEF3D

PETTER FORNES[1], HANS BIHS[2], VIKAS THAKUR[3] & STEINAR NORDAL[4]

[1, 2, 3, 4]Department of Civil and Environmental Engineering, Norwegian University of Science and Technology (NTNU), Trondheim, Norway
petter.fornes@ntnu.no

ABSTRACT

Landslides triggered by hydro-meteorological processes are a serious natural hazard in many areas of the world. The landslides of the debris flow type are often triggered by extreme precipitation events. These landslides are composed of water and poorly graded soil particles, and usually form a dense flow. To predict the runout distance of such landslides and to design countermeasures to reduce their consequences, a solid understanding and description of the debris flow mechanism is essential. Debris flows are often modeled with depth-averaged models, which are fast to simulate. To better capture the physics of the problem, computational fluid dynamics (CFD) can be used. A non-Newtonian rheology for modeling the behavior of the dense fluid phase, representing fine solids suspended in water, is implemented in the open-source CFD code REEF3D. The three-dimensional numerical model employs the level set method for representing the free surface. This approach can handle the complex air-debris flow interface topology. The Reynolds-Averaged Navier-Stokes (RANS) equations are discretized with the fifth-order accurate Weighted Essentially Non-Oscillatory (WENO) scheme in space and with a third-order Runge-Kutta based fractional step scheme in time. The model behavior is validated through comparisons with laboratory model tests with slurry of water and fine grained soil.

Keywords: CFD; non-Newtonian rheology; free surface; debris flow; REEF3D.

1 INTRODUCTION

Rapid debris flows, debris avalanches, earth flows, landslides, rock avalanches and failures of loose fill are among the most dangerous and most damaging of all landslide phenomena. Their runout determines a large portion of the consequences and the risk associated with the landslides. Runout parameters include the maximum distance reached, flow velocities, thickness and distribution of deposits, as well as the behavior at obstacles in the flow path (Crosta et al., 2003; Rickenman, 2005; Hungr, 2005; Lacasse, 2013; Hungr, 2016; Strand et al., 2017).

The landslides of the debris flow type are typically triggered by hydro-meteorological processes during extreme precipitation events. Debris flows are often composed of water and poorly graded soil particles, forming a dense flow (Iverson, 1997). To predict the runout distance of such landslides and to design countermeasures to reduce their consequences, a solid understanding and description of the debris flow mechanism is necessary. Complete understanding of the mechanisms involved in debris flow is a complex and challenging task. However, owing to the crucial nature of assessing the initiation and mobility of debris flow, researchers and practitioners have attempted to address such problems in pragmatic approaches that involve several logical simplifications.

In engineering practice, the propagation of these flows is traditionally simulated with depth-averaged models. The main advantage of integrating over the height of the flow is to reduce the problem from three dimensions to two, and thereby reducing the simulation time significantly. However, this simplification reduces the accuracy, by applying all the resistance through the base friction and using an average over the height shear rate profile. The traditional depth averaged methods often use a single phase rheology, modeling the debris flow as a continuum, for example using Voellmy rheology. If so, the base shear is applied as a constant frictional resistance term and viscous term non-linear dependent on the average shear rate. The material parameters in these models typically have to be calibrated based on field cases, in order to make any predictions. With the recent increases in computer power, it might be more feasible to consider a full three dimensional solution of the debris flows propagation. Computational fluid dynamics (CFD) can therefore be used to try to capture more of the problem physics.

Such complex problems have also been approached by focusing on certain selected aspects of the problem at a time, one of which is to understand the flow behavior of remolded debris. This paper addresses and validates this aspect, numerically, in light of laboratory measurements. The objective of this work is then to model only the behavior of the dense fluid phase of debris flow landslides, using CFD. Here, the flow is in this three dimensional method modeled as a single-phase continuum, even though a single-phase viscoplastic

rheology is not sufficient to capture all the complex mechanisms of debris flows (Iverson, 2003). Full debris flow behavior, including the friction between the larger sized grains, the buildup of excess pore pressure, and temporal and spatial rheological changes, cannot realistically be captured when modeled as a single phase continuum fluid. To account for this, while still considering the debris flow as a continuum, a multiphase approach seems necessary (von Boetticher et al., 2015). However, that is outside the scope of this paper. Regardless, a viscoplastic non-Newtonian rheology may be sufficient for the interstitial fluid phase of a debris flow, consisting of water with fine particles in suspension (Laigle and Coussot, 1997). It may also be appropriate for other fluidized fine-grained soils, such as mudflows and flow slides in sensitive clays (Jeong et al., 2012). For this purpose, a non-Newtonian viscoplastic rheology has been implemented in the open-source CFD code REEF3D (Bihs et al., 2016).

2 NUMERICAL MODEL

The open-source CFD code REEF3D is documented by Bihs et al. (2016). The three-dimensional finite difference numerical model solves the Navier-Stokes equations, which govern the behavior of viscous and incompressible fluids. For mass and momentum conservation of the fluid domain, the continuity and Reynolds Averaged Navier-Stokes (RANS) equations are considered:

$$\frac{\partial u_i}{\partial x_i} = 0 \qquad [1]$$

$$\frac{\partial u_i}{\partial t} + u_j \frac{\partial u_i}{\partial x_j} = -\frac{1}{\rho}\frac{\partial p}{\partial x_i} + \frac{\partial}{\partial x_j}\left[\left(\nu + \nu_t\right)\left(\frac{\partial u_i}{\partial x_j} + \frac{\partial u_j}{\partial x_i}\right)\right] + g_i \qquad [2]$$

where u is the velocity, ρ is the fluid density, p is the pressure, ν is the kinematic viscosity, ν_t is the eddy viscosity, g is the gravitational acceleration. On the left hand side of the RANS equations are the transient and convective velocity terms. On the right hand side are the surface and volume forces, the viscous and pressure terms, and the gravity, respectively. The Reynold stress term capturing the turbulence is modeled separately.

The RANS equations are discretized with the fifth-order accurate Weighted Essentially Non-Oscillatory (WENO) scheme in space (Jiang and Shu, 1996) and with a third-order Runge-Kutta based fractional step scheme in time (Shu and Osher, 1988).

The pressure gradient is modeled with Chorin's projection method (Chorin, 1968) for incompressible flow. A staggered grid is used to avoid decoupling of velocity and pressure. The momentum equation with the pressure gradient removed is solved for an intermediate velocity field u_i^*. The pressure for the new time step p^{n+1} is determined and used to correct the velocity field. In order to create divergence free flow field, the pressure needs to fulfill the following equation:

$$\frac{\partial}{\partial x_i}\left(\frac{1}{\rho(\phi^n)}\frac{\partial p^{n+1}}{\partial x_i}\right) = \frac{1}{\Delta t}\frac{\partial u_i^*}{\partial x_i} \qquad [3]$$

The level set method proposed by Osher and Sethian (1988) is employed for locating the free surface. This approach can handle the complex air-debris flow interface topology. To define the interface between the two fluids, the following continuous signed distance function is used:

$$\phi(\vec{x},t)\begin{cases} > 0 & \text{if } \vec{x} \text{ is in phase 1} \\ = 0 & \text{if } \vec{x} \text{ is at the interface} \\ < 0 & \text{if } \vec{x} \text{ is in phase 2} \end{cases} \qquad [4]$$

The level set function $\phi(\vec{x}, t)$ is coupled to the velocity field u_j with a convection equation, and the spatial discretization is determined with the Hamilton-Jacobi WENO scheme version (Jiang and Peng, 2000):

$$\frac{\partial \phi}{\partial t} + u_j \frac{\partial \phi}{\partial x_j} = 0 \qquad [5]$$

3 NON-NEWTONIAN RHEOLOGY

For modeling the interstitial fluid of debris flows, consisting of water with fine particles in suspension, the viscoplastic Herschel-Bulkley rheology may be appropriate. Kaitna and Rickenmann (2007) and Kaitna et al. (2007) found that Herschel-Bulkley can be fitted to experiments on debris flow material with small particle diameters and high clay content. Coussot et al. (1998) determined Herschel-Bulkley parameters for debris flow deposit samples (without the largest particles).

The non-newtonian viscoplastic Herschel-Bulkley rheology features a yield stress τ_0 and a non-linear stress relationship with the shear rate $\dot{\gamma}$. In order to have shear deformation, the shear stress acting on the fluid must supersede the yield stress. For shear stress lower than the yield stress, the shear rate is zero. The Herschel-Bulkley rheology is defined by the shear stress and shear rate relation:

$$\tau = \tau_o + K\dot{\gamma}^n \quad [6]$$

$$\dot{\gamma} = \begin{cases} 0 & \text{if } \tau < \tau_0 \\ \left(\frac{1}{K}(\tau - \tau_0)\right)^{\frac{1}{n}} & \text{if } \tau \geq \tau_0 \end{cases} \quad [7]$$

where τ is the shear stress, $\dot{\gamma}$ is the shear rate, τ_0 is the yield stress, K is the consistency parameter, n is the Herschel-Bulkley exponent. If n> 1 shear-thickening behavior is defined, and n< 1 defines shear-thinning behavior. If n = 1 the equations provide the Bingham rheology, and if additionally τ_0 = 0, they provide the Newtonian rheology. The Herschel-Bulkley rheology can be considered as a generalized Newtonian fluid by determining the apparent shear rate dependent dynamic viscosityμ, as the shear stress divided by the shear rate. As the shear rate decreases towards zero, the apparent viscosity increases towards infinity:

$$\mu = \frac{\tau}{\dot{\gamma}} = \frac{\tau_o}{\dot{\gamma}} + K\dot{\gamma}^{n-1} \quad [8]$$

The Herschel-Bulkley rheology has been implemented in the REEF3D CFD code. The kinematic viscosity $\nu = \mu/\rho$ in the Navier-Stokes equations Eq. [2] is determined locally for each cell every time step since it varies spatially and temporally. It is determined by normalizing the apparent dynamic viscosity by the fluid density, and a maximum value ν_0 is specified to avoid numerical problems:

$$\nu = \min\left[\nu_0, \left(\frac{\tau_o}{\dot{\gamma}} + K\dot{\gamma}^{n-1}\right)\Big/\rho\right] \quad [9]$$

where τ_0 is the yield stress, K is the consistency parameter, n is the Herschel-Bulkley exponent, ρ is the density and ν_0 is a maximum kinematic viscosity value used for small shear rates when the apparent viscosity approaches infinity. The viscosity is considered isotropic, and the scalar shear rate magnitude $\dot{\gamma}$ is determined from the shear rate tensor:

$$\dot{\gamma} = \sqrt{\frac{1}{2}\sum_{i=1}^{3}\sum_{j=1}^{3}\dot{\gamma}_{ij}\dot{\gamma}_{ij}} \quad [10]$$

The implementation in Eq. [9] results in a material with a very high viscosity for low shear rates instead of a yield stress preventing deformation. This means that the flowing material will never come fully to rest with a sloped angle, which can be expected for a landslide deposited at a flat area. However, when the magnitude of velocity is several orders of magnitude lower than while propagating, it will be considered to have stopped. The implementation is bi-viscous, making the rheology discontinuous. Instead, a regularization parameter could be employed (Saramito and Wachs, 2016), which may improve the accuracy. It would also help to obtain rigid body motion for the unyielded material, but it has not been considered necessary to obtain the precise location of solid material.

4 EXPERIMENTS

To validate the implementation of the Herschel-Bulkley rheology in REEF3D, laboratory experiments with fine-grained soil materials were considered. Sensitive clays are fine grained soil materials that exhibit viscoplastic flow behavior when remolded (Locat and Demers, 1988). When these clays are deformed, their intact structure disintegrates and they can transform from a solid material to essentially a fluid with potentially less than 1kPa shear strength ('quick'). This brittle behavior has caused many landslides to develop retrogressively and the consequences can become large (Thakur et al., 2013).

When remolded and thus fluidized, sensitive clays can be considered to be viscoplastic single phase continuum material (Jeong et al., 2012). Thus, laboratory experiments on remolded sensitive clay were considered for validation of the Herschel-Bulkley implementation. Grue et al. (2017) reports viscometer test results on Norwegian remolded sensitive clays. They established correlations between the Herschel-Bulkley model parameters τ_0, K and n, and the soil characterization parameter Liquidity Index (I_L).

For validation of the Herschel-Bulkley rheology implementation, simulation had been done of a new laboratory test called a 'quickness test', proposed by Thakur and Degago (2012) for determining the run out potential of sensitive clay landslides. This test was performed by first filling a standardized cylinder (height x diameter = 120 mm x 100 mm) resting on a flat smooth surface with remolded clay material, see Figure 1. Afterwards, the cylinder was slowly lifted vertically, and the gravity causes the material to radially flow out to the sides from underneath the cylinder, see Figure 3. The collapse height and deposition diameter were noted. The results of this laboratory test can be used for making correlations with landslide runout distances, and evaluating the susceptibility of long runout distances.

The tests done by Thakur and Degago (2012) were with material from Heimdal, Norway. The material is characterized in Table 1. Samples of the clay with different remolded shear strengths c_{ur} were tested, having correspondingly different degrees of fluidization.

Figure 1. Cylinder (internal height 120 mm, diameter 100 mm) filled with remolded sensitive clay, standing on glass plate. (Photo: Thakur, V.).

Table 1. Heimdal clay properties, Thakur and Degago (2012).

Sampling depth [m]	6-10
Clay fractions (< 2 μm) [%]	30
Water content (w) [%]	22-34
Plasticity index (I_P) [%]	5-7
Liquidity index (I_L) [-]	0.7-2.0
Undisturbed undrained shear strength (c_{ui}) [kPa]	12-58
Remolded undrained shear strength (c_{ur}) [kPa]	0-2
Sensitivity (S_t) [-]	16-29
Over consolidation ratio (OCR) [-]	1.8-2.0

The quickness test was simulated with REEF3D as cylindrical dam break test. The domain considered was 400 mm x 400 mm x 180 mm, with cell length 2 mm, resulting in a mesh with 3.6 million cells. A cylinder of Herschel-Bulkley fluid with initial dimension height 120 mm and diameter 100 mm was immediately released and allowed to flow out due to gravity. The rest of the domain was filled with a fluid phase given Newtonian rheology with the properties of air. Turbulence was not considered in the simulation.

The rheological parameters used in the numerical simulation for the remolded clay were based on the data produced by Grue et al. (2017), due to no viscometer test done for the quickness test material. The sensitive clays used by Thakur and Degago (2012) and Grue et al. (2017) were collected from two different sensitive clay deposits located in Trondheim, Norway. However, the grain size distribution, salt contents, and the mineralogical characteristics of these sensitive clays deposits are rather similar (Thakur et al., 2017). Therefore, the data reported by Grue et al. (2017) had been used as a reference to establish best estimate values of Herschel-Bulkley model parameters for the Heimdal clay with remolded shear strength c_{ur} = 0.2 kPa, see Table 2. Figure 2 shows the corresponding rheology curve according to Eq. [6].

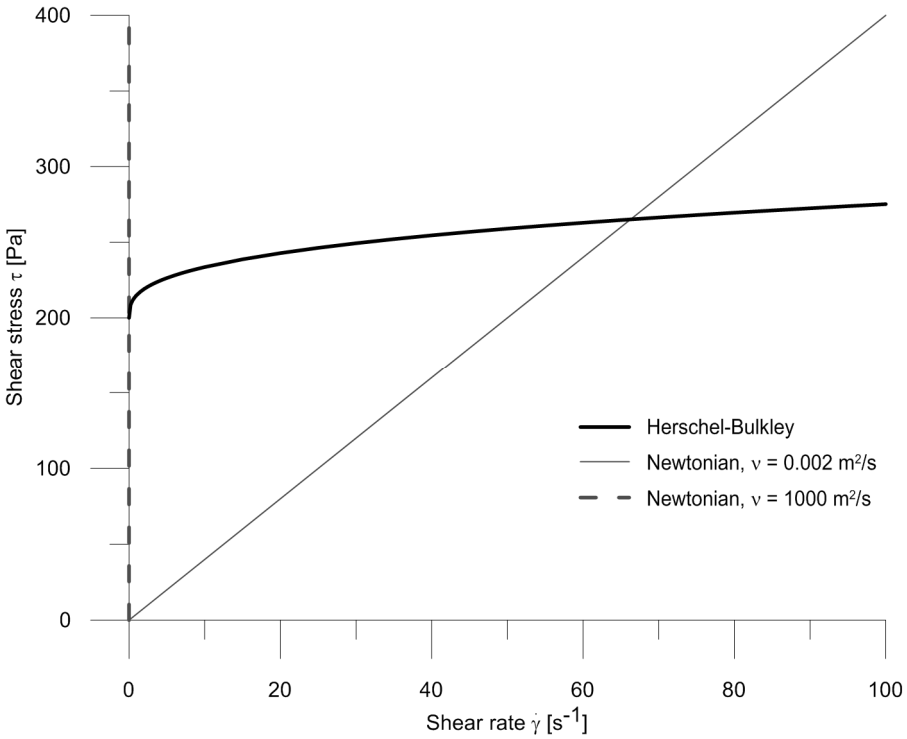

Figure 2. Shear stress and shear rate relation for best estimate Herschel-Bulkley parameters, compared to Newtonian rheology with dynamic viscosity μ = 4.0 and $2 \cdot 10^6$Pa·s (corresponding to kinematic viscosity ν = 0.002 and 1000 m^2/s, for density ρ = 2000 kg/m^3).

Table 2. Herschel-Bulkley model parameters, REEF3D simulation.

Density (ρ) [kg/m^3]	2000
Maximum kinematic viscosity (ν_0) [m^2/s]	1000
Yield stress (τ_0) [Pa]	200
Herschel-Bulkley exponent (n) [-]	0.35
Consistency parameter (K) [$Pa \cdot s^n$]	15

5 RESULTS

In the laboratory tests by Thakur and Degago (2012), it was observed a significant change in the material flow behavior for remolded shear strength c_{ur} from 0.2 to 0.5 kPa. For lower shear strength, the material is highly liquid, and for higher strength its shape remains more intact. In the in-between range it behaves like a dense fluid with yield stress. Figure 3 shows the final deposition shape of the sample with remolded shear strength c_{ur} = 0.2 kPa. The final deposition height was 40 mm and the diameter 237 mm. The deformed shape is irregular due to variable speed of lifting the cylinder.

Figure 4 shows the simulation results using the Herschel-Bulkley rheology with the parameters in Table 2. The overall deposition of the simulation matched relatively well with the experiments, see Figure 5. The height at rest (low velocity), was lower than in the laboratory experiment. It can be due to the laboratory execution, which resulted in an irregular shape or due to the friction between the material and the surface on which the material was flowing. Without these, the maximum height would probably be slightly lower.

In the simulation, the material was released from the cylinder immediately. The magnitude of deformation velocity reduces significantly after time T = 0.3 s, and the fluid is considered as being at rest. Conversely, the laboratory experiment was performed by lifting the cylinder slowly and unevenly, and thus took longer time to obtain the final deposition.

The material in the simulation was perfectly homogenous, and the starting conditions were symmetric. One would therefore expect a symmetrical deposition pattern. This is not the case, due to the high viscosity considered for this fluid. Numerically, the treatment of the diffusion term in the momentum equation is handled with a staggered grid, and the interpolation algorithms used may introduce an asymmetrical solution. This is not expressed when considering viscosities closer to the value for water.

In this simulation, best estimate rheological parameters were used, established based on correlations with I_L from similar clays. The match could be improved with further calibration of the rheological parameters, or by performing viscometer tests on the actual sample material.

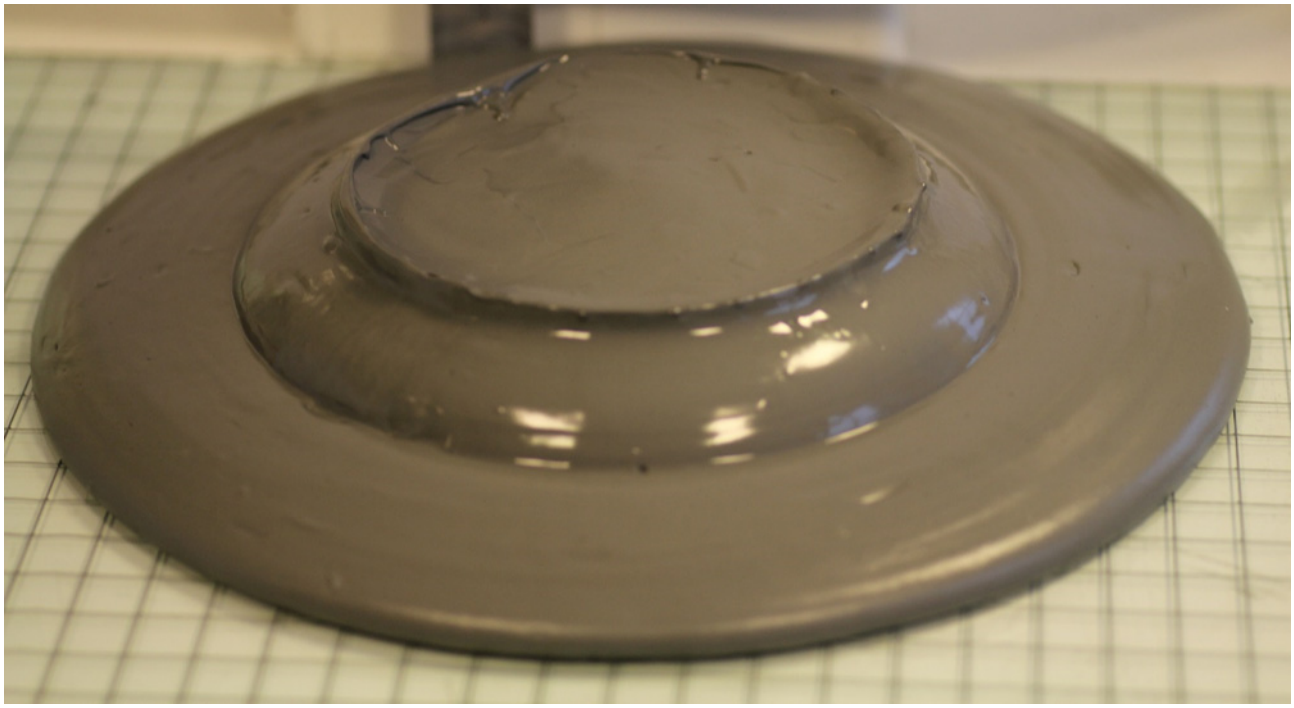

Figure 3. Final shape laboratory quickness test (height 40 mm, diameter 237 mm), Heimdal clay, remolded shear strength c_{ur} = 0.2 kPa (Photo: Thakur, V.)

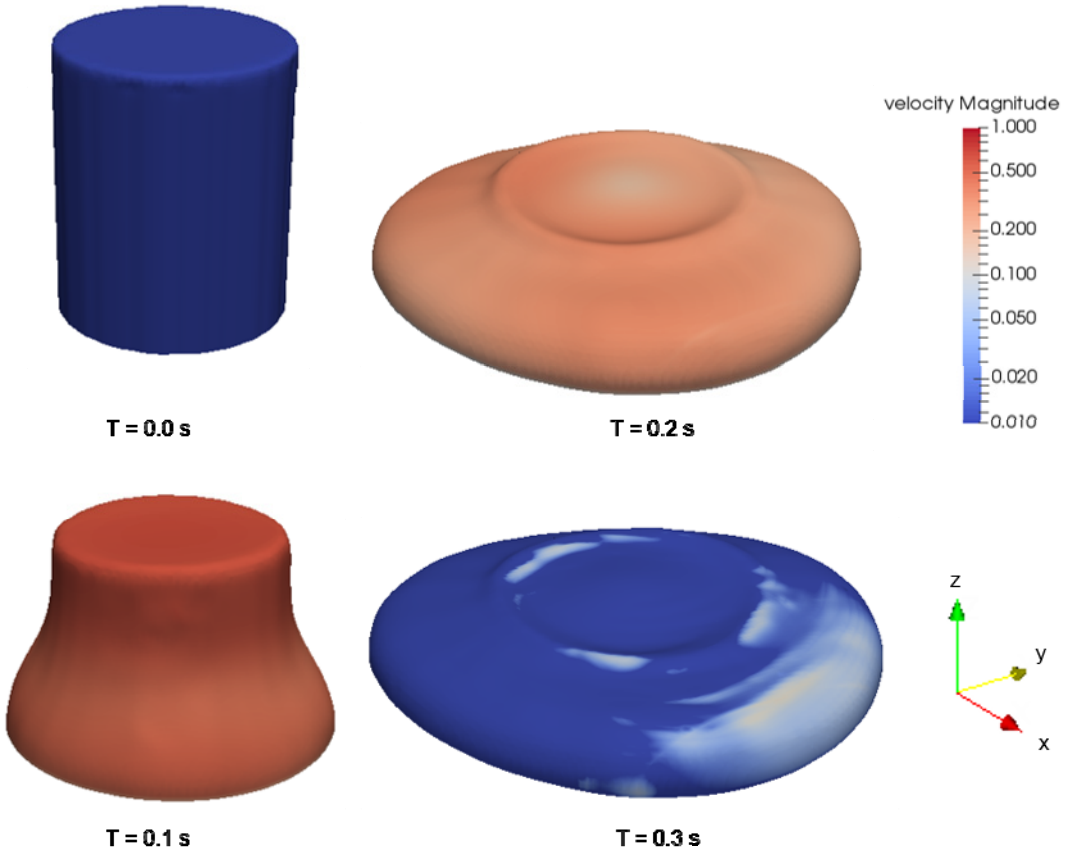

Figure 4. Simulation of quickness test, velocity contours during deformation from time T = 0.0-0.3 s.

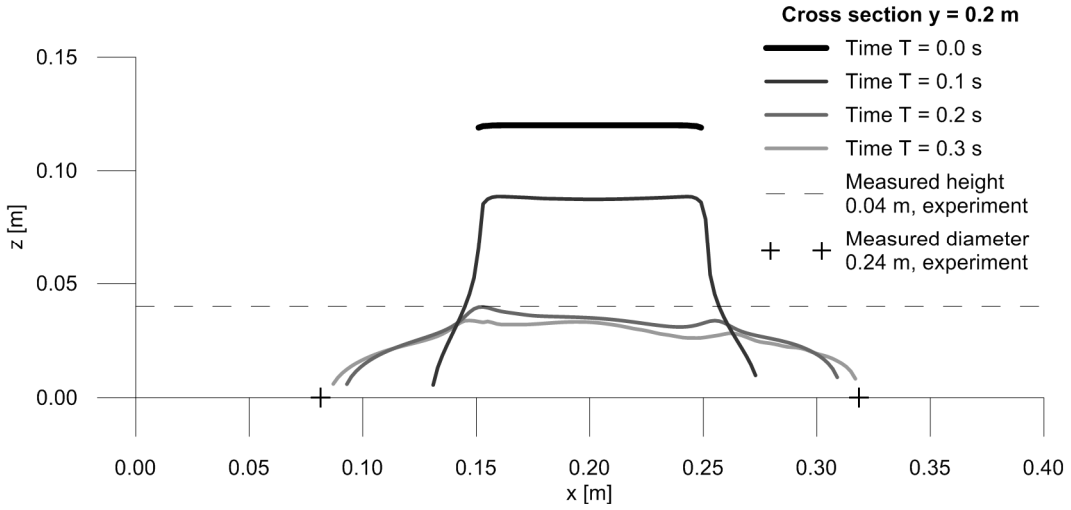

Figure 5. Simulated free surface elevation for the Herschel-Bulkley fluid at cross section y = 0.2 m (middle).

6 CONCLUSIONS

The implementation of the non-Newtonian Herchel-Bulkey rheology in the REEF3D open-source CFD code has been validated for laboratory experiments on remolded sensitive clay. This material can be described as a single-phase viscoplastic fluid for low remolded shear strengths. Despite some simplifications and assumptions, the flow behaviors observed in the laboratory are captured quite well in the numerical simulation.

With the current implementation, the yield stress is modeled as a very high viscosity for low shear rates. The deformation of a fluid modeled this way will finally slow down significantly, but never stop completely without resting with a level surface. To obtain a steady state solution where the material can stop with a sloped surface, the yield stress should be accounted for more realistically.

Although the Herschel-Bulkley rheology can be appropriate for the interstitial fluid of debris flows, a more advanced multiphase model is necessary for capturing full debris flow behavior using a continuum approach in CFD.

ACKNOWLEDGEMENTS

This work has been done as a part of the project Klima 2050, which is a Centre for Research-based Innovation with many Norwegian partners from the private and public sector and research & education. Great help and support has been provided by the team at NTNU Marine Civil Engineering developing the REEF3D open-source code. The work presented in this paper is relevant for other ongoing research activities at NTNU such as GEOFUTURE II project.

REFERENCES

Bihs, H., Kamath, A., Chella, M.A., Aggarwal, A. & Arntsen, Ø.A. (2016). A New Level Set Numerical Wave Tank with Improved Density Interpolation for Complex Wave Hydrodynamics. *Computers & Fluids*, 140, 191-208.

Chorin, A.J. (1968). Numerical Solution of Navier-Stokes Equations. *Mathematics of Computation*, 22(104), 745-762.

Coussot, P., Laigle, D., Arattano, M., Deganutti, A. & Marchi, L. (1998). Direct Determination of Rheological Characteristics of Debris Flow. *Journal of Hydraulic Engineering-ASCE*, 124(8), 865-868.

Crosta, G.B., Cucchiaro, S. & Frattini, P. (2003). Validation of Semi-Empirical Relationships for the Definition of Debris-Flow Behavior in Granular Materials. *Debris-Flow Hazards Mitigation: Mechanics, Prediction and Assessment,* 1(2), 821-831.

Grue, R., Issler, D., L'Heureux, J.S. & Thakur, V. (2017). Viscometric Tests of Sensitive Clay from Byneset, Norway, and Fit to the Herschel–Bulkley model. Second International Workshop on Landslides in Sensitive Clays, June 2017. *Springer Book Series Advances on Natural and Technological Hazards Research*. (In print)

Hungr, O. (2005). *Classification and Terminology.* Debris-flow Hazards and Related Phenomena, Springer, 9-23

Hungr, O. (2016). *A Review of Landslide Hazard and Risk Assessment Methodology, Landslides and Engineered Slopes.* Experience, Theory and Practice, CRC Press, 3-27.

Iverson, R.M. (1997). The Physics of Debris Flows. *Reviews of Geophysics*, 35(3), 245-296.

Iverson, R.M. (2003). The Debris-Flow Rheology Myth. *Debris-Flow Hazards Mitigation: Mechanics, Prediction, and Assessment,* 1(2), 303-314.

Jeong, S.W., Locat, J. & Leroueil, S. (2012). The Effects of Salinity and Shear History on the Rheological Characteristics of Illite-Rich and Na-Montmorillonite-Rich Clays. *Clays and Clay Minerals*, 60(2), 108-120.

Jiang, G.S. & Peng, D.P. (2000). Weighted ENO Schemes for Hamilton-Jacobi Equations. *Siam Journal on Scientific Computing,* 21(6), 2126-2143.

Jiang, G.S. & Shu, C.W. (1996). Efficient Implementation of Weighted ENO Schemes. *Journal of Computational Physics*, 126(1), 202-228.

Kaitna, R. & Rickenmann, D. (2007). Flow of Different Material Mixtures in a Rotating Drum. Paper Presented at the Debris-Flow Hazards Mitigation: Mechanics, Prediction, and Assessment. *Proceedings of the 4th International DFHM Conference,* Chengdu, China.

Kaitna, R., Rickenmann, D. & Schatzmann, M. (2007). Experimental Study on Rheologic Behaviour of Debris Flow Material. *Acta Geotechnica*, 2(2), 71-85.

Lacasse, S. (2013). 8thTerzaghi Oration Protecting Society from Landslides– The Role of the Geotechnical Engineer. *Proceedings of the 18th International Conference on Soil Mechanics and Geotechnical Engineering,* Paris.

Laigle, D. & Coussot, P. (1997). Numerical Modeling of Mudflows. *Journal of Hydraulic Engineering-ASCE*, 123(7), 617-623.

Locat, J. & Demers, D. (1988). Viscosity, Yield Stress, Remolded Strength and Liquidity Index Relationships for Sensitive Clays. *Canadian Geotechnical Journal*, 25(4), 799-806.

Osher, S. & Sethian, J.A. (1988). Fronts Propagating with Curvature-Dependent Speed - Algorithms Based on Hamilton-Jacobi Formulations. *Journal of Computational Physics*, 79(1), 12-49.

Rickenmann, D. (2005). Runout Prediction Methods. *Debris-Flow Hazards and Related Phenomena,* 305-324, Springer.

Saramito, P. & Wachs, A. (2016). Progress in Numerical Simulation of Yield Stress Fluid Flows. *Rheologica Acta*, 1-20.

Shu, C.W. & Osher, S. (1988). Efficient Implementation of Essentially Non-Oscillatory Shock-Capturing Schemes. *Journal of Computational Physics*, 77(2), 439-471.

Strand, S.A., Thakur, V., L'Heureux, J.S., Lacasse, S., Karlsrud, K., Nyheim, T., Aunaas, K., Ottesen, H., Gjelsvik, V., Fauskerud, O.A., Sandven, R. & Rosenquist, A. (2017). Runout of Landslides in Sensitive Clays. Second International Workshop on Landslides in Sensitive Clays. June 2017. *Springer Book Series Advances on Natural and Technological Hazards Research*. (In print)

Thakur, V., Degago, S., Oset, F., Dolva, B. & Aaboe, R. (2013). A New Approach to assess the Potential for Flow Slide in Sensitive Clays. *Proceeding of 18th International Conference on Soil Mechanics and Geotechnical Engineering.*

Thakur, V. & Degago, S.A. (2012). Quickness of Sensitive Clays. *Géotechnique Letters*, 2, 87-95.

Thakur, V., Gjelsvik, V., Fauskerud, O.A., Christensen, S., Oset, F., Viklund, M. & Strand, S.A. (2017). Recommended Practice for the Use of Strength Anisotropy Factors in Stability Calculations. 2nd International Workshop on Landslides in Sensitive Clays. *Natural Hazards book: Advances in Natural and Technological Hazards Research.* (In print)

Von Boetticher, A., Turowski, J., McArdell, B., Rickenmann, D. & Kirchner, J. (2015). Debris Inter Mixing-2.3: A Finite Volume Solver for Three Dimensional Debris Flow Simulations based on a Single Calibration Parameter-Part 1: Model Description. Geo Scientific Model Development Discussions, 8(8).

Proceedings of the 37th IAHR World Congress
August 13 – 18, 2017, Kuala Lumpur, Malaysia

ESTIMATION OF PEAK AND SURGE SHAPE OF DEBRIS FLOW USING CCTV CAMERA AND SEISMOMETER

SATORU MATSUDA[(1)], YOTARO NISHI[(2)], TSUYOSHI IKESHIMA[(3)], TAKAHIRO ITOH[(4)] & TAKAHISA MIZUYAMA[(5)]

[(1,4)] Research and Development Center, Nippon Koei Co., Ltd., Tsukuba, Japan.
a7148@n-koei.co.jp
[(2)] Nagoya Branch Office, Nippon Koei Co., Ltd., Nagoya, Japan.
[(3)] Nippon Koei Co., Ltd., Tokyo, Japan.
[(5)] National Graduate Institute for Policy Studies (GRIPS), Tokyo, Japan

ABSTRACT

Debris flow disaster had taken place at Nashi-zawa creek in Kiso River basin, Nagano Prefecture on 9th July in 2014 due to intensive rainfall of the typhoon Neoguri. A CCTV camera and a high sensitivity seismometer are installed along Nashi-zawa creek, a high sensitivity seismometer is at the ground about 104 m in depth, 10 m apart from the river center of Nashi-zawa creek and in around 500 m downstream reach from CCTV camera. Surges of debris flows are recorded by CCTV camera, though the camera is destroyed by those surges. Acceleration of the vibration recorded by seismometer took place two peak of acceleration when debris flows runoff is estimated by hearing survey to local residential persons. There is no research related to estimation of debris flows hydrograph using a high sensitivity seismometer, though there have been researches related to the estimation of peak discharge of debris flow using a high sensitivity seismometer. In present study, hydrograph is estimated using discharge by CCTV camera data and fitting curve of relations of between debris flow discharge and acceleration of vibration. Peak discharge extrapolated from peak acceleration of the vibration is estimated about 756 m^3/s. The estimation is similar to peak discharge (490.5 to 889.6 m^3/s) through free surface traces by field survey just after disaster. In addition, relationship between estimated peak discharge and total discharge with estimated hydrograph took almost same order value in comparison with previous data.

Keywords: Debris flow; peak discharge; hydrograph; vibration meter.

1 INTRODUCTION

In Kiso River basin, the sediment movements such as debris flows are called "Jya-nuke", in which "Jya" means debris flow movements seems to be snakes and "Nuke" means sediment runoff from torrents occurs suddenly. Sediment yielding is active and sediment is transported directly in the basin.

Debris flow disaster triggered by rainfall of the typhoon Neoguri took place at Nashi-zawa creek in Kiso River basin, Nagano Prefecture on 9th July in 2014. A part of debris flow run out downstream and into Kiso River, though a part of debris flow was caught by some sabo dam. Debris flow caused devastating damage to houses, railway tracks and Route 19 of national road. Tragically one person was killed and three injured (Hiramatsu et al., 2014).

After the debris flow disaster, estimation of magnitude of the debris flows in this disaster were carried out based on field survey of free surface traces. However, there are some discrepancies of the peak of debris flow discharge that is 490.5 to 899.6 m^3/s.

On the other hand, CCTV camera and high sensitivity seismometer have been installed along Nashi-zawa creek. Surges of debris flows were recorded by CCTV camera, though the camera was destroyed by those surges. High sensitivity seismometer were installed at 782 observatories in Japan in order to monitor weak ground shaking by micro-earthquakes. High sensitivity seismometer measured temporal changes of vibration of debris flow at Nagiso high sensitivity seismometer observatory. There were researches related to estimation of debris flows magnitude using a high sensitivity seismometer (Suwa, et al., 1999), however, there is no previous study related to estimation of temporal change of debris flows discharge that is hydrograph of debris flow.

In the present study, the peak of debris flow and the temporal change of debris flow that occurred at Nashi-zawa creek on 9th July in 2014 were estimated using the image of CCTV camera and the acceleration of the vibration measured by a high sensitivity seismometer.

.

2 STUDY SITE

Nashi-zawa creek, in the upper reach of Kiso River basin in Nagano Prefecture, Japan (Figure 1). Nashi-zawa basin is composed of Onashi-zawa (The area of basin, A=2.55 km^2, average bed slope=1/3.4) and Konashi-zawa (A=0.73 km^2, average bed slope=1/2.9). Geologically, this area consists of granite, and there

are many boulders around 2 m in diameter on the bed. Vegetation consists of Japanese cypress in the upstream and consists of planted Japanese cypress and Japanese cedar and broadleaf tree in the middle to downstream reach. Annual rainfall is about 2400 mm at Nagiso rainfall observation station (a part of AMeDAS; Automated Meteorological Data Acquisition System) which is nearest rainfall observing station of Nashi-zawa torrent. Annual rainfall depth in this area is larger than that of annual average in Japan.

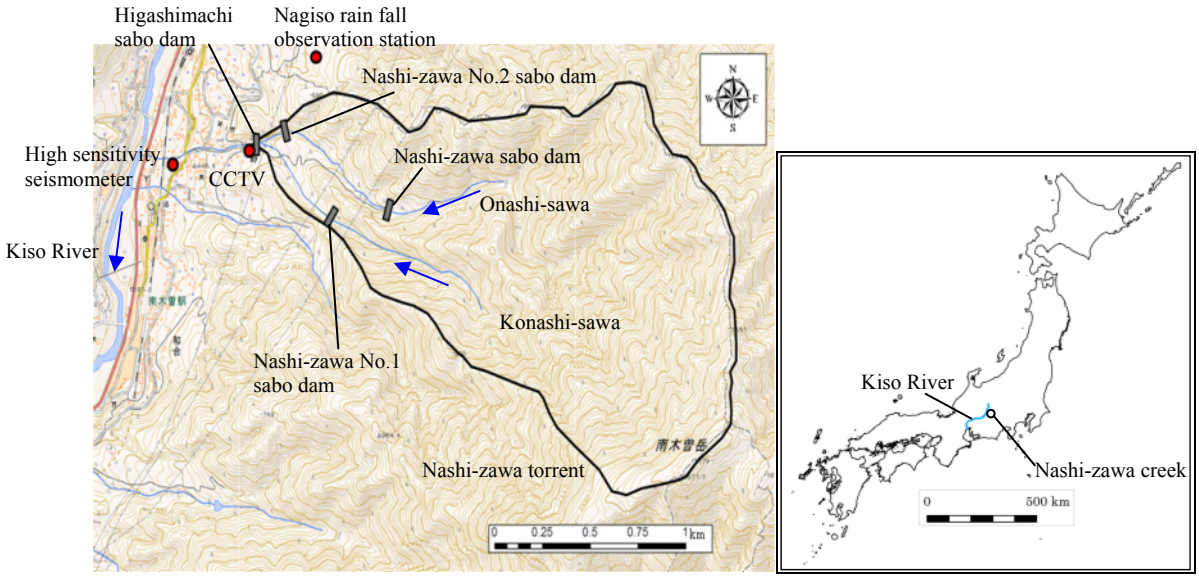

Figure 1. Location of Nashi-zawa torrent and some observatories.

Three sabo dams were installed in upper stream reach of Nashi-zawa basin. Nashi-zawa sabo dam and Nashi-zawa No.2 sabo dam were installed in Onashi-sawa, and Nashi-zawa No.1 sabo dam were installed in Konashi-sawa, respectively. Higashimachi sabo dam was installed in just downstream of confluence of Onashi-sawa and Konashi-sawa. The waterway was installed along downstream of Nashi-zawa from Higashimachi sabo dam. The angle of view of a CCTV is located and directed in spillway of Higashimachi sabo dam. A high sensitivity seismometer is located at the ground about 104 m in depth, 10 m apart from the river center of Nashi-zawa creek and in around 500 m downstream reach from a CCTV camera.

Debris flow disaster occurred at Nashi-zawa because of intensive rainfall. Accumulated rainfall depth is 93.5 mm (duration of rainfall: 6 hours), maximum rainfall intensity is 70.0 mm/h at Nagiso rainfall observation station. The return period of accumulated rainfall depth is 1.2 years in those two rainfalls on July 9th in 2014.

Figure 2 shows downstream of Nashi-zawa after debris flow events on July 11th in 2014. Many houses are at the downstream of Nashi-zawa. Some houses on the Nashi-zawa fan were destroyed by this debris flows.

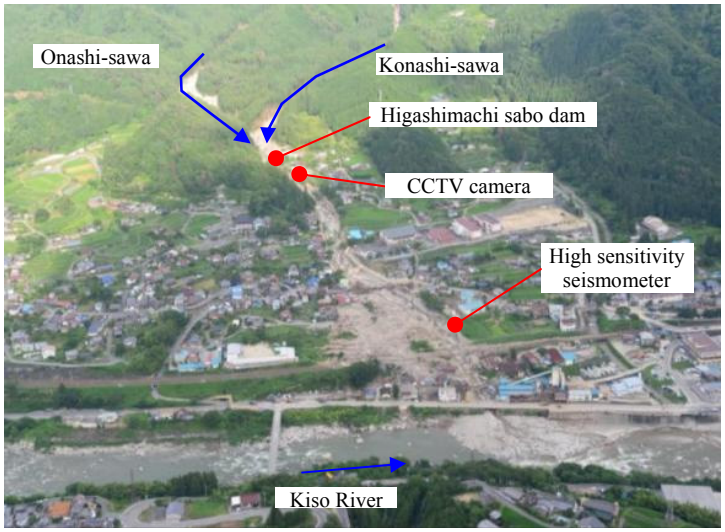

Figure 2. Aerial photo at Nashi-zawa basin on July 11th in 2014 (after debris flow events).

3 ESTIMATION OF DISCHARGE OF DEBRIS FLOW USING CCTV CAMERA DATA

3.1 Setting for photo analysis

Figure 3 shows a view from CCTV camera for a part of spillway of Higashimachi sabo dam during debris flow, scale is based on the plan view and front view of Higashimachi sabo dam (Figure 4), and is drawn in Figure 5. Water level and surface velocity were measured by image of CCTV camera in every two seconds in order to be clarified temporal change of discharge. However, the velocity based on photo analysis means surface velocity (Figure 5). Therefore average velocity was estimated from surface velocity. Surface velocity is corrected using the relationship that mean velocity is 3/5 times of surface value (Mizuyama et al., 1984; Takahashi, 2014).

Figure 3. Images of CCTV camera (Left: before occurrence of debris flow, Right: during debris flow).

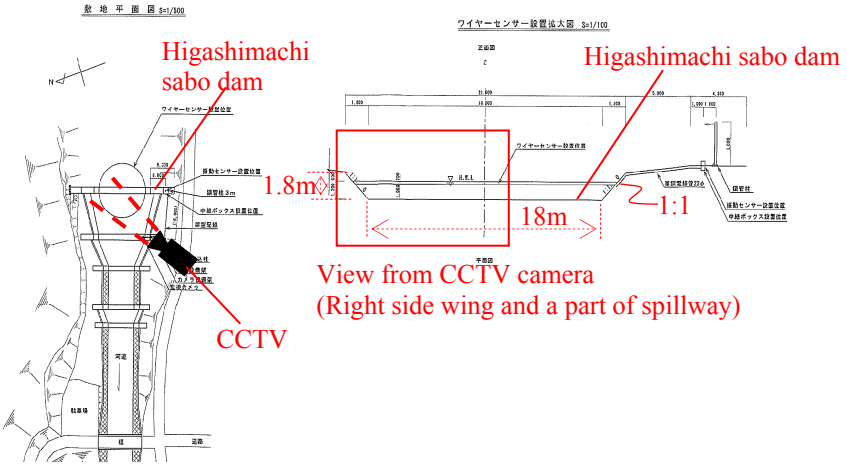

Figure 4. Location of CCTV camera and a view from CCTV camera (Left: plan view, Right: front view).

Figure 5. Photo analysis of surface velocity (during 1/15 seconds).

3.2 Photo analysis and the synchronizing with the high sensitivity seismometer data

Some testimonies by a hearing survey were conducted with local residents, it was determined that there were the two large scale of debris flows, however there was debris deposition in Kiso River before those surges. Figure 6 shows the acceleration of the vibration was measured by a high sensitivity seismometer calculated using root mean square (RMS) in every one second, and there are two peaks of acceleration at 17:43:27 (in the time unit as h: m: s) and 17:46:11 on 9th July in 2014. On the other hand, debris flow run off through the spillway of Higashimachi sabo dam was recorded by CCTV camera at 17:41:39. It seems that the acceleration of the vibration by the debris flow could occur after 17:41:39 and before remarkable peaks at 17:43:27 because of recorded time of CCTV camera and some testimonies. The peak time of acceleration and discharge by photo analysis are synchronized at the time when increasing and decreasing stage were overlapped. Temporal change of discharge by photo analysis shows increasing and decreasing stage after the discharge within the range of 1 to 2 m^3/s. The time when increasing and decreasing stage of discharge is similar temporal change of acceleration at 17:42:34(Figure 7). As a result, peak time of acceleration and discharge by photo analysis is estimated 17:42:34.

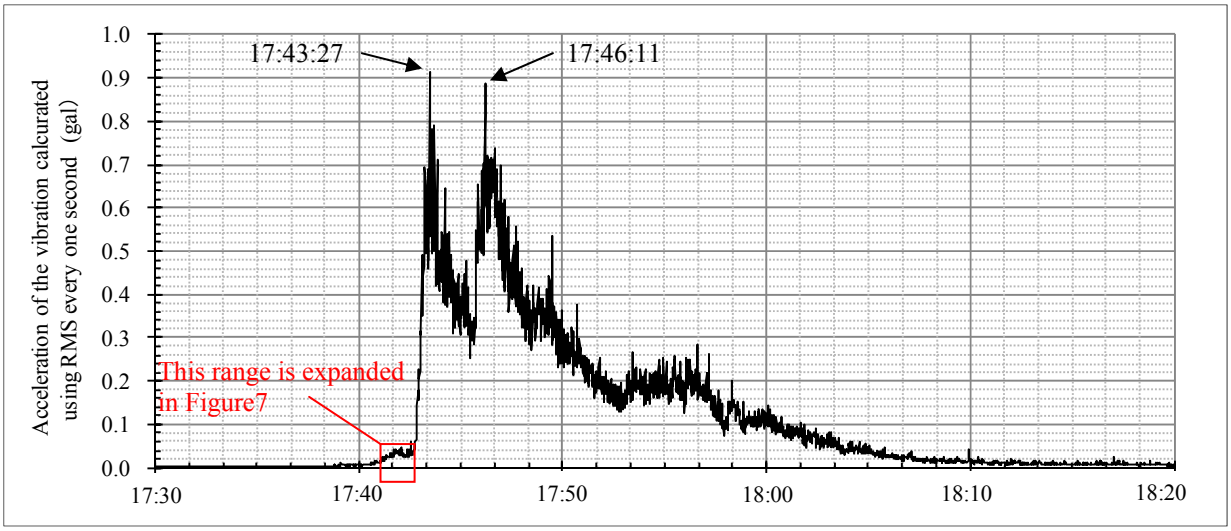

Figure 6. The acceleration of the vibration by a high sensitivity seismometer calculated using RMS.

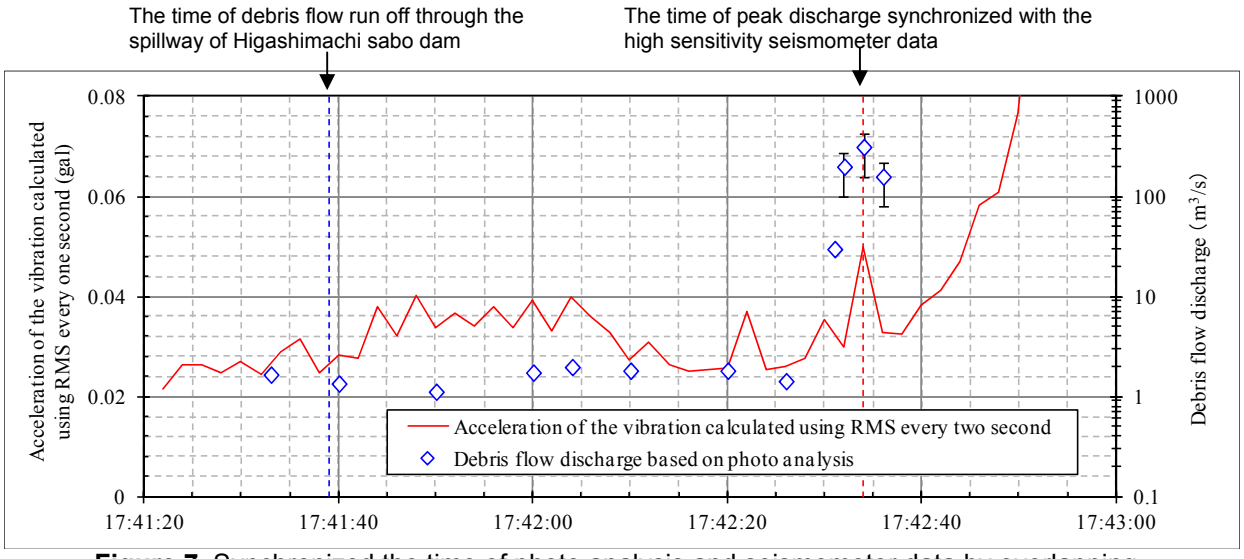

Figure 7. Synchronized the time of photo analysis and seismometer data by overlapping.

4 ESTIMATION OF PEAK DISCHARGE OF DEBRIS FLOW USING SEISMOMETER

Referring to Suwa et al. (1999), the relationships between discharge and acceleration of the vibration were evaluated for those peak values. In present study, the relationships between discharge and acceleration of the vibration using same method of Suwa et al. (1999) assuming that small peak of vibration shows the proportional relation with a same order. The impulse force by a round boulder collision using the boulder diameter, D, and mean velocity, V, yields the following equation.

$$P \propto D^2 \, V^{\frac{6}{5}} \quad [1]$$

The notation "$\propto$ " means the proportional relation with a same order. The empirical relationship (Suwa. et al., 1999) between the boulder diameter, D, and discharge, Q, is as follows.

$$D \propto Q^{\frac{3}{5}} \quad [2]$$

Applying Manning formula for mean velocity, V, and the depth, H, of the debris flow yields following relations in a prismatic channel.

$$V \propto H^{\frac{2}{3}} \quad [3]$$

Suwa et al. (1999) assume that the flow width, B, and H were proportional. On the other hand, in this study, flow width in the waterway of Nashi-zawa creek is constant because debris flow runs off inside of waterway, though over flow takes place a part of debris flow. Discharge was shown by using Eq. [3].

$$Q \propto BHV \propto BH^{\frac{3}{5}} = BV^{\frac{2}{5}} \quad [4]$$

Substituting Eq. [2] and Eq. [4] into Eq. [1] yields the following equation for constant flow width.

$$Q = P^{\frac{25}{42}} \quad [5]$$

Equation [5] can be re-written using the acceleration of vibration, G (gal), instead of P.

$$Q = a\,(G-b)^{\frac{25}{42}} \quad [6]$$

The form of is shown using Eq. [6] and extrapolative fitting curve is obtained by both estimated discharge analyzed by CCTV camera image and acceleration of the vibration calculated in every two seconds where a and b are empirical coefficient. Values of a and b were specified by the least-squares method to minimize deviation between fitting curve using Eq. [6] and estimated discharge analyzed by CCTV camera image where a is 850 ($m^3/s/gal^{(25/42)}$) and b is 0.025 (gal). Figure 9 shows estimated hydrograph of debris flow using the fitting curve. Peak discharge extrapolated from peak acceleration of the vibration is about 756 m^3/s (Figure 9 and Figure 10). The estimation was similar to peak discharge (490.5 m^3/s to 889.6 m^3/s) by free surface traces by field survey just after disaster.

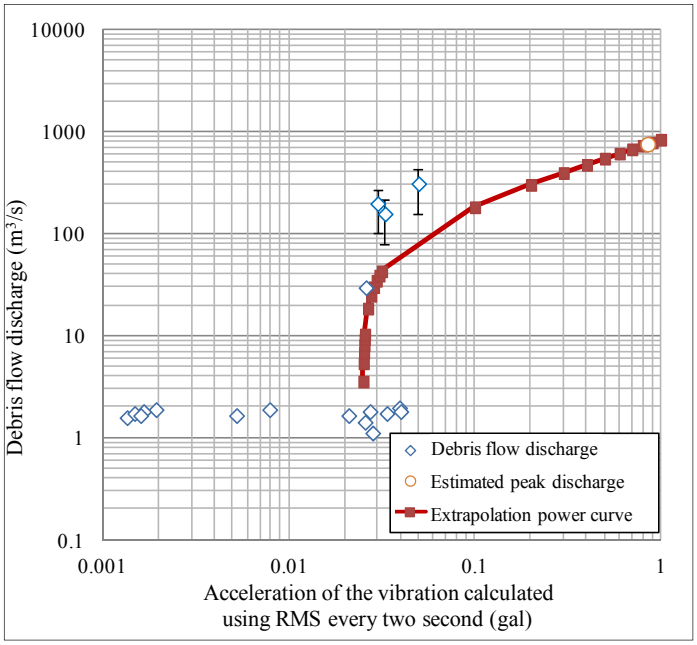

Figure 8. Relation between debris flow discharge and acceleration of the vibration calculated in every two seconds.

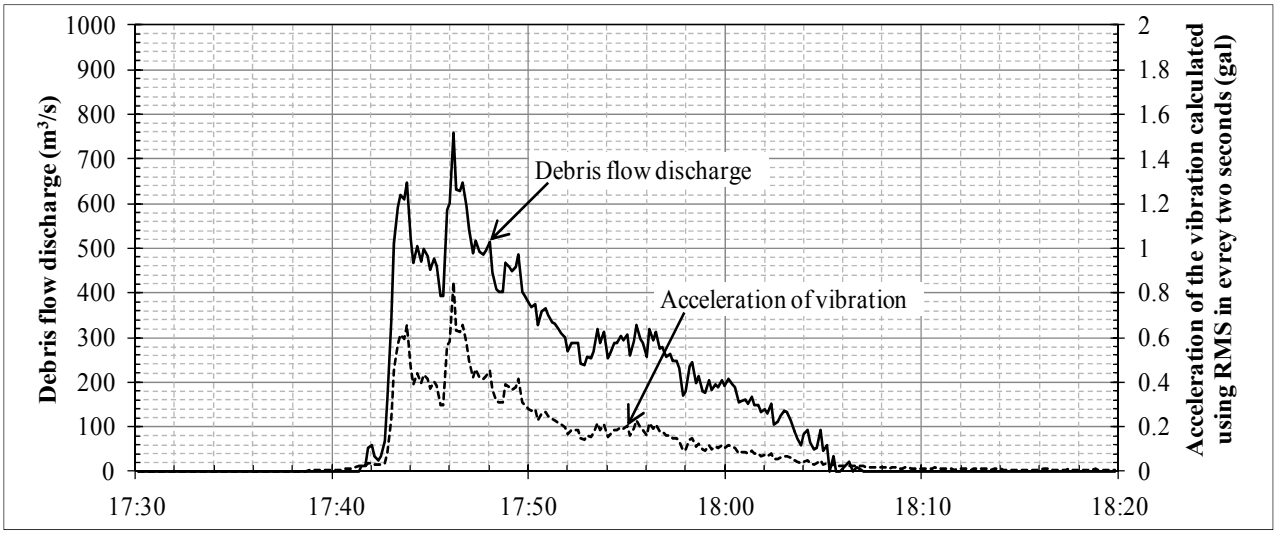

Figure 9. Estimated hydrograph of debris flow.

5 RELATIONSHIP BETWEEN ESTIMATED PEAK DISCHARGE AND TOTAL DISCHARGE OF DEBRIS FLOW

There is relation between the peak discharge of debris flow and total discharge (Ou et al., 1991; Rickenmann D., 1999), which were used to plan sabo dam. Relation between the peak discharge of debris flow and total discharge based on the result of present study are compared with relation of previous study. Total discharge at Higashimachi sabo dam was calculated using time integration estimated hydrograph. Relationship between estimated peak discharge and total discharge that is estimated by field survey carried out after the disaster took almost same order value in comparison with previous data (Ou et al., 1991). The plot in present study is on the regression line for data obtained in Kamikamihori-sawa creek (Figure 10).

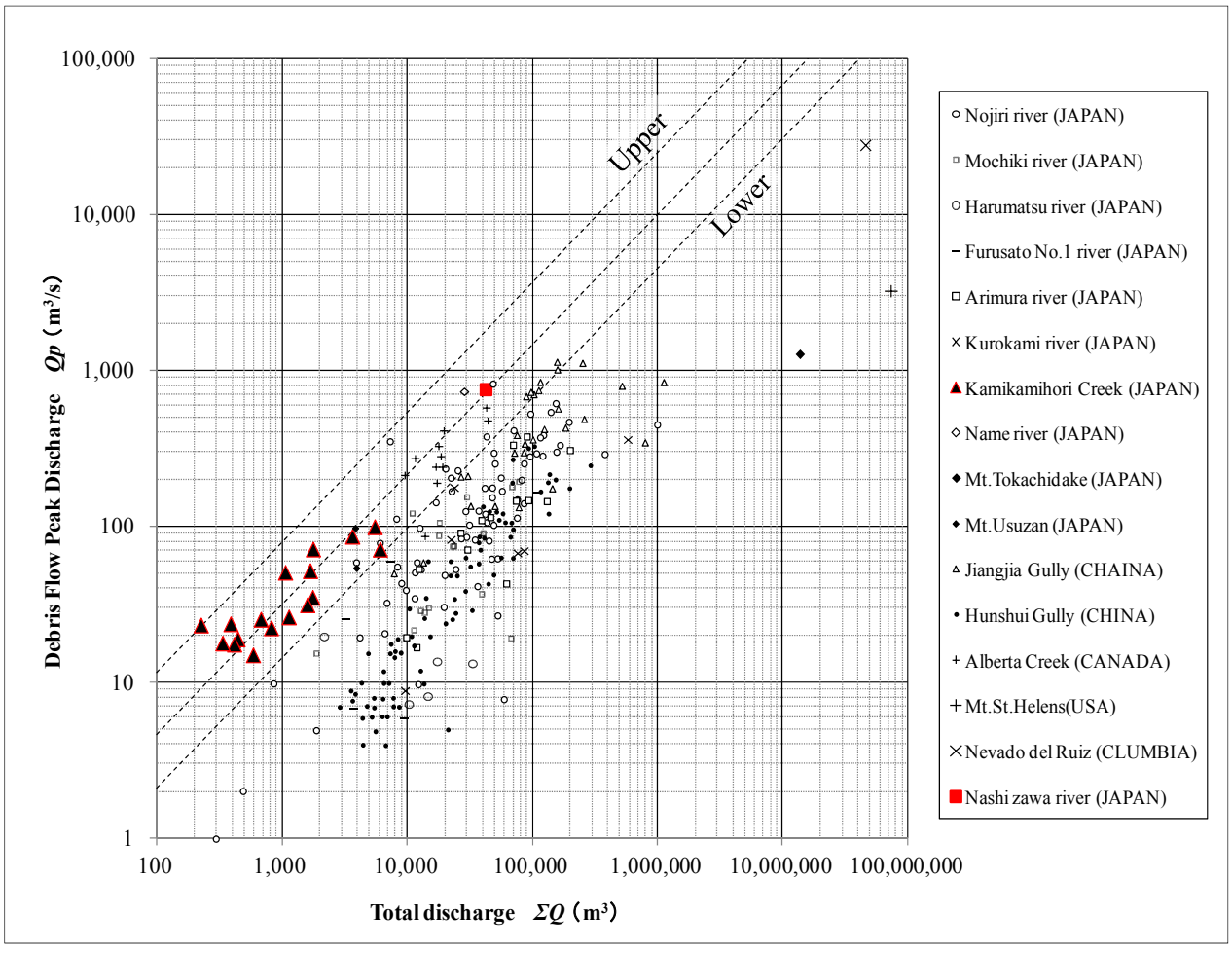

Figure 10. Relationship between estimated total discharge and peak discharge.

6 CONCLUSIONS

These results obtained in present study are summarized as follows:

(1) Estimated peak discharge of debris flow on 9th July in 2014 is similar to peak discharge by field survey, and the estimation is 756 m^3/s.

(2) Hydrograph of debris flow on 9th July in 2014 is estimated using temporal change of acceleration of vibration measured by high sensitivity seismometer and estimated peak discharge. One of method of estimation of hydrograph of debris flow is proposed.

(3) Relationship between estimated peak discharge and total discharge by estimations took almost same order value in comparison with previous data. The plot in present study is on the regression line for data obtained in Kamikamihori-sawa creek.

Present study showed one of method of estimation discharge and hydrograph of debris flows. Unfortunately, CCTV camera was destroyed by debris flow. Therefore, when draw the fitting curve of relation between discharge of debris flow and acceleration of vibration, there is small discharge data of debris flow. Especially, there is not plot when acceleration of vibration is over 0.05 gal. In Japan, a lot of observatories of high sensitivity seismometer are monitoring. If some observatories were installed near the creek such as Nagiso high sensitivity seismometer observatory, high sensitivity seismometer could record acceleration of vibration of debris flow and peak discharge and temporal change of discharge could be estimated by acceleration of vibration data.

ACKNOWLEDGEMENTS

Authors should be thankful for Tajimi office of Sabo and National Highway of Ministry of Land, Infrastructure, Transport and Tourism (MLIT) in Japan to give us useful comments and discussions.

REFERENCES

Hiramatsu, S., Fukuyama, T., Yamada, T., Ohsaka, O., Nakatani, K., Matsumoto, N., Fujimura, N., Kato, N., Shimada, T., Kubo, T., Matsuo, S., Nishio, Y. & Yoshino, K. (2014). Disaster Report on the Debris Flow Occurred in Nagiso, Nagano Prefecture. *Journal of the Japan Society of Erosion Control Engineering*, 67(4), 38-48. (In Japanese)

Ou, G., Kobashi, S. & Mizuyma, T. (1991). Prediction of Debris Flow Peak Discharge. *Journal of the Japan Society of Erosion Control Engineering*, 44(4), 24-29. (In Japanese)

Mizuyama, T. & Uehara, S. (1984). Observed Data of the Depth and Velocity of Debris Flow. *Journal of the Japan Society of Erosion Control Engineering*, 37(4), 23-26. (In Japanese)

Rickenmann, D. (1999). Empirical Relationships for Debris Flows. *Natural Hazards*, 19, 47-77.

Suwa, H., Yamakoshi, T. & Sato, K. (1999). Estimation of Debris Flow Discharge by Monitoring Ground Tremor. *Journal of the Japan Society of Erosion Control Engineering*, 52(2), 5-13. (In Japanese)

Takahashi, T. (2014). *Debris Flow -Mechanics, Prediction and Countermeasures-*. Taylor & Francis, 80.

SEDIMENT YIELD ESTIMATION ON A RESERVOIR IN SEVERELY ERODING RIVER BASIN

DEVARAJA PATHIRAGE CHANAKA LAKNATH [(1)] & THOTAPITIYA ARACHCHILLAGE JEEWANTHI GANGANI SIRISENA [(2)]

[(1)]Lanka Hydraulic Institute (LHI), Moratuwa, Sri Lanka,
chanaka.laknath@gmail.com

[(2)] UNESCO-IHE Institute for Water Education, Delft, The Netherlands,University of Twente, Enschede, The Netherlands
jeewanthisri@gmail.com

ABSTRACT

The sediment study in a basin is a prerequisite for any dam construction. In the context of field measurements inadequacy, the estimation of soil erosion in a given catchment is a tedious and complex process. Generally, all the eroded materials neither enter the stream system nor deposit in the reservoir. Hence, to estimate the soil loss from the catchment, sediment delivery ratio (SDR) was considered in order to estimate the sediment yield at the reservoir. Thus, sediment yield was estimated for a proposed dam across the Nyabarongo River in African continent. Accordingly, the applicability of two widely used empirical erosion models (i.e. *USLE & RUSLE*) was assessed for a reservoir in severely eroding river basin. Comparing with sediment yields estimated by other researchers for the watersheds in African continent as well as predicted global mean values, the estimated sediment yield values by USLE and RUSLE were recognized as reliable values for the proposed dam site.

Keywords: Nyabarongo River; soil erosion; empirical models; SDR; annual sediment yield.

1 INTRODUCTION

Each part of the world today faces some degrees of soil erosion. The on-site impacts of increasing soil loss are coupled with serious off-site impacts, which are related to the increasing of sediment mobilization and its delivery to drainage networks. The sediment study in a basin has become a major requirement before any dam construction. The estimation of soil erosion in a given catchment is a complex process as it depends on several factors like rainfall intensity, geology, topography, land use, drainage network, and sediment characteristics which are interrelated. There are no standard procedures established to quantify the erosion rates that can be generally used for any given watershed. The estimation of erosion rates are usually based on the empirical formulae that have been developed using data collected from specific geographical areas and hence, the application of those equations are generally limited to those areas represented in the base data.

This study presents the detailed analysis carried out to estimate the sediment yield for a proposed dam across the Nyabarongo River in Rwanda. Sediment yield is an essential parameter to determine the capacity requirement for dead storage of the reservoir.

The main objective of this study is to assess the possibility of using some of the widely used empirical formulae, (i.e. USLE (Wischmeier and Smith, 1978) and RUSLE (Renard et al., 1991)) for estimating soil erosion rates. Thus, it was attempted to derive a reasonable value of sediment yield for the proposed reservoir site by using the available limited field data.

2 STUDY AREA

Sediment study was carried out by focusing a potential dam site at a suitable location in the middle reaches of Nyabarongo River in Rwanda (Figure 1). The dam site is situated approximately 30 km northeast to Kigali, which is the capital and largest city of Rwanda. Rwanda has two principal basins called the Eastern Nile Basin (85 % of entire basin) and the Western Congo Basin (remaining 15 % of entire basin). These basins are divided by Congo-Nile alpine regions. The Nyabarongo and Akanyaru rivers of this study area belong to the Nile basin. The Nyabarongo and Akanyaru tributaries consist of a catchment area of over 16,000 km^2. The proposed dam could aim to cater for the municipal and irrigation water, power needs of the country and stabilization of Nyabarongo River for flood control (Laknath & Sirisena, 2016). Drainage area of the dam site is 6489 km^2 and most of the area is over 1400 m MSL. Generally, the Nyabarongo catchment has been recognized as a severely eroding one. These areas as senescent regions look like a shape of a typical meandering. Apart from that, high density turbidity currents occur throughout the year due to the severe disturbance of surface soil by the nature of soil and cultivation practices in upstream of the river. 78 % of total catchment areas are utilized for rain-fed agricultural crops. Based on the areal precipitation calculation for the dam site, February-May and September-December receive significantly high rainfall than that of other months

and the highest rainfall falls in April. According to the SCCE (2011), the average temperature in Rwanda is around 20 ^{0}C. The river flow regime follows the same rainfall pattern.

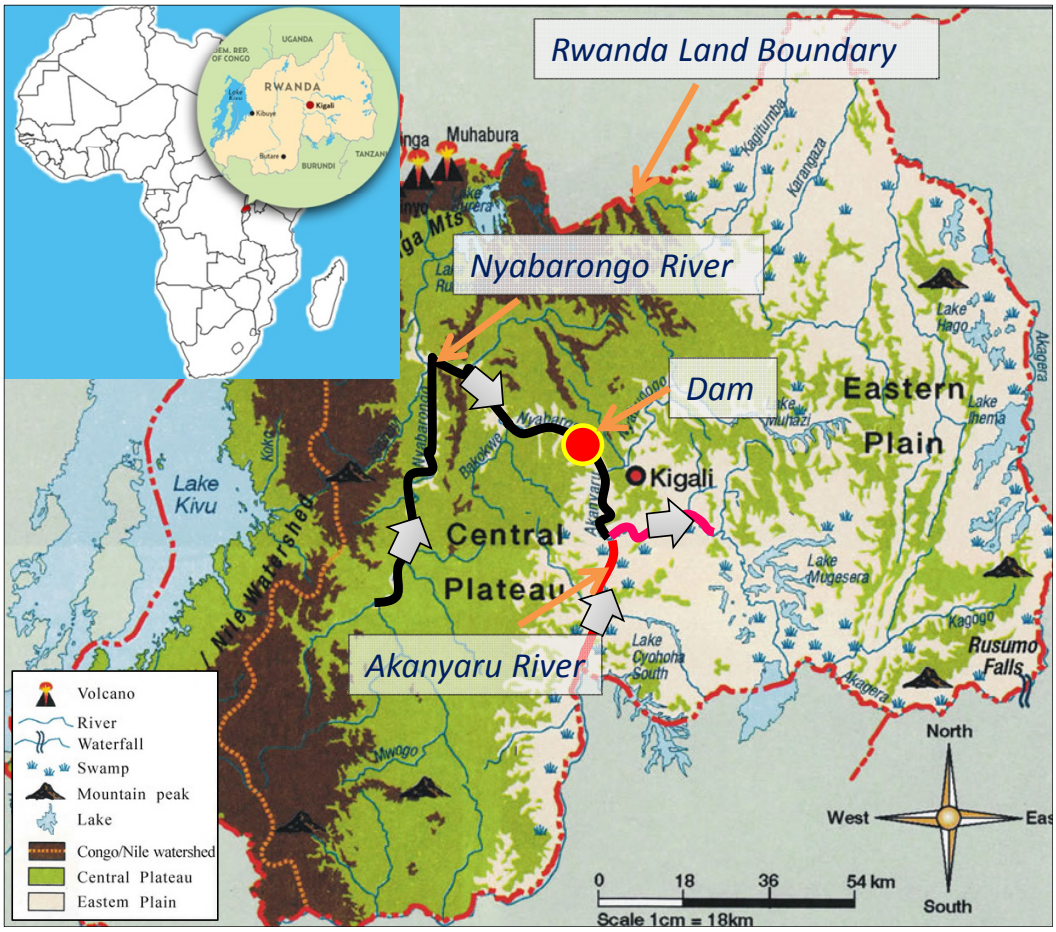

Figure 1. Rwanda: Physical features–Nyabarongo River and proposed dam site (Source: Laknath & Sirisena, 2016; Henninger, 2013).

3 EMPIRICAL MODELS: DEVELOPMENT FROM USLE TO RUSLE

The estimation of soil erosion rate in a given catchment is a complex process as it requires much field data. In addition, there are no standard procedures established to quantify the erosion rates that can be generally used for any given watershed. The estimation of erosion rates are usually based on the empirical formulae that have been developed using data collected from specific geographical areas and hence, the application of those equations are generally limited to those areas represented in the base data. However, the possibility of using some of the widely used empirical formulae to estimate the soil erosion rates was analyzed and a reasonable value of sediment yield to the proposed reservoir site was derived using the limited field data available for the present study. Most of the available formulae to quantify soil loss are usually developed empirically based on the field data collected from specific areas. An empirical relationship developed by Wischmeieir and Smith, namely Universal Soil-Loss Equation (USLE) (Wischmeier & Smith, 1965) is widely used to determine soil erosion in agricultural areas. It is a simple multiplicative model based on the mathematical formulation as given by Eq. [1];

$$E = R.K.L.S.C.P \qquad [1]$$

where, E is the mean annual soil loss (t/ac/yr), R is the rainfall erosivity index, K is the soil erodibility index, L is the slope length, S is the slope steepness, C is the crop factor, and P is the conservation practice factor. The factors of slope length (L) and slope steepness (S) are combined in a single factor, named as 'LS factor'. Though the USLE is simple to use and conceptually easy to understand, it gives erroneous results when estimating soil loss from a single storm event. This method has been generally recommended for the prediction of long-term average annual soil loss on individual erosion plots. Therefore, the application of USLE to estimate the average annual soil loss from the Nyabarongo catchment in the proposed study could be justified. However, the field sizes and slope gradients of the catchment in the present study area are somewhat higher than the values originally considered in the formulation of USLE. However, this has been

given special attention when preparing LS factors as the input parameters for the model, which is described in the subsequent sections. In addition, the erosion rates predicted by the model on the areas having steep gradients need to be interpreted with care.

USLE was modified in 1978. It is one of the most widely used and accepted empirical soil erosion models developed for sheet and rill erosion based on a large set of experimental data from agricultural plots. The USLE has been updated during last 30 to 40 years. Modified Universal Soil Loss Equation (MUSLE) (Williams, 1977), Areal Nonpoint Source Watershed Environmental Resources Simulation (ANSWERS) (Beasley, 1989), Unit Stream Power Based Erosion Deposition (USPED) (Mitasova et. al, 1996) and Revised Universal Soil Loss Equation (RUSLE) (Renard et. al, 1997) are based on the extensive review of USLE and its database, and are represented as an improvement of the former (Sirisena et.al, 2016).

The Nyabarongo catchment with 12 sub basins (*M1-M5* & *R1-R7*) was considered for the sediment analysis in this study (Figure 2).

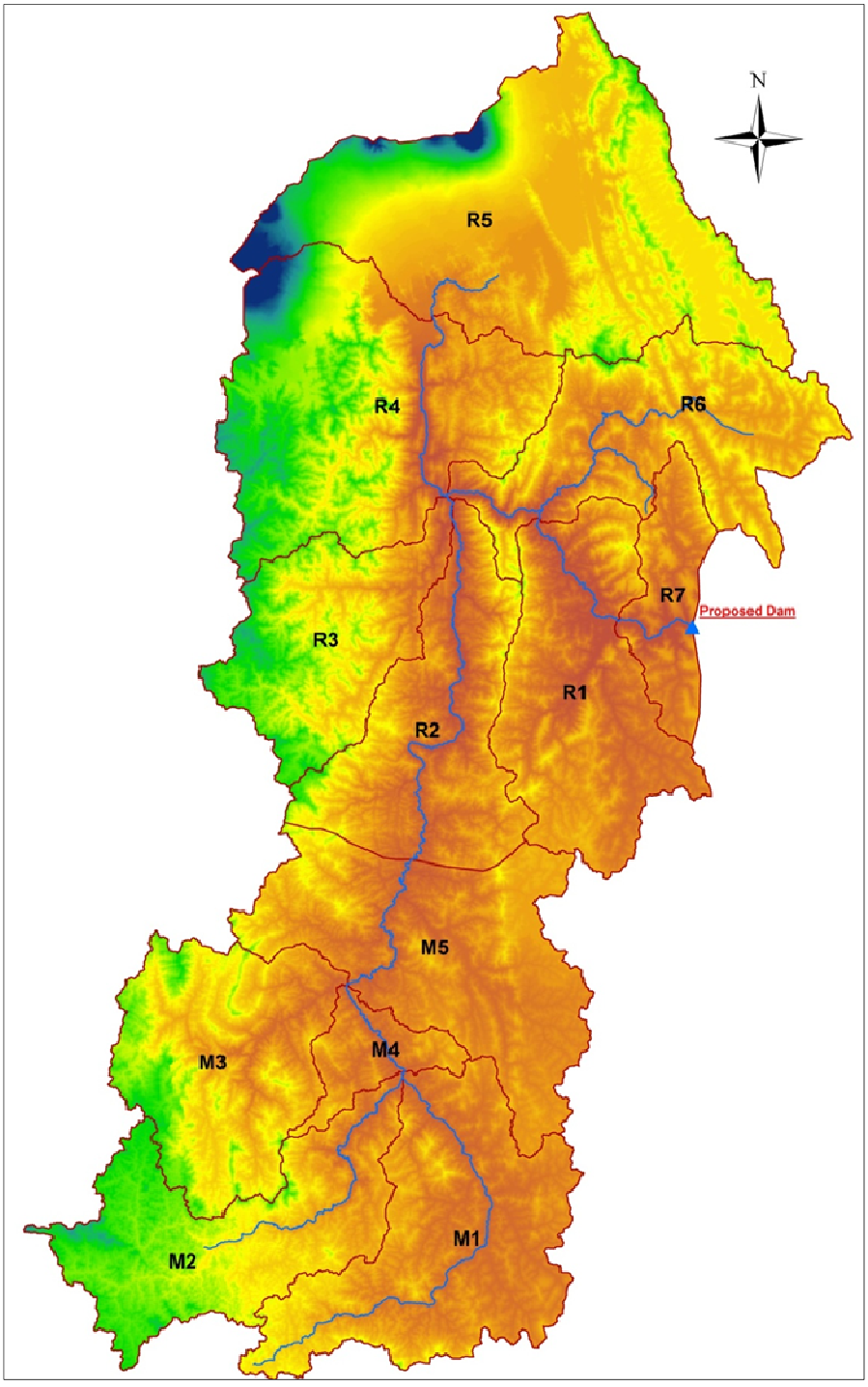

Figure 2. Nyabarongo catchment area of different sub basins.

4 UNIVERSAL SOIL LOSS EQUATION (USLE):SOIL EROSION ESTIMATION

4.1 Parameter estimation

4.1.1 Rainfall erosivity index (R)

The rainfall erosivity index represents the energy input that drives the sheet and rill erosion process, and it is a measure of the erosive force of a specific rainfall. From the origin of USLE, the *R* index is defined as mean annual EI_{30}/100, where *E* is the total storm kinetic energy and I_{30} is the maximum rainfall intensity in 30 minutes. Many different mathematical formulations can be found in literature for computing *R* factor. But, each of these formulae had been derived for specific catchment areas. As the availability of required field data in the Nyabarongo catchment is limited, it is not possible to select a suitable method to compute *R* factor directly or to carry out any sort of model calibration. Therefore, it is decided to apply different mathematical formulations as suggested by various researchers (*i.e.* Roose (1975), Morgan (1974), Foster et al (1981), Arnoldous (1980), Renald & Freimund (1994), Kassam et al (1992) and Singh et al (1981)). Then, an appropriate method was selected to compute *R* index for the Nyabarongo catchment based on the relative comparison of erosion rate predictions. By taking the average values of R factors identified using aforementioned methods for each sub basin, lower and upper limits of soil erosion rates were used for computation of USLE (see Table 1).

Table 1. Higher and lower values of R obtained from different methods specified in Section 4.1.1.

Sub Basin	Rainfall Erosivity Index (*R*)	
	Lower limit	Upper limit
M1	148.0	492.6
M2	171.0	540.9
M3	305.2	826.0
M4	175.8	540.5
M5	145.7	481.2
R1	167.9	527.1
R2	150.0	489.3
R3	148.5	480.6
R4	157.9	493.9
R5	139.6	460.2
R6	166.1	519.8
R7	174.9	543.3

4.1.2 Soil erodibility index (K)

Soil erodibility index expresses the soil susceptibility to the detachment and transport of soil particles (*i.e.* grains or crumbs), subjected to the amount and rate of runoff for a specific rainfall, as measured under the standard plot. This is defined as mean annual soil loss per unit of erosivity for a standard condition of bare soil, with no conservation practices. The K factor is rated on a scale from 0 to 1, where, 0 refers to soils with the least susceptibility to erosion and 1 refers to soils that are highly susceptible to erosion by water. The grain size distribution curves available at the dam sites, which have been identified in KOICA (2008), was the only information available regarding the soil properties in the Nyabarongo catchment. Based on the limited data, the soil properties in the catchment were taken as percentage of silt and very fine sand as 30 %, percentage of sand and organic matter as 10 % and 2 %, respectively, soil structure as fine granular, and permeability in the range of slow to moderate. Accordingly, the nomograph gives the soil erodibility index of the catchment is about 0.13 and it was decided to use the same value of K factors for all the sub basins, due to the non-availability of field data in each sub basins.

4.1.3 Slope Length (L) and Slope Steepness (S) factors

In the USLE, these two parameters are not treated separately. Instead, they are combined to a single parameter called ‘slope factor (LS)’ as both the L and S factors have a strong co-variation. The estimation of slope factor should be done accurately in order to represent the topographical features of the catchment by taking into account the complex slope assemblies. Accordingly, the catchment area of each sub basin was divided into different slope categories and the corresponding slope lengths and land areas covering each slope category were extracted from the digital maps of the Nyabarongo catchment. The LS factor represents a ratio of soil loss under given conditions to that of the "standard" slope steepness of 5 % and slope length of 22.13 m (72.6 ft) to give a value of 1.0. The appropriate value of LS factor can be estimated using the following equation (Morgan, 1986):

$$LS = \sqrt{\frac{L}{22.13}}\left[0.065 + 0.045S + 0.0065S^2\right] \qquad [2]$$

where, L is in m and S is in percent.

Table 2 gives the slope factors computed using Eq. [2] for different sub basins.

Table 2. LS factors computed for different sub basins.

Sub Basin	*LS* Factors									Weighted Avg. *LS* Factor
	Less than 5^0	5 – 10^0	10 – 15^0	15 – 20^0	20 – 25^0	25 – 30^0	30 – 35^0	35 – 40^0	Greater than 40^0	
M1	0.549	3.910	8.808	16.010	27.060	42.851	62.351	0.000	0.000	9.187
M2	0.531	3.410	7.708	15.149	25.807	41.243	54.472	78.626	79.543	10.018
M3	0.542	3.276	7.491	14.463	25.246	39.436	55.254	55.314	72.762	13.747
M4	0.560	3.568	8.448	16.286	27.073	45.047	64.323	0.000	0.000	10.649
M5	0.586	4.074	8.476	15.755	26.811	42.636	65.114	0.000	0.000	8.825
R1	0.543	3.748	8.572	15.338	25.413	41.345	60.976	91.137	0.000	12.734
R2	0.550	3.221	7.592	14.959	25.545	41.064	60.937	88.716	0.000	14.322
R3	0.573	3.116	6.856	14.129	26.064	42.300	60.945	82.746	0.000	15.630
R4	1.037	3.414	7.341	14.420	25.620	40.962	62.154	83.827	94.830	14.989
R5	1.353	4.031	7.712	14.045	24.708	41.968	64.030	82.376	79.813	10.132
R6	0.606	3.274	7.145	13.655	24.352	41.820	61.450	88.812	93.021	18.981
R7	0.577	3.679	8.267	14.952	25.891	42.158	60.705	91.529	0.000	14.981

It could be noted that the slope factors calculated for steeper slope areas are somewhat higher as compared to those computed for milder slopes. The LS factors proposed for the USLE were derived based on the field experiments, where the maximum slope angle used in the field tests is about 20 percent and is approximately equal to a slope angle of 12^0. However, the LS factors for slopes beyond this steepness have not been analyzed. Therefore, the application of Eq. [2] to estimate the slope factors for catchment areas with steep slopes has to be done with care, as the extrapolation of Eq. [2] to a region where the validity of the equation has not been verified. This may result in high erosion rates that are very far from the actual soil loss.

In addition, the land areas corresponding to steep slopes (say above 25^0 or 30^0) are relatively small and hence, the contribution of soil erosion in steep areas to the final erosion rate of the catchment appears to be small. Considering all these aspects, it was decided to use Eq. [2] to compute LS factors for different sub basins up to the slope angle of 15^0 maximum. These maximum LS values were used for all other steeper slopes in the catchment so as not to overestimate the slope factors in steep areas beyond realistic values. The updated LS factors for each basin in the Nyabarongo catchment are tabulated in Table 3.

Table 3. Updated LS factors for different sub basins.

Sub Basin	*LS*Factors				Weighted Avg. *LS* factors
	Less than 5^0	5 – 10^0	10 – 15^0	Greater than 15^0	
M1	0.549	3.910	8.808	8.808	6.169
M2	0.531	3.410	7.708	7.708	5.809
M3	0.542	3.276	7.491	7.491	6.346
M4	0.560	3.568	8.448	8.448	6.430
M5	0.586	4.074	8.476	8.476	5.693
R1	0.543	3.748	8.572	8.572	6.679
R2	0.550	3.221	7.592	7.592	6.465
R3	0.573	3.116	6.856	6.856	6.064
R4	1.037	3.414	7.341	7.341	5.959
R5	1.353	4.031	7.712	7.712	4.635
R6	0.606	3.274	7.145	7.145	6.114
R7	0.577	3.679	8.267	8.267	6.745
Weighted average *LS* factor (mean value)					**6.092**

4.1.4 Conservation practice factor (P)

This parameter gives the ratio of soil loss where any soil conservation practices, such as contouring, contour strip-cropping, etc. are adopted to that of no such conservation practices. With no conservation measures, the value of P is 1.0. In this study, the P-factor is taken as 1.0.

4.2 Sediment yield

The *Sediment Delivery Ratio* (SDR) is a widely used parameter to quantify the amount of sediments that reach at a given point in the watershed, which is also known as '*Sediment Yield'*, once the gross amount of soil erosion from the catchment is estimated. The sediment delivery ratio is defined as the ratio between sediment yield and the mean annual soil loss computed using different empirical methods. SDR depends on many factors, such as drainage area, topography, soil texture, and land use. There are no generalized SDR values defined for any given catchments. Hence, various methods suggested by researchers were compared here in order to select the suitable SDR values for different sub basins in the Nyabarongo catchment. The sub basins are combined into three main groups, depending on their locations to increase the basin area. The corresponding SDR values were computed and are presented in Table 4. It can be noted that SDR values of these basin groups are slightly smaller than the previous values and are more realistic for the given catchment areas.

Table 4. Sediment delivery ratio (%) computed by combining several sub basins.

Sub Basins	Area (km^2)	SDR (%)				
		Renfro (1975)	Vanoni (1975)	USDA SCS (1979)	Average of all three methods	Average of Renfro and USDA SCS
M1 – M4	1791.8	21	19	25	22	23
M5 & R1 – R3	2088.3	21	18	24	21	23
R4 – R7	2609.1	20	18	24	21	22

The sediment delivery ratios computed for different sub basins are used to convert the mean annual soil erosion rates estimated by USLE to the total sediment yield (ton/yr) at the proposed reservoir site, as tabulated in Table 5. Figure 3 shows the contribution to annual sediment yield from different sub basins for lower and upper limits of soil erosion rates.

Table 5. Annual sediment yield computed using USLE.

Sub Basin	Area (km^2)	Mean Annual Soil Loss (tons)		Sediment Yield (ton/yr)	
		Lower Limit	Upper Limit	Lower Limit	Upper Limit
M1	632.5	4,201,432	13,983,955	966,329	3,216,310
M2	529.9	3,058,316	9,673,937	703,413	2,225,006
M3	511.0	8,634,487	23,368,565	1,985,932	5,374,770
M4	118.4	1,170,269	3,598,011	269,162	827,542
M5	635.6	4,603,211	15,202,916	1,058,738	3,496,671
R1	539.8	5,290,199	16,607,885	1,216,746	3,819,814
R2	503.1	4,265,109	13,912,787	980,975	3,199,941
R3	409.9	3,221,533	10,426,051	708,737	2,293,731
R4	803.4	6,602,523	20,652,224	1,452,555	4,543,489
R5	1081.7	3,050,161	10,055,043	671,035	2,212,110
R6	540.0	3,191,521	9,987,674	734,050	2,297,165
R7	183.9	1,894,937	5,886,331	416,886	1,294,993
Total	**6489**	**49,183,698**	**153,355,380**	**11,164,559**	**34,801,541**

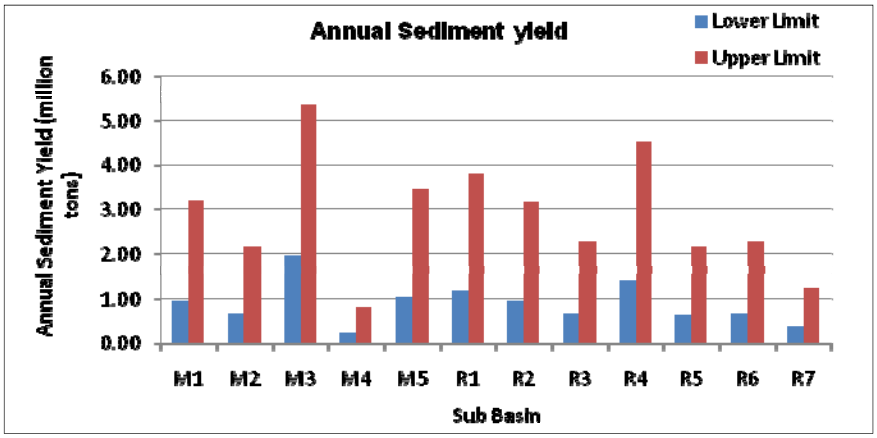

Figure 3. The contribution to annual sediment yield from different sub basins.

It can be noted that the sediment yield of the proposed reservoir is in the range of 11.2 to 34.8 million tons per year. The area-specific sediment yield varies between 17.2 to 53.7 ton/ha/yr with a mean value of 35.5 ton/ha/yr. Based on the soil erosion studies carried out in African continent, Abwubi et al., (2009) stated that area-specific sediment yields in Tigray and Ethiopia were in the range of 3 to 49 ton/ha/yr with a mean value of 19 ton/ha/yr. It is also reported that the sediment yield of a global mean value is around 15 ton/ha/yr whilst in African continent is about 9 ton/ha/yr. Comparing with the present study, the sediment yield computed at lower limit appears to be more reasonable; however this needs further analysis, which is discussed in the following section (*Section 5*).

5 REVISED UNIVERSAL SOIL LOSS EQUATION (RUSLE):SOIL EROSION ESTIMATION

In order to solve several drawbacks in USLE, certain amendments were incorporated to this method while retaining the basic structure of the Eq.1 (Renard et al., 1991).The revised equation, RUSLE has the same coefficients used in USLE, but several improvements were made in the estimation of R, K and LS factors. The K factor has been made time varying and corrections were made to rock fragments in the soil profile. The slope factor (LS) has been revised to account for the relation between rill and inter-rill erosion. The C factor has also been improved to represent a continuous function of prior land use, surface cover in detail and soil moisture, etc. However, due to the non-availability of sufficient field data, the full advantage of these updates in RUSLE could not be achieved. But, we could update only the estimation of LS factor as suggested in RUSLE. The values used for other model parameters, such as R, K, C and P factors were same as the values used for USLE. The mean annual soil loss computed using RUSLE for different sub basins are tabulated in Table 6. By using the same SDR values derived for different sub basins, the sediment yield to the proposed reservoir site was calculated, as shown in the same table. Figure 4 shows the contribution to annual sediment yield from different sub basins for lower and upper limits of soil erosion rates computed using RUSLE.

Table 6. Mean annual soil loss and sediment yield computed using RUSLE.

Sub Basin	Area (km^2)	Mean Annual Soil Loss (tons)		Sediment Yield (ton/yr)	
		Lower Limit	Upper Limit	Lower Limit	Upper Limit
M1	632.5	4,239,219	14,109,723	847,844	2,821,945
M2	529.9	3,254,912	10,295,799	650,982	2,059,160
M3	511.0	9,629,095	26,060,395	1,925,819	5,212,079
M4	118.4	1,254,655	3,857,459	276,024	848,641
M5	635.6	4,725,904	15,608,135	1,039,699	3,433,790
R1	539.8	5,530,908	17,363,560	1,216,800	3,819,983
R2	503.1	4,874,417	15,900,349	1,072,372	3,498,077
R3	409.9	3,876,586	12,546,043	852,849	2,760,129
R4	803.4	7,671,822	23,996,916	1,764,519	5,519,291
R5	1081.7	3,274,825	10,795,661	753,210	2,483,002
R6	540.0	3,664,347	11,467,355	842,800	2,637,492
R7	183.9	2,053,621	6,379,259	472,333	1,467,230
Total	**6489**	**54,050,312**	**168,380,655**	**11,715,250**	**36,560,818**

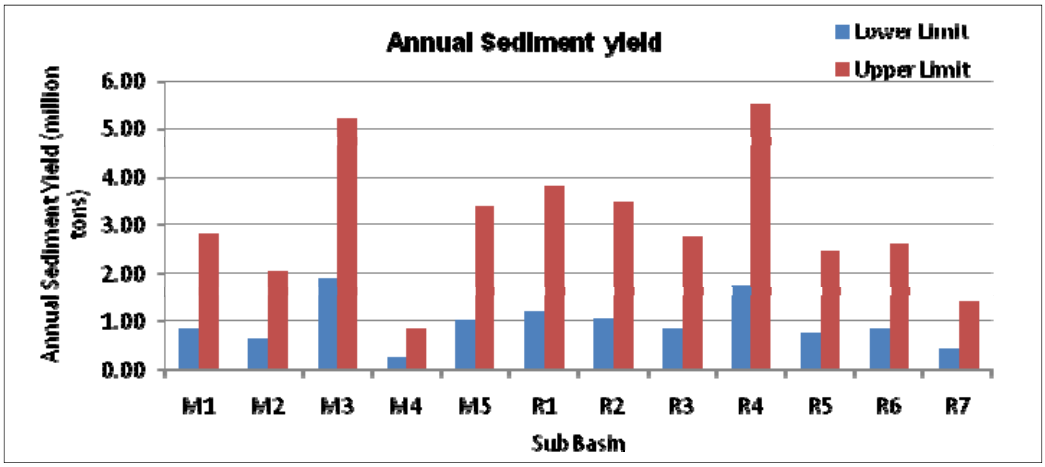

Figure 4. The contribution to annual sediment yield from different sub basins.

The results show that the sediment yield to the proposed reservoir is in the range of 11.7 to 36.6 million tons per year, which is nearly the same as the values obtained using USLE. The area-specific sediment yield varies between 18.1 and 56.4 ton/ha/yr with a mean value of 37.3 ton/ha/yr. The proposed dam site and turbidity of river due to erosion are given in Figure 5.

6 SUMMARY OF SEDIMENT YIELD COMPUTATION

Table 7 compares the annual sediment yield estimated to the proposed reservoir site using USLE and RUSLE models.

Table 7. Summary of annual sediment yield (SY).

Sub Basin	USLE		RUSLE	
	Lower Limit	Upper Limit	Lower Limit	Upper Limit
M1	966,329	3,216,310	847,844	2,821,945
M2	703,413	2,225,006	650,982	2,059,160
M3	1,985,932	5,374,770	1,925,819	5,212,079
M4	269,162	827,542	276,024	848,641
M5	1,058,738	3,496,671	1,039,699	3,433,790
R1	1,216,746	3,819,814	1,216,800	3,819,983
R2	980,975	3,199,941	1,072,372	3,498,077
R3	708,737	2,293,731	852,849	2,760,129
R4	1,452,555	4,543,489	1,764,519	5,519,291
R5	671,035	2,212,110	753,210	2,483,002
R6	734,050	2,297,165	842,800	2,637,492
R7	416,886	1,294,993	472,333	1,467,230
Total *SY* (tons/yr)	**11,164,559**	**34,801,541**	**11,715,250**	**36,560,818**
Area specific SY (tons/ha/ yr)	**17.5**	**53.7**	**18.1**	**56.4**

As stated previously, the area-specific sediment yields estimated for the watersheds in Tigray and Ethiopia in African continent were reported to be in the range of 3 to 49 ton/ha/yr with a mean value of 19 ton/ha/yr (Abwubi et al., 2009). It has also been reported that the sediment yield of a global mean value is predicted to be around 15 ton/ha/yr whilst in African continent is about 9 ton/ha/yr. According to the previous study carried out by KOICA (2008) for the same catchment area, it has been derived that the annual sediment yield of a watershed area of 5,750 km^2 is around 7.5 million tons, which corresponds to the specific sediment yield of 13 tons/ha/yr.

Considering the sediment yields of the proposed reservoir site using different methods with the values generally predicted in this region, it is decided to drop the higher values of sediment yields obtained using USLE and RUSLE as the upper limit, so as not to overestimate the sediment yield to the proposed reservoir. Therefore, the sediment yield to the proposed reservoir site is finally taken as the average of the remaining values and this value was computed as 11.44 million tons. The specific sediment yield of the catchment was 17.8 tons/ha/yr.

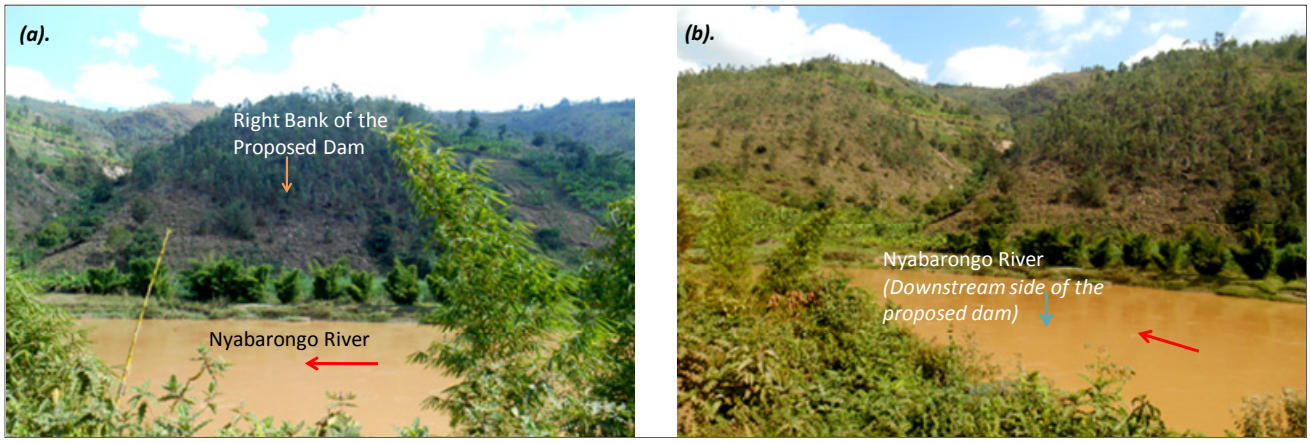

Figure 5. (a) Proposed dam location; (b) High turbidity of river water due to weathering of rocks and heavy erosion in the upstream catchment (Source: Filed Visit, July 2014)

7 CONCLUSIONS

In this study, the sediment yield was estimated for a proposed dam across the Nyabarongo River in Rwanda in African continent. First, to estimate the soil loss from the catchment, Sediment Delivery Ratio (SDR) was considered in order to estimate the sediment yield at the reservoir. Generally, in the context of field measurements inadequacy, the estimation of soil erosion in a given catchment is a complex processes. Hence, by using two widely used empirical erosion models (*i.e. USLE & RUSLE*), the sediment yield at the proposed reservoir in severely eroding river basin was estimated and assessed.

Though the USLE is simple to use and conceptually easy to understand, it gives erroneous results when estimating soil loss from a single storm event. This method has been generally recommended for the prediction of long-term average annual soil loss on individual erosion plots. Therefore, the application of USLE to estimate the average annual soil loss from the Nyabarongo catchment in the proposed study was justified. However, the field sizes and slope gradients of the catchment in the present study area are somewhat higher than the values originally considered in the formulation of USLE. This has been given special attention when preparing LS factors as the input parameters for the model. The revised equation, RUSLE has the same coefficients used in USLE, but several improvements were made in the estimation of R, K and LS factors. By using the same SDR values derived for different sub basins, sediment yield to the proposed reservoir site was calculated by using RUSLE. Generally, RUSLE model gave higher values than the USLE model. Thus, the sediment yield to the proposed reservoir site was computed as 11.44 million tons. The specific sediment yield of the catchment was 17.8 tons/ha/yr. Comparing with sediment yields estimated by other researchers for the watersheds in African continent as well as predicted global mean values, the estimated sediment yield values by USLE and RUSLE were justified.

REFERENCES

Adwubi, A., Amegashie, B.K., Agyare, W.A, Tamene, L., Odai, S.N. & Quansah, C. (2009). Assessing Sediment Inputs to Small Reservoirs in Upper East Region, Ghana.Lakes & Reservoirs. *Research and Management*, 14(4), 279-287.

Arnoldus, H.M.J. (1980).*An Approximation of The Rainfall Factor in The Universal Soil Loss Equation*. In: De Boodt, M. and Gabriels, D. (Eds) Assessment of Erosion. John Wiley and Sons, Chichester, England, 127-132.

Beasley, D.B. & Thomas, D.L. (1989). *Applications of Water Quality Models for Agricultural and Forested Watersheds*, Southern Cooperative Series Bulletin, No. 338.

Foster, G.R., McCool, D.K., Renard, K.G. & Moldenhauer, W.C. (1981). Conversion of Universal Soil Loss Equation to SI Metric Units.*Journal of Soil and Water Conservation*, 36(6), 355-359.

Henninger, S.M. (2013). Does the global warming modify the local Rwanda climate. *Natural Science*, 5(1A), 124-129.

Kassam, A.H., Velthuizen, H.T., Mitchell, A.J.B., Fischer, G.W. & Shah, M.M. (1992). *Agro-Ecological Land Resources Assessment for Agricultural Development planning.* Land and Water Development Division Food and Agriculture Organization of the United Nations and International Institute for Applied Systems Analysis.

KOICA (2008).*Feasibility Study of Water Resources Development in Nyabarango River in Rwanda, Final Report*, Korea International Cooperation Agency, Korea Water Resources Cooperation.

Laknath, D.P.C. & Sirisena, T.A.J.G. (2016). Application of Hydrological Study Methodologies Used in African Context for Water Security in Asian Countries. *Conference Proceedings in International conference on Water security and Climate Change: Challenge and Opportunities in Asia,* Bangkok, Thailand.

Mitasova, H. (1996). *GIS Tool for Erosion/Deposition Modelling and Multidimensional Visualization. Part III: Process based erosion simulation.* Geographic modelling system laboratory, University of Illinois: Illinois.

Morgan, R.P.C. (1986).*Soil Erosion and Conservation*. Longman Group Limited, United Kingdom.

Renard, K.G., Foster, G.R., Weesies, G.A. & Portor, J.P. (1991). Revised Universal Soil Loss Equation, *Journal of Soil and Water Conservation*, 30-33.

Renard, K.G. & Freimund, J.R. (1994). Using Monthly Precipitation Data to Estimate the R-Factor in the Revised USLE. *Journal of Hydrology*, 157, 287-306.

Renfro, G.W. (1975). *Use of Erosion Equations and Sediment Delivery Ratio's for Predicting Sediment Yields and Sources*. U.S. Department of Agricultural Research Services Publication, S-40, 33-45.

Roose, E.J. (1975). *Use of the Universal Soil Loss Equation to Predict Erosion in West Africa. In: Soil Erosion, Prediction and control*. Soil and Water Conservation Society Ankeny, IA, 60-74.

SCEE (2011). *Rwanda's Climate: Observations and Projections, Smith School of Enterprise and the Environment*. University of Oxford, UK.

Singh, G., Babu, R. & Chandra, S. (1981). *Soil Loss Prediction Research in India*. Central Soil and Water Conservation Research and Training Institute.

Sirisena, T.A.J.G., Subasinghe, S.M.C.K., Dharmadasa, V., Senarathne, D.E.N., Ranasinghe, D.P.L., Nandalal, K.D.W. & Raveenthiran, K. (2016). Hydrological Investigations to Facilitate the Design of Demodara Dam. *E-Proceedings of 20th Congress of Asia Pacific Division of IAHR, IAHRAPD/paper/3D006, 1-9.*

USDA-SCS (1979). *Hydrology.* National Engineering Hand Book, Section 4. United States Department of Agriculture Soil Conservation Service

Vanoni, V.A. (1975). *Sedimentation Engineering*, ASCE Task Committee for the Preparation of the Manual on Sedimentation of the Sedimentation Committee of the Hydraulics Division.

Williams, J.R. & Berndt, H.D. (1977). *Sediment Yield Prediction Based on Watershed Hydrology*, Transactions of the ASAE, 1100 – 1104.

Wischmeier, W.H. & Smith, D.D. (1965).*Predicting Rainfall-Erosion Losses from Cropland East of the Rocky Mountains*. Agricultural Handbook No. 282, U.S. Department of Agricultural, Washington DC.

Wischmeier, W.H. & Smith, D.D. (1978).*Predicting Rainfall Erosion Losses: A Guide to Conservation Planning*. Agriculture, Handbook No. 537, U.S. Department of Agricultural, Washington DC.

FIELD EXPERIMENT OF BEDLOAD TRANSPORT RATE MEASUREMENT AT SEDIMENT BYPASS TUNNEL

TAKAHIRO KOSHIBA[(1)], SAMEH AHMED KANTOUSH[(2)] & TETSUYA SUMI[(3)]

[(1,2,3)] Disaster Prevention Research Institute, Kyoto University, Japan
koshiba.takahiro.47v@st.kyoto-u.ac.jp, kantoush.samehahmed.2n@kyoto-u.ac.jp, sumi.tetsuya.2s@kyoto-u.ac.jp

ABSTRACT

In order to prevent reservoir sedimentation, Sediment Bypass Tunnels (SBTs) to reduce the sediment inflow by diverting sediments around a dam is an attractive solution. However, SBTs are prone to severe invert abrasion caused by high sediment flux. To estimate abrasion damage, it is important to establish a sediment transport measurement system because abrasion prediction model is basically depending on actual bedload flux in the SBT. For this purpose, impact plates, one surrogate bedload monitoring system, have been installed at the outlet of the Koshibu SBT. Field-based calibration test where 10 cases of experiments, varying grain size, water discharge, and sediment volume, were conducted with the sediment artificially damped inside the tunnel and flushed down with clean water from the inlet of SBT. Several recorded data showed that the impact plates worked well by indicating the timing of sediment passage, and showing a good correlation with the grain size. In particular, the number of waveform spikes possess the characteristics of transported particle size. In this study, the spatial distribution of transported particle size is computed by using the number of spikes. Finally, it is found that the sediment with large grain size flows faster than the smaller particles. Furthermore, another finding is that tunnel curve affects the spanwise sediment concentration of the bypassed flow is in line with the past experience observed through SBTs operation in Japan and Switzerland.

Keywords: Sediment Bypass Tunnels (SBTs); reservoir sedimentation; geophone; hydrophone; sediment transport.

1 INTRODUCTION

With the nature of reservoirs impounded by dam, they are inevitable to store sediment from the upstream reach likewise water. Reservoir sedimentation has been one of the topical issues affecting sustainable use of dams not only in Japan but worldwide. Various problems are led by reservoir sedimentation: (1) decrease of the reservoir active capacity directly affects the functions of the dam, supplying drinking and irrigation water, hydroelectricity production, and flood disaster mitigation, (2) affecting dam or hydropower generation equipment, such as abrasion of gates or turbines (Boes et al., 2014; Sumi et al., 2009), (3) downstream reach deterioration caused by the lack of sediment, such as river bed incision which inhibits aquatic life activities, and coastal line recession (Kondolf et al., 2014). Current gross storage capacity in the world, 6,000 km^3 with 45,000 large dams (higher than 15 m), is affected by 570 km^3 (12 %) of capacity loss. In average, annual sedimentation rate is 31 km^3/year (0.52 %) and can be accelerated due to global climate change (Sumi et al., 2004). What is worse, this rate exceeds the increase rate of reservoir capacity, leading the surely future when reservoirs would be filled with sediment completely and useless, unless adequate countermeasures are taken (Auel, 2016). Figure 1 shows one example of reservoir compromised by sedimentation, Ikawa reservoir in Japan. In a worse case, a fully-silted reservoir is reported overseas (Chanson, 1998). Therefore, a number of studies have been worked on sedimentation prevention. Generally, the concept of the countermeasures can be classified into broad three categories: (1) reduce incoming sediment from upstream reach including sabo (check) dam construction, reforestation, and erosion control, (2) removing sediment deposited in the reservoir by dredging, dry excavation, and flushing, and (3) sediment routing around or through the reservoir (Kondolf et al. 2014; Kantoush and Sumi 2010; Morris and Fan, 1998).

In particular, the third category includes sluicing and turbid density currents but also one advanced technique of Sediment Bypass Tunnels (SBTs), which are implemented to reduce suspended and bedload deposition in reservoirs by routing the incoming sediment around the dam (Auel and Boes 2011b; Sumi et al. 2004; Vischer 1997). SBT generally consists of guiding structure in the reservoir in order not to let sediment with large grain size flow into the tunnel, an inlet with gates, short tunnel section with steel bed to induce sediment flow, bypass tunnel section with mild slope, and outlet structure (Figure 2) (Sumi, 2015). Although the applicability of SBTs depends on the attribution of the reservoir with favor of curved shape, relatively small size, it can be said that the SBTs have notable advantages among other strategies (Sumi and Kantoush, 2011). First, SBTs are proven to be able to divert around 77 % to 94 % of the incoming sediments to the downstream reaches (Auel et al. 2016a). For instance, regular sedimentation volume measurement in Asahi dam in Japan unveiled that after the commencement of SBT operation in 1998, almost no additional sedimentation occurred (Fukuroi, 2012).

The other unique merit is that SBTs can restore the environment of the downstream reaches in respect of sediment supply (Martin et al., 2015; Kondolf et al. 2014). Because SBTs connect upstream and downstream reach of the dam directly, it can supply natural flood water directly without including the unnaturally concentrated sediment flow likewise flushing or lowering the water level affecting hydropower generation as sluicing (Kondolf et al., 2014; Quadroni et al., 2016).

Figure 1. Reservoir sedimentation (Ikawa dam reservoir in Japan).

Figure 2. Outlet of the Koshibu dam SBT.

Japan and Switzerland are the leading countries where more than five SBTs are operating although more than two SBTs are constructed and planned in Taiwan (Lai et al., 2015; Fukuda et al., 2012). However, SBTs tend to be affected by the combination of high flow velocity and high sediment flux, causing invert abrasion, which increase SBTs maintenance costs besides the relatively expensive SBTs tunnel construction costs (Auel and Boes 2011b, Baumer and Radogna 2015, Jacobs and Hagmann 2015). Figure 3 shows the present abrasion situation of Asahi dam SBT in Nara prefecture, Japan where the abrasion situation is severe (Nakajima et al. 2015). The tunnel invert is abraded largely, and rock and steel reinforcements are exposed in part, thus for the safe SBT operation, the tunnel owner (Kansai Electric Power Co., Inc.) needs to spend irregular expense for reinforcement works of the tunnel invert. Therefore, to realize appropriate invert abrasion management and quantifying the amount of abrasion are the noteworthy research subjects. For that, it is important to establish a sediment transport measurement system because abrasion prediction model is basically depending on actual bedload flux in the SBT (Auel et al., 2016b; Ishibashi, 1983). Moreover, the sediments transport volumes, which are diverted downstream of the dam during floods, is useful information for comprehensive river basin management and also important regarding environmental aspects, as morphologic variability is enhanced (Facchini et al., 2015).

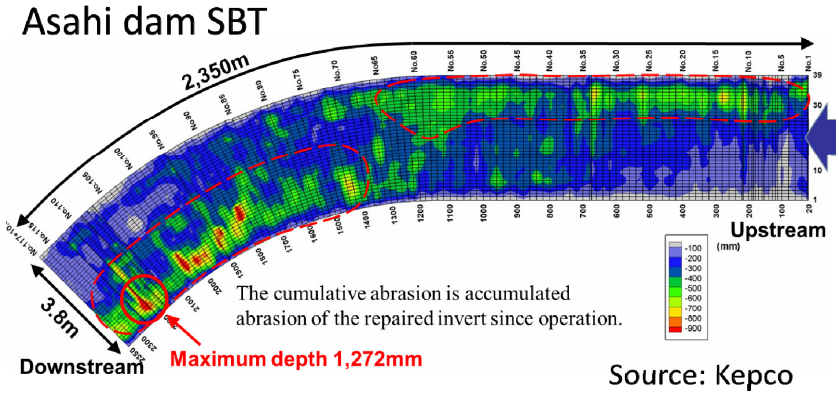

Figure 3. Accumulated abrasion depth (1998 to 2011) at Asahi dam SBT (Nakajima et al., 2015).

A significant number of research to measure bedload transport has been conducted (Tsakiris et al., 2014; Gray et al., 2010; Helley and Smith, 1971). Analogous to the studies all over the world, Japanese Pipe Microphone (JPM), one surrogate bedload monitoring system, was developed and has been widely used in Japan. The JPM is composed of a steel pipe equipped with a microphone inside the pipe and mounted on the river bed. The JPM detects the sound of sediment particle impacts, which includes the information of transported sediment characteristics, e.g. gran size, sediment volume and particle velocity (Mizuyama et al., 2010).

In this paper, a new bedload monitoring system named Impact plate devised based on the JPM is introduced and calibrated with the full scale experiment at Koshibu SBT in Japan. The impact plate has same concept as the JPM but consists of a steel plate instead of a pipe with referring Swiss Plate Geophone (SPG), one most widely used surrogate bedload monitoring systems in Europe (Rickenmann et al., 2012). The plate is expected to possess adequate robustness against the intensive condition of SBTs where the flow velocity exceeds 10 m/s (Auel and Boes, 2011a). Moreover, an acceleration sensor is also employed and mounted in a steel plate in addition to a microphone for expecting wide frequency range of measurement.

2 BEDLOAD MONITORING SYSTEMS

2.1 Impact plates and hydrophone

In the Koshibu SBTs, seven impact plates (Figure 4) and two JPMs (Figure 5), manufactured by Hydrotech Co., Ltd. (Japan), are installed for measuring spatial distribution of the transported sediment. As noted above, the impact plate consists of four units as: a steel plate, microphone, acceleration sensor (GH-313A and GA-223 as a converter, manufactured by KEYENCE, Japan) and data-logger. The steel plate is 49.2 cm in width, 35.8 cm in length in flow direction and 1.5 cm in thickness. The JPMs has a length of 80 cm and 48.6 mm in diameter, which is the similar to those widely used in Japan. A detailed information about the JPM is reported in the study by Goto et al. (2014). Both microphone and acceleration sensor record the sound and vibration of the sediment particle impacts transmitted to the sensor through the plate respectively as a voltage [V] at 50 kHz of sampling frequency. Figure 5 (i) shows the raw waveform data of microphone output performed in the laboratory tests where several particles of gravels were transported over the plate with the diameter of 50 mm at the water velocity of 4.5 m/s (Koshiba et al. 2016a). Even though such raw waveform data are useful in analyzing transported sediment attributions, *i.e.* volume, grain size and particle transport mode (sliding, rolling, and saltation), a significant volume of its data amount doesn't allow to continuously collect raw data. Therefore, some data processing methods for decreasing data amount while remaining the characteristics of transported particle were developed for the JPMs in Japan and were also employed for observation using impact plates. During full scale trail experiment, the raw waveform data were collected in part, but the following data processing was conducted throughout every runs.

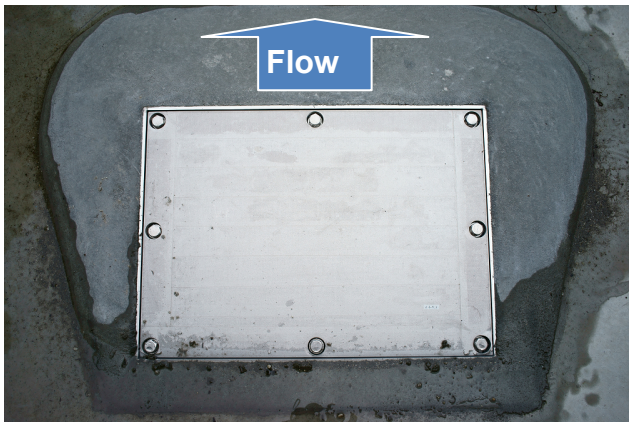

Figure 4. Impact plate.

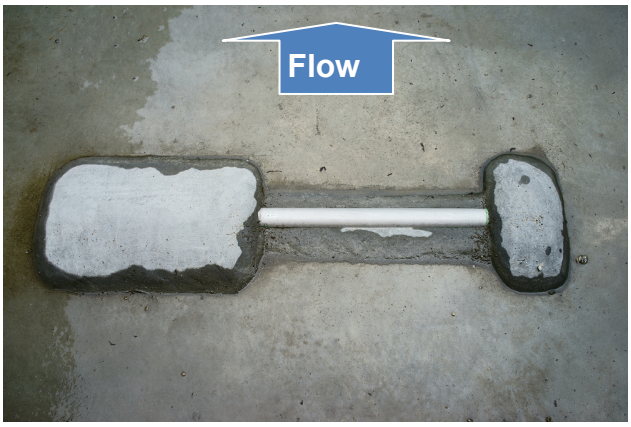

Figure 5. Japanese pipe microphone (JPM).

2.2 Data Processing

In accordance with the previous observations by the JPM (Mizuyama et al., 2008; Suzuki et al., 2010), the following two parameters were computed by the impact plate during each experiment: the number of impulses, I_p and the average value of sound pressure, S_p. Both values are obtained through analog signal processing in a data logger, and thus calculated simultaneously with the recording of the raw waveform data. Due to the technical limitation, *i.e.* the limited memory of PC and electricity power supply, these variables were computed only for the microphone signal.

The recorded number of impulses (I_p) represents the number of particles that hitting the plate, and the analogous method is employed not only for the JPMs but also for the SPG, as one of the simplest methods for quantifying the Bedload transport rate (Wyss et al. 2016). This parameter works to significantly decrease the accumulated data amount rather than collecting all signal raw waveform data while maintaining some extends of information on the frequency and amplitude fractions of the signal of particle impacts. To compute I_p, the following steps are conducted with the data logger simultaneously to the raw waveform recording, as shown in Figure 6 step (i)-(iv). First, the registered raw waveform (i) is proceeded through a band-path filter to extract the frequency of approximately 4.6 kHz (ii), which was previously computed as the most effective frequency for distinguishing particle impacts on the plate.

Subsequently, the filtered waveform is transformed into an absolute value, and the envelope curve is generated (iii). Then, the enveloped data are exported to 10 different channels, where the wave is amplified with amplification factor, *Amp* of 2, 4, 8, 16, 32, 64, 128, 256, 512, and 1024 times. Finally, I_p for each amplification factor is defined as the number of impulses, grouping the distributed signals above a predefined threshold of 2 V (iv). In figure 6 (iv), envelope curve and the amplified curves with *Amp* = 4 and 16 are exemplified. In the example, when *Amp* = 4, no peak of the amplified curve reaches the threshold and hence I_p = 0. In contrast, the amplified curve with *Amp* = 16 touch the threshold four times, hence I_p = 4.

Although I_p is already commonly used for field observations in Japan, it is also reported that I_p can lead to underestimations, due to the overlapping of each single impulse when the sediment transport rate is high as well as when several gravel particles hit the plate simultaneously (Mizuyama et al., 2010). To address this shortcoming, bedload measurements were taken using the enveloped data in the process of calculating I_p, as suggested by Suzuki et al. (2010), and also automatically recorded for all runs as S_p, which is referred to as *average value of sound pressure* in Japan. S_p is defined as the value of the enveloped signal data (Figure 6 (iii)) averaged over every 10 s duration. S_p can be regarded as a parameter that represents the integrated value of raw waveform, which is less affected by the overlapping of particle impacts than I_p.

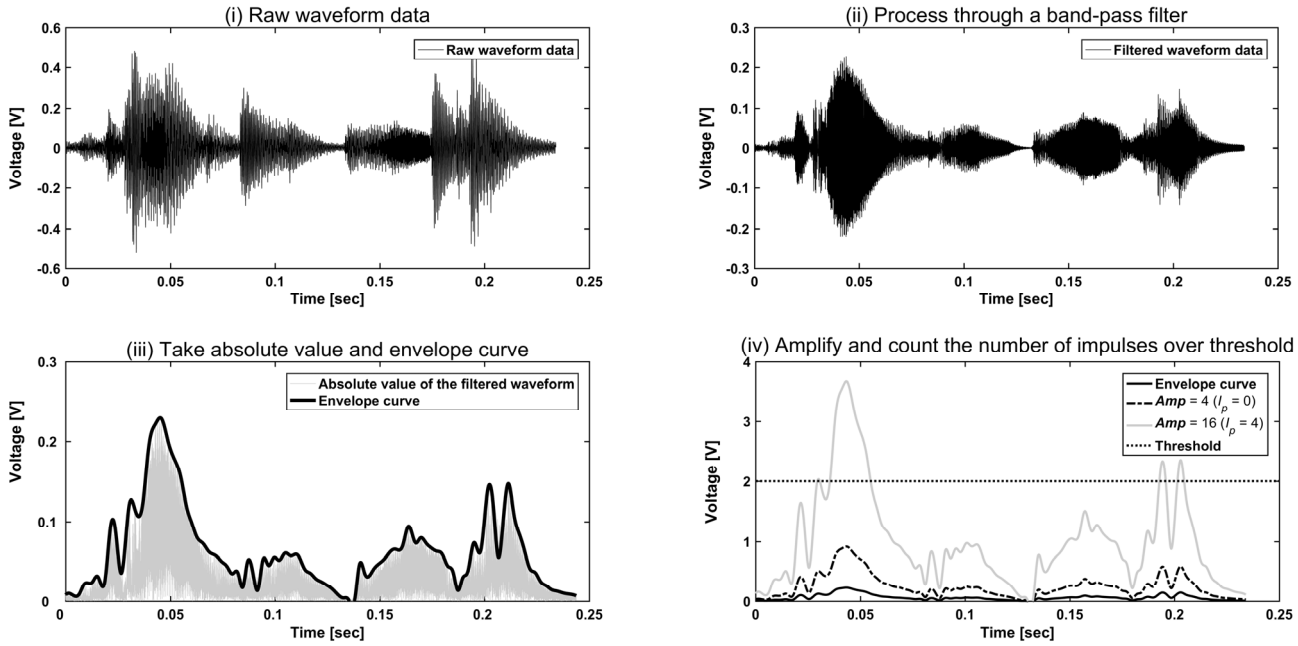

Figure 6. Illustration of the signal processing for counting the number of impulses (I_p). (i) Raw waveform data collected by a microphone. (ii) Filtered raw waveform data through band-pass filter, (iii) Filtered waveform data transformed to the absolute value and envelope curve is extracted. (iv) Envelope curve is amplified with the amplification factor (*Amp*) ranging from 2 to 1024 times and the number of impulses (I_p) over the threshold is counted. (*Amp* = 4 and 16 are exemplified).

3 KOSHIBU SBT

The Koshibu dam is located at the Koshibu river catchment in Nagano prefecture, Japan, and is operated by the Ministry of Land, Infrastructure, Transport and Tourism (MLIT) for flood prevention, water supply and hydropower generation. The dam was built in 1969, and is 105 m high with a width of 293.3 m. The catchment area is 288 km^2 and mostly covered by forest and sediment supply prone areas. Moreover, the reservoir received enormous severe floods and thus rapid sedimentation rate has been an issue for the dam management. Indeed, in 2015, the sedimentation volume exceeds 15.6 million m^3 (MCM), almost reaching to 20.0 MCM of original designed sedimentation capacity. Therefore, MLIT initiated the construction of Koshibu SBT and the first operation was successfully achieved during 21st and 23rd of September 2016 during the typhoon Malakas. The length of the SBT is 3,982 m with a circular cross section and a plain invert with a slope of 2 %. The width and height are 5.5 m and 7.9 m, respectively. Most of the parts are rectilinear tunnel but the last approximately 600 m from the outlet is curved on the orographic right direction (Radius, R = 1000 m). Most of the tunnel invert is paved with the high strength concrete (50 N/mm^2), particularly in the first 20 m of the inlet facility and the next 30 m where the tunnel inclination is relatively high for accelerating incoming flow are reinforced with rubber-steel and steel-lining materials, respectively. The impact plates are installed at the outlet (Figure 2) and observation is started from the first SBT operation.

4 FULL SCALE EXPERIMENT

4.1 Sediment monitoring design

Figure 7 shows the arrangement of measurement devices at the Koshibu SBT outlet (Figure 2). Five impact plates named t15 are mounted in order to measure the cross sectional distribution of transported sediment. Moreover, as in Figure 7, two additional impact plates are mounted namely, t12 and t15 inclined. Original impact plate (t15) has the thickness of 15 mm, whereas t12 is an impact plate with the thickness of 12 mm. On the other, t15 inclined is an original impact plate but the plate is inclined with 10°. These are employed for comparative study with the original impact plates to investigate the difference of detection efficiency due to the different thickness and inclination respectively. In particular, the increase of sensitivity by inclining a plate is confirmed in the past study by Auel and Boes (2011b). We chose the inclination angle of 10° according to the study where the value showed the highest detection rate.

To compare the experimental results with existing studies on the JPM and SPG, the JPM and geophone sensor (Geospace GS-20DX, manufactured by Geospace Technologies, Houston, Texas) are also employed for the observation. As in Figure 7, two JPMs are installed at both left and right sides and the geophone sensors were mounted underneath the plate 3, t12, and t15 inclined in addition to the microphone and the acceleration sensor. Moreover, five pipe pits are also built at the outlet vertically to collect bypassed water at five different height fractions so as to measure vertical turbidity distribution because the impact plates are not good at gaining the vertical sediment flow profiles. Figure 8 is a photo of the outlet taken from the outside.

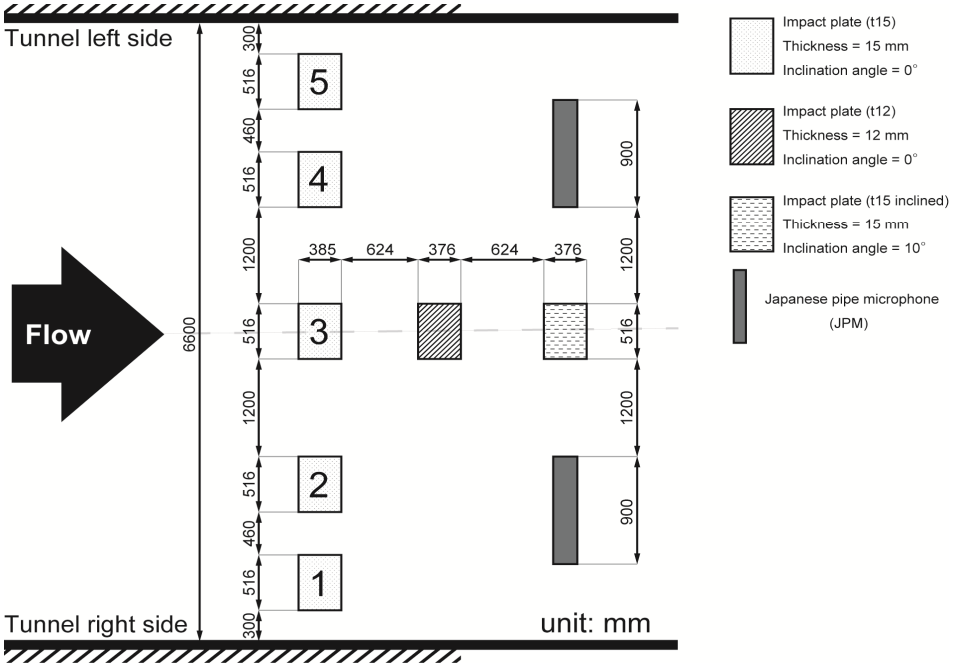

Figure 7. Plan view of bedload measurement apparatuses on the Koshibu dam SBT.

4.2 Experimental setup

To calibrate the bedload monitoring systems, a series of field experiments were conducted at Koshibu SBT by artificially flush sediment over the devices through the tunnel. The experiments were performed in three sunny days sequentially from 22nd August in 2016 to 24th. As in Table 1, 10 cases of experimental conditions were selected at various grain sizes (D_s = 5, 10, 50 mm), sediment volumes (V = 1, 3, 5, 9 m^3), and water discharges (Q = 5, 10, 50 m^3/s). At Case 8 and 10, the mixed grain size sediment were tried so that all include D_s with V = 3 m^3 for each. The grain sizes are determined based on the Koshibu SBT's design that only sediment of D_s smaller than 100 mm is bypassed by collecting larger sediment particles at a divert equipment nearby the inlet. Although the Q is much smaller than the SBT capacity of 370 m^3, it was decided in order to lessen the negative impact of sediment flushing to the downstream reaches as much as possible. The test sediment was derived from the quarrying area from the immediate downstream of the SBT and was carried by a dump truck into the SBT just before every run.

Observing the effect of the tunnel section where SBT makes a turn in the last 600 m, the sediment was placed 800 m upstream from the outlet (Figure 9). Indeed, the sediment transport observation of Solis SBT in Switzerland using the SPGs showed that the tunnel's horizontal curve can cause the sediment concentration at the inner side of the tunnel bend in the cross sectional direction (Albayrak et al., 2015).

Figure 3 also shows the consequential uneven abrasion distribution, the severest abrasion occurs at inner side of the tunnel curve, in Asahi SBT in Japan (Nakajima et al., 2015). After confirming everyone exits the tunnel, the designated amount of water was drawn by opening the inlet gate for 20 minutes (T_{flush}) in each run. The natural riverine water stored in a pool impounded by diversion equipment was used for the experiment and in order not to allow sediment in the pool passes into the tunnel while experiment is in progress, previous gate open operation was conducted to flush the deposited sediment entirely. All impact plates and the JPMs continuously registered the variables (I_p and S_p) throughout the experimental flushing except for the raw waveform data. Since the raw waveform data volume is extremely high and difficult to be measured continuously at the desirable sampling frequency of 50 kHz, the raw waveforms were recorded from just before the incipient of the sediment flow reaches the outlet to the time when all sediment passes the outlet completely, with five seconds of recording and ten seconds in interval. Several cameras were also installed at both tunnels; inside where the sediment is placed, the outlet of the tunnel. The flow depth at the outlet was estimated based on the video recorded data of the outlet camera. After every experimental runs, several persons entered into the tunnel and visually observed the condition of the hydroabrasion on the invert.

Table 1. Experimental conditions.

Experimental conditions						Experimental results					
Case	Date	D_s [mm]	V [m^3]	Q [m^3/s]	T_{flush} [min]	h_{max} [mm]	h_{min} [mm]	h_{mean} [mm]	V_w [m/s]	Fr [-]	T_{reach} [min]
1	22/8	10	1	10	20	592	112	232	2.60	1.72	11.9
2	22/8	10	3	5	20	388	14	135	1.98	1.72	14.3
3	22/8	50	3	5	20	416	65	151	1.85	1.52	14.9
4	22/8	5	3	5	20	460	28	143	1.67	1.41	15.0
5	23/8	10	5	5	20	379	18	124	2.03	1.84	15.4
6	23/8	10	9	5	20	411	36	136	1.87	1.62	15.3
7	23/8	10	9	20	20	840	92	358	3.66	1.95	10.0
8	23/8	5/10/50	3/3/3	5	20	406	28	163	1.89	1.50	15.5
9	24/8	50	9	20	20	920	151	372	3.34	1.75	9.2
10	24/8	5/10/50	3/3/3	20	20	773	67	372	3.98	2.08	10.4

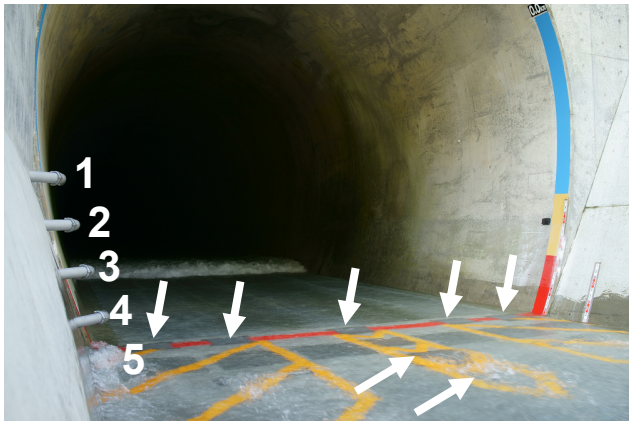

Figure 8. Koshibu SBT outlet. White arrows show impact plates, numbers show the water collect pit.

Figure 9. Input sediment (D_s = 10 mm, V = 5 m^3/s).

5 RESULT

5.1 General findings

All experiments were successfully conducted within the planned date, as shown in Table 1. T_{flush} is the duration when the SBT gate was opened and closed, being fixed at 20 minutes. T_{reach} is the duration from the gate opening to the moment the flow front arrives at the outlet where bedload monitoring systems are installed. T_{reach} has good negative linear correlation with the Q (R^2 = 0.95) concurrently with the positive correlation with the average flow velocity, V_w calculated by flow measured mean flow depth and Q (R^2 = 0.96). However, the water flow in all runs exhibit significant roll-waves, thus the water depth undulates in the range of 14 mm to 920 mm as h_{max} and h_{min} exhibit. Hence, although the average water velocity, V_w calculated from the average water depth is shown in the table, it should be reminded that the V_w is also likely to vary in a large range during each run.

5.2 Mixed grain size test (Case 8)

Figure 10 shows one of the results that exhibiting significant behaviour for the difference of D_s at Case 8 where the mixed grain size with V = 9 m^3 was flashed at Q = 5 m^3/s. The results include S_p (bar chart), I_p with *Amp* of 1024, 256, 64, 16, 4 times, and abscissa notes the time from the impact plates started observation when clear water already reached the outlet. Apparently, it shows that the sediment reaches the outlet at around T = 0.75 and passed completely around T = 4.5. Throughout the observation, I_p increases as the amplification factor increases in the nature of the I_p's definition. Considering only the clean water flows at T = 5, where all variables detect no signals, the noise of water flow does not affect the accurate measuring of S_p and I_p. The result, especially S_p shows that the sediment flow is not constant and includes some extends of fluctuation. General speaking, the result can be separated into two parts at around T = 3. In the first half, relatively high amount of S_p are recorded. When it comes to I_p, almost same values are recorded for I_p at *Amp* = 1024 and 256, but the I_p at *Amp* = 64 and 16 gradually decreases in the second half, especially at *Amp* = 4, I_p is almost zero. Since the impact amplitude is highly dependent on the grain size of impinged particles, this result implicates the difference of grain size distribution between the first and latter half (Koshiba et al. 2016a).

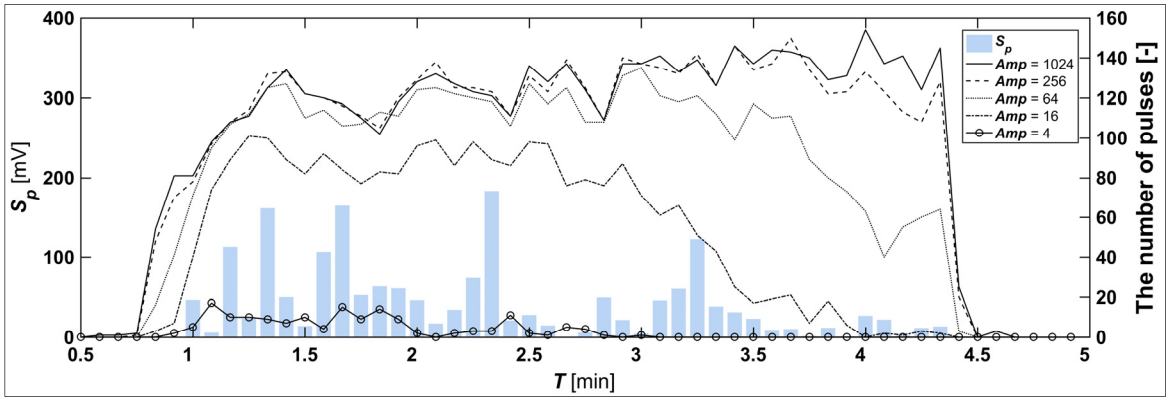

Figure 10. The S_p and I_p (*Amp* = 1024, 256, 64 and 4) registered during the experiment of Case 8.

For further investigation, the raw waveform data is shown in Figure 11. Waveform (a), (b), and (c) are collected by the microphone and three points of time in Figure 10 and were selected namely T = 2, 3, and 4 respectively for clarifying the time series variation. Obviously, the wave amplitude decreases over time, and presumably the shift of I_p in Figure 10 is influenced by the shift of amplitude. For reference, Figure 11 also shows the raw waveform data in Case 3, 5, and 4, thus the impact of uniform grain size sediment with D_s = (d) 50 mm, (e) 10 mm, and (f) 5 mm are registered respectively. According to (d) – (f), it can be expected that the waveform (a) is predominantly composed of sediment flow with D_s = 50 mm and (c) is with D_s = 5 mm. Therefore, Case 8 flow investigated that the large particles reached the outlet first and subsequently small particles arrived. Supposing this process is correct, the different characteristics of I_p between the first and latter half can be reasonably understood. In the first half, only large particles, causing relatively large waveform amplitudes, are flushed, thus the I_p is entirely registered even for *Amp* = 4 being the lowest sensitivity. On the other hand, in the latter half, the D_s of predominant sediment gradually decreases, accordingly I_ps at low *Amp,* meaning low sensitivity, also decreases.

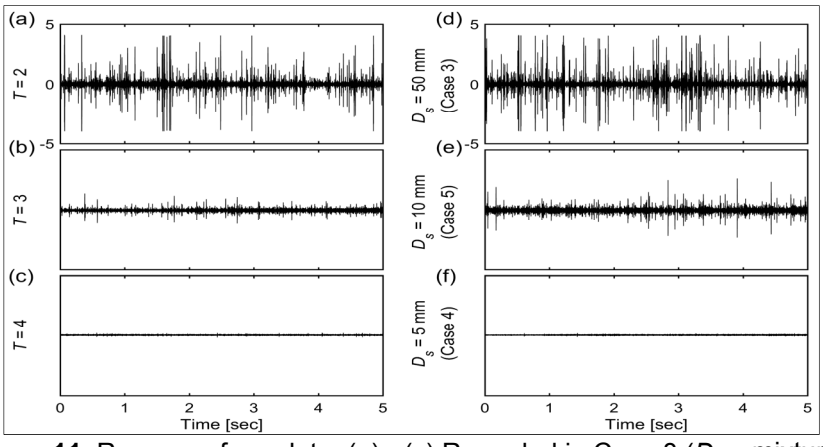

Figure 11. Raw waveform data. (a) - (c) Recorded in Case 8 (D_s = mixture), each T corresponding to the T in Figure 8, (d) Case 3 (D_s = 50 mm), (e) Case 5 (D_s = 10 mm), (f) Case 4 (D_s = 5 mm).

5.3 The centroid amplitude factor.

However, if only the I_p at Amp = 1024 and 256 are focused, the I_p in the latter half is slightly higher than the first half. It seemed to be brought on by the much higher number of transported sediment particles in the latter half. Because, as shown in Table 1, the amount of the sediment was measured in volume-base, the higher number of particles is flushed in the cases with smaller D_s. These findings clarify the meaningful outcome that the grain size distribution of sediment flow can be extracted only with using the information of I_p.

The discussion above revealed that the fraction of I_p is likely to depend on the predominant grain size of the sediment flow. The centroid amplitude, $Amp_{centroid}$ is computed to characterize the I_p profile in the amplification factor domain. $Amp_{centroid}$ is calculated as Eq. [1].

$$Amp_{centroid} = 10 - \frac{\sum I_p \cdot \log_2 Amp}{\sum I_p} \qquad [1]$$

It expresses the centroid of the graph I_p versus Amp. For instance, in Figure 10, $Amp_{centroid}$ at T = 2 is calculated as higher value than T = 4, because entirely I_ps at T = 2 are located at higher value than the I_ps at T = 4. Hence, it means that the centroid of the Amp spectrum at T = 2 is posed higher than the T = 2. As this example, the $Amp_{centroid}$ expresses the deviation of the I_ps, which indicates the predominant grain size as a single value in each measurement time point. The reason to take the logarithm of Amp is that the Amp has the wide range of order, thus the $Amp_{centroid}$ is extremely concentrated on the higher Amp direction without any preliminaries.

The result applying the $Amp_{centroid}$ to all cases and plates is in Figure 12. These show that the computation results at first 250 seconds from the time just before the sediment flow incipient reaches the outlet including most of the sediment flow in all cases. The vertical ticks indicate that the Plate 1 to 5 as shown in Case 1, thus the bottom side of each figure corresponds to the inner side of SBT curve. Apparently, the results can be classified into three groups based on the magnitude of $Amp_{centroid}$. The lowest group is only Case 4, the middle group including Case 1, 2, 5, 6, and 7, and the highest group Case 3, 8, 9 ,and 10. This classification clearly matches the maximum grain size in the transported sediment, in turn the lowest with D_s = 5 mm, middle with D_s = 10 mm, and highest with D_s = 50 mm. The result of Case 8, especially, is worthy of notice since the shift of dominant grain size over the time found in Figure 10 and 11 are reflected on. As in the result of Case 8, the large grain size sediment (red color) flows first and the color gradually changes into blue color through yellow as the shift of major sediment grain size.

The sediment spatial concentration such as the example of Asahi dam SBT (Figure 3) can be also seen in the results. In particular, Case 2, 3, 5, and 10 markedly show that the sediment transport continued longer in the tunnel inner side than the other side. However, even though the difference of flow duration is found between the both side, the grain size fraction is symmetric between both sides and sediment with large grain size tend to concentrate on the center of streamline than the both sides.

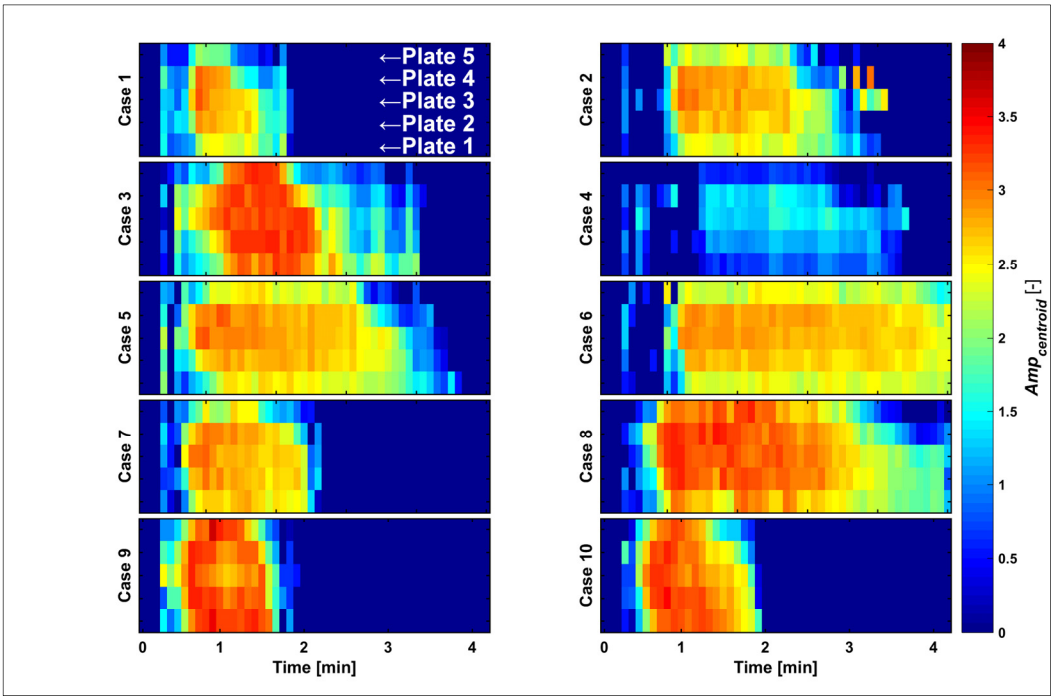

Figure 12. $Amp_{centroid}$ over time for all plates (Case1 - 10).

6 CONCLUSION

Accurate sediment monitoring in SBTs are necessary for coming up with appropriate maintenance approach and the quantification of bypassing efficiency. This study introduced the impact plates firstly for measuring bedload transport in SBTs and conducted a full scale calibration experiment.

The calibration was successfully carried out and the impact plates worked under the high flow condition with sediment transport. The outcomes through the experiment might be concluded as:

(a) The impact plates worked under the high flow condition with sediment transport adequately.
(b) The profile of I_p is strongly dependent on the predominant D_s in the sediment flow. $Amp_{centroid}$ characterizes I_p profile is calculated and confirmed to exhibit the predominant D_s based on the raw waveform data.
(c) Spatial distribution of $Amp_{centroid}$ in the tunnel shows that the spanwise deviation of the sediment flow. This result well corresponds to the abrasion situation in Asahi dam SBT in Japan.

For further study, not only the grain size information but also the transported sediment volume and other necessary parameters for abrasion estimation, should be unveiled. Moreover, the theoretical meaning of $Amp_{centroid}$ is also needed to be figured out for extracting the grain size distribution in addition to the predominant grain size. For these aims, the raw waveform data analysis using signal processing have been actively ongoing.

ACKNOWLEDGEMENTS

The authors acknowledge the support by JSPS KAKENHI (Grant Number 26257304) and by regional research project of river and sediment management technology development by MLIT. The authors also would like to appreciate Michinobu Nonaka, the president of Hydrotech Co., Ltd for his many meaningful advice and support about the impact sensor.

REFERENCES

Auel, C. & Boes, R.M. (2011a). Sediment Bypass Tunnel Design – Review and Outlook. *Proc. ICOLD Symposium Dams under Changing Challenges (A.J. Schleiss and R.M. Boes, Eds.), 79th Annual Meeting, Lucerne*. Taylor and Francis, London, UK, 403-412.

Auel, C. & Boes, R.M. (2011b). Sediment Bypass Tunnel Design–Hydraulic Model Tests. *Proc. Hydro 2011 - Practical Solutions for a Sustainable Future*, No.29.03. Aqua-Media International Ltd. Prague, Czech Republic.

Auel, C., Kantoush, S.A. & Sumi, T. (2016a). Positive Effects of Reservoir Sedimentation Management on Reservoir Life : Examples from Japan. *84th Annual Meeting of ICOLD*, Johannesburg, South Africa.

Auel, C., Boes, R.M. & Sumi, T. (2016b). Abrasion prediction at Asahi Sediment Bypass Tunnel Based on Ishibashi's formula. *Journal of Applied Water Engineering and Research*, 1-14.

Baumer, A. & Radogna, R. (2015). Rehabilitation of the Palagnedra Sediment Bypass Tunnel (2011-2013). *Proc. Int. Workshop on Sediment Bypass Tunnels*, VAW-Mitteilung 232 (Boes, R.M, ed.), ETH Zurich, Switzerland, 235-245.

Boes, R.M., Auel, C., Hagmann, M. & Albayrak, I. (2014). Sediment Bypass Tunnels to Mitigate Reservoir Sedimentation and Restore Sediment Continuity. *Reservoir Sedimentation*, 221-228.

Chanson, H. (1998). Extreme Reservoir Sedimentation in Australia: A review. *International Journal of Sediment Research*, 13(3), 55-63.

Facchini, M., Siviglia, A. & Boes, R.M. (2015). Downstream Morphological Impact of a Sediment Bypass Tunnel – Preliminary Results and Forthcoming Actions. *Proc. International Workshop on Sediment Bypass Tunnels*, VAW-Mitteilung 232 (Boes, R.M, ed.), ETH Zurich, Switzerland, 137-146.

Fukuda, T., Yamashita, K., Osada, K. & Fukuoka, S. (2012). Study on Flushing Mechanism of Dam Reservoir Sedimentation and Recovery of Riffle-Pool in Downstream Reach by a Flushing bypass Tunnel. *Proc. International Symposium on Dams for a Changing World,* Kyoto, Japan.

Fukuroi, H. (2012). Damage from Typhoon Talas to Civil Engineering Structures for Hydropower and the Effect of the Sediment Bypass System at Asahi Dam. *Proc. International Symposium on Dams for a Changing World,* Kyoto, Japan.

Goto, K., Itoh, T., Nagayama, T., Kasai, M. & Marutani, T. (2014). Experimental and Theoretical Tools for Estimating Bedload Transport Using a Japanese Pipe Hydrophone. *International Journal of Erosion Control Engineering*, 7(4), 101-110.

Gray, J.R., Laronne, J.B. & Marr, J.D. (2010). *Bedload-Surrogate Monitoring Technologies*. US Department of The Interior, US Geological Survey.

Helley, E.J. & Smith, W. (1971). *Development and Calibration of a Pressure-Difference Bedload Sampler*. U.S. Geological Survey, Water Resources Division, Open-File Rep., (No. 73-108).

Ishibashi, T. (1983). A Hydraulic Study on Protection for Erosion of Sediment Flush Equipments of Dams. *Proc. Japan Society of Civil Engineers* 1983(334), 103-112 (In Japanese).

Jacobs, F. & Hagmann, M. (2015). Sediment Bypass Tunnel Runcahez: Invert abrasion 1995-2014. *Proc. Int. Workshop on Sediment Bypass Tunnels*, VAW-Mitteilung 232 (Boes, R.M, ed.), ETH Zurich, Switzerland, 211-221.

Kondolf, M., Gao, Y., Annandale, G., Morris, G., Jiang, E., Zhang, J., Carling, P., Fu, K., Guo, Q., Hotchkiss, R., Peteuil, C., Sumi, T., Wang, H.W., Wang, Z., Wei, Z., Wu, B. & Yang, C.T. (2014). Sustainable Sediment Management in Reservoirs and Regulated Rivers: Experiences from Five Continents. *Earth's Future* 2(5), 256-280.

Koshiba, T., Sumi, T., Takemon, Y. & Tsutsumi, D. (2016). Flume Experiment on Bedload Measurement with a Plate Microphone. *Annuals of Disaster Prevention Research Institute*, Kyoto University, No.58 B.

Lai, J.S., Lee, F.Z., Wu, C.H., Tan, Y.C., & Sumi, T. (2015). Sediment Bypass Tunnels of the Shihmen Reservoir in Taiwan. *Proc. Int. Workshop on Sediment Bypass Tunnels*, VAW-Mitteilung 232 (Boes, R.M, ed.), ETH Zurich, Switzerland, 55-70.

Martín, E.J., Doering, M. & Robinson, C.T. (2015). Ecological Effects of Sediment Bypass Tunnels. *Proc. International Workshop on Sediment Bypass Tunnels*, VAW-Mitteilung 232 (Boes, R.M, ed.), ETH Zurich, Switzerland, 147-156.

Mizuyama, T., Matsuoka, M. & Nonaka, M. (2008). Bedload Measurement by Acoustic Energy with Hydrophone for High Sediment Transport Rate. *Journal of the Japan Society of Erosion Control Engineering*, 61(1), 35-38. (In Japanese)

Mizuyama, T., Oda, A., Laronne, J.B., Nonaka, M. & Matsuoka, M. (2010). *Laboratory Tests of Japanese Pipe Geophone for Continuous Acoustic Monitoring of Coarse Bedload*, US Geological Survey Scientific Investigations Report, 5091, 319-335.

Morris, G.L. & Fan, J. (1998). *Reservoir Sedimentation Handbook: Design and Management of Dams, Reservoirs and Watersheds for Sustainable Use*. McGraw Hill Professional.

Nakajima, H., Otsubo, Y. & Omoto, Y. (2015). Abrasion and Corrective Measures of a Sediment Bypass System at Asahi Dam. *Proc. Int. Workshop on Sediment Bypass Tunnels*, VAW-Mitteilung 232 (Boes, R.M, ed.), ETH Zurich, Switzerland, 21-32.

Quadroni, S., Brignoli, M.L., Crosa, G., Gentili, G., Salmaso, F., Zaccara, S. & Espa, P. (2016). Effects of Sediment Flushing from a Small Alpine Reservoir on Downstream Aquatic Fauna. *Ecohydrology*, 9(7), 1276–1288.

Rickenmann, D., Turowski, J.M., Fritschi, B., Klaiber, A., & Ludwig, A. (2012). Bedload Transport Measurements at the Erlenbach Stream with Geophones and Automated Basket Samplers. *Earth Surface Processes and Landforms*, 37(9), 1000-1011.

Sumi, T., Okano, M. & Takata, Y. (2004). Reservoir Sedimentation Management with Bypass Tunnels in Japan. *Proceedings of the Ninth International Symposium on River Sedimentation,* Vol. 2, 1036-1043.

Sumi, T., Kobayshi, K., Yamaguchi, K. & Takata, Y. (2009). Study on the Applicability of the Asset Management for Reservoir Sediment Management. *In International Congress on Large Dams*, Brasilia.

Sumi, T. & Kantoush, S.A. (2011). Comprehensive Sediment Management Strategies in Japan: Sediment bypass tunnels. *In 34th IAHR World Congress*, Brisbane, Australia.

Sumi, T. (2015). Comprehensive Reservoir Sedimentation Countermeasures in Japan, *Proc. International Workshop on Sediment Bypass Tunnels*, VAW-Mitteilung 232 (Boes, R.M, ed.), ETH Zurich, Switzerland, 1-20.

Suzuki, T., Mizuno, H., Osanai, N., Hirasawa, R. & Hasegawa, Y. (2010). Basic Study on Sediment Rate Measurement with a Hydrophone on The Basis of Sound Pressure Data. *Journal of the Japan Society of Erosion Control Engineering*, 62(5), 18-26. (In Japanese)

Tsakiris, A.G., Papanicolaou, A.T.N. & Lauth, T.J. (2014). Signature of bedload particle transport mode in The Acoustic Signal of a Geophone. *Journal of Hydraulic Research*, 52(2), 185-204.

Vischer, D.L., Hager, W.H., Casanova, C., Joos, B., Lier, P. & Martini, O. (1997). Bypass Tunnels to Prevent Reservoir Sedimentation. *In Transactions of the International Congress on Large Dams,* Vol. 3, 605-624.

Wyss, C.R., Rickenmann, D., Fritschi, B., Turowski, J.M., Weitbrecht, V. & Boes, R.M. (2016). Laboratory Flume Experiments with the Swiss Plate Geophone Bed Load Monitoring System: 1. Impulse Counts and Particle Size Identification. *Water Resources Research*, 52(10), 7744-7759.

DETECTION OF DEBRIS FLOWS BY COMBINATION OF LVP AND WIRE SENSORS

TAKAHIRO ITOH[(1)], TAKAHISA MIZUYAMA[(2)], MICHINOBU NONAKA[(3)], SATOSHI TAGATA[(4)] & SATORU MATSUDA[(5)]

[(1)] Research and Development Center, Nippon Koei Co., Ltd., Tsukuba, Japan
e-mail a6556@n-koei.co.jp
[(2)] National Graduate Institute for Policy Studies (GRIPS), Tokyo, Japan
e-mail byk01260@nifty.com
[(3)] Hydrotec Co., Ltd., Shiga, Japan
e-mail rishin@hydro.co.jp
[(4)] Nippon Koei Co., Ltd., Tokyo, Japan
e-mail a5672@n-koei.co.jp

ABSTRACT

A LVP sensor is consisted of load cell, acceleration meter and pressure meter, and some sensors can detect debris flows occurrences even if the other sensors are broken for continuous detections of debris flow. The flame of the sensor is made by stainless, the thickness of top plate (force plate) is 25 mm and the load is measured by a centered round plate with 60 mm in diameter. The small size of a force plate for load measurement is designed to avoid direct collisions due to boulders to the plate. The LVP sensor is better to use together with a wire sensor, and the sensor, which is modified several times, is installed on the bed at Nojiri No. 7 sabo dam on February 6th, 2015 in Sakurajima Island. There are several patterns of detections of debris flows such that the LVP sensor detected at almost same time to disconnected wires, the LVP sensor could detect several surges after disconnected wires and the LVP sensor could not detect perfectly because of transverse flow shifting. Referring to relationships between the flow depth and load, between the flow depth and vibration at the time of disconnected wires, there seem to be some threshold for debris flow event, though the sediment concentration could take various value for the flow depth. The threshold value for debris flow occurrences is estimated at 400 kgf/m^2 in load and 200 mVolt in vibration, though more data collections are necessary. Supposing combination both a wire and LVP sensor, the data for debris flow detections were collected by the LVP sensor in every debris flow event, and the threshold value are tried to determine through continuous monitoring by the LVP sensor.

Keywords: Debris flow; bed pressure; vibration; detection; lvp sensor.

1 INTRODUCTION

A lot of debris flows have occurred in Sakura-jima Island until 2000, and recently taken place there after falling volcanic ash by volcanic activities since 2010. Sakura-jima is in southern west region of Kyusyu area in Japan, and the ash depositions often take place due to volcanic activity. Debris flows occur due to the rainfall after eruption, and the huge volume of sediment is transported there by debris flows. For detection of debris flows occurrences after eruption, various kinds of sensors installation have been proposed, such as wire sensor, acceleration sensor and so on (Osumi Construction Office, 1988). Recently, in Europe, geophone (e.g. Arattano et al., 2008) is usually used though the applicability is not confirmed in Japan, and however, a wire sensor is still now used for debris flow detection in Japan because of the cheap cost and easy maintenance for the setting. In Sakura-jima, the numbers of debris flow occurrences are defined as disconnected numbers of a wire sensor, and three wires are set vertically at the height of 60 cm, 120 cm, 180 cm from the bed, respectively, to know magnitude of frontal part of debris flow.

A LVP sensor, which consists of a load cell, acceleration meter and pressure meter, was developed to detect the debris flow occurrences in real-time by measuring temporal changes of debris flow quantities. In fact, wires cannot detect continuously debris flow events during the disconnection after debris flows occurrences. Additionally, wires are sometimes disconnected by the movements of logs and animal activities. Present studies indicate the objective for development of a LVP sensor, the installation in Sakura-jima Island and some knowledge through data obtained by the LVP sensor.

2 DEBRIS FLOW DETECTIONS BY SENSORS

2.1 Previous attempts by sensors

Several sensors were installed to detect debris flow passing through the observation section. Electric, optical and vibration media were mainly selected, respectively, and the sensor is wire sensor, optical beam and acceleration sensor (vibration meter) corresponding to each media, respectively (e.g. Okuda et al., 1980,

Hirano et al., 1999, Suwa et al., 2011). The wire sensor has been usually used for the debris flow detection through there were a lot of attempts for the debris flow detections through various kinds of sensors, though there are still now a lot of attempts for debris flow monitoring using sensors (e.g. Scott et al., 2011). The geophone has an acceleration meter and is developed based on previous attempts for debris flow monitoring as described above. However, the geophone is mainly used in Europe. In Sakura-jima Island, the wire sensor is used formally for detections of debris flow occurrences and the numbers of debris flow occurrences are counted by disconnected wires, and the magnitude of the flow is judged by disconnection of three wires, which is set vertically at the height of 60 cm, 120 cm and 180 cm. New development is needed for debris flow detection considering either new type sensor or the combination of present sensors.

2.2 Development and modifications of LVP sensor

The LVP sensor is consisted of load cell (for load), acceleration meter (for vibration) and pressure meter (for flow depth), and the sensor call as LVP sensor, because debris flow monitoring using load cell can be known as effective tools (e.g. McArdell et al., 2007; Osaka et al, 2014). The LVP sensor is modified by try and error through the direct debris flow monitoring in field site. Additionally, the LVP sensor is installed on the bed of the river to directly measure several values of debris flow, and the feature of the installation is quite interesting.

Figure 1 shows the schematics of continuous detection for debris flow by the combination of a wire and LVP sensors, and the LVP sensor is better to use together with a wire sensor, as shown in Figure 1. Figure 2 shows the longitudinal bed profiles along the Nojiri River in Sakura-jima Island. The sensor, which is modified and installed on the bed at Nojiri No. 7 sabo dam on February 6th, 2015, detected 12 times of debris flow events in 13 times occurrences of debris flows after installation. A wire also detected 12 times of debris flows because the disconnected wire could not be maintained due to active eruption during the middle to the end of August in 2015, while the LVP sensor detected debris flows with around 60 cm in depth.

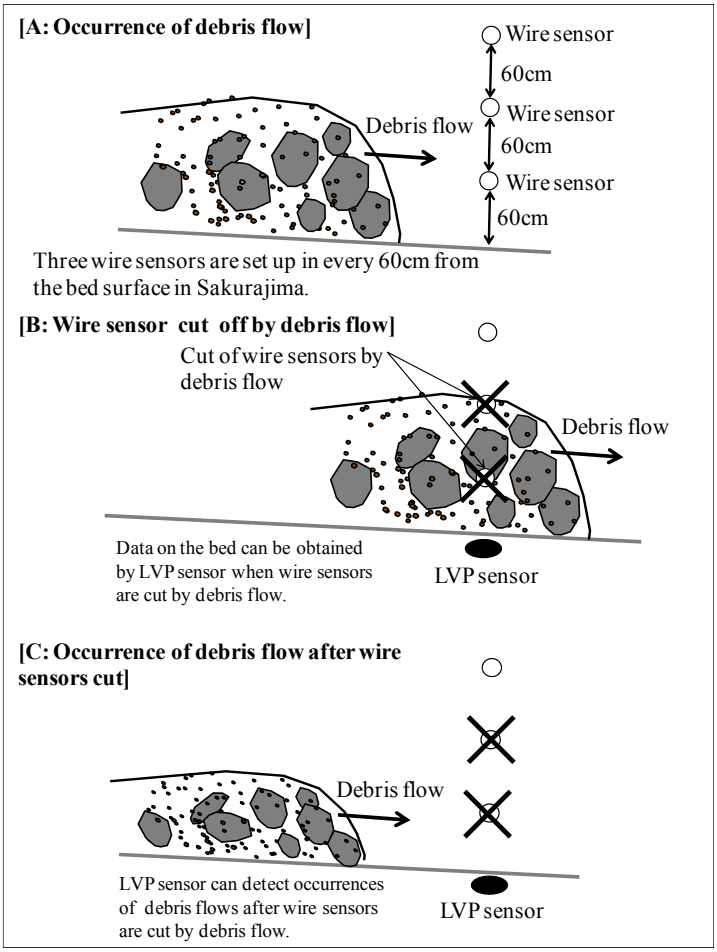

Figure 1. Schematics of debris flow detections by combination of a wire and a LVP sensors.

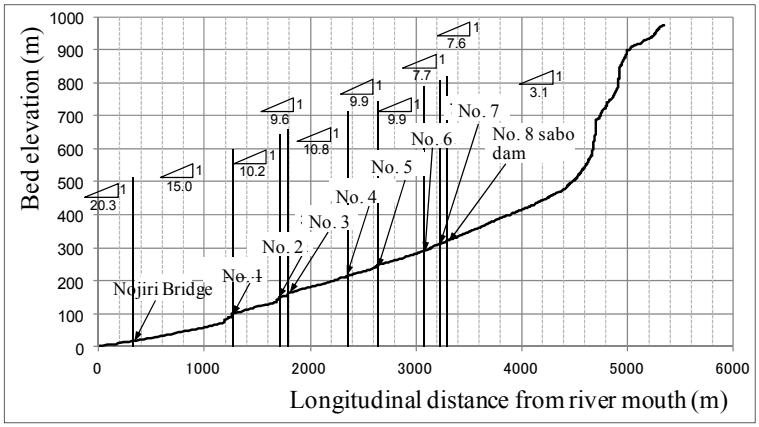

Figure 2. Longitudinal bed profiles and sabo dam layout along the Nojiri River in Sakura-jima Island.

The No. 1 sensor with a force plate, which is 25 cm in width and 35 cm in length, were installed on March 15th in 2014 and detected 14 times of debris flow occurrences. In the debris flow events on June 20th to 21st in 2014, the load cell was broken due to the direct collisions of large boulders in debris flow surge, but the debris flows were detected by a "VP sensor", which consists of the pressure and acceleration meters until February 5th, 2015. Data obtained by the No. 1 LVP sensor showed that the sensor could detect the debris flows even if some sensors are broken. The No. 2 sensor is modified and developed to avoid direct collisions of large boulders, and has small size of a force plate, which is 6 cm in diameter, as shown in Figure 3. The force plate seems to be appropriate for only load measurement by load cell to detect the debris flow passing, and the measured load does not have accuracy because of the debris flow detection by measured weight with the load cell. Herein, data sampling rate is 10 Hz and measured data can be shown by every 10 Hz and every one minute. Those data are deposited at a personal computer set at the field site.

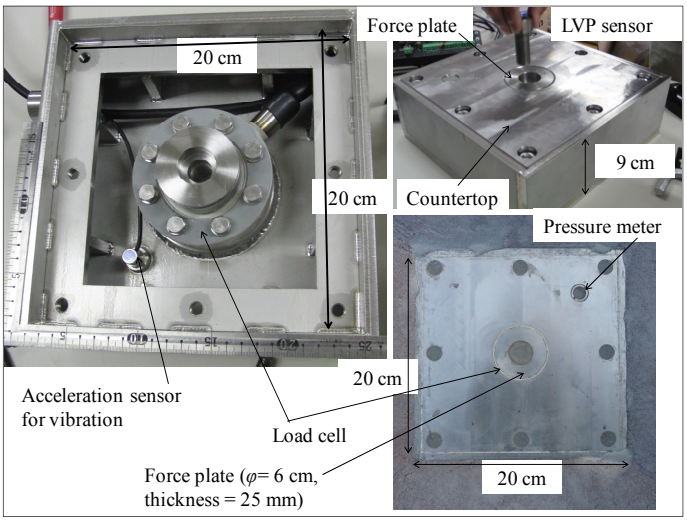

Figure 3. Developed LVP sensor (No. 2 LVP sensor).

The modified No. 2 LVP is detected 12 times of debris flow events in 13 times occurrences of debris flows during a year in 2015 after installation. Meanwhile, a wire also detected 12 times of debris flows, because the disconnected wire could not be maintained due to active eruption during the middle to the end of August in 2015. During those days, the LVP sensor detected the debris flows with around 60 cm in depth (August 30th, 2015). It indicated that the LVP sensor can detect the debris flows after disconnection of wire sensor without the maintenance for wires. Debris flows are detected well by a combination of a wire, and the LVP sensor can detect multiple debris flow occurrences after disconnected wires.

2.3 Measured debris flow events

Several typical data are obtained using the LVP sensor: Debris flow events on June 8th, April 6th and April 19th in 2015, respectively. Those are examples for debris flows detections by a wire and LVP sensor, such that the LVP sensor detected at almost same time to the disconnected wires, the LVP sensor could detect several surges after disconnected wires and the LVP sensor could not detect perfectly.

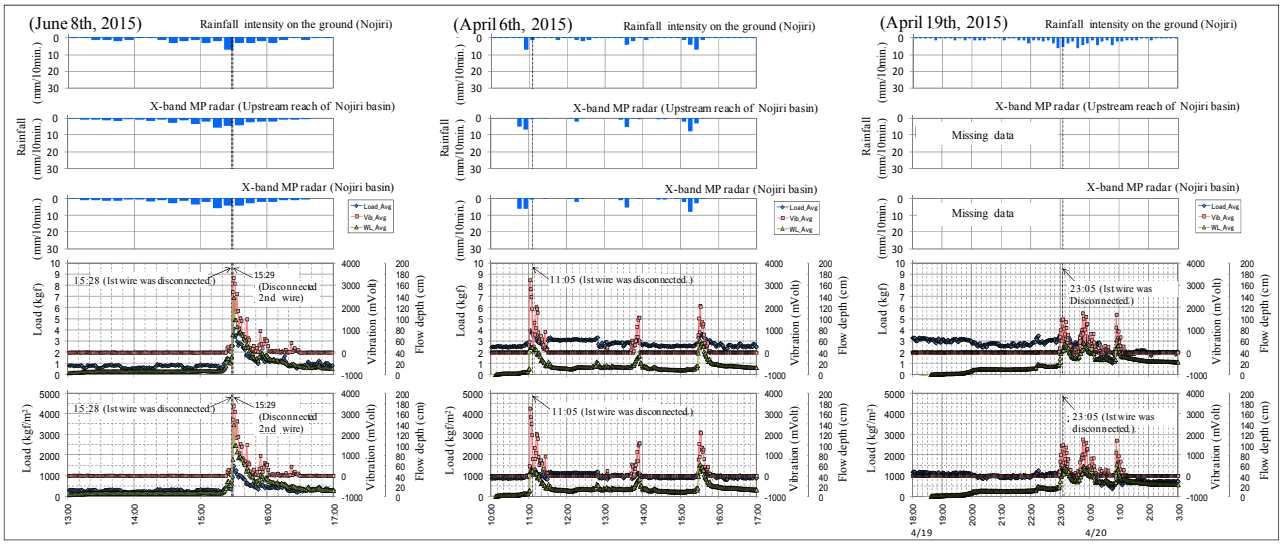

Figures 4. Typical debris flows detected by LVP sensor on June 8th, April 6th and April 19th in 2015.

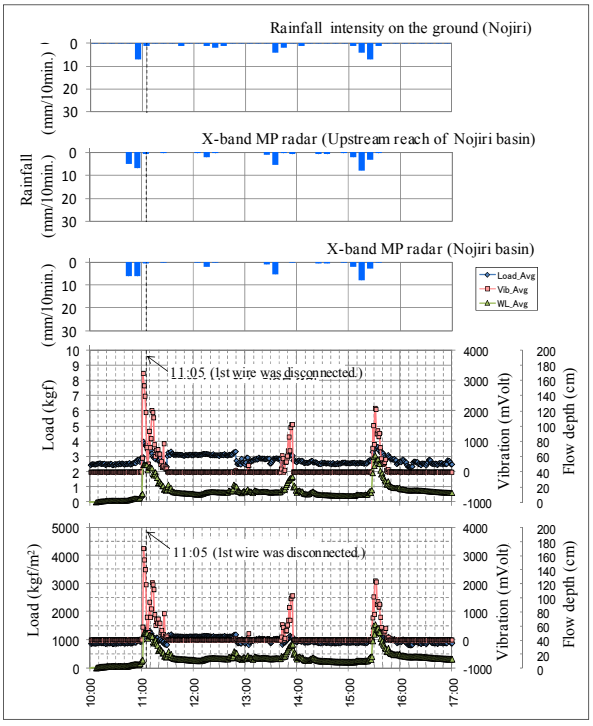

Figure 5. Data obtained by the LVP sensor for debris flow events with multiple surges on April 6th in 2015.

Figures 4 shows those typical data obtained by LVP sensor. In those figures, flow depth, load and vibration are shown in units of cm, kgf, kgf/m^2 and mVolt, and time and the numbers of disconnected wires are also shown. As shown in Figure 4, there are several patterns of the detections of debris flows such that the LVP sensor detected at almost same time to disconnected wires, the LVP sensor could detect several surges after disconnected wires. Figure 5 shows the debris flow events on April 6th in 2015, and the figure indicates that the debris flows are detected well by a combination of a wire, and the LVP sensor can detect multiple debris flow occurrences after disconnected the wires. While, the LVP sensor could not detect perfectly, because of transverse flow shifting. Figures 6 and 7 show debris flow events taken place on April 19th in 2015. It seems that several installations of the sensor could be better to avoid transverse flow shifting of debris flows.

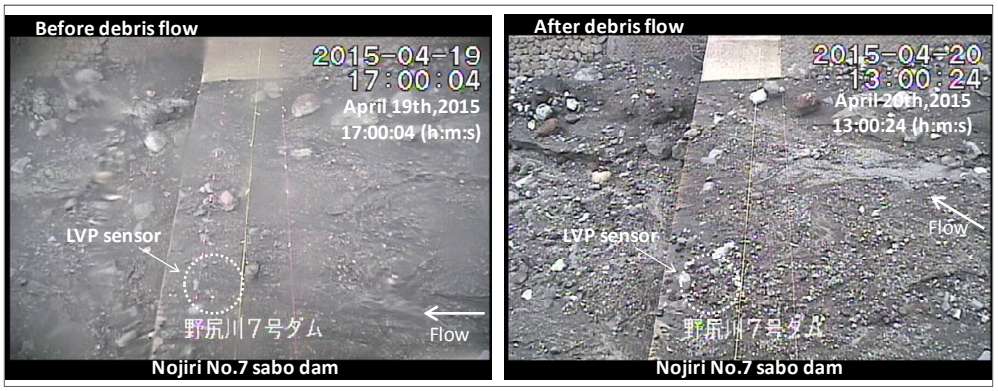

Figures 6. Debris flow events with transverse flow shifting on April 19th in 2015.

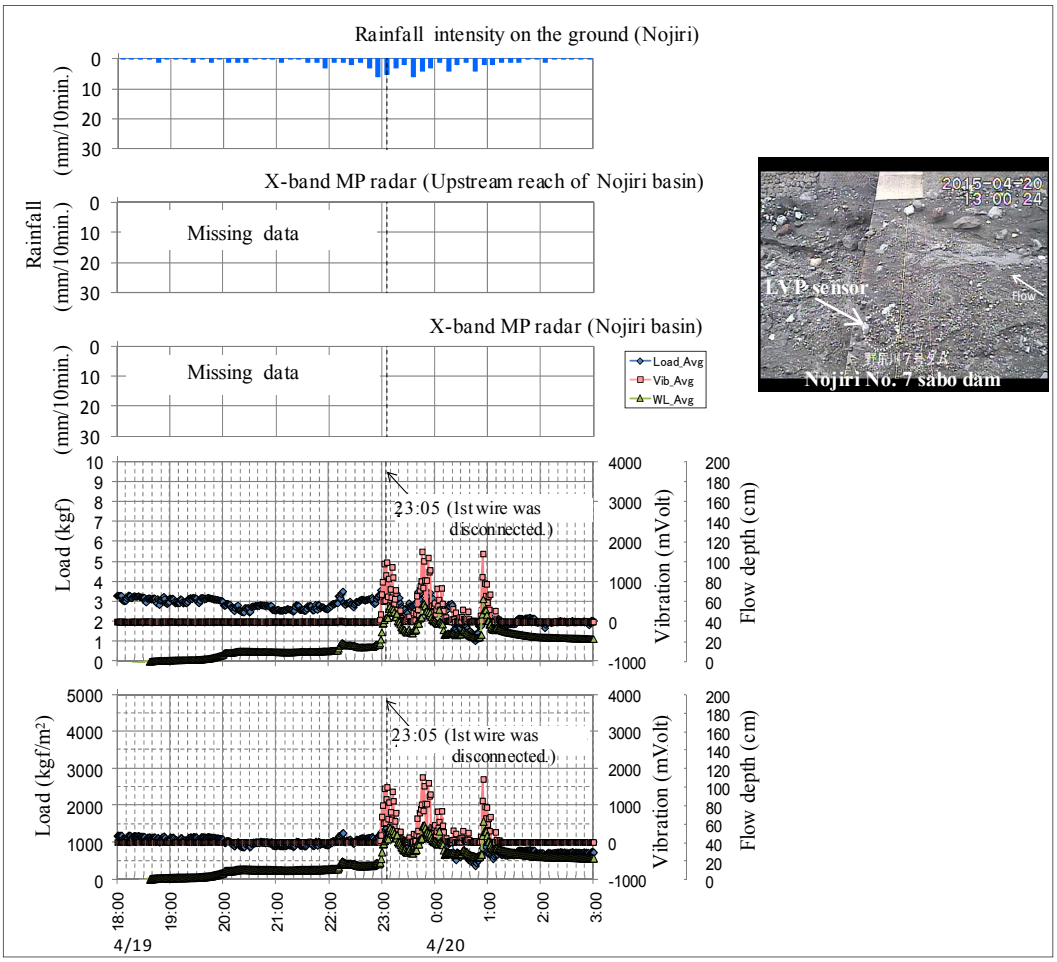

Figure 7. Data obtained by the LVP sensor for debris flow events with transverse flow shifting on April 19th in 2015.

3 EVALUATIONS OF THRESHOUD VALUE FOR DEBRIS FLOW OCCURENCES

Let us see the relationships between the flow depth and load, between the flow depth and vibration at the time of disconnected wires. There seem to be some threshold for the occurrences of the debris flow events, though the sediment concentration takes various values for the flow depth.

Figure 8 shows an example for attempts for threshold values for the debris flow occurrences, which are estimated by obtained data using a LVP sensor in case of debris flow weight. Figure 9 shows examples for attempts for threshold values for the vibrations or acceleration due to vibration as well as in Figure 8. Though more data collections are needed for discussions, the threshold value for the debris flow occurrences could be estimated as 400 kgf/m^2 in load and 200 mVolt in vibration, though more data collections are necessary.

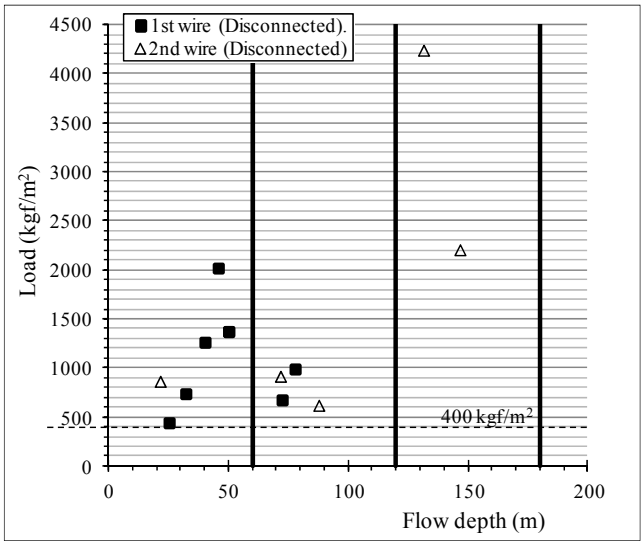

Figure 8. Threshold values for debris flow occurrences, which are estimated by obtained data using a No. 2 LVP sensor (Weight).

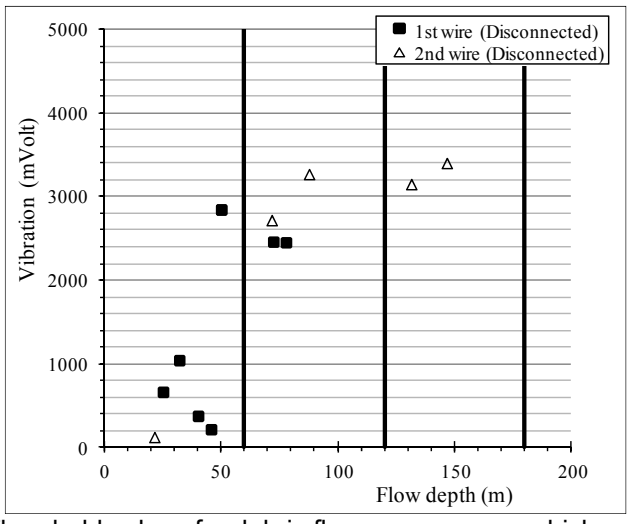

Figure 9. Threshold values for debris flow occurrences, which are estimated by obtained data using a No. 2 LVP sensor (Vibration).

4 CONCLUSIONS

The LVP sensor was developed and installed for continuous debris flow detections at Nojiri No. 7 sabo dam, supposing the combination of both a wire and LVP sensor. Through data collections using the No. 1 LVP sensor, knowledge for measurements with the LVP sensor yields the modified LVP sensor (No. 2) for the debris flow detection without large boulder collision to the sensor. Data for debris flow detections were collected by the LVP sensor in every debris flow event, and threshold values are tried to determine through continuous monitoring on the bed by temporal changes of flow depth, weight and vibration, which are measured by those sensors.

ACKNOWLEDGEMENTS

Authors should be thankful for Osumi Office of River and National Highway, Kyushu Regional Development Bureau, Ministry of Land in Japan (MLIT) for monitoring data useful advice, and be thankful for Dr. Koji YOKOYAMA about useful discussions for LVP sensor development. Additionally, authors are thankful for research budget (KAKENHI: Scientific Research C, No. 15K07502) from Japan Society for the Promotion of Science (JSPS) for parts of present study.

REFERENCES

Arattano, M. & Marchi, L. (2008): Systems and Sensors for Debris-Flow Monitoring and Warning. *Sensors*, 8, 2436-2452.

Hirano, M., Hashimoto, H., Park, K., Kouno, M. & Onda, K. (1999). Field Measurements of Debris Flows in the Mizunashi and Nakao Rivers on Mt Unzen-Hugen Dake. *Journal of JSCE*, 635(49), 49-65 (In Japanese with English Abstract).

McArdell, B. W., Perry, B. & Julia, K. (2007). Field Observations of Basal Forces and Fluid Pore Pressure in a Debris Flow, *Geophysical Research Letters*. 34 (L07406), 1-4.

Osaka T., Utsunomiya R., Tagata S., Itoh T. & Mizuyama T. (2014). Debris Flow Monitoring using Load Cells in Sakurajima Island. *Proceedings of the Interpraevent 2014 Pacific Rim (edited by Fujita, M. et al.), November 25-28, Nara, Japan,* O-14.pdf in DVD.

Okuda, S., Suwa, H., Okunishi, K., Yokoyama, K. & Nakano, M. (1980). Observation of the Motion of Debris Flow and its Geomorphological Effects. *Zeitschrift fur Geomorphology, Suppl*, *Bd*, 35, 142–163.

Osumi Construction Office in the Ministry of Construction (1988). *Debris Flow in Sakura-jima Island,* SABO Publicity Center, 65pp (In Japanese).

Scott, W. M., Coe, J. A., Kean, J. W., Turker, G. E., Staley, D. M. & Wasklewicz, T. A. (2011). Observations of Debris Flows at Chalk Criffs, Colorado, USA: Part1, *Italian Journal of Engineering Geology and Environment*, 1, 65-75.

Suwa, H., Okano, K. & Kanno, T (2011): *Forty years of debris-flow monitoring at Kamikamihorizawa Creek, Mount Yakedake, Japan.* Debris-Flow Hazards Mitigation Ed. By Genevois, Hamilton & Prestinzi©2011, Casa Editrice, Università La Sapienza, 605-613.

Proceedings of the 37th IAHR World Congress
August 13 – 18, 2017, Kuala Lumpur, Malaysia

ESTIMATION OF RESERVOIR SEDIMENTATION OF UKAI RESERVOIR USING SRS TECHNIQUE BETWEEN SPECIFIC WATER SURFACE ELEVATIONS

GANESH D. KALE[(1)], RITESHKUMAR H. SHOBHAVAT[(2)] & AMIT KUMAR SHARMA[(3)]

[(1)] Asst. Professor, Civil Engineering Department, SV NIT, Surat, Gujarat, India.
kale.gd@gmail.com
[(2)] M. Tech (WRE) Student, Civil Engineering Department, SV NIT, Surat, Gujarat, India.
riteshshobhavat@gmail.com
[(3)] Junior Research Fellow, Department of Civil Engineering, IISc, Bangalore, India.
amitsharma.isro@gmail.com

ABSTRACT

Efficient reservoir management calls for periodic assessment of its capacity. Remote sensing (SRS) technique offers acquisition of data over a long time span and broad spectral range and thus it is better than conventional methods. Earlier studies have been using the commercially available remote sensing data for the estimation of reservoir sedimentation. Cost of the imageries is significant financial element in the estimation of reservoir sedimentation using SRS technique. So, in the present study the reservoir sedimentation of Ukai reservoir located in Surat district of Gujarat State of India, is estimated using SRS technique with free landsat data, for the water years 2003 and 2010 to identify potential of free landsat data in reservoir sedimentation estimation. The daily water level data of reservoir and free Landsat data are used in the study. The reservoir sedimentation estimation by SRS technique for the water year 2003 is used to compare with previous hydrographic survey carried out at study area. Capacities of reservoir at water surface elevations above 98.1 m estimated by hydrographic survey (water year 2003) are more than corresponding original reservoir capacities while that of estimated by SRS method are lower than the original reservoir capacities. The loss of reservoir capacity between water surface elevations 91.1 m to 104.7 m for the period 1972 to 2010 is 470.4 MCM and corresponding loss in percentage is 9.1%. So, present study has shown that with use of free Landsat imageries and SRS technique the reservoir sedimentation can be estimated with fair accuracy and less cost.

Keywords: SRS technique; reservoir sedimentation estimation; capacity of reservoir.

1 INTRODUCTION

One of the most important natural resource is the water. There is unequal distribution of freshwater in both space and time. Time variations of the water requirement and water availability are managed by reservoirs. Storage reservoirs play important role in many ways observing long-term benefits. The rapid increase in uncontrolled population along with development activities in domestic and industrial field throughout the globe, have increased tremendous stress on the water resources (Roman, 2007).

India is a very huge country having high variability of rainfall in temporal and spatial domain. For tapping existing water resources and to use water as per the needs, many river valley projects have been built for serving different purposes like domestic and industrial water supply, hydropower generation, irrigation etc. One of the major factors affecting the lifespan of such projects is sediment accumulation in reservoirs. Sedimentation decreases reservoir storage capacity and hence their capability of conserving water for different intended aims. Sedimentation also decreases the aquatic species survival and constrains the utility of water for various purposes. Sedimentation further increases evaporation due to increment in exposed water surface area (NIH Roorkee, 1998). Gully, sheet and stream erosions are responsible for the decrease in reservoir storage capacity to about 40% of its designed capacity (Rao et al., 2006).

For optimum use of available storage of water in reservoirs, only reservoir capacity estimation by reservoir sedimentation estimation is not adequate but trapped sediment distribution in different reservoir zones is equally important for water use planning (Roman, 2007). Following are the various methods of estimation / prediction of deposition of sediments in reservoirs as given in Roman (2007):

I. Streamflow analysis
II. Hydrographic surveys/reservoir capacity surveys
III. Satellite remote sensing (SRS) technique
IV. Empirical methods - Area reduction technique
V. Mathematical models

Mathematical models and Empirical methods are useful for prediction of sedimentation of reservoir during planning stage while other three methods are useful for estimation of sedimentation during operation stage. Data of daily measurements of water and sediment flows at downstream and upstream of reservoir from

reservoir impoundment day are required for stream flow analysis method. Thus large data collection is required for the streamflow analysis method. While modern hi-tech survey systems consisting of differential global positioning system (DGPS) and depth measuring instruments such as echo sounders are required for the hydrographic survey. The hydrographic surveys for reservoirs with thick vegetation around and within reservoir in hilly region pose great difficulties. In spite of modern systems, hydrographic surveys of large reservoirs of fan shape need time span of 12 to 18 months or more. Apart from factor of time, these hydrographic surveys are costly, so cannot be carried out frequently at short intervals for reservoir sedimentation monitoring (Roman, 2007).

On the other hand remote sensing (RS) and geographical information system (GIS) techniques have become essential and an important tool for solving many civil engineering problems. RS is the art and science of acquiring information of material, area, objects or phenomenon, without its physical contact (Saha, 2010).

A Geographic Information System (GIS) is an integration of hardware, software and data to capture, manage, analyze and display geographically referenced information of all forms. GIS also permit the integration of data sets for gaining meaningful information and outputting the information derived in the form of map or table. In three ways a GIS can be viewed: 1) database view, 2) map view, 3) model view. RS observations provide data of resources of earth in a spatial format and GIS correlates different spatial data and their attributes (Saha, 2010).

Moreover, remote sensing technique offers acquisition of data over a long time span and broad spectral range and thus it is better than conventional methods. The benefit of satellite data over conventional methods includes coverage of a given area repeatedly at interval of few days, synoptic view availability and availability of almost instantaneous spatial data of the area of interest. More accurate data of reservoir water spread area on a given date could be collected instantaneously by remote sensing technique which is practically not possible even for high-tech survey systems. These advantages lead to development of SRS technique for reservoir sedimentation study (Roman, 2007).

The optimum utilization of water resources for different uses is possible if the available water storage in the reservoir is known. By sedimentation surveys, the available water quantity in reservoir can be known and this information can be used for optimum allocation of water resources for different water needs like domestic, industrial and irrigation etc. Thus assessment of storage capacity of reservoir is essential for reservoir water management. The information regarding the water availability is not only necessary for efficient reservoir management, but also required for planning of appropriate measures to minimize excessive siltation of reservoir or for recovering a fraction of lost capacity by removal of deposited sediment to obtain projected benefits during the reservoir planned life. Periodical reservoir capacity surveys in a basin are required for arriving at a realistic sedimentation index for catchment which will be useful in planning of reservoir projects in future in the basin. So, efficient management of reservoir calls for periodic assessment of its capacity by capacity surveys (Roman, 2007).

2 LITERATURE REVIEW

For the assessment of pattern of deposition of sediment in a reservoir, periodically systematic capacity surveys are carried out. With the advancement of technology of RS, reservoir sedimentation estimation has become commodious and economic (Goel et al., 2002). The number of studies in India used SRS technique for estimation of reservoir sedimentation (NIH Roorkee, 1998; Goel et al., 2002; Jain et al., 2002; Durbude and Purandare, 2005; Rathore et al., 2006; Roman, 2007; Mukherjee et al., 2007; Mani and Chakravorty, 2007). Roman (2007) is the main reference used in the present study. Some studies estimated reservoir capacity for entire reservoir while other studies estimated reservoir capacity between specific water surface elevations. All aforesaid studies used the commercially available remote sensing data for the estimation of reservoir sedimentation. Cost of the imageries is a significant financial element in the estimation of reservoir sedimentation using SRS technique. Use of freely available satellite imageries in SRS technique will reduce the cost of reservoir sedimentation estimation. As reservoir sedimentation estimation is carried out periodically for each important reservoir and there are many such reservoirs in India, crores of rupees can be saved by using free Landsat data in SRS technique.

So, objective of the present study is to find out reservoir sedimentation of Ukai reservoir for water years 2003 and 2010 between reservoir water surface elevations 91.1 m to 104.7 m, by using SRS technique and free Landsat data to to identify potential of free landsat data in reservoir sedimentation estimation. The use of free Landsat data will decrease the cost required for estimation of reservoir sedimentation using SRS technique. Water year is period of 12 months for any given year starting from 1 October and ending on 30 September of next year (U.S. Geological Survey 2016). But in the present study period Sept. 2002 to June 2003 is considered as water year 2003 while period Oct. 2007 to June 2010 is considered as water year 2010. The reservoir sedimentation estimation by SRS technique for water year 2003 is used to compare with previous hydrographic survey carried out at study area.

3 MATERIALS AND METHODS

The information about study area and catchment characteristics is referred from NIH Roorkee (1998).

3.1 Study area

Ukai Reservoir: It is the largest multipurpose project completed so far in state of Gujarat. The Ukai dam is constructed across Tapi River near Ukai Village of taluka Fort-Songadh in Surat district of Gujarat State. Ukai reservoir is positioned between latitudes 20^0 5' 0" N to 22^0 52' 30" N and longitudes 73^0 32' 25" E to 78^0 36' 30" E. The location of dam is about 29 km upstream of Kakrapar Weir. Ukai Reservoir total catchment area is 62,225 km^2 lying in the Deccan Plateau. The catchment of the dam is spread across 12 districts of three states Maharashtra, Madhya Pradesh and Gujarat of India. Survey of India toposheet maps 46 (G, H, K, L, O, P) and 55 (C, D, G, N and K) are covering entire catchment area of Ukai dam.

The dam consists of a 4927 m long composite earth cum masonry dam constructed across the Tapi River. The reservoir live storage capacity is $0.71x10^4$ million cubic metre (MCM) at full reservoir level (FRL) 105.156 m. The storage provides irrigation facilities to 3,76,000 acres area under the Ukai Left Bank Canal and 5,62,250 acres under Ukai Right Bank Canal under the command area of pick up weir located at Kakrapar. The hydropower house consisting of four units of 75 MW each, constructed at the foot of the dam. An average of 190 MW of hydropower is generated at present in addition to irrigation benefits. Also partial flood control was provided by dam to the downstream areas like Surat city.

3.2 Data collection

3.2.1 Topographical data

The topographical details of Ukai reservoir are obtained from Survey of India (SOI) toposheets. The details of toposheets of study area are obtained from SOI, Gandhinagar along with latitude and longitude information of study area and these are given below:

I. Toposheet No's.:- 46 G/11 and 12, 46 G/15 and 16.
II. Scale: - 1: 50,000.
III. Latitude:- 21^0 05' 00" to 21^0 35' 00" N
IV. Longitude: - 73^0 30' 00" to 74^0 10' 00" E

3.2.2 Field data

For accurate estimate of reservoir sedimentation reliable ground truth data is required (Roman, 2007). The salient features of the reservoir, original elevation–area–capacity table (1972) and curve, revised capacity table and curve for hydrographic survey of the water year 2003 and index map for Ukai catchment are collected from the Irrigation Dept., Surat, Gujarat. Daily reservoir water level data for the period 2000 to 2010 is collected from Irrigation Dept., Surat, Gujarat and database of Centre of Excellence on 'Water Resources and Flood Management', Civil Engineering Department, SV NIT, Surat. The details of important levels of Ukai reservoir and the corresponding areas and capacities are obtained from original elevation-area-capacity table (1972) and these are shown in Table 1 below. Data of important levels given below and their corresponding elevations is also available in salient features of reservoir.

Table 1. Important levels of Ukai reservoir.

Sr. No	Reservoir Level	Elevation (m)	Area (Mm^2)	Capacity (MCM)
1	River Bed	42.672	0	0
2	Minimum Draw Down Level (MDDL)	82.296	139.622	1418.5
3	Full Reservoir Level (FRL)	105.156	586.815	8511.012

Location of Ukai Dam in Tapi Basin is shown in Figure 1, while the original elevation capacity curve for the Ukai reservoir is shown in Figure 2. Revised elevation capacity curve found out by the hydrographic survey for water year 2003 is shown in Figure 3. The daily water level data for the periods Sept. 2002 to June 2003 and Oct. 2007 to June 2010 are used in the analysis.

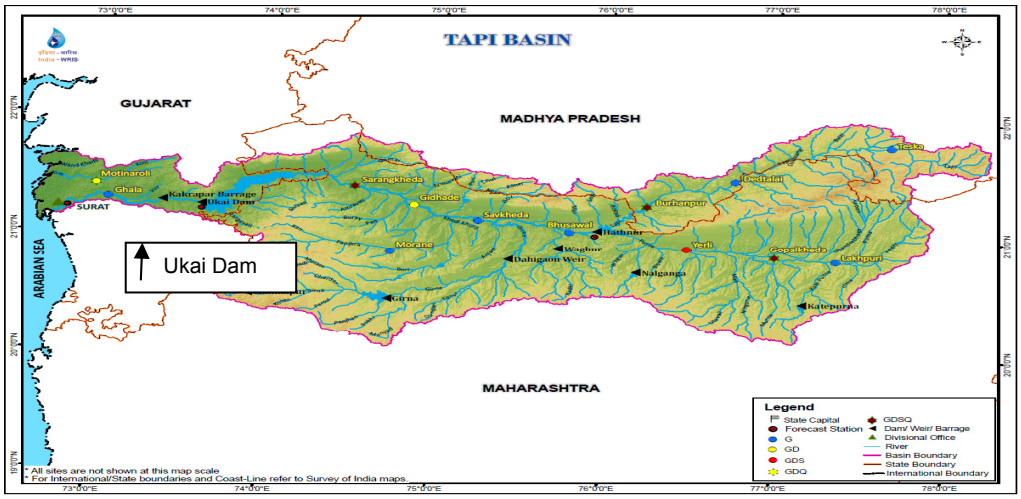

Figure 1. Map of Tapi basin.
(National Remote Sensing Centre 2015)

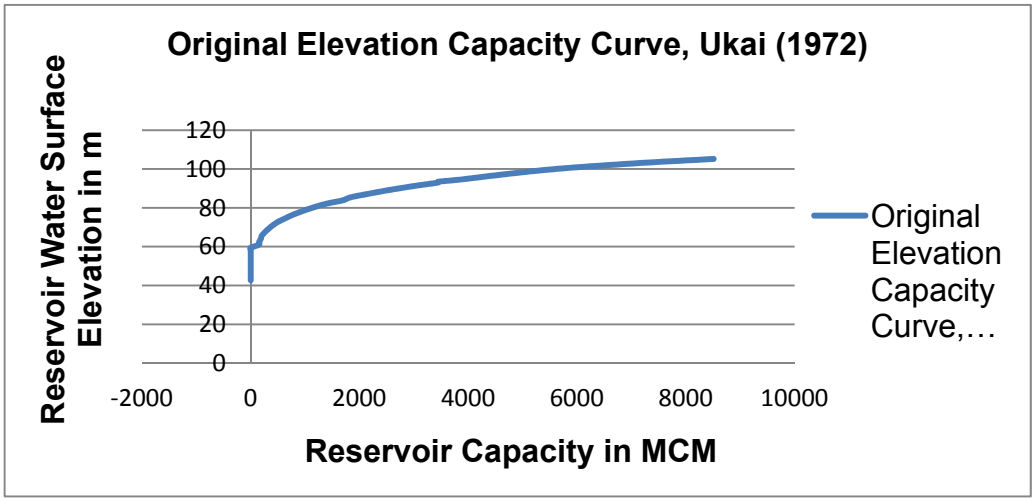

Figure 2. Original elevation capacity curve (1972).

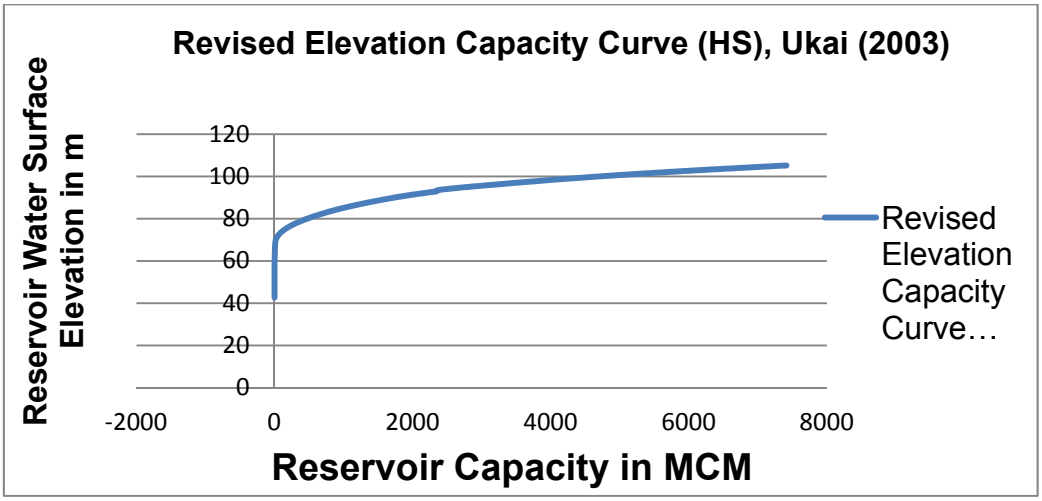

Figure 3. Revised elevation capacity curve by hydrographic survey (2003).

3.2.3 Satellite data

The raw optical data of Landsat satellite for enhanced thematic mapper sensor (ETM+) (L7 ETM SLC ON up to 2003 and 2003 onwards SLC OFF) was available for periods of analysis and same is used for the study. These imageries in ".JPG" format are downloaded from website "http://edcsns17.cr.usgs.gov/ NewEarthExplorer/" and presently these imageries can be downloaded from U.S. Geological Survey, (2017a).

The digital elevation modal (DEM) is downloaded from "www.gdem.aster.ersdac.or.jp" and presently it can be downloaded from U.S. Geological Survey, (2017b).

The ETM+ sensor data of Landsat-7 satellite having resolution of 30 m and three spectral bands is used in the study. The revisit period of Landsat-7 satellite is 16 days while its coverage area is 170 x 183 km^2 (Landsat Technical Guide, 2004). The Ukai reservoir water spread is covered in one scene of path 147 and row 45 of Landsat satellite.

3.3 SRS technique

Information about SRS method is taken from Roman (2007). SRS method for estimation of reservoir sedimentation uses the fact of decreasing water spread areas at various water surface elevations because of sedimentation of reservoir. The reservoir water spread areas at different water levels between FRL to MDDL in different months of the year are estimated from satellite imageries. Knowing the water spread areas and reservoir water surface levels corresponding to date of satellite pass, new elevation-capacity curve can be obtained and compared with original elevation capacity curve or with elevation capacity curve of earlier survey. Shift in the capacity curves shows reservoir capacity loss. Step by step procedure is followed for calculating loss of reservoir capacity using SRS technique:

I. Daily reservoir water levels analysis
II. To determine the period of analysis on the basis of availability of cloud free image data and maximum variation between the maximum and minimum water surface elevations of reservoir in the given period.
III. Satellite data analysis
IV. Water spread area estimation from analysis of satellite data
V. New area elevation curve generation
VI. Calculation of reservoir volumes at different elevations of reservoir
VII. Sediment deposition estimation in different zones of reservoir
VIII. Comparison of results with original and past hydrographic / SRS survey
IX. Calculation of sediment index of catchment

Following are some benefits and limitations of SRS technique used for estimating reservoir capacity.

Advantages: Cost effective, less time required for analysis, less manpower is required, possible to select appropriate water year for analysis on the basis of availability of cloud free imageries and maximum fluctuation between maximum and minimum water levels, sedimentation of past years can also be calculated at desired intervals of time and better accuracy for fan shaped large reservoirs.

Limitations: Revised capacity above MWL (gross storage + flood storage) and below MDDL cannot be estimated, less but skilled manpower is required, special care has to be taken in separation of land and water pixels, perceptivity in to reservoir under flood situations and some experience are needed in extended tail separation and less accuracy for elongated reservoirs.

3.4 Analysis of data

3.4.1 Determination of period of analysis

To decide the appropriate periods of analysis is an essential first step in determination of sedimentation by SRS technique. The selection of appropriate period for the analysis depends on the availability of cloud free data in the given period and maximum variation in the observed reservoir water levels in the given analysis period (Roman, 2007). From Ukai daily reservoir water level data from year 2000 to 2010, maximum and minimum daily reservoir water levels for water years in the aforesaid period were found out.

The first period of analysis is taken from Sept. 2002 to June 2003 i.e. 2003 water year because for the same period the revised elevation-area-capacity data of hydrographic survey was available for the comparison. Second period of analysis is taken from Oct. 2007 to June 2010 because the loss of capacity up to water year 2010 is to be determined and difference of reservoir water levels was enough for duration of Oct. 2007 to June 2010 to have large no. of water levels in between.

3.4.2 Analysis of satellite imageries

The methodology of analysis of satellite imageries is studied from Roman (2007) and modified as per the need of the present study. The analysis of satellite imageries is carried out by steps given below. The detailed information about the below steps is available in Shobhavat (2011).

I. Conversion of raw image in ".jpg" format to ".img" format.
II. Geo-referencing of satellite images
III. Area of interest separation
IV. Delineation of water-land boundary
V. Delineating land and water pixels
VI. Computation of water spread areas

After delineation of land water interface by contour generation, the vector editor displays selected closed vector contour area. These water spread areas, after performing following corrections are used for estimation of capacities of reservoir at different elevations:

- Removal of isolated water patches within the reservoir
- Cloud effect elimination
- Island areas removal
- Discontinuous pixels removal
- Noise elimination
- Extended tail and channel removal

The superimposed water spread areas of the reservoir for the period of analysis October 2007–June 2010 are shown in Figure 4.

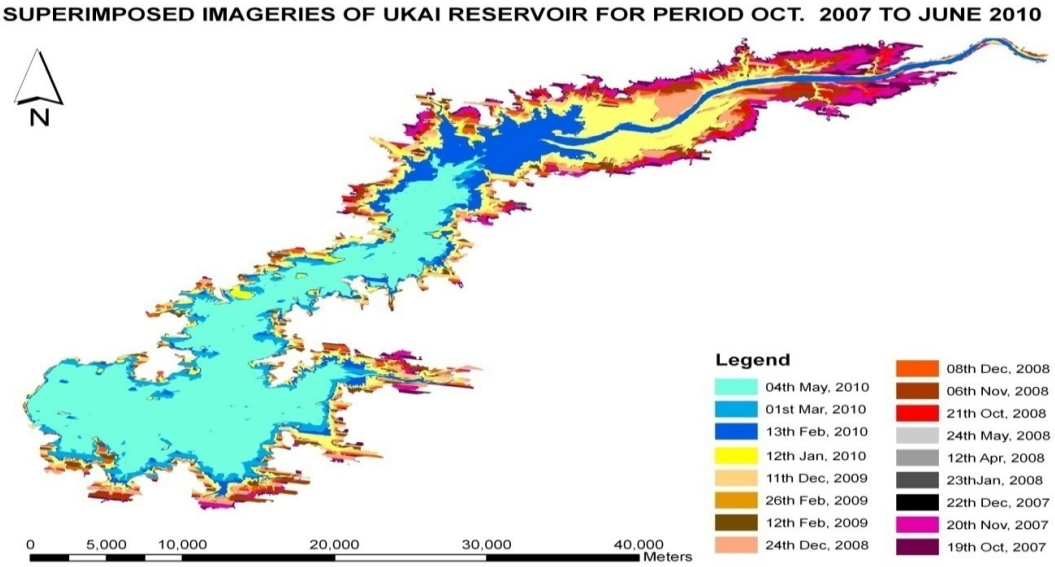

Figure 4. Super imposed areas for all 17 cloud free images for period October 2007 to June 2010.

4 RESULTS AND DISCUSSION

4.1 Estimation of latest area-elevation curve

Water spread areas corresponding to different dates of satellite overpass are estimated by digital analysis of satellite imageries corresponding to different water surface elevations and they are plotted to create area-elevation curve (Roman, 2007). As remote-sensing technique is able to estimate water spread areas mainly in live storage zone (Roman, 2007) and in the present study the fluctuation of water surface level is considered from 91.1 m to 104.7 m, therefore the water spread areas below FRL are available. The water surface levels 91.1 m to 104.7 m are considered in the present analysis because these are minimum and maximum water levels among water levels corresponding to dates of satellite pass. Linear interpolation/extrapolation techniques are used to estimate areas. The revised water spread areas for the different dates of pass of satellite in the analysis period Sept. 2002 to June 2003 are shown in Table 2. Water spread areas in Table 2 corresponding to hydrographic survey are obtained from analysis of satellite imageries. The water spread areas of original (1972) and Revised SRS (2003) in Table 2 are obtained by linear interpolation and extrapolation from their corresponding area-elevation-capacity tables. Similarly revised water spread areas for the different dates of pass of satellite for the analysis period Oct. 2007–June 2010 are calculated and are shown in the Table 3.

The water spread area below 92.2 m water level was not available for 2003 water year analysis by SRS technique. So, water spread area for water surface level 91.1 m for water year 2003 is estimated by linear extrapolation in Table 3.

Table 2. Reservoir water surface elevations and water spread areas for different dates of satellite overpass during September 2002 to June 2003.

Sr. No.	Date of Satellite Pass	Observed Water Level (m)	Area (10^6 m^2) Original 1972	Revised 2003 (HS)	Revised 2003 (SRS)
1	05-10-2002	103.1	508.5	538.7	473.9
2	22-11-2002	101.0	454.3	472.2	402.6
3	24-12-2002	99.8	414.8	438.1	401.7
4	10-02-2003	97.6	365.5	380.7	360.9
5	30-03-2003	95.2	315.6	331.4	296.8
6	17-05-2003	92.2	260.0	217.2	220.6

(HS-Hydrographic Survey, SRS-Satellite Remote Sensing)

Table 3. Reservoir water surface elevations and water spread areas for different dates of satellite overpass during October 2007 to June 2010.

Sr. No.	Date of Satellite Pass	Observed Water Level (m)	Area (10^6 m^2) Original 1972	Revised 2003 (HS)	Revised 2003 (SRS)	Revised 2010 (SRS)
1	19-10-2007	104.7	568.7	595.7	481.3	513.6
2	20-11-2007	103.7	528.8	558.8	476.7	488.9
3	22-12-2007	102.4	485.2	515.6	450.1	466.2
4	23-01-2008	101.4	456.7	484.4	416.2	433.0
5	12-04-2008	97.3	359.2	374.3	352.9	342.3
6	24-05-2008	94.4	299.0	309.5	276.5	208.3
7	21-10-2008	102.0	472.7	502.7	436.6	449.1
8	06-11-2008	101.5	459.4	487.5	419.6	439.8
9	08-12-2008	100.2	425.1	449.1	402.0	417.1
10	24-12-2008	100.0	419.9	443.6	401.9	414.6
11	10-02-2009	98.1	375.8	393.5	370.2	371.3
12	26-02-2009	97.3	359.2	374.3	352.9	331.3
13	11-12-2009	98.1	375.8	393.5	370.2	361.6
14	12-01-2010	96.7	346.5	362.2	336.9	328.6
15	13-02-2010	95.9	329.6	345.9	315.5	293.1
16	01-03-2010	95.0	311.6	327.2	291.7	285.6
17	04-05-2010	91.1	241.9	197.4	218.0	200.4

4.2 Estimation of reservoir volumes at different elevations

The capacity of reservoir between two elevations is estimated by Prismoidal formula using corresponding water spread areas. The formula is as follows:

$$\Delta V_{1-2} = \frac{\Delta H}{3}(A_1 + A_2 + \sqrt{A_1 A_2}) \quad [1]$$

Where, $\Delta V_{1\text{-}2}$ is volume between elevations E_1 and E_2 ($E_2 > E_1$), Δh is difference between elevations E_2 and E_1 i.e. (E_2-E_1) and A_1, A_2 are water spread areas at water surface elevations E_1 and E_2. The above formula and information about different terms used in the above formula are referred from Roman (2007). The original and revised cumulative capacities (by using SRS method) of Ukai reservoir for both periods of analysis are calculated and these are shown in Table 4. The data in the table is arranged in ascending order of water surface elevations of reservoir.

The loss of reservoir capacity between reservoir water surface elevations 91.1 m to 104.7 m for years 1972-2003 is 351.7 MCM and corresponding loss in percentage is 6.8%. The loss of capacity between reservoir water surface elevations 91.1 m to 104.7 m for years 1972-2010 is 470.4 MCM and corresponding loss in percentage is 9.1%. Also it is observed from Table 4 that capacities of reservoir at water surface elevations above 98.1 m estimated by hydrographic survey carried out in water year 2003 are more than corresponding original reservoir capacities while on the other hand corresponding estimates in present study are lower than the original reservoir capacities. So, the results of the present study confirm that SRS technique and free Landsat data can be used for estimation of reservoir sedimentation with fair accuracy and less cost.

Table 4. Revised capacities and loss of capacity of Ukai reservoir for different water years.

Sr. No.	Date of Satellite Pass	Observed Water Level (m)	Cumulative Capacity (MCM)				Loss in Cumulative Capacity (MCM)	
			Original 1972	Revised 2003 (HS)	Revised 2003 (SRS)	Revised 2010 (SRS)	SRS 2003	SRS 2010
1	4-5-2010	91.1						
2	24-05-2008	94.4	890.8	829.5	814.0	674.3	76.8	216.5
3	1-3-2010	95.0	1074.0	1020.5	984.4	821.9	89.5	252.1
4	13-02-2010	95.9	1362.5	1323.3	1257.6	1082.3	104.9	280.2
5	12-1-2010	96.7	1632.9	1606.6	1518.5	1330.8	114.4	302.1
6	26-02-2009	97.3	1844.6	1827.5	1725.4	1528.8	119.1	315.8
7	12-4-2008	97.3	1844.6	1827.5	1725.4	1528.8	119.1	315.8
8	10-2-2009	98.1	2138.6	2134.6	2014.7	1814.2	123.9	324.4
9	11-12-2009	98.1	2138.6	2134.6	2014.7	1814.2	123.9	324.4
10	24-12-2008	100.0	2894.1	2929.4	2747.9	2551.0	146.1	343.1
11	8-12-2008	100.2	2978.6	3018.6	2828.3	2634.2	150.2	344.4
12	23-01-2008	101.4	3507.5	3578.6	3319.2	3144.2	188.3	363.4
13	6-11-2008	101.5	3553.4	3627.2	3361.0	3187.8	192.3	365.5
14	21-10-2008	102.0	3786.4	3874.7	3575.1	3410.0	211.3	376.3
15	22-12-2007	102.4	3977.9	4078.4	3752.4	3593.1	225.6	384.9
16	20-11-2007	103.7	4636.8	4776.6	4354.7	4213.9	282.1	423.0
17	19-10-2007	104.7	5185.5	5353.7	4833.7	4715.1	351.7	470.4

4.3 Estimation of sediment deposition in reservoir and erosion rate per year

As mentioned earlier, the Ukai dam was constructed in the year 1972. As per available records, the first impoundment of reservoir was occurred in year 1972. The reservoir gross storage capacity in 1972 was 8511.012 MCM at FRL (105.156 m). Original elevation capacity curve of 1972 is shown in Fig. 2. In order to estimate loss in storage and sedimentation rate, capacity surveys by remote sensing technique are carried out in the present study for the periods Sept. 2002-June 2003 and Oct. 2007-June 2010. The variation in the cumulative capacities of original (1972) and latest (2003, 2010) SRS surveys has given loss of storage between reservoir water surface elevations 91.1 m to 104.7 m as shown in Table 4. The elevation capacity curves for the year 1972 (original) and two periods of analysis in the present study are shown in Fig. 5. Table 5 gives the loss in capacity of Ukai reservoir between water surface elevations 91.1 m to 104.7 m, at the two periods of analysis along with annual siltation rate and percentage loss in capacity since 1972.

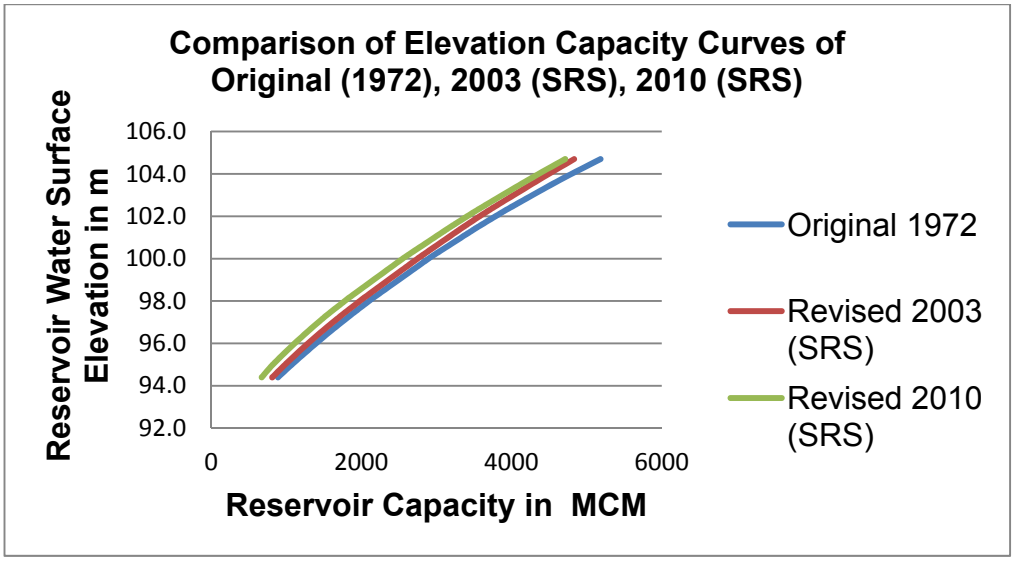

Figure 5. Comparison of elevation capacity curves for 1972, 2003 (SRS) and 2010 (SRS).

The sediment index estimated considering total sediment deposition of 351.7 MCM from year 1972 to 2003 (31 years) taking 62,225 km^2 catchment area is 182.3 m^3/km^2/year which is equivalent to 255.2 T/km^2/year (assuming dry density of 1.4 T/m^3). The sediment index estimated considering total sediment deposition of 470.4 MCM from 1972 to 2010 (38 years) taking 62,225 km^2 catchment area is 198.9 m^3/km^2/year which is equivalent to 278.5 T/km^2/year (assuming dry density of 1.4 T/ m^3). Average annual loss in storage capacity of reservoir in percentage from year 1972 to 2003 is 0.2%. Average annual loss in storage capacity of reservoir in percentage from year 1972 to 2010 is 0.2%.

Table 5. Loss of storage in Ukai Reservoir.

Year	Reservoir capacity MCM (91.1 m to 104.7)	Loss of Capacity MCM		Period (years)		Rate of siltation MCM/yr		% loss of capacity from 1972	% annual loss from 1972
		From 1972	From previous survey	From 1972	From previous survey	From 1972	Between two surveys		
1972	5185.5	0	0	0	0	0	0	0	0
2003 (SRS)	4833.7	351.7	351.7	31	31	11.3	11.3	6.8	0.2
2010 (SRS)	4715.1	470.4	118.7	38	7	12.4	17	9.1	0.2

5 RESULTS AND DISCUSSION

I. The loss of reservoir capacity between reservoir water surface elevations 91.1 m to 104.7 m for years 1972-2003 is 351.7 MCM and corresponding loss in percentage is 6.8%. The loss of capacity between reservoir water surface elevations 91.1 m to 104.7 m for years 1972-2010 is 470.4 MCM and corresponding loss in percentage is 9.1%.

II. The sediment index estimated considering total sediment deposition of 351.7 MCM from year 1972 to 2003 (31 years) taking 62,225 km^2 catchment area is 182.3 m^3/km^2/year which is equivalent to 255.2 T/km^2/year (assuming dry density of 1.4 T/m^3). The sediment index estimated considering total sediment deposition of 470.4 MCM from 1972 to 2010 (38 years) taking 62,225 km^2 catchment area is 198.9 m^3/km^2/year which is equivalent to 278.5 T/km^2/year (assuming dry density of 1.4 T/ m^3).

III. Average annual loss in storage capacity of reservoir in percentage from year 1972 to 2003 is 0.2%. Average annual loss in storage capacity of reservoir in percentage from year 1972 to 2010 is 0.2%.

6 CONCLUSIONS

I. As compared to 1972 to 2003, the rate of siltation has been increased during 2003 to 2010.

II. The SRS technique is fast and fairly accurate technique of the estimation of reservoir sedimentation.

III. With SRS technique and free satellite data like Landsat data, the estimation of reservoir sedimentation can become more economical.

ACKNOWLEDGEMENTS

The authors are thankful to concerned authorities of U.S. Geological Survey, Survey of India, Gandhinagar, Irrigation Department, Surat, Gujarat and Centre of Excellence on 'Water Resources and Flood Management', Civil Engineering Department, SV NIT, Surat for providing the necessary data required for the study. Also authors are thankful to all who have directly and indirectly helped in data collection.

REFERENCES

Durbude, D.G. & Purandare, B.K. (2005). Assessment of Sedimentation in the Linganmakki Reservoir using Remote Sensing. *Journal of Indian Society of Remote Sensing,* 33(4), 503-509.

Goel, M.K., Jain, S.K. & Agarwal, P.K. (2002). Assessment of Sediment Deposition Rate in Bargi Reservoir using Digital Image Processing. *Hydrological Sciences-Journal-Des Sciences Hydrologiques,* 47(S), S81-S92.

Jain, S.K., Singh, P. & Seth, S.M. (2002). Assessment of Sedimentation in Bhakra Reservoir in the Western Himalayan Region using Remotely Sensed Data. *Hydrological Sciences-Journal-des Sciences Hydrologiques,* 47(2), 203-212.

Landsat Technical Guide. (2004). *Global Land Cover Facility,* University of Maryland Institute for Advanced Computer Studies, University of Maryland Department of Geography. Available at: http://glcf.umd.edu/library/guide/techguide_landsat.pdf

Mani, P. & Chakravorty, V. (2007). Remote Sensing based Sedimentation Study of Maithon Reservoir. *Journal of the Indian Society of Remote Sensing,* 35(1), 117-120.

Mukherjee, S., Veer, V., Tyagi, S.K. & Sharma, V. (2007). Sedimentation Study of Hirakud Reservoir through Remote Sensing Techniques. *Journal of Spatial Hydrology,* 7(1), 122-130.

National Remote Sensing Centre (2015), last accessed on 13 February 2017, <http://india-wris.nrsc.gov.in/wrpinfo/index.php?title=Tapi>

Roorkee, N.I.H. (1998). *Reservoir Sedimentation Study for Ukai Dam using Satellite Data,* A Technical Study Report submitted in NIH Roorkee, India.

Rao, P.J., Harikrishnan, P. & Rao, S.P.B. (2006). Studies on Silt Deposition in Gambhiram Reservoir-a Remote Sensing Approach. *Journal of Indian Geophysical Union,* 10(4), 285-292.

Rathore, D.S., Choudhary, A. & Agarwal, R.K. (2006). Assessment of Sedimentation in Hirakud Reservoir using Digital Remote Sensing Technique. *Journal of the Indian Society of Remote Sensing,* 34(4), 377-383.

Roman, U.C. (2007). Application of Remote Sensing for Reservoir Sedimentation, *Ph. D.* Seminar, Civil Engineering Department, SV NIT, Surat.

Saha, S. (2010). Application of Remote Sensing and GIS in Civil Engineering. *FOSET Academic Meet 2010, Civil and Architecture Section,* West Bengal University of Technology, BF-142, Sector-I, Salt Lake, Kolkata, India.

Shobhavat, R.H. (2011). Application of SRS Technique for Estimation of Reservoir Sedimentation: A Case Study of Ukai Reservoir, *M. Tech (WRE) Dissertation.* Submitted in Civil Engineering Department, SV NIT, Surat.

U.S. Geological Survey (2016), last accessed on 13 February 2017, <http://water.usgs.gov/nwc/explain_data.html>

U.S. Geological Survey (2017a), last accessed on 13 February 2017, <http://earthexplorer.usgs.gov/>

U.S. Geological Survey (2017b), last accessed on 13 February 2017, <https://gdex.cr.usgs.gov/gdex/>

Proceedings of the 37th IAHR World Congress
August 13 – 18, 2017, Kuala Lumpur, Malaysia

DIRECT DEBRIS FLOW MONITORING USING LOAD CELL SYSTEMS IN SAKURAJIMA ISLAND

TAKAHIRO ITOH[(1)], TAKAHISA MIZUYAMA[(2)] & SATOSHI TAGATA[(3)]

[(1)] Research and Development Center, Nippon Koei Co., Ltd., Tsukuba, Japan,
a6556@n-koei.co.jp
[(2)] National Graduate Institute for Policy Studies (GRIPS), Tokyo, Japan,
byk01260@nifty.com
[(3)] Nippon Koei Co., Ltd., Tokyo, Japan,
a5672@n-koei.co.jp

ABSTRACT

In debris flow monitoring in Sakurajima Island in Japan, temporal changes of flow depth, discharge and bed profiles have been tried to be collected using ultrasonic sensors and video camera, and profiles of bed elevations are also monitored along the channel for longitudinal deposition and near river mouth in the sea using a sounding machine to evaluate sediment runoff volume from river mouth. However, it was quite difficult to obtain continuous data for sediment discharge and the runoff volume due to debris flows. Debris flows are observed by the newly installed debris flow measurement system with loadcell and pressure sensor (DFLP), and sediment concentration of both coarse sediment phase and suspended & liquid phase can be calculated using data measured by the DFLP (Osaka et al., 2014). In Arimura River, debris flow took place 13 times in 2014, and debris flows have been observed on June 27th, July 30th, August 29th and November 1st, and debris flows on June 27th are obtained by DFLP systems. While, in Nojiri River, debris flow took place 17 times in 2014, and debris flows have been observed on May 14th, June 21st, June 27th, July 9th, August 1st and November 1st. Debris flows on June 21st and 27th are measured by three DFLP systems in Nojiri River. In present study, temporal changes of specific weight, sediment concentration and sediment volume of debris flow are newly calculated using data obtained by DFLP systems in Nojiri and Arimura Rivers in 2014. Sediment concentration and specific weight are calculated such as 0.552 (left side), 0.667 (center), 0.816 (right side) and 1.94 (left side), 2.13 (center), 2.38 (right side), respectively, in Nojiri River (June 27th, 2014). In Arimura River, sediment concentration and specific weight are calculated as 0.463 and 1.76, respectively, on June 27th, 2014.

Keywords: Debris flow monitoring; loadcell; debris flow measurement system with loadcell and pressure sensor system (DFLP); sediment concentration, specific weight.

1 INTRODUCTION

Numerous debris flows have recently taken place frequently in Sakurajima Island, which is located at southern-west in Japan, due to rainfall events after deposition of volcanic ash by volcanic activities since 2010, and the number of debris flow occurrences has been gradually increasing though volcanic activities were active in 1980s there and the number of debris flows occurrences decreased in 1990s to 2000s due to decrease of volcanic activities. The numbers of debris flow occurrences are counted by the numbers of disconnected wire sensors in Sakurajima. Many kinds of measurements have been carried out to evaluate flow characteristics of debris flows not only in Sakurajima but also abroad (e.g., Arattano et al., 2008; Itakura et al., 2005; Osumi Construction Office, 1988; Scott et al., 2011). In those monitoring, temporal changes of flow depth, discharge and bed profiles tried to be collected using ultrasonic sensors and video camera, and profiles of bed elevations were also monitored along the channel for longitudinal deposition and near river mouth in the sea using a sounding machine to evaluate sediment runoff volume from river mouth. Sediment in debris flow bodies tried to be measure using a sampler box produced by an iron bucket (e.g., Osumi Construction Office, 1988). However, it was quite difficult to obtain continuous data for sediment discharge and the runoff volume due to debris flows.

A modified debris flow measurement system with loadcell and pressure sensor (DFLP) system, that is firstly proposed in Switzerland (McArdell et al., 2007), using load cells and an iron plate was installed to evaluate flow characteristics of debris flows at the Arimura River No. 3 sabo dam in June in 2012 (Osaka et al., 2014). After the installation in Arimura River, a system with small size of loadcell and iron plate without accuracy change of measurements was discussed for easier maintenance, and the newly modified three systems with an iron plate (1 m in width and 1 m in length) were installed transversely at the No. 1 sabo dam in Nojiri River in March in 2013.

In present study, temporal changes of specific weight, sediment concentration and sediment volume of debris flow using data measured by the DFLP systems in Nojiri and Arimura Rivers in 2014 were calculated because of well measured data. Sediment concentration and specific weight were calculated such as 0.552 (left side), 0.667 (center), 0.816 (right side) and 1.94 (left side), 2.13 (center), 2.38 (right side), respectively, in Nojiri River (June 27th, 2014). In Arimura River, sediment concentration and specific weight are calculated as 0.463 and 1.76, respectively, on June 27th, 2014, and those monitored data are shown since installation in 2012, because of necessity for several data collections in present monitoring.

2 INSTALLATON AND MODIFICATON OF DFLP

Figures 1 to 4 show the plan view and longitudinal bed profies of Noji River and Arimura River, respectively. Nojiri River is southern-west area in Sakurajima, and is with a watershed area 2.99 km^2, bed slope 4.5 % and flow width 13.2 m at the Nojiri No. 1 sabo dam (see Figures 1 and 2). Arimura River is in southern-east area in Sakurajima, and is with a watershed area 1.35 km^2, bed slope 19% and flow width 20.5 m at the Arimura No. 3 sabo dam (see Figures 3 and 4), though those information are shown in previous research (Osaka et al., 2014).

Focused on several rivers where debris flows take place frequently, the number of debris flow occurrences in Arimura River has gradually increased: e.g., 6 times in 2010, 6 times in 2011, 9 times in 2012, 5 times in 2013, 16 times in 2014, 15 times in 2015 and 6 times in 2016 and while 18 times in 2010, 10 times in 2011, 21 times in 2012, 12 times in 2013, 17 times in 2014, 13 times in 2015 and 11 times in 2016 in Nojiri River.

In Arimura River, debris flow measurement system with loadcell and pressure sensor (DFLP) system was installed in June in 2012, and ultrasonic velocity meter was also set up in 2013 (Osaka et al., 2014). Measurements using a DFLP system on the bed can obtain temporal changes of data without disturbing debris flow body. Flow discharge and depth are measured by image analyses of CCTV or ultra-sonic wave meter. Data of loadcells and pressure meter are measured by 100 Hz of sampling rate, and are converted using the low-pass filter and the converter (JFE Advantech production). Those data are collected by the NR600 (Keyence production), and the same data sampling system and collections are used in Nojiri river, which is shown below (Osaka et al., 2014).

In Nojiri river, after the installation in Arimura River in 2012, a system with small size of loadcell and iron plate without accuracy change of measurements was discussed for easier maintenance against mechanical troubles and the newly modified three systems with an iron plate (1 m in width and 1 m in length) was developed and installed transversely at the No. 1 sabo dam in March in 2013, as shown in a picture in Figure 1.

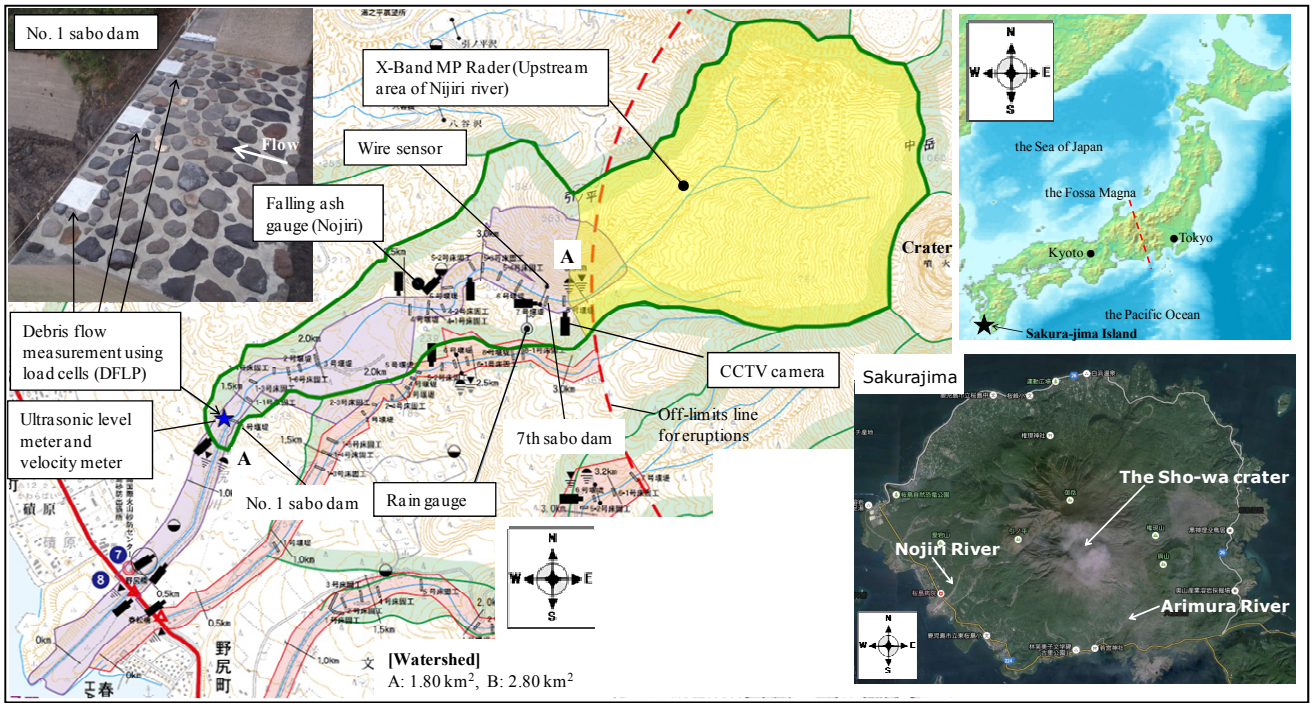

Figure 1. Plan view of Nojiri River basin and installed various sensors for debris flow monitoring.

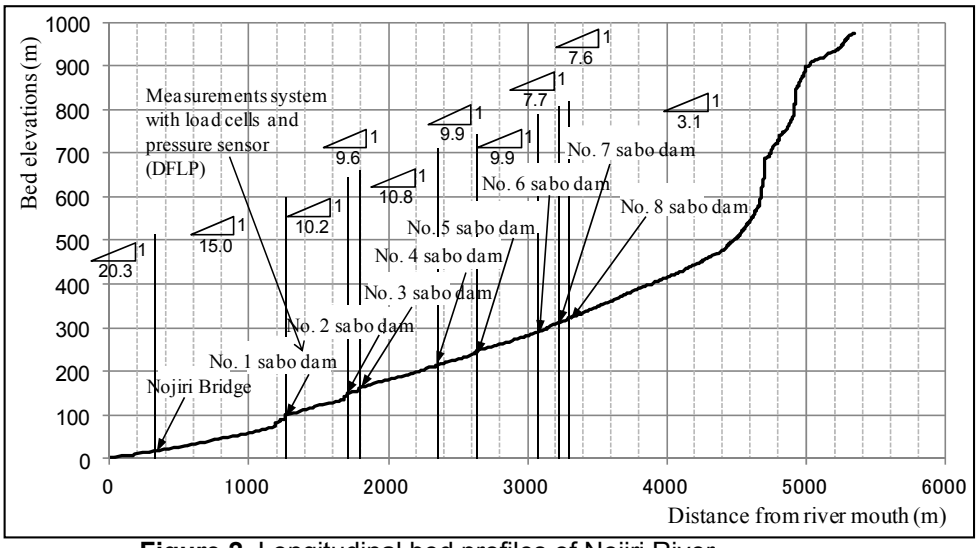

Figure 2. Longitudinal bed profiles of Nojiri River.

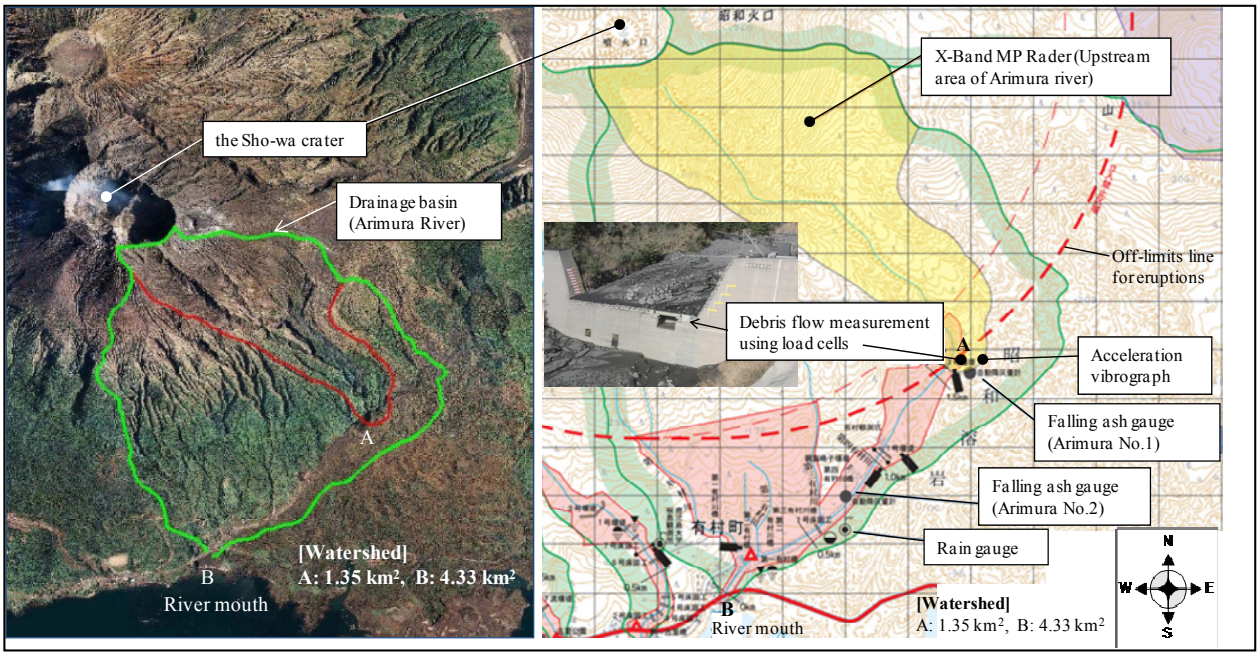

Figure 3. Plan view of Arimura River basin and installed various sensors for debris flow monitoring.

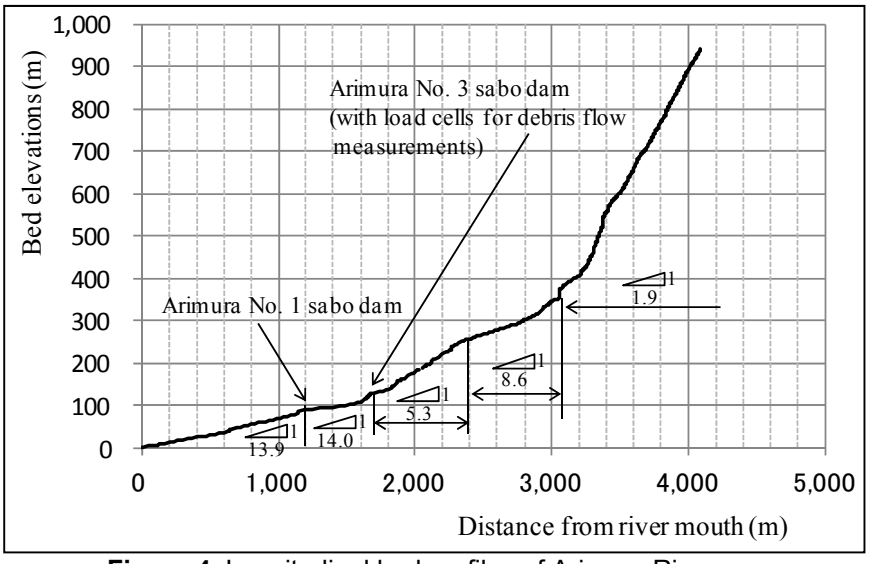

Figure 4. Longitudinal bed profiles of Arimura River.

3 TYPICAL DEBRIS FLOWS MEASURED BY DFLP

3.1 Flow discharge, weight and pressure

In order to measure occurrence and runoff of debris flow, many sensors have been installed (see Figures 1 and 3), and those are as follows: Rain gauge on the bed, X - band MP rader, ultrasonic water level meter, wire sensor, falling ash gauge, acceleration vibrograph (in only Arimura River) and CCTV camera in Arimura and Nojiri River.

In Sakurajima Island, the numbers of debris flow occurrences are counted by the numbers of disconnected wires of wire sensor and wires are installed at the height of 60 cm, 120 cm and 180 cm from the bed surface to know debris flow magnitude. In Arimura River, debris flow took place 16 times in 2014, and debris flows with middle magnitude were observed on June 27th, July 30th, August 29th and November 1st, and debris flows on June 27th were observed by the DFLP systems. While, in Nojiri River, debris flow took place 17 times in 2014, and debris flows with middle magnitude were observed on May 14th, June 21st, June 27th, July 9th, August 1st and November 1st. Debris flows on June 21st and 27th were measured by three DFLP systems in Nojiri River.

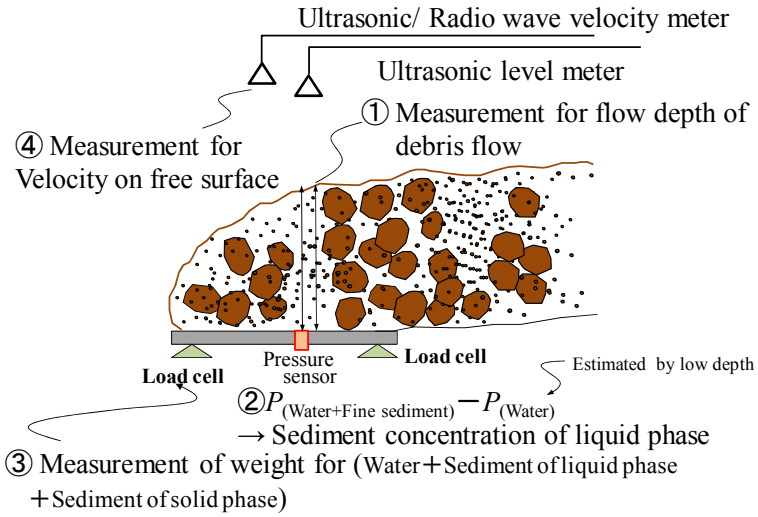

(a) Schematics

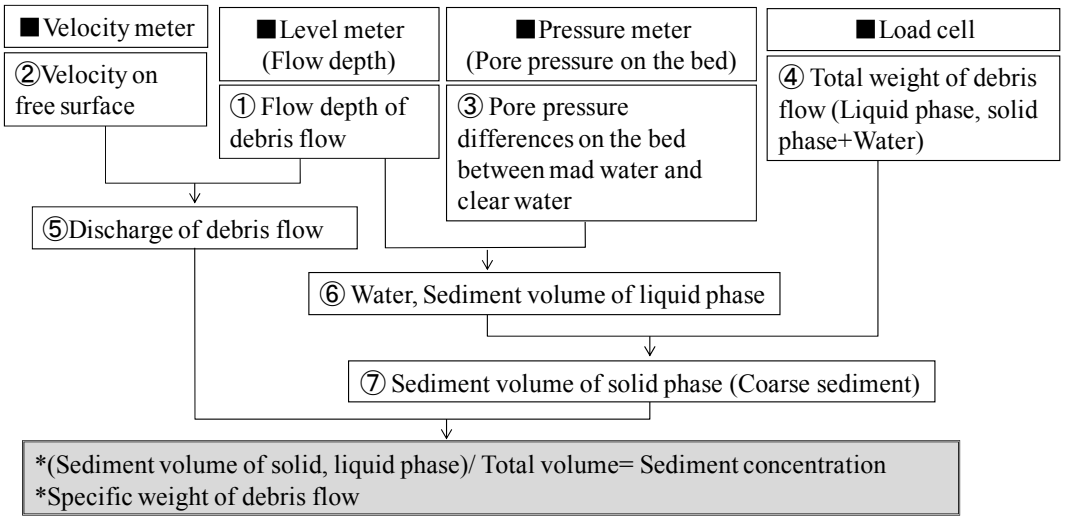

(b) Flow chart

Figure 5. Flow chart for calculations of mass density and sediment concentration using data obtained by sensors.

In Arimura River, debris flows are observed by the DFLP system as shown in Figure 3, and sediment concentration of both coarse sediment phase and suspended & liquid phase can be estimated by data measured by the DFLP system and calculations (Osaka et al., 2014) as shown in Figures 5 (a) and (b).

In debris flow events on 27th June in 2014, two debris flow surges were observed with magnitude of 64.4 m^3/s in peak discharge, 1.1 m in a depth and 13.8 m/s in surface velocity at Arimura River. Debris flows with

one surge took place with magnitude of 1.0 m in peak flow depth at Nojiri River in the day. The velocity and flow depth are analyzed by image analyses of CCTV video camera in Arimura River, and by data of CCTV video camera and ultrasonic meter in Nojiri River.

Figure 6 shows temporal changes of rainfall depth, surface velocity and flow discharge, and pressure head and weight on the bed, which are observed at Arimura River. Figure 7 shows temporal changes of rainfall depth, surface velocity and flow depth measured by ultra-sonic meters, pressure head and weight by the DFLP system at Nojiri River. In addition, two pressure meters on the iron plate are set longitudinally with 50 cm in a distance, and the pressure differences are measured though the value of zero for each pressure meter is moving before events. Those debris surges can be observed well, and temporal changes of those data are compared with time of disconnected wires. Wire sensors are at downstream of the monitoring section in Arimura river and, whereas, wire sensors are at upstream of the monitoring section in Nojiri river. Differences between arrival time of peak values and disconnected time of wire appear clearly, and travel time of debris flow is also measured with several sensors.

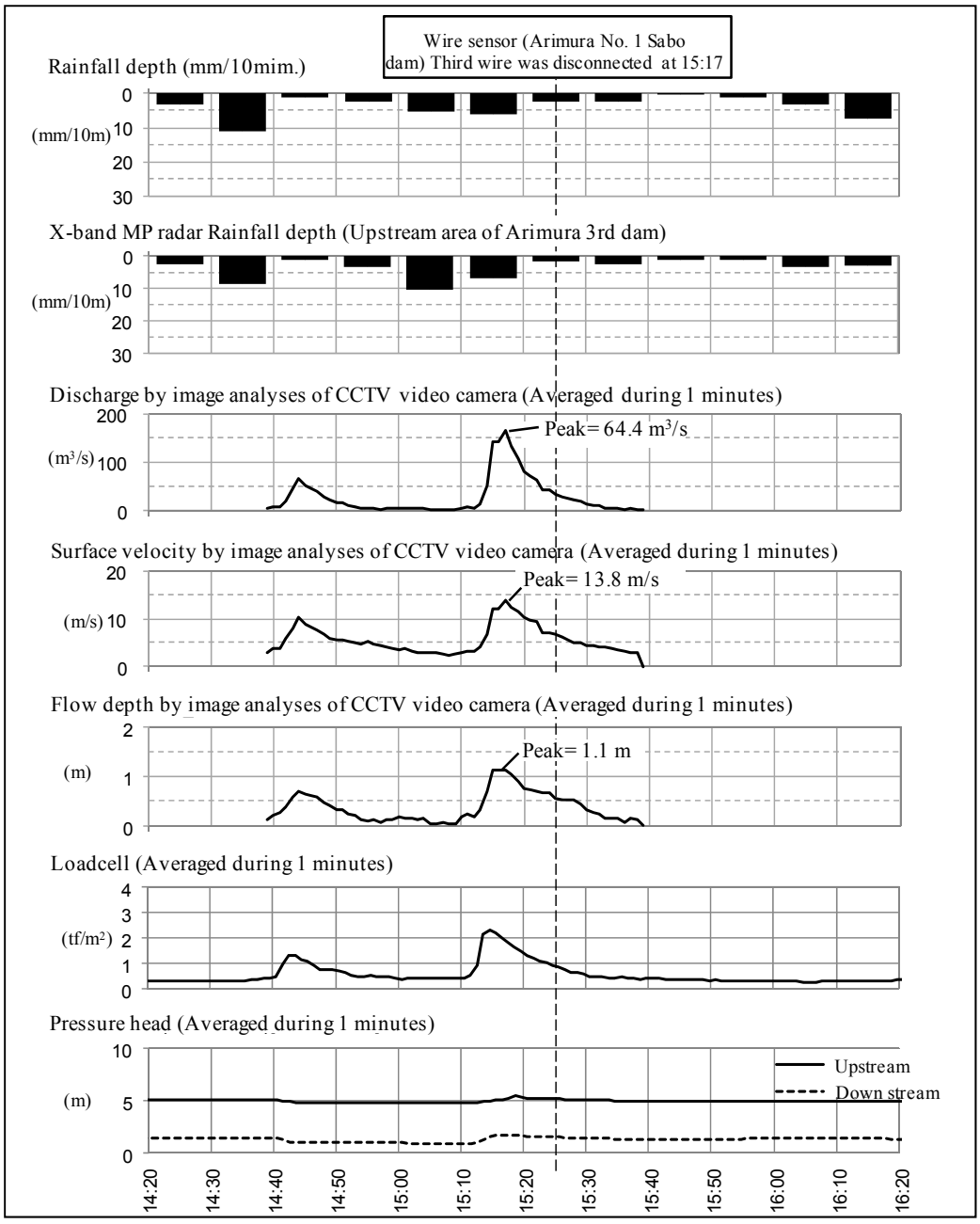

Figure 6. Temporal changes of rainfall depth, flow discharge, surface velocity and flow depth, and weight and pressure head on the bed, observed at Arimura River (Debris flow events on 27th June in 2014).

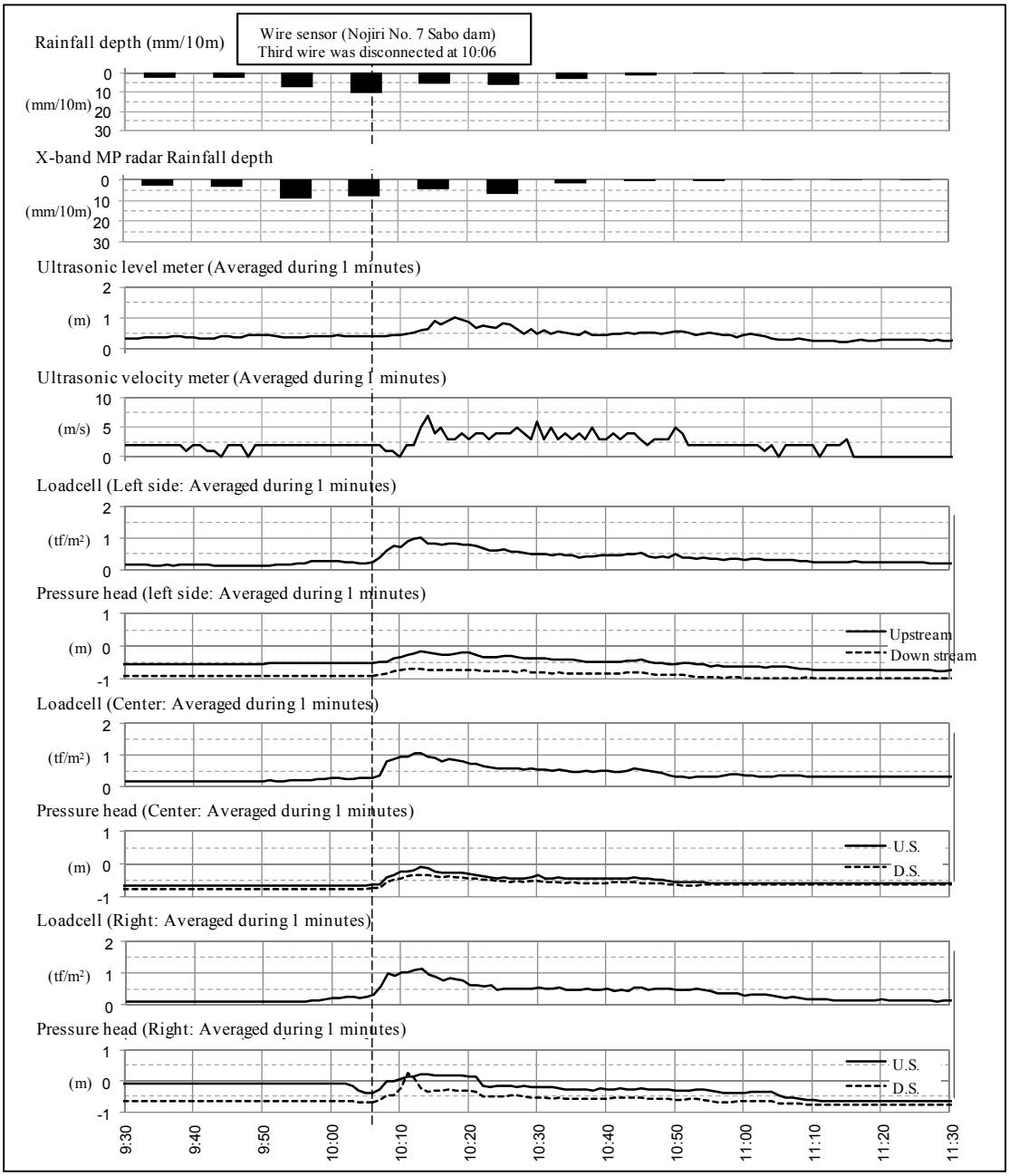

Figure 7. Temporal changes of rainfall depth, surface velocity and flow depth measured by ultra-sonic meters, pressure head and weight on the bed by the DFLP system in Nojiri River (Debris flow events on 27th June in 2014).

3.2 Specific weight and sediment concentration

Temporal changes of specific weight, sediment concentration and sediment volume of debris flow using data obtained by DFLP systems are calculated through calculation flow shown in Figures 5, in Nojiri and Arimura Rivers in 2014, because of well measured data using DFLP system. Herein, equations sets for calculations of specific weight and sediment concentration are already introduced in Osaka et al. (2014). Limitation such as maximum sediment concentration is not set in calculation of sediment concentration.

Figures 8 (a) to (b) show calculated sediment concentration, specific weight of debris flow, and sediment discharge rate for events on June 27th, 2014 in Arimura River. Figures 9 (a) to (c) shows calculated sediment concentration and specific weight of debris flow measured at left, center and right side, respectively, in Nojiri River.

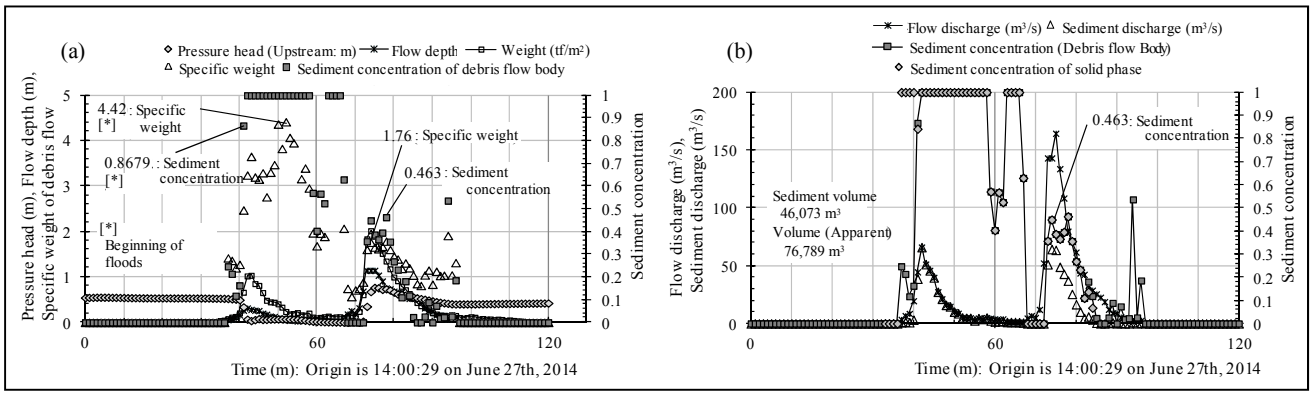

Figure 8. Calculated sediment concentration, specific weight of debris flow, and sediment discharge rate for events on June 27th, 2014 in Arimura River.

In Arimura River, sediment concentration and specific weight are calculated as 0.463 and 1.76, respectively, on June 27th, 2014, and sediment discharge is calculated as 46,073 m^3 in total surges and 22,656 m^3 in second surge as shown in Figures 8. Temporal changes of specific weight and sediment concentration can be calculated during debris flow events using DFLP system. In addition, data for sediment concentration of debris flow is obtained by eight debris flow events, and the averaged sediment concentration, which is averaged near peak of debris flow surge, is 0.419 during June in 2012 to March 2016 in Arimura River (see Table 1). Table 1 lists calculated sediment concentration near peak stage by the DFLP system at Arimura River. Disconnected wire, accumulated rainfall depth and rainfall depth during 10 minutes before debris flow occurrences are also listed in the table.

Meanwhile, sediment concentration and specific weight were calculated such as 0.552 (left side), 0.667 (center), 0.816 (right side) and 1.94 (left side), 2.13 (center), 2.38 (right side), respectively, in Nojiri River (On 27th in June, 2014). Effects of channel shifting on mass density and sediment concentration are clearly shown in measurements in Nojiri River, though the characteristics could depends on flow magnitude of debris flow.
Table 2 lists calculated sediment concentration and so on at Noriji No. 1 sabo dam as well as in Table 1. Sediment concentration seems to be independent on rainfall intensity in Arimura and Nojiri River. Figure 10 shows calculated sediment volume for solid and liquid phase obtained by data in Figure 9. Total runoff sediment volume is 1,920 m^3, and sediment volume of solid and liquid phase are estimated 1,781 m^3 and 139 m^3, respectively.

Table 1. Estimated sediment concentration of debris flow near peak stage (Arimura No. 3 sabo dam).

Time (y/m/d)	Disconnected wire (1st, 2nd, 3rd)	Sediment concentration near peak stage	Rainfall depth (mm) (*)	Rainfall depth during 10 min. (mm) (**)
2012/6/15	2	0.290	39.0	14.0
2012/6/21	1	0.371	122	10.0
2014/6/27	3	0.288	34.0	11.0
2014/8/1	2	0.295	21.0	15.0
2014/8/29	2	0.515	13.0	6.0
2015/6/3	2	0.491	52.0	7.0
2015/6/11	2	0.554	10.0	9.0
2015/6/14	2	0.551	23.0	7.0
Average	-	0.419	39.3	9.88

(*) Accumulated rainfall before debris flow occurrences
(**) Maximum rainfall depth during 10 minutes before debris flow occurrences (mm)

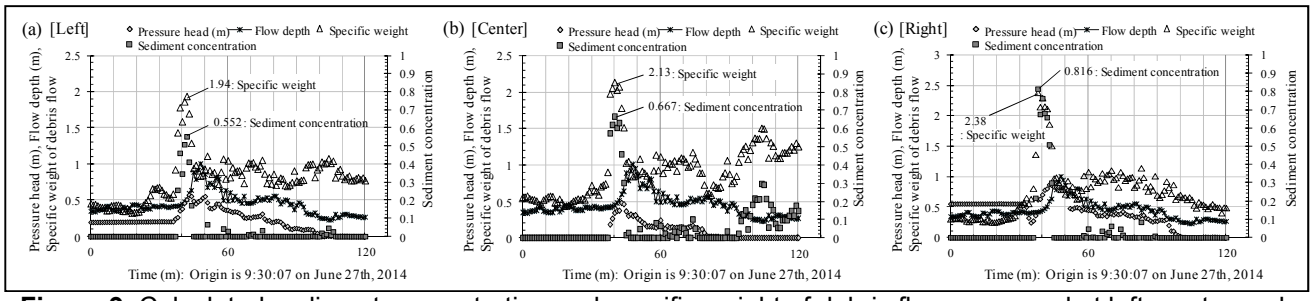

Figure 9. Calculated sediment concentration and specific weight of debris flow measured at left, center and right side, respectively (Debris flow events on June 27th, 2014 in Nojiri River).

Table 2. Estimated sediment concentration of debris flow near peak stage (Nojiri No. 1 sabo dam).

Time (y/m/d)	Disconnected wire (1st, 2nd, 3rd)	Sediment concentration near peak stage	Rainfall depth (mm) (*)	Rainfall depth during 10 min. (mm) (**)
2014/6/21	2	0.156	12.0	5.0
2014/6/27	1	0.191	55.0	10.0
2015/3/19	3	0.435	16.0	6.0
2015/4/6	1	0.371	8.00	7.0
2015/6/6	2	0.187	24.0	7.0
Average	-	0.268	23.0	7.00

(*) Accumulated rainfall before debris flow occurrences
(**) Maximum rainfall depth during 10 minutes before debris flow occurrences (mm)

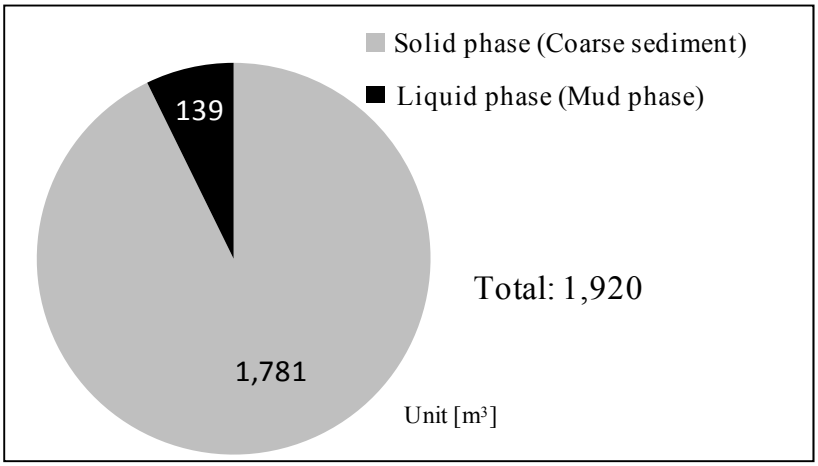

Figure 10. Calculated sediment volume for solid and liquid phase obtained by data shown in Figure 9 (Debris flow events on June 27th, 2014 in Nojiri River).

4 CONCLUSIOS

Debris flows quantities such as temporal changes are desired to evaluate through direct measurements. Results obtained in present study are summarized as follows:

1) Debris flow measurement system with loadcell and pressure sensor (DFLP) were developed by modification of proto-type proposed in Switzerland (McArdell et al., 2007), in order to almost directly measure temporal changes of debris flows.
2) In Nojiri and Arimura Rivers in Sakurajima Island, where debris flows took place many times, DFLP systems were installed in March of 2013 and June of 2012, respectively. Several typical debris flows were measured by present DFLP system.
3) Mass density and sediment concentration of debris flows were calculated using data obtained by the DFLP system. Mass density was calculated by pressure head measured on the bed and flow depth of debris flows, and sediment concentration was calculated by mass density of debris flow body. Temporal changes of specific weight, sediment concentration and sediment volume of debris flow were calculated using data measured by the DFLP system in Nojiri and Arimura Rivers in 2014

because data was well measured in the year. On June 27th in 2014, sediment concentration and specific weight were calculated such as 0.552 (left side), 0.667 (center), 0.816 (right side) and 1.94 (left side), 2.13 (center), 2.38 (right side), respectively, in Nojiri River. In Arimura River, sediment concentration and specific weight were calculated as 0.463 and 1.76, respectively, on June 27th in 2014.

ACKNOWLEDGEMENTS

Authors should be thankful for Osumi Office of River and National Highway, Kyushu Regional Development Bureau, Ministry of Land in Japan (MLIT) for usage of monitoring data, and for Volcano and Debris flow Research Team in Tsukuba Central Research Institute of Public Works Research Institute (PWRI) in Japan to give useful discussions and suggestions for present research.

REFERENCES

Arattano, M. & Marchi, L. (2008). Systems and Sensors for Debris-Flow Monitoring and Warning. *Sensors,* 8(4), 2436-2452.

Itakura, Y., Inaba, H. & Sawada, T. (2005). A Debris-Flow Monitoring Devices and Methods Bibliography. *Natural Hazards and Earth System Sciences*, 5, 971-977.

McArdell, B. W., Bartelt, P. & Kowalski, J. (2007). Field Observations of Basal Forces and Fluid Pore Pressure in a Debris Flow. *Geophysical Research Letters*, 34(7), 1-4.

Osaka, T., Utsunomiya, R., Tagata, S., Itoh, T. & Mizuyama, T. (2014). Debris Flow Monitoring using Load Cells in Sakurajima Island. *Proceedings of the Interpraevent 2014 Pacific Rim,* Nara, Japan.

Osumi Construction Office in the Ministry of Construction (1988). *Debris Flow in Sakura-Jima Island*, SABO Publicity Center, 65. (in Japanese)

Scott, W.M., Coe, J.A., Kean, J.W., Turker, G.E., Staley, D.M. & Wasklewicz, T.A. (2011). Observations of Debris Flows at Chalk Criffs, Colorado, USA: Part1. *Italian Journal of Engineering Geology and Environment*, 1(11), 65-75.

DEBRIS AND MUDFLOW COMPUTER MODEL

NORLIDA MOHD DOM[1], SANDRA LIGONG[2] & A. RAZAK BAHAROM[3]

[1,2] The Regional Humid Tropics Hydrology and Water Resources Centre for Southeast Asia and The Pacific (HTC KL), Kuala Lumpur, Malaysia,
norlidamd@water.gov.my

[3] Servis Eda Sdn. Bhd, Kuala Lumpur, Malaysia

ABSTRACT

Malaysia has long had a history of disastrous debris and mud floods that have wreaked havoc on human lives and properties. With the increase in human activities on hillsides, incidents of debris and mud floods have also increased. Not surprisingly, these incidents tend to occur on average once a year during the monsoon season, when there is heavy rainfall. Thus, recordkeeping of rainfall is crucial to the management of debris- and mudflow-related disasters. Based on the works on correlating rainfall and debris and mudflows in Cameron Highlands, a computer model was needed to automatically monitor rainfall events that could lead to future debris and mud floods. By automating this process, rainfall can be monitored to forecast critical events. A computer application was developed for calibration process to allow hydrologists to create their own model for the use of forecasting debris and mudflow events for Cameron Highlands or other interest location and area. This paper describes the development of a web-based computer application of the calibration model of debris and mudflow. Rainfall records go back to the late 19th century, and record keeping now falls under the jurisdiction of a government agency called Department of Irrigation and Drainage (DID). Since its inception, a major function of DID has been to continuously augment its rainfall data keeping by adding rainfall stations all over the country. To date, there are 1,200 automated rainfall stations nationwide. However, the rainfall data are archived for use in flood forensic, flood forecasting, and urban drainage planning. With major debris and mud flood incidents occurring on a frequent basis, there is an urgent need to utilize rainfall data for yet another use, which is debris and mud flood monitoring and forecasting. DID has been instrumental in monitoring these incidents as landslides that bring debris and mud begin to find its way to rivers and cause even greater damage. This paper describes the calibration methodology required to extract the information from rainfall data for use in debris and mud flood forensics, forecasting, and monitoring. Using a mathematical computer-based rainfall analysis model, many warning and evacuation line sets can be drawn into a graph for fast evaluation and verification of the final debris and mudflow warning model and graph at a particular interest area.

Keywords: Debris and mudflow warning system; landslides; Cameron Highlands; rainfall; debris.

1 INTRODUCTION

In Malaysia, rainfall has long been associated with floods. Flood is the most significant natural hazard in Malaysia in terms of population affected, frequency, area extent, flood duration and social economic damage. Malaysia has 189 main river basins and the 2,986 rivers and their corridors of flood plains fulfill a variety of functions both for human use and for the natural ecosystem. The North-East Monsoon generates heavy rainfall especially to a heightened level as certain parts of the country, particularly the East Coast of Peninsular Malaysia, are especially vulnerable to devastating debris and mud floods when average annual rainfall is above an average rainfall 2500mm/year. Debris flow is a natural phenomenon in mountainous terrains where uphill valleys or streams are fed by high annual rainfalls. The occurrences of debris flows have been well documented in some countries such as Hong Kong and Japan where the monitoring mountainous terrain areas use rainfall as a triggering factor from the local data. This study follows the Japanese methods and the guideline provided by the Ministry of Land, Transport and Infrastructure (MLIT) Japan during the Working Group of Hydrology (WGH) of Typhoon Committee in 2000.

2 DEVELOPMENT OF DEBRIS AND MUDFLOW WARNING MODEL IN MALAYSIA

As a developing country, Malaysia has utilized most of its flat lands in the major conurbations. In order to continue growing economically, urban and agricultural development have been encroaching into the hillside areas. While monsoon flood was relatively less severe since 2008, flash floods and mud floods have been increasing and causing greater damage. The most susceptible debris and mud flood in Malaysia focuses on the slope area along the highways and federal roads especially in Cameron Highlands, Pahang, Malaysia. It has now become one of major natural disasters in Malaysia. Furthermore, The National Slope Master Plan 2009-2023 (NSMP) details the elements of a comprehensive and effective national policy, strategy and action

plan for reducing risk from landslides (PWD, 2009). Based on the plan, DID function in the water security, especially in this case is flood issue which is then further identified as major contributing areas to the disaster, whereby the natural disaster such as mud flood flows into the river.

Due to the magnitude and frequency of debris and mud floods, a number of studies have been made in Malaysia by Norlida and Nasehir (2006) and Tan and Ting (2008) to estimate critical rainfall conditions that induce landslides and debris flows. More attentions have been placed on the correlation between rainfall and debris flow. In Malaysia, the occurrences of debris flow in the mountainous terrains do give intangible impact especially on human lives, psychology and economic losses. It is when human lives and/or infrastructures are impacted that such debris flow incidents are investigated and reported through a special forensic committee established at Slope Division, Public Works Department, Ministry of Public Works, Malaysia in 2008 and later Mineral and Geoscience Department, Ministry of Natural Resources and Environment, Malaysia in 2014.

Increased in natural disasters severity derived intangible losses, Cameron Highlands was chosen as a pilot study area of the development of the debris and mudflow warning model (DMFWM). The first initiative on the debris and mud flow was identified during the WGH in 2000 and the first model was successfully developed in Malaysia in 2005 with data from 1994 to 2002. Of late, two major incidents occurred in Cameron. In October 2012 and November 2013, debris and mudflow disasters hit the Bertam River in the agricultural town of Bertam Valley, south of Cameron Highlands area. These disasters caused millions of Malaysian Ringgit in damages and took several lives. The Cameron Highlands mud flood became a major threat to the residences living there. The 5th November 2014 debris and mud flood triggered political urged and DID to provide a warning model for the following nine major towns in Cameron Highlands; Blue Valley, Kg Raja, Kg. Kuala Kerla, Tringkap, Kea Farm, Tanah Rata, Habu, Bertam Valley and Ringlet. In early 2015, DID took first steps to model a rainfall-debris and mudflow correlation in Cameron Highlands with some additional data. Emphasis was placed on collating rainfall data from other two rainfall stations within Cameron Highlands and all records of landslides, and debris and mud flood events. This resulted in a system development in Phase 1 called the Debris and Mudflow Warning System (DMFWS). DID has taken a responsibility in providing the mud flood warning model into a system connecting to the online rainfall data in Brinchang by improving the 2005 model as a source model to be upgraded into the new mathematical computer-based model. The first proof of concept model without a database was approved by the Information and communication technology (ICT) Committee at Ministry level in 2015 and the model was successfully uploaded into the system in February 2016.

This paper presents the development of debris and mudflows 2016 mathematical computer-based model of Cameron Highlands to provide an early warning to public and stakeholders to fulfill the government responsibility in reducing tangible and intangible losses of the country due to natural causes triggered by rainfall.

3 METHODOLOGY

A 2004 paper by Low and Norlida extols the benefits of flood hazard maps as a useful tool in predicting the onset of potential debris flow events. It goes further to introduce a warning and evacuation methods for debris flow called the “Debris and Mudflow Warning System in Cameron Highlands”. It introduces a chart of hourly and warranted rain that juxtaposes a snake line and a critical line, warning line, and evacuation line. The concept is introduced as a future enhancement to be taken up for further research and development in the field of debris flow warning.

In 2011, Suhaimi et al. asserted that any landslide early warning systems to be developed in Malaysia should be implemented based on empirical correlation of rainfall data and landslide cases. It highlighted the benefits of an empirical approach over a physically based approach, especially at a regional level. The study looked at two types of empirical rainfall thresholds: (i) Intensity vs Duration (ID) and (ii) Intensity vs Working Rainfall. It studied three locations within the country using these threshold methods: the Intensity vs Duration (ID) method was used for Ampang / Hulu Kelang and Penang areas, while the Intensity vs Working Rainfall method was used for Cameron Highland area.

In the last decade, also of great concern is the increased occurrences of other flood related disasters such as debris flood flow, mud flow and landslides in mountain streams and hill slopes (Norlida and Nasehir, 2004). Such incidences have claimed high casualties at Post Dipang Mud flood in 1996 with 44 number of casualties (Low and Norlida, 2004). These number of casualties could be reduced if the warning can be disseminated through National Security Council (*Majlis Keselamatan Negara),* (which is now managed by National Disaster Management Agency (NADMA) to the local residence in the Post Dipang catchment, Perak.

Since 2005 Cameron Highlands model development, there has been no significant incidence of mud flood into the river that can be directly predicted by the rain threshold at 35 mm/hr. The recorded 14-day rainfall model did not exceed the threshold rain value and the requirement procedure frequently stop the model to activate when threshold data was not exceeded. However, an occurrence of high rainfall in 2006, the 20mm/hr for few hours of rain amount less than 35mm/hr provided an opportunity for DID to recalibrate the model by following the rainfall pattern on the correlation graph but no mud flood was reported. Therefore, this

rain event suggested that the incidence occur along the small slopes and the slope failure including sediment movement did not flow into the nearest DID river as mud flood.

In 2014, the Slope Engineering Unit of the Public Works Department (PWD) carried out a study at four locations that have experienced devastating debris flows, namely Lentang, Genting Sempah, Fraser's Hill, and Gunung Pulai. Comparisons between worldwide threshold data compiled by Jakob et al. (2005) and Peninsular Malaysia data carried out showed that the trigger thresholds are generally higher for Malaysia. In comparison between rainfall intensity-duration threshold for debris flow in Europe based on works by Jakob and Hungr (2005) and four (4) sites in Peninsular Malaysia shows that Malaysian data are plotted around the threshold at the upper limits of the European data (Suhaimi et al., 2014).

Kuraoka and Mori (2015) highlighted a study carried out by PWD estimated the potential damage of debris flows and landslides and was instrumental in preparing preliminary guidelines for conducting debris flow hazard assessment. In the study, it explored empirical criteria for estimating the onset of landslides and debris flows such as intensity-duration (I-D) thresholds, snake curves, and soil water index (SWI).

At the same time, Mohamed Roseli et al. (2016) gave a description of the methodology for the development of DID's debris and mud flow warning system. It starts with the representation of the area for survey as well as the debris flow hazard area. Next is the collection of arrangement of rainfall data. The rainfall index is developed using rainfall intensity and total rainfall. The result is a plotting of rainfall groups along an abscissa and ordinate delineating safe and unsafe zones where debris flows may occur. Critical lines are inserted, along with the snake curve and the warning and evacuation lines.

This paper announces the development of a mathematical computer-based model system to forecast debris and mudflow in Cameron Highlands. How this system works is the crux of this paper's topic, which shall be explained in the next topic of this paper. The method explains the procedure taken for the development of the warning model. The computerised calculation derived from Norlida and Nasehir (2006) mathematical model is called the Debris and Mudflow Forecast Computer Model (DMFWM).

The System is made up of two (2) modules. The first module, Rainfall Analysis, is to filter and extract rainfall data from files generated from Hydrological Database, Time Dependent Database (TiDEDA). TiDEDA provide automatic data extraction at any interval data duration by selecting the rainfall station. The second is a web-based system that reads the filtered rainfall data and presents them in a graphical format for the user to determine critical parameters of the Debris and Mudflow Computer Model.

In the Rainfall Analysis, the latest 24-hour accumulated rain is multiplied by 1, the second 24-hour accumulated rain is multiplied by the half-life factor of 0.5 (n), the subsequent previous 24-hour is multiplied by n/2 (MLIT, 2004). The formula is as follows:

$$Working\ Rain, W_{0.5} = A_d + \sum_{t=1}^{23} \frac{0.5}{2^t} A_{d-t} \quad [1]$$

where,

A_d is the accumulated 24-hour rain, and

A_{d-t} is the subsequently previous 24-hour accumulated rain

In the second method, working rain is also calculated but with a half-life factor of 0.25. The formula is as follows:

$$Working\ Rain, W_{0.25} = A_d + \sum_{t=1}^{23} \frac{0.25}{2^t} A_{d-t} \quad [2]$$

where,

A_d is the accumulated 24-hour rain, and

A_{d-t} is the subsequently previous 24-hour accumulated rain

Both resulting working rains are recorded in the same file. The requirements for DMFWS is that the results of both methods are needed to provide the options for the user to select.

3.1 The Rainfall Analysis module

Rainfall in TiDEDA is registered every second. TiDEDA can be retrieved at any interval of rain data. This time resolution is enough to support several of DIDs' flood monitoring and forecasting systems. Each rain data or data point comes with three key data: a unique rainfall gauging station identifier, the date and time it was recorded and the value of the rainfall in the last minutes.

The Rainfall Analysis module is an executable that was designed for MS-DOS, where the user can execute them in a DOS shell command. The executable software is called RainfallAnalysis.exe. Rainfall Analysis reads a file from TiDEDA and generates rainfall data specifically for debris and mudflow calibration model. The model requires several information that is extracted from the rainfall data in order to correlate rainfall and debris and mud flood events.

Thus, Rainfall Analysis detects rainfall events from the information and classifies them as potential triggering events. A rainfall event is defined as continuous rainfall from the moment it starts to rain until it stops. If the rain stops momentarily for at least 10 minutes and then continues, Rainfall Analysis considers that as a second rainfall event.

The development of the graph is dependent on the type of events whether it is occurrence event (debris and mud flood) or non-occurrence event. Each data point of the event is calculated based on maximum hourly rain versus working rain. The rain event records the rainfall in a 1-day and to be total up to 14-day until it reaches let say 40mm/14-day, then the model will trigger to find out the next 10-hour to get the maximum 1-hour rain let say equal to 30 mm/hr. The 14-day total rain (A_{d-i}) is calculated using equation 1 or 2 as a working rain. Then the calculated working rain will be plotted against hourly maximum rain in the axis as a point of either occurrence or non-occurrence rain.

Each snake line point is also calculated by an equation 1 or 2 except that the model starts to activate the first point of the snake line calculation when the daily rain is equal to let say 40mm and the next 2-hour rain is equal to let say 30mm. When the two conditions applied, the daily rain is calculated by equation 1 to become a warranted rain. Later it will be added to A_{d}, the accumulated 24-hour rain to become a working rain point of the snake line. Rainfall Analysis software further calculates and determines working rain for the entire hourly rainfall data as a point of snake line data against the hourly data. There is a running working rain value for every hourly.

With this information, the debris and mudflow model could be executed and determine to plot the graph of intensity rainfall versus working rain as a snake line. Otherwise, the Rainfall Analysis ignores the snake line plot when triggering values of the two criteria (40, 30) does not meet and there will be no snake line plotting.

3.2 Rainfall data architecture

Rainfall Analysis reads the TiDEDA data, processes it and generates three sets of outputs. The first is the working rainfall data and its associated data, then the trigger rainfall data, and finally a series of annual rainfall. Wherever the software is located in the computer, the TiDEDA file is stored in a relative local folder called Input. The output is in a folder called Output. Figure 1 illustrates the rainfall data architecture.

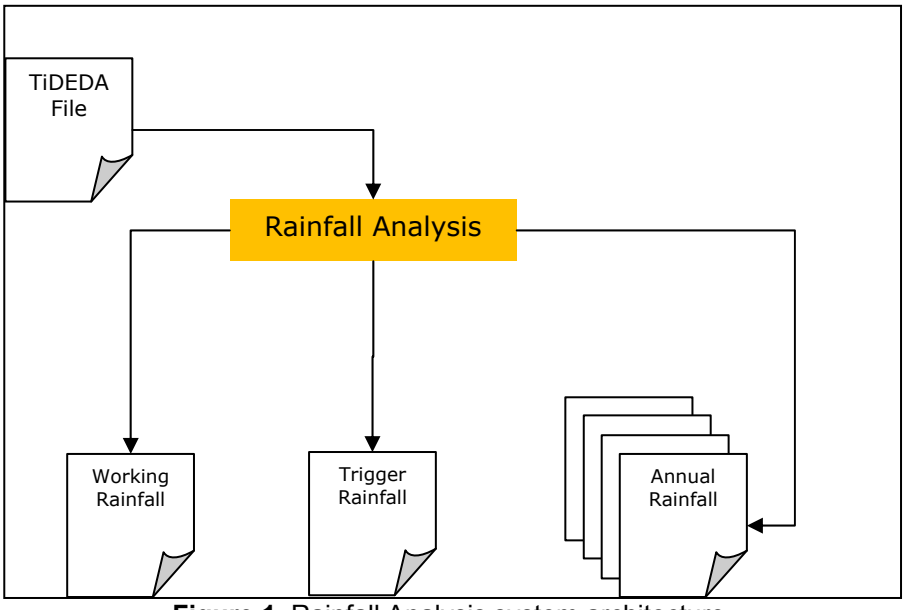

Figure 1. Rainfall Analysis system architecture.

3.3 Command line execution

Rainfall Analysis in Figure 2 is triggered using an MS-DOS command line. The file name for the input TiDEDA file must be the unique rainfall gauging station identifier. Subsequently, the output files generated still carries the identifier name with several extensions to it.

While processing, Rainfall Analysis displays on the command line the tasks that are currently being undertaken. Figure 2 clearly illustrates a typical run of Rainfall Analysis. After reading the TiDEDA file, it

calculates the accumulated rainfall and the working rain. It then generates all the necessary output files as show an example in Figure 3.

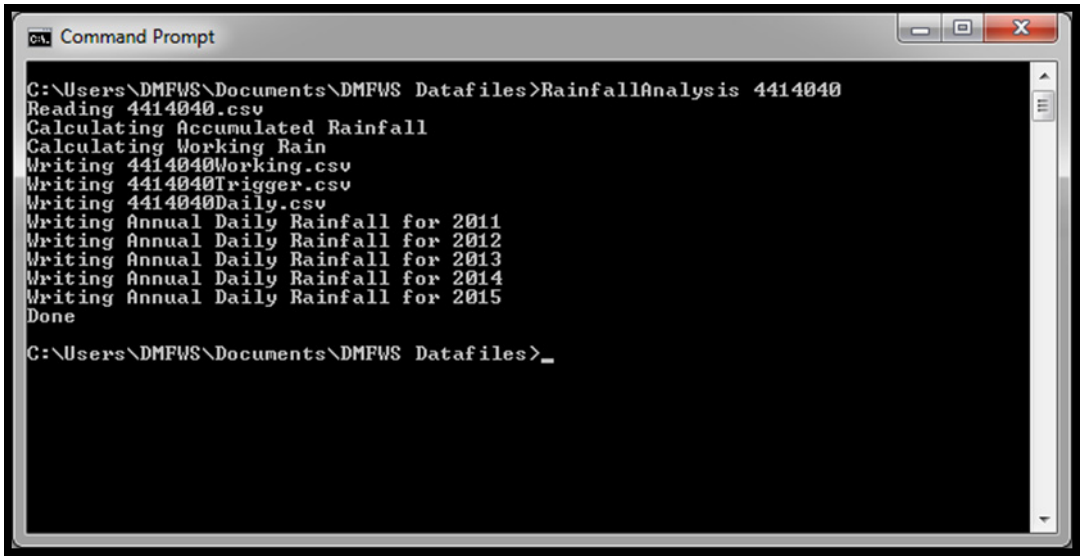

Figure 2. Rainfall Analysis command line execution.

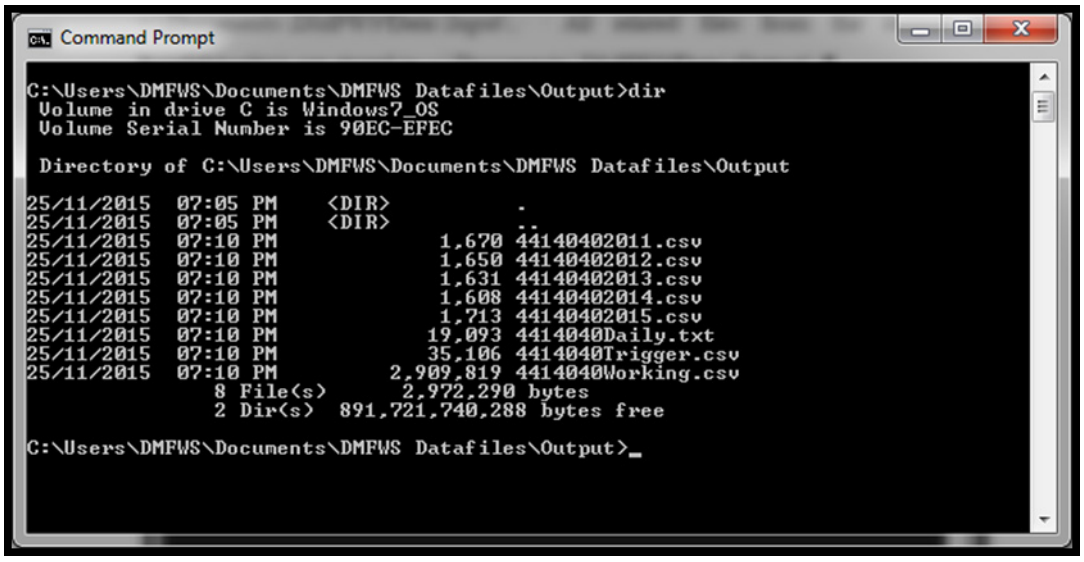

Figure 3. Rainfall Analysis generated output files.

3.4 Working rain output

There are two accumulated rainfall inputs that are required by the debris and mudflow model. The first is the daily accumulated rainfall that begins at 1am every day and ends at the subsequent midnight. The second is the accumulated rainfall event.

From the 15 minutes' rainfall data, Rainfall Analysis recalculates to produce hourly rainfall. The associated accumulated rainfalls are based on the hourly rates. Table 1 shows the result calculations. In addition, Rainfall Analysis also calculates the working rain every hour. There are two working methods that Rainfall Analysis uses as stated in equation 1 (working rainfall 1) and equation 2 (working rainfall 2). In the first method, the latest 24-hour accumulated rain is multiplied by 1, the second 24-hour accumulated rain is multiplied by the half-life factor of 0.5 (n), and the subsequent previous 24-hour is multiplied by n/2. Both resulting working rains are recorded in the same file. The requirements for DMFWS is that the results of both methods are need to provide the options for the user to select.

Table 1. Sample of accumulated rainfall for 6 May, 2013.

Date	Rainfall	Hours	Accumulated Rain Event	Trigger	24H Acc	Working1	Working2
6/5/2013 1:00	0.0	0.0	0.0	0.0	4.4	8.8	13.2
6/5/2013 2:00	0.0	0.0	0.0	0.0	4.4	8.7	13.0
6/5/2013 3:00	0.0	0.0	0.0	0.0	4.1	8.5	12.8
6/5/2013 4:00	0.0	0.0	0.0	0.0	3.5	7.9	12.3
6/5/2013 5:00	0.0	0.0	0.0	0.0	3.5	7.9	12.3
6/5/2013 6:00	0.0	0.0	0.0	0.0	3.5	7.9	12.3
6/5/2013 7:00	0.0	0.0	0.0	0.0	3.5	7.9	12.3
6/5/2013 8:00	0.0	0.0	0.0	0.0	3.5	7.9	12.3
6/5/2013 9:00	0.3	1.0	0.3	0.0	3.8	8.2	12.6
6/5/2013 10:00	0.2	2.0	0.5	0.0	4.0	8.4	12.8
6/5/2013 11:00	0.1	3.0	0.6	0.0	4.1	8.5	12.9
6/5/2013 12:00	0.1	4.0	0.7	0.0	4.2	8.6	13.0
6/5/2013 13:00	0.1	5.0	0.8	0.0	4.3	8.7	13.0
6/5/2013 14:00	0.1	6.0	0.9	0.0	4.4	8.7	13.0

3.5 Trigger rainfall output

The trigger rainfall output file is a summary of known rainfall events from the rainfall gauging station. This file is used by DMFWS to plot the chart of Intensity Rainfall versus Working Rain. A sample output trigger rainfall is show in Table 2. From the table, Trigger is the accumulated rainfall for each rainfall event. The Rainfall column is the highest hourly rainfall for that event, and the Next H column is the next hour reading subsequent hourly rainfall. RH2m is the sum of Rainfall and next hour rain (Next H).

Working 1 and Working 2 are the working rain using the 0.25 and 0.5 half-life respectively. Finally, Duration is the number of hours of rainfall event.

Thus, each record represents a rainfall event as recorded from the DID rainfall gauging station. When DMFWS read the trigger rainfall output files, it automatically plots out the graph.

Table 2. Sample trigger rainfall output file.

Trigger	Date	Rainfall	Next H	RH2m	Sum	Working1	Working2	Duration
24.6	03/01/2011 15:00:00	7.1	4.8	11.9	24.6	0.0	0.0	7
10.7	05/01/2011 21:00:00	3.6	3.6	7.2	10.7	0.0	0.0	13
26.7	14/01/2011 03:00:00	12.9	6.4	19.3	26.7	0.0	0.0	19
18.4	15/01/2011 18:00:00	16.2	1.4	17.6	19.4	0.0	0.0	10
27.0	28/01/2011 07:00:00	1.3	0.8	2.1	10.8	15.80	20.84	47
34.2	31/01/2011 05:00:00	1.9	0.9	2.8	14.7	19.81	24.91	69
19.6	15/02/2011 18:00:00	17.1	0	17.1	19.6	20.86	22.12	10
10.5	24/02/2011 15:00:00	6.1	3.9	10.0	10.5	10.54	10.58	7
10.0	25/02/2011 22:00:00	4.8	2.2	7.0	10	12.64	15.27	14
17.4	07/03/2011 04:00:00	9.1	0.3	9.4	17.4	19.35	21.30	20
37.8	08/03/2011 15:00:00	11.5	2.9	14.4	37.1	41.89	46.67	31
10.6	12/03/2011 05:00:00	1.4	0.4	1.8	10.6	12.83	15.052	21

3.6 Annual rainfall output

Finally, Rainfall Analysis generates the annual rainfall output file. Unlike TiDEDA, Rainfall Analysis reorganizes the rainfall data into daily rainfall per annum. The number of files generated for this series depends on the duration of the rainfall data from TiDEDA. In TiDEDA, rainfall data is in a sequence manner of rainfall value every 15 minutes. Rainfall Analysis calculates them into accumulated daily rainfall. It then creates the respective annual file writing across the rows from the month of January and subsequently up to December. In Figure 4, the first row is the daily rainfall for the first day of the month. This is followed by the second row of daily rainfall for the second day of the month. This continues until the thirty-first row representing the last day of the month. If a month is less days that 31, Rainfall Analysis leaves it blank. The Figure 4 helps the modeler to understand the rainfall distribution for example at Tanah Rata.

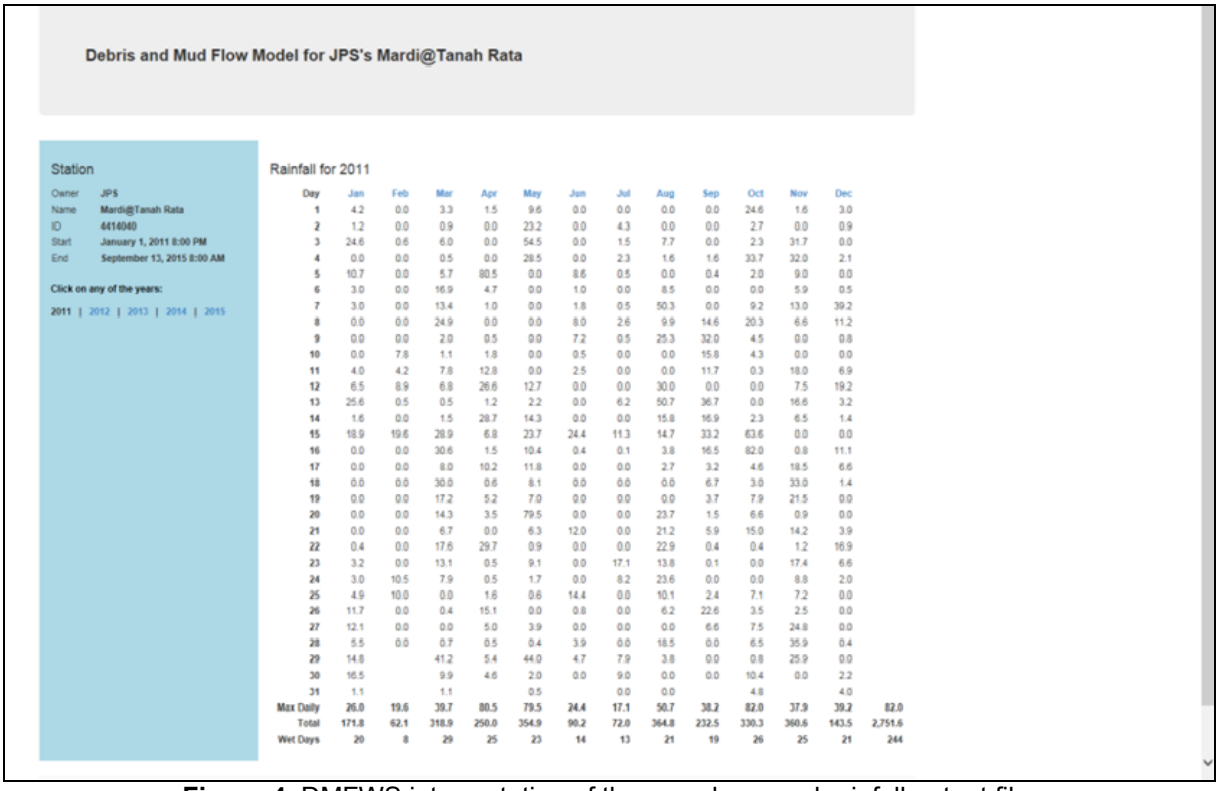

Debris and Mud Flow Model for JPS's Mardi@Tanah Rata

Station

Owner	JPS
Name	Mardi@Tanah Rata
ID	4414040
Start	January 1, 2011 8:00 PM
End	September 13, 2015 8:00 AM

Click on any of the years:

2011 | 2012 | 2013 | 2014 | 2015

Rainfall for 2011

Day	Jan	Feb	Mar	Apr	May	Jun	Jul	Aug	Sep	Oct	Nov	Dec	
1	4.2	0.0	3.3	1.5	9.6	0.0	0.0	0.0	0.0	24.6	1.6	3.0	
2	1.2	0.0	0.9	0.0	23.2	0.0	4.3	0.0	0.0	2.7	0.0	0.9	
3	24.6	0.6	6.0	0.0	54.5	0.0	1.5	7.7	0.0	2.3	31.7	0.0	
4	0.0	0.0	0.5	0.0	28.5	0.0	2.3	1.6	1.6	33.7	32.0	2.1	
5	10.7	0.0	5.7	80.5	0.0	8.6	0.5	0.0	0.4	2.0	9.0	0.0	
6	3.0	0.0	16.9	4.7	0.0	1.0	0.0	8.5	0.0	0.0	5.9	0.5	
7	3.0	0.0	13.4	1.0	0.0	1.8	0.5	50.3	0.0	9.2	13.0	39.2	
8	0.0	0.0	24.9	0.0	0.0	8.0	2.6	9.9	14.6	20.3	6.6	11.2	
9	0.0	0.0	2.0	0.5	0.0	7.2	0.5	25.3	32.0	4.5	0.0	0.8	
10	0.0	7.8	1.1	1.8	0.0	0.5	0.0	0.0	15.8	4.3	0.0	0.0	
11	4.0	4.2	7.8	12.8	0.0	2.5	0.0	0.0	11.7	0.3	18.0	6.9	
12	6.5	8.9	6.8	26.6	12.7	0.0	0.0	30.0	0.0	0.0	7.5	19.2	
13	25.6	0.5	0.5	1.2	2.2	0.0	6.2	50.7	36.7	0.0	16.6	3.2	
14	1.6	0.0	1.5	28.7	14.3	0.0	0.0	15.8	16.9	2.3	6.5	1.4	
15	18.9	19.6	28.9	6.8	23.7	24.4	11.3	14.7	33.2	63.6	0.0	0.0	
16	0.0	0.0	30.6	1.5	10.4	0.4	0.1	3.8	16.5	82.0	0.8	11.1	
17	0.0	0.0	8.0	10.2	11.8	0.0	0.0	2.7	3.2	4.6	18.5	6.6	
18	0.0	0.0	30.0	0.6	8.1	0.0	0.0	0.0	6.7	3.0	33.0	1.4	
19	0.0	0.0	17.2	5.2	7.0	0.0	0.0	0.0	3.7	7.9	21.5	0.0	
20	0.0	0.0	14.3	3.5	79.5	0.0	0.0	23.7	1.5	6.6	0.9	0.0	
21	0.0	0.0	6.7	0.0	6.3	12.0	0.0	21.2	5.9	15.0	14.2	3.9	
22	0.4	0.0	17.6	29.7	0.9	0.0	0.0	22.9	0.4	0.4	1.2	16.9	
23	3.2	0.0	13.1	0.5	9.1	0.0	17.1	13.8	0.1	0.0	17.4	6.6	
24	3.0	10.5	7.9	0.5	1.7	0.0	8.2	23.6	0.0	0.0	8.8	2.0	
25	4.9	10.0	0.0	1.6	0.6	14.4	0.0	10.1	2.4	7.1	7.2	0.0	
26	11.7	0.0	0.4	15.1	0.0	0.8	0.0	6.2	22.6	3.5	2.5	0.0	
27	12.1	0.0	0.0	5.0	3.9	0.0	0.0	0.0	6.6	7.5	24.8	0.0	
28	5.5	0.0	0.7	0.5	0.4	3.9	0.0	18.5	0.0	6.5	35.9	0.4	
29	14.8		41.2	5.4	44.0	4.7	7.9	3.8	0.0	0.8	25.9	0.0	
30	16.5		9.9	4.6	2.0	0.0	9.0	0.0	0.0	10.4	0.0	2.2	
31	1.1		1.1		0.5		0.0	0.0		4.8		4.0	
Max Daily	26.0	19.6	39.7	80.5	79.5	24.4	17.1	50.7	36.2	82.0	37.9	39.2	82.0
Total	171.8	62.1	318.9	250.0	354.9	90.2	72.0	364.8	232.5	330.3	360.6	143.5	2,751.6
Wet Days	20	8	29	25	23	14	13	21	19	26	25	21	244

Figure 4. DMFWS interpretation of the sample annual rainfall output file.

Figure 5 shows real time landslide monitoring uploaded in 2005 by using calibrated data from 1994-2002 and manual calculation using a spread sheet. The snake line is the line in brown colour shows the changes of two rainfall indices with time. The snake line depicts at an interval of one hour. If the interval is made shorter, judgment will become more accurate. Therefore, to avoid misinterpretation, care is needed when monitoring the snake line against the critical line in. The working rainfall is derived by the addition of the antecedent warranted rainfall to the continuous rainfall and will drop when the recorded rain getting less. The snake line in Figure 5 always goes upward relative to the abscissa during the period of rain. As a result, if moderate amount of rainfall continuous to occur for a long time or during a prolong rainfall event, the snake line will still be possible to exceed the Warning Line and progressively proceed to the Evacuation Line of exceeded period and the snake line will be continuously plotted. This causes a problem especially when attempting to cancel or issue a warning or an evacuation instruction, since the affected people would not like to be evacuated for prolong a period of time.

Further data model and data filter were introduced to the source data and Figure 6 shows the constructed graph based on the latest data extraction from 1994-2013. This model was tested on the actual reported occurrence event on 5th November 2014. The reconstructed snake line shows the snake line crossed the critical line. When these lines cross each other (blue circled), it means the occurrence of the debris and mud flood event in Cameron Highlands has happened. It is concluded that when the triggering point starts to plot the snake line, there will be a high possibility that the debris and mud flood will occur when the rain continuously fall. This information is very critical before the point of the snake line cross the critical line. In this scenario, the warning can be disseminated at least 4-hour before the event.

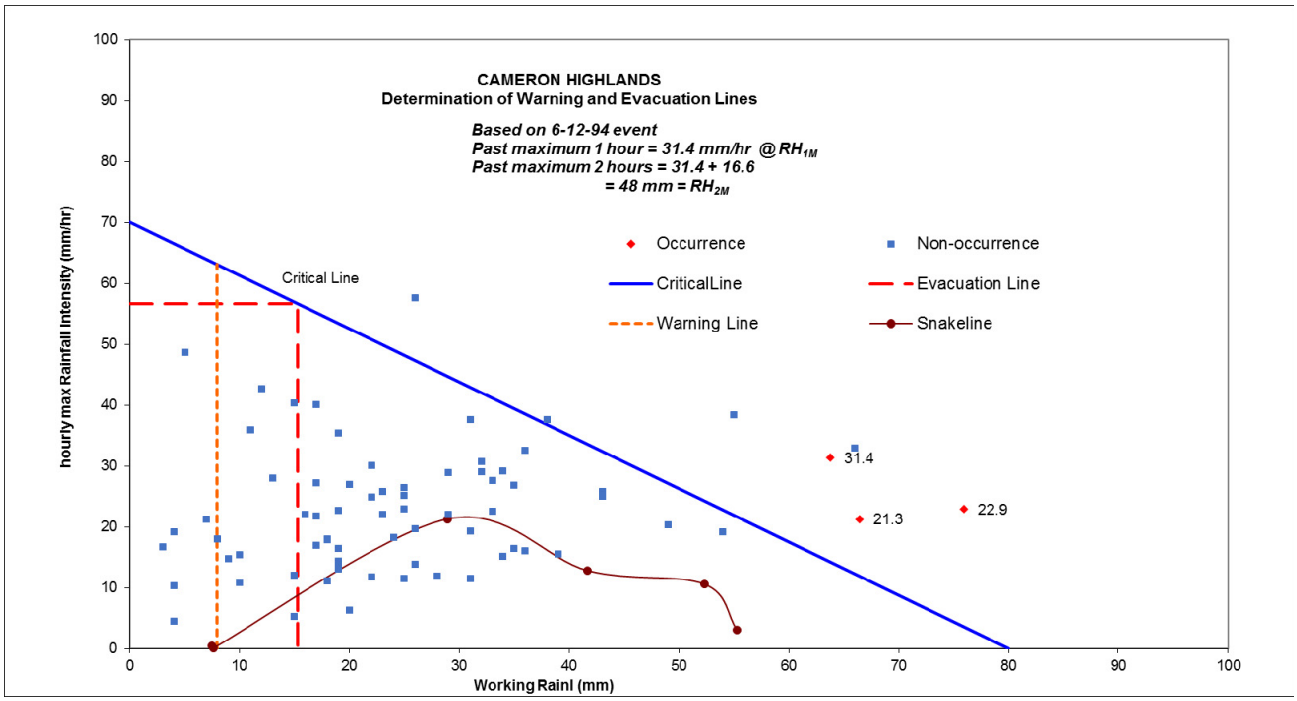

Figure 5. DMFWS intensity rainfall versus working rain (manual calculation- using spreadsheet) data (1994-2002).

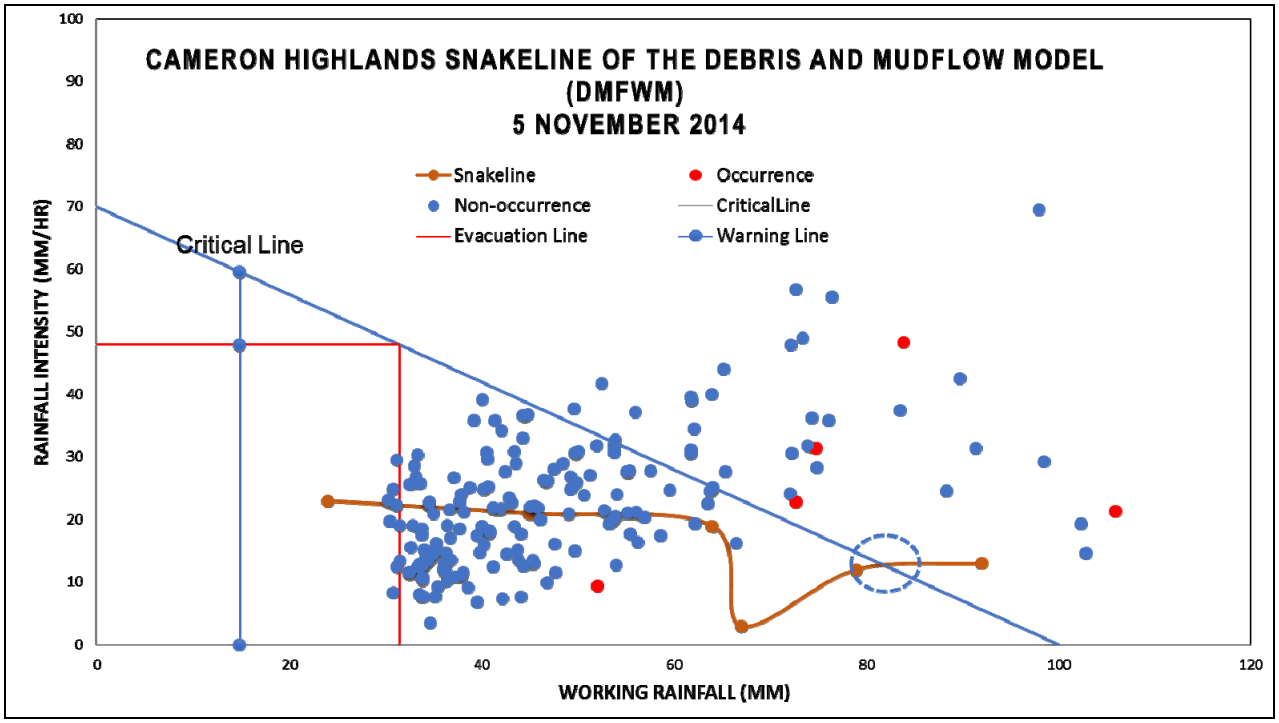

Figure 6. DMFWS intensity rainfall versus working rain (1994-2013) computerised model

Figure 7 shows the software capabilities in plotting each working rain against maximum rain in an hour when the rain threshold is varied. Figure 5, 6 and 7 show different working rain is plotted at different rain threshold and the working rain distribution can result in different critical line development. The model in Figure 6 and 7 represent the variation of with different rain thresholds was applied with additional new data from 1995-2013 and the case study was uploaded in 2015. Moreover, the data from 1994-2013 were computerised and filtered, and events were evaluated based on the truth events except with different rain thresholds. The blue dots represent a mathematical working rain computer-based model of non-occurrence events while the red dots are the recorded debris and mud flood or events occurred. It provides a single record from the trigger rainfall output file and uses the 0.50 working rain calculations. This computerised calculation model is more consistence with its own equation in the model. Figure 6 and 7 show the possibility of having unidentified debris and mud flood around the area as they were not reported officially. These are shown in the graph

where the blue dots are above the critical line. Therefore, the critical line placement is subject to the accuracy of the defined data. Figure 6 shows many occurrence event data exceeded critical line. This suggests for further investigation of these points are above the critical line.

Moriyama and Hikida (2004) stated that it is not clear how to decide the critical line of the occurrence of debris flow and the hourly rain is not suitable for the analysis of debris flows. Moriyama and Hikida (2004) suggested that the debris flow needs higher temporal resolution as 10 minutes or less as the concentration time of debris flow is 45 minutes in Sakurajima for volcano debris type.

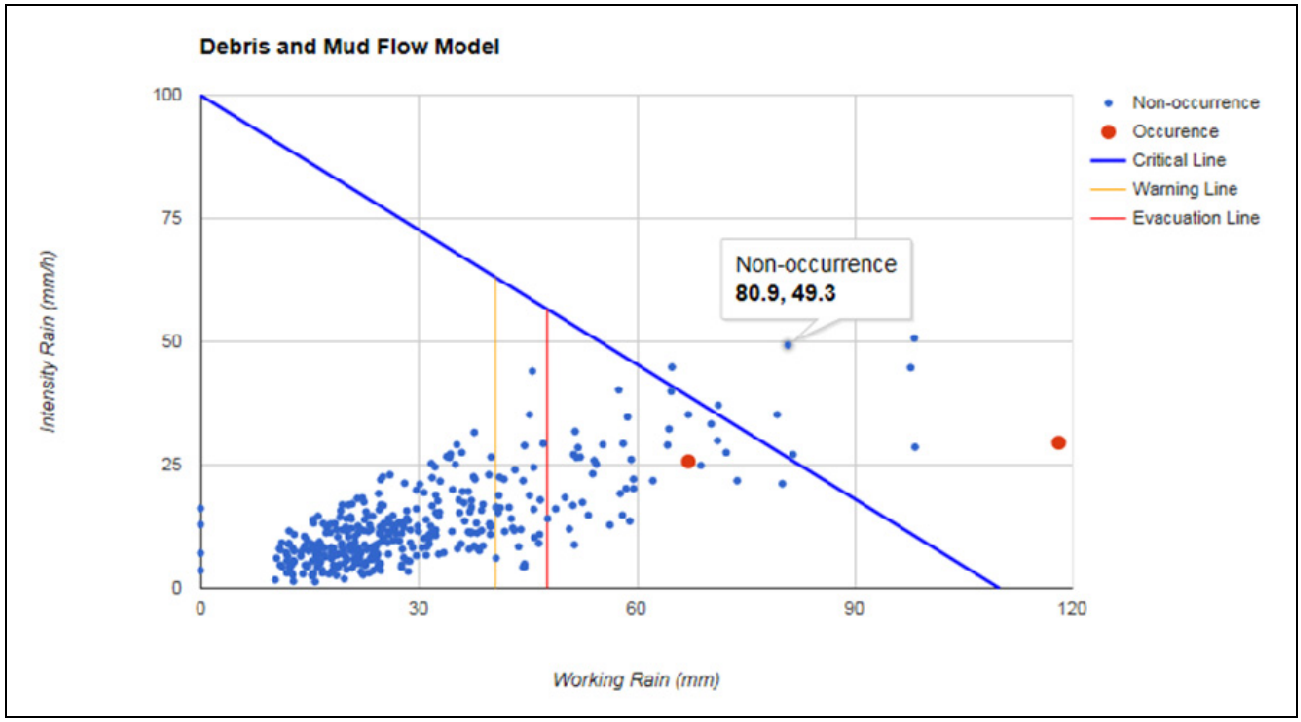

Figure 7. DMFWS intensity rainfall versus working rain chart (a mathematical computer-based model) (1994-2015).

4 CONCLUSIONS

Rainfall Analysis is a useful software tool to prepare for DMFWS. It pre-calculates the rainfall data from any recorded database and generates the necessary files. It analyses the performance of the implemented software relative to other approaches existing in hydrology in general such as working a calculation in worksheet format. Otherwise, for the DMFWM to calculate the raw rainfall data, the process is very time consuming. The 2015 mathematical computer-based model is able to generate calculations within a second without human errors and speed up the process of the model recalibration. This computer-based model development provided many sets of graphs for post calibration. The 2015 model derived points are available for the modeler to verify with other suitable methods. The identified SWI method will provide ground water and soil moisture in the ground through tank model concept. The additional parameter SWI is currently incooperated in the current project phase 2B. This study also proposes that rain data interval less than an hour should be investigated.

ACKNOWLEDGEMENTS

The research team acknowledges the Flood Mitigation Division, Department of Irrigation and Drainage (DID) for providing the research fund and to the Hydrology and Water Resources Management Division of DID for the technical support in this project. Special thanks are extended to the DID Top Management on their policy support of this pilot Project.

REFERENCES

Tan, B.K. & Ting, W.H. (2008). Some Case Studies on Debris Flow in Peninsular Malaysia. *Geotechnical Engineering for Disaster Mitigation and Rehabilitation*, 231-235.

Kuraoka, S. & Mori, M. (2014). Examples of Technology Transfer Projects for Mitigation of Debris Flow in Peninsular Malaysia and Landslides in El Salvador. *Japan Landslide Association Symposi*um, 1-24.

Norlida, M.D. & Low, K.S. (2004). Coping with Risk: UNESCAP Typhoon Committee Hydrological Component. *XXXI International Association of Hydraulic Engineering and Research Congress*, Seoul, Korea.

Mohamed Roseli, Z.A. & Norlida, M.D. (2015). Debris and Mudflow Warning Modeling: Case Study of Cameron Highlands, Malaysia. *Strategic Strengthening for South-South Cooperation for Modelling and Managing Hydro-Hazards*, Indonesia.

Ministry of Land, Infrastructure, Transport and Tourism (MLIT). (2004). Guidelines for Construction Technology Transfer: Development of Warning and Evacuation System Against Sediment Disasters in Developing Countries, Infrastructure Development Institute, Japan.

Norlida, M.D., Nasehir, K. & Yahya, E.M. (2006). Development and Evaluation of Debris and Mudflow Warning Model in High Risk Hilly Slopes in Malaysia, *Proceedings of the National Conference on Water for Sustainable Development Towards a Developed Nation by 2020*, Port Dickson, Malaysia.

Public Works Department (PWD). (2009). National Slope Master Plan 2009-2023, Ministry of Public Works, Malaysia.

Suhaimi, J., Che Hassandi, A. & Norhidayu, K. (2014). Rainfall Intensity and Duration for Debris Flow Triggering in Peninsular Malaysia, *Proceedings of World Landslide Forum*, Beijing, China.

Suhaimi, J., Che Hassandi, A. & Norhidayu, K. (2010). Characteristics and Mechanisms of Debris Flow Occurrence in Peninsular Malaysia. *Journal of the Japan Society of Erosion Control Engineering*.

Suhaimi, J. & Faisal, A. (2011). An Overview of Some Empirical Correlations between Rainfall and Shallow Landslides and Their Applications in Malaysia. *Electronic Journal of Geotechnical Engineering*, 16, 1429-1440.

Moriyama, T. & Hikida, M. (2004). Rainfall Analysis of Debris Flow Occurrence in 2003, Minamata, Japan, *Proc. of 2nd Asia Pacific Association of Hydrology and Water Resources Conference*, 1-6.

NUMERICAL SIMULATION OF FLOW AND SEDIMENT TRANSPORT IN TANKS WITH THE INFLUENCE OF CAVITY

ABDELLAH GHENAIM[1], YI LIU[2]; ABDELALI TERFOUS[3] & PIERRE-ANDRE GARAMBOIS[4]

[1,2,3] INSA de Strasbourg, ICUBE - Mécanique des fluides,
abdellah.ghenaim@insa-strasbourg.fr , yi.liu@insa-strasbourg.fr abdelali.terfous@insa-strasbourg.fr
[4] INSA de Strasbourg, ICUBE
pierre-andre.garambois@insa-strasbourg.fr

ABSTRACT

With the increase of urbanization worldwide, it is crucial to sustainably manage sediment flows in urban networks and especially in stormwater detention basins. One key aspect is to propose optimized designs for detention tanks in order to best reduce flood peak flows and in the meantime to settle particles. It is therefore necessary to understand the complex flows patterns and sediment deposition conditions in stormwater detention basins. The aim of this paper is to study the flow structure and particle deposition pattern for a given tank geometry in view to control and maximize sediment deposition. As a matter of facts, numerical modelling is a useful tool to investigate those complex flow structures. The approach presented here is based on the resolution of the Reynolds averaged Navier Stokes equations to account for turbulent effects and also a passive particle transport model. Given the difficulty involved in those modellings, especially with regard to complex and variables velocity fields and the few existing models for sediment deposition conditions, the choice is made here to test a simple parallelepiped geometry. An analysis of particle deposition conditions is presented in this paper in terms of flow velocities and turbulence patterns. Then sediment deposition zones are presented thanks to the modelling with particle tracking method. It is shown that two recirculation zones seem to significantly influence sediment deposition. Due to the possible overestimation of particle trap efficiency with standard wall functions and stick conditions, further investigations seem required for basal boundary conditions based on turbulent kinetic energy and shear stress. As the trap conditions neglect the resuspension of the particles, a new boundary condition based on shield curves was implemented to the simulation, which can promote the prediction of the trap efficiency and particle distribution zone.

Keywords: Storm sewers; sediment tank; sediment transport; sediment deposition; numerical simulation.

1 INTRODUCTION

Sanitary system might be the closest way that contacts normal people to the sediment. With the development of urbanization both the quantity and quality of stormwater runoff delivered to urban water system have changed. In recent decades, people pay more and more attention to the pollutants, which is because of the importance of environment management of urban stormwater. As we all know, suspended solids and sediments are the main components of pollutants in sewer detention system, so the treatment of particles will become more and more important. Sedimentation is the last procedure before the effluent is discharged to the external, so it's crucial to make sedimentation tank to work effectively.

It's of great importance of sewage system in the process of urbanization, which also impels the treatment of sediment become more and more crucial. Sediments in the sewage system usually originates from five principal sources, which are the atmosphere, the surface of the catchment, domestic sewage, the environment and processes inside the drainage/sewer system, industrial and commercial effluents and solids from construction sites. Without efficient management of those sediments unexpected result will happen, which may be very harmful to the environment and even to human being.

Based on the purpose of collection, the sewer can be divided into combined, separate and above ground/underground sewer. Based on the purpose of transport, the sewer can be divided into gravity, pressure and vacuum sewer. In total, the type of the sewer system can be combined sewers, separate sewers, simpified sewers, solid free sewers, pressurised sewers, vacuum sewers and open channel drains. In those sewers, sedimentation tank can store water temporarily to regulate a flood.

The use of sediment tank is mainly for removing particles in the sanitary system. However, the design of a sediment tank could not be obtained before it is constructed, which means the cost spent on constructing a tank will be wasted if the tank could not perform as it was supposed to be. With the development of computer science, it becomes possible to simulate flow in sediment tank with CFD codes, which is also called numerical computation.

There are two criterions for assessing the performance of sediment tank, one is the capacity of storage of water volume, the other is the maximum value of the pollution the tank can discharge. Flow condition in the sediment tank plays a very important role in the frame of mechanic fluid. As the fluid cannot maintain a fix

form independently, the flow conditions rely on not only the characteristics of the fluid and also the medium where the fluid move in.

In Germany there are over 13,000 combined sewer overflow(CSO) control tanks working for the goal of capturing 80% of the settleable solids (Pitt, 2014). Detention-sedimentation basins are also widely used for water storage and improving the quality of the water. Table 1 shows the efficiency of detention basins and Table 2 shows the trap efficiency of detention basins in UK.

Table 1. Efficiency of detention basins (Nascimento, 1999)

	Ulis Sud a detention basin			Pollutant reduction after 2h of decantation (%)
	Yearly inflow load (kg/ha imp.)	Yearly outflow load(kg/ha imp.)	Yearly removal efficiency (%)	
TSS	3902	387	90.1	88
BOD5	829	107	87.1	76
COD	2598	521	79.9	–
TKN	189	91	51.8	–
P total	44	22	50.6	–
Pb	0.893	0.054	94	65
Zn	5.12	0.66	87.1	77
Cd	0.031	0.0051	83.7	–
Cu	–	–	–	69
Hydrocarbons	65	4	94.2	–

Table 2. Trap efficiency of detention basins (Nascimento, 1999)

Pollutants	Imhoff settleability (24h)	Detention basin 2h removal (%)	Detention basin 6h removal (%)	Range
TSS	68	34	84	49-91
BOD5	32	13	48	14-53
Ptot	46	20	58	20-70
Pb	62	30	66	46-78
Oil/hydrocarbons	69	18	62	20-78
Total coliforms	71	60	72	47-73

2 NUMERICAL METHODS

2.1 Flow modeling

In the field of fluid mechanic, there are always three basic equations which are used to achieve the solution: continuity equation, momentum equation, energy equation. These three equations which provide theoretical basement in fluid mechanics: mass is conserved, Newton's second law, energy is conserved.

Continuity equation:

$$\frac{\partial \rho}{\partial t} + \nabla \cdot \left(\rho \vec{V}\right) = 0 \quad [1]$$

Momentum equation:

$$\frac{\partial (\rho u)}{\partial t} + \nabla \cdot \left(\rho u \vec{V}\right) = -\frac{\partial p}{\partial x} + \frac{\partial \tau_{xx}}{\partial x} + \frac{\partial \tau_{yx}}{\partial y} + \frac{\partial \tau_{zx}}{\partial z} + \rho f_x \quad [2a]$$

$$\frac{\partial (\rho v)}{\partial t} + \nabla \cdot \left(\rho v \vec{V}\right) = -\frac{\partial p}{\partial y} + \frac{\partial \tau_{xy}}{\partial x} + \frac{\partial \tau_{yy}}{\partial y} + \frac{\partial \tau_{zy}}{\partial z} + \rho f_y \quad [2b]$$

$$\frac{\partial (\rho w)}{\partial t} + \nabla \cdot \left(\rho w \vec{V}\right) = -\frac{\partial p}{\partial z} + \frac{\partial \tau_{xz}}{\partial x} + \frac{\partial \tau_{yz}}{\partial y} + \frac{\partial \tau_{zz}}{\partial z} + \rho f_z \quad [2c]$$

Energy equation:

$$\frac{\partial}{\partial t}\left[\rho\left(e + \frac{V^2}{2}\right)\right] + \nabla \cdot \left[\rho\left(e + \frac{V^2}{2}\vec{V}\right)\right] = \rho \dot{q} + \frac{\partial}{\partial x}\left(k \frac{\partial T}{\partial x}\right) + \frac{\partial}{\partial y}\left(k \frac{\partial T}{\partial y}\right) + \frac{\partial}{\partial z}\left(k \frac{\partial T}{\partial z}\right) - \frac{\partial (up)}{\partial x} - \frac{\partial (vp)}{\partial y} - \frac{\partial (wp)}{\partial z} + \frac{\partial (u\tau_{xx})}{\partial x} + \frac{\partial (u\tau_{yx})}{\partial y} + \frac{\partial (u\tau_{zx})}{\partial z} + \frac{\partial (v\tau_{xy})}{\partial x} + \frac{\partial (v\tau_{yy})}{\partial y} + \frac{\partial (v\tau_{yz})}{\partial z} + \frac{\partial (w\tau_{xz})}{\partial x} + \frac{\partial (w\tau_{yz})}{\partial y} + \frac{\partial (w\tau_{zz})}{\partial z} + \rho \vec{f} \cdot \vec{V} \quad [3]$$

All the equations are in the Cartesian coordinates system, where ρ is the density of the fluid, $\vec{V} = (u, v, w)$ is the instant velocity vector, τ is the stress tensor, f is the volume force, p is the pressure, T is the temperature, e is the specific energy of the fluid, $\dot{q}$ is the energy source term. Those equations are derived from a small element of fluid, and under the circumstance that the fluid is a compressible Newtonian fluid.

2.2 Particle trajectory

In CFD, the trajectories of particles are usually completed by two different frames, namely the Euler-Eulerian method and the Lagrangian-Eulerian method.

The Euler-Eulerian method treats all the involved phase as continuum medium. Each of the involved phases is defined as volume fraction, in the calculation the volume fraction in each cell of the mesh is calculated. In Fluent codes, several model based on the Euler-Euler method are provided, including VOF, mixture model, Euler model and level-set model. Normally, VOF is used for the simulation of stratified flow, where the different phases are not miscible and the equation for a single phase with average properties is solved. With more mixed phase in the flow, the used model should be more complex. In mixture model, the velocity difference and interaction between continuum phase and discrete phase is taken into consideration, the different phases are also not miscible and the parameters for solving the equation are averaged by different phases. Eulerian model can solve all the single phase separately, and the equation for each phase is independent, which allow Eulerian model suitable for different conditions, however due to separate iteration for each single phase, the requirement on the calculation resources is also larger.

The Lagrangian-Eulerian method treat the fluid as continuum medium, and for the movement of the particle, the calculation is finished by Lagrangian method.

DPM is a typical Lagrangian-Eulerian method, where the particle trajectory can be tracked separately, however the effect of particle on the fluid is ignored, so DPM can be only used in the condition where the volume of particle phase is less than 10%.In DPM, trajectories of particles/droplets/bubbles are computed in a Lagrangian frame. Particles can exchange heat, mass, and momentum with the continuous fluid phase. As the trajectory of a particle is computed, the heat, mass, momentum gained or lost by the particle stream is tracked, where trajectory and these quantities can be incorporated in the subsequent continuous phase calculations. Thus, the effect of the discrete phase trajectories on the continuum can be incorporated due to the impact of the continuous phase on the discrete phase. This two-way coupling is accomplished by alternately solving the discrete and the continuous phase equations until the solutions in both phases have stopped changing. Each trajectory represents a group of particles of the same initial properties. Particle-particle interactions are neglected.

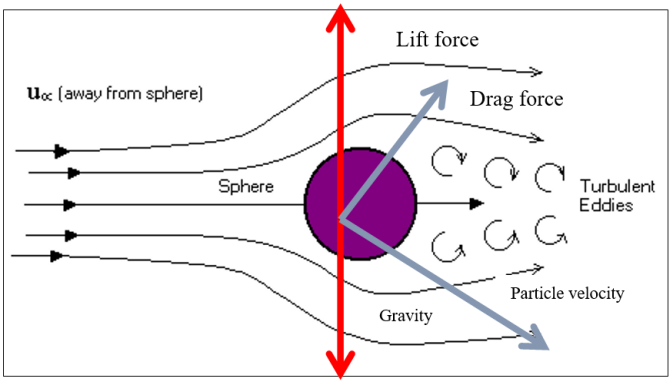

Figure 1. Mechanical analysis of particle in the fluid

The particle in the fluid is under the interactions of many different kinds of forces, including gravity force, lift force, drag force, pressure gradient force, additional body force, Magnus force, Basset force and Saffman force.

Fluent codes present the mechanical analysis of particle in the fluid in a mathematical expression as follows:

$$\frac{du_i^p}{dt} = F_D(u_i - u_i^p) + \frac{g_i(\rho_P - \rho)}{\rho_P} + F_i/\rho_P \qquad [4]$$

Where u_i is the fluid phase velocity, u_i^p is the particle velocity, ρ is the density of fluid, ρ_P is the density of particle, g_i is the gravity acceleration and F_i are the additional forces.

3 SIMULATION RESULTS OF FLOW

3.1 Geometry and mesh

The model used in this article is rectangular reservoir with free surface, pipe inlet and pipe outlet. The dimensions of the model are all derived from the experiment device. The first model in this thesis is derived from the experiment work. The dimensions of the first rectangular reservoir are 4240mm*760mm*405mm, two circular pipe with the diameter equals to 80mm. The second model is of the same dimension with the second model, but with the addition of a cavity at the bottom, the dimension of the cavity is 760mm*325mm*80mm. In order to decrease the difficulty in creating the mesh for the simulations, some simplifications were done on the geometry. The details of the model are showed in the figure as follow.

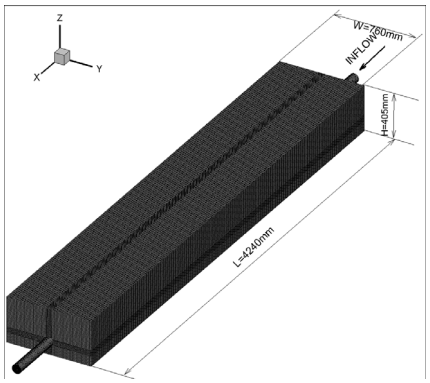

Figure 2. Detailed geometry and mesh of the tank

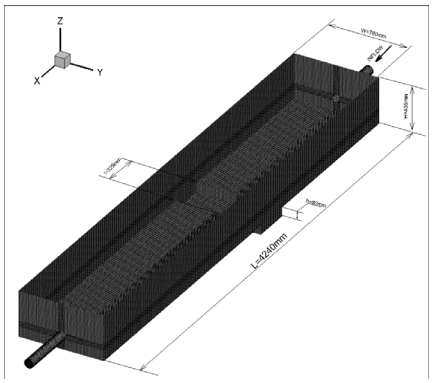

Figure 3. Detailed geometry and mesh of the tank with cavity

Usually, there are two types of the mesh, tetrahedron and hexahedron, and tetrahedral mesh is always used in the condition where the geometry is very complicated. At the beginning, in multi-dimension condition, the main factor for the numerical errors is numerical diffusion, which is also called false diffusion, as it is not a real physical phenomenon, the effect on flow calculation of which is similar to increasing real diffusion coefficient. Numerical diffusion is really significant when the physical diffusion of the flow is relatively low. All the real numerical design about fluid flow include limit quantity of numerical diffusion, which is because of truncation error, the result of present the discrete form of the fluid flow equation. Corresponsively, the total numerical diffusion depends on the discretization of the mesh. In most situations, hexahedral mesh can provide a minimum numerical diffusion due to the flow is in accordance with the mesh. Furthermore, in a same model hexahedral mesh needs less cells than tetrahedral mesh, and less cells of mesh means less occupied computational resources in calculation. So it's more economic by choosing the hexahedral mesh to process the simulation. In the end, another important factor for numerical simulation is accuracy and convergence. The characteristic the hexahedral cells is tolerating larger aspect ratio than tetrahedral cells. A large aspect ratio in the tetrahedral cell can always affect the skewness of the cell, which is not expected, as it can hamper the accuracy and convergence of the computation. All in all, in consideration of the geometry in this research, the hexahedral mesh can provide better solution.

The mesh used for simulation is accomplished by Ansys ICEM, a professional mesh create software. As it is mentioned above, a hexahedral mesh is chosen for all the simulation in the work.

3.2 Mesh sensitivity

In a simulation process, the first step is to determine the accuracy of the numerical results. Discrete method is the cause of the numerical errors, the solver will calculate all the value in the mesh points, in which the truncation error exist, in order to make the computation process continuously, the truncation error will be neglected, for each iteration the truncation error will accumulate, this is called the numerical error. If the numerical error is too high, the simulation result can be wrong. The solution to the numerical errors is to refine the mesh, however boundlessly refining the mesh means huge increasing of computational resources. In practice, users will find a point between numerical accuracy and computational resources; this is so called grid independence verification or mesh sensitivity verification. Normally, the accuracy of a numerical simulation will depend on the quality and the number of the mesh. Errors will exist if the mesh number of the model and the quality of the mesh are not appropriate, and errors will accumulate with the continuous numerical calculation process. The parameter chosen for examine the mesh sensitivity are volume flow rate at the outlet and the range of interface. The mesh number chosen for the test are as follows: 0.468, 0.616, 0.808, 1.145, 1.305, 2.259(million). The increasing of the mesh is not just based on numbers, it's by increasing the global variable factor and refining the part mesh by changing the point distribution in the edge.

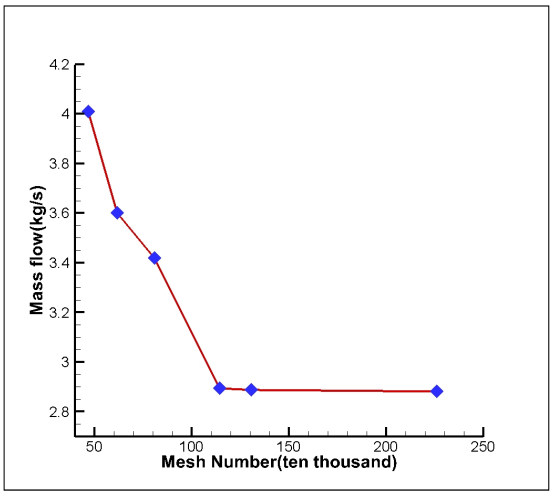

Figure 4. Variation of mass flow at outlet along the mesh number

From the curve, it turns out the numerical results will be stable if the mesh number is larger than 130 million. However, the geometry in the research will change, so the number can't be the criterion for all the geometry. To solve this problem, the global variable factor used in creating the mesh will be the criterion, the global variable factor is a parameter to determine the size of each mesh cell, in a same topology structure and global variable factor, the mesh will be similar in different geometry.

The number of the mesh do not only affect the flow properties but also affect the interface tracking. With coarse mesh the range of the volume fraction between 0 and 1 is larger than the result with refiner mesh. The ranges of the volume fraction become stable when the mesh number arrives at 130million.

3.3 Water level

The purpose of the showing this parameter is to show the ability of tracking the interface between water and air. In the method of VOF, when the water volume fraction equals to 1, it means the cell is occupied by water, and when the water volume fraction equals to 0, it means the cell is occupied by air, in the end, the interface exists in the zone where the water volume fraction is between 0 to 1.

In this simulation, the water level is from 14cm to about 22cm ranging from the volume flow rate. The variation of the water level in the tank with the increasing of the entrance volume flow rate is similar to the situation of simulation in the short tank.

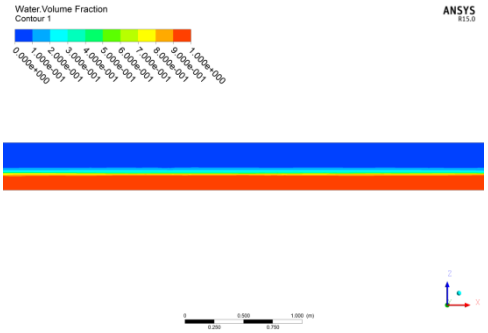

Figure 5. Water volume fraction at volume flow rate 1L/s

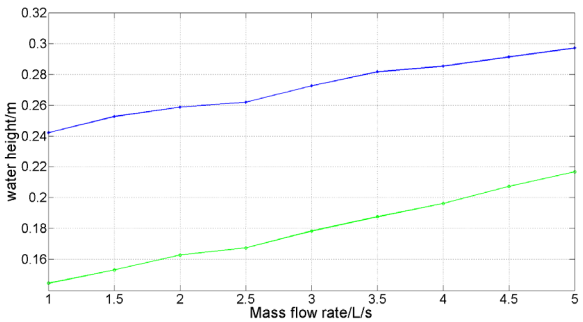

Figure 6. Averaged water level along increasing entrance volume flow rate

3.4 Flow patterns

The flow patterns in the tank means the eddy distributions, in the simulation results the streamlines at the horizontal plane where the height of the plane is at the center of the inlet pipe are chosen to show the size and location of the recirculation. The criterion for choosing the height of plane is based on the center of the injection, at which the streamlines is most representative.

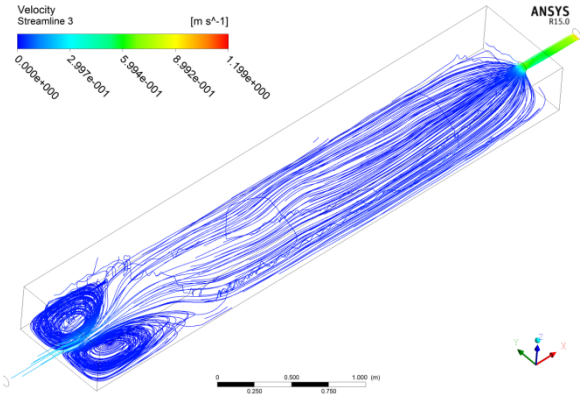

Figure 7. 3D streamlines at volume flow rate 1L/s

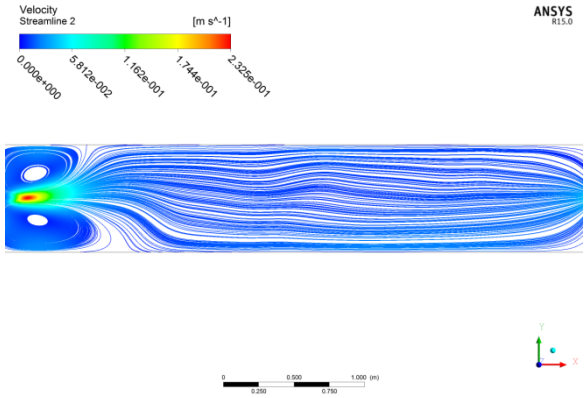

Figure 8. 2D streamlines at Z=0.04m at volume flow rate 1L/s

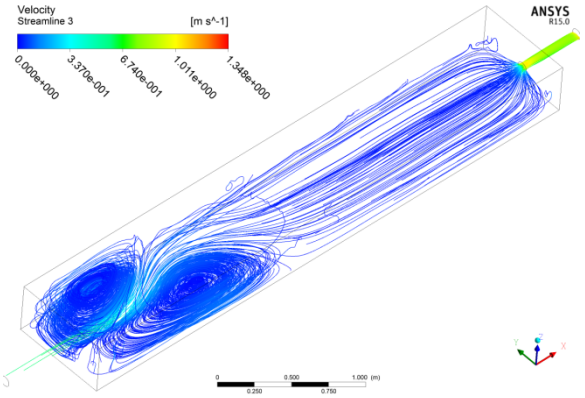

Figure 9. 3D streamlines at volume flow rate 3L/s

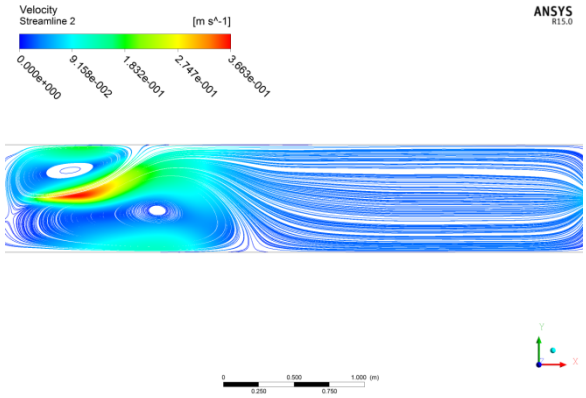

Figure 10. 2D streamlines at Z=0.04m at volume flow rate 3L/s

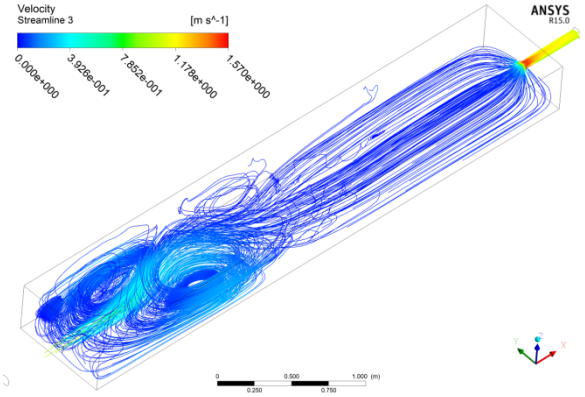

Figure 11.3D streamlines at volume flow rate 5L/s

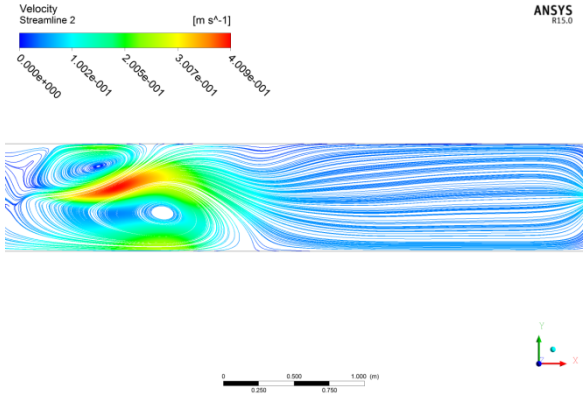

Figure 12. 2D streamlines at Z=0.04m at volume flow rate 5L/s

The Flow domain is mainly dominated by two eddy in the front of the tank and a uniform flow part in the back of the tank, the differences among different volume flow rate are the size and location of the recirculation, in the backward the flow become more smooth and the velocity is quite low comparing to the entrance velocity. The symmetric flow patterns do not exist when the water level is low, the reason might be that the injection is near to the free surface, less pressure from the water is impacted on the injection, which leads to the injection develop with less limitation.

Basically, the flow field in the tank with cavity is mainly dominated by two eddies and a uniform flow part, which is similar to the flow field in the tank without cavity.

The existence of the cavity do not change the number of the eddy in the front part, however it change the distribution, location and size of the eddy, the existence of the cavity can swift the flow pattern to symmetry in some extent. The variation differs depending on the ratio of length to width of the cavity.

Table 3. Flow patterns under low water level

Entrance volume flow rate(L/s)	Averaged water depth(cm)		Flow patterns	
	No cavity	With cavity	No cavity	With cavity
1	14.46	14.48	Quasi-symmetry	Symmetry
1.5	15.32	15.23	Quasi-symmetry	Symmetry
2	16.29	15.88	Quasi-symmetry	Symmetry
2.5	16.74	16.73	Quasi-symmetry	Asymmetry
3	17.83	17.62	Asymmetry	Asymmetry
3.5	18.75	18.62	Asymmetry	Asymmetry
4	19.61	19.57	Asymmetry	Asymmetry
4.5	20.72	20.61	Asymmetry	Asymmetry
5	21.65	21.82	Asymmetry	Asymmetry

Table 4. Flow patterns under high water level

Entrance volume flow rate(L/s)	Averaged water depth(cm)		Flow patterns	
	No cavity	With cavity	No cavity	With cavity
1	24.25	24.00	Symmetry	Asymmetry
1.5	25.28	24.46	Symmetry	Quasi-symmetry
2	25.89	25.34	Symmetry	Quasi-symmetry
2.5	26.22	26.24	Asymmetry	Symmetry
3	27.27	27.11	Quasi-symmetry	Symmetry
3.5	28.18	27.90	Symmetry	Asymmetry
4	28.54	28.51	Symmetry	Asymmetry
4.5	29.14	29.31	Quasi-symmetry	Asymmetry
5	29.72	29.73	Asymmetry	Asymmetry

4 SIMULATION RESULTS OF SEDIMENT TRANSPORT

4.1 Bed shear stress

Bed shear stress was treated as a criterion for the sedimentation of particle since Shields (1936). In the numerical simulation, there is no good model for the settling of particles, the trap condition used in the Fluent codes estimates the trap efficiencies much higher than real condition. Adamsson et al. (2003) put forward that the boundary condition at the bottom of the tank should be given careful consideration, as the prediction of trap efficiency and deposition zone of the trap condition is not available. The prediction of trap efficiency is too high and the deposition zone is vast. A useful criterion, which is a critical bed shear stress is used to implement the defect of Fluent codes,. The method based on bed shear stress shows better agreement with measured sedimentation efficiency data, and the spatial distribution of sediment is more similar to the laboratorial work.

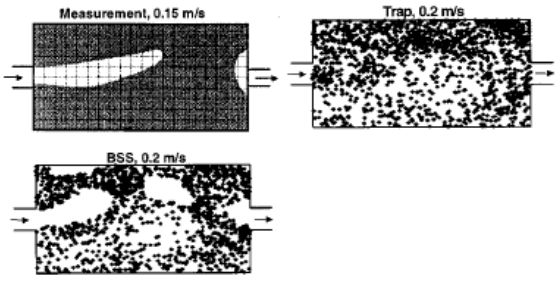

Figure 13. Spatial distribution of sediment in measurements and in simulations.

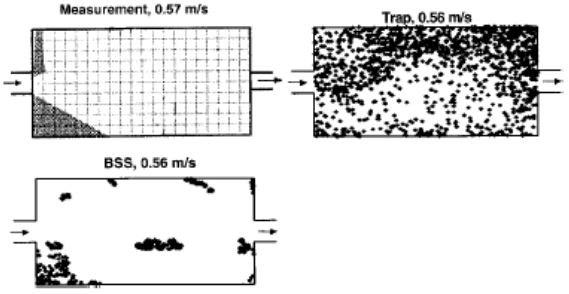

Figure 14. Spatial distribution of sediment in measurements and in simulations.

4.2 Simulation setup

In Fluent codes, Turbulent dispersion of particles due to turbulence in the fluid phase can be modeled using either stochastic tracking or a “particle cloud” model. By the use of stochastic methods the effect of instantaneous turbulent velocity fluctuation on the particle trajectories is included in the stochastic tracking (random walk) model. The statistical evolution of a cloud of particle about a mean trajectory is tracked in the particle cloud model, where a Gaussian probability density about the mean trajectory is used to represent the concentration of particles within the cloud.The removal efficiencies of the tank rely on the time scale factor in discrete random walk model (DRWM).Dufresne(2008) and Yan(2013) tested the effect of the time scale factor on the removal efficiencies, and it turned out with smaller time scale factor, the simulated removal efficiencies was more close to the real condition. In this article, the time scale factor is selected as 0.05.

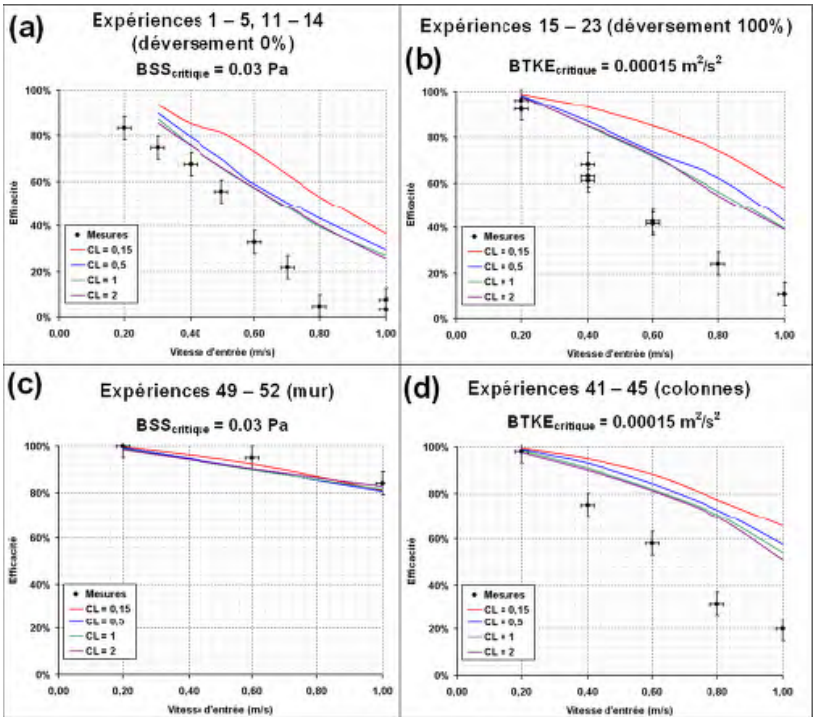

Figure 15. Comparison between experiment results and numerical simulation with different time scale factor (Dufresne,2008)

4.3 Modelling of sediment transport

In this article, the injected particles are set to be inertia. For the size distribution of the particles, firstly the complete range of sizes is divided into an adequate number of discrete intervals, each interval are represented by a mean diameter for which trajectory calculations are performed, secondly using the Rosin-Rammler distribution to obtain the mass fraction of the particle. The mass fraction distribution of particle in this article is from the experimental measurements.

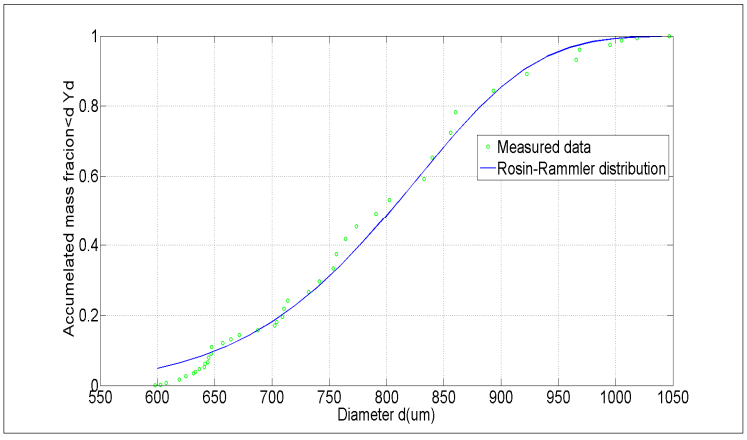

Figure 16. Accumulated mass fraction along diameter

According to the fitting of experiment data to the mathematical expression of the Rosin-Rammler distribution, the spread number $n = 9$, and the diameter constant $\bar{d} = 837\mu m$.

The calculation of particle trajectory starts when the particle enters the flow domain at the inlet part, the calculation of particle trajectory terminates when the particle leaves the flow domain at the exit part. The escape type boundary condition is used at the inlet, outlet part and the free-surface, indeed the particle remains in the fluid and won't go to the air phase, so no particle escape the flow domain from the free-surface.

Figures 17 to 21 show the particle trajectory in the rectangular tank with a cavity. The movement of the particle in the tank corresponds to the flow pattern of the fluid, at the beginning the particle is mainly in the flow injection and then the particle will move to other parts of the tank when it leaves the part influenced by the flow injection.

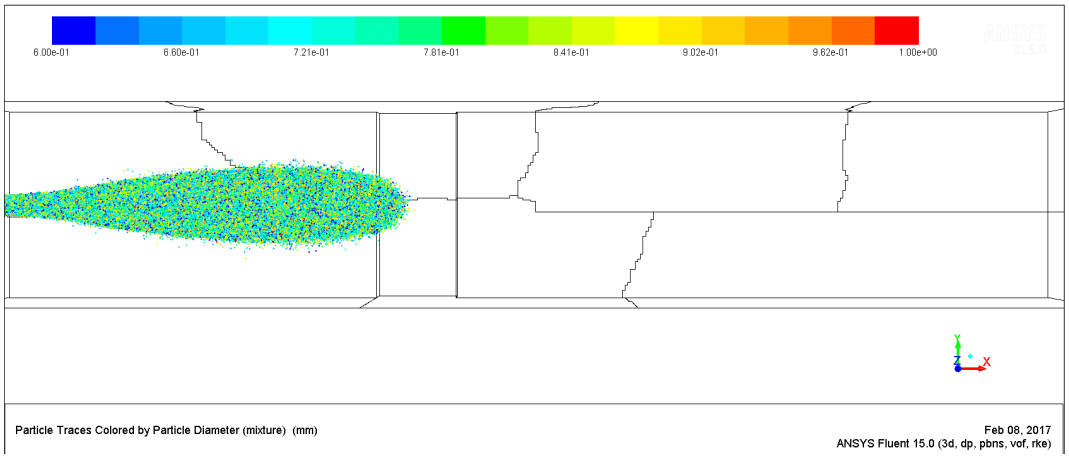

Figure 17. Particle tracking at 5000 iteration steps

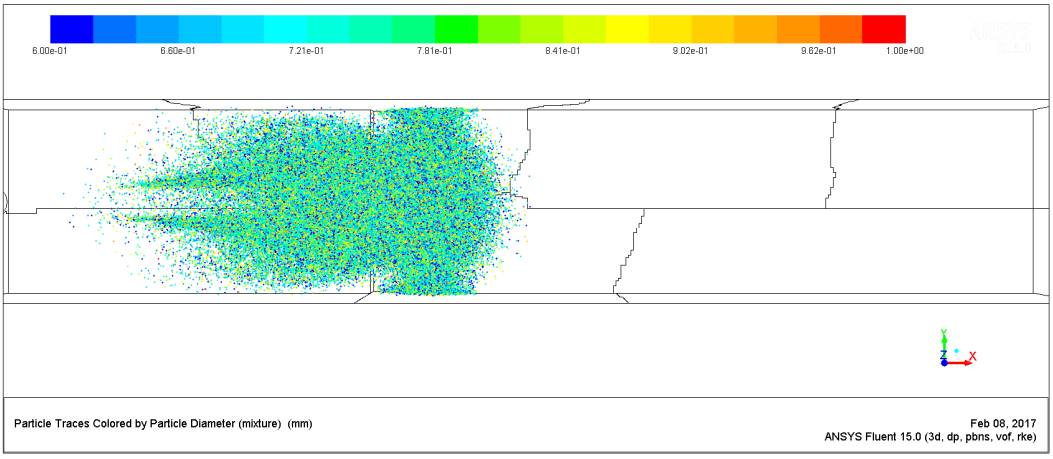

Figure 18. Particle tracking at 15000 iteration steps

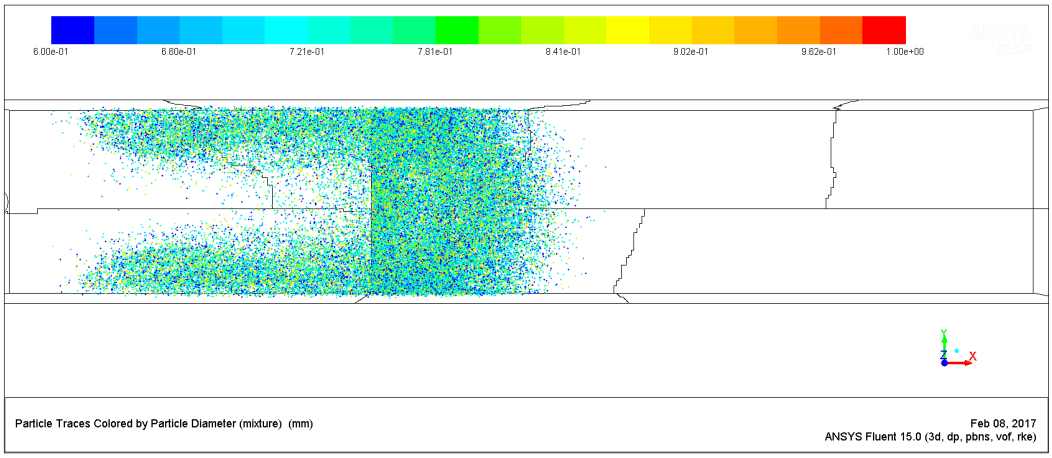

Figure 19. Particle tracking at 25000 iteration steps

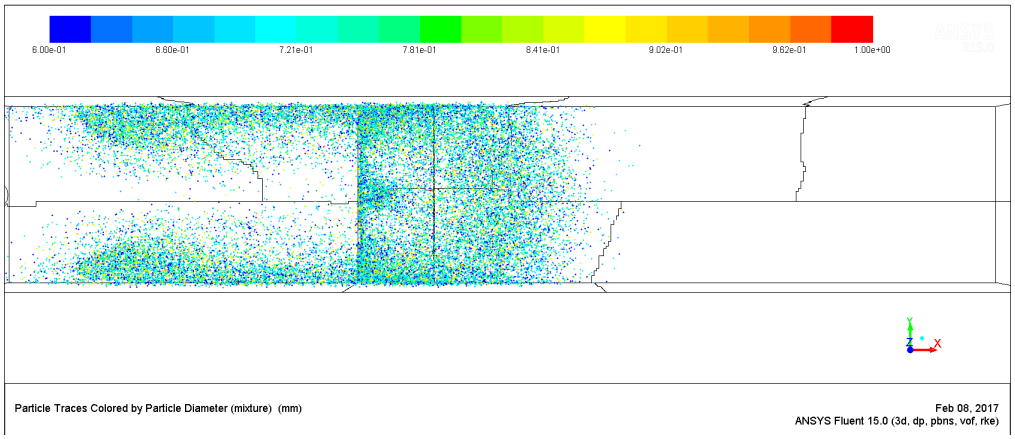

Figure 20. Particle tracking at 35000 iteration steps

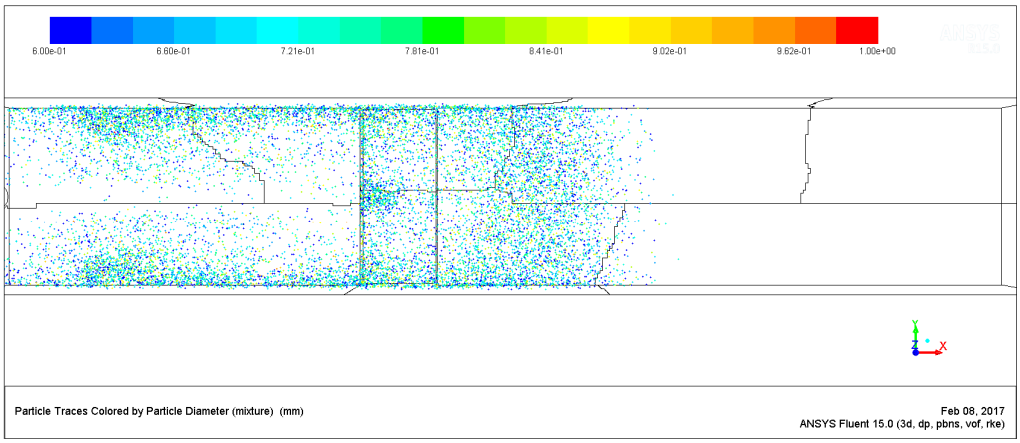

Figure 21. Particle tracking at 45000 iteration steps

5 CONCLUSIONS

The existence of the cavity do not change the flow field essentially, the function of the cavity is to change the parameter distribution in the flow field and create a part with low value of wall shear stress and turbulent kinetic energy. All in all, the flow field in the rectangular tank is really complicated, entrance volume flow rate, water level in the tank and geometry of the tank are factors that can change the flow pattern and flow parameter distribution.

The flow pattern is the main factor that influences the movement of the particle in a rectangular tank. The existence of the cavity creates a part where is capable of settling the particle easily. The boundary condition for the particle should be taken care of, otherwise the trap efficiency will be overestimated.

ACKNOWLEDGEMENTS

The research reported here is sponsored by Institute National des Sciences Appliquees Strasbourg and China Scholarship Council. The author would like to present great thankfulness to INSA Strasbourg and CSC.

REFERENCES

Adamsson, Å., Stovin, V. & Bergdahl, L. (2004). Closure to “Bed Shear Stress Boundary Condition for Storage Tank Sedimentation” by Åsa Adamsson, Virginia Stovin, and Lars Bergdahl. *Journal of Environmental Engineering*, 130(9), 1068-1069.

Adamsson, Å., Bergdahl, L. & Lyngfelt, S. (2005). Measurement and Three-Dimensional Simulation of Flow in a Rectangular Detention Tank. *Urban Water Journal*, 2(4), 277-287.

Dufresne, M. F. D. (2008). *La modélisation 3D du transport solide dans les bassins en assainissement: du pilote expérimental à l’ouvrage réel* (Doctoral dissertation, INSA de Strasbourg).

Shields, A. (1936). *Anwendung der Aehnlichkeitsmechanik und der Turbulenzforschung auf die Geschiebebewegung*. Preussischen Versuchsanstalt für Wasserbau.

Yan, H. (2013). Experiments and 3D modelling of hydrodynamics, sediment transport, settling and resuspension under unsteady conditions in an urban stormwater detention basin, *Doctoral Dissertation*. INSA de Lyon.

INFLUENCE OF THE UPPER YANGTZE RIVER SEDIMENT DECREASING ON SEDIMENTATION IN THREE GORGES RESERVOIR

WENJIE LI[(1)], SHENGFA YANG[(2)], PINGYI WANG[(3)], YI XIAO[(4)] , JIANG HU[(5)] & XUHUI FU[(6)]

[(1, 2, 3)]National Inland Waterway Regulation Engineering Research Center (NIWRERC),
Chongqing Jiaotong University, Chongqing, China,
li_wj1984@163.com; ysf777@163.com; 429582608@qq.com
[(4, 5, 6)]Key Laboratory of Ministry of Education for Hydraulic and Water Transport Engineering (KLMEHWTE),
Chongqing Jiaotong University, Chongqing, China,
409705911@qq.com; hujiang77@163.com; fuxuhui@hotmail.com

ABSTRACT

Sedimentation in the Three Gorges Reservoir (TGR) has been studied concerning mainly the amount change due to the decrease in sediment inflow. In this study, the sediment-decrease-induced sedimentation was investigated using the sediment budget and topographical methods, and the mechanism underlying the influences were analyzed based on the field data sets. The total sedimentation reduced significantly to about half of the predicted value, while the deposition ratio increased by 15.8 %. The sedimentation mainly consisted of fine sediments, and presented a spatial pattern of 'segment siltation' rather than the expected 'continuous siltation'. At wide reaches, flow velocities were slowed down significantly and flocculation occurred, hence the sediment carrying capacities decreased to below the sediment concentrations, resulting in fine sediment deposition. While at gorges, flows were still energetic and the flocs were likely to be disrupted, hence the sediment carrying capacities decreased slightly and remained bigger than sediment concentrations, resulting in no cumulative deposition. The future sedimentation equilibrium with no unified bed slope and deposition delta was expected due to the decreasing of sediment inflow, facilitating the TGR's functions significantly.

Keywords: Decreasing of sediment inflow; sedimentation; fine sediment; sediment carrying capacity; Three Gorges Reservoir.

1 INTRODUCTION

Through controlling floods, generating power, and facilitating navigation, et al., dams have played an important role in the development of human society for thousands of years. China, as a country with abundant hydropower resources, is particularly active in dam constructions and has built more than half of the world's largest dams since 1950 (Fuggle and Smith, 2000). Most of these dams were built on the Yangtze River, which is ranked fifth in the world in terms of water discharge and fourth in terms of sediment load (Milliman and Syvitski, 1992). Known as the largest hydroelectric project in the world, the Three Gorges Dam (TGD) was constructed at Yichang (Figure 1) with the height of 185 m and the length of 2335 m (Zhao et al., 2000).

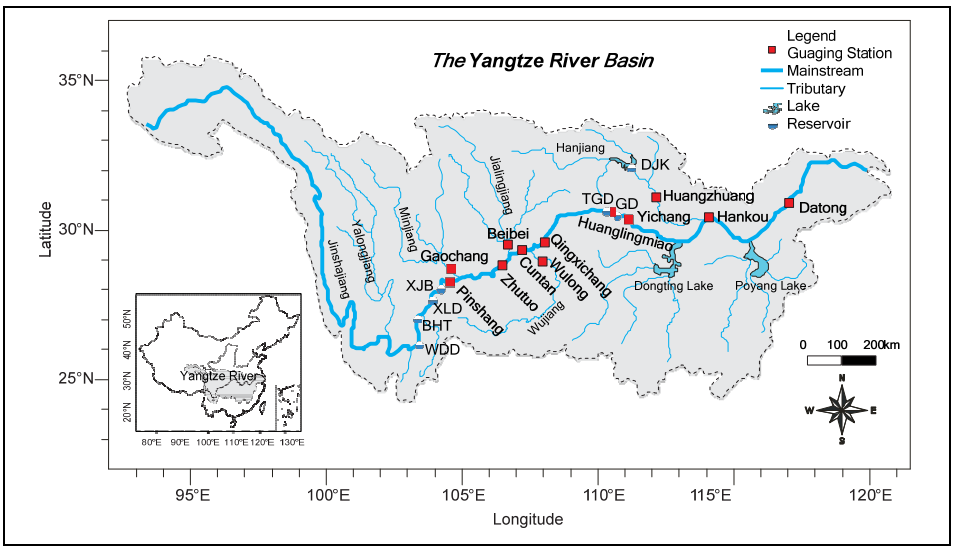

Figure 1. Yangtze River basin (GD, Gezhouba Dam; TGD, Three Gorges Dam; XJB, Xiangjiaba Reservoir; XLD, Xiluodu Reservoir; BHT, Baihetan Reservoir; and WDD, Wudongde Reservoir).

In June 2003, the TGD began to impound water and trap sediments and had a water level of 135 m, which increased to 156 m in 2006, to 172 m in 2009, and to full capacity in 2010 (175 – 155 – 145 m scheme, where 175 m is the normal pool level, and 145 m is the flood control level). With a total water storage capacity of 39.3 billion m^3, the TGR plays significant roles in controlling floods, generating power and improving navigation (Jordi and Marta, 2006), the frequency of major flooding downstream could be reduced from once every 10 years to once every 100 years, approximately 4 % of the nation's electricity needs in 2011 could be provided, the navigation from Yichang to Chongqing could be improved dramatically due to the deepening and widening of the river channel.

Sedimentation in a reservoir is of global concern because the sediment retention can reduce the reservoir capacity significantly. It is estimated that approximately 1% of the world's total reservoir capacity is lost each year as a result of sedimentation (WCD, 2000). Therefore, sediment issues are of great interest to scientists and have been highly emphasized in discussions of the TGD both domestically and internationally. For example, based on the Yangtze River sediment discharge in the period of 1950-2000, the amount of the sedimentation in TGR was predicted by Tsinghua University, China's Institute of Water Resource and Hydropower Research, and Yangtze River Scientific Research Institute in the demonstration phase (Science and Technology Department of Ministry of Water Conservancy and Electric Power, 1988; Lin and Zhang, 1989; Sediment Experts Group of the Three Gorges Project Construction Committee Executive Office, 2002). The main results stated that, (1) the sediment finer than 0.01 mm were wash load and would not deposit in TGR, (2) if the 175–155–145 m scheme was followed, the amount of sediment deposition would be approximately 3 billion tons with the sediment export ratio being about 40% during the first decade, (3) the deposition was expected to be continuous and the deposition delta would be created between the entrance and outlet of TGR, finally forming an equilibrium bed slope which would lead to the increase of the reservoir tail water level.

Recently, due to the water and soil conservation projects and sediment retentions of the newly constructed upstream cascade reservoirs (e.g. XJB Reservoir, XLD Reservoir, et al.), although the flow discharge of the Yangtze River remains almost unchanged, the sediment load has decreased significantly from about 0.5 billion tons in pre-TGD period to about 0.2 billion tons in post-TGD period (Lu et al., 2011; Xu et al., 2013; Yang, et al., 2014; Gao et al., 2015). Consequently, the actual sedimentation was found much less than that predicted in the demonstration phase (Dai et al., 2006; Yang et al., 2006; Yang et al., 2007; Chen et al., 2008; Xu and Milliman, 2009; Hu et al., 2009; Li et al., 2011; Yang, et al., 2014; among others). However, the influences of the sediment inflow decrease on the sedimentation in TGR are still not fully clarified. For example, the Huanghuacheng reach which is about 350 km away from the TGD, is suffering from serious sedimentation, the local deposition thickness exceeds 40m that the river bed elevation is approaching 145m and the navigation is forbidden at the period of low water level, while no sedimentation is found at the nearby narrow reaches; lots of sediment finer than 0.01mm which were expected to be wash load are found deposited (Yang, 2013).

The previous studies mainly focused on the decrease of the sedimentation amount, failed to delineate the overall influences and analyze the reasons. The objective of this paper is to provide more details about the influences of the sediment inflow decrease on the sedimentation in TGR and to analyze the reasons, including (1) deposition amount of different particle size, (2) spatial pattern of the sedimentation, and (3) the mechanism underlying the influences. Finally, the sedimentation equilibrium trend is discussed. It is expected that this work could deepen our understandings of the sedimentation in TGR and lay the foundation for the scientific operation and management of TGR.

2 DATA AND METHODOLOGY

2.1 Data collection

As shown in Figure 1, Zhutuo, Cuntan, Qingxichang, Huanglingmiao and Yichang are five gauging stations on the Yangtze River, Beibei and Wulong stations are located on the Jialingjiang and Wujiang tributaries, respectively. The station that controls the water and sediment inflow of TGR was Qingxichang station in 2003-2006, but with the upstream backwater extension due to the increasing water level before TGD, the controlling stations in 2007-2008 were Cuntan and Wulong stations, and after 2009, the controlling stations were Zhutuo, Beibei and Wulong. The Huanglingmiao station is located 12 km downstream of the TGD site, and control the water and sediment outflow of TGR.

Hydrological data of these gauging stations, including flow discharges, sediment concentrations and particle sizes to quantify the deposition amount of each particle size, are collected from the Bulletin of Changjiang Sediment (CRWC, 2003-2014) and the Report on prototype observation of sedimentation in the TGR navigation channel (Yang, 2013). The annual profiles (2003-2011) of 340 cross sections arranged from TGD site to the end of the backwater are compiled from the Report on prototype observation of sedimentation in the TGR navigation channel (Yang, 2013), to determine the spatial pattern. The along-TGR daily water levels (2003-2011) of 29 water level stations are collected, combined with the daily flow discharges, annual cross section profiles and monthly particle sizes, to calculate the sediment carrying capacity.

2.2 Methodology for estimating sedimentation

The sediment budget method (SBM) was widely used in previous studies (Dai et al., 2006; Yang et al., 2006; Yang et al., 2007; Chen et al., 2008; Xu and Milliman, 2009; Hu et al., 2009; Li et al., 2011; Gao et al., 2015), and the improved-SBM (ISBM) was proposed recently to involve the sediment inflow of ungauged areas (Yang et al., 2014). While no particle size information of the ungauged sediment inflow can be acquired, and the SBM is used finally in this study to quantify the deposition amount of each particle size. Although most previous studies used the Yichang station as the TGR output station, the Huanglingmiao station which is closer to TGD is used, expected to produce more accurate results.

The spatial deposition pattern is delineated through the topographical method. Based on the annual profile changes of the 340 cross sections, it is assumed that the sediment volume deposited between two adjacent sections equals to the average deposition area of the two sections multiplied by the distance.

In China, the reservoir sedimentation is usually calculated using the sediment carrying capacity, defined as the critical maximum of the sediment concentration under equilibrium sediment transport conditions, measured as the percentage of weight per unit volume, commonly expressed as follows:

$$S_* = k\left(\frac{U^3}{gR\omega}\right)^m \quad [1]$$

Where S_* = cross-sectional averaged sediment carrying capacity (kg/m^3), U = cross-sectional averaged flow velocity (m/s), g = gravitational acceleration (m/s^2), R = hydraulic radius (m), ω = settling velocity (m/s), and k and m = model coefficients, which are 0.02 and 0.92 respectively in the TGR case (Zhou, 2005).

3 INFLUENCES ON SEDIMENTATION DURING THE INITIAL OPERATION STAGE

3.1 Sediment trapped in the TGR

Based on the upper Yangtze River flow and sediment discharge from 1950s to 2000s, the sedimentation in TGR was predicted during the Pre-TGD period. It was expected that the deposition amount would be approximately 3 billion tons during the first decade. In Table 1, the sediment inflows are slightly less than the sediment outflows in 1950s – 1990s, reflecting the sediment inflow of ungauged areas that was not considered in the demonstration phase. The SBM is used to determine the sedimentation after TGR's operation, as shown in Table 1.

Table 1. Annual runoff, sediment flow and sedimentation in TGR.

Years	Runoff (10^8 m^3)	Sediment discharge (10^8 t)		
		Inflow[a]	Outflow[b]	sedimentation
1950s	3881.05	5.16	5.25	
1960s	4206.22	5.15	5.56	Pre-TGD period
1970s	3782.51	4.14	4.80	
1980s	3988.60	5.03	5.41	
1990s	3910.40	3.77	4.17	
2003	3733.33	2.08	0.84	1.24
2004	3696.06	1.66	0.64	1.02
2005	4187.91	2.54	1.03	1.51
2006	2692.02	1.02	0.09	0.93
2007	3599.24	2.20	0.50	1.70
2008	3820.88	2.18	0.32	1.86
2009	3483.54	1.83	0.36	1.47
2010	3719.33	2.29	0.33	1.96
2011	3031.69	1.02	0.07	0.95
2012	4173.82	2.19	0.45	1.74
2013	3353.47	1.27	0.33	0.94
2014	3837.61	0.55	0.11	0.44
2015	3357.80	0.32	0.04	0.28
2003-2015	3591.28	1.63	0.39	1.23

Due to the decrease in sediment inflow, the total sedimentation from 2003 to 2015 was about 1.6 billion tons, with a deposition rate of 123 million tons per year. The expected deposition ratio (defined as the ratios of the sedimentation to the sediment inflow) was 60 % in Pre-TGD period. The actual deposition ratio was 75.8 %, which was bigger than the expected value, although the total sedimentation reduced. The SBM is used for each size group at monthly scale from 2003 to 2015, as shown in Figure 2.

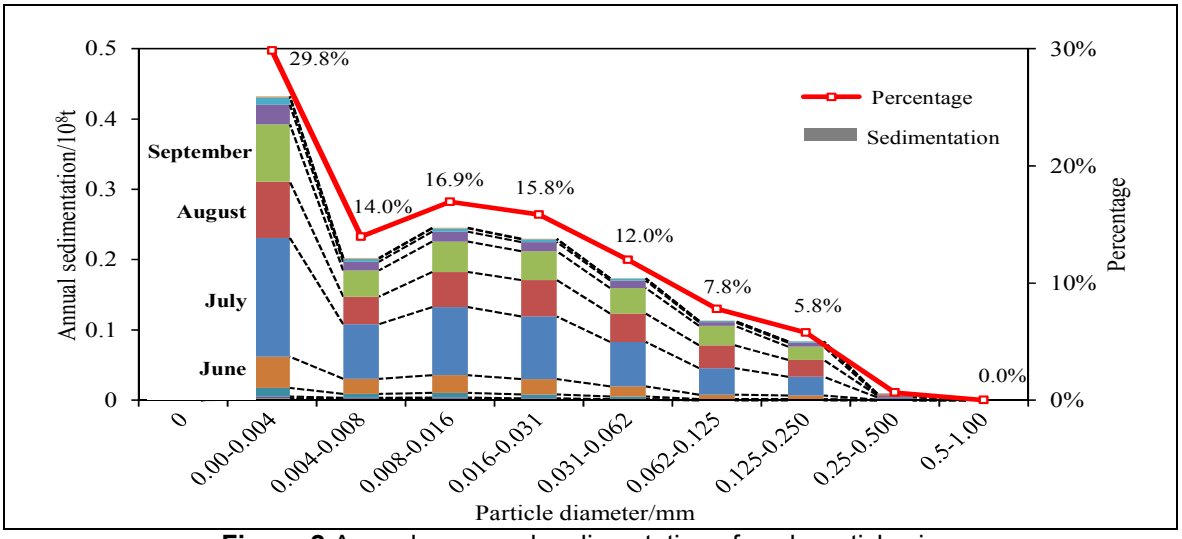

Figure 2. Annual-averaged sedimentation of each particle size.

It is expected that the sediment finer than 0.01 mm were wash load and would not deposit in TGR. Figure 2 illustrates that massive sediment finer than 0.008 mm were trapped in TGR with a ratio of 44 % of the total sedimentation, and that finer than 0.016 mm had a ratio of more than 60 %. Additionally, these fine sediment deposition mainly occurred during the flood season from June to September.

In overall, due to the decrease in sediment inflow, the total sedimentation reduced significantly to about half of the predicted value, while the actual deposition ratio was larger than that expected previously. Additionally, with the decrease of sediment particle size, sediment finer than 0.008 mm deposited with a proportion of 44 % in total sedimentation instead of the expected situation that the sediment finer than 0.01 mm would not deposit in TGR.

3.2 Spatial pattern of the sedimentation

The topographical method is conducted for the typical cross sections, as shown in Figure 3.

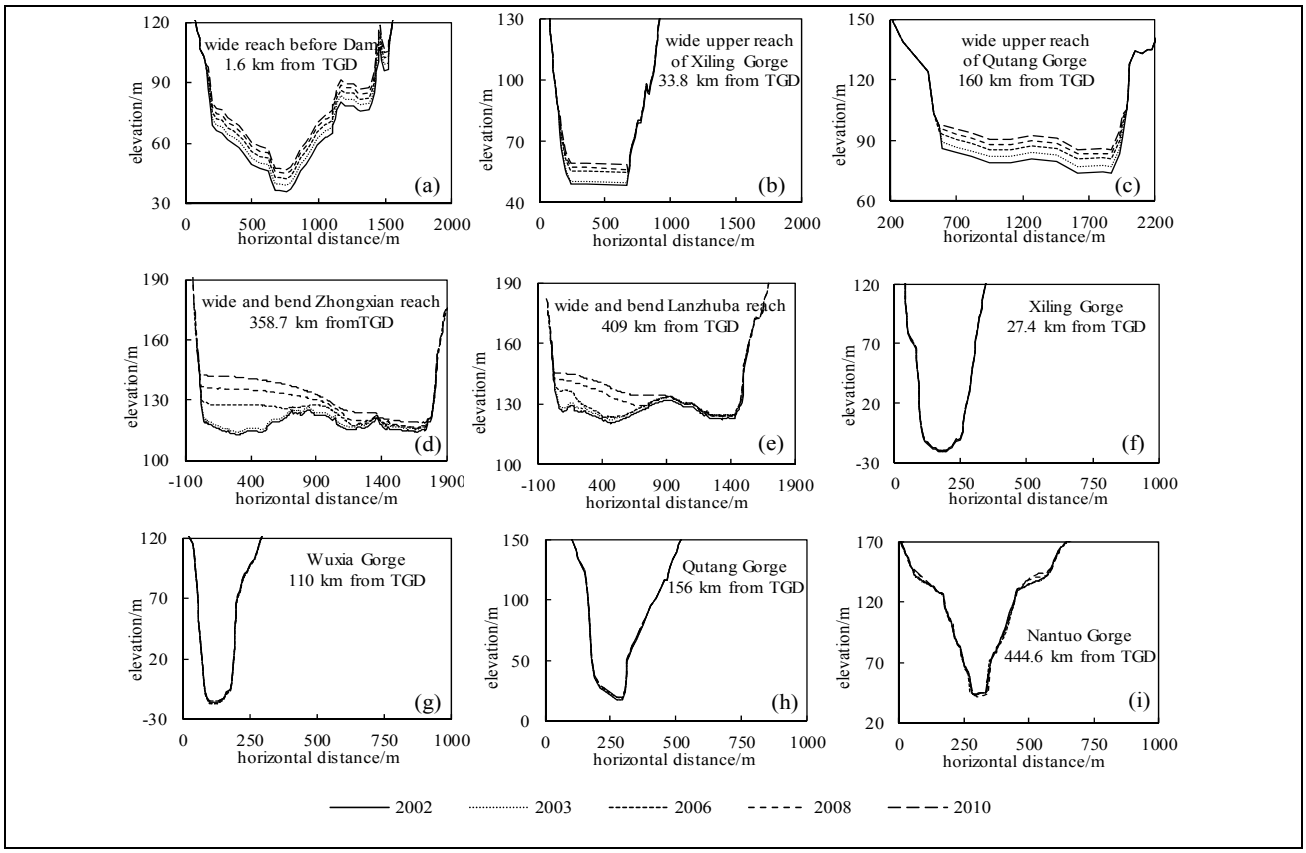

Figure 3. Topographical changes of the typical sections.

It is indicated that severe deposition occurred in the wide reaches, which width is generally larger than 1000 m when the water level before TGD is 145 m (see Figure 3(a), (b), (c), (d), (e)). No cumulative deposition existed in the gorges, which generally have widths less than 500 m when the water level before TGD is 145 m (see Figure 3(f), (g), (h), (i)). The topographical change of each section reflects the deposition area of the section, which can also represent the deposition volume per unit length, defined as the deposition strength. Thus, based on the topographical changes of 340 sections from 2003 to 2011, the distribution of the deposition strength in TGR is calculated as shown in Figure 4. The sedimentation primarily occurred at certain reaches in the permanent backwater region rather than in the fluctuating backwater region, such as the reach before the TGD, the upper reaches of the Xiling, Wuxia and Qutang Gorges, the Yunyang reach, the Wanzhou reach, the Zhongxian reach, the Lanzhuba reach, and the Tunaozi reach. The TGR is approximately 668 km long, and the total length of the depositing reaches is approximately 227 km, indicating that more than 80 % of the deposition occurred in one-third of the entire backwater region.

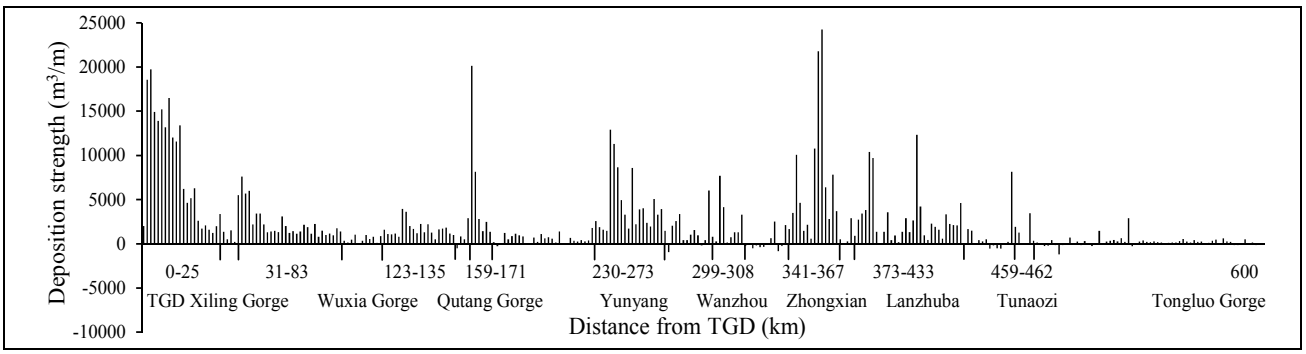

Figure 4. Distribution of the deposition strength in TGR.

In overall, the spatial pattern of the sedimentation in TGR is more complicated than expected. The sedimentation was expected to be continuous between the entrance and outlet of TGR. However, following the decrease of sediment inflow, sedimentation mainly occurred in wide reaches and no deposition was found in gorges, presenting the form of 'segment siltation' rather than the expected 'continuous siltation'.

4 MECHANISM UNDERLYING THE INFLUENCES

4.1 Analysis of fine sediment deposition

Base on the field measurements (Li et al., 2013), the vertical particle size distribution measured using laser particle size analyzer and particle settling velocities deduced using ADV-measured flow velocities and back scattered acoustic intensities are illustrated in Figure 5.

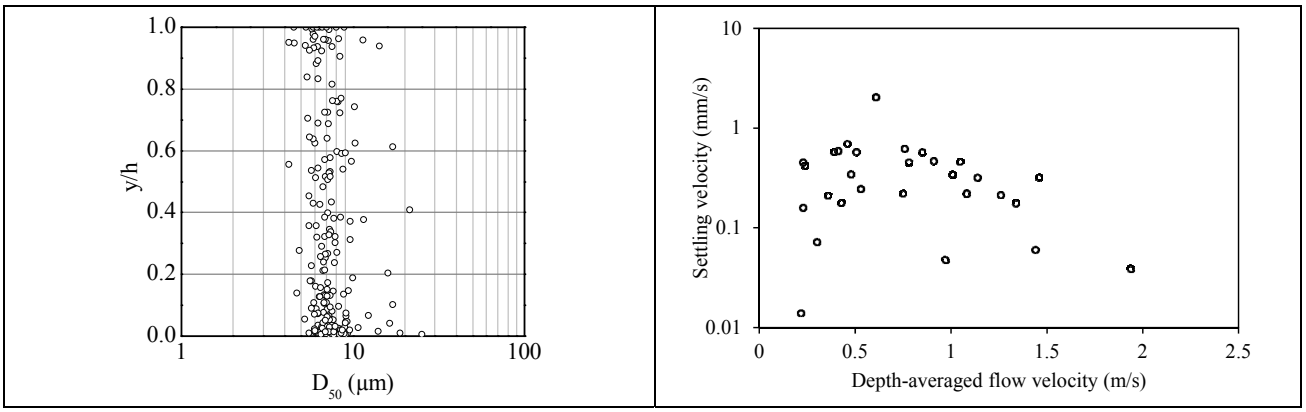

Figure 5.(a) Vertical distributions of median particle diameter. (b) Settling velocities.

It can be seen that the particle diameters keep almost the same along the water depth, and the diameters of bed materials are similar with those of the suspended particles, indicating that all the particles of different size may settle together instead of the settlement of only larger particles. The median particle diameters are in the range of 4 ~ 10 μm and the corresponding settling velocities are 0.01 ~ 0.09 mm/s following the Stokes equation, while the measured settling velocities are mostly between 0.01 – 2 mm/s and bigger than those of their primary particles. These results inspire us to believe that the flocculation is likely to occur in TGR. It is known that turbulent motion can cause fine particles to collide and form flocs, turbulent shear can also cause flocs to break up (Chien and Wan, 1999; Winterwerp, 2002). Figure 5b illustrates that the settling velocity

increases with the increasing flow velocity, and then decreases when the flow velocity exceeds about 0.7 m/s, indicating the above mentioned turbulent effects. Therefore, it is concluded that the turbulent motion results in the flocculation, which is responsible to the fine sediment deposition in TGR.

4.2 Analysis of sedimentation spatial pattern

Based on equation (1), the sediment carrying capacities of the typical sections are calculated and compared to the sediment concentrations as shown in Figure 6.

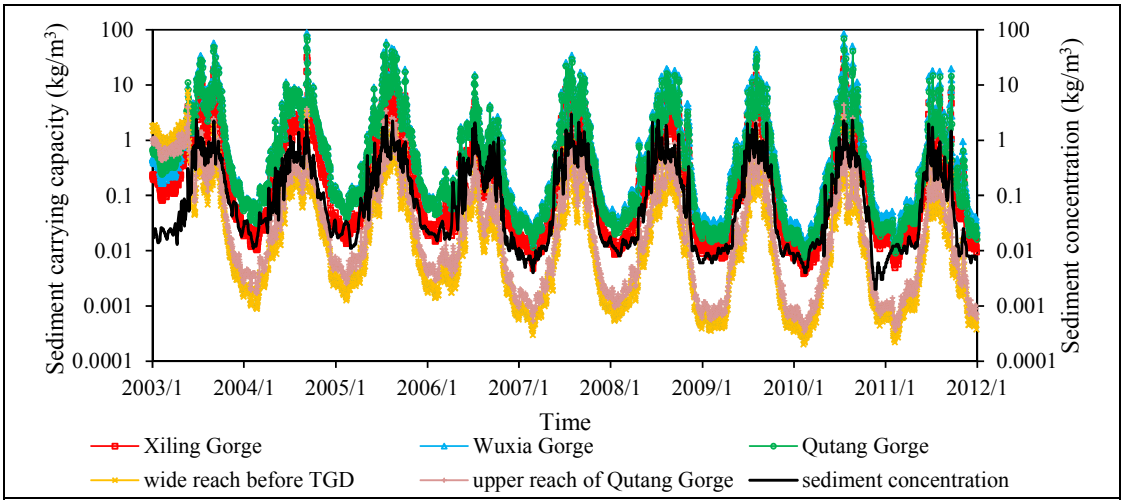

Figure 6. Sediment carrying capacities of the typical sections compared with the sediment concentrations.

Although the sediment carrying capacities decreased following the operation of TGD, the sediment concentrations decreased at the same time. At the wide reaches, the sediment carrying capacities experienced larger reductions compared with sediment concentrations and were always lower than sediment concentrations, resulting in sedimentation. However, the gorge reaches are usually narrow, thereby the increase of flow section areas were significantly less than those at wide reaches at the same water level, hence less reduction of flow velocities. Consequently, the sediment carrying capacities at gorges experienced less reduction as compared to sediment concentrations and remained larger than the sediment concentrations. It should be noted that the slow flow velocities at wide reaches can lead to flocculation, resulting in the increase of settling velocity and thereby the strong decrease of sediment carrying capacity. While the flocculation is likely to be disrupted due to the energetic flows at gorges, hence slight decrease of sediment carrying capacity is expected.

To clarify clearly the relationship between sediment carrying capacities and sediment concentrations, their differences are plotted against flow discharges at two sections in Figure 7.

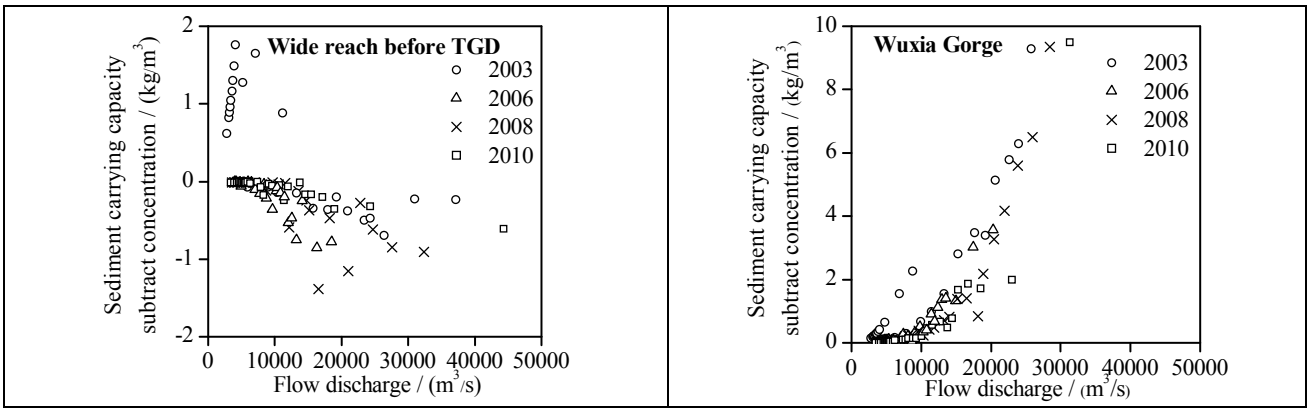

Figure 7. Differences between sediment carrying capacities and concentrations against flow discharges.

It can be seen that the sediment carrying capacities are bigger than the sediment concentrations with the increasing flow discharge at the wide reach, while the opposite at the gorge. It is indicated that sedimentation at wide reaches occurred mainly during flood seasons, although sedimentation may occur at gorges during non-flood seasons, they were likely to be eroded during flood seasons. Consequently, no accumulative sedimentation occurred at gorges.

In overall, the sediment carrying capacities and the sediment concentrations decreased at the same time. The sediment carrying capacities at wide reaches decreased significantly to below the sediment concentrations,

while that at gorges decreased slightly and remained bigger than the sediment concentrations. As a result, sedimentation occurred in wide reaches, and no cumulative deposition existed at gorges, presenting the form of 'segment siltation' rather than the expected 'continuous siltation'.

5 DISCUSSION ON THE FUTURE TREND OF THE SEDIMENTATION IN TGR

According to the analysis above, the sedimentation amount decreased significantly and the 'segment siltation' spatial pattern occurred due to the decrease of sediment inflow. However, it is still not clarified whether the previously expected sedimentation equilibrium is delayed and the unified equilibrium bed slope will be formed after a longer time period, or a new equilibrium will be generated.

Based on the annual profiles of 340 cross sections, the longitudinal profile change is plotted in Figure 8.

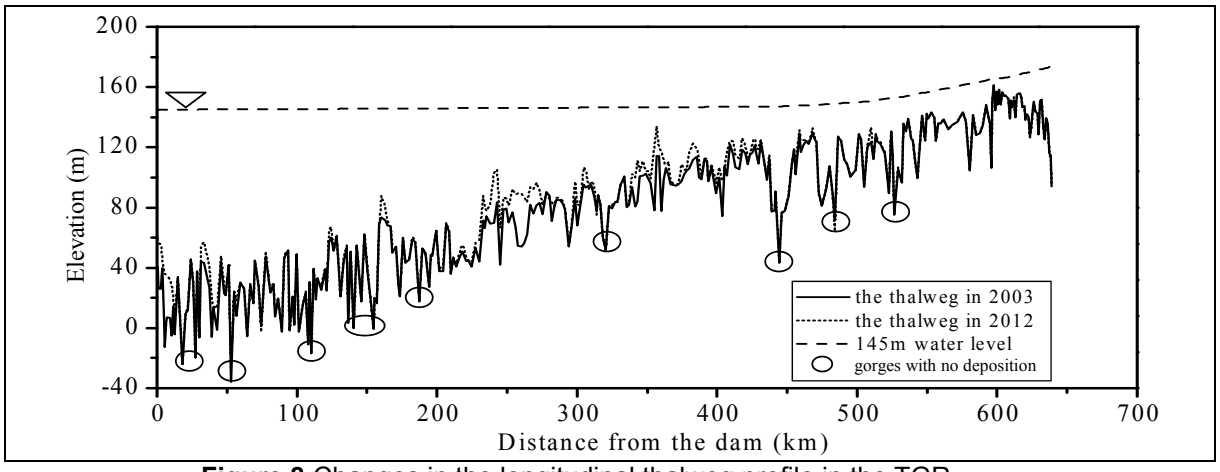

Figure 8. Changes in the longitudinal thalweg profile in the TGR.

It can be seen that the maximum thalweg changes at the Yunyang and Zhongxian reaches are about 40 m, while no thalweg changes are found at the nearby and other typical gorges, illustrating no trend of unified equilibrium bed slope.

During the initial operation stage of TGR, the effective areas of the flow sections were the largest and the corresponding sediment carrying capacities were the lowest. The lowest sediment carrying capacities were still bigger than the sediment concentrations and no deposition occurred at gorges. If deposition occurs at these gorges later, the effective areas of the flow sections will decrease and the sediment carrying capacity will increase. This will contradict the fact that no deposition occurred at the lowest sediment carrying capacities during the initial operation stage. Considering that the decrease of sediment inflow will be maintained for a long Post-TGD period (Yang et al., 2014), the surplus sediment carrying capacity will exist at the gorges where no deposition occurred now, and no deposition is expected in the future. In TGR, wide reaches are interlaced with gorges, these gorges will display as local base levels of erosion, and a new sedimentation equilibrium state with no deposition delta and unified equilibrium bed slope is expected.

Consequently, the deposition amount under the final equilibrium state in TGR will be much less than previously predicted. Smaller deposition amount will weaken the reduction in the storage capacity and benefits the flood control of downstream significantly. In addition, the increase in the tail water level will be limited due to the less sediment deposition, which would significantly facilitate flood control and navigation in the fluctuating backwater region.

In overall, due to the decrease of sediment inflow, it is deduced that the sedimentation equilibrium is changed rather than delayed, and the unified equilibrium bed slope will not be formed in the future. Under the new equilibrium state, the deposition amount will be much lesser than that of predicted during the demonstration phase, facilitating the TGR's functions significantly.

6 CONCLUSIONS

The sediment issue in TGR has been of interest to many scientists since its demonstration phase. The amount and particle size of sediment inflow are undergoing significant decrease after the impoundment of TGR, and the influences on sedimentation are investigated using the sediment budget and topographical methods based on the field data sets. The main contributions are as follows:

i. The total sedimentation from 2003 to 2014 reduced to about half of the predicted value, while the deposition ratio increased from 60 % (expected) to 75.6 % (measured). Additionally, lots of sediments are finer than 0.01 mm deposited instead of expected sluicing.
ii. The sedimentation mainly occurred at wide reaches and no deposition at gorges, presenting the form of 'segment siltation' rather than the expected 'continuous siltation'.

iii. It was found that the flocculation was likely to occur because of the turbulent motion, and should be responsible for the sedimentation of fine particles in TGR.
iv. The sediment carrying capacities and concentrations in TGR reduced at the same time. At wide reaches, the sediment carrying capacities decreased significantly to below the sediment concentrations, while the sediment carrying capacities decreased slightly and remained bigger than sediment concentrations at gorges. As a result, sedimentation occurred in wide reaches, and no cumulative deposition existed at gorges.
v. Considering that the decrease of sediment inflow will be maintained, the sedimentation equilibrium with no unified bed slope is expected rather than that the predicted sedimentation equilibrium will be delayed.

A new overview of the sedimentation in TGR due to the decrease of sediment inflow is addressed in current study, but the sedimentation trend in the future requires more field data and theoretical analysis, and should be further verified.

ACKNOWLEDGEMENTS

This work is financially supported by the National Natural Science Foundation of China (51679019), National Key Research and Development Program of China (2016YFC0402103), and the Basic Research Project of China Ministry of Transport (2014329814310).

REFERENCES

Changjiang Water Resources Commission (CRWC). (2014). *Bulletin of Changjiang Sediment*. Available At: Http://Www.Cjh.Com.Cn (In Chinese).

Chen, X.Q., Yan, Y.X., Fu, R.S., Dou, X.P. & Zhang, E.F. (2008). Sediment Transport from the Yangtze River, China, Into the Sea over the Post-Three Gorge Dam Period: *A Discussion. Quaternary International,* 186(1), 55-64.

Chien, N. & Wan, Z.H. (1999). *Mechanics of Sediment Transport*. ASCE, Reston, Va.

Dai, S.B., Yang, S.L. & Li P. (2006). Regulation of the Main River Channel to the Sediment Discharge of Yangtze Catchment. *Acta Geographica Sinica*, 61(5), 461-470 (In Chinese).

Fuggle, R. & Smith, W. (2000). *Large Dams in Water and Energy Resource Development in the People's Republic of China (PRC).* Country Review Paper Prepared as an Input to the World Commission on Dams, Cape Town, South Africa.

Gao, P., Wang, Z.Y. & Siegel, D. (2015). Spatial and Temporal Changes of Sedimentation in Three Gorges Reservoir of China. *Lakes and Reservoirs: Research and Management*, 20, 1-10.

Hu, B.Q., Yang, Z.S., Wang, H.J., Sun, X.X., Bi, N.S. & Li, G.G. (2009). Sedimentation in the Three Gorges Dam and the Future Trend of Changjiang (Yangtze River) Sediment Flux to the Sea. *Hydrology and Earth System Sciences*, 13(11), 2253-2264.

Jordi, L. P. & Marta, P. (2006). The Three Gorges Dam Project in China: History and Consequences. *Revista Hmic Història Moderna I Contemporània,* 4, 151-188.

Li, Q.F., Yu, M.X., Lu, G.B., Cai, T., Bai, X. & Xia, Z.Q. (2011). Impacts of the Gezhouba and Three Gorges Reservoirs on the Sediment Regime in The Yangtze River, China. *Journal of Hydrology*, 403(3), 224-233.

Li, W.J., Wang, J.J. & Zhang, S.S. (2013). Field Measurements of Sediment Transport in the Permanent Backwater Region of the Three Gorges Reservoir. *The 3rd Biennial Symposium of the International Society for River Science*, Beijing, 584-591.

Li, W.J. (2013). Suspended Particle Settling Velocities in the Three Gorges Reservoir. *The 35th IAHR World Congress,* Chengdu, 1-8.

Lin, B.N. & Zhang, R. (1989). On Some Key Sedimentation Problems of Three Gorges Project (TGP). *International Journal of Sediment Research*, 4(1).

Lu, J.Y., Huang, Y. & Wang, J. (2011). The Analysis on Reservoir Sediment Deposition and Downstream River Channel Scouring After Impoundment and Operation of TGP. *Engineering Sciences (China),* 9, 113-120.

Milliman, J.D. & Syvitski, J.P.M. (1992). Geomorphic/Tectonic Control of Sediment Discharge to the Ocean: The Importance of Small Mountainous Rivers. *Journal of Geology*, 100(5), 525-544.

Science and Technology Department of Ministry of Water Conservancy and Electric Power. (1988). *Reports Collection on The Sediment Issues of the Three Gorges Reservoir*, Beijing, China (In Chinese).

Sediment Experts Group of the Three Gorges Project Construction Committee Executive Office. (2002). *Sediment Research of the Three Gorges Project from 1996 to 2000*, Intellectual Property Press, Beijing, China (In Chinese).

World Commission on Dams (WCD). (2000). *Dams and Development: A New Framework for Decision-Making*. London and Sterling (VA, USA), Earthscan Publications.

Winterwerp, J.C. (2002). On The Flocculation And Settling Velocity Of Estuarine Mud. *Continental Shelf Research*, 22(9), 1339-1360.

Xu, K.H. & Milliman, J.D. (2009). Seasonal Variations of Sediment Discharge from the Yangtze River Before and After Impoundment of the Three Gorges Dam. *Geomorphology*, 104(3), 276-283.

Xu, X., Tan, Y. & Yang, G. (2013). Environmental Impact Assessments of the Three Gorges Project in China: Issues and Interventions. *Earth-Science Reviews,* 124(9), 115-125.

Yang, S.F. (2013). *Report On Prototype Observation Of Sedimentation in the Three Gorges Reservoir Navigation Channel*, Chongqing Jiaotong University, China (In Chinese).

Yang, S.L., Milliman, J.D., Xu, K.H., Deng, B., Zhang, X.Y. & Luo, X.X. (2014). Downstream Sedimentary and Geomorphic Impacts of the Three Gorges Dam on the Yangtze River. *Earth-Science Reviews*, 138, 469-486.

Yang, S.L., Zhang, J. & Xu, X.J. (2007). Influence of the Three Gorges Dam on Downstream Delivery of Sediment and Its Environmental Implications, Yangtze River. *Geophysical Research Letters*, 34(10), 1-5.

Yang, S.L., Zhao, Q.Y. & Belkin, I.M. (2002). Temporal Variation in the Sediment Load of the Yangtze River and the Influences of Human Activities. *Journal of Hydrology*, 263(1), 56-71.

Yang, Z., Wang, H., Saito, Y., Milliman, J.D., Xu, K., Qiao, S. & Shi, G. (2006). Dam Impacts on the Changjiang (Yangtze) River Sediment Discharge To the Sea: The Past 55 Years and After the Three Gorges Dam. *Water Resource Research*, 42(4), 1-10.

Zhao, C.H., Zhu, Z.H. & Zhou, D.Z. (2000). *Worldwide Rivers and Dams*. China Water Conservancy and Hydroelectric Press, Beijing (In Chinese).

Zhou, J.J. (2005). Discussion on the Reliability of Sediment Computations Employed in the Feasibility Studies Of Three Gorges Project. *Journal of Hydroelectric Engineering*, 24(1), 33-39 (In Chinese).

